frontiers | Research Topics

Linking subaqueous, subglacial, and subaerial volcanism: How water influences eruption dynamics and creation of volcanic products

Edited by
Tobias Dürig, Kristen Fauria, Alison Hollomon Graettinger,
Martin Jutzeler and John L. Smellie

Published in
Frontiers in Earth Science

ISSN 1664-8714
ISBN 978-2-8325-3669-8
DOI 10.3389/978-2-8325-3669-8

About Frontiers

Frontiers is more than just an open access publisher of scholarly articles: it is a pioneering approach to the world of academia, radically improving the way scholarly research is managed. The grand vision of Frontiers is a world where all people have an equal opportunity to seek, share and generate knowledge. Frontiers provides immediate and permanent online open access to all its publications, but this alone is not enough to realize our grand goals.

Frontiers journal series

The Frontiers journal series is a multi-tier and interdisciplinary set of open-access, online journals, promising a paradigm shift from the current review, selection and dissemination processes in academic publishing. All Frontiers journals are driven by researchers for researchers; therefore, they constitute a service to the scholarly community. At the same time, the *Frontiers journal series* operates on a revolutionary invention, the tiered publishing system, initially addressing specific communities of scholars, and gradually climbing up to broader public understanding, thus serving the interests of the lay society, too.

Dedication to quality

Each Frontiers article is a landmark of the highest quality, thanks to genuinely collaborative interactions between authors and review editors, who include some of the world's best academicians. Research must be certified by peers before entering a stream of knowledge that may eventually reach the public - and shape society; therefore, Frontiers only applies the most rigorous and unbiased reviews. Frontiers revolutionizes research publishing by freely delivering the most outstanding research, evaluated with no bias from both the academic and social point of view. By applying the most advanced information technologies, Frontiers is catapulting scholarly publishing into a new generation.

What are Frontiers Research Topics?

Frontiers Research Topics are very popular trademarks of the *Frontiers journals series*: they are collections of at least ten articles, all centered on a particular subject. With their unique mix of varied contributions from Original Research to Review Articles, Frontiers Research Topics unify the most influential researchers, the latest key findings and historical advances in a hot research area.

Find out more on how to host your own Frontiers Research Topic or contribute to one as an author by contacting the Frontiers editorial office: frontiersin.org/about/contact

Linking subaqueous, subglacial, and subaerial volcanism: How water influences eruption dynamics and creation of volcanic products

Topic editors
Tobias Dürig — University of Iceland, Iceland
Kristen Fauria — Vanderbilt University, United States
Alison Hollomon Graettinger — University of Missouri–Kansas City, United States
Martin Jutzeler — University of Tasmania, Australia
John L. Smellie — University of Leicester, United Kingdom

Citation
Dürig, T., Fauria, K., Graettinger, A. H., Jutzeler, M., Smellie, J. L., eds. (2023). *Linking subaqueous, subglacial, and subaerial volcanism: How water influences eruption dynamics and creation of volcanic products*. Lausanne: Frontiers Media SA.
doi: 10.3389/978-2-8325-3669-8

Table of contents

frontiers | Frontiers in Earth Science

TYPE Editorial
PUBLISHED 25 September 2023
DOI 10.3389/feart.2023.1290315

OPEN ACCESS

EDITED AND REVIEWED BY
Valerio Acocella,
Roma Tre University, Italy

*CORRESPONDENCE
Tobias Dürig,
✉ tobi@hi.is

RECEIVED 07 September 2023
ACCEPTED 18 September 2023
PUBLISHED 25 September 2023

CITATION
Dürig T, Fauria K, Graettinger AH, Jutzeler M and Smellie JL (2023), Editorial: Linking subaqueous, subglacial, and subaerial volcanism: how water influences eruption dynamics and creation of volcanic products. *Front. Earth Sci.* 11:1290315. doi: 10.3389/feart.2023.1290315

Editorial: Linking subaqueous, subglacial, and subaerial volcanism: how water influences eruption dynamics and creation of volcanic products

Tobias Dürig[1]*, Kristen Fauria[2], Alison H. Graettinger[3], Martin Jutzeler[4] and John L. Smellie[5]

[1]Institute of Earth Sciences, University of Iceland, Reykjavik, Iceland, [2]Department of Earth and Environmental Sciences, Vanderbilt Universiy, Nashville, TN, United States, [3]School of Science and Engineering, University of Missouri–Kansas City, Kansas City, MO, United States, [4]School of Natural Sciences, University of Tasmania, Hobart, TAS, Australia, [5]School of Geography, Geology & The Environment, University of Leicester, Leicester, United Kingdom

KEYWORDS

magma water interaction, phreatomagmatic activity, subglacial volcanism, submarine volcanic activity, subaqueous volcanism

Editorial on the Research Topic
Linking subaqueous, subglacial, and subaerial volcanism: how water influences eruption dynamics and creation of volcanic products

This Research Topic addresses the latest volcanological advances concerning magma-water interactions and their distinctive landforms and eruptive products wherever they occur, in the hydrosphere, cryosphere or atmosphere. The common thread of this article Research Topic, which contains nine contributions is the involvement and impact of magma interacting with water in all its forms, including snow and ice. It seeks to improve our understanding of the different ways in which water affects volcanism, including eruptions with only minor water input but which materially transforms the resulting eruptive processes in distinctive ways.

Water is ubiquitous on Earth and interaction with magma is common, however many processes involving magma-water interaction are only partially understood. Most of Earth's volcanism takes place in submarine settings, particularly at mid-oceanic ridges and oceanic arcs, but the vast majority of eruptions involving water, including those occurring under ice, are unobserved, thereby limiting our understanding of the eruptive processes and mechanisms involved. Being able to reliably detect new eruptive events that occur under the sea surface is an important step forward towards better understanding submarine eruptions. Using machine learning techniques, a novel analysis framework developed by Zheng et al., will help researchers to uncover new submarine eruptions by semi-automatically identifying active pumice rafts recorded in high-definition global satellite imagery. This technique is particularly relevant for eruptions occurring at remote seamounts that may not be detected by any other type of warning system. An example for how modern technological advancements enhance our capabilities to monitor eruptive processes in deep-sea settings with increasing detail is provided by Saurel et al. Their study describes how hydro-acoustic signals can be utilized to reconstruct the short-term spatial evolution of submarine lava flows and constrain the effusion rates.

Analysis of deposits from subaqueous eruptions is another crucial instrument to shed light on relevant eruptive processes. Using geochemical analysis of submarine samples, Tamura et al. not only confirmed that a shift from effusive to more explosive volcanism at Nishinoshima Volcano (Japan) was coincident with a change in magma composition, but used trace elements and isotopic analysis to fingerprint the source conditions of the magmas (see Figure 1).

The eruptive style is considerably influenced by external water, resulting in powerful explosions that fuel phreatomagmatic eruptions and generate fine ash that can be difficult to forecast and, at another extreme, may be implicated in devastating poorly understood violent-Strombolian events. Volcanologists distinguish between two thermohydraulic explosion mechanisms (Dürig et al., 2020a): molten fuel-coolant interaction (MFCI) and induced fuel coolant interaction (IFCI). In IFCI, water acts as a "thermohydraulic wedge," which boosts the efficiency of a primary magma fragmentation process. IFCI was identified as a key driver for an explosive phase that produced fine tephra during the 2012 eruption of Havre volcano (Dürig et al., 2020b), a submarine caldera which is situated in the Kermadec arc. MFCI, on the other hand, requires a pre-mixing phase, during which the magma is separated from the liquid phase of water by a thin vapor film (Büttner and Zimanowski, 1998). The experimental findings of Sonder and Moitra help us to better understand the complex physical mechanisms that sustain such a vapor film, and explain why the stability of the vapor film decreases under increasing ambient pressures, reducing the likelihood of MFCI to occur.

Finding out what controls the efficiency of MFCI explosions is also the research focus of the study by Schmith and Swanson, who combined field observations with granulometric and morphometric analysis of ash samples to examine how magma structure and magma-water mixing conditions controlled phreatomagmatic explosions at Kīlauea Volcano, Hawaii.

The dynamics of subglacial eruptions are fundamentally controlled by the presence (or absence) of water, be it in the form of snow, ice, or meltwater, whilst the resulting landforms can be different due particularly to the physical constraints of eruptions confined by ice. This is unusually well demonstrated by multiple monogenetic volcanic edifices that are part of the Mount Melbourne Volcanic Field in Antarctica, within the West Antarctic Rift System, described by Smellie et al. They erect a hierarchy of landforms that reflects the different eruptive conditions (water, ice) experienced by erupting magmas and which was used to define the varying environments that prevailed in the volcanic field over the last 4 million years. Exceptional sections exposed across a pillow-dominated volcanic ridge at Undirhlíðar, Iceland, also permitted Pollock et al. to demonstrate that alternating effusive and explosive eruptions were involved in its construction. The ridge was also fed incrementally in space and time by multiple magma batches from separate crustal magma bodies, thus shedding light on the unexpectedly varied physical and compositional processes involved in a seemingly simple pile of pillow lavas erupted in a glacial setting.

Understanding how glacial and deglacial effects influence eruption dynamics is also fundamental to better anticipating and thus mitigating

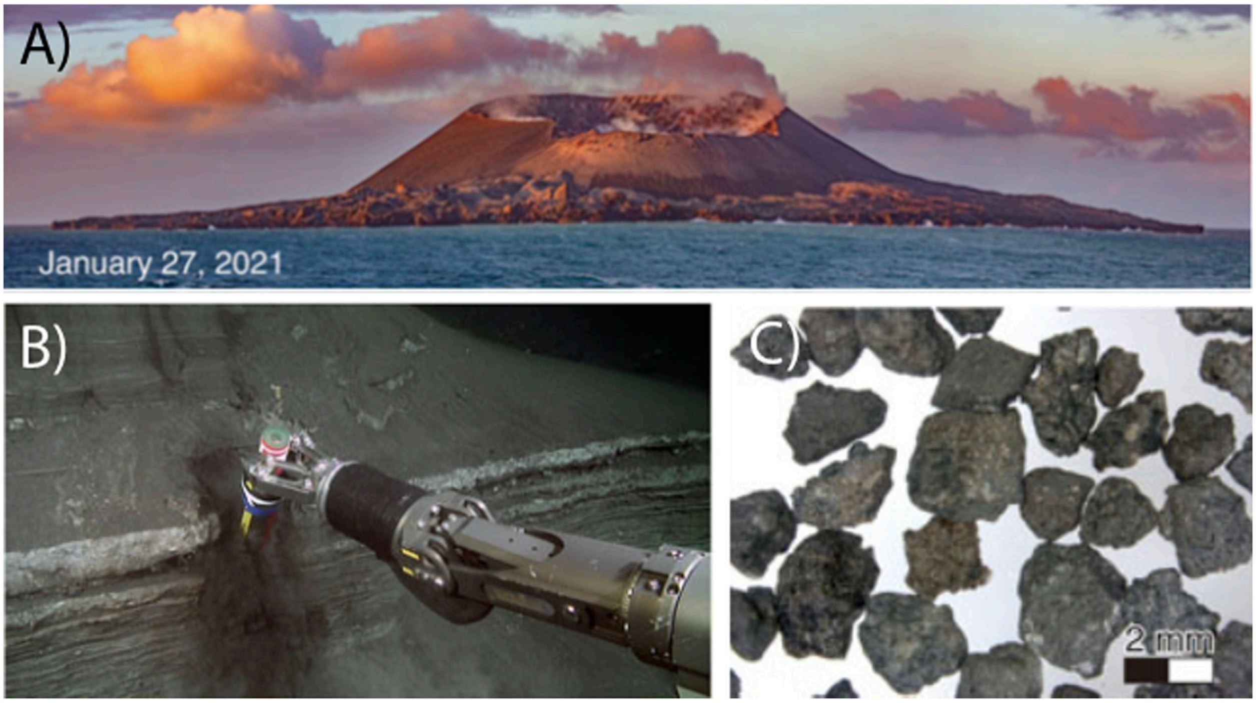

FIGURE 1
Scales of volcanism in marine environments modified from Tamura et al. **(A)** Slightly emergent edifice of Nishinoshima Volcano, Japan. The height of the central cone is ~250 m. **(B)** Sampling of Nishinoshima submarine tephra deposits by a remotely operated vehicle. **(C)** Scoria particles recovered from the tephras in **(B)**.

future hazards. Conway et al. review the time-volume-composition trends for 33 Pleistocene-Holocene volcanoes worldwide and examine the impact of changes in glaciation on erupted volumes and compositions of the edifice-forming products. Despite the apparent link between rapid deglaciation, release of crustal stress and enhanced eruption rates, the study showed that such a link is still difficult to demonstrate unambiguously due to ongoing limitations in the published datasets, particularly a lack of reliable chronologies.

Experiments with simple materials can often illustrate complex geological processes better than complicated scientific texts, and attract young budding scientists into scientific careers. Conway et al. present a series of innovative, fun and informative experiments using everyday kitchen materials to illustrate what happens when effusive eruptions occur on ice-clad volcanoes. They show how the presence or absence of ice affects the physical distribution of the lavas and thus influences the construction of volcanoes in many important ways.

The studies of this Research Topic highlight the continued value of multipronged research avenues including direct observations of eruptions, deposit characterizations, petrologic investigations and analogue experiments to better understand the physics, hazards, and records of magma water interactions around the globe. We cannot understand these complex systems without attacking them from all angles as demonstrated in this research volume.

Author contributions

TD: Conceptualization, Writing–original draft, Writing–review and editing. KF: Writing–review and editing. AG: Writing–review and editing. MJ: Writing–review and editing. JS: Writing–review and editing.

Conflict of interest

The authors declare that the research was conducted in the absence of any commercial or financial relationships that could be construed as a potential conflict of interest.

Publisher's note

References

Büttner, R., and Zimanowski, B. (1998). Physics of thermohydraulic explosions. *Phys. Rev. E* 57, 5726–5729. doi:10.1103/PhysRevE.57.5726

Dürig, T., White, J. D. L., Murch, A. P., Zimanowski, B., Büttner, R., Mele, D., et al. (2020a). Deep-sea eruptions boosted by induced fuel–coolant explosions. *Nat. Geosci.* 13, 498–503. doi:10.1038/s41561-020-0603-4

Dürig, T., White, J. D. L., Zimanowski, B., Büttner, R., Murch, A., and Carey, R. J. (2020b). Deep-sea fragmentation style of Havre revealed by dendrogrammatic analyses of particle morphometry. *Bull. Volcanol.* 82, 67. doi:10.1007/s00445-020-01408-1

frontiers | Frontiers in Earth Science

BRIEF RESEARCH REPORT
published: 28 April 2022
doi: 10.3389/feart.2022.838532

Pumice Raft Detection Using Machine-Learning on Multispectral Satellite Imagery

Maggie Zheng[1], Tushar Mittal[1]*, Kristen E. Fauria[2], Ajit Subramaniam[3] and Martin Jutzeler[4]*

[1]Department of Earth, Atmospheric and Planetary Sciences, Massachusetts Institute of Technology, Cambridge, MA, United States, [2]Department of Earth and Environmental Sciences, Vanderbilt University, Nashville, TN, United States, [3]Lamont-Doherty Earth Observatory, Columbia University, Palisades, NY, United States, [4]Centre for Ore Deposit and Earth Sciences (CODES), University of Tasmania, Hobart, TAS, Australia

Most of Earth's volcanic eruptions occur underwater, and these submarine eruptions can significantly impact large-scale Earth systems (e.g., enhancing local primary production by phytoplankton). However, detecting submarine eruptions is challenging due to their remote locations, short eruption durations, lack of sea surface signature (if eruptions do not breach the surface), and the transient nature of the surface manifestations of an eruption (e.g., floating pumice clasts, hydrothermal fluids). We can utilize global satellite imagery of 10–30 m resolution (e.g., Landsat 8, Sentinel-2) to detect new eruptions; however, the large data volumes make it challenging to systematically analyze satellite imagery globally. In this study, we address these challenges by developing a new semi-automated analysis framework to detect submarine eruptions through supervised classification of satellite images on Google Earth Engine. We train our algorithm using images from rafts produced by the August 2019 eruption of Volcano F in the Tofua Arc and present a case study using our methodology on satellite imagery from the Rabaul caldera region in Papua New Guinea. We potentially find a large number of new unreported pumice rafts (in ~16% of images from 2017–present). After analysis of the spatial pattern of raft sightings and ancillary geophysical and visual observations, we interpret that these rafts are not the result of a new eruption. Instead, we posit that the observed rafts represent remobilization of pumice clasts from previous historical eruptions. This novel process of raft remobilization may be common at near-shore/partially submarine caldera systems (e.g., Rabaul, Krakatau) and may have significant implications for new submarine eruption detection and volcanic stratigraphy.

Keywords: submarine volcano monitoring, pumice raft dispersal, machine learning (ML), sentinel-2, Google Earth engine (GEE)

Edited by:
Max Rudolph,
University of California, Davis,
United States

Reviewed by:
Simon Carn,
Michigan Technological University,
United States
Scott Edward Bryan,
Queensland University of Technology,
Australia

****Correspondence:***
Maggie Zheng
mzhengxi@mit.edu
Tushar Mittal
tmittal2@mit.edu

Specialty section:
This article was submitted to Volcanology, a section of the journal Frontiers in Earth Science

Received: *17 December 2021*
Accepted: *04 April 2022*
Published: *28 April 2022*

Citation:
Zheng M, Mittal T, Fauria KE, Subramaniam A and Jutzeler M (2022) Pumice Raft Detection Using Machine-Learning on Multispectral Satellite Imagery. Front. Earth Sci. 10:838532. doi: 10.3389/feart.2022.838532

1 INTRODUCTION

Submarine volcanism is an important driver for Earth's climate and geochemical cycles on global scales (mid-ocean ridge volcanic system and submarine large igneous provinces) as well as on regional scales (Embley et al., 2004; Santana-Casiano et al., 2013; Tilstone et al., 2014; Kelley, 2017; Mittal and Delbridge, 2019). For instance, submarine eruptions inject ash, pumice, and magmatic volatiles (with nutrients such as Fe) into the water column and the atmosphere (White et al., 2015). Pumice rafts, one of the key signatures of some submarine eruptions, can transport volcanic products

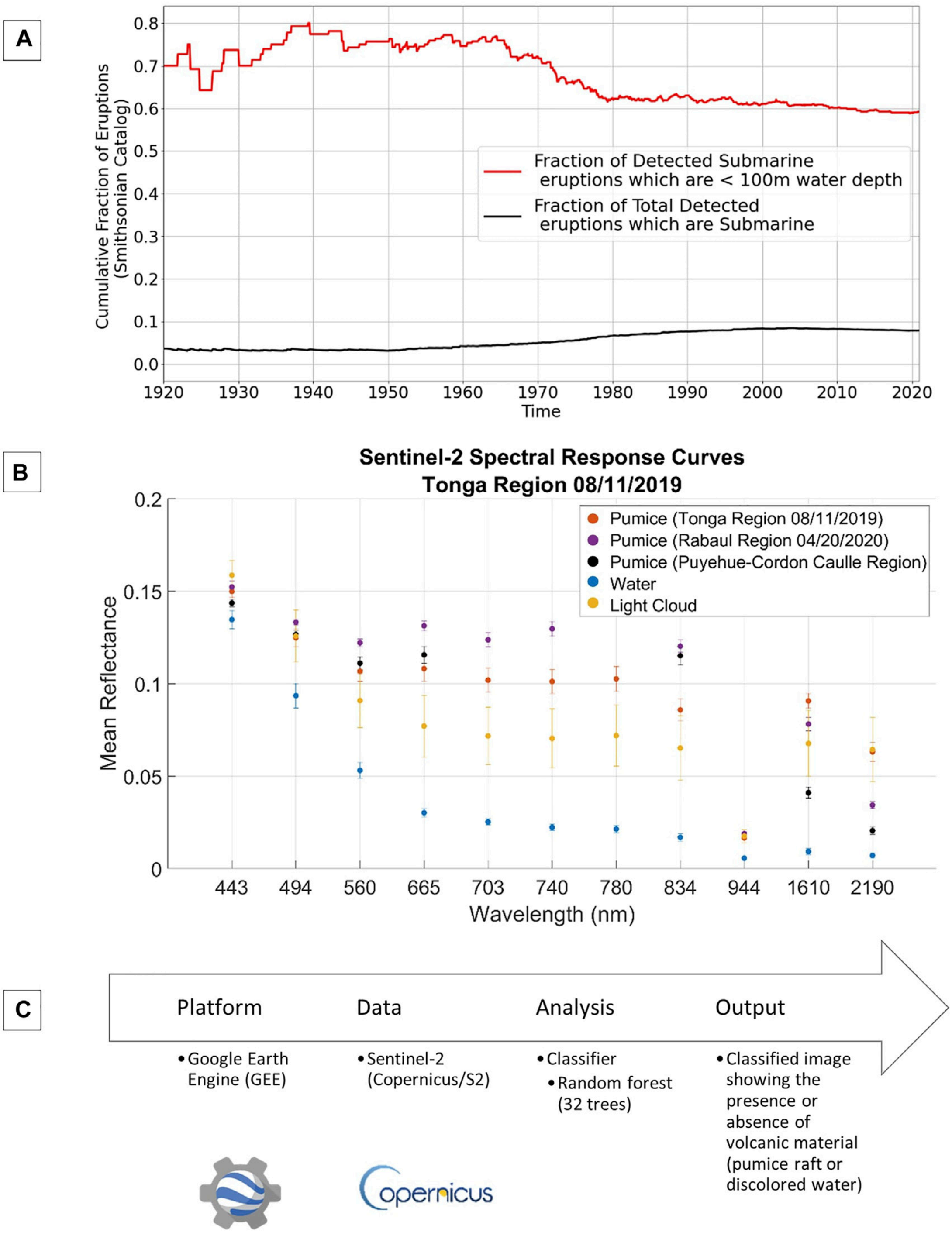

FIGURE 1 | (A) Fraction of all detected submarine eruptions out of total eruptions and fraction of detected shallow submarine eruptions (less than 100 m water depth) out of all detected submarine eruptions (Global Volcanism Program, 2013). Only a small fraction of submarine eruptions are pumice-forming. **(B)** Mean spectral response curves generated for a Sentinel-2 raft image in the Tonga region (11 August 2019). Error bars are generated from the standard deviation measured for each wavelength. Spectral response curves for pumice from the Rabaul region (20 April 2020) and a lake near Puyehue-Cordón Caulle are also provided for comparison. For Puyehue-Cordón Caulle, Sentinel-2 imagery was not available, so Landsat 8 imagery was used instead, and mean reflectance values were averaged between two dates (19 June 2013 and 5 October 2013). **(C)** Schematic of workflow used in this study.

and marine organisms across thousands of kilometers, potentially dispersing nutrients and increasing microbial biomass and biodiversity in areas geographically distant from the site of the eruption (DeVantier, 1992; Risso et al., 2002; Bryan et al., 2012). Pumice rafts can also be a significant hazard for human maritime activities, especially by clogging harbors and affecting near shore sea life and fisheries, disrupting local economies (Bryan et al., 2012; Jutzeler et al., 2020), as observed in the recent raft dispersal from the 2021 eruption of Fukutoku-Okanoba volcano, a submarine volcano in the Bonin Arc (24.285° N, 141.481° E) (Fauria et al., 2022; Yoshida et al., 2022).

Modern day submarine volcanism includes both mid-ocean ridge and ocean-island volcanism as well as fully/partially submarine subduction zone volcanism (e.g., Kermadec-Tonga Arc, Izu-Bonin Arc, Papua New Guinea Arc) (White et al., 2006; Global Volcanism Program, 2013). Overall, submarine volcanism potentially represents the majority ($>70\%$) of Earth's present-day volcanism (White et al., 2006; White et al., 2015; ERUPT, 2017; Rubin et al., 2012). However, we have historically detected only a very small fraction of expected underwater eruptions. In fact, only ~10% of all eruptions in the Smithsonian Global Volcanism database (Global Volcanism Program, 2013) over the past 100 years are submarine (**Figure 1A**, (White et al., 2006)) and the majority of detected eruptions are shallow ($<$ 100 m water depth; **Figure 1A**).

One of the key reasons for this strong bias in our submarine eruption detection ability is the remote location of submarine volcanoes, as well as the difficulty in detecting eruptions that may or may not breach the sea surface. In addition, unlike subaerial volcanoes, precursory gas emissions or thermal anomalies are much more difficult to detect beneath the water surface. Although multiple new approaches have been proposed to improve submarine volcanism detection, including hydro-acoustics [e.g., (Heaney et al., 2013; Tepp et al., 2019)], seismic and ground deformation with ocean bottom seismometers (Wilcock et al., 2016; Matsumoto et al., 2019; Cesca et al., 2020; Tepp and Dziak, 2021), and ocean thermal anomalies (Baker et al., 1989; Mittal and Delbridge, 2019), challenges remain due to limited global instrumental coverage. In this study, we describe another dataset—satellite imagery—that can be used to efficiently detect and characterize products of submarine volcanism.

Automated satellite image analysis has already proven to be very useful for global subaerial eruption detections based on thermal anomalies, ash-rich subaerial plumes, and sulfur dioxide emissions (Wright et al., 2004; Brenot et al., 2014; Furtney et al., 2018; Poland et al., 2020; Engwell et al., 2021). However these methods are not adapted for submarine eruptions where the presence of water obscures/reduces these signatures. Satellite imagery has been used to map the eruptive products (e.g., pumice, ash, hydrothermal fluids) from submarine eruptions (Bryan et al., 2004; Jutzeler et al., 2014; O'Malley et al., 2014; Jutzeler et al., 2020; Sakuno, 2021; Whiteside et al., 2021) on an event-by-event basis. For example, a pumice raft from the 7 August 2019 Tonga eruption of an unnamed submarine volcano (sometimes referred to as Volcano F, 18.325°S, 174.365°W) in the Tofua Arc was tracked in near-real-time by Sentinel-2 (~10 m/pixel) and Landsat 8 (~30 m/pixel) satellite imagery (Jutzeler et al., 2020). However, this was done by manual hand-tracing and visual tracking through various satellite images. Although this process is fairly accurate for large rafts, it introduces subjectivity in tracing, especially for smaller rafts. Consequently, it is difficult to quantify uncertainties and biases across different studies. An ancillary challenge with using satellite imagery is the large data volume associated with satellite collections. For example, a single day in the Tonga region is composed of about forty individual 100 × 100 km image granules, each containing about 600 MB of data. Thus, analyzing entire global collections over extended time periods, and for multiple different satellites, would require handling enormous amounts of data and requisite computing resources.

Our study aims to address these challenges of submarine eruption detection by developing a semi-automated Machine-Learning (ML) based methodology using global, publicly available, high resolution (~ <30 m/pixel) satellite data products (**Figure 1C**). This method utilizes Google Earth Engine (Gorelick et al., 2017), in order to remove the large data storage need that is typical for analyzing satellite collections. Our primary focus is on detecting rafts formed from floating pumice (or pumiceous material, **Supplementary Text S16**) emitted by intermediate to silicic volcanism, but our approach can be applied to other signatures of submarine eruptions (e.g., discolored water from hydrothermal fluids). Our analysis is complementary to recent work on detection of large submarine eruptions using specific global, low resolution ($>$ 250 m/pixel) satellite products (O'Malley et al., 2014; Qi et al., 2020; Whiteside et al., 2021).

As a complementary question, we also seek to examine whether individual pumice raft detections necessarily indicate a new eruption. Previous work has examined the remobilization of pumice clasts, which may have been deposited in the area immediately surrounding the vent, or stranded a distance away after traveling as a raft, following large eruptions (Mandeville et al., 1996; Shane et al., 1998; Manville et al., 2002; Jutzeler et al., 2020). Using our automated detection algorithms, we can improve raft detection (of scales of at least a few pixel scale, e.g., a few 100 m^2 for Sentinel-2 imagery and even smaller with commercial sub-m pixel scale imagery). These observational constraints on pumice raft occurrence, along with field studies of the detected rafts and textural analysis, can help understand the re-rafting mobility and floatation ability of pumice of different sizes on timescales ranging from days to hundreds of years after the original eruption (Brasier et al., 2011; Bryan et al., 2012).

In **Section 2**, we describe our detection algorithm and its implementation in Google Earth Engine. In **Section 3**, we illustrate our method's accuracy using satellite imagery from the 2019 Tonga submarine eruption (Jutzeler et al., 2020) and then use our method to analyze pumice rafts in a region close to the Rabaul volcano in Papua New Guinea (partially submerged caldera). In **Section 4**, we discuss what our new pumice raft detections from Rabaul suggest in regards to suspension of pumice material, potentially from pumice clasts or rafts previously washed up on shores or eroded on riverbanks or coastal cliffs. Finally, we briefly discuss areas for future algorithmic improvements.

2 MATERIALS AND METHODS

2.1 Google Earth Engine

We developed and implemented our Machine Learning (ML) detection algorithm for pumice raft detection on the Google Earth Engine (GEE) platform (Gorelick et al., 2017). GEE is a web-based, publicly available platform that enables access to a vast catalog of satellite images and the resources to run global-scale analyses without the need to download or export large amounts of data. There are various satellite collections offered through GEE, such as low resolution (MODIS) and medium-high resolution imagery (Landsat, Sentinel-2). Although some other super-high-resolution image collections are available outside of GEE (e.g., Planet labs—3 m/pixel, Digital Globe—50 cm/pixel), they are typically not publicly available without commercial licenses. Thus, for this study, we have primarily focused on using GEE resources for the ML algorithm.

Specifically, we use GEE collections from the Sentinel-2 Multi-Spectral Instrument (MSI) as our baseline satellite product. Sentinel-2 (a pair of two satellites, each with MSI instrumentation) offers both high-resolution imagery (10–60 m/pixel), good coverage in regions of interest, and a relatively frequent repeat time (~global 5-day revisits; **Supplementary Text S6**). Sentinel-2 data products are also freely available through the European Space Agency's Copernicus Open Access Hub as well as other cloud environments. For our study, we chose to use Sentinel-2 as its high resolution imagery could be used to detect much smaller rafts than a lower resolution satellite (e.g., MODIS). In addition, Sentinel-2's MSI collects data across 13 different spectral bands, with finer spectral coverage than other high resolution satellite image collections (e.g., Landsat 7 and 8) (See spectral response curve for Landsat 8 image of Puyehue-Cordón Caulle pumice in **Figure 1B**). An initial method using thresholds on only the visual bands to detect pumice rafts was insufficient, so the additional spectral bands are necessary in our ML algorithm (**Supplementary Text S1**). As illustrated by the variable importance in the Random Forest classifier (RF, **Supplementary Figure S11**), the multi-wavelength information is critical for accurate classification with a dominant role of the visible bands. In particular, the reflectance of pumice in the near-infrared (NIR) bands (700–900 nm) is much higher than the reflectance at those bands of most biological phenomena that are near the surface but still underwater (i.e., algal blooms, coral spawn, seaweed) (Biermann et al., 2020; Qi et al., 2020), so the NIR bands are critical for distinguishing between pumice and other visually similar-looking biological blooms. Our overall methodology is general and can be applied to other satellite collections in the future (**Supplementary Text S10**).

2.2 Machine-Learning Algorithm

To identify spectral characteristics that can be used to classify Sentinel-2 image pixels as pumice rafts, we generated spectral response curves for pumice and other categories of interest in **Figure 1B**. Spectral response curves record the mean reflectance or brightness of an image pixel for a range of wavelengths. We used the Tonga pumice raft from 11 August 2019 to generate the spectral response curves (**Figure 1B**), as the particular eruption and the associated raft has been extensively analyzed by previous work (Brandl et al., 2020; Jutzeler et al., 2020). We also show the variance around the mean spectral response curve calculated for all of the pixels for each class (pumice, water, light clouds).

A key result from this analysis is that there is a significant difference between the spectral response curves of pumice, water, and light clouds (**Figure 1B**). Additionally, we find relatively minor (compared to differences with other classes) variation in the reflectance from pumice pixels within a single geo-temporal area, such as a specific day in Tonga (**Figure 1B**) or comparing across multiple days for the same raft (**Supplementary Figure S16**). Although there is some variation in pumice spectral response curves when comparing rafts from different chemical compositions, sources, and times (**Figure 1B**, comparison with Rabaul raft and Puyehue-Cordón Caulle raft), the general shape of the reflectance curve remains very similar. This characteristic shape of the spectral response curve for pumice pixels allows for an algorithm to identify pumice and differentiate from other classes (e.g., water, clouds) across a broad range of regions and time periods. Details for the Puyehue-Cordón Caulle raft are provided in **Supplementary Text S13**.

Our machine-learning algorithm uses a Random Forest classifier to read in an RGB Sentinel-2 image and return a classified image, where each pixel is colored according to the assigned class. The algorithm specifics are detailed in **Supplementary Text S4**. Since RF is a supervised learning algorithm, we need to train it on a set of manually demarcated and classified pixels. Our primary training data for pumice, ocean water, light cloud cover, and heavy cloud cover was sampled from the Tonga raft on 11 August 2019 (**Figure 2A**, only a small part of the raft pixels were used for training). We also included additional data from a Sentinel-2 scene of Rabaul, Papua New Guinea, on 20 April 2020 (**Figure 2B**, spectrally this is representative of the potential rafts from other days also). This image includes a large, distinct pumice raft as well as ocean water, light cloud cover, pumice mixture classes, and two different discolored water classes (additional information for the discolored water classes are included in **Supplementary Text S9**). Since the discolored water classes are not the primary focus of this study, our primary optimization for the RF algorithm was to ensure accurate detection of pumice rafts. We provide all the scripts, with step-by-step instructions for usage, used in our analysis in a publicly available repository (**Supplementary Material**—GEE Script Links).

3 RESULTS

3.1 Single Image Analysis Results

We applied our classification algorithm to Sentinel-2 images from different geo-temporal regions to test model accuracy (**Figure 2**). In the Tonga area on 11 August 2019 (**Figure 2A**), the classifier displays pumice pixels in red, water in blue, light cloud cover in orange, and heavy cloud cover in white. The shape of the large raft is distinctly visible in the classified image. In the Rabaul region, on

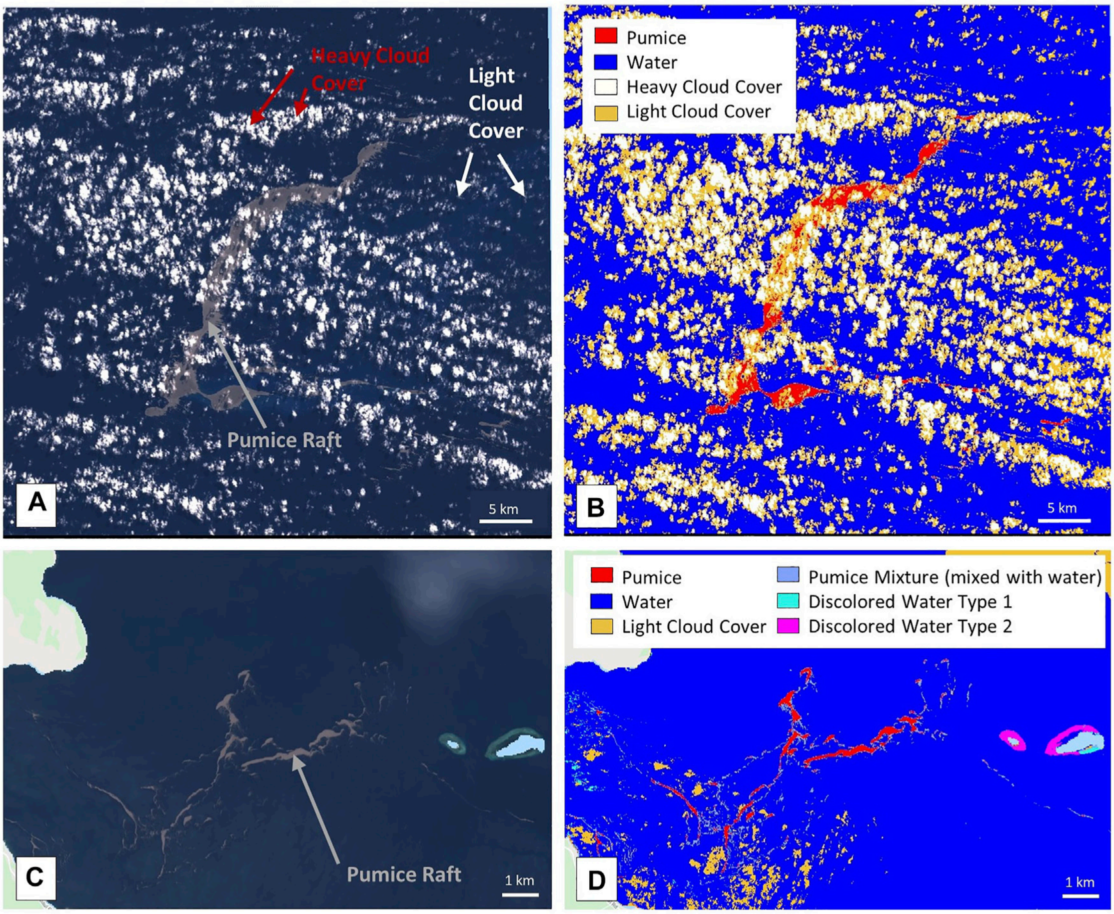

FIGURE 2 | (A) Land-masked RGB image of Tonga region on 08/11/2019 **(B)** Classified image of Tonga region on 08/11/2019 **(C)** Land-masked RGB image of Rabaul on 04/20/2020 **(D)** Land-masked classified image of Rabaul on 04/20/2020.

20 April 2020 (**Figure 2A**), the classifier also includes additional classes: mixed/faint pumice—a mixture of water and pumice—shown in light blue, and two different classes of discolored water shown in turquoise and magenta. Overall, our algorithm is efficient at identifying pumice from other backgrounds though the accuracy of discolored water detection (mixing with corals) and shallow cloud is not great at present. Algorithm validation methods and results are included in **Supplementary Text S5**.

3.2 Regional Results

To assess the utility of our algorithm for new submarine eruption detection, we applied the classifier over a single region for an extended period of time. We focused on Rabaul, a partially submarine volcano located on the Gazelle Peninsula's tip at the northeast end of New Britain in Papua New Guinea (**Figure 3A**). The Rabaul caldera (~8 × 14 km size) was formed as a consequence of multiple large explosive eruptions in the past few hundred thousand years, with the present day shape due to an eruption ~1,400 years ago (GVP and wunderman, 1994). The caldera is mostly shallow submarine (< 200 m water depth) and is connected to the sea on the east through a wide opening (Blanche Bay). The main raft-forming eruptions for this volcano occurred in 1878, 1937, and 1994, and no raft formation has been recorded since 1994 (GVP and Wunderman, 1994; GVP and Wunderman, 2006). No activity has been recorded at either of the main vents (Vulcan and Tavurvur) since 2014 (Bernard and Bouvet de Maisonneuve, 2020). More detailed eruption history is provided in **Supplementary Text S8**.

In the Rabaul area, we applied our algorithm from November 2015 (start of the Sentinel-2 coverage for the Rabaul region) to August 2020—a total of 239 distinct days with images. More details on our algorithm application method are included in **Supplementary Text S7**.

Of these 239 days, we found that 74 days were too cloudy for the classifier to detect any pumice meaningfully. Cloudy days were filtered out by manually examining classified images and removing images in which every pixel was labeled as heavy or light cloud cover. In the future, this step can be automated by explicitly filtering the images based on the classified heavy cloud fraction. We detected potential rafts in 28 (red lines, **Figure 3B**)

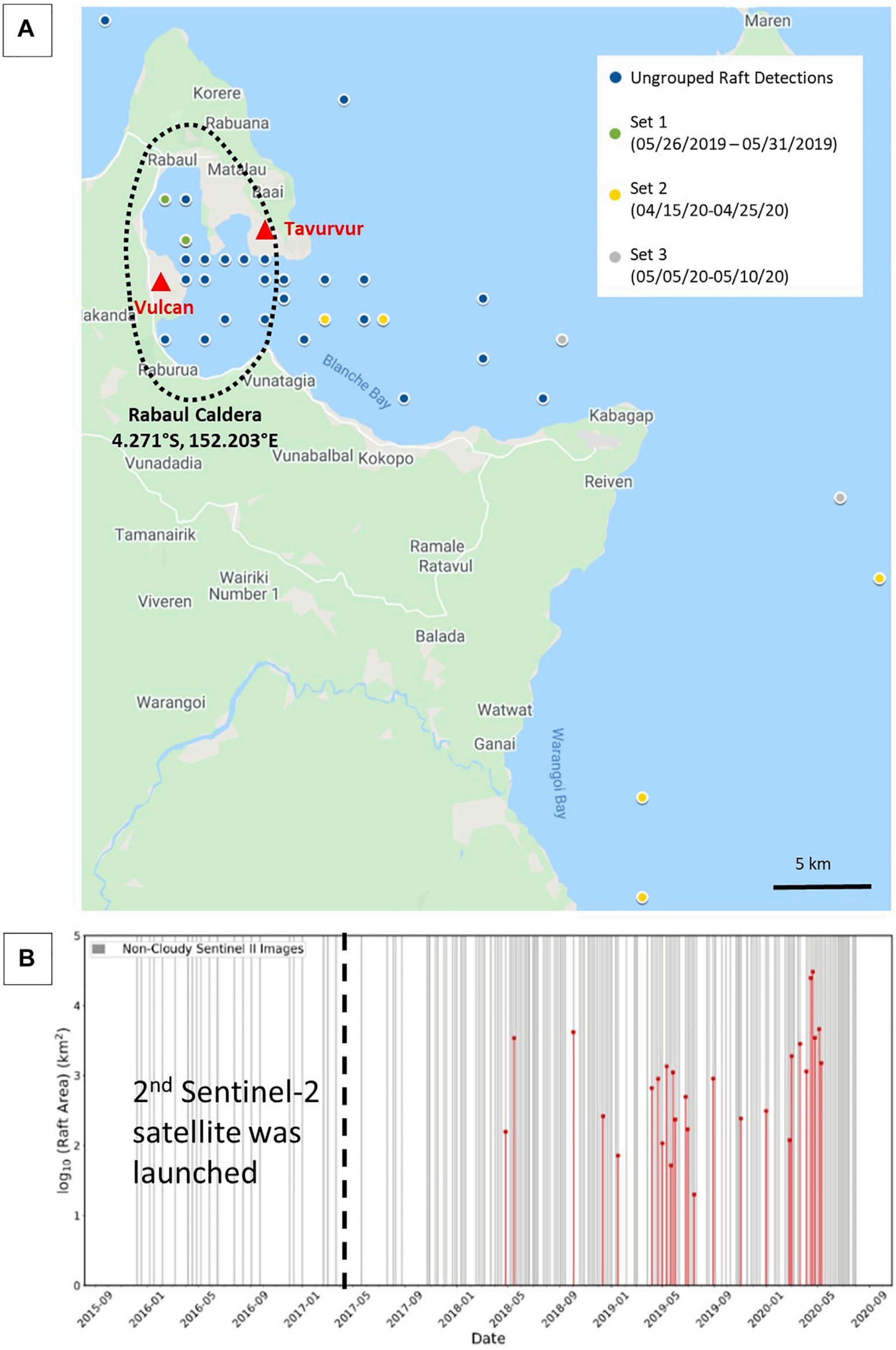

FIGURE 3 | (A) Map of pumice raft detection locations in Rabaul area. Main vent locations are marked with red triangles. Groupings of raft detections (by proximity in time and location) are indicated by the different colored icons **(B)** Non-cloudy days during Sentinel-2 coverage period, with raft detections in red (height indicating raft area).

of the remaining 165 days (gray lines, **Figure 3B**), leading to a detection rate of 16.97%. As illustrated in **Figure 3B**, most of our raft detections were after January 2018 (**Figure 3B**). This is likely a consequence of increased revisit frequency (~5-day) after the second Sentinel-2 satellite launch. Before 2018, when only one Sentinel-2 satellite was in operation, there are significantly fewer images available. It is noteworthy that none of the rafts detected in our analysis had been previously reported in the scientific literature (to the best of our knowledge) or the Smithsonian Global Volcanism Catalog (Global Volcanism Program, 2013). The sizes of our detected rafts varied greatly, with raft areas as small as 20 km^2 to as great as 10,000 km^2. At present, we do not have any direct ground truthing of our detections. However, considering the distinctive spectral features of pumice compared to other biological sources, especially in the Near Infrared (Biermann et al., 2020; Qi et al., 2020), we interpret the classified features as rafts of pumiceous material - pumice rafts (**Supplementary Text S16** for discussion regarding difference between "true" pumice and more general pumiceous material).

3.2.1 Source of New Rafts in Rabaul

Given our new raft detections, there is a natural follow-up question—do these rafts represent previously unreported submarine eruptions, or are they suspended pumiceous material remobilized from known previous eruption deposits from Rabaul or pumice produced by eruptions from other volcanoes in the region that subsequently drifted into the Rabaul harbor? These are the three primary end-member models, with the remobilization of pumice (or pumiceous material) from previous eruptions being a process that has been documented following the dispersal of large pumice rafts. For example, the Tonga 2019 pumice raft was stranded in near coastal regions in multiple islands in Fiji (in particular Lakeba island) in early-mid September 2019. However, some of this raft material in Lakeba island was not remobilized till late October-early November 2019 (Jutzeler et al., 2020, observations from Sentinel-2 Imagery). Redeposition and remobilization of volcanic products such as ash fall (Etyemezian et al., 2019; Del Bello et al., 2021) as well as subaerial [e.g., from Pinatubo 1991 eruption, Torres et al. (1996)] and subaqueous pyroclastic material has been recorded after initial deposition (Mandeville et al., 1996; Manville et al., 2002; Park and Schmincke, 2020). However, the majority of this work has focused on a short time frame—on the order of days to months after the eruption though there are some exceptions—e.g., secondary pumice rafts from Socorro Island in January 2009 (Ochoa, 2009, Personal Comm. from Scott Bryan) and secondary pumice rafts in Brasier et al. (2011). Here, if our hypothesis is correct, the pumiceous material we are seeing is remobilized tens or even hundreds of years after the original eruption since the last major raft forming eruption in Rabaul was in 1994.

We assess the likelihood of new submarine eruptions by analyzing the reported volcanic activity for Rabaul in the Smithsonian Volcano Catalog (Global Volcanism Program, 2013). The Rabaul Volcano Observatory has recorded no large eruptions since 2014 (Global Volcanism Program, 2013) and/or any significant submarine activity besides hydrothermal discharge near the Tavurvur vent. Because rafts initiating from point sources can indicate new eruptions, we test this further by recording each of our raft detections' spatial location and considering the spread of each sighting. We have tried to manually aggregate three sets of raft locations together (**Figure 3A**). These sets are of sequential images, in which the raft detections were somewhat close, not only in time, but in location as well. Conclusively tracking the rafts as they are advected around by local ocean currents is challenging due to repeat frequency (5-day gap between images), cloud cover, and complex shallow-water ocean currents in the regions. In aggregate, the detections are scattered over a broad area in the caldera and surrounding sea, rather than primarily located near any known vents (**Figure 3A**).

We also used Sentinel-2 imagery as well as ancillary datasets [e.g., higher spatial and temporal resolution Planet Labs imagery (Planet Team, 2021)] to check if the rafts are associated with any other eruptive signatures expected for shallow submarine eruptions (e.g., aerial plumes, discolored water). We did not find any aerial plumes and, while there was some discolored water around the Tavurvur vent location, we did not find any relationship between the days with raft detections and days with discolored water around the vent (**Supplementary Text S14**). Thus, we interpret that the detected rafts are not actually products from a new submarine eruption.

Instead, we propose that they are secondary rafts [like the rafts in Socorro Island in January 2009 (Ochoa (2009), Personal Comm. from Scott Bryan); also see Richards (1958), Lee (1979), Kent and Frick (1984), Thiel and Gutow (2004) for related discussion] that have been suspended after being deposited on surrounding shores and riverbanks following their initial eruptions tens to hundreds of years ago (**Section 4** for the potential processes). This is a new, novel physical process that has not been fully documented before, especially in the modern/satellite era. Our analysis is the first study, to the best of our knowledge, to carefully document the secondary raft process on timescales of years or longer using satellite imagery, further validating the importance of this process as suggested by previous studies (Pullar et al., 1977; Osborne et al., 1991; Shane et al., 1998; Bryan et al., 2012; Jutzeler et al., 2014). This secondary raft process is likely relevant for the dispersal of eruptive products from many volcanic systems in coastal regions (e.g., Krakatau in Indonesia, Tonga-Fiji region). Although the secondary rafts are much smaller scale individually compared to large pumice rafts associated with new eruptions such as the Havre 2012 and the Krakatau 1883 eruption, they can be much more frequent. Thus, they may potentially still be important for material transport and local/regional scale biology. We acknowledge that a systematic analysis of secondary rafts on regional/global scales is needed to quantify this effect (if any). Without any specimens of the pumice that we detected, we are presently unable to ascertain a specific source eruption of the rafts. In addition, even with samples, it may still be difficult to determine the original source eruption or eruptions, as pumice material from the 1878 eruption and subsequent eruptions have very similar overall composition and texture (Bernard and Bouvet de Maisonneuve, 2020). However, the morphology of the pumice samples (angular vs. rounded, presence of biological material) can at least provide some constraints on whether the pumice represents a new eruption or remobilized material (from Rabaul or other farther eruptions, based on composition).

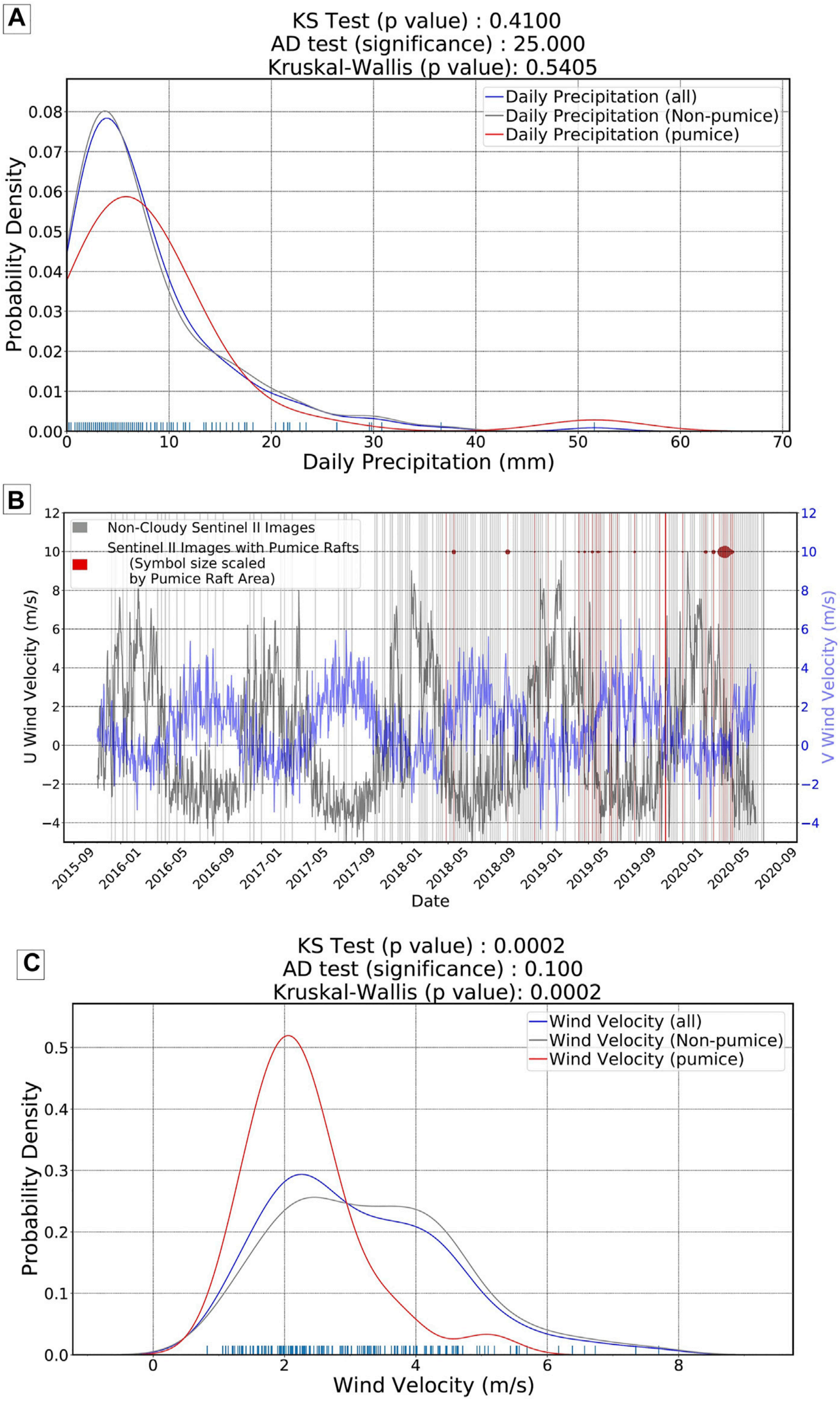

FIGURE 4 | (A) Probability density function for the daily precipitation in the Rabaul region (5 days rolling window) **(B)** Time series of daily wind directionality in the Rabaul region—U wind velocity is the eastward component of wind while the V wind velocity is the northward component **(C)** Probability density function for daily wind magnitude in the Rabaul region (5 days rolling window).

Furthermore, field work in the Rabaul region can ground truth our conclusions and help test whether there is enough erodible material in the coastal areas to form rafts.

4 DISCUSSION

4.1 Source of Pumice Remobilization: Influence of Weather Factors

Considering our interpretation that the detected rafts in Rabaul are secondary rafts, an important question to consider is what potential physical mechanisms are responsible for the mobilization of pumiceous material. One possibility is that resuspension is a consequence of local climatological conditions, e.g., high rainfall events, high wind conditions that dislodge pumice along coastlines and riverbanks back into the water. Local weather can lead to landslides and dislodgement of small pumice rafts [e.g., local pumice raft from rockslide in the Askja caldera, Iceland on 21 July 2014 (Icelandic Meteorological, 2014)]. Using ERA5 Daily Aggregate Reanalysis Product (Hersbach et al., 2020) (directly accessible through GEE), we generated time series of various atmospheric properties—daily mean air temperature, wind magnitude, wind direction, and precipitation. These time series were all sampled from the same location, directly on top of one of Rabaul's vents, and the time series spanned the entire Sentinel-2 coverage period in the area. We did not observe any significant correlation between the daily mean air temperature and the detection of pumice rafts in the area (**Supplementary Figure S3**). We also explored potential correlations with weather parameters up to 10 days before raft detection to allow for some unknown advection time (**Supplementary Data**). Overall, we did not find significantly different results across these windows. The main statistically robust relationships in our dataset are between raft detection and wind and precipitation.

4.1.1 Precipitation

To compare the impact of wind, precipitation, and other weather parameters on raft detection, we construct and compare probability density distributions (PDF). A PDF is a function that provides the relative likelihood of an event (raft detection) given another parameter (e.g. wind speed, recorded rainfall). We find that the PDF for the days with sighted pumice rafts (red curve, **Figure 4A**) were slightly different from the curves for the total days in the coverage period (blue curve, **Figure 4A**) and the days where no rafts were detected (gray curve, **Figure 4A**) (using 5 day rolling window, other windows have similar results). However, this difference is not statistically significant when using either the Anderson-Darling (AD) test statistic (Scholz and Stephens, 1987) or the Epps-Singleton (ES) test statistic (Epps and Singleton, 1986). The medians of the raft vs. non-raft precipitation PDFs are potentially different, as shown by the lower *p*-value for the Kruskal-Wallis test (Kruskal and Wallis, 1952). We also do not find any clear correlation between precipitation values and raft area.

We analyzed the long-term precipitation history in the Rabaul area to help elucidate the remobilization process. We used ERA5 data to consider 3-day rolling sums of precipitation values in Rabaul since 1990. From the long-term history, we observe the peak precipitation occurred in February 2018. All of our detected rafts in Sentinel-2 imagery are post 2018 (further analysis using Landsat imagery is included in **Supplementary Text S15**). This may be a consequence of increased frequency of sampling in the Rabaul area after the second Sentinel-2 satellite launch in March of 2017. Alternatively, the detection of rafts after the precipitation peak in early 2018 suggests that a large storm or significant weather event made rafts easier to remobilize post-2017. More detailed work, especially in the field in Rabaul, is needed to test these hypothesis and ascertain which coastal areas have significant amounts of pumice ready to mobilize.

Overall, we find that there is only a weak correlation between precipitation and raft detection. We posit that the slightly higher values for precipitation before raft detection compared to non-raft days suggest a role for higher precipitation to increase erosion and consequently encourage raft remobilization. However, it is clear that precipitation is not a unique factor since days of high precipitation are not always followed by raft detections (**Figure 4A**, **Supplementary Figure S2**).

4.1.2 Wind

In addition to precipitation, we also considered the role of wind in raft formation. **Figure 4B** shows the daily wind direction [U (eastward), V (northward) components] in Rabaul along with red vertical lines highlighting days with raft detections. We find that the general wind direction in Rabaul has a strong seasonal cycle which is relatively stable over the past 5 years. Interestingly, most of our pumice raft sightings were around the March–May window despite having a number of non-cloudy images for other months. This suggests that there is some seasonality to the raft remobilization process.

In order to assess the role of overall wind magnitude, we show the probability distribution curves for wind velocity for all days in the Sentinel-2 coverage period (blue curve, **Figure 4C**), days without raft sightings (gray curve, **Figure 4C**), and days with raft sightings (red curve, **Figure 4C**) (using 5 day rolling window, other windows have similar results). We find that days where rafts were detected produced a significantly different probability distribution curve (**Figure 4C**). There is also a high correlation between wind amplitude and raft area (**Supplementary Figure S3**). However, since there are not many high raft area data points, the correlation may be biased by outliers. Overall, we see most of our raft sightings are in the distinct range of wind velocities (1 to 4 m/s) compared to the overall distribution. Even when accounting for different sample sizes, this difference is statically significant [Anderson-Darling (AD) test statistic (Scholz and Stephens, 1987); the Epps-Singleton (ES) test statistic (Epps and Singleton, 1986); Kolmogorov-Smirnov (KS) test (Hodges, 1958)]. We conclude that the high wind velocities likely break up and disperse the secondary rafts too rapidly for Sentinel-2 to capture. We would note that there are number of non-cloudy days with low wind velocity and no raft detection (**Figure 4C**, grey curve). Thus, wind condition is not the only parameter that controls the temporal pattern of raft detection with an additional role of seasonality.

4.2 Open Challenges for Global Pumice Detection Algorithm

Although our ML algorithm is reasonably successful for pumice raft detection, it is not fully automated. The classification process requires manual checks to filter out incorrect classifications of pumice and cloud cover. In particular, the light cloud cover with a flat spectral response curve can at times be misclassified as pumice (and vice versa). Also, the satellite's viewing geometry may create a "Sun glint" in certain images, where all of the pixels in the RGB rendering are affected and off-colored. The classifier subsequently has difficulty correctly identifying the correct class of each pixel. There are some ways these issues can be addressed. Better atmospheric corrected products, specifically for oceanic regions, would help improve detection. For instance, in some cases, using the atmosphere corrected Surface Reflectance (Level-2A) product can allow us to detect pumice rafts on images discolored due to atmospheric effects (**Supplementary Figure S10**). Alternatively, more stringent data filtering for satellite viewing angle and cloudiness bounds can help reduce potential false positives. Finally, incorporating additional satellite imagery data e.g., geostationary imagery with high temporal frequency (more detailed raft tracking as well as better cloud detection based on motion) and radar imagery (sensitive to surface roughness and reduced sensitivity to atmospheric effects) could help improve detection accuracy. Additional potential options for algorithmic improvement are described in **Supplementary Text S11**.

5 CONCLUSION

In this study, we show that GEE and RF classifiers can be successfully used to detect pumice rafts. This can be useful to efficiently track pumice rafts, which can pose as hazards and disruptions to boats and harbors (Jutzeler et al., 2014; Jutzeler et al., 2020) and thus help with hazard mitigation and coordination services along populated shorelines (e.g., ongoing raft arrival on mainland Japan from the August 2021 eruption of Fukutoku-Okanoba volcano). Our methodology can help address our current strong bias in eruption detection and improve the detection of submarine eruptions globally. Using GEE removes the large data storage requirement and allows for a semi-automated, easily scalable classification with minimal subjective biases. Using the Rabaul caldera regions in Papua New Guinea as a case study, we show that not all detected pumice rafts necessarily correlate with a new eruption. Indeed, in some coastal regions, remobilization is likely to be a widespread phenomenon and can affect the spatial pattern of how products from an eruption are deposited as well as pumice remobilization after large storms/coastal tsunamis (e.g., Anak Krakatau 2018; Hunga Tonga Hunga Ha'apai 2022 eruption). Since these spatial patterns serve as the basis for estimating volcanic eruptive volumes, as well as long-distance (on tens to hundreds of kilometers scale) stratigraphic correlations (Shane et al., 1998; Mouginis-Mark and Zimbelman, 2020; Freundt et al., 2021), the raft remobilization process needs to be further analyzed. Finally, if drifting, remobilized pumice is common, its presence can impact the detection of future submarine eruptions, especially small eruptions in near coastal regions. Thus understanding the morphology, abrasion, and lifetime of the remobilized rafts (i.e., how they fragment over time and any differences from newly erupted rafts) is critical to remove this false positive for new eruption detection.

DATA AVAILABILITY STATEMENT

The original contributions presented in the study are publicly available. This data can be found here: https://figshare.com/projects/Pumice_Raft_Detection_Using_Machine-Learning_on_Multispectral_Satellite_Imagery/126466.

AUTHOR CONTRIBUTIONS

TM and MZ conceived the study and were in charge of overall direction and planning. MZ wrote the algorithm scripts and applied algorithm in case study. TM and MZ analysed the data and wrote the manuscript with input from all authors.

ACKNOWLEDGMENTS

We thank Amber Madden-Nadeau, Samantha L. Engwell, Sebastian Watt, Michael Cassidy, Ralf Bennartz, Ashok Gupta, Liam Kelly, John Rausch for useful discussions and suggestions for the manuscript text. We thank the editor and the reviewers for their valuable comments and suggestions. We thank Planet Labs, Sentinel-2, Landsat 7/8, and Google Earth Engine platform for providing the satellite imagery and computational tools. MZ acknowledges support from the MIT UROP program, TM acknowledges funding support from the Crosby Postdoc Fellowship at MIT, and KF acknowledges funding support from the NASA Grant 80NSSC20K1450.

SUPPLEMENTARY MATERIAL

The Supplementary Material for this article can be found online at: https://www.frontiersin.org/articles/10.3389/feart.2022.838532/full#supplementary-material

REFERENCES

Baker, E. T., Lavelle, J. W., Feely, R. A., Massoth, G. J., Walker, S. L., and Lupton, J. E. (1989). Episodic Venting of Hydrothermal Fluids From the Juan de Fuca Ridge. *J. Geophys. Res.* 94, 9237–9250. doi:10.1029/jb094ib07p09237

Bernard, O., and Bouvet de Maisonneuve, C. (2020). Controls on Eruption Style at Rabaul, Papua New Guinea - Insights from Microlites, Porosity and Permeability Measurements. *J. Volcanology Geothermal Res.* 406, 107068. doi:10.1016/j.jvolgeores.2020.107068

Biermann, L., Clewley, D., Martinez-Vicente, V., and Topouzelis, K. (2020). Finding Plastic Patches in Coastal Waters Using Optical Satellite Data. *Sci. Rep.* 10, 5364. doi:10.1038/s41598-020-62298-z

Brandl, P. A., Schmid, F., Augustin, N., Grevemeyer, I., Arculus, R. J., Devey, C. W., et al. (2020). The 6-8 Aug 2019 Eruption of 'Volcano F' in the Tofua Arc, Tonga. *J. Volcanology Geothermal Res.* 390, 106695. doi:10.1016/j.jvolgeores.2019.106695

Brasier, M. D., Matthewman, R., McMahon, S., and Wacey, D. (2011). Pumice as a Remarkable Substrate for the Origin of Life. *Astrobiology* 11, 725–735. doi:10.1089/ast.2010.0546

Brenot, H., Theys, N., Clarisse, L., van Geffen, J., van Gent, J., Van Roozendael, M., et al. (2014). Support to Aviation Control Service (SACS): an Online Service for Near-Real-Time Satellite Monitoring of Volcanic Plumes. *Nat. Hazards Earth Syst. Sci.* 14, 1099–1123. doi:10.5194/nhess-14-1099-2014

Bryan, S. E., Cook, A., Evans, J. P., Colls, P. W., Wells, M. G., Lawrence, M. G., et al. (2004). Pumice Rafting and Faunal Dispersion during 2001-2002 in the Southwest Pacific: Record of a Dacitic Submarine Explosive Eruption from Tonga. *Earth Planet. Sci. Lett.* 227, 135–154. doi:10.1016/j.epsl.2004.08.009

Bryan, S. E., Cook, A. G., Evans, J. P., Hebden, K., Hurrey, L., Colls, P., et al. (2012). Rapid, Long-Distance Dispersal by Pumice Rafting. *PloS one* 7, e40583. doi:10.1371/journal.pone.0040583

Cesca, S., Letort, J., Razafindrakoto, H. N. T., Heimann, S., Rivalta, E., Isken, M. P., et al. (2020). Drainage of a Deep Magma Reservoir Near Mayotte Inferred from Seismicity and Deformation. *Nat. Geosci.* 13, 87–93. doi:10.1038/s41561-019-0505-5

Del Bello, E., Taddeucci, J., Merrison, J. P., Rasmussen, K. R., Andronico, D., Ricci, T., et al. (2021). Field-Based Measurements of Volcanic Ash Resuspension by Wind. *Earth Planet. Sci. Lett.* 554, 116684. doi:10.1016/j.epsl.2020.116684

DeVantier, L. (1992). Rafting of Tropical Marine Organisms on Buoyant Corolla. *Mar. Ecol. Prog. Ser.* 86, 301–302. doi:10.3354/meps086301

Embley, R. W., Baker, E. T., Chadwick, W. W., Lupton, J. E., Resing, J. A., Massoth, G. J., et al. (2004). Explorations of Mariana Arc Volcanoes Reveal New Hydrothermal Systems. *Eos Trans. AGU* 85, 37–40. doi:10.1029/2004eo040001

Engwell, S., Mastin, L., Tupper, A., Kibler, J., Acethorp, P., Lord, G., et al. (2021). Near-real-time Volcanic Cloud Monitoring: Insights into Global Explosive Volcanic Eruptive Activity through Analysis of Volcanic Ash Advisories. *Bull. Volcanology* 83, 1–17. doi:10.1007/s00445-020-01419-y

Epps, T. W., and Singleton, K. J. (1986). An Omnibus Test for the Two-Sample Problem Using the Empirical Characteristic Function. *J. Stat. Comput. Simulation* 26, 177–203. doi:10.1080/00949658608810963

Erupt (2017). *Volcanic Eruptions and Their Repose, Unrest, Precursors, and Timing*. Washington, DC: The National Academies Press. doi:10.17226/24650

Etyemezian, V., Gillies, J. A., Mastin, L. G., Crawford, A., Hasson, R., Van Eaton, A. R., et al. (2019). Laboratory Experiments of Volcanic Ash Resuspension by Wind. *J. Geophys. Res. Atmos.* 124, 9534–9560. doi:10.1029/2018jd030076

Fauria, K., Jutzeler, M., Mittal, T., Gupta, A., Kelly, L., Rausch, J., et al. (2022). Simultaneous Creation of a Large Vapor Plume and Pumice Raft by a Shallow Submarine Eruption. *Earth Space Sci. Open Archive*. doi:10.1002/essoar.10510412.1

Freundt, A., Schindlbeck-Belo, J. C., Kutterolf, S., and Hopkins, J. L. (2021). *Tephra Layers in the Marine Environment: A Review of Properties and Emplacement Processes*. London: Geological Society. *Special Publications* 520.

Furtney, M. A., Pritchard, M. E., Biggs, J., Carn, S. A., Ebmeier, S. K., Jay, J. A., et al. (2018). Synthesizing Multi-Sensor, Multi-Satellite, Multi-Decadal Datasets for Global Volcano Monitoring. *J. Volcanology Geothermal Res.* 365, 38–56. doi:10.1016/j.jvolgeores.2018.10.002

Gorelick, N., Hancher, M., Dixon, M., Ilyushchenko, S., Thau, D., and Moore, R. (2017). Google Earth Engine: Planetary-Scale Geospatial Analysis for Everyone. *Remote sensing Environ.* 202, 18–27. doi:10.1016/j.rse.2017.06.031

Global Volcanism Program (2013). "Global Volcanism Program," in *Volcanoes of the World*. Editor E. Venzke (Smithsonian Institution), 2, 4–6. doi:10.5479/si.GVP.VOTW4-2013

Gvp (1994). "Report on Rabaul (Papua New Guinea)," in *Bulletin of the Global Volcanism Network*. Editor R. Wunderman (Smithsonian Institution), 19, 8. doi:10.5479/si.GVP.BGVN199408-252140

Gvp (2006). "Report on Rabaul (Papua New Guinea),". Editor R. Wunderman (Smithsonian Institution), 31, 9. doi:10.5479/si.GVP.BGVN200609-252140*Bull. Glob. volcanism Netw.*

Heaney, K. D., Campbell, R. L., and Snellen, M. (2013). Long Range Acoustic Measurements of an Undersea Volcano. *The J. Acoust. Soc. America* 134, 3299–3306. doi:10.1121/1.4818844

Hersbach, H., Bell, B., Berrisford, P., Hirahara, S., Horányi, A., Muñoz-Sabater, J., et al. (2020). The ERA5 Global Reanalysis. *Q.J.R. Meteorol. Soc.* 146, 1999–2049. doi:10.1002/qj.3803

Hodges, J. L. (1958). The Significance Probability of the Smirnov Two-Sample Test. *Ark. Mat.* 3, 469–486. doi:10.1007/bf02589501

Icelandic Meteorological Office (2014). *Rockslide in Askja, July 21 2014 - Preliminary Results of Observations*.

Jutzeler, M., Marsh, R., Carey, R. J., White, J. D., Talling, P. J., and Karlstrom, L. (2014). On the Fate of Pumice Rafts Formed during the 2012 Havre Submarine Eruption. *Nat. Commun.* 5, 3660. doi:10.1038/ncomms4660

Jutzeler, M., Marsh, R., van Sebille, E., Mittal, T., Carey, R. J., Fauria, K. E., et al. (2020). Ongoing Dispersal of the 7 August 2019 Pumice Raft from the Tonga Arc in the Southwestern Pacific Ocean. *Geophys. Res. Lett.* 47, e1701121. doi:10.1029/2019gl086768

Kelley, D. (2017). Volcanology: Vulcan Rule beneath the Sea. *Nat. Geosci.* 10, 251–253. doi:10.1038/ngeo2929

Kent, L., and Frick, C. (1984). Drift Pumice in the Indian and South Atlantic Oceans. *South. Afr. J. Geology.* 87, 19–33.

Kruskal, W. H., and Wallis, W. A. (1952). Use of Ranks in One-Criterion Variance Analysis. *J. Am. Stat. Assoc.* 47, 583–621. doi:10.1080/01621459.1952.10483441

Lee, V. F. (1979). Maritime Pseudoscorpions of Baja California, Mexico (Arachnida: Pseudoscorpionida).

Mandeville, C. W., Carey, S., and Sigurdsson, H. (1996). Sedimentology of the Krakatau 1883 Submarine Pyroclastic Deposits. *Bull. Volcanol* 57, 512–529. doi:10.1007/BF00304436

Manville, V., Segschneider, B., and White, J. D. L. (2002). Hydrodynamic Behaviour of Taupo 1800a Pumice: Implications for the Sedimentology of Remobilized Pyroclasts. *Sedimentology* 49, 955–976. doi:10.1046/j.1365-3091.2002.00485.x

Matsumoto, H., Zampolli, M., Haralabus, G., Stanley, J., Mattila, J., and Meral Özel, N. (2019). Interpretation of Detections of Volcanic Activity at Ioto Island Obtained from *In Situ* Seismometers and Remote Hydrophones of the International Monitoring System. *Sci. Rep.* 9, 19519. doi:10.1038/s41598-019-55918-w

Mittal, T., and Delbridge, B. (2019). Detection of the 2012 Havre Submarine Eruption Plume Using Argo Floats and its Implications for Ocean Dynamics. *Earth Planet. Sci. Lett.* 511, 105–116. doi:10.1016/j.epsl.2019.01.035

Mouginis-Mark, P. J., and Zimbelman, J. R. (2020). Rafted Pumice: A New Model for the Formation of the Medusae Fossae Formation, Mars. *Icarus* 343, 113684. doi:10.1016/j.icarus.2020.113684

Ochoa, C. N. (2009). *Report of Drift Pumice Near Socorro Island (25 January to 3 February 2009)*.

O'Malley, R. T., Behrenfeld, M. J., Westberry, T. K., Milligan, A. J., Reese, D. C., and Halsey, K. H. (2014). Improbability Mapping: a Metric for Satellite-Detection of Submarine Volcanic Eruptions. *Remote sensing Environ.* 140, 596–603.

Osborne, N. M., Enright, N. J., and Parnell, K. E. (1991). The Age and Stratigraphic Significance of Sea-Rafted Loisels Pumice in Northern New Zealand. *J. R. Soc. New Zealand* 21, 357–371. doi:10.1080/03036758.1991.10420833

Park, C., and Schmincke, H.-U. (2020). Multistage Damming of the Rhine River by Tephra Fallout during the 12,900 Bp Plinian Laacher See Eruption (germany). Syn-Eruptive Rhine Damming I. *J. Volcanology Geothermal Res.* 389, 106688. doi:10.1016/j.jvolgeores.2019.106688

Planet Team (2021). "Planet Application Program Interface," in *Space for Life on Earth*.

Poland, M. P., Lopez, T., Wright, R., and Pavolonis, M. J. (2020). Forecasting, Detecting, and Tracking Volcanic Eruptions from Space. *Remote Sens Earth Syst. Sci.* 3, 55–94. doi:10.1007/s41976-020-00034-x

Pullar, W. A., Kohn, B. P., and Cox, J. E. (1977). Air-Fall Kaharoa Ash and Taupo Pumice, and Sea-Rafted Loisels Pumice, Taupo Pumice, and Leigh Pumice in Northern and Eastern Parts of the North Island, New Zealand. *New Zealand Journal Geology. Geophysics* 20, 697–717. doi:10.1080/00288306.1977.10430729

Qi, L., Hu, C., Mikelsons, K., Wang, M., Lance, V., Sun, S., et al. (2020). In Search of Floating Algae and Other Organisms in Global Oceans and Lakes. *Remote Sensing Environ.* 239, 111659. doi:10.1016/j.rse.2020.111659

Richards, A. F. (1958). Transpacific Distribution of Floating Pumice from Isla San Benedicto, Mexico. *Deep Sea Res. (1953)* 5, 29–35. doi:10.1016/S0146-6291(58)80005-3

Risso, C., Scasso, R. A., and Aparicio, A. (2002). Presence of Large Pumice Blocks on Tierra Del Fuego and South Shetland Islands Shorelines, From 1962 South Sandwich Islands Eruption. *Mar. Geology.* 186, 413–422. doi:10.1016/s0025-3227(02)00190-1

Rubin, K., Soule, S. A., Chadwick, W., Jr, Fornari, D., Clague, D., Embley, R., et al. (2012). Volcanic Eruptions in the Deep Sea. *oceanog* 25, 142–157. doi:10.5670/oceanog.2012.12

Sakuno, Y. (2021). Trial of Chemical Composition Estimation Related to Submarine Volcano Activity Using Discolored Seawater Color Data Obtained from GCOM-C SGLI. A Case Study of Nishinoshima Island, Japan, in 2020. *Water* 13, 1100. doi:10.3390/w13081100

Santana-Casiano, J. M., González-Dávila, M., Fraile-Nuez, E., De Armas, D., González, A. G., Domínguez-Yanes, J. F., et al. (2013). The Natural Ocean Acidification and Fertilization Event Caused by the Submarine Eruption of El Hierro. *Sci. Rep.* 3, 1140. doi:10.1038/srep01140

Scholz, F. W., and Stephens, M. A. (1987). K-Sample Anderson-Darling Tests. *J. Am. Stat. Assoc.* 82, 918–924. doi:10.1080/01621459.1987.10478517

Shane, P., Froggatt, P., Smith, I., and Gregory, M. (1998). Multiple Sources for Sea-Rafted Loisels Pumice, New Zealand. *Quat. Res.* 49, 271–279. doi:10.1006/qres.1998.1968

Tepp, G., Chadwick, W. W., Jr, Haney, M. M., Lyons, J. J., Dziak, R. P., Merle, S. G., et al. (2019). Hydroacoustic, Seismic, and Bathymetric Observations of the 2014 Submarine Eruption at Ahyi Seamount, Mariana Arc. *Geochem. Geophys. Geosyst.* 20, 3608–3627. doi:10.1029/2019gc008311

Tepp, G., and Dziak, R. P. (2021). The Seismo-Acoustics of Submarine Volcanic Eruptions. *J. Geophys. Res. Solid Earth* 126, e2020JB020912. doi:10.1029/2020jb020912

Thiel, M., and Gutow, L. (2004). The Ecology of Rafting in the Marine Environment. I. The Floating Substrata. *Oceanography Mar. Biol. Annu. Rev.* 42, 181–263. doi:10.1201/9780203507810.ch6

Tilstone, G. H., Miller, P. I., Brewin, R. J. W., and Priede, I. G. (2014). Enhancement of Primary Production in the North Atlantic Outside of the Spring Bloom, Identified by Remote Sensing of Ocean Colour and Temperature. *Remote sensing Environ.* 146, 77–86. doi:10.1016/j.rse.2013.04.021

Torres, R. C., Self, S., Martinez, M. M. L., Newhall, C., and Punongbayan, R. (1996). *Secondary Pyroclastic Flows from the June 15, 1991, Ignimbrite of Mount Pinatubo Fire and Mud: Eruptions and Lahars of Mount Pinatubo*. Philippines, 665–678.

White, J. D. L., Schipper, C. I., and Kano, K. (2015). "Submarine Explosive Eruptions," in *The Encyclopedia of Volcanoes*. Editor H. Sigurdsson. Second EditionSecond edition edn (Amsterdam: Academic Press), 553–569. doi:10.1016/B978-0-12-385938-9.00031-6

White, S. M., Crisp, J. A., and Spera, F. J. (2006). Long-term Volumetric Eruption Rates and Magma Budgets. *Geochem. Geophys. Geosystems* 7. doi:10.1029/2005gc001002

Whiteside, A., Dupouy, C., Singh, A., Frouin, R., Menkes, C., and Lefèvre, J. (2021). Automatic Detection of Optical Signatures within and Around Floating Tonga-Fiji Pumice Rafts Using MODIS, VIIRS, and OLCI Satellite Sensors. *Remote Sensing* 13, 501. doi:10.3390/rs13030501

Wilcock, W. S. D., Tolstoy, M., Waldhauser, F., Garcia, C., Tan, Y. J., Bohnenstiehl, D. R., et al. (2016). Seismic Constraints on Caldera Dynamics from the 2015 Axial Seamount Eruption. *Science* 354, 1395–1399. doi:10.1126/science.aah5563

Wright, R., Flynn, L. P., Garbeil, H., Harris, A. J. L., and Pilger, E. (2004). Modvolc: Near-Real-Time Thermal Monitoring of Global Volcanism. *J. Volcanology Geothermal Res.* 135, 29–49. doi:10.1016/j.jvolgeores.2003.12.008

Yoshida, K., Tamura, Y., Sato, T., Hanyu, T., Usui, Y., Chang, Q., et al. (2022). Variety of the Drift Pumice Clasts from the 2021 Fukutoku-Oka-no-Ba Eruption, Japan. *Isl. Arc* 31. doi:10.1111/iar.12441

Conflict of Interest: The authors declare that the research was conducted in the absence of any commercial or financial relationships that could be construed as a potential conflict of interest.

frontiers | Frontiers in Earth Science

TYPE Original Research
PUBLISHED 03 October 2022
DOI 10.3389/feart.2022.983112

Experimental constraints on the stability and oscillation of water vapor film—a precursor for phreatomagmatic and explosive submarine eruptions

Ingo Sonder[1]* and Pranabendu Moitra[2]

[1]Center for Geohazards Studies, Department of Geology, University at Buffalo, Buffalo, NY, United States, [2]Department of Geosciences, University of Arizona, Tucson, AZ, United States

OPEN ACCESS

EDITED BY
Tobias Dürig,
University of Iceland, Iceland

REVIEWED BY
Karoly Nemeth,
Massey University, New Zealand
Arran Peter Murch,
National Museum of Nature and Science, Japan
Pierfrancesco Dellino,
University of Bari Aldo Moro, Italy

*CORRESPONDENCE
Ingo Sonder,
ingomark@buffalo.edu

SPECIALTY SECTION
This article was submitted to Volcanology,
a section of the journal
Frontiers in Earth Science

RECEIVED 30 June 2022
ACCEPTED 12 September 2022
PUBLISHED 03 October 2022

CITATION
Sonder I and Moitra P (2022), Experimental constraints on the stability and oscillation of water vapor film—a precursor for phreatomagmatic and explosive submarine eruptions.
Front. Earth Sci. 10:983112.
doi: 10.3389/feart.2022.983112

Pre-mixing of magma and external water plays a key role in driving explosive phreatomagmatic and submarine volcanic eruptions. A thin film of water vapor forms at the magma–water interface as soon as hot magma comes in direct contact with the cold water (Leidenfrost effect). The presence of a stable vapor film drives efficient mixing and mingling between magma and water, as well as magma and wet and water-saturated sediments. Such mixing occurs before explosive molten fuel–coolant type interactions. Using high-temperature laboratory experiments, we investigate the effect of magma and water temperatures on the stability of vapor film, which has not been performed systematically for a magmatic heat source. The experiments were performed with re-melted volcanic rock material, from which spherically-shaped rock samples were produced. These samples were heated to 1,110°C and then submerged in a water pool with a constant temperature (3–93°C). The experiments were recorded on video, and, synchronously, sample and water temperatures were measured using thermocouples. The time-dependent thickness of the vapor film was measured from the video material. The vapor film tends to oscillate with time on the order of 10^2 Hz. We find that the vertical collapse rates of vapor films along the sample–water interfaces are $13.7\,\mathrm{mm\,s^{-1}}$ and $4.2\,\mathrm{mm\,s^{-1}}$ for water temperatures of 3.0°C and 65°C, respectively. For a given initial sample temperature, the thickness and stability time scales decrease with decreasing water temperature, which has implications for the efficiency of pre-mixing required for explosive eruptions. Using thermodynamics and previously measured material parameters, it is shown that a sudden collapse of the vapor film can start brittle fragmentation of the melt and thus serves as the starting point of thermohydraulic explosions.

KEYWORDS

magma–water interaction, vapor film, film boiling, Leidenfrost effect, phreatomagmatic, submarine volcanic eruptions, thermohydraulic explosion

1 Introduction

Energetic interaction between magma and ground water results in explosive phreatomagmatic eruptions. Magma, in phreatomagmatic eruptions, either directly interacts with ground water or mingles with ground water-laden crystal rocks or sediments (McBirney, 1963; Kokelaar, 1986; White, 1996; Zimanowski, 1998; Zimanowski and Büttner, 2003; Soule et al., 2006; White and Ross, 2011; Valentine and White, 2012; Graettinger et al., 2013; Wohletz et al., 2013; Houghton et al., 2015; Liu et al., 2015; van Otterloo et al., 2015; Fitch et al., 2017; Sonder et al., 2018). Such energetic interactions between magma and water are also common under planetary environments (Wilson and Head, 2004; Hamilton et al., 2011; Moitra et al., 2021). During submarine eruptions, magma comes in direct contact with seawater and causes explosive and non-explosive styles of eruption (Allen et al., 2008; Chadwick et al., 2008; Sonder et al., 2011; Schipper et al., 2013; Fauria and Manga, 2018; Manga et al., 2018; Dürig et al., 2020; Murch et al., 2020; Cahalan and Dufek, 2021). In explosive scenarios, heat transfer from magma to water is rapid and causes brittle fragmentation of larger amounts of magma in a short time, an overall very explosive process termed molten fuel coolant interaction (MFCI, Németh and Kósik, 2020; Zimanowski et al., 1997a). Therefore, understanding the dynamics of interaction between magma and water is key to better assessing hazards associated with the resulting explosive volcanic eruptions.

When magma comes in direct contact with water, the high temperature difference causes evaporation of water in the direct vicinity of the interface, forming a thin film there. The phenomenon is not limited to magma–water heat transfer, but is considered a general phenomenon of heat transfer to water and other substances at high temperature drops and is also known as the "Leidenfrost effect" (Leidenfrost, 1966; Dhir, 1998; Incropera et al., 2007). As magma cools, the vapor film collapses. In its place, numerous steam bubbles form at the magma–water interface, transitioning from a film-boiling regime to a nucleate-boiling regime. The source temperature at which this collapse takes place is called a Leidenfrost point (Incropera et al., 2007). The Leidenfrost temperature and the extent of heat flux from magma to water also depend on the water temperature, with heat flux increasing with decreasing water temperature (Moitra et al., 2020).

The formation of a vapor film is thought to be a key phenomenon that results in energetic magma–water interaction (Wohletz et al., 2013, and references therein). The explosive interaction of magma and water, termed molten fuel–coolant interaction (MFCI) or also thermohydraulic explosion (Büttner and Zimanowski, 1998), relies on a pre-mixing stage before an explosion in which magma and liquid water mingle (for the highest explosivity into cm-sized water domains trapped inside the melt). Mixing liquids as different as magma and water is only possible in a limited time window. The Leidenfrost effect enables a vapor film to exist at such temperatures, and it limits the heat flux from melt to water as long as the melt temperature at the interface is above the Leidenfrost point (Moitra et al., 2020). The quasi-stable nature of the vapor film is also relevant since it can collapse rapidly if a small but steep pressure pulse passes through the film (Fletcher, 1995; Büttner and Zimanowski, 1998; Zimanowski et al., 2015). In that case, heat transfer increases rapidly, and if the collapse area is large enough, the melt breaks instantaneously before vapor is produced (Zimanowski et al., 1997b) due to thermal expansion of the water side and contraction of the melt side imposing high pressure across the interface, which initiates the explosion. Peperites are viewed as non-exploded relics of such mixing between magma and wet sediments (Skilling et al., 2002). To a somewhat lesser extent, film boiling states also play a role in non-explosive magma–water interaction, such as the thermal granulation of magma into small- and medium-sized particles. There, the film's lifetime influences the average heat transfer rates, cooling rates, and produced particles (Schmid et al., 2010; Sonder et al., 2011).

Vapor film lifetime and stability were measured at metallic and other heat sources (Dhir, 1998; Vakarelski et al., 2012). On a magmatic heat source, film boiling was observed and described (Sonder et al., 2011; Schipper et al., 2013), but was not systematically investigated at varying water temperatures. In this study, we investigated the dynamics of the film boiling regime as magma comes in direct contact with water. We performed high temperature laboratory experiments with remelted rocks to investigate the film boiling regime due to the interaction between magmatic materials and water. Using the empirical results, we evaluated the stability and oscillatory behavior of the vapor of the film that has implications for explosive volcanic eruptions.

2 Laboratory experiments

2.1 Experimental methods

The magma–water interaction experiments in this study are modified versions of the heat transfer experiments in Moitra et al. (2020). Here, we explore vapor film thickness and collapse rates, which were not quantified before. The experiments were performed in two steps: 1) sample preparation and 2) experiments in the film boiling regime, which are described as follows.

2.1.1 Sample preparation

We first prepared spherical samples of about 3 cm diameter from remelted mafic rocks. The rocks were acquired from a quarry in Texas and have low silica content (Table 1 and Sonder et al. (2018)). After working with a few different rock types, we used this low-Si rock as it was readily available and the material

TABLE 1 Oxides of major elements in the source rock, measured on volatile-free basis, as initially published by Sonder et al. (2018).

Oxides	SiO_2	TiO_2	Al_2O_3	FeO	MnO	MgO	CaO	Na_2O_3	K_2O	P_2O_5
wt%	38.03	3.79	9.81	12.20	0.20	15.22	12.61	3.05	1.19	0.83

was homogeneous. The material has a relatively low viscosity, which made it possible to cast a cm-sized sample. Centimeter-sized rock chips were melted in an argon-purged furnace and then were poured into an insulated spherical stainless steel mold. The spherical shape was chosen for consistent sample production and to allow for similar heat transfer conditions across the magma–water interface. Sharp corners, for example, such as those in cuboides, cool more rapidly than the main body. The spherical symmetry allows for better separate effects of geometry from the physical process. The sample shape is also convenient for building a model framework to quantify magmatic heat transfer rates (Moitra et al., 2018; Moitra et al., 2020). While casting the melt, a thin and hollow alumina tube was placed inside each sample through which later, for the heat transfer experiment, a thermocouple was inserted to measure the change in sample temperature. Each sample had a small tail with a negligible effect on heat transfer (Moitra et al., 2018). This small tail was used to hold the sample during the heat transfer experiment. After pouring and inserting the alumina tube, the sample was cooled under an insulated chamber to prevent any quench-induced fracturing. After solidification, the spherical molds were carefully removed from the samples.

To prepare a sample, several physical processes have to be balanced: 1) thermally induced stress, caused by rapid cooling which leads to large temperature gradients, can lead to crack formation ("thermal shock"); therefore, the cooling rate after casting the melt into the mold has to be low enough. 2) When cooling is too slow the melt contact with the steel mold becomes too adhesive and the sample breaks after cooling when the mold is removed. 3) If the initial temperature of the steel mold is too high, the mold's diameter will decrease more than that of the sample when the temperature drops. Since the thermal expansion of steel is much higher than that of any igneous material, the mold can eventually break the sample.

It was found that the right amount of heat applied to the steel mold in combination with the right cooling rate and the relatively low melt viscosity can balance these contradicting processes to create the samples. The result is the previously described approximate sphere. The surface texture is not quenched, but microcrystalline, and the porosity is less than 3%.

2.1.2 Experiments in film boiling regime

During the experiment, a sample was heated to 1,110°C in an argon-purged furnace and kept at this temperature for several hours. To ensure constant temperature, a thermocouple was inserted into the sample through the alumina tube before placing the sample assembly inside the furnace. When ready, the sample was taken quickly from the furnace and submerged in distilled water (Figure 1). The water pool was prepared in a 30 cm × 30 cm plexiglass tank and was about 15 cm deep so that the dimensions were much greater than the sample size of about 3 cm in diameter. To determine vapor film behavior at different degrees of subcooling, the experiments were performed at different water pool temperatures ranging from 3 to 93°C. Both water pool and sample temperatures were recorded at 100 Hz. Experiments were recorded by different cameras: two Sony™ FDR-AX100 were used from two different angles, one was recorded with 1,920 px × 1,080 px at 59.94 fps and the other was recorded with 1,280 px × 720 px at 119.88 fps. Two of the experiments were also recorded with a high-speed camera (pco. 1,200 hs) at 978 fps.

2.2 Data analysis

To measure the vapor film location, thickness, and direct melt-water contact area, video material was split into separate frames and then manually marked up in the ImageJ program (Schindelin et al., 2012). Polygons were drawn outlining regions of interest. To handle the resulting lists of image coordinates efficiently, an ImageJ plugin was written that allows to store all the drawn polygons of a video in a single JSON (JavaScript Object Notation) formatted text file. This file was read by Python scripts for further analysis.

A video record has to meet three main requirements to enable the data analysis described as follows. 1) The shutter

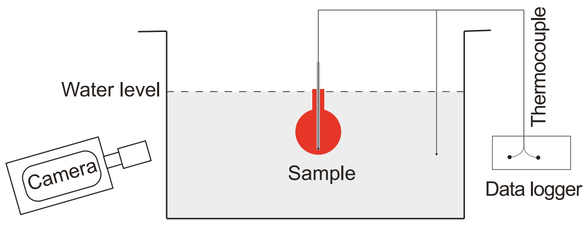

FIGURE 1
Schematic diagram showing the experimental set-up (not to scale). A spherical sample of magma, initially at 1,110°C, is submerged in a Plexiglas tank filled with distilled water, where thermocouples and data logger record the temperature data of the sample and the water, and the cameras record the experiment.

speed of the camera has to be short enough so that the rapid film oscillations do not completely blur regions of interest. 2) Spacial image resolution has to be high enough so that the film's thickness measures at least a couple of pixels on the camera sensor. 3) The video recording has to include at least one frame in which the sample is visibly in direct contact with water (no film boiling present) so that the sample size can be measured accurately. This is because even though the vapor film is transparent, the refraction index of vapor is different from that of liquid water such that the sample, including its boundaries, behind the film appears distorted (Figure 2).

To measure film thickness in each analyzed video frame, a polygon outlining the outside of the vapor film was drawn (Figure 2). The use of the lower frame rate video has the advantage of higher image resolution and a continuous video stream through the complete boiling regime. In the end, the sample is visible without film boiling or distorting vapor bubbles. Then, it is possible to measure the sample size precisely from the same camera perspective as the film boiling is measured. The high-speed records only allowed to record less than 4 s, and the sample without film or bubble at the interface is not available.

Vertical dependencies for film thickness and direct contact area were measured by splitting the drawn polygons into segments according to their vertical (y) coordinate. For a total of 10 vertical and equidistant bands, the polygons were split into nine segments on either side of the sample, corresponding to the nine upper bands plus one bottom segment connecting the two sides, resulting in 19 sub-polygons which, when concatenated, reproduce the original polygon (see also Figure 2B).

2.2.1 Film thickness

The vapor film thickness was determined as the average distance between the two polygons outlining the sample and the film's outer boundary. The thickness can be retrieved directly from the two-dimensional video material because the observed boundaries are parallel to the camera's sensor and 2D geometry is sufficient to treat the problem.

An arbitrary simple curve S without loops may be approximated by a polygon represented as a sequence of N Cartesian coordinate pairs, $\boldsymbol{s}_i$, which are connected by straight lines. Here, i is a running integer $\in [1, N]$. An arbitrary point on S is accessible using the segment number i and a parameter u that scales the connection vector between points $\boldsymbol{s}_i$ and $\boldsymbol{s}_{i+1}$:

$$\boldsymbol{s}_i(u) = \boldsymbol{s}_i + u\,(\boldsymbol{s}_{i+1} - \boldsymbol{s}_i), \quad u \in [0, 1]. \tag{1}$$

The minimum distance $\delta_i(\boldsymbol{r})$ of an arbitrary point $\boldsymbol{r} = (x, y)$ to the ith polygon segment is given by minimizing the absolute value of the difference

$$\frac{d}{du}\left|\boldsymbol{r} - \boldsymbol{s}_i(u)\right|^2 = 0, \tag{2}$$

which requires that

$$u_{S,\min}(\boldsymbol{r}) = \frac{\left(s_{i+1,x} - s_{i,x}\right)\left(x - s_{i,x}\right) + \left(s_{i+1,y} - s_{i,y}\right)\left(y - s_{i,y}\right)}{\left(s_{i+1,x} - s_{i,x}\right)^2 + \left(s_{i+1,y} - s_{i,y}\right)^2}. \tag{3}$$

If u determined that way is larger 1, the point closest to $\boldsymbol{r}$ lies outside the segment; but since the direction of a straight line does not change, the closest point within the segment is then $\boldsymbol{s}_i(1)$, that is, $\boldsymbol{s}_{i+1}$. Similarly, if $u < 0$ the closest point within the ith segment

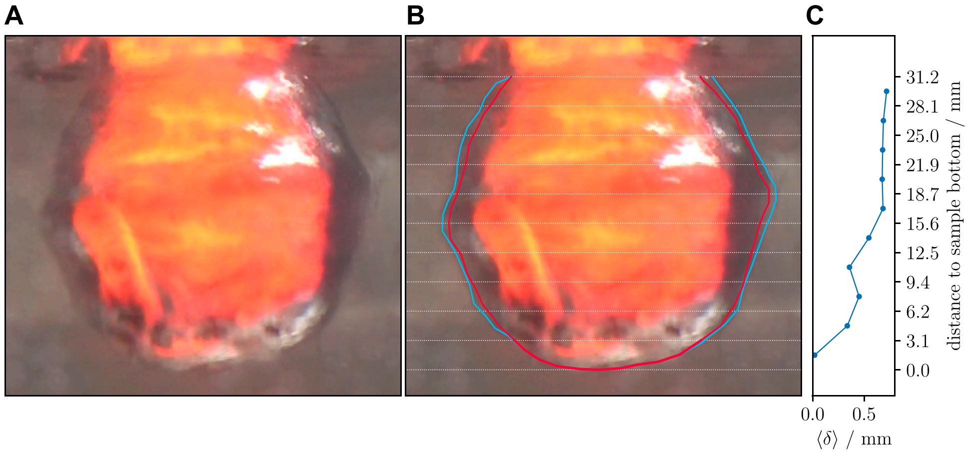

FIGURE 2
Film boiling example at 65°C pool water temperature. **(A)** Film boiling at T_w = 65°C, 0.25 s after initial water contact. Large parts of the sample are covered by the vapor film. Toward the sample bottom, there are smaller areas where the film becomes unstable. **(B)** Same video frame as **(A)** with added markup used to measure film thickness. The red polygon is the sample outline, determined after heat transfer (in the same video record). The blue polygon is the outline of the vapor film. White lines mark the 10 segments in which the film thickness was averaged. **(C)** Measured vapor film thickness, ⟨δ⟩, averaged for each of the 10 vertical segments. Broadly speaking, film thickness increases with distance from the sample bottom. In the particular frame shown, thickness has negligible values at the sample bottom and has its maximum of 0.72 mm at the top.

is $\boldsymbol{s}_i(0) = \boldsymbol{s}_i$. The absolute minimum distance of point $\boldsymbol{r}$ from S can be determined by computing u from Equation 3 for all segments, determining the distance for those u, and selecting the minimum.

$$\delta_{S,\min}(\boldsymbol{r}) = \min\left(\left|\boldsymbol{r} - \boldsymbol{s}_i\left(u_{S,\min}(\boldsymbol{r})\right)\right|\right) \quad \forall\ i. \tag{4}$$

The average distance, $\langle\delta\rangle$, between two non-intersecting curves S and F (F is approximated by a polygon of M points $\boldsymbol{f}_k$) can be determined by integrating the minimal distance of each point of F (Equation 4) to S, $\delta_{S,\min}(\boldsymbol{f}_k)$, and dividing by the length of F:

$$\langle\delta\rangle = \frac{1}{L}\int_0^L \delta_{S,\min}\left(\boldsymbol{f}_k(u)\right) dl. \tag{5}$$

Here, L is the total length of F, the sum of lengths of the $M - 1$ connection vectors

$$L = \sum_{k=1}^{M-1}\left|\boldsymbol{f}_{k+1} - \boldsymbol{f}_k\right| = \sum_{k=1}^{M-1} L_k. \tag{6}$$

Integration can be split into the individual line segments of F

$$\begin{aligned}\langle\delta\rangle &= \frac{1}{L}\sum_{k=1}^{M-1}\int_0^1 \delta_{S,\min}\left(\boldsymbol{f}_k(u)\right) L_k\, du \\ &= \frac{1}{L}\sum_{k=1}^{M-1} L_k \int_0^1 \min\left(\left|\boldsymbol{f}_k(u) - \boldsymbol{s}_i\left(u_{S,\min}\left(\boldsymbol{f}_k(u)\right)\right)\right|\right) du. \end{aligned} \tag{7}$$

This is a form that can be implemented in a fairly straightforward way. The remaining integral was evaluated with the trapezoidal rule.

As described earlier, each of the raw polygons was split into 19 parts. Pairs of parts were built that belong to the same vertical band and same sample side, one describing the sample surface and the other the film. Averaged distances between those pairs were interpreted as the average film thickness in this y-band. Even though it makes no principal difference, for this analysis, polygon parts describing the sample surface were defined as S, whereas parts describing the film boundary were defined as F. That means the film's polygon parts were used for integration.

2.2.2 Direct contact area

Areas of the sample surface where the vapor film had collapsed were outlined with polygons. Direct sample–water contact can be identified by a slightly higher color contrast of the sample surface and by a relatively undisturbed view of the surface details. It typically occurs at a small distance from the boundary of the area of the sample which is hot enough to appear in red or orange color on the video and is always covered by the vapor film (see Figure 3A; Supplementary Videos S1, S3, S4 and S5; and the archived source video material in Sonder and Moitra (2022)).

Each analyzed video frame can contain more than one such closed polygon (Figure 3B). To track the vertical dependency, vertices to each pixel of a frame were created, and for each vertex, it was determined if it is contained by one of the polygons or not. Then, the polygon-contained vertices were associated with one of the y-segments, depending on their vertical coordinate (Figure 3D). The total direct contact area of a y-segment, A_{direct}, is then the number of pixels fulfilling these conditions multiplied by the area of one square pixel, which is the square of the image resolution. Each pixel is assumed to be either fully inside or fully outside a polygon. For many pixels, their number is a good measure of the total area they represent. Here, typical areas measured this way are of the order of 10^3 px^2 to 10^4 px^2.

A scalable definition of vapor film collapse cannot be given as an absolute area. Therefore, the relative direct contact area, the ratio $A_{\text{direct}}/A_{\text{ref}}$, can be used, where the reference area, A_{ref}, is the sample's surface area (in each y-segment). As a criterion that the vapor film has collapsed, the following analysis assumes 90% direct contact, that is, $A_{\text{direct}}/A_{\text{ref}} \geq 0.9$.

3 Results

3.1 Qualitative observations

The experimental videos show that a thin film of water vapor forms instantaneously as soon as the hot sample is submerged in water. The film tends to oscillate over time as the sample cools and retreats, starting at the bottom and moving to the top of the sample, at any given water temperature. Parts of the sample surface which are covered by the vapor film stay hot longer than those parts in direct liquid water contact. This can be seen from the red radiation ("glow") of the sample, which only occurs at high temperatures and which is only observed under the vapor film. As the film retreats, quench-induced dendritic cooling patterns were observed on the surface of the samples. The thickness of the film, from qualitative observations, decreases overall with decreasing water temperature. The film is thickest at 93°C water temperature, and it is the thinnest at 3°C water temperature (see Section 3.2).

Visually, the shape of the vapor film is most stable at 65°C water temperature, even though the thickness of the film is relatively small (~ 0.5 mm) as compared to the higher water temperature experiment (~ 0.5 cm). At 3°C, the vapor film forms only at the lower part of the sample and collapses within fractions of a second. At 93°C water temperature, the film is relatively thick but remains highly unsteady for the duration of its stability. However, at 65°C, the film is more quiescently present, making the measurement of film thickness possible.

3.2 Film thickness

Film thickness could only be measured for the T = 65°C experiment. In the 3°C experiment, the thickness was below the measurable threshold of one camera pixel (px) from the beginning. At 93°C, water temperature thickness often approaches values similar to the sample radius, but then rapidly collapses. Even though the camera shutter is fast

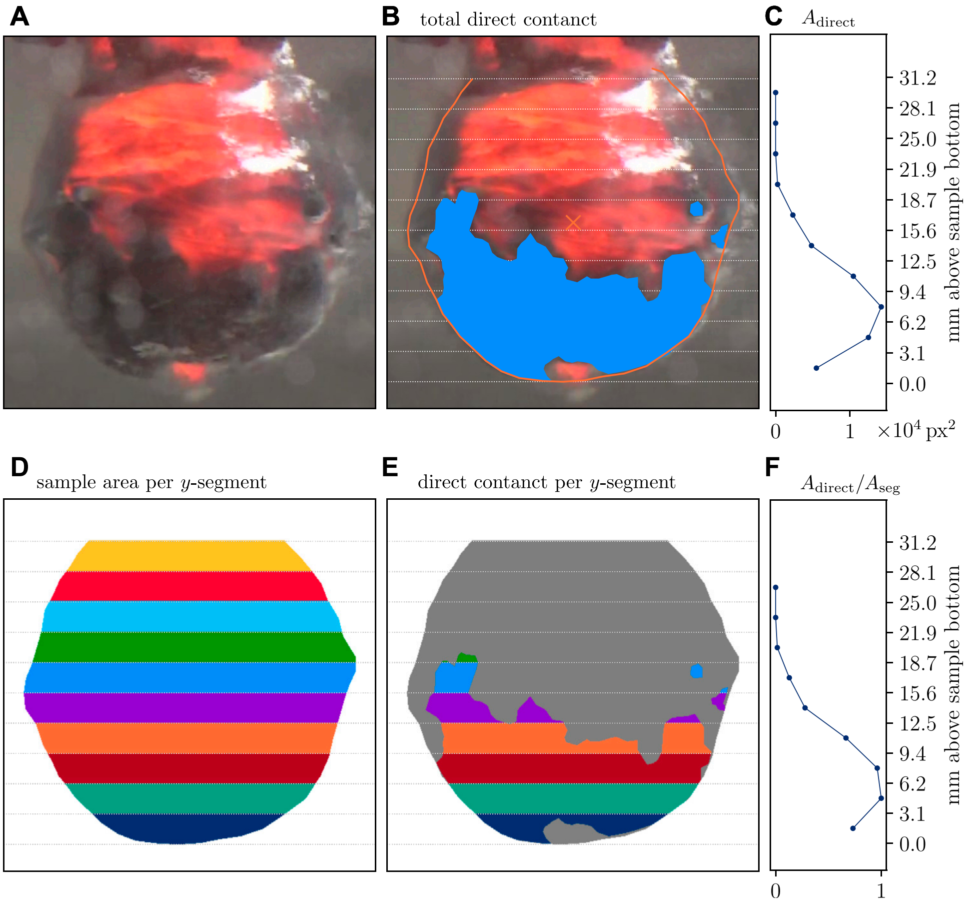

FIGURE 3
Area-based tracking of direct melt–water contact. Analysis of one frame of the $T_w = 65$°C run is shown. **(A)** Blank frame without marked areas for comparison. The translucent gray circular patches are caused by condensing water at the outside of the water container wall. **(B)** Three polygons outlining the direct contact area. **(C)** Vertical dependency of direct contact. **(D)** Area of the projected sample colored by the y-segments (A_{seg}). **(E)** Direct contact area (A_{direct}) of this frame. Gray background is the film-covered sample. **(F)** The ratio of areas colored in **(D)** and **(E)** is the relative direct contact area $A_{\mathrm{rel}} = A_{\mathrm{direct}}/A_{\mathrm{seg}}$. The bottom part of the sample has higher amounts of direct contact. The lower value of A_{rel} in the lowest segment is likely caused by a small crack at the sample's bottom, which produced local film boiling over an extended period.

enough to suppress motion blur, the frame rate was not high enough to clearly observe the oscillation's amplitudes.

At 65°C, the overall behavior is that thickness increases with vertical distance from the sample bottom; and thickness decreases over time. The data for the lower sample half roughly follow an exponential decay

$$\langle \delta \rangle = \delta_0 \, e^{-t/t_{0,i}}, \tag{8}$$

where $i = 1, 2, \ldots$ refers to the ith y-segment, starting at the sample bottom and relates to the vertical distance by

$$y = (i - 1/2)\, \Delta y. \tag{9}$$

Values for Δy are listed in Table 2. A fit of Equation 8 to the lower sample half ($i = 1 \ldots 5$) shows increasing values for time constants, $t_{0,i}$, with vertical distance i (Figure 4). The average and extrapolated value

TABLE 2 Data on experimental setup and conditions. T_0: initial sample temperature. T_w: initial water pool temperature. Sample diameter: the characteristic size from which the spatial resolution was determined (camera pixels were converted to length). Errors associated with measuring sample radius, T_w, and T_0, were within ± 0.5 mm, ± 0.5 K, and ± 2 K, respectively. Δy: height of one of the 10 y-segments.

run	Sample			Video		Δy
	T_w °C	T_0 °C	Diameter mm	Spatial res. mm/px	Frame rate frames/s	mm
1	65	1,110	34.10	0.0768	59.94	3.125
2	3.0	1,110	34.0	0.0798	119.88	3.105
3	93	1,110	33.60	0.142	119.88	3.088

TABLE 3 Material properties of water and a magmatic melt that were used to calculate Δp (Equation 16). Water properties were derived with help of the IAPWS steam tables (Huber et al., 2012). Melt properties were taken from three different publications: ρ, c_p, k from Moitra et al. (2018), α_p from Büttner et al. (1998) and β_T from Kuryaeva and Kirkinskii (1997).

Property	Value		Unit
	water	*melt*	
c_p	4.2×10^3	1.2×10^3	J kg^{-1}K^{-1}
ρ	0.98×10^3	2.95×10^3	kg m^{-3}
k	0.675	2.0	W m^{-1} K^{-1}
α_p	7×10^{-4}	8.3×10^{-5}	K^{-1}
β_T	4.5×10^{-10}	2.5×10^{-11}	Pa^{-1}

for the initial thickness, δ_0, for all y-segments is $\delta_0 = 2.05$ mm. It became clear during the analysis that the thickness decreases to a lower limit which cannot be resolved by the video material. However, the same material shows that the film then still exists for a while longer. We set the lower threshold for the film thickness to about 1 px (ca. 0.07 mm). Over time, thickness drops below this threshold starting from the sample bottom upwards. The speed at which the lower thickness threshold was approached was ca. 20 mm s^{-1} (Figure 8).

3.3 Direct contact area

Following the decrease of the film's thickness with some delay, direct contact starts to grow from the sample bottom upwards. The time dependency of the relative direct contact area $A_{\text{rel}} = A_{\text{direct}}/A_{\text{ref}}$ follows a smoothed step function starting from 0 and gradually growing to 1 (Figure 5). Comparing the time axes of $T_{\text{w}} = 3^{\circ}$C and 65°C cases shows that in the former case, film collapse is roughly a factor 5 faster than the latter (Figures 5A–D, respectively).

In contrast to the thickness measurements, the detection of the existence of film boiling was successful in all three experiments. The most difficult case was for $T_{\text{w}} = 93^{\circ}$C, where the strong film oscillations obstructed straightforward measurement as in the other two experiments. For this case, instead of continuous tracking of A_{direct}, the largest values of A_{direct} were measured, and the corresponding film lifetime values, therefore, represent minimum estimates.

The shape of this time dependency is best approximated by a function of the form

$$A_{\text{rel}}(t) = 1 - e^{-\left(\frac{t-t_1}{t_2}\right)^2}. \tag{10}$$

Here, t_1 and t_2 are two positive fit parameters, describing a constant shift on the time axis and the width (and maximal slope) of the step, respectively. As this function approaches 1 asymptotically, we assume 90 percentile direct contact for the film collapse condition, that is, $A_{\text{rel}}(t_{\text{coll}}) = 0.9$. Solving Equation 10 for collapse time t_{coll} yields for the 90 percentile area-based film lifetime

$$t_{\text{coll},90} = t_1 - t_2\sqrt{\ln 10}. \tag{11}$$

For $T_{\text{w}} = 3^{\circ}$C, there is no measurable delay between the lowest three vertical segments ($y \leq 9.3$ mm). Only the fourth segment shows a short delay (Figure 6). The lifetime for this temperature lies between 0.13 and 0.16 s. A very rough estimate for the vertical collapse speed of ca. 180 mm s^{-1} can be given.

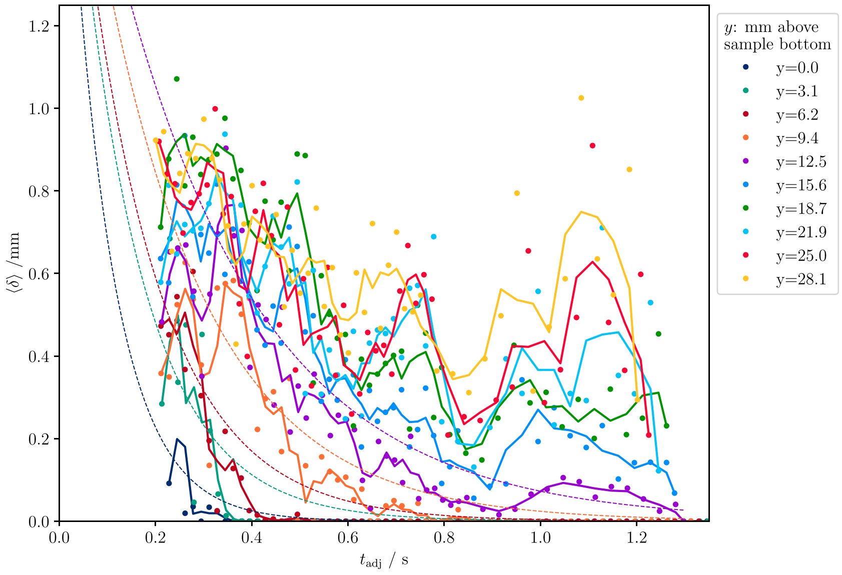

FIGURE 4
Average film thickness for each vertical segment of the $T = 65^{\circ}$C experiment. Dots show measured thicknesses. Solid lines show a moving average of three samples, and the dashed lines show a fit of an exponential (Equation 8) to the lowest five segments (lower half of the sample). Film thickness increases with distance from the sample bottom. Segments in the upper sample half show larger oscillations than the lower half.

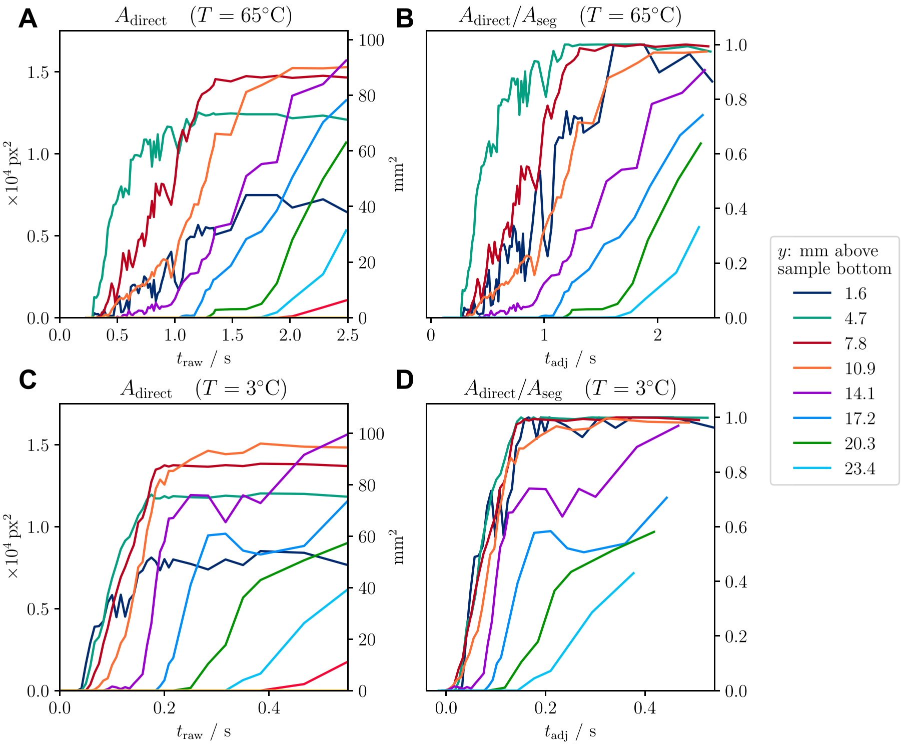

FIGURE 5
Measured direct contact area against time in each of the vertical segments. **(A)** and **(B)** show data of the T = 65°C experiment, and **(C)** and **(D)**, data of the T = 3°C experiment. The center of each segment is given in the legend. Timescales of both experiments show that film collapse occurs roughly 5 times faster at T = 3°C than the T = 65°C case. **(A)** and **(C)**: raw direct contact time dependencies show that film collapse starts at the sample bottom and progresses vertically with time, segment by segment. For larger times, areas approach different but constant values, which correspond to the sample's segment areas (A_{seg}). **(B)** and **(D)**: relative direct contact areas for the vertical segments plotted against a time axis that was adjusted to compensate for the sample motion (t_{adj}): for each vertical segment, the time of first water contact was determined and set as 0 s. The total duration until the sample is fully submerged was 0.16 s for the 65°C experiments and 0.25 s for the 3°C experiments. Graph **(D)** shows that in the adjusted timeline, the small time delays visible in the lower segments in the raw timeline in **(C)** are not present.

At 65°C water temperature, film lifetime increases linearly from 0.78 to 2.89 s for the vertical range 4.7 mm ≤ y ≤ 17.2 mm. The film vanishes upwards at 5.6 mm s^{-1} (Figures 7, Figure 8). As mentioned earlier, the T_w = 93°C case shows massive film oscillations which are hard to interpret. Despite these instabilities, the minimum film lifetime measured here is greater than 10 s (Figure 8).

4 Discussion

The film lifetime dependency on the vertical coordinate may be explained by convection: Heat transfer from the melt effectively increases water temperature at the interface above a given point, but less effectively below due to the changes in the density of liquid water and steam when heated. As mentioned in Section 2.1.1, we use spherical-shaped samples for reproducible results and quantification of heat transfer parameters. More research is necessary to quantify the geometric dependency in order to investigate its importance relative to the many other factors relevant to magma–water interaction, such as the magma's own motion and deformation, external water flow (Moitra and Sonder, 2022), water salinity, and pressure (Gregg, 2013; Wohletz et al., 2013; Zimanowski et al., 2015).

4.1 Initiation of fragmentation in thermohydraulic explosions

The vapor film is often called "quasi-stable" because despite its remarkable stability at high temperatures, it may break down quickly if passed by a steep, but not necessarily large, pressure pulse. Previous research that recorded high-speed image material of thermohydraulic explosions showed immediate crack formation in the melt prior to steam production directly after film collapse (Zimanowski et al., 1997b). This implies that at least the start of melt fragmentation in the MFCI process is not caused by steam, but by direct liquid water to melt contact (Zimanowski, 1998). The only

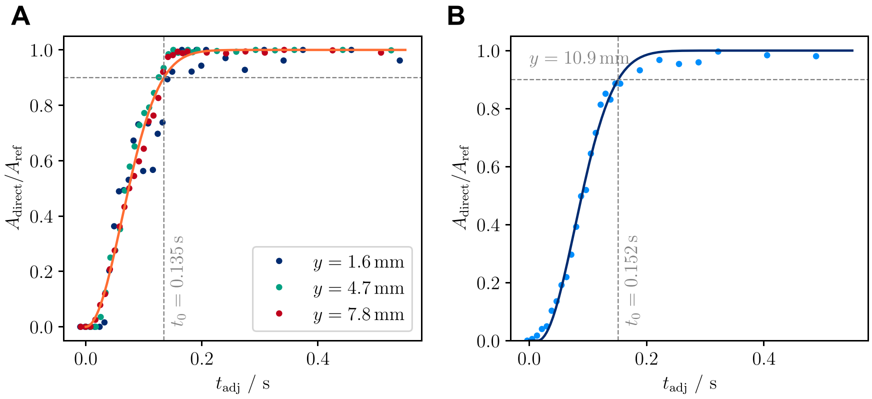

FIGURE 6
Measurement of vapor film lifetime at 3.0°C water temperature, using area-based measurements: relative direct contact area (Figures 5B,D) plotted against the sample motion-adjusted time since first contact. **(A)** Dots show the relative direct contact area of the first three y-segments for which no delay could be detected. A smeared-out step function is used to define the time window, t_0, of film collapse (at $t = t_0$ the relative direct contact area is 90%). The best fit time window is $t_0 = 0.135$ s (orange curve). **(B)** Same as **(A)**, but for the segment at $y = 10.9$°mm, the only other segment that yielded a conclusive result in this experiment. The 90% film lifetime here is 0.152 s.

remaining physical reasons for crack formation at that point in time is a thermal expansion on the colder (water) side and thermal contraction on the hot (melt) side of the two hydraulically coupled liquids.

An estimate of the pressure that this thermohydraulic coupling can create may be given by computing the integral of the pressure change with respect to temperature on either side of the magma–water interface and expressing this with material parameters. At this point of the process, by assumption, pressure and temperature change rapidly. Therefore, the pressure change with temperature of an adiabatic (constant entropy) and an isochoric (constant volume) process are calculated for two temperatures, T_1 and T_2, which will be specified later:

$$\Delta p = \int_{T_1}^{T_2} \left(\frac{\partial p}{\partial T}\right)_{S\,\mathrm{or}\,V} dT. \tag{12}$$

Section 1.1 of the Supplementary Material shows that the derivatives can be expressed by the temperature and material parameters measured at constant pressure:

$$\left(\frac{\partial p}{\partial T}\right)_S = \frac{\rho c_p}{\alpha_p T}, \tag{13}$$

$$\left(\frac{\partial p}{\partial T}\right)_V = \frac{\alpha_p}{\beta_T}. \tag{14}$$

Here ρ, c_p, α_p, and β_T, respectively, are the mass density, specific heat capacity, volumetric thermal expansion coefficient, and compressibility. The adiabatic case, in Equation 13, does not contain a compressibility term. Also, it predicts a larger pressure change for a lower thermal expansion coefficient. Both of these points are counter-intuitive and arise from the constant entropy condition in which temperature change is predominantly achieved by volume change. The isochoric case, in Equation 14, follows the common intuition: pressure change increases with rising thermal expansion coefficient and decreases with rising compressibility. Therefore, in the following, an isochoric process is assumed. The constant volume case is applicable as long as acceleration dominates over velocity (here volume change). A couple of microseconds after direct contact fractures are present in the melt, and constant volume is the wrong assumption then.

In the instance of film collapse, heat transfer is only possible by conduction, since convection material has to be accelerated into motion from (approximately) rest. It should be noted that even though known for relatively slow heat transfer, heat conduction supports high heat transfer rates, if the temperature gradient is large enough. The heat equation $\partial T/\partial t = a\,\mathrm{div}\,(\mathrm{grad}\ T)$ shows that a rapid temperature change (left-hand side) means a large temperature gradient (right-hand side) without any time delay (Landau and Lifshitz, 1970). For conductive heat transfer between two materials, which are thick compared to the region of the temperature gradient, a contact temperature is given by (Incropera et al., 2007)

$$T_c = \frac{T_m j_m + T_w j_w}{j_m + j_w}. \tag{15}$$

The subscripts $_w$ and $_m$ refer to the water and melt materials, respectively. The weights j are given in terms of the thermal conductivity, k, and thermal diffusivity, a, for each material: $j = k/\sqrt{a}$.

For liquid water and melt temperatures relevant to volcanic eruptions, the contact temperature lies above 850 K and therefore

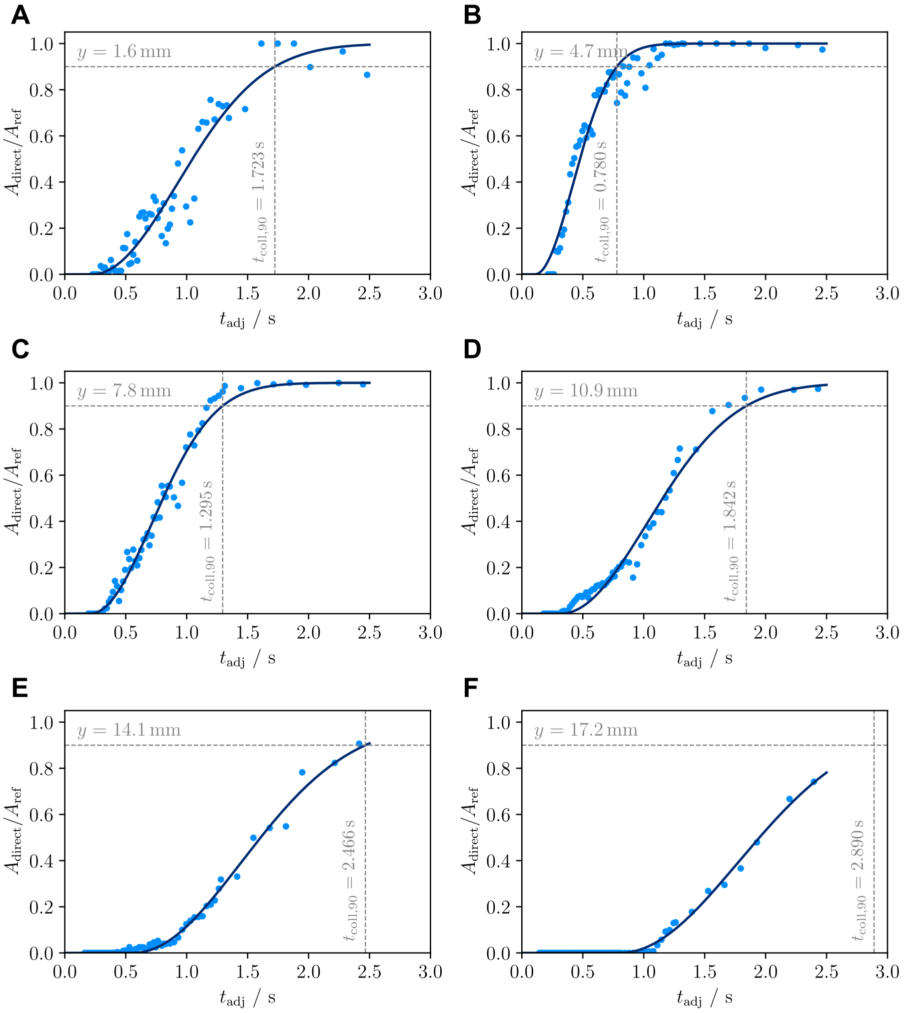

FIGURE 7
Time dependence of the relative direct contact area for the lowest six segments of the sample at T_w = 65°C (**A**: lowest, **F**: sixth lowest segment). The time axis was adjusted for the sample motion. Generally, the lifetime increases with an increase in the distance from the sample bottom. Similarly, the growth rate of direct contact (maximum slope) decreases with increasing *y*. We attribute the longer lifetime in the lowest segment to a small crack, which causes local film production over a relatively long period of time.

above the spontaneous nucleation temperature of water (max. 647 K). In the absence of many nucleation cores, when heated rapidly, liquid water may assume such superheated temperatures for a short time (Apfel, 1972). Since by assumption (and observation) water has not evaporated until crack formation, water temperature is assumed to stay below that threshold. Another research study on MFCI (Cronenberg, 1980), which is followed here, pragmatically assumes vapor formation starts at $T_N = 0.9 \times 647\ \mathrm{K} \simeq 583\ \mathrm{K}$.

With these assumptions, the integration boundaries of Equation 12, T_1 and T_2 become, respectively, for water and melt T_w, T_N and T_c, T_m; T_w and T_m are the water and melt temperature before direct contact and are now far from the interface. The pressure change in the two materials becomes

$$\begin{aligned}\Delta p_w &= \int_{T_w}^{T_N} \left(\frac{\partial p_w}{\partial T}\right)_V dT = \frac{\alpha_w}{\beta_{p,w}} (T_N - T_w)\\ \Delta p_m &= \int_{T_c}^{T_m} \left(\frac{\partial p_m}{\partial T}\right)_V dT = \frac{\alpha_m}{\beta_{p,m}} (T_m - T_c).\end{aligned} \tag{16}$$

It is noteworthy that the formulas are of the form $(T_1 - T_2)\alpha/\beta$, which is also obtained by solving the thermoelastic problem for the surface stress of a heated sphere (Kingery, 1955; Landau and Lifshitz, 1970). With melt properties as listed in Table 3 this expression yields values for Δp_w between 1.2 and 1.5 GPa for water temperatures between 4 and 90°C and melt temperatures between 1,050°C and 1,250°C (Figure 9). The pressure change in water, Δp_w, has values between 300 and 500 MPa. For

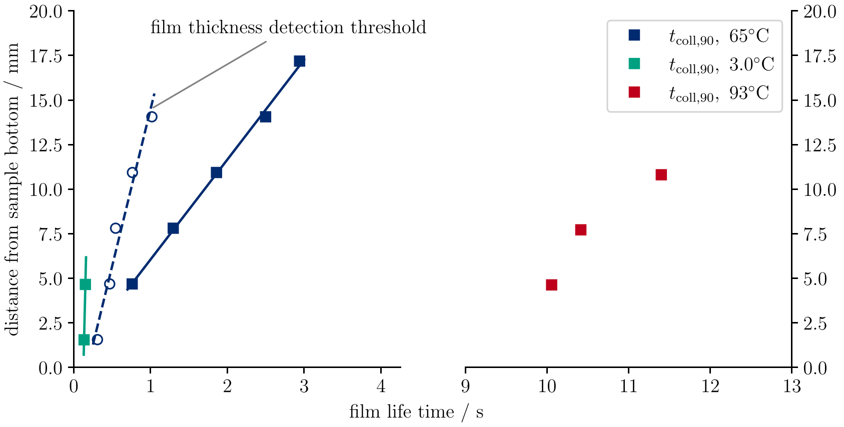

FIGURE 8
Vapor film lifetime dependence on vertical elevation above the bottom of the heat source. Squares show the film lifetime based on 90% relative direct contact area. Open circles show the 1 px (0.07 mm) film thickness detection threshold. Vertical collapse rates (slopes of the linear fits) are ca. 180 mm s^{-1} for 3.0°C and 5.6 mm s^{-1} for the 65°C experiments. For the 93°C run, the slope is not very different from 65°C; however, the measurement accuracy is low due to the oscillatory nature of the film boiling there.

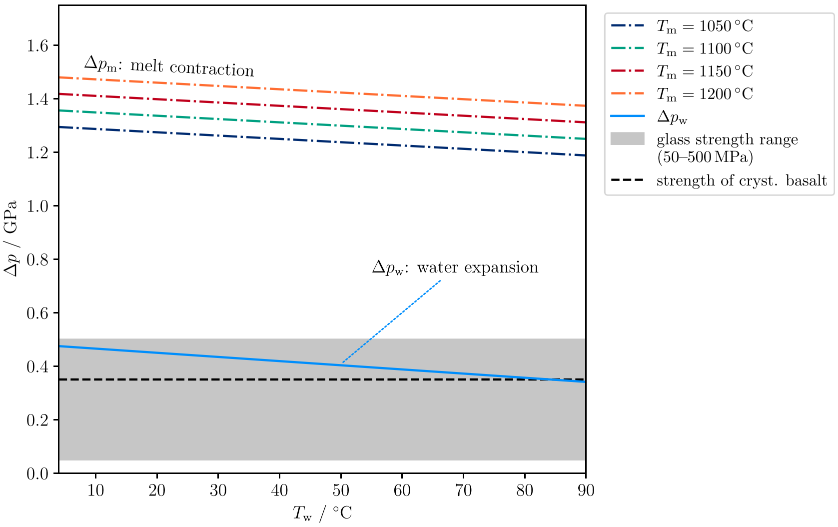

FIGURE 9
Estimate of pressure change in melt and water due to the sudden contact of the two liquid phases. Dash-dotted lines show the pressure change in the melt. The blue line shows the pressure change in the water. The gray area shows typical values for the compressive strength of glass (ca. 50–500 MPa, Brückner, 1970). The dashed black line (350 MPa) is a typical value for the compressive strength of crystalline basalt (Waltham, 2009).

comparison, estimates for the strength of glass vary in a wide range, likely between 50 and 500 MPa (Brückner, 1970). The compressive strength of crystalline basalt is of the order of 350 MPa (Waltham, 2009). This shows that the thermohydraulic shock overcomes the material strength by more than a factor of 5, and pressure changes on either side of the interface are larger than the material strength of the melt.

Clearly, some caveats in this rough estimate exist: the temperature gap in the integration between T_N and T_c is on the order of 200 K. It is clear that this temperature difference adds to the heat flux and thermal expansion, but is neglected here. Therefore, Equation 16 likely underestimates the acting pressure. The material properties are assumed to be constant. At least the heat capacity of water is known to increase in superheated states

(Lienhard, 1977), and the material strengths of silicate melts under thermal shock conditions are likely not as high as their thermally stable counterparts. Therefore, one or both of Δp_w and Δp_m is likely underestimated here, while the strength may be overestimated. The nucleation temperature of the water is typically measured at constant pressure, and its sensitivity to pressure change is unclear, and subject to surface properties, such as wetting angles and roughness (Debenedetti, 1996). Another shortcoming of this formulation is that the two systems are only "coupled" by the temperature condition. It is clear that at least the confining pressure also plays a role. Δp_w and Δp_m only describe the thermally induced stress in each material. The total pressure acting across the interface depends on the specific geometry and the resulting material acceleration. However, each of the contributions Δp_w and Δp_m is large enough to overcome the compressive strength of the melt alone.

5 Conclusion

Our experiments show that water temperature is the primary factor that determines vapor film lifetime: between water temperatures of 3 and 93°C, the lifetime increases by a factor of 85. For a given water temperature, film lifetime increases by a factor of 3 over a distance of ca. 15 mm. Such small vertical changes are easily overcome in any realistic natural scenario. Therefore, when modeling magma–water heat transfer, film boiling lifetime should only assume ambient water temperatures locally around the lowest point of the heat source. Due to the sensitivity to vertical elevation, the question is not if film lifetime is increased compared to a static scenario, but how effective other factors, such as water flow, melt motion, deformation, and fracture generation, are. Neglecting these other factors, magma in contact with cold water will effectively create its own warm water conditions some cm above the lowest contact point, which allows for film lifetimes of several seconds, possibly more than 10 s. Whether or not it is possible to borrow from heat transfer of metal-based heat sources, which are thermally highly conductive as compared to magmatic materials, remains to be investigated.

The stability of vapor film plays a key role in efficiently pre-mixing magma and water, which is required for explosive molten–fuel coolant interaction. Using high-temperature laboratory experiments, this study systematically quantifies the time scale, thickness, and spatial dependency of vapor film. While our experiments were not designed to investigate energetic interactions between magma and water, the results obtained in this study likely provide better insights into the pre-mixing conditions during phreatomagmatic and explosive submarine volcanic eruptions. The presence and duration of stable vapor film also affect the non-explosive fragmentation of lava (Schmid et al., 2010; Sonder et al., 2011). The quantification of vapor film properties for a range of magmatic and water temperatures study sheds light on the dynamics of lava–water interaction during the non-explosive fragmentation and the generation of hyaloclastites, particularly under shallow submarine conditions. This study provides a basis for future investigation into the generation and stability of vapor films in contact with magma at elevated pressure conditions suitable under deep magmatic plumbing systems and submarine eruption settings.

The thermodynamic considerations in Section 3.4 show that rapid heat conduction is realistic and able to create large enough thermal stress to overcome the melt's material strength and start fragmentation of liquid melt, emphasizing the role of film boiling in the MFCI process. The film collapse observed in our experiments was not forced by an external event, but occurred from the decreasing surface temperature of the melt sample. Therefore, the time scale of the collapse is a factor 10^5 to 10^7 larger than the estimated time scale for the initial direct liquid water to melt contact. To estimate thermal stresses as they occur in thermal granulation processes and other non-explosive situations, steady-state considerations are likely more appropriate (Kingery, 1955; Strobl et al., 2018; Moitra et al., 2020).

Data availability statement

All experimental data was compiled into a dataset and is publicly available at Zenodo (Sonder and Moitra, 2022, doi: 10.5281/zenodo.6950485). The complete code of the data analysis is available at the authors' gitlab page (gitlab.com/isonder/vaporfilm-experiments) and is further specified in the Supplementary Material.

Author contributions

IS and PM conceptualized the project. PM worked on the experimental design and IS performed the experimental data analysis presented in this study. IS wrote the first draft. IS and PM edited and finalized the manuscript.

Funding

This work is supported by US National Science Foundation (NSF) grant OCE-2113770 to Sonder and OCE-2113709 to Moitra.

Acknowledgments

The authors would like to thank the three reviewers Nemeth, Murch and Dellino, as well as the editors Dürig and Acocella for their helpful comments, which very much improved the quality of this manuscript.

Conflict of interest

The authors declare that the research was conducted in the absence of any commercial or financial relationships that could be construed as a potential conflict of interest.

Publisher's note

Supplementary material

The Supplementary Material for this article can be found online at: https://www.frontiersin.org/articles/10.3389/feart.2022.983112/full#supplementary-material

References

Allen, S., Fiske, R. S., and Cashman, K. (2008). Quenching of steam-charged pumice: Implications for submarine pyroclastic volcanism. *Earth Planet. Sci. Lett.* 274, 40–49. doi:10.1016/j.epsl.2008.06.050

Apfel, R. E. (1972). Water superheated to 279.5° C at atmospheric pressure. *Nat. Phys. Sci.* 238, 63–64. doi:10.1038/physci238063a0

Brückner, R. (1970). Properties and structure of vitreous silica. I. *J. Non-Crystalline Solids* 5, 123–175. doi:10.1016/0022-3093(70)90190-0

Büttner, R., Zimanowski, B., Blumm, J., and Hagemann, L. (1998). Thermal conductivity of a volcanic rock material (olivine-melilitite) in the temperature range between 288 and 1470 k. *J. Volcanol. Geotherm. Res.* 80, 293–302. doi:10.1016/s0377-0273(97)00050-4

Büttner, R., and Zimanowski, B. (1998). Physics of thermohydraulic explosions. *Phys. Rev. E* 57, 5726–5729. doi:10.1103/PhysRevE.57.5726

Cahalan, R., and Dufek, J. (2021). Explosive submarine eruptions: The role of condensable gas jets in underwater eruptions. *J. Geophys. Res. Solid Earth* 126, e2020JB020969. doi:10.1029/2020jb020969

Chadwick, W., Cashman, K., Embley, R., Matsumoto, H., Dziak, R., De Ronde, C., et al. (2008). Direct video and hydrophone observations of submarine explosive eruptions at nw rota-1 volcano, mariana arc. *J. Geophys. Res.* 113. doi:10.1029/2007jb005215

Cronenberg, A. W. (1980). Recent developments in the understanding of energetic molten fuel-coolant interactions. *Nucl. Saf.* 3, 319–337.

Debenedetti, P. G. (1996). Metastable liquids: Concepts and principles. *Physical chemistry*. Princeton, N.J: Princeton University Press.

Dhir, V. (1998). Boiling heat transfer. *Annu. Rev. Fluid Mech.* 30, 365–401. doi:10.1146/annurev.fluid.30.1.365

Dürig, T., White, J. D. L., Murch, A. P., Zimanowski, B., Büttner, R., Mele, D., et al. (2020). Deep-sea eruptions boosted by induced fuel–coolant explosions. *Nat. Geosci.* 13, 498–503. doi:10.1038/s41561-020-0603-4

Fauria, K. E., and Manga, M. (2018). Pyroclast cooling and saturation in water. *J. Volcanol. Geotherm. Res.* 362, 17–31. doi:10.1016/j.jvolgeores.2018.07.002

Fitch, E. P., Fagents, S. A., Thordarson, T., and Hamilton, C. W. (2017). Fragmentation mechanisms associated with explosive lava–water interactions in a lacustrine environment. *Bull. Volcanol.* 79, 12–16. doi:10.1007/s00445-016-1087-3

Fletcher, D. (1995). Steam explosion triggering: A review of theoretical and experimental investigations. *Nucl. Eng. Des.* 155, 27–36. doi:10.1016/0029-5493(94)00865-V

Graettinger, A. H., Skilling, I., McGarvie, D., and Höskuldsson, Á. (2013). Subaqueous basaltic magmatic explosions trigger phreatomagmatism: a case study from askja, Iceland. *J. Volcanol. Geotherm. Res.* 264, 17–35. doi:10.1016/j.jvolgeores.2013.08.001

Gregg, T. K. (2013). *Deep-sea eruptions*. New York: Cambridge University Press.

Hamilton, C. W., Fagents, S. A., and Thordarson, T. (2011). Lava–ground ice interactions in elysium planitia, Mars: geomorphological and geospatial analysis of the tartarus colles cone groups. *J. Geophys. Res.* 116, E03004. doi:10.1029/2010je003657

Houghton, B., White, J. D., and Van Eaton, A. R. (2015). "Phreatomagmatic and related eruption styles," in *The encyclopedia of volcanoes* (Netherlands: Elsevier), 537–552.

Huber, M. L., Perkins, R. A., Friend, D. G., Sengers, J. V., Assael, M. J., Metaxa, I. N., et al. (2012). New international formulation for the thermal conductivity of H2O. *J. Phys. Chem. Reference Data* 41, 033102. doi:10.1063/1.4738955

Incropera, F. P., DeWitt, D. P., Bergman, T. L., and Lavine, A. S. (2007). *Introduction to heat transfer*. New Jersey: John Wiley & Sons.

Kingery, W. D. (1955). Factors affecting thermal stress resistance of ceramic materials. *J. Am. Ceram. Soc.* 38, 3–15. doi:10.1111/j.1151-2916.1955.tb14545.x

Kokelaar, P. (1986). Magma-water interactions in subaqueous and emergent basaltic. *Bull. Volcanol.* 48, 275–289. doi:10.1007/bf01081756

Kuryaeva, R. G., and Kirkinskii, V. A. (1997). Influence of high pressure on the refractive index and density of tholeiite basalt glass. *Phys. Chem. Minerals* 25, 48–54. doi:10.1007/s002690050085

Landau, L. D., and Lifshitz, E. M. (1970). *Theory of elasticity of* Course of theoretical physics. second edn. Oxford: Pergamon Press.

Leidenfrost, J. G. (1966). On the fixation of water in diverse fire. *Int. J. Heat Mass Transf.* 9, 1153–1166. doi:10.1016/0017-9310(66)90111-6

Lienhard, J. H. (1977). Estimation of specific heat of superheated water. *Nucl. Sci. Eng.* 62, 302–304. doi:10.13182/NSE77-A26965

Liu, E., Cashman, K., Rust, A., and Gislason, S. (2015). The role of bubbles in generating fine ash during hydromagmatic eruptions. *Geology* 43, 239–242. doi:10.1130/g36336.1

Manga, M., Fauria, K. E., Lin, C., Mitchell, S. J., Jones, M., Conway, C. E., et al. (2018). The pumice raft-forming 2012 havre submarine eruption was effusive. *Earth Planet. Sci. Lett.* 489, 49–58. doi:10.1016/j.epsl.2018.02.025

McBirney, A. R. (1963). Factors governing the nature of submarine volcanism. *Bull. Volcanol.* 26, 455–469. doi:10.1007/bf02597304

Moitra, P., Horvath, D. G., and Andrews-Hanna, J. C. (2021). Investigating the roles of magmatic volatiles, ground ice and impact-triggering on a very recent and highly explosive volcanic eruption on Mars. *Earth Planet. Sci. Lett.* 567, 116986. doi:10.1016/j.epsl.2021.116986

Moitra, P., Sonder, I., and Valentine, G. A. (2018). Effects of size and temperature-dependent thermal conductivity on the cooling of pyroclasts in air. *Geochem. Geophys. Geosyst.* 19, 3623–3636. doi:10.1029/2018GC007510

Moitra, P., Sonder, I., and Valentine, G. A. (2020). The role of external water on rapid cooling and fragmentation of magma. *Earth Planet. Sci. Lett.* 537, 116194. doi:10.1016/j.epsl.2020.116194

Moitra, P., and Sonder, I. (2022). Vapor bubbles and velocity control on the cooling rates of lava and pyroclasts during submarine eruptions. *JGR. Solid Earth* 127, e2022JB024665. doi:10.1029/2022jb024665

Murch, A. P., White, J. D., Barreyre, T., Carey, R. J., Mundana, R., and Ikegami, F. (2020). Volcaniclastic dispersal during submarine lava effusion: the 2012 eruption of havre volcano, kermadec arc, New Zealand. *Front. Earth Sci. (Lausanne).* 8, 237. doi:10.3389/feart.2020.00237

Németh, K., and Kósik, S. (2020). Review of explosive hydrovolcanism. *Geosciences* 10, 44. doi:10.3390/geosciences10020044

Schindelin, J., Arganda-Carreras, I., Frise, E., Kaynig, V., Longair, M., Pietzsch, T., et al. (2012). Fiji: An open-source platform for biological-image analysis. *Nat. Methods* 9, 676–682. doi:10.1038/nmeth.2019

Schipper, C. I., Sonder, I., Schmid, A., White, J. D., Dürig, T., Zimanowski, B., et al. (2013). Vapour dynamics during magma–water interaction experiments: hydromagmatic origins of submarine volcaniclastic particles (limu o pele). *Geophys. J. Int.* 192, 1109–1115. doi:10.1093/gji/ggs099

Schmid, A., Sonder, I., Seegelken, R., Zimanowski, B., Büttner, R., Gudmundsson, M. T., et al. (2010). Experiments on the heat discharge at the dynamic magma-water-interface. *Geophys. Res. Lett.* 37, L20311. doi:10.1029/2010GL044963

Skilling, I. P., White, J. D., and McPhie, J. (2002). Peperite: a review of magma–sediment mingling. *J. Volcanol. Geotherm. Res.* 114, 1–17. doi:10.1016/s0377-0273(01)00278-5

Sonder, I., Harp, A. G., Graettinger, A. H., Moitra, P., Valentine, G. A., Büttner, R., et al. (2018). Meter-scale experiments on magma-water interaction. *J. Geophys. Res. Solid Earth* 123, 10597–10615. doi:10.1029/2018jb015682

Sonder, I., and Moitra, P. (2022). Vapor film lifetime at magma-water interface. doi:10.5281/ZENODO.6950485

Sonder, I., Schmid, A., Seegelken, R., Zimanowski, B., and Büttner, R. (2011). Heat source or heat sink: What dominates behavior of non-explosive magma-water interaction? *J. Geophys. Res.* 116, B09203. doi:10.1029/2011jb008280

Soule, S. A., Fornari, D. J., Perfit, M. R., Ridley, W. I., Reed, M. H., and Cann, J. R. (2006). Incorporation of seawater into mid-ocean ridge lava flows during emplacement. *Earth Planet. Sci. Lett.* 252, 289–307. doi:10.1016/j.epsl.2006.09.043

Strobl, S., Adlmann, F.-A., Supancic, P., Lube, T., Danzer, R., and Schöppl, O. (2018). Fracture toughness of silicon nitride balls via thermal shock. *J. Eur. Ceram. Soc.* 38, 1278–1287. doi:10.1016/j.jeurceramsoc.2017.11.005

Vakarelski, I. U., Patankar, N. A., Marston, J. O., Chan, D. Y., and Thoroddsen, S. T. (2012). Stabilization of leidenfrost vapour layer by textured superhydrophobic surfaces. *Nature* 489, 274–277. doi:10.1038/nature11418

Valentine, G. A., and White, J. D. (2012). Revised conceptual model for maar-diatremes: Subsurface processes, energetics, and eruptive products. *Geology* 40, 1111–1114. doi:10.1130/g33411.1

van Otterloo, J., Cas, R. A., and Scutter, C. R. (2015). The fracture behaviour of volcanic glass and relevance to quench fragmentation during formation of hyaloclastite and phreatomagmatism. *Earth-Science Rev.* 151, 79–116. doi:10.1016/j.earscirev.2015.10.003

Waltham, T. (2009). *Foundations of engineering geology*. 3rd ed edn. London ; New York: Spon Press.

White, J. D., and Ross, P.-S. (2011). Maar-diatreme volcanoes: a review. *J. Volcanol. Geotherm. Res.* 201, 1–29. doi:10.1016/j.jvolgeores.2011.01.010

White, J. (1996). Impure coolants and interaction dynamics of phreatomagmatic eruptions. *J. Volcanol. Geotherm. Res.* 74, 155–170. doi:10.1016/s0377-0273(96)00061-3

Wilson, L., and Head, J. W., III (2004). Evidence for a massive phreatomagmatic eruption in the initial stages of formation of the mangala valles outflow channel, Mars. *Geophys. Res. Lett.* 31, L15701. doi:10.1029/2004gl020322

Wohletz, K., Zimanowski, B., and Büttner, R. (2013). *Magma-water interactions*. Modeling volcanic processes. New York: Cambridge University Press, 230–257.

Zimanowski, B., and Büttner, R. (2003). "Explosive subaqueous volcanism," in *Phreatomagmatic explosions in subaqueous eruptions* (USA: American Geophysical Union Geophysical Monograph Series), 140, 51.

Zimanowski, B., Büttner, R., and Lorenz, V. (1997a). Premixing of magma and water in mfci experiments. *Bull. Volcanol.* 58, 491–495. doi:10.1007/s004450050157

Zimanowski, B., Büttner, R., and Nestler, J. (1997b). Britte reaction of a high-temperature ion melt. *Europhys. Lett.* 38, 285–290. doi:10.1209/epl/i1997-00239-3

Zimanowski, B., Dellino, P., and Büttner, R. (2015). "Magma-water interaction and phreatomagmatic fragmentation," in *The encyclopedia of volcanoes*. Editors H. Sigurdsson, B. Houghton, H. Rymer, J. Stix, and S. McNutt. Second edn (Cambridge: Academic Press), 473–484. chap. 26. doi:10.1016/B978-0-12-385938-9.00026-2

Zimanowski, B. (1998). "Phreatomagmatic explosions," in *From magma to tephra, developments in Volcanology 4*. Editors A. Freundt, and M. Rosi (Amsterdam: Elsevier), 25–54.

frontiers | Frontiers in Earth Science

TYPE Brief Research Report
PUBLISHED 05 October 2022
DOI 10.3389/feart.2022.983051

Combining hydro-acoustic sources and bathymetric differences to track the vent evolution of the Mayotte eruption, Mozambique Channel

Jean-Marie Saurel[1]*, Lise Retailleau[1,2], Christine Deplus[1], Benoît Loubrieu[3], Delphine Pierre[3], Michel Frangieh[1], Nassim Khelifi[1], Robin Bonnet[3], Valérie Ferrazzini[1,2], Sara Bazin[3], Pierre Guyavarch[3], Maryline Moulin[3], REVOSIMA Seismology group and REVOSIMA Bathymetry group

[1]Université Paris Cité, Institut de physique du globe de Paris, CNRS, Paris, France, [2]Observatoire volcanologique du Piton de la Fournaise, Institut de physique du globe de Paris, La Plaine des Câfres, Réunion, [3]University Brest, CNRS, Ifremer, Plouzane, France

EDITED BY
Tobias Dürig,
University of Iceland, Iceland

REVIEWED BY
Luis E. Lara,
Servicio Nacional de Geología y Minería de Chile, Chile
Paolo Favali,
ERIC foundation, Italy

*CORRESPONDENCE
Jean-Marie Saurel,
saurel@ipgp.fr

SPECIALTY SECTION
This article was submitted to Volcanology, a section of the journal Frontiers in Earth Science

RECEIVED 30 June 2022
ACCEPTED 23 August 2022
PUBLISHED 05 October 2022

CITATION
Saurel J-M, Retailleau L, Deplus C, Loubrieu B, Pierre D, Frangieh M, Khelifi N, Bonnet R, Ferrazzini V, Bazin S, Guyavarch P, Moulin M, REVOSIMA Seismology group, REVOSIMA Bathymetry group (2022), Combining hydro-acoustic sources and bathymetric differences to track the vent evolution of the Mayotte eruption, Mozambique Channel.
Front. Earth Sci. 10:983051.
doi: 10.3389/feart.2022.983051

The majority of Earth volcanism takes place in the deep ocean. Deep-sea volcanoes are particularly complicated to study due to their remoteness. Very different methods can be used and their combination can lead to crucial information about submarine volcanoes behavior. In Mayotte, Comoros archipelago, efforts have been made to study and monitor the deep volcanic activity (~3000 m) currently occurring east of Mayotte through various methods and campaigns on land and at sea. In October 2020, a line of 10 Ocean Bottom Seismometers was deployed during 10 days, leading to a hand-picked catalog of more than a thousand of hydro-acoustic signals, which have been associated with reactions between hot lava and deep cold ocean waters. During the same period, repeated swath bathymetry surveys were performed over an active lava flow field. We compare the time evolution of the hydro-acoustic events locations and bathymetry differences observed between each survey. While bathymetric information gives absolute location of new lava flows, hydro-acoustic events give detailed relative time variations leading to short-term spatial evolution. Bathymetric information thus provides snapshots of the eruptive area evolution at specific times, when hydro-acoustic signals show its continuous evolution. By combining both complementary analyses we are able to clearly define the detailed evolution of the lava flows pattern in the short time period of 10 days. Applied to the data already acquired on Mayotte since 2019, this method could allow us to estimate more precisely the volcano effusion rate and its evolution, giving further insights on the feeding system.

KEYWORDS

hydro-acoustic analysis, bathymetric analysis, multi-beam echo sounder, submarine eruption, Mayotte, lava flows, ocean bottom seismometer

1 Introduction

The majority of volcanism on Earth occurs underwater, under hundreds to thousands of meters of sea water. Submarine volcanoes are particularly difficult to study due to lack of access. Their activity can remain unknown because the seafloor, of which only 20% had been mapped in 2021 (GEBCO, 2021), is largely invisible and unreachable. Unless the products of the eruption get close to the surface, satellite can not be of any help.

Like volcanoes on land, submarine volcanoes generate various seismic signals that give indication about magma sources, propagation and eruptive processes (McNutt and Roman, 2015). Because submarine eruptions are often far away from land (for example, along mid-ocean ridges), common land-based monitoring means (e.g. seismicity, deformation) have limited performances due to distance. These eruptions also generate signals that propagate through the water column. A wide variety of hydro-acoustic signals emitted by active submarine volcanoes can be recorded at sea and are part of the global oceanic soundscape (Yun et al., 2021). They range from high frequency bubbling noise in shallow waters (Longo et al., 2021) to broadband explosion signals in deep waters (Haxel and Dziak, 2005; Dziak et al., 2008). Eruption can also generate long-duration low-frequency tremor (Dziak et al., 2008; Heaney et al., 2013). Such hydro-acoustic signals, generated through different processes (earthquakes, landslides, lava-water interactions, explosions), are transmitted into the water column and can be recorded in near field by Ocean Bottom Seismometers (OBS), by moored hydrophones in near and far field, or through converted T-waves by shore-based seismic stations. Tepp and Dziak (2021) showed that, since 1939, 47% of the 119 submarine eruptions reported in the literature were detected thanks to hydro-acoustics recordings around the world. 82% of those 119 eruptions were associated with land-based detections and half of these detections were based on the study of T-waves when they reach the shorelines.

Once discovered, some active submarine volcanoes are then studied with marine surveys, to confirm their existence and understand their mechanism. During these surveys, *in situ* methods are performed to observe and characterize the detected activity (e.g. with towed cameras, dredges, profiling CTDs). One of the main method is to perform repeated swath bathymetry campaigns with a multi beam echo sounder (MBES). The resulting seafloor topography maps can be compared in order to identify and constrain the extent of morphological changes (Chadwick et al., 1991; Fox et al., 1992; Caress et al., 2012; Carey et al., 2018). In volcanic contexts, negative depth changes are interpreted as collapse or landslides (Chadwick et al., 2008; Watts et al., 2012), and positive depth changes are interpreted as new volcanic material (e.g. volcaniclastic deposits, lava flows or edifices, Clague et al., 2011; Chadwick et al., 2019; Feuillet et al., 2021). When possible, underwater vehicles, autonomous - AUV or remotely operated - ROV, are used to acquire swath bathymetry with higher resolution. AUV and ROV navigate much closer to the seafloor, yielding bathymetry with ~1 m lateral resolution, but can only survey a limited surface. Ship-based MBES surveys can cover a much wider surface, but their lateral resolution is limited to tens of meters in deep waters.

Several volcanoes have been discovered and studied with these combined methods. In the early 1980s, the mapping of the Juan de Fuca ridge, off the coast of Oregon (United States of America), led to the discovery of Axial Seamount volcano (Delaney et al., 1981). Since then, this active volcano has been intensively studied. In 2006, several OBS were moored nearby and regularly recovered. Those instruments allowed the understanding of the 2011 eruption timing and the reconstruction of the precursory phase (Dziak et al., 2012). In 2014, the Ocean Observatories Initiave [OOI, (Kelley et al., 2014)] deployed a permanent cabled network of instruments around Axial Seamount, including OBS equipped with hydrophones. In 2015, an eruption and its signals were recorded in real-time by the network (Wilcock et al., 2016). The hydro-acoustic signals were located on the north rift zone, 10 km away from the main caldera. This led to a marine survey a few month later that mapped fresh lava flows with ship-based MBES. Higher resolution maps were also acquired using an AUV-based MBES. These surveys showed that lava flows were spread over 19 km along the main caldera and the north rift zone (Chadwick et al., 2016; Clague et al., 2017), and their location matched the hydro-acoustics events locations. Using both bathymetry difference maps and the hydrophone recordings, Le Saout et al. (2020) were then able to reconstruct the eruption dynamics and quantify the lava propagation rates and edifice constructions.

Similarly, in the south-west of the Pacific Ocean, the West Mata submarine volcano, part of the Mata volcanic chain is also frequently erupting and used as an underwater volcano laboratory to better document and understand deep sea eruptions. With 11 bathymetry surveys performed on site since 1996, the different morphological changes on West Mata have been mapped (Clague et al., 2011; Embley et al., 2014; Chadwick et al., 2019). In May 2009, a combination of close-distance hydrophone, *in-situ* ROV videos and ship based surveys allowed the recording and understanding of deep-sea active degassing and explosive activity (Dziak et al., 2015).

These studies showed that hydro-acoustic signals recordings combined with MBES surveys can help reconstruct eruption dynamics, which is crucial in submarine contexts where continuous visual observation is difficult to achieve.

East of Mayotte island, in the Comoros archipelago, a major eruption started in 2018, preceded by strong seismic activity in May of that year (Cesca et al., 2020; Lemoine et al., 2020). An oceanographic cruise conducted in May 2019 [Mayobs1, (Feuillet, 2019)] led to the discovery of a new volcanic edifice

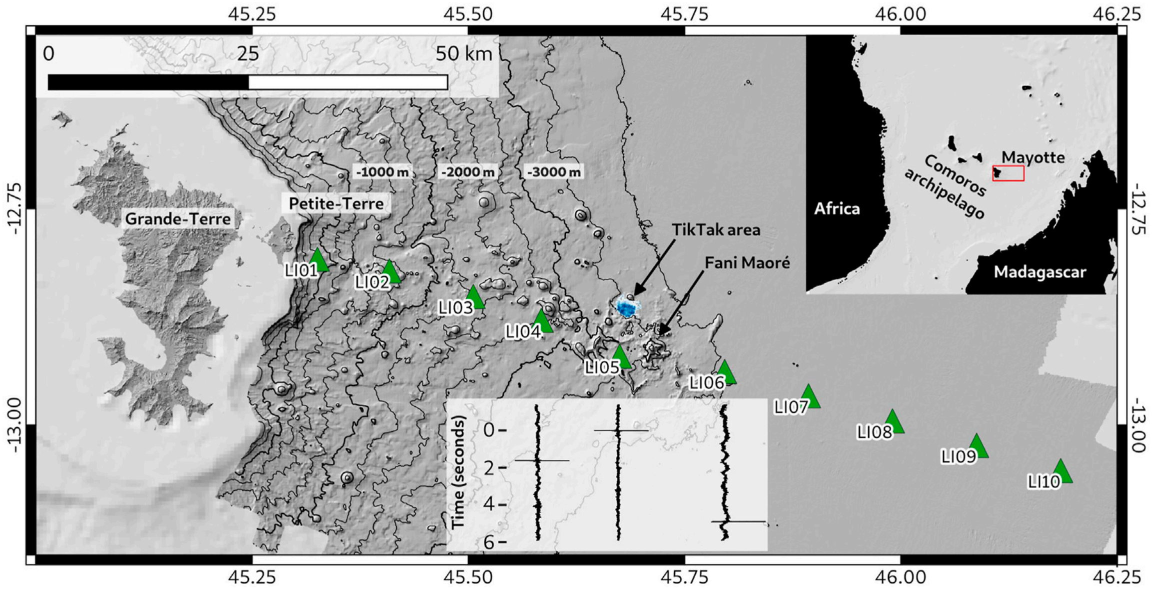

FIGURE 1
Bathymetry (Feuillet et al., 2019) of the eastern Mayotte submarine volcanic area with depth contours every 1000 m (thick contours) and 250 m (light contours). The green triangles represent the line of OBS deployed from October 7 to October 17, 2020. The new volcanic edifice (Fani Maoré) lies at the eastern tip of the volcanic chain, close to LI05. The TikTak volcanic area, active during the deployment, is shown in blue. Top right insert: regional setting of the Comoros archipelago, north of Mozambique Channel, between Africa and Madagascar. Insert below the stations: example of an hydro-acoustic event recording, synchronized with LI05 first arrival.

(named Fani Maoré) 50 km south east of the island (Feuillet et al., 2021). Many efforts are made to monitor the activity by a reinforced land network of seismic stations and oceanographic cruises (REVOSIMA, 2021), to understand the current volcanic activity as well as past activity. Amongst these methods, OBS stations are regularly installed and their data analyzed (Saurel et al., 2022). Multi-Beam Echo Sounder (MBES) measurements are also performed to study the building of the volcanic structure (Deplus et al., 2019).

We analyzed the data recorded by the hydrophone channel of a set of OBS stations distributed along a 100 km-long line from Petite-Terre to the south-west, with a 10 km inter station distance (Figure 1). They were deployed between October 7 and October 17, 2020. The closest instrument was only a few kilometers south from the active lava flows (blue patch on Figure 1). During this deployment, a scientific cruise [Mayobs15, (Rinnert et al., 2020)] was conducted on board French R/V Marion Dufresne with MBES profiling over the Fani Maoré volcano and its surroundings. Successive bathymetry surveys revealed that the eruption was ongoing all along the duration of the cruise, in an area north-west of the main edifice, hereafter named the TikTak area. Their careful analysis allowed to recover very fine depth changes between each survey and to map the location of volcanic activity on the seafloor at several times between October 7 and October 17.

We show in this paper that bathymetry surveys can quantify the overall extent of new lava flows, which is not possible using hydro-acoustic monitoring alone. On the other hand, hydro-acoustic monitoring can track the relative evolution of the activity in time with hourly details and metric spatial resolution, which cannot be attained with the limited spatial resolution and the sporadic recurrence of bathymetry surveys. Combining the two methods allowed to recover absolute and fine information of the lava flow evolution of the Mayotte eruption with high time resolution.

2 Materials and methods

We present in this section the methodologies used to map bathymetry changes and to extract hydro-acoustic signals source locations.

2.1 Multi-Beam Echo Sounder surveys

During Mayobs15 cruise, several bathymetry surveys of various quality were carried out. A high quality survey of the whole Fani Maoré volcano and its surroundings, made up of east/west and north/south lines, was performed on October 9 and 10.

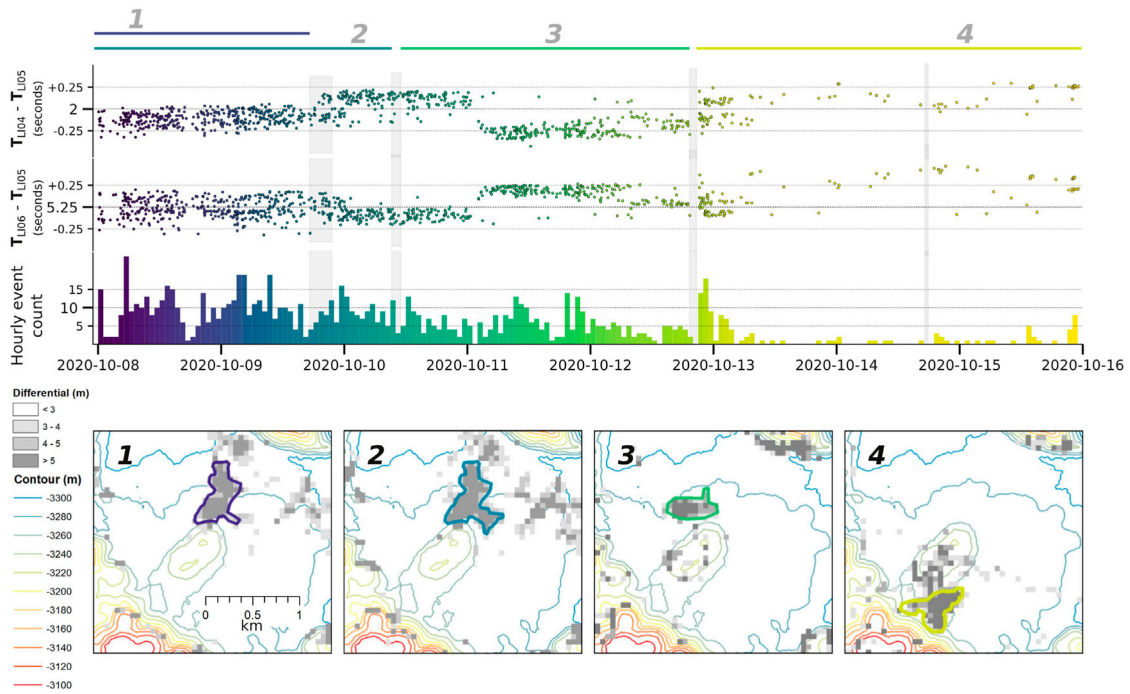

FIGURE 2
Top panel: time span corresponding to each bathymetry difference map. Hydro-acoustic events arrival time differences between LI04 and LI05 and between LI06 and LI05. Middle panel: hourly number of hydro-acoustic events detected from October 8 to October 16. The gray vertical bars indicate the occurrence of each MBES survey used to produce elevation difference maps. Bottom panel: maps of the TikTak area showing depth differences greater than 3 m (gray scale) between MBES surveys (1: October 6–9; 2: October 6–10; 3: October 10–12; 4: October 12–17). The same color is used on the maps to outline the reliable depth differences interpreted as new volcanic material.

On October 22, a set of 4 good quality lines was also acquired over the active lava flows field. In between, good quality profiles were acquired on the same area on October 12 and 17, as well as an additional transit line on October 14. Another transit line has been collected before the October 9–10 survey, on October 6.

R/V Marion Dufresne is equipped with a Kongsberg EM122 MBES (12 kHz, 1° × 1° beam width). Good quality lines are conducted at low speed (5–6 knots), the swath bathymetry width is cut at 50° for both starboard and portside and adjacent lines overlap from central to external beams. Thanks to these acquisition standards, the MBES vertical accuracy can be constrained to 0.2–0.3% of the water depth. All bathymetry data are processed using the GLOBE software (Poncelet et al., 2019), according to a single and common workflow, resulting in standardized grids for depth changes analysis. Due to the depth of the area (~3000 m) and thanks to the redundancy of the soundings, the data can be gridded down to a 30 m cellsize. For each pixel, a standard deviation layer (based on the valid soundings in the cell) is computed: for low slopes, at 3000 m water-depth, it does not exceed 4 m, which support a robust analysis of thin new morphological features. As a result of this statistical analysis, we consider that changes in bathymetry exceeding 5 m in elevation over a minimum of 3x3 pixels surface in flat areas are the result of new lava flows.

In addition, the MBES acquisitions are regularly calibrated in an area known for being stable, outside of the eruption site. A statistical analysis of the differences between two successive grids is performed: the vertical bias between the two surveys can be identified and corrected as an average level in bathymetry differences; moreover, resulting standard deviation over such a stable area helps for validating observations. Low quality data, that do not permit to accurately quantify small depth changes, can however be used to track-down the moving main spot of volcanic activity on the seafloor if they form a coherent unit with elevation differences above the 5 m threshold.

Finally, after computing differences between the bathymetry grids in the TikTak area, outlines of areas with reliable depth changes between two successive surveys have been designed using the 5 m threshold (Figure 2). Their locations were confirmed by analysing bathymetry differences between the high quality surveys of October 9–10 and 22.

2.2 Hydro-acoustic signals analysis

The waves emitted at underwater eruption sites propagate upwards in the water column and can later reflect at the ocean surface and the seafloor. They can be recorded by hydrophones

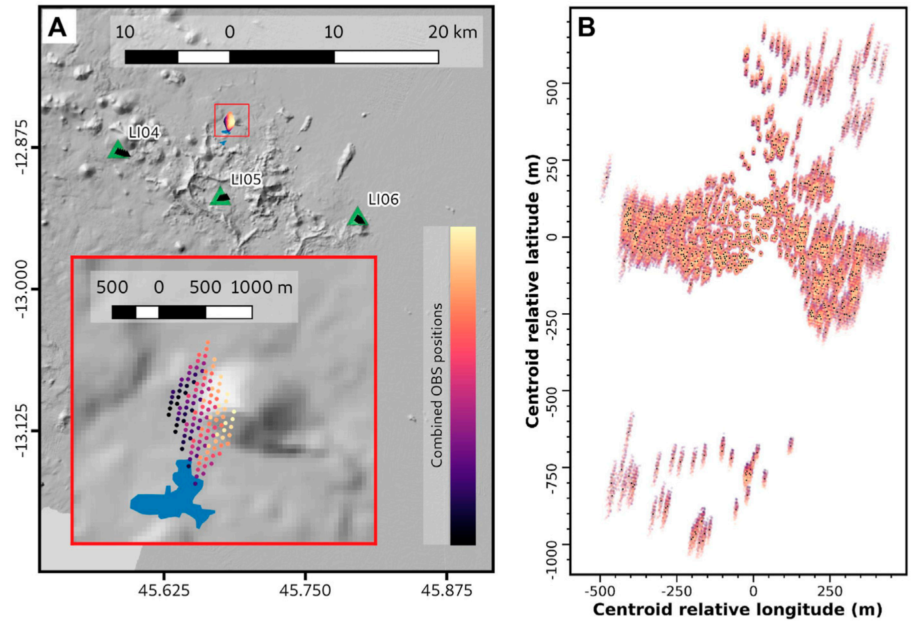

FIGURE 3
(A): Centroid of the source locations computed with each of the 125 OBS network configurations (represented with the color scale). The green triangles represent the deployment locations of the three stations we used. The black triangles on top represent the station location variations we tested. The insert shows a zoom on the events locations (red square). The blue patch corresponds to the area of reliable depth changes deduced from MBES surveys over the whole survey. **(B)**: Events locations (color dots for each event) relative to the centroid point for all the network configurations. The color scale indicate the set of OBS positions used.

located in the water column or on the seafloor. In Mayotte, Bazin et al. (2021) showed the distinct signature of these signals using hydrophones moored in the SOFAR (SOund Fixing and RAnging) channel. Part of the hydro-acoustic energy is also converted into seismic waves and is transmitted in the Earth crust. Indeed, some geophones of the OBS array recorded such signals but their data analysis is more complex.

Among the 10 OBS, LI05 was the closest to the active lava flows at the time of deployment and therefore served as reference. We chose here to only use the 3 closest OBS (LI04, LI05 and LI06) to analyse the best waveforms (highest signal to noise ratios).

The continuous records were manually scanned to identify hydro-acoustic events by the REVOSIMA seismology group during a pickathon (Saurel et al., 2022). These events are characterized by a short and impulsive signal, and several seconds time-delay between stations (Figure 1) due to the slow propagation of the hydro-acoustic waves through water at ~1500 m/s. This led to a manual catalog of 1328 events. Because the bathymetry difference maps do not show any significant changes between October 14 and 17 and because very few events occurred on October 16, we chose to limit our analysis up to the end of October 15.

For each event we automatically picked the first arrival on the hydrophone record, in a 25 s data-window. After detrending the signals, we filtered them above 1.5 Hz to remove unwanted long-period noise. On each station, the absolute maximum value of the trace was picked and labelled as the first arrival. This first arrival corresponds to an acoustic wave propagation with a single reflection on the ocean surface.

To locate the sources, we performed a grid search to fit the inter-station arrival time differences. We generated synthetic time-arrivals on a 10 m grid on the seafloor by using NonLinLoc Time2EQ software (Lomax, 2008). The travel-time tables for a signal reflected on the ocean surface were calculated using the Pirocko Cake library (Heimann et al., 2017). We used a 1D velocity model derived from a CTD profile (conductivity, temperature, depth) on the volcano acquired during Mayobs1 (Feuillet, 2019). We calculated the two synthetic arrival time differences between LI04 and LI06, respectively, and the reference LI05 station. Our location result corresponded to the grid point where we minimized the residuals root mean square between observed and synthetic arrival-time differences. We also tested a simpler global 1D velocity model to assess how sensitive our locations were compared to water celerity. We noted that it did not produced a significant variation in the absolute locations.

The OBS stations location on the seafloor could not be determined and we only knew the ship position during the instrument deployment and its recovery, with an accuracy of 10 m. Since there are strong oceanic currents around Mayotte, the OBS can drift several hundred of meters during its descent

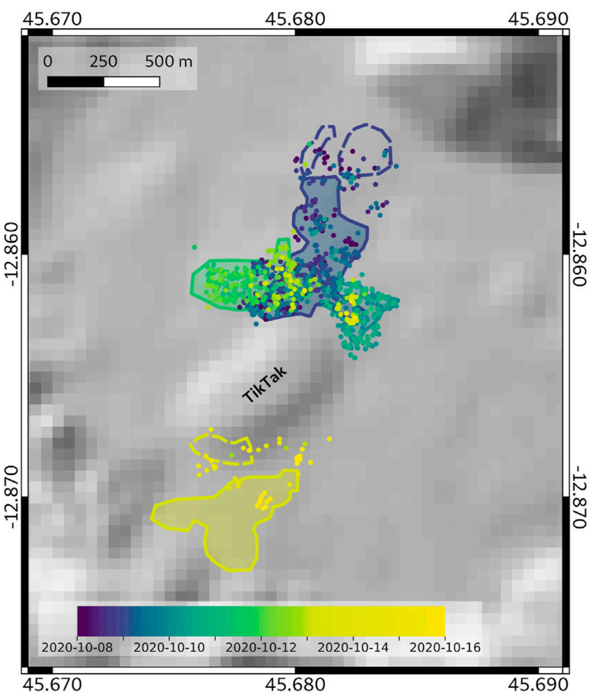

FIGURE 4
Locations of hydro-acoustic events superimposed on bathymetry differences contours. Same colorscale as in Figure 2. Dots show the hydro-acoustic events relative locations. Plain lines contours are the outlines of reliable depth differences from Figure 2 interpreted as new lava flows. Dashed contours show the outlines of questionable depth changes, that we further confirmed as new volcanic material thanks to hydro-acoustic events relative locations.

and ascent. Indeed, we observed that the distances between deployment and pick up locations varied between 300 m and 900 m. To estimate the influence of the OBS location uncertainty on our location results, we calculated the locations of all the events of our catalog using 5 different locations for each of the 3 OBS (Figure 3A). The 5 locations were uniformly spread between deployment and recovery points for each instrument and they led to 125 sets of OBS array configurations.

Our results (Figure 3A) show that absolute source locations greatly depend on the OBS positions and are spread over ~0.7 km square. Moreover, these absolute locations are not collocated with the mapped changes of bathymetry (Figure 3A insert) and are always located north of the mapped lava flows. Relative positions can be obtained by removing the centroid of the events from each set built with the 125 station configurations (Figure 3B). While the absolute locations differ, the relative variations between events remain consistent for all configurations of stations. The relative variations are limited to 7 m in longitude and 26 m in latitude for 95% of the events. Consequently, we can translate the centroid of the events to match the contour of the sea-floor bathymetry changes identified with the MBES surveys, in order to analyze the relative variations of the locations with time.

In the next sections, we refer as source location, the average position of the events obtained with the 125 station distributions.

3 Results

Between October 7 and 17, 2020, various periods of activity can be identified through both hydro-acoustic signals and bathymetry analysis (Figure 2).

Relative time arrivals of the hydro-acoustic events between different stations (Figure 2) and the resulting relative locations of the hydro-acoustic events (Figure 4) show both progressive and sudden migrations. Simultaneously, bathymetry analysis shows the evolution of the lava flow pattern (Figures 2, 4).

The bathymetry differences highlight 3 different areas of morphology changes during the period of study (Figure 2, bottom panels). They were located at the north and at the south of the elongated mount named TikTak (Figure 4). Until October 10 around 12:00 UTC, the activity was concentrated in the north of the area, with some late extension towards the south eastern tip. Between October 10 and October 13, the activity shifted to the south west of the previously active zone. Starting from October 13, depth changes were only present in the south of the area, about 1 km away from the other active zones we highlight.

Relative hydro-acoustic event locations evolution adds insight into the short time evolution of the lava flows. Figure 2 shows the evolution of arrival times, number of events and depth changes during the 8 days of the study. On the upper panel, we show the evolution of the arrival time difference between stations LI04 (and LI06) and the reference station LI05. We can see that the extension of activity to the eastern tip of the northern patch at the end of October 9 happened gradually. In contrast, on October 11, the western patch started being active quite suddenly. The arrival time differences show a clear shift in average values compared to the previous activity period followed by a smooth and rapid variation during the first hours. On October 13, hydro-acoustic events migrated sharply again, which is consistent with the migration of the areas of significant depth changes to the south.

Figure 4 shows that some hydro-acoustic events occured outside the contours defined by reliable depth changes (plain lines). On the eastern tip, which was active at the end of October 10, the event locations were more extended than the bathymetry contours, suggesting areas covered with lava flows thinner than our depth change threshold. In the north, they seemed to correspond to some cluster of pixels indicating bathymetry differences (blue dashed contour, Figure 4). These pixels were located at the edge of the bathymetry swath and were difficult to discriminate from noise. Swath bathymetry data standard deviations are also higher in areas with high slopes. Consequently, the depth differences observed at the southern edge of the TikTak mount (yellow dashed contour, Figure 4) had not been initially associated with reliable changes in bathymetry. However, during this period of sparse activity (hourly events count, Figure 2), some hydro-acoustic events were located on the southern edge of TikTak, which suggests that the southern dashed contour (Figure 4) also bounds a real bathymetry change.

The hydro-acoustic events activity varied during the period of study. The northern lava flows was the most active, with around 10 to 15 events per hour. The number of events decreased when the lava flows expanded toward the east, but regained in intensity again when the western area suddenly became active. This could be an indication that the strength of activity and the lava flow rate (expected to be higher at the onset of a new outbreak) are correlated.

4 Discussion and conclusion

As discussed in the Materials and methods section, the results of the absolute locations of the hydro-acoustic events vary with station locations. As explained by Le Saout et al. (2020) the sea-floor topography and variations in the water celerity also have an influence on hydro-acoustic waves propagation. Our approximation of this parameters was then transferred to the absolute localization results of the hydro-acoustic events. However, we showed that localizing their relative positions is robust against uncertainties in the positions of the recording stations. Thus, hydro-acoustic events can be used to study the temporal evolution of lava flows.

On the other hand, maps of bathymetry differences give correct absolute locations but integrate all the differences over the time window between two surveys. Maps of bathymetry differences are not able to show the temporal evolution of what happened between the surveys. Consequently, bathymetry surveys and hydro-acoustic events location are very complementary. By combining both methods, we are able to observe short-term variations of the lava flows of the Mayotte eruption between October 8 and 16. While the flows can progressively extend through an area, the volcanic activity location can also suddenly change, as we showed in the previous section (Figure 2). This highlights that the eruption was not a steady and continuous process with a single lava outbreak on the seafloor, even if it might have been fed by a single dyke. Furthermore, like on onland volcanoes, lava outputs cool at some locations, closing the active outbreak, and the lava finds new paths toward the seafloor, either via lava tunnels or shallow propagation from the main dyke.

Areas with high variations in slopes scatter the echo-sounder beams in multiple directions, leading to false bathymetry differences. Similarly, the edges of the bathymetry swath are noisy and generate artifacts on bathymetry difference maps. Consequently, it makes it difficult to distinguish small real bathymetry changes from noisy signals. When coupled with the hydro-acoustic event relative locations, such small questionable differences can be confirmed (or not) as new areas of volcanic activity. Hydro-acoustic event locations and analyses of depth changes are complementary to give information on the evolution of the lava flows through time and thus the eruption dynamic. Consequently, lava flows starting and ending times can be narrowed down to the hour. We showed in this study that areas that were considered doubtful during the bathymetry analysis (southern rim of the TikTak structure and north of the area) were real zones of recent volcanic activity, using hydro-acoustic events location.

In the past 20 years, two main mechanisms have been proposed to explain hydro-acoustic impulsive signals generated at submarine volcanoes. They could either result from rapid expansion and explosion of cold water entrapped into the molten lava: depending on the water depth, cold water can be heated to steam (Caplan-Auerbach et al., 2017) or supercritical state (Schipper and White, 2010). Or, the impulsive signals could be generated by gas bubbles: gas-rich magma exsolves bubbles (Clague et al., 2003) which can burst in shallow waters or implode in deeper waters (depending on the gas critical point).

The hydro-acoustic sources we recorded near Mayotte were very impulsive. The instrument 250 Hz sampling rate can theoretically recover signals with a frequency content up to 125 Hz. However, with a signal length typically shorter than 0.05 s, the impulsive events were recorded with less than 10 samples. Consequently, we were not able to reliably recover their complete frequency content, which is likely above 50 Hz. This frequency content seems however comparable with the hydro-acoustic signals analysed by Le Saout et al. (2020) that present a similarity between them up to high frequencies between 50 and 100 Hz. Because we could not recover the complete frequency band of the signal, we cannot know if we recovered the correct polarity of the dominant source. This polarity would give information on whether the source of the hydro-acoustic signals was explosive (starting with compression) or implosive (starting with decompression).

There is a debate whether explosive sources are possible in deep water. Depending on salinity, the critical point of sea-water, where water-vapour phase in not possible anymore, is between 295 and 302 bars (Bischoff and Rosenbauer, 1984), which corresponds to a depth of 3000 m (Fofonoff and Millard, 1983). Since the active area near Mayotte is deeper than 3200 m (Figure 2 lower panels), it is supposed that sea-water cannot exist in the vapour phase. In that case, a steam-burst explosive type source as evidenced at 1600 m depth on Axial Seamount during 2015 eruption (Caplan-Auerbach et al., 2017) would not be compatible with Mayotte eruption depth. However, Schipper and White (2010) demonstrated that lava could heat entrapped sea-water to supercritical state at depth below 3000 m with a rapid phase transition allowing explosive sources. More recently, Dürig et al. (2020) showed that induced fuel-coolant process (IFCI, that do not involve any vapour phase) are very effective in deep ocean and produce fine ash at explosive rate on the lava-water boundary. Such highly effective fragmentation process could produce numerous impulsive hydro-acoustic signals at the lava-water boundary. Another explanation could involve CO_2 or other volcanic gases. Clague et al. (2003) proposed that supercritical CO_2 bubbles exsolved from the magma quickly collapse into liquid CO_2 when the bubble cools down. Cui et al. (2016) showed the existence of cavitation when bubbles collapse and rebound, generating pressure pulse at each collapse and rebound. Bubble collapse, whether they are produced by exsolved CO_2 or other volcanic gases, would produce repetitive implosive hydro-acoustic signals. The June 2019 fresh lava samples (Fouquet and Feuillet, 2019) from the second phase of the eruption showed a significant amount of vesicularity and some of them still contained vesicle-trapped volatiles (popping rocks) when brought on-board (Berthod et al., 2021). Assuming the lava composition from 2020 TikTak lava flows was similar, a high vesicularity, compatible with a high volatile content, could be in favor of underwater implosions driven by rapidly cooling gas bubbles.

Preliminary analysis of the speed of the hydro-acoustic sources migration during October 12th shows velocity values around 0.0044 m/s (Green to yellow zone in Figure 4). Those values are similar to the lowest flow front velocities estimated by Le Saout et al. during 2015 eruption on Axial Seamount and interpreted as corresponding to the latest stages of the activity. On Fani Maoré volcano, the volcanic activity we described happened more than 2 years after the beginning of the eruption (Mittal et al., 2022) and the low flow-front velocities could correspond to the latest stages of the eruption.

Combining the repeated swath bathymetry surveys with the continuous OBS hydrophone records can give insights into the eruption evolution and constrains the time boundaries of its lava flow activities at the hour level. We showed three cases where hydro-acoustic events helped confirm small bathymetry changes. When only ship-based bathymetry is available, outlines of the new lava flows can also be made more finely thanks to hydro-acoustic events relative locations and this will have consequences on the emitted volumes estimation. This information can then be used to estimate the lava flow extrusion rate with an accuracy and precision greater than with bathymetry alone, and have a better idea of the eruption mechanism and dynamics.

We show the success of this methodology for a 8-days time window. In the next steps, the hydro-acoustic events will be analyzed using the OBS data recorded since early 2019 near Mayotte and compared with bathymetric surveys performed during the successive Mayobs campaigns (Feuillet et al., 2019). Since events cannot be picked manually for such long term records, on-going work focuses on the automatic detection and classification of hydro-acoustic events. Simultaneously, work is being done to reconstruct the phases of the eruption and to estimate the volumes of new material and flow rates throughout the eruption from the repeated bathymetric surveys near Mayotte (Deplus et al., 2019).

Data availability statement

The datasets analyzed for this study can be found in the Sismer Mayobs15 (Rinnert et al., 2020; http://data.ifremer.fr/SISMER) and Volobsis (REVOSIMA, 2021; http://volobsis.ipgp.fr) repositories upon request.

Author contributions

J-MS, LR, CD, BL and DP contributed to conception and design of the study. DP, BL, RB and CD performed the bathymetry analysis. J-MS, LR, MF, NK and VF performed the hydro-acoustic events analysis. SB helped interpreting the hydro-acoustic signals. J-MS and LR wrote the first draft of the manuscript. CD and BL wrote the MBES method section. PG performed the OBS deployment, data conversion and quality assessment. MM designed the OBS deployment. The REVOSIMA seismology group manual picked the hydro-acoustic events. The REVOSIMA bathymetry group designed the MBES data processing protocol and assessed the accuracy and resolution limits. All authors contributed to manuscript revision, read, and approved the submitted version.

Funding

Since June 2019, Mayotte eruption monitoring is funded by le Ministère de l’Enseignement Supérieur, de la Recherche et de l’Innovation (MESRI), le Ministère de la Transition Ecologique (MTE) and le Ministère des Outremers (MOM) with the support of le Ministère de l’Intérieur (MI) and le Ministère des Armées (MINARM) through the REVOSIMA (REVOSIMA, 2021).

Acknowledgments

J-MS and LR thank William Chadwick, William Wilcock and David Clague for fruitful discussions on impulsive hydro-acoustic events possible sources at the beginning of the project. The authors thank Genavir and Louis Dreyfus

Armateur crews who operated the R/V Marion Dufresne Mayobs15 survey and the cruise leaders (Emmanuel Rinnert, Isabelle Thinon and Nathalie Feuillet). Members of the REVOSIMA Seismology group who picked the hydro-acoustic events that have been used in this study: Chastity Aiken, Sara Bazin, Kévin Canjamalé, Océane Foix, Cyprien Griot, Aude Lavayssière, Nicolas Mercury, J-MS. REVOSIMA Bathymetry group: Jean-Marie Augustin, Patrick Bachèlery, Sylvain Bermell, Christine Deplus, Nathalie Feuillet, Jean-Christophe Komorowski, Elodie Lebas, Anne Le Friant, Benoît Loubrieu, Fabien Paquet, Delphine Pierre, Emmanuel Rinnert, Carla Scalabrin, Isabelle Thinon. Numerical computations of hydro-acoustic events location were performed on the S-CAPAD/DANTE platform, IPGP, France.

Conflict of interest

The authors declare that the research was conducted in the absence of any commercial or financial relationships that could be construed as a potential conflict of interest.

Publisher's note

References

Bazin, S., Royer, J.-Y., Dubost, F., Paquet, F., Loubrieu, B., Lavayssière, A., et al. (2021). Initial results from a hydroacoustic network to monitor submarine lava flows near Mayotte island. *Comptes Rendus Géoscience*. (accepted). doi:10.5802/crgeos.119

Berthod, C., Médard, E., Bachèlery, P., Gurioli, L., Di Muro, A., Peltier, A., et al. (2021). The 2018-ongoing Mayotte submarine eruption: Magma migration imaged by petrological monitoring. *Earth Planet. Sci. Lett.* 571, 117085. doi:10.1016/j.epsl.2021.117085

Bischoff, J. L., and Rosenbauer, R. J. (1984). The critical point and two-phase boundary of seawater, 200–500°C. *Earth Planet. Sci. Lett.* 68, 172–180. doi:10.1016/0012-821X(84)90149-3

Caplan-Auerbach, J., Dziak, R., Haxel, J., Bohnenstiehl, D., and Garcia, C. (2017). Explosive processes during the 2015 eruption of axial seamount, as recorded by seafloor hydrophones. *Geochem. Geophys. Geosyst.* 18, 1761–1774. doi:10.1002/2016gc006734

Caress, D., Clague, D., Paduan, J., Martin, J., Dreyer, B., Chadwick, W., Jr, et al. (2012). Repeat bathymetric surveys at 1-metre resolution of lava flows erupted at Axial Seamount in April 2011. *Nat. Geosci.* 5, 483–488. doi:10.1038/ngeo1496

Carey, R., Soule, S. A., Manga, M., White, J. D., McPhie, J., Wysoczanski, R., et al. (2018). The largest deep-ocean silicic volcanic eruption of the past century. *Sci. Adv.* 4, e1701121. doi:10.1126/sciadv.1701121

Cesca, S., Letort, J., Razafindrakoto, H. N., Heimann, S., Rivalta, E., Isken, M. P., et al. (2020). Drainage of a deep magma reservoir near Mayotte inferred from seismicity and deformation. *Nat. Geosci.* 13, 87–93. doi:10.1038/s41561-019-0505-5

Chadwick, W., Jr, Wright, I., Schwarz-Schampera, U., Hyvernaud, O., Reymond, D., and De Ronde, C. (2008). Cyclic eruptions and sector collapses at monowai submarine volcano, kermadec arc: 1998–2007. *Geochem. Geophys. Geosyst.* 9. doi:10.1029/2008gc002113

Chadwick, W. W., Embley, R. W., and Fox, C. G. (1991). Evidence for volcanic eruption on the southern juan de fuca ridge between 1981 and 1987. *Nature* 350, 416–418. doi:10.1038/350416a0

Chadwick, W. W., Jr, Paduan, J. B., Clague, D. A., Dreyer, B. M., Merle, S. G., Bobbitt, A. M., et al. (2016). Voluminous eruption from a zoned magma body after an increase in supply rate at axial seamount. *Geophys. Res. Lett.* 43, 12063–12070. doi:10.1002/2016GL071327

Chadwick, W. W., Rubin, K. H., Merle, S. G., Bobbitt, A. M., Kwasnitschka, T., and Embley, R. W. (2019). Recent eruptions between 2012 and 2018 discovered at west mata submarine volcano (ne lau basin, sw Pacific) and characterized by new ship, auv, and rov data. *Front. Mar. Sci.* 6. doi:10.3389/fmars.2019.00495

Clague, D. A., Davis, A. S., and Dixon, J. E. (2003). Submarine strombolian eruptions on the gorda mid-ocean ridge. *Explos. Subaqueous Volcanism*, 111–128. doi:10.1029/140gm07

Clague, D. A., Paduan, J. B., Caress, D. W., Chadwick, W. W., Jr, Le Saout, M., Dreyer, B. M., et al. (2017). High-resolution auv mapping and targeted rov observations of three historical lava flows at axial seamount. *Oceanogr. Wash. D. C).* 30, 82–99. doi:10.5670/oceanog.2017.426

Clague, D., Paduan, J., Caress, D., Thomas, H., Chadwick, W., and Merle, S. (2011). Volcanic morphology of West Mata Volcano, NE Lau Basin, based on high-resolution bathymetry and depth changes. *Geochem. Geophys. Geosyst.* 12. doi:10.1029/2011gc003791

Cui, P., Zhang, A., and Wang, S. (2016). Small-charge underwater explosion bubble experiments under various boundary conditions. *Phys. Fluids* 28, 117103. doi:10.1063/1.4967700

Delaney, J. R., Johnson, H. P., and Karsten, J. L. (1981). The juan de Fuca ridge—Hot spot—Propagating rift system: New tectonic, geochemical, and magnetic data. *J. Geophys. Res.* 86, 11747–11750. doi:10.1029/JB086iB12p11747

Deplus, C., Feuillet, N., Bachelery, P., Fouquet, Y., Jorry, S., Thinon, I., et al. (2019). Early development and growth of a deep seafloor volcano: Preliminary results from the mayobs cruises. *AGU Fall Meet. Abstr.* 2019, V43I–V0227.

Dürig, T., White, J. D., Murch, A., Zimanowski, B., Büttner, R., Mele, D., et al. (2020). Deep-sea eruptions boosted by induced fuel–coolant explosions. *Nat. Geosci.* 13, 498–503. doi:10.1038/s41561-020-0603-4

Dziak, R., Haxel, J., Bohnenstiehl, D., Chadwick, W., Nooner, S. L., Fowler, M., et al. (2012). Seismic precursors and magma ascent before the april 2011 eruption at axial seamount. *Nat. Geosci.* 5, 478–482. doi:10.1038/ngeo1490

Dziak, R. P., Bohnenstiehl, D. R., Baker, E. T., Matsumoto, H., Caplan-Auerbach, J., Embley, R. W., et al. (2015). Long-term explosive degassing and debris flow activity at west mata submarine volcano. *Geophys. Res. Lett.* 42, 1480–1487. doi:10.1002/2014GL062603

Dziak, R., Royer, J., Haxel, J., Delatre, M., Bohnensteihl, D., Matsumoto, H., et al. (2008). *AGU Fall Meeting Abstracts*, 2008. T51B–1888.Hydroacoustic detection of recent seafloor volcanic activity in the southern indian ocean

Embley, R. W., Merle, S. G., Baker, E. T., Rubin, K. H., Lupton, J. E., Resing, J. A., et al. (2014). Eruptive modes and hiatus of volcanism at West Mata seamount, ne lau basin: 1996–2012. *Geochem. Geophys. Geosyst.* 15, 4093–4115. doi:10.1002/2014gc005387

Feuillet, N., Jorry, S., Crawford, W., Deplus, C., Thinon, I., Jacques, E., et al. (2021). Birth of a large volcanic edifice through lithosphere-scale dyking offshore Mayotte (Indian Ocean). *Nat. Geosci.* 14, 787–795. doi:10.1038/s41561-021-00809-x

Feuillet, N., Jorry, S., Rinnert, E., Thinon, I., Fouquet, Y., Paquet, F., et al. (2019). *Mayobs*. doi:10.18142/291

Feuillet, N. (2019). *MD220/Mayobs1 cruise, Marion Dufresne R/V*. doi:10.17600/18001217

Fofonoff, N., and Millard, R. (1983). Algorithms for computation of fundamental properties of seawater. *UNESCO Tech. Pap. Mar. Sci.* 44.

Fouquet, Y., and Feuillet, N. (2019). *MD223/Mayobs4 cruise, Marion Dufresne R/V*. doi:10.17600/18001238

Fox, C. G., Chadwick, W. W., Jr, and Embley, R. W. (1992). Detection of changes in ridge-crest morphology using repeated multibeam sonar surveys. *J. Geophys. Res.* 97, 11149–11162. doi:10.1029/92jb00601

GEBCO (2021). *About the seabed 2030 project*. Available at: https://seabed2030.org/about-us (Accessed 08 02, 2022).

Haxel, J., and Dziak, R. (2005). Evidence of explosive seafloor volcanic activity from the Walvis ridge, south atlantic ocean. *Geophys. Res. Lett.* 32, L13609. doi:10.1029/2005gl023205

Heaney, K. D., Campbell, R. L., and Snellen, M. (2013). Long range acoustic measurements of an undersea volcano. *J. Acoust. Soc. Am.* 134, 3299–3306. doi:10.1121/1.4818844

Heimann, S., Kriegerowski, M., Isken, M., Cesca, S., Daout, S., Grigoli, F., et al. (2017). *Pyrocko: A versatile seismology toolkit for Python.* doi:10.5880/GFZ.2.1.2017.001

Kelley, D. S., Delaney, J. R., and Juniper, S. K. (2014). Establishing a new era of submarine volcanic observatories: Cabling Axial Seamount and the endeavour segment of the Juan de Fuca ridge. *Mar. Geol.Anniversary Spec. Issue* 352, 426–450. doi:10.1016/j.margeo.2014.03.010

Le Saout, M., Bohnenstiehl, D. R., Paduan, J. B., and Clague, D. A. (2020). Quantification of eruption dynamics on the north rift at Axial Seamount, Juan de Fuca ridge. *Geochem. Geophys. Geosyst.* 21, e2020GC009136. doi:10.1029/2020gc009136

Lemoine, A., Briole, P., Bertil, D., Roullé, A., Foumelis, M., Thinon, I., et al. (2020). The 2018–2019 seismo-volcanic crisis east of Mayotte, Comoros islands: Seismicity and ground deformation markers of an exceptional submarine eruption. *Geophys. J. Int.* 223, 22–44. doi:10.1093/gji/ggaa273

Lomax, A. (2008). *The NonLinLoc software guide*. Mouans-SartouxFrance: ALomax Scientific. Available at: http://alomax.free.fr/nlloc.

Longo, M., Lazzaro, G., Caruso, C. G., Corbo, A., Scappuzzo, S. S., Italiano, F., et al. (2021). *Hydro-acoustic signals from the Panarea shallow hydrothermal field: New inferences of a direct link with stromboli*. London: Geological Society. Special Publications 519.

McNutt, S. R., and Roman, D. C. (2015). "Volcanic seismicity," in *The encyclopedia of volcanoes* (Elsevier), 1011–1034.

Mittal, T., Jordan, J. S., Retailleau, L., Beauducel, F., and Peltier, A. (2022). Mayotte 2018 eruption likely sourced from a magmatic mush. *Earth Planet. Sci. Lett.* 590, 117566. doi:10.1016/j.epsl.2022.117566

Poncelet, C., Billant, G., and Corre, M.-P. (2019). *Globe (global oceanographic bathymetry explorer) software*.

REVOSIMA (Mayotte Volcanological And Seismological Monitoring Network) (2021). *Institut de physique du globe de Paris (IPGP), Bureau de recherches géologiques et minières (BRGM), Institut français de recherche pour l'exploitation de la mer (IFREMER), and Centre national de la recherche scientifique (CNRS).* Data collection of the Mayotte volcanological and seismological monitoring network (REVOSIMA). doi:10.18715/MAYOTTE.REVOSIMA

Rinnert, E., Thinon, I., and Feuillet, N. (2020). *MD228/Mayobs15 cruise, Marion Dufresne R/V*. doi:10.17600/18001745

Saurel, J.-M., Jacques, E., Aiken, C., Lemoine, A., Retailleau, L., Lavayssière, A., et al. (2022). Mayotte seismic crisis: Building knowledge in near real-time by combining land and ocean-bottom seismometers, first results. *Geophys. J. Int.* 228, 1281–1293. doi:10.1093/gji/ggab392

Schipper, C. I., and White, J. D. (2010). No depth limit to hydrovolcanic limu o pele: Analysis of limu from Lō`ihi seamount, Hawai`i. *Bull. Volcanol.* 72, 149–164. doi:10.1007/s00445-009-0315-5

Tepp, G., and Dziak, R. P. (2021). The seismo-acoustics of submarine volcanic eruptions. *J. Geophys. Res. Solid Earth* 126, e2020JB020912. doi:10.1029/2020jb020912

Watts, A., Peirce, C., Grevemeyer, I., Paulatto, M., Stratford, W., Bassett, D., et al. (2012). Rapid rates of growth and collapse of Monowai submarine volcano in the Kermadec arc. *Nat. Geosci.* 5, 510–515. doi:10.1038/ngeo1473

Wilcock, W. S. D., Tolstoy, M., Waldhauser, F., Garcia, C., Tan, Y. J., Bohnenstiehl, D. R., et al. (2016). Seismic constraints on caldera dynamics from the 2015 Axial Seamount eruption. *Science* 354, 1395–1399. doi:10.1126/science.aah5563

Yun, S., Lee, W. S., Dziak, R. P., Roche, L., Matsumoto, H., Lau, T.-K., et al. (2021). Quantifying soundscapes in the Ross sea, Antarctica using long-term autonomous hydroacoustic monitoring systems. *Front. Mar. Sci.* 1549. doi:10.3389/fmars.2021.703411

frontiers | Frontiers in Earth Science

TYPE Original Research
PUBLISHED 13 January 2023
DOI 10.3389/feart.2022.1061515

OPEN ACCESS

EDITED BY
Luis E. Lara,
Servicio Nacional de Geología y Minería de Chile (SERNAGEOMIN), Chile

REVIEWED BY
Rosie Cole,
University of Iceland, Iceland
Raymond A. F. Cas,
Monash University, Australia
Meagen Pollock,
College of Wooster, United States

*CORRESPONDENCE
J. L. Smellie,
✉ jls55@le.ac.uk

SPECIALTY SECTION
This article was submitted to Volcanology, a section of the journal Frontiers in Earth Science

RECEIVED 04 October 2022
ACCEPTED 15 December 2022
PUBLISHED 13 January 2023

CITATION
Smellie JL, Rocchi S and Di Vincenzo G (2023), Controlling influence of water and ice on eruptive style and edifice construction in the Mount Melbourne Volcanic Field (northern Victoria Land, Antarctica).
Front. Earth Sci. 10:1061515.
doi: 10.3389/feart.2022.1061515

Controlling influence of water and ice on eruptive style and edifice construction in the Mount Melbourne Volcanic Field (northern Victoria Land, Antarctica)

J. L. Smellie[1]*, S. Rocchi[2] and G. Di Vincenzo[3]

[1]School of Geography, Geology and the Environment, University of Leicester, Leicester, United Kingdom, [2]Dipartimento di Scienze della Terra, Università di Pisa, Pisa, Italy, [3]Istituto di Geoscienze e Georisorse, Consiglio Nazionale delle Ricerche, Pisa, Italy

The Mount Melbourne Volcanic Field (MMVF) is part of the West Antarctic Rift System, one of Earth's largest intra-continental rift zones. It contains numerous small, compositionally diverse (alkali basalt–benmoreite) flank and satellite vents of Late Miocene–Pliocene age (≤12.50 Ma; mainly less than 2.5 Ma). They demonstrate a wide range of morphologies and eruptive mechanisms despite overlapping compositions and elevations, and they occur in a relatively small area surrounding the active Mount Melbourne stratovolcano. The volcanic outcrops fall into several main categories based on eruptive style: scoria cones, tuff cones, megapillow complexes, and shield volcanoes. Using the analysis of lithofacies and appraisal of the internal architectures of the outcrops, we have interpreted the likely eruptive setting for each center and examined the links between the environmental conditions and the resulting volcanic edifice types. Previous investigations assumed a glacial setting for most of the centers but without giving supporting evidence. We demonstrate that the local contemporary environmental conditions exerted a dominant control on the resulting volcanic edifices (i.e., the presence or absence of water, including ice or snow). The scoria cones erupted under dry subaerial conditions. Products of highly explosive hydrovolcanic eruptions are represented by tuff cones. The water involved was mainly glacial (meltwater) but may have been marine in a few examples, based on a comparison of the contrasting internal architectures of tuff cones erupted in confined (glacial) and unconfined (marine, lacustrine) settings. One of the glaciovolcanic tuff cones ceased activity shortly after it began transitioning to a tuya. The megapillow complexes are highly distinctive and have not been previously recognized in glaciovolcanic successions. They are subglacial effusive sequences emplaced as interconnected megapillows, lobes, and thick simple sheet lavas. They are believed to have erupted at moderately high discharge and reduced cooling rates in partially drained englacial vaults under ice, probably several hundred meters in thickness. Finally, several overlapping small shield volcanoes crop out mainly in the Cape Washington peninsula area. They are constructed of previously unrecognized multiple ʻaʻā lava-fed deltas, erupted in association with a thin draping ice cover c. 50–145 m thick. Our study highlights how effectively water in all its forms (e.g., snow, ice, and any meltwater) or its absence exerts a fundamental control on eruption dynamics and volcano construction. When linked to published ages and ^{40}Ar/^{39}Ar dates produced by this study, the new environmental information indicates that the Late Pliocene–Pleistocene landscape was mainly an icefield rather than a persistent topography-drowning ice sheet. Ice thicknesses also generally increased toward the present.

KEYWORDS

glaciovolcanic, tuff cone, megapillow, A'ā lava, lava-fed delta, tuya, Plio–Pleistocene environment, ice sheet

1 Introduction

Volcanoes erupt in various environmental settings, including subaerial, subaqueous (lacustrine, marine), and subglacial. Each environment differently influences the erupting magma, resulting in varied eruptive styles and different types of edifices constructed (Cas and Simmons, 2018; Edwards et al., 2022). For example, notwithstanding localized explosivity due to induced fuel–coolant interaction (IFCI) of magmas highly strained during the eruption (Dürig et al., 2020), under deep water conditions, volatile exsolution is largely inhibited, molten fuel–coolant interactions (MFCI) are suppressed, and lava effusion dominates, usually as pillow lava (Kokelaar, 1986; Schmincke and Bednarz, 1990; Clague and Paduan, 2009). At shallower depths, vigorous volatile exsolution and MFCI promote intimate interaction with the surrounding water, resulting in explosive hydrovolcanic eruptions and the generation of abundant lapilli tuffs in tuff cones and tuff rings (Sohn, 1996; White, 1996; Cole et al., 2001; Brand and Clarke, 2009). By contrast, eruptions under fully subaerial conditions, in the absence of surface water or groundwater, are primarily magmatic and construct scoria cones and lava fields (Houghton and Hackett, 1984; Vespermann and Schmincke, 2000). Environmental overburden pressures also directly affect eruptions under ice, known as glaciovolcanic eruptions (Smellie and Edwards, 2016). Thick ice (i.e., high ambient pressures) suppresses explosive eruptions in favor of lava effusion (pillow lavas), and thin ice promotes the construction of tuff cones (Jones, 1969; 1970; Höskuldsson et al., 2006; Schopka et al., 2006; Pollock et al., 2014). Additionally, because of the buttressing effects of ice, the resulting glaciovolcanic edifices typically have higher aspect ratios (height:basal width) than those formed in unconfined (lacustrine, marine) settings; the latter are much broader and have lower profiles (Smellie, 2013; Pedersen et al., 2020). Thus, the eruptive setting imposed by local environmental conditions can exert a dominating influence on eruption dynamics and edifice construction. Interpreting the eruptive setting can therefore be used as a dipstick to reconstruct past environments and thereby document climate change (Smellie, 2018; Edwards et al., 2022).

We have investigated the flank and satellite centers in the Mount Melbourne Volcanic Field (MMVF), northern Victoria Land, Antarctica (Figure 1) to assess how effective the presence or absence of water has been in determining eruptive styles and edifice construction. Probably because of the glacial environment prevailing today, a glaciovolcanic origin has generally been assumed by previous authors, but supporting evidence has only rarely been presented (*cf.* Wörner and Viereck, 1987; Wörner and Viereck, 1989; Giordano et al., 2012; Smellie et al., 2018). The centers are mainly small scoria cones but, unusually for volcanism in the West Antarctic Rift System (Smellie, 2021; Wilch et al., 2021), they include several tuff cones, outcrops formed of megapillows and large lava lobes (herein called megapillow complexes), and volcanic shields composed

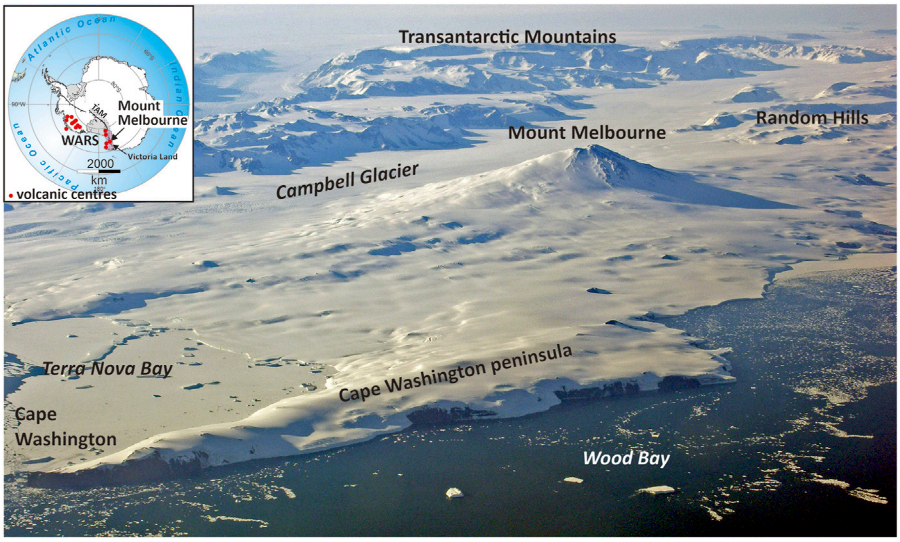

FIGURE 1
Aerial view of the Mount Melbourne Volcanic Field, looking west-northwest. The area is dominated by the prominent symmetrical stratocone of Mount Melbourne. Cape Washington peninsula is formed from several small Late Pliocene coalesced shield volcanoes intruded by Pleistocene strombolian vents. Numerous small centers can be seen as isolated nunataks protruding through the snow at low elevations surrounding Mount Melbourne. The inset shows the location of Mount Melbourne and other large volcanic centers within the West Antarctic Rift System (WARS). TAM–Transantarctic Mountains (stippled). The boundary of the WARS is after LeMasurier (2008).

of multiple lava–breccia couplets (lava-fed deltas), which were previously unrecognized. In this study, the physical volcanology of the centers within the MMVF is described, and the eruptive settings are deduced. Our interpretation of the centers demonstrates that variable local environmental conditions were the dominating control on the eruptive styles and edifices constructed. We show that the variations in eruptive styles and the resulting primary volcanic landforms were overwhelmingly influenced by the presence or absence of water in all its forms (snow, ice, meltwater, and seawater), which, in turn, is linked inextricably to the prevailing climate. Our results are also placed within a comprehensive chronology based mainly on new ^{40}Ar/^{39}Ar age determinations. This has enabled a unique view of the terrestrial glacial/interglacial environmental history of the region to be constructed.

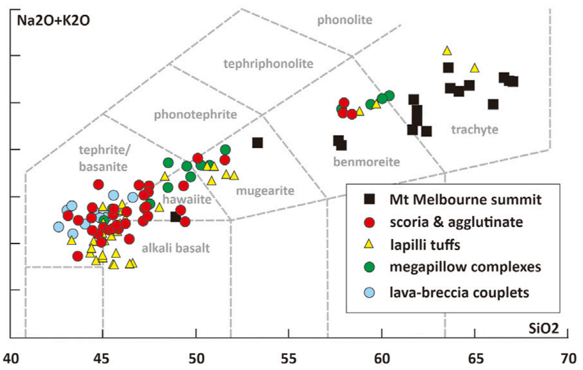

FIGURE 2
TAS diagram (after Le Maitre et al., 2002) for the MMVF showing the wide range of compositions that characterizes the flank and satellite centers and the much more restricted mainly trachytic compositions of volcanic products erupted from the summit of Mount Melbourne. Data from Armienti et al. (1991), Giordano et al. (2012), and unpublished information of the authors.

2 Geological setting

Antarctica is host to one of Earth's great volcanic rifts, known as the West Antarctic Rift System (WARS) (LeMasurier (2008); Jordan et al., 2020; Siddoway, 2021; Figure 1). Active in stages since the mid-Cretaceous, much of the regional extension probably ceased at c. 26 or possibly 11 Ma, with younger extension focused on the western margin in the Terror Rift and continuing to modern times (Granot and Dyment, 2018; Jordan et al., 2020; Siddoway, 2021). Volcanism has been widespread throughout the WARS. It forms an alkaline association broadly bimodal overall (LeMasurier and Thomson, 1990; Martin et al., 2021; Panter et al., 2021; Rocchi and Smellie, 2021). In Victoria Land, volcanism is contained within the McMurdo Volcanic Group, divided into three large volcanic provinces (Smellie and Martin, 2021; Smellie and Rocchi, 2021). The volcanic edifices throughout Victoria Land consist of (1) polygenetic stratocones characteristic of the inland centers and (2) coalesced shield volcanoes linked to coast-parallel faulting in coastal areas (Hamilton, 1972). There are also numerous small-volume monogenetic centers, mainly scoria cones, scattered over a wide area and known as the Northern Local Suite (Smellie and Rocchi, 2021). The magmatic source for volcanism in northern Victoria Land was initially thought to have originated in an active or fossil mantle plume or a source metasomatized by Palaeozoic subduction. However, the evidence for a mantle plume origin has been strongly criticized (Rocchi et al., 2003; 2005; Rocchi and Smellie, 2021). It is now thought more likely to be related to a combination of (1) generation of an incipient intra-plate boundary between southern Australia and the Ross Sea; (2) craton-directed mantle flow (edge flow) leading to coast-parallel necking and decompression melting; and (3) emplacement of melts along north–south faults and northwest–southeast reactivated Palaeozoic translithospheric transfer faults (Salvini et al., 1997; Storti et al., 2007; Panter et al., 2018; Rocchi and Smellie, 2021).

2.1 Mount Melbourne Volcanic Field

The MMVF is situated in northern Victoria Land. It is part of the Melbourne volcanic province, which contains four other volcanic fields (Smellie and Rocchi, 2021). The MMVF has been described by Wörner and Viereck (1987), Wörner and Viereck (1990), Wörner et al. (1989), Wörner and Orsi (1990), and Giordano et al. (2012) and is summarized here. The petrology is described by Armienti et al. (1991), Wörner and Viereck (1990), Beccaluva et al. (1991), Lee et al. (2015), and Gambino et al. (2021). Compositionally, the MMVF is a Na-alkaline series, ranging from tephrite/basanite/alkali basalt to trachyte (Figure 2).

Mount Melbourne has a crater or possibly a small caldera 700 m in diameter. The summit is mainly constructed of trachyte to benmoreite domes, scoria and phreatomagmatic cones, and lavas from which the youngest published ages have been obtained (Giordano et al., 2012; Lee et al., 2015). Tephras are also present, including welded fall, and basaltic bombs scattered around the summit attest to recent mafic activity. The crater and upper slope on the north side also contain areas of heated ground and fumaroles (Lyon and Giggenbach, 1974; Lyon, 1986; Wörner et al., 1989; Gambino et al., 2021). The most recent eruption dates back to c. AD 1892–1922 (Lyon, 1986; Wörner et al., 1989), but numerous cryptotephras found in ice cores extend the recent explosive history of Mount Melbourne back to Eemian time, at least 124 ka, possibly 137 ka (Del Carlo et al., 2015; Narcisi and Petit, 2021). Outcrops at lower elevations, which represent flank and satellite vents, are the focus of this study and are scattered widely surrounding Mount Melbourne. They are generally isolated and small, with the largest snow-free outcrops at Edmonson Point and Shield Nunatak. Apart from a small isolated trachyte dome or lava c. 3 km west-northwest of Edmonson Point, the flank and satellite outcrops are tephrite/basanite to benmoreite in composition. They are mainly scoria cones showing variable degrees of degradation, but there are also outcrops of palagonitized lapilli tuffs described as tuff rings, together with enigmatic outcrops composed of megapillows and large lava lobes. Additionally, our study identified several outcrops composed of ʻaʻā lava-fed deltas mainly confined to the Cape Washington peninsula (Figure 3).

Radioisotopic ages for rocks in the MMVF are mainly based on K-Ar data (Armstrong, 1978; Wörner et al., 1989; Armienti et al., 1991; Lee et al., 2015), mostly without analytical details. More recently, Giordano et al. (2012) reported ^{40}Ar/^{39}Ar data. The previously published results were based on old constants (decay constants and/or the age of the reference mineral) and are therefore

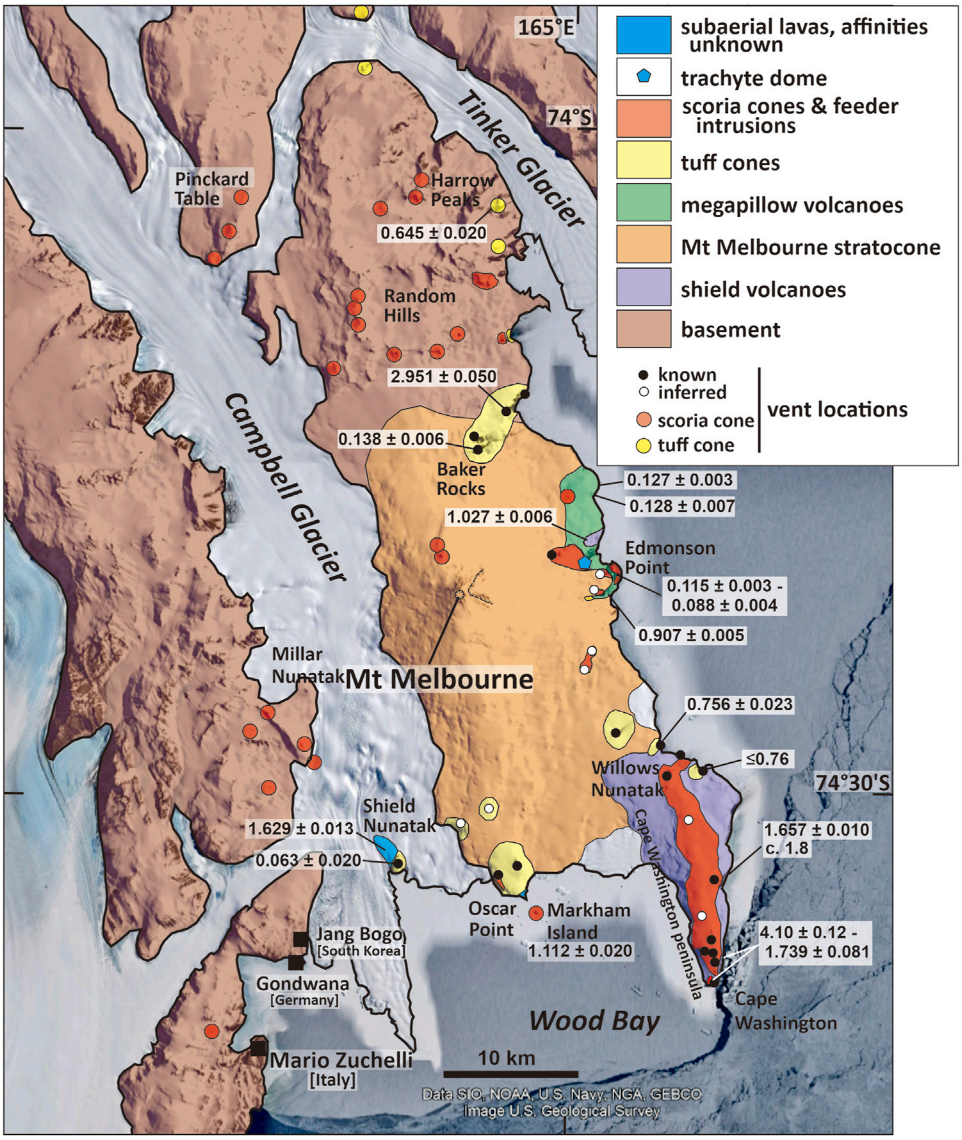

FIGURE 3
Map of the solid geology of the Mount Melbourne Volcanic Field. The sizes of some of the smaller outcrops are exaggerated for clarity. The $^{40}Ar/^{39}Ar$ ages (Ma) determined by this study are also shown, followed by ± 2σ internal uncertainties. For the locations of other published ages, see Supplementary Figure S1. Several scoria cone and a few of the tuff cone outcrops were not visited during this investigation. Their locations are culled from Wörner et al. (1989) and Armienti et al. (1991) and from our binocular observations.

expected to be c. ≤ 1% younger, but these variations fall largely within the analytical uncertainties. The radioisotopic ages suggest that volcanism began in the Late Miocene (c. 12.5 Ma) but became widespread from the Pliocene (from c. 4 Ma but mainly after c. 2.5 Ma). It continues today, although no eruptions have been witnessed (Wörner et al., 1989; Giordano et al., 2012; Gambino et al., 2021). Units dated by the K-Ar method are mainly intrusions in tuff cones and range in age from 2.96 ± 0.2 to 0.2 ± 0.04 Ma but including an outlier age of 12.50 ± 0.18 Ma (Supplementary Figure S1). $^{40}Ar/^{39}Ar$ ages published by Giordano et al. (2012) included samples from Edmonson Point, Shield Nunatak, Markham Island, Harrow Peaks, and Random Hills (Figure 3). The dated outcrops vary from scoria cones and associated lava fields to ignimbrite and a lava in one of the megapillow complexes. The localities do not overlap with those dated by K-Ar, and the ages range between 1.368 ± 0.009 and 0.0907 ± 0.019 ka. The 2-σ uncertainties are generally quite high.

3 Methods

Fieldwork occurred in 2005–2006, 2011, and 2014, using helicopter logistics provided by the Programma Nazionale di Recherche in Antartide (PNRA) of Italy. The localities visited are shown in Supplementary Figure S2. A new lithostratigraphic geological map is presented in Figure 3, together with the first detailed geological maps of many outcrops. Rock samples were taken for petrography, radioisotopic dating, and whole-rock analyses. More than 100 thin sections were examined, and 22 samples were analyzed by the $^{40}Ar/^{39}Ar$ dating method.

TABLE 1 Characteristics of lithofacies in flank and satellite centers of the Mount Melbourne Volcanic Field.

Lithofacies	Characteristics
Sheet lava [sL][a]	Thin sheets and lenses of vesicular finely crystalline ‘a‘ā lava. Two types of occurrence: (1) small lava fields sourced in scoria cones and (2) shallow-dipping (c. 5°) sequences overlying lava lobe-bearing breccia. In (1), the sequences are up to a few tens of meters thick; the lavas have massive centers c. 0.3–0.5 m thick (rarely up to 20 m) with coarse irregular to columnar joints and grey to red oxidized autobreccias up to 3 m thick (Figure 4B). Also occur as a capping sequence 60 m thick on the tuff cone forming Shield Nunatak; those lavas, probably sourced in a summit scoria cone, transform down-dip into invasive lavas within lapilli tuffs. In (2), the lava sequences vary from 15 to >80 m thick, comprising 2–4 m of massive lava (rarely up to c. 20 m) associated with a similar thickness of autobreccia in which the clinkers are commonly oxidized; the lavas pass down into lava lobe-bearing breccia (lithofacies cB), with which they form cogenetic lava–breccia couplets; the outcrops are mainly confined to Cape Washington peninsula
Compound lava [cL]	Pāhoehoe lava is present at one locality only (4.5 km northwest of Edmonson Point); includes tumuli and entrail pāhoehoe; flow directions suggest derivation from a source upslope to the west, probably the prominent large scoria cone present there, with which there is a compositional match
Pillow lava [pL]	Minor lithofacies; occurs as invasive lava pillows at Baker Rocks (south) between 400 and 600 m asl; the pillows have irregular shapes and are 0.7–3 m across, showing fluidal surfaces and marginal peperite (Figure 4F); stratification is destroyed in adjacent lapilli tuffs; associated with irregular lava tubes 2–6 m thick and up to 50 m long. Pillows also locally developed at margins of invasive lavas intruding lapilli tuffs at Shield Nunatak (Figure 4H)
Megapillows, lobes, and sheets [MpL]	Highly distinctive lithofacies, seen at Edmonson Point (benmoreite to Si-poor trachyte) and to the north, northwest and southwest of Edmonson Point (hawaiite and mugearite); outcrops mostly extend up to c. 200 m asl but highest elevation is c. 400 m asl in nunatak northwest of Edmonson Point; the lava masses are interconnected, comprising irregularly shaped megapillows 4–12 m in diameter, and lobes and sheets a few tens of meters high and a few tens of meters (lobes) to a few hundred meters (sheets) long (Figures 9A–C); rare lava pillows 25–40 cm in diameter (rarely to 1 m) present locally at base of some lava sheets; dark grey aphanitic margins c. 10 cm thick with patchy glassy rinds c. 1–2 cm thick; pale grey and fine grained internally; prominent jointing, of several types (Figure 10; terminology after Lescinsky and Fink, 2000): marginal closely spaced (≤10 cm, down to mm scale) sheeting joints prevalent; they are cross-cut by more widely spaced (c. 20 cm) sheet-like joints, which give way internally to entablature with small prismatic columns (20–50 cm wide; usually <30 cm); entablatures ubiquitous, especially prominent in the lava sheets (Figures 9B,C); some of the larger lava lobes also have basal colonnades developed intermittently, which are much thinner (few meters) than the overlying entablatures (Figure 9C); the smaller megapillows and rare lava pillows (lithofacies pL) are often radial jointed; blocky joints are well developed where exposed surfaces cut deeply into lobes or megapillows, often accompanied by subordinate pseudopillow joints; joint surfaces occasionally show multiple glassy/aphanitic rinds; some lobes and megapillows show alternating bands of abundant vesicles and non-vesicular lava that are parallel to the lava margins; the vesicles vary from spherical to stretched in an outward direction; the paired bands are up to 2 m thick and pass down into massive non-vesicular lava forming the lava interiors; many lobes and megapillows also have giant ovoid (arched-roof) to spherical vesicles <15 cm in diameter (rarely up to 40 cm); rare irregularly shaped cavities also present, varying from 1 to a few meters in diameter, with fretted glassy internal surfaces (Figure 9D); minor autobreccias present, a few dm to rarely a meter thick, formed of vesicular aphanitic to glassy clinkers 1–10 cm in diameter with strongly stretched vesicles; many clinkers have broken fluidal shapes and often have a weak maroon or rusty brown coloration
Basalt intrusions, irregular and sheet-like [iL]	Pale grey irregular masses and sheets of intrusive basalt occurring in two situations: (1) invading massive to crudely stratified oxidized scoria lapillistones (lithofacies LP), which occur as screens and foundered masses; and (2) within stratified lapilli tuffs (lithofacies LT). Spectacular exposures of (1) are present in the eastern cliffs north of Cape Washington; the basalts are massive to coarsely columnar jointed. In (2), the basalts are spectacularly entablature jointed throughout, sometimes with megapillows developed marginally (Figure 4G); similar intrusive necks, but entablature-jointed, intrude scoria lapillistones at Shield Nunatak and the outcrop east of Willows Nunatak (Figures 6, 7)
Scoria and agglutinate [LP]	Commonest lithofacies in the MMVF. Mainly amorphous piles of scoria; a few have snow-filled craters. The greatest vertical exposure is c. 90 m at Markham Island (Figure 4A). Massive to weakly bedded coarse scoria and broken bombs, including dense cannonball bombs and armored bombs with scoria cores, usually oxidized. Lenses of weakly welded agglutinate up to 15 m thick, with flattened bombs up to 1.7 m and clastogenic lavas
Lapilli tuff, diffusely stratified [dsLT]	Common volcaniclastic lithofacies. Lapilli tuff with prevalent diffuse stratification lacking sag structures below outsize clasts; 1%–2% accessory lava blocks up to 20 cm in diameter; accidental (bedrock-derived) clasts absent but may occur in basal lapilli tuff beds at Harrow Peaks (Giordano et al., 2012). Ash-coated lapilli noted at three localities (Shield Nunatak, northern Baker Rocks, and Harrow Peaks). Outcrops strongly eroded, but craters rarely preserved (at south Baker Rocks, summit of Shield Nunatak, and Oscar Point summit); crater-rim unconformities seen at Baker Rocks (north) and northeast of Baker Rocks. Stratification is disturbed and often destroyed in lapilli tuffs in large areas within outcrops at Shield Nunatak and Harrow Peaks (Smellie et al., 2018). Deformation (slumps, slides) prominent in “Oscar cliff” outcrop (Figure 16)
Lapilli tuffs, well-bedded, graded [glLT]	Minor lithofacies; fine lapilli tuffs forming well-defined beds a few dm to 3 m thick, laterally continuous except where amalgamated (common); reverse-graded bases and normal-graded tops with faint planar laminations; loading structures seen in fine (tuffaceous) tops of beds (Figure 4D)
Coarse tuff, diffusely stratified to dune-bedded [dsT; xT]	Minor lithofacies; very similar to diffusely stratified lapilli tuff lithofacies but thinner stratification and with uncommon steep-faced dune bedforms
Thin-bedded coarse and fine tuffs [bT]	Minor lithofacies; alternating beds 10–15 cm thick with planar and ripple cross laminations
Fine tuff, laminated [glT]	Minor lithofacies; planar laminations, normal grading, amalgamation; rare ripple cross laminations, flame structures, slumping

(Continued on following page)

TABLE 1 (*Continued*) **Characteristics of lithofacies in flank and satellite centers of the Mount Melbourne Volcanic Field.**

Lithofacies	Characteristics
Hyaloclastite [H]	Minor lithofacies occurring as lenses usually <30 cm thick and a few meters in extent associated with megapillows, lobes and lava sheets at Edmonson Point, with which they are compositionally identical; fines-poor, formed of blocky, glassy to aphanitic lava fragments typically 1–3 cm in diameter (Figure 9E); usually massive but some show laminated coarse sand to granule-grade bases overlain by coarser reverse-graded to normal-graded hyaloclastite; intact and fragmented small lava pillows common
Pumice lapilli tuff [pLT]	Minor lithofacies only found as lenses 1.5–4 m thick and up to 20 m long associated with compositionally identical megapillow, lobes, and lava sheets at Edmonson Point; weakly lithified to unlithified, variably tuffaceous, and full of white to fawn-brown-colored, angular to abraded pumices up to 12 cm in diameter (mainly 1–10 mm) and up to 5%–10% of aphanitic lava clasts; rare small lava pillows (Figure 9F); varies to fine lapillistone; rare faint planar lamination basally, then reverse- to normal-grading above. The Thickest deposit occurs on the high ridge on the inland side of Edmonson Point, overlying megapillow complex; it may be >20 m thick, comprising diffusely stratified fine pumiceous lapilli tuffs with numerous bombs up to 35 cm across, some breadcrusted, others flattened and dense (obsidian-like); the deposit also contains rare thin (<6 cm) lenses of wavy planar laminated tuff
Lava lobe-bearing breccia [cB]	Varies from c. 25 to >115 m thick; always associated with capping ʻaʻā lava sequences, with which they form cogenetic lava–breccia couplets; the host breccia is massive or rarely crudely homoclinally stratified and formed of coarse aphanitic lava clasts (Figure 9G), generally fines-free or with a minor, patchy coarse or very coarse sand-grade matrix; lava clasts are blocky with planar faces and poorly or non-vesicular; mostly dominated (up to c. 95%) by irregular prismatic and blocky-jointed lava lobes of aphanitic lava up to c. 7 m thick showing closely spaced (1 or 2 dm) irregular joints, blocky joints or entablature with narrow columns (individually typically c. 25 cm wide) that may break up marginally into massive lava breccia; some lobes are partially encased in autobreccia with oxidized clinkers; the breccia in the outcrop north of Edmonson Point is distinguished by two prominent parallel and essentially horizontal orange color bands c. 70 cm thick each, caused by enhanced alteration (Figure 9H)

[a]Lithofacies notations after Smellie and Edwards (2016), slightly modified.

Radioisotopic dating was carried out at the Istituto di Geoscienze e Georisorse, Consiglio Nazionale delle Ricerche (Pisa, Italy). ^{40}Ar/^{39}Ar dates are consistent with the age reported for the reference mineral Fish Canyon sanidine by Kuiper et al. (2008). Full descriptions of the dating results and methods used are presented in Supplementary Figure S3. Elevations and unit thicknesses were determined by hand-held GPS (Garmin eTrex), adjusted for daily pressure drift, and calibrated to fixed locations in the field, with an estimated error of ± 10 m. The terminology for volcaniclastic rocks follows that of White and Houghton (2006), modified to include lapillistones (after Smellie and Edwards, 2016). Additionally, "accessory" and "accidental" refer to cognate lithic clasts and bedrock-derived clasts unrelated to the volcanic center, respectively (Fisher and Schmincke, 1984). Rock compositional names are after Le Maitre et al. (2002).

4 Eruptive styles of flank and satellite centers in the Mount Melbourne Volcanic Field

The volcanic sequences in the MMVF are composed of a comparatively small number of lithofacies and architectures, which together define at least four categories as follows: 1) scoria lapillistones and lava fields, 2) lapilli tuffs and tuffs, 3) megapillow complexes, and 4) lava–breccia couplets. Their principal characteristics and the lithofacies notations used are described in Table 1. Additionally, the trachyte lava or dome present northwest of Edmonson Point (Figure 3) is >180 m thick, multi-colored (pale khaki yellow, green-grey, and cream) with a sugary crystalline texture. It is unconformably overlain by unrelated ʻaʻā lavas, but it is an isolated occurrence. Its age is unknown (older than 112 ± 84 ka; Supplementary Figure S1). Neither the upper nor lower contacts of the trachyte are exposed, and it is not considered further.

4.1 Scoria lapillistones and lava fields

The scoria deposits form variably degraded pyroclastic cones constructed mainly of massive to crudely bedded fines-free deposits dominated by oxidized scoria (LP; Figure 4A). They are associated with agglutinate, clastogenic lavas, and ʻaʻā (sL; rarely pāhoehoe [cL]) lava fields (Figure 4B). The lavas have oxidized autobreccias. Additionally, prominent thick, irregular crystalline intrusions with coarse, crude prismatic joints occur at depth in outcrops on the Cape Washington peninsula (iL; Figure 5). The characteristics of the outcrops are indicative of weakly explosive and effusive magmatic eruptions in the absence of groundwater or surface water (or snow/ice).

4.2 Lapilli tuffs and tuffs

At least 12 discrete outcrops formed of lapilli tuff and tuff are present in the MMVF (Figure 3). They are strongly eroded. All the outcrops are dominated by khaki-yellow fine lapilli tuffs with dips often between 18 and 24 but varying to horizontal (Figures 6, 7). Crater-rim unconformities are preserved in strata high in the outcrops at northern Baker Rocks and on the coast northeast of Baker Rocks. Important characteristics include predominant planar, diffuse, discontinuous stratification, rare low-angle cross-stratification, and monomict compositions, with minor accessory lava clasts and scarcity of impact structures beneath outsize clasts (dsLT, dsT). Clasts are blocky and variably vesicular sideromelane and poorly sorted, they often contain abundant fine ash-size matrix, and some contain ash-coated lapilli. These are characteristics shared by deposits formed from dilute pyroclastic density currents (PDCs) during explosive hydrovolcanic eruptions (Branney and Kokelaar, 2002). They result in the construction of tuff cones and tuff rings, but the absence of accidental (bedrock-derived) clasts (except possibly in basal beds at

TABLE 2 Summary of new ^{40}Ar/^{39}Ar ages for volcanic rocks of the Mt Melbourne Volcanic Field[a]

Sample #	PNRA #	Locality	Lithology	Analyzed material	Total gas age (Ma)[b]	±2σ	Plateau age (Ma)[b]	±2σ	^{39}Ar$_{(K)}$ % plateau or number of grains in the weighted mean	Preferred age
Irradiation PAV-66										
T5.5.4	11.12.05JS4	Harrow Peaks	Lava (intrusion in tuff cone)	Groundmass	0.619	0.020	**0.645**	**0.020**	51.4	Plateau
T5.3.4	07.12.05JS4	N of Willows Nun	Lava (intrusion in tuff cone)	Groundmass	0.769	0.025	**0.756**	**0.023**	74.1	Plateau
T5.4.6	09.12.05JS3	Shield Nunatak	Lava	Groundmass	0.064	0.028	**0.063**	**0.020**	95.7	Plateau
T5.17.1	25.12.05JL1	Shield Nunatak	Lava	Groundmass	1.663	0.015	**1.629**	**0.013**	80.9	Plateau
T5.10.2	14.12.05JS2	Markham Island	Lava, clastogenic	Groundmass	1.104	0.026	**1.112**	**0.020**	99.7	Plateau
T5.15.1	20.12.05JA1	Baker Rocks, south	Lava pillow (intrusive; in tuff cone)	Groundmass	0.139	0.009	**0.138**	**0.006**	100.0	Plateau
T5.36.3	09.01.06JS3	NE of Baker Rocks	Lava (intrusion in tuff cone)	Groundmass	2.958	0.055	**2.951**	**0.050**	83.0	Plateau
T5.18.1	25.12.05JL6	7 km north of Edmonson Point	Lava, megapillow	Groundmass	0.127	0.010	**0.1284**	**0.0066**	100.0	Plateau
T5.34.1	08.01.06JS1	Edmonson Point	Lava	Groundmass	0.0984	0.0047	**0.0877**	**0.0043**	70.9	Plateau
T5.34.3	08.01.06JS3	Edmonson Point	Pumice (ignimbrite)	Alkali feldspar	0.1157	0.0029	**0.1147**	**0.0028**	11/11	Plateau
T5.37.3	11.01.06JS3	Cape Washington summit	Lava (juvenile clast in tuff cone)	Groundmass	1.86	0.10	**1.739**	**0.081**	61.6	Plateau
T5.37.5	11.01.06JS5	Cape Washington summit	Lava; local delta #4	Groundmass	2.976	0.037	**2.903**	**0.037**	60.6	Plateau
Irradiation PAV-87										
T11.1.3	18.11.11JS3	Southern Cape Washington peninsula	Lava; local delta #1	Groundmass	4.21	0.10	**4.10**	**0.12**	43.4	Plateau
T11.1.6	18.11.11JS6	Southern Cape Washington peninsula	Lava; local delta #2	Groundmass	3.71	0.12	**3.271**	**0.039**	52.7	Plateau
T11.4.4	21.11.11JS4	Cape Washington	Lava (intrusion in Strombolian vent)	Groundmass	3.018	0.017	**2.913**	**0.012**	83.5	Plateau
T11.22.2	02.12.11JS8	West flank Cape Washington peninsula	Lava; local delta #4	Groundmass	3.156	0.013	**3.161**	**0.011**	56.6	Plateau
T11.5.2	21.11.11JS6	8 km N of Cape Washington	Lava (intrusion in Strombolian vent)	Groundmass	1.650	0.017	**1.657**	**0.010**	79.9	Plateau
T11.5.3	21.11.11JS7	8 km N of Cape Washington	Lava; from lava lobe-rich breccia of lava-fed delta	Groundmass	1.966	0.016	1.792	0.011	33.5	**~1.8**
T11.6.3	22.11211JS3	E of Willows Nunatak, Cape Washington peninsula	Lava (intrudes scoria lapillistones)	Groundmass	0.892	0.012	No plateau	–	–	≤ **0.76** Ma
T11.9.1	24.11.11JS1	3 km NW of Edmonson Pt	Lava; lava-fed delta	Groundmass	1.0260	0.0063	**1.0265**	**0.0059**	73.5	Plateau
T11.23.3	03.12.11JS3	2 km SW of Edmonson Pt	Lava, megapillow	Groundmass	0.9193	0.0052	**0.9071**	**0.0047**	79.7	Plateau
T14.20.1	15.12.14JS1	c. 8 km north of Edmonson Pt	Lava, megapillow	Groundmass	0.1281	0.0035	**0.1274**	**0.0029**	100.0	Plateau

[a]See Supplementary Figure S3 for analytical details and the full dataset.

[b]Preferred ages shown in bold; ages are relative to either the reference material Fish Canyon sanidine [FCs, age 28.201 ± 0.046 Ma (Kuiper et al., 2008)—irradiation PAV-66] or the Alder Creek sanidine [ACs, age 1.1848 ± 0.0012 Ma (Niespolo et al., 2017)—irradiation PAV-87].

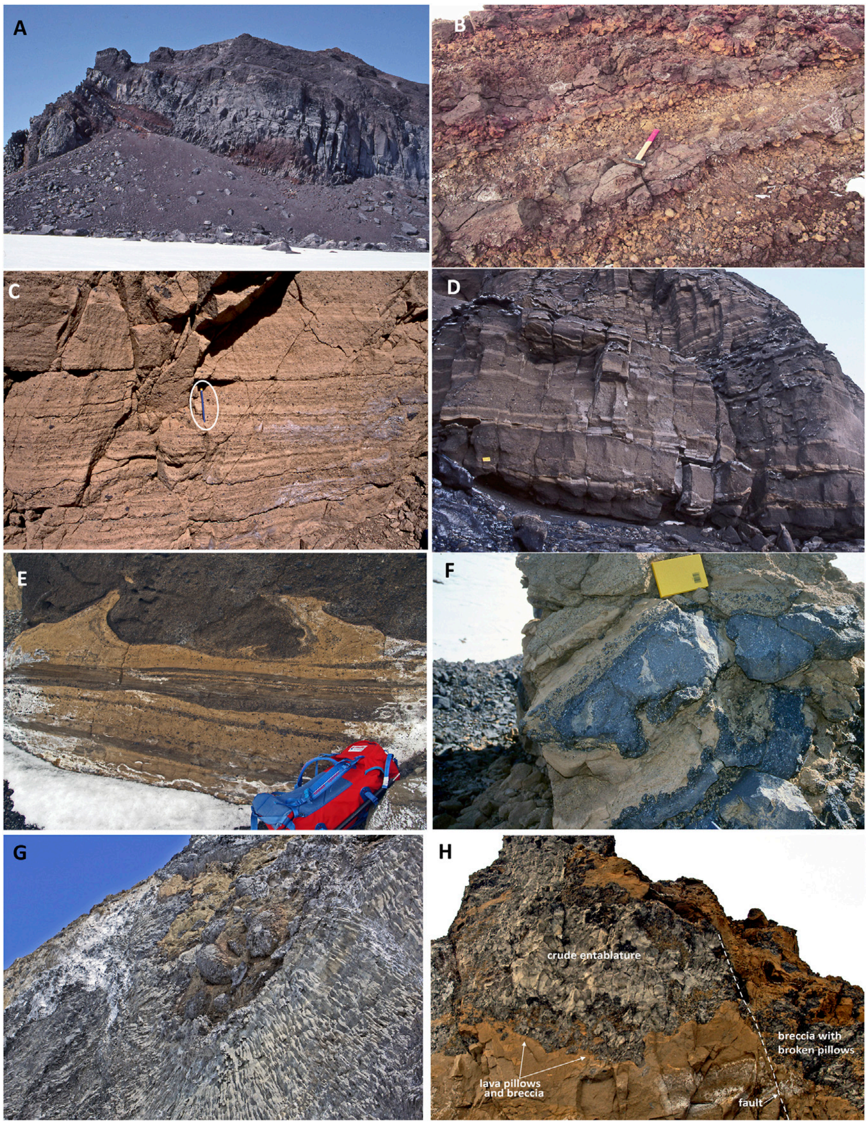

FIGURE 4
Photo compilation showing features of selected lithofacies in scoria and tuff cones in the MMVF. **(A)** View of oxidized scoria, agglutinate, and clastogenic lavas; Markham Island north face; the cliff face is c. 90 m high. **(B)** Close view of ʻaʻā lavas and autobreccias; west flank of Cape Washington peninsula, 3.5 km north-northwest of Cape Washington; the hammer is 40 cm long. **(C)** Diffusely stratified fine lapilli tuffs characteristic of the lapilli tuff outcrops; the individual beds are massive, and the bedding surfaces are ill-defined and essentially gradational; Baker Rocks, north; the pencil (ringed) is c. 13 cm long. **(D)** Well-stratified lapilli tuffs and tuffs; the bed surfaces are much better defined than in C; the strata are laterally continuous, often amalgamated, and internally well-structured (normal and reverse grading, planar and wavy lamination, minor soft-state deformation), all features of subaqueous density current deposits (Mulder and Alexander, 2001; Moorhouse and White, 2016); the wavy laminations are probably transitional to ripples; the strata crop out at an elevation of c. 300 m asl; outcrop northeast of Baker Rocks; the notebook is 17 cm long. **(E)** Close view of lapilli tuff beds showing prominent soft-state deformation (load and flame structures) developed in water-saturated tephra; Shield Nunatak; the rucksack is c. 85 cm long. **(F)** Close view of intrusive lava pillows in lapilli tuffs and tuffs; note the fluidal textures on the surface of the basal pillow shown, the development of peperite, and the disturbance of adjacent stratification; Baker Rocks, south; the notebook is 17 cm long. **(G)** Large dyke-like neck within lapilli tuff outcrop; the intrusion is entablature jointed throughout and develops large pillows marginally where they intrude adjacent lapilli tuffs; the lava pillows are 3–5 m in diameter; outcrop c. 2.4 km north-northwest of Willows Nunatak. **(H)** View looking up at invasive lava within massive fine lapilli tuffs in the western cliffs of Shield Nunatak; the lava can be traced to subaerial sheet lavas out of the view beyond the skyline; it develops lava pillows marginally and breaks up into breccia beyond the small-displacement fault seen at right; the breccia on the right may be due to interaction between the invasive lava and wet tephra or brittle breakage linked to the generation of the fault shown; the rock face is c. 20 m high.

Harrow Peaks; Giordano et al., 2012) is more typical of tuff cones, with the loci of explosions high in the eruptive pile rather than in bedrock. Bedrock-sourced explosions, typically resulting in a high proportion of bedrock clasts (>10 vol%; Sohn, 1996; Ort et al., 2018; Latutrie and Ross, 2020), result in the construction of tuff rings and maars, whereas tuff cones typically form where magma interacts with shallow surface water (lakes or the sea), although they can also form above free-flowing readily recharged aquifers (Sohn and Chough, 1992). The absence of basal pillow lava mounds and pillow lava fragments as clasts in the outcrops indicates that volatile exsolution and explosivity were not suppressed at the outset consistent with low ambient pressures and thus relatively shallow water depths, or possibly relatively thin

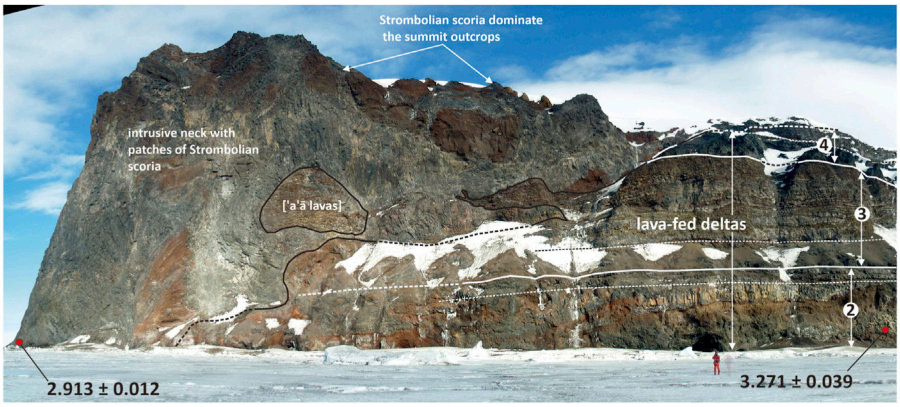

FIGURE 5
View of the east side of Cape Washington showing a sequence of 'a'ā lava-fed deltas intruded by intrusive necks and sheets associated with coeval oxidized Strombolian scoria deposits (see also Figure 11). The fine dashed lines indicate the approximate positions of passage zones (subaqueous–subaerial transitions) associated with each lava-fed delta. The locations and $^{40}Ar/^{39}Ar$ ages (Ma) of dated samples are also shown, with ± 2σ internal uncertainties. The cliff is c. 250 m high.

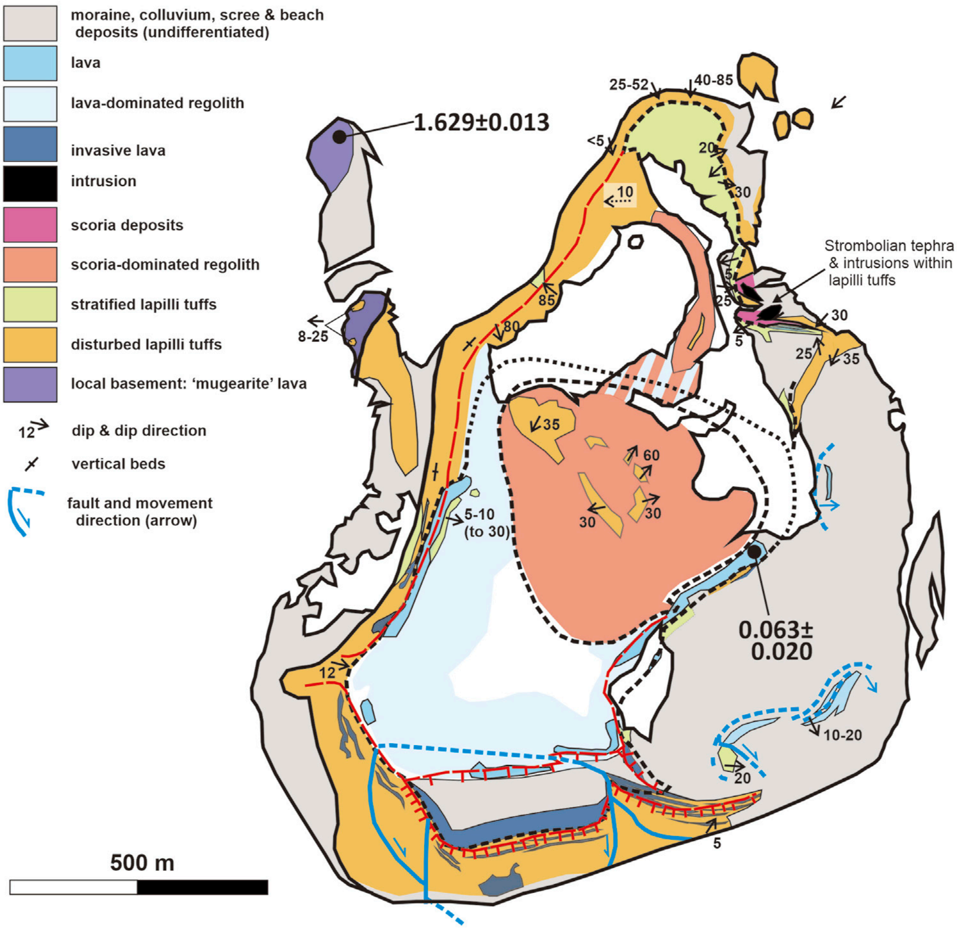

FIGURE 6
Geological map of Shield Nunatak. The locations and $^{40}Ar/^{39}Ar$ ages (Ma) of dated samples are also shown, with ± 2σ internal uncertainties. Note (1) the often gently inward-dipping upper lapilli tuff strata and (2) the occurrence of scoria lapillistone deposits at two levels (at the summit and within lapilli tuffs in the northeastern cliff face; the latter outcrop also includes entablature-jointed intrusions). Both are features consistent with the eruption in an ice-confined glacial vault involving variable water levels and multiple vents. Very similar relationships also occur in the outcrop east of Willows Nunatak (Figure 7).

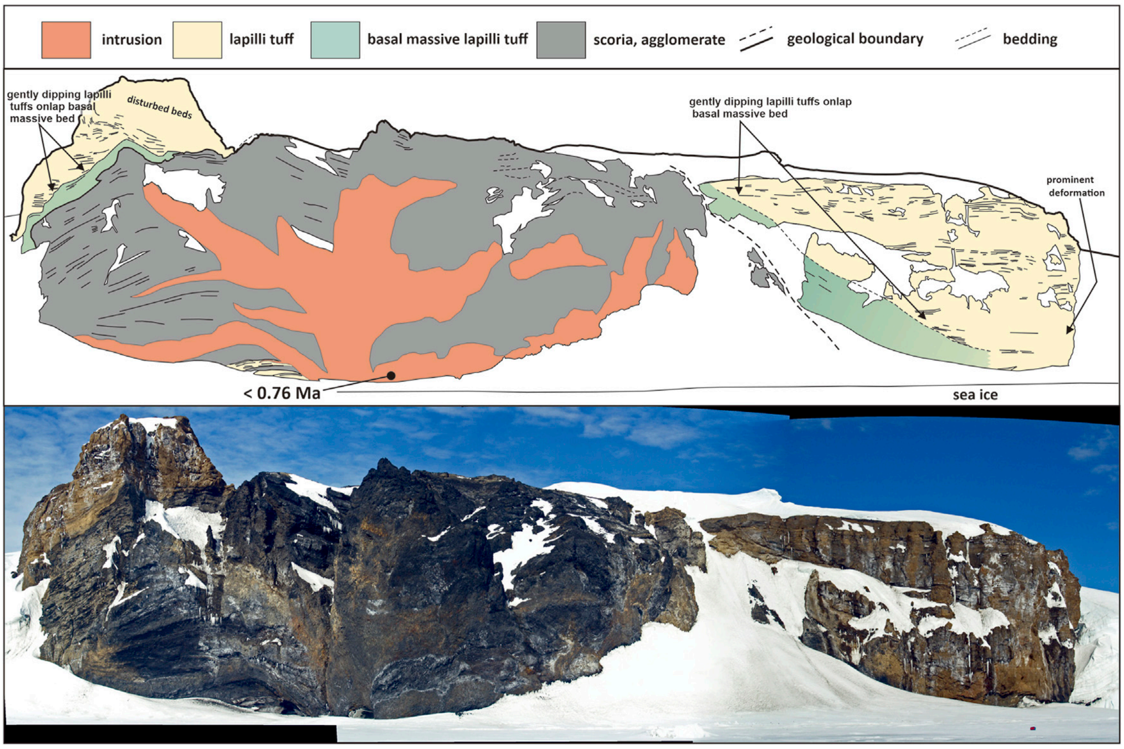

FIGURE 7
Sketch of outcrop east of Willows Nunatak showing the principal lithofacies present. The location and ^{40}Ar/^{39}Ar age (Ma) of the dated sample are also shown, with ± 2σ internal uncertainty. Note the very low dips of the upper (lapilli tuff) strata, consistent with banking against surrounding high ice walls and eruption in a glacially confined vault. Although the central intrusion invades scoria lapillistones, it is pervasively entablature-jointed with blocky and pseudopillow joints, suggesting that the scoria deposit was water saturated by the time the neck was emplaced. Note also the thin lapilli tuff units formed from hydrovolcanic eruptions at the base of the scoria deposits, left of the intrusive neck. The outcrop is petrologically similar throughout (basanite) and was constructed from products of more than one vent, with later vent-clearing hydrovolcanic explosive eruptions forming the massive deposit (green color) that drapes the slightly earlier scoria unit. An eruptive history involving variable water levels and multiple vents is indicated as also occurred at Shield Nunatak, but the outcrop lacks the thin capping sequence of subaerial lavas present at Shield Nunatak (*cf.* Figure 6). The cliff is c. 100 m high.

overlying ice. Although it is thought that powerful explosive MFCI hydrovolcanic eruptions are increasingly unlikely at water depths exceeding 100 m (Zimanowski and Büttner, 2003; Dürig et al., 2020), the depth of the effusive to explosive transition for mafic magmas is not well defined. Estimates typically range between 100 and 200 m (Jones, 1970; Allen, 1980; White et al., 2003; Schopka et al., 2006; Valentine et al., 2014). Explosivity at greater depths is theoretically possible but probably requires special circumstances (IFCI: Dürig et al., 2020), and the relatively high hydraulic pressures at depths greater than 100–200 m seem likely to severely restrict explosivity (*cf.* Wohletz, 2003; Chadwick et al., 2008; Resing et al., 2011).

The pervasive diffuse stratification of the dominant lapilli tuff lithofacies, with its ill-defined bedding surfaces (Figure 4C), indicates rapid deposition from PDCs during vertical aggradation of the eruption-fed tephra piles, probably accompanying a sustained continuous-uprush style of explosive activity (White, 2000; Smellie, 2001). The deposits are not diagnostic of depositional settings, which can be subaerial or subaqueous (Sohn et al., 2008; Russell et al., 2013; Sohn and Sohn, 2019). However, the preservation of ash-coated lapilli (sensu Brown et al., 2012) is unlikely if the lapilli fell into and sank through water. They occur in outcrops at northern Baker Rocks, Oscar cliff, Shield Nunatak, and east of Willows Nunatak. In each case, they are confined to the uppermost strata, consistent with subaerial exposure of the tuff cone in its final eruptive stages. In a few examples, the final eruptive activity consisted of scoria cones, signifying "dry" subaerial conditions [Baker Rocks (south), Shield Nunatak]. Uncommon occurrences of ash-coated lapilli at lower elevations (e.g., at Oscar cliff) might be reworked during discrete mass flow events in which the lapilli were transported while isolated from the overlying water by relatively concentrated PDCs rich in fine tuff. However, tuff cone eruptions within a water-flooded vent occur through repeated ejection and recycling of water-saturated slurries (Kokelaar, 1983). It is an environment that will probably reduce the formation of ash-coated particles and ash aggregates because of the lack of surface tension effects (Go et al., 2017). Ash-coated particles and aggregates are common in the subaerially constructed summit cones formed after the vent is no longer flooded (Sohn et al., 2008).

By contrast, the associated, less common lithofacies may have been deposited mainly under subaqueous conditions. They include lithofacies glLT, dsT, xT, bT and glT (Table 1). They consist of well-structured laterally continuous beds with sharp surfaces and a variety of structures, including amalgamation, reverse- and normal-grading, syn-sedimentary instability (flame structures, soft-state deformation), ripple bedforms, and planar and wavy laminations (Figures 4D,E), which collectively probably indicate subaqueous transport and deposition. Beds of lapilli tuff with well-defined (rather than diffuse) bedding surfaces have been interpreted as

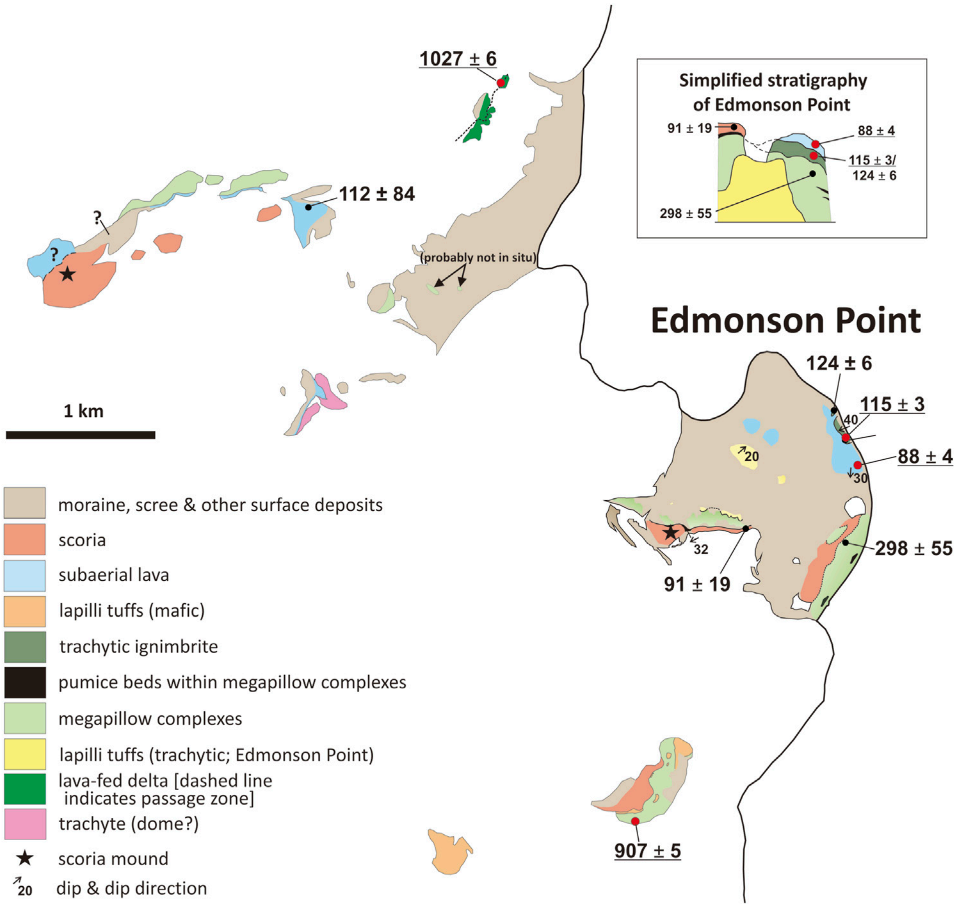

FIGURE 8
Geological map of Edmonson Point and areas inland. ^{40}Ar/^{39}Ar ages (ka) are given with ± 2σ internal uncertainties. The ages presented in this study are underlined. Other ages are culled from Giordano et al. (2012). The inset is a schematic composite sketch section to show the relationships between the major geological units (not to scale).

products of intermittent jetting activity in Surtseyan tuff cones resulting in discrete pulses of tephra cascading down the subaqueous flanks as gravity flows (White, 1996; White, 2000; Smellie, 2001; Sohn et al., 2008). Although there is a resemblance to subaerial deposits (e.g., Sohn and Chough, 1992; Sohn, 1996; Solgevik et al., 2007), it is unlikely that fast-moving subaerial pyroclastic density currents are capable of creating the deposits with (admittedly rare) small (<c. 5 cm amplitude) ripples with steep lee faces, whereas they are a common bedform in subaqueous sequences (Skilling, 1994; White, 1996; White, 2000; Sohn et al., 2008; Moorhouse and White, 2016; Sohn and Sohn, 2019). The soft-state deformation is also more likely to occur in a water-saturated substrate. The absence of steep-sided erosion surfaces, such as incised rills and other channels cut by surface wash, and the absence of ash-coated lapilli are also indirect evidence for a subaqueous depositional setting (Sohn et al., 2008). Additional support is provided by the presence of intrusions at high elevations in the tephra piles showing pervasive entablature or closely spaced irregular jointing and intrusive lava pillows (iL; Figure 4F). The style of jointing and development of lava pillows indicates a water-rich environment. Hence, the tephra piles were water-saturated and presumably surrounded by a lake. Entablature jointing in the coeval intrusions typically extends up to c. 200 m above sea level (asl) but may exceed 300 m asl in the outcrop northeast of Baker Rocks. The neck or large dyke in the outcrop north of Willows Nunatak also includes marginal megapillows invading adjacent lapilli tuffs (Figure 4G). Finally, the tuff cone outcrop at Shield Nunatak has a capping unit of sheet-like ʻaʻā lavas. In part, they are coarsely jointed and finely crystalline consistent with subaerial emplacement, although lacking oxidation of the autobreccias. They were probably sourced from the small summit scoria cone present (Figure 6). However, the lavas transform down-dip into invasive sheets showing the development of aphanitic breccias and pillows (Figure 4H), indicating intrusion into the tephra deposits, which were water saturated and unlithified, and a high coeval water level. Scoria deposits also occur in other lapilli tuff outcrops in the MMVF [east of Willows Nunatak (Figure 7), Baker Rocks (south)]. In summary, the tuff cone outcrops show evidence for subaqueous and subaerial eruptions consistent with an origin as Surtseyan (subaqueous to emergent) tuff cone edifices.

4.3 Megapillow complexes

Outcrops composed of interconnected megapillows, lobes, and lava sheets (MpL) are restricted to the east side of the Mount Melbourne peninsula, at Edmonson Point, and in surrounding

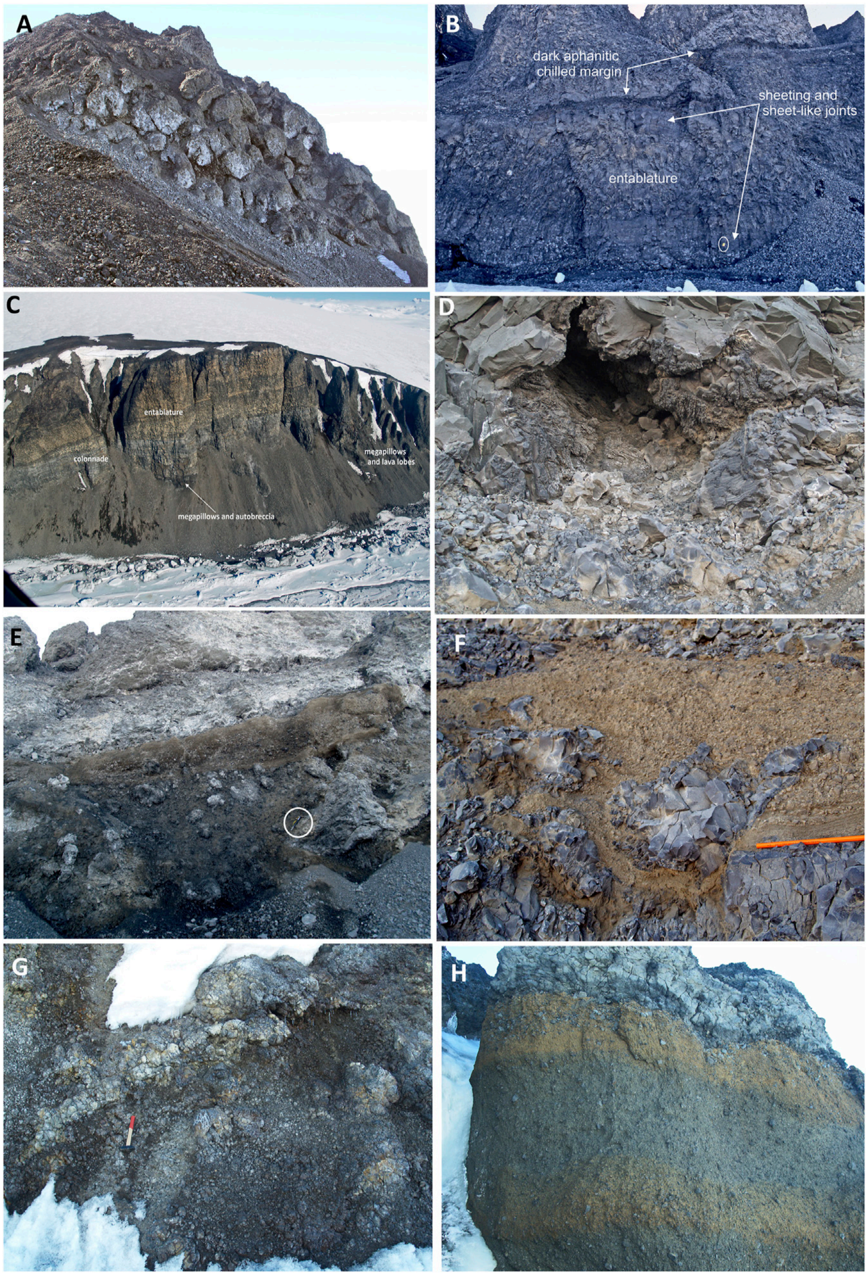

FIGURE 9
Photo compilation showing features of selected lithofacies in the MMVF: megapillow complexes and lava-fed deltas. **(A)** Cluster of close-packed megapillows; the megapillows in this group are unusually well defined; individual megapillows are 4–8 m in diameter; southern Edmonson Point. **(B)** Lava lobe or small sheet 7 km north of Edmonson Point; the lobe is dominated by pervasive closely spaced cooling joints, mainly marginal sheeting joints and prominent central entablature. Sheet-like joints cut perpendicularly across the marginal sheeting joints; the notebook (ringed) is 17 cm long. **(C)** Large lava sheet >500 m long with a thin basal colonnade (pale grey) and overlying much thicker entablature (brown); the lava changes to megapillows and lobes to the right and below; outcrop 7 km north of Edmonson Point; the cliff is c. 200 m high. **(D)** Large void c. 1 m in diameter with fretted glassy surface situated between megapillows, interpreted as a likely ice-block melt-out cavity; southern Edmonson Point. **(E)** Unusually thick lens of massive fine hyaloclastite with dispersed intact and fragmented lava pillows between lava masses; southern Edmonson Point; the ice axe (ringed) is c. 70 cm long. **(F)** Lens of trachytic pumice lapillistone with lava pillows; the pumice deposit shows planar laminations to base; southern Edmonson Point; the pencil shown is 13 cm in length. **(G)** Massive breccia formed of angular, blocky, monomict, aphanitic lava fragments with numerous closely jointed, irregular, water-cooled lava lobes; lava-fed delta outcrop c. 9 km north of Cape Washington; the hammer is 40 cm in length. **(H)** View of lava-fed delta passage zone in the outcrop c. 3.5 km north-northwest of Edmonson Point; the closely jointed lava at the top of the outcrop is water cooled and invades the underlying monomict lava breccia; the breccia also shows two prominent pervasive orange-stained alteration zones, each c. 70 cm thick, interpreted as possible alteration fronts caused by at least two water levels coeval with emplacement of the delta.

nunataks (Figures 3, 8, 9A–C). The division into several morphologies is based on size (terminology after Goto and McPhie, 2004). However, the exposure is only in two dimensions, so the full three-dimensional morphologies of the lava bodies are unknown. Although megapillow shapes can reasonably be inferred for some outcrops (Figure 9A), other megapillows might be cross-sections through tubes. All lava

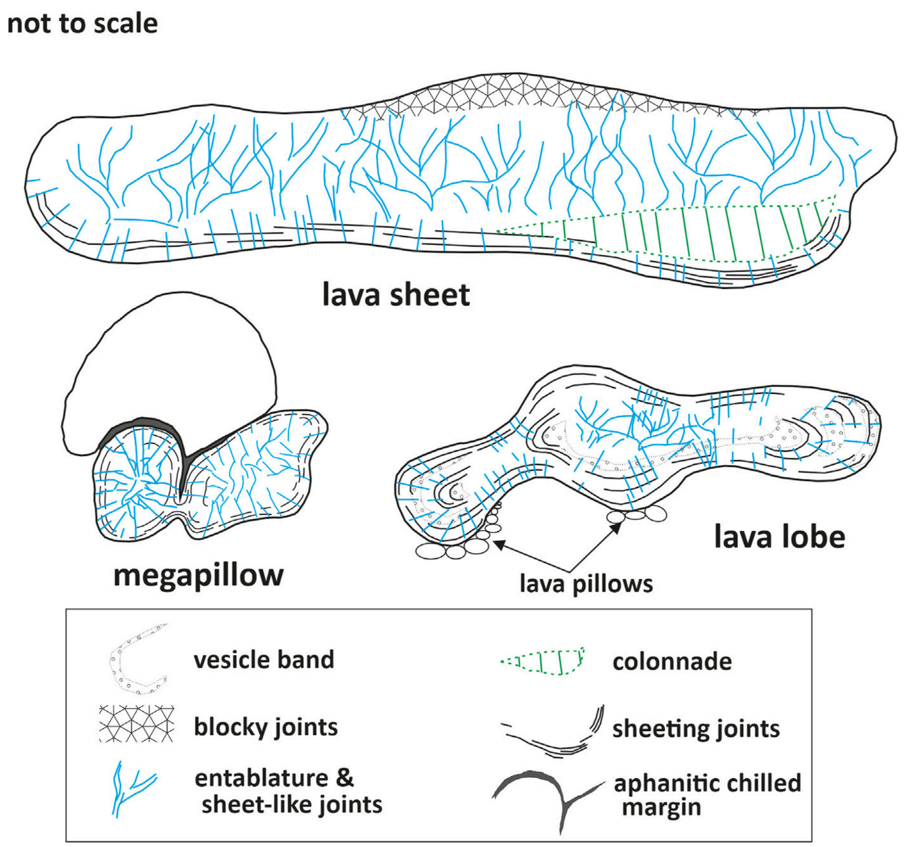

FIGURE 10
Sketches illustrating the shapes of megapillows, lobes, and lava sheets in the megapillow complexes of the MMVF and the spatial relations between the different jointing styles. The morphologies grade into one another. Megapillows are typically 4–8 m in diameter and broadly circular to somewhat oblate in two dimensions (Figure 9A); lobes are a few to c. 10 m high and up to a few tens of meters long (Figure 9B); lava sheets are typically several tens of meters high and extend up to a few hundred meters in length (Figure 9C).

masses are characterized by multiple sets of prominent cooling fractures, including sheeting, entablature, sheet-like, blocky, and pseudopillow (Figures 9B,C). Blocky joints (also called cube joints or hackly joints) are a more densely fractured version of entablature caused by interaction with larger amounts of coolant and a faster cooling rate (Forbes et al., 2014). The spatial development of the joint types is the same in each outcrop and is concentric to the lava morphology (Figure 10). All the joints are extensional structures, and the style of fracturing and fracture spacing reflect (1) the position of the fractures relative to the lava margins and (2) the cooling history of the lava, that is, progressive inward cooling (Lescinsky and Fink, 2000). They are caused by the rapid chilling of lava against water or ice, and the fracture spacing is inversely proportional to the cooling rate (Long and Wood, 1986; Grossenbacher and McDuffie, 1995; Lescinsky and Fink, 2000; Goehring and Morris, 2008). The marginal sheeting joints wrap around and mimic the shape of the individual lava bodies. They form after the lava has substantially crystallized and are thought to be related to late-stage shear within the lava (Bonnichsen and Kauffmann, 1987). In the absence of exposed surfaces, they are often the best indicator of the overall morphology of the individual lava masses. Moreover, observations of the sheeting joint orientations have shown that most of the lava masses in the MMVF outcrops are probably interconnected. The multiple bands of vesicles observed in some megapillows and lobes are vesicle zones characteristic of lava inflation (Self et al., 1996; Self et al., 1998). The autobreccia clinkers are also vesicular. Together with the vesicle zones, the features suggest that the lavas were not fully degassed when they erupted.

Lava pillows and megapillows are thought to characterize subaqueous lava emplacement (Batiza and White, 2000; Goto and McPhie, 2004; Hungerford et al., 2014). In the megapillow complexes of the MMVF, the presence of lava pillows and megapillows with glassy rims and lenses of hyaloclastite indicates rapid water chilling. Moreover, entablatures and pseudopillow fractures form by steam and water penetrating down extensional fractures (Long and Wood, 1986; Lescinsky and Fink, 2000; Forbes et al., 2012; Forbes et al., 2014). However, the lava masses typically have dm-thick dark grey rims that are aphanitic or hypohyaline (Figure 9B), and glassy (holohyaline) rims are poorly developed in general. The presence of relatively thin colonnades below some of the lava sheets (Figure 9C) also indicates slow conductive cooling. The observations are inconsistent with the rapid cooling of subaqueous lavas. The sedimentary features of the interbedded lenses of pumiceous lapilli tuff (pLT; Table 1) indicate transport and deposition by tractional and density currents (planar lamination and variable grading; *cf.* Mulder and Alexander, 2001). The abundant highly vesicular pumice is likely to float, suggesting that transport was fluvial unless the pumice was hot when it fell onto the water and ingested water, causing it to rapidly become waterlogged and to sink (Witham and Sparks, 1986). The abrasion observed in

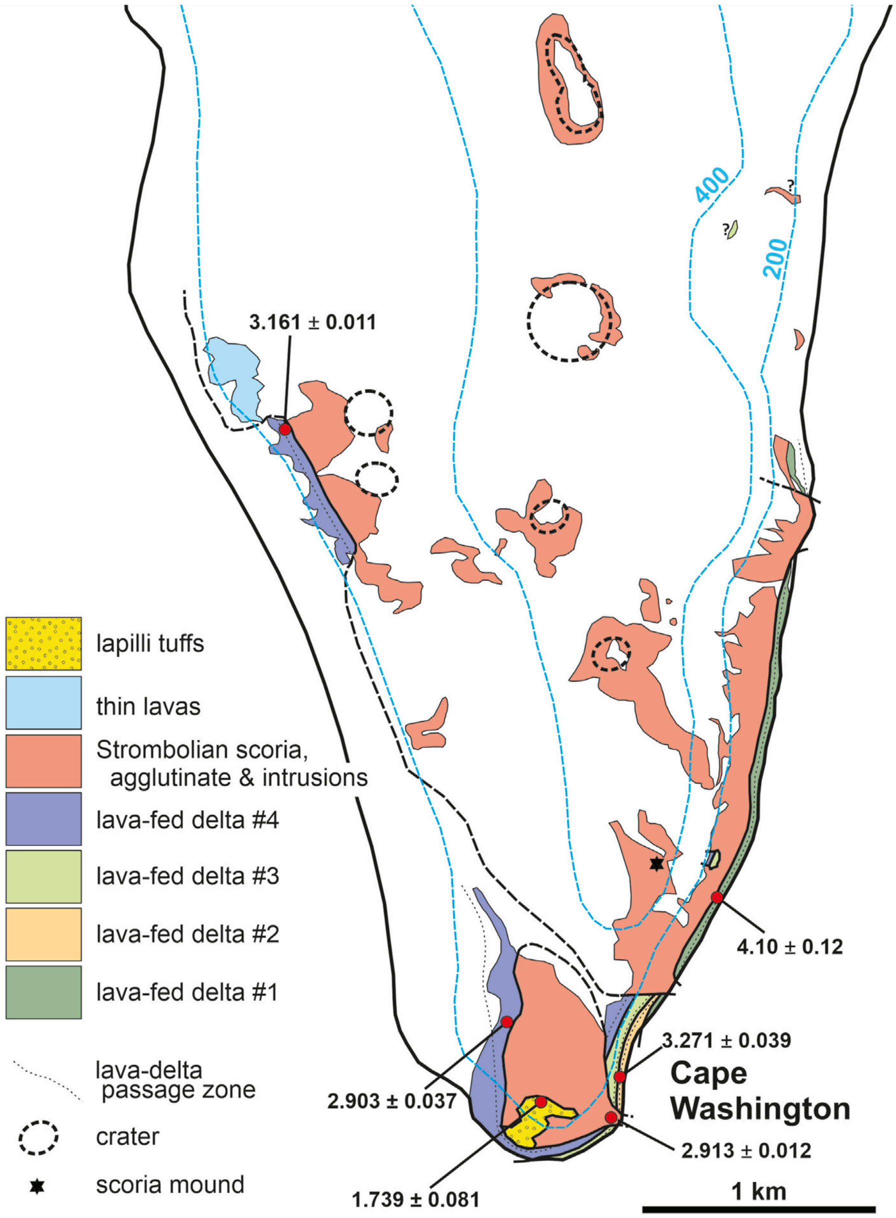

FIGURE 11
Geological map of the southern Cape Washington peninsula, consisting of Pliocene ʻaʻā lava-fed deltas cut across by several Strombolian vents. The latter were aligned in a north–south direction and were probably fault-controlled. They comprise prominent tephrite/basanite intrusions that constructed multiple scoria cones formed of oxidized scoria and at least one fed a small field of ʻaʻā lava. The locations and ^{40}Ar/^{39}Ar ages (Ma) of dated samples are also shown, with ± 2σ internal uncertainties. See also Figure 5.

many of the pumices is also consistent with fluvial transport. The aphanitic lava fragments forming the autobreccias, with their fluidal and planar broken faces, resemble the broken crusts seen in many pāhoehoe lavas, but the absence of oxidation suggests that emplacement was not subaerial (i.e., “dry” conditions; Self et al., 1996; Bondre et al., 2004). Thus, the evidence suggests that although water cooling played a prominent part in the emplacement of the megapillow complexes, the individual lava masses may not have been fully submerged (see Section 6.1.3).

Subaqueous lavas are typically categorized on the basis of their morphology as pillowed, lobate, or lava sheets (e.g., Fox et al., 1987; Schmincke and Bednarz, 1990; Gregg and Fink, 1995; Batiza and White, 2000; Goto and McPhie, 2004; Clague and Paduan, 2009; Hungerford et al., 2014). The distinction is based principally on size, although the lavas also become more flattened as they become larger, and, as described above, they display regular cooling joint patterns (Figure 10; Lescinsky and Fink, 2000). The morphological differences have been related to composition, eruption temperature, cooling rate, effusion rate, viscosity, and crystallinity (Schmincke and Bednarz, 1990; Griffiths and Fink, 1992; Gregg and Fink, 1995, and references therein). However, analog models and studies of ocean-floor lavas have demonstrated that the principal link is to discharge rate and bedrock gradient (Gregg and Fink, 1995; Batiza and White, 2000; Clague and Paduan, 2009). Although pillow

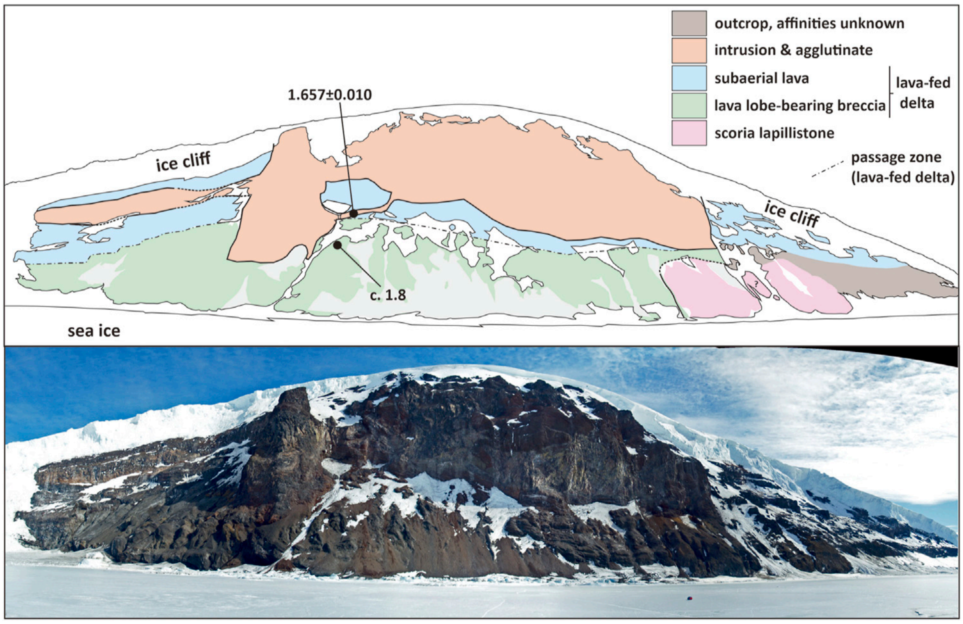

FIGURE 12
Sketch of an outcrop c. 9 km north of Cape Washington with the geology indicated. The exposure cuts through the flank of a small (original basal diameter c. 3 km) isolated Middle Pleistocene shield volcano. The locations and $^{40}Ar/^{39}Ar$ ages (Ma) of dated samples are also shown, with ± 2σ internal uncertainties. The outcrop is dominated by a thick ʻaʻā lava-fed delta. The delta rests on a scoria lapillistone deposit at the right and is cut across by intrusions and associated oxidized scoria of a much younger Strombolian vent. The relationships are the same as at Cape Washington (Figures 5, 11), but the two outcrop areas differ in age. The cliffs shown are c. 150–200 m in height.

diameter is known to increase in more evolved magmas (Walker, 1992), studies have shown that a wide spectrum of flow morphologies (i.e., pillow lavas to lava sheets) can occur with negligible compositional differences (Batiza et al., 1989; Batiza and White, 2000) and the rheological effects of composition, temperature, viscosity, and crystallinity are interlinked. There is no compositional dependence evident in the MMVF. Despite the wide range of compositions present in the megapillow complexes (alkali basalt to Si-poor trachyte; Figure 2), similar lava morphologies occur in each outcrop. Moreover, in some (e.g., outcrop 7 km north of Edmonson Point), the lava masses increase in size up through the lava pile despite no obvious compositional variation. Thus, we suggest that the progression of morphologies, from rare pillows through megapillows and lobes to lava sheets, probably reflects increasing discharge rates, with the generally large dimensions due to relatively slow cooling. We suggest that the slower cooling was due to only partial submergence in water; pillow lavas emplaced fully submerged are faster-cooled and, therefore, smaller. Bedrock gradient might have been a contributing factor affecting flow rate, but the observed variations in morphology, which are usually random in the outcrops, would require that the bedrock gradient varied during the course of the individual effusive eruption, which is unlikely unless the lava piled up around the vent, thus increasing the surface gradient over time. Therefore, we suggest that increasing discharge rates at the vent and environmentally imposed slower cooling rates were the likely dominant factors that led to the different lava morphologies in the megapillow complexes. The lowest effusion rates and highest cooling rates were probably responsible for the pillow lavas, the highest effusion rates and slower cooling led to the lava sheets, and intermediate rates were responsible for the megapillows and lava lobes.

4.4 Lava–breccia couplets

A discovery of the present study was the recognition of multiple lava–breccia couplets within the MMVF. They crop out mainly on the Cape Washington peninsula, particularly close to Cape Washington (Figure 11), but there is an additional small isolated outcrop a few kilometers north of Edmonson Point (Figure 3). The combination of massive chaotic aphanitic lava breccia with abundant irregular lava lobes (cB) capped by subaerially emplaced ʻaʻā lavas (sL) is diagnostic of ʻaʻā lava-fed deltas (Smellie et al., 2011a; Smellie et al., 2013). The lava-fed deltas have shallow dips of c. 5 consistent with original shield-like landforms. The bedding attitudes of additional outcrops with deltas on the east side of the Cape Washington peninsula indicate that multiple small shield-like volcanoes are present (Figure 12). The upper surfaces of only two lava-fed deltas (#1 and #3) were accessible. They are erosive (Figure 13), resulting in the capping ʻaʻā lava sequences of both deltas thinning markedly in a southerly direction. The thickest sequence (c. 250 m) is at Cape Washington and comprises four superimposed lava-fed deltas (Figures 5, 11). The lava lobes in the breccia lithosomes show strong evidence for water chilling in the form of diagnostic joint patterns (mainly closely spaced, irregular, or blocky), and the lobes often break up marginally into aphanitic lava breccia. Oxidized clinkers are also dispersed in the breccias and partially encase lava lobes, which are distinctive features of water-chilled lavas and breccias in ʻaʻā lava-fed deltas (Smellie et al., 2013). The number of lava lobes increases up toward the

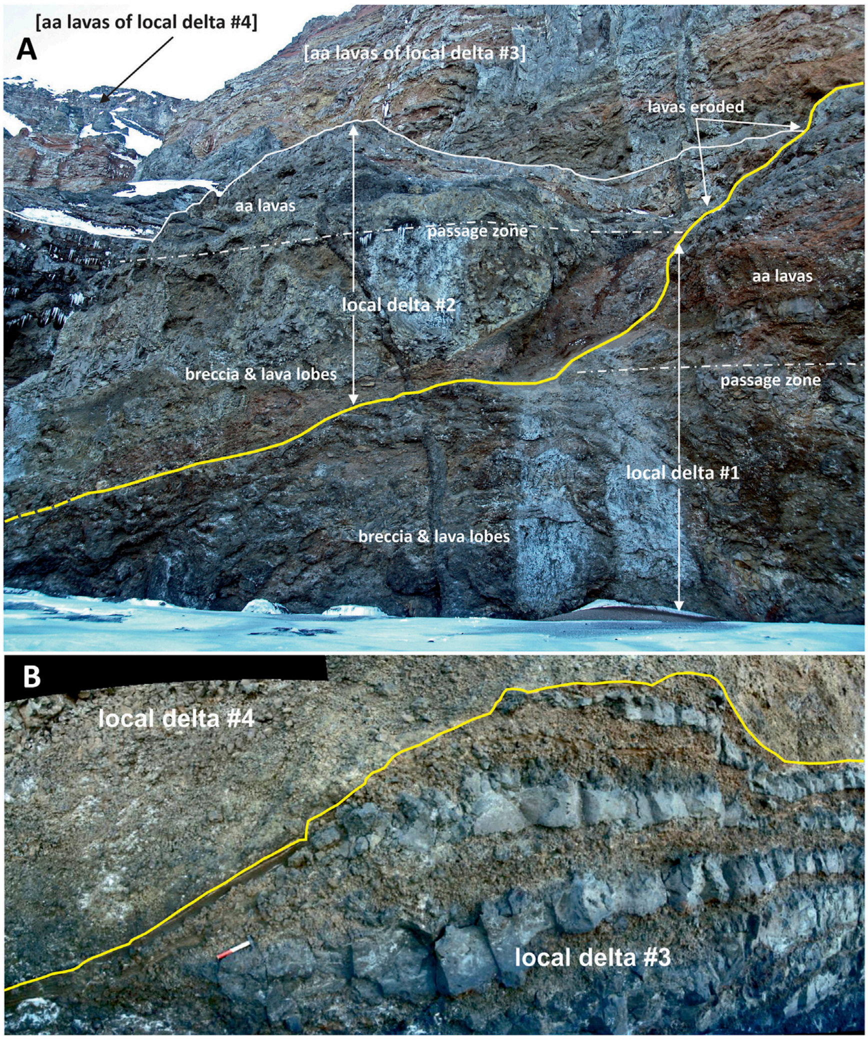

FIGURE 13
Views of upper eroded surfaces (bold yellow lines) of lava-fed deltas at Cape Washington. **(A)** Local lava-fed delta #1; the upper surface of delta #2 is inaccessible, and the uneven appearance is an effect of perspective. **(B)** Local lava-fed delta #3; the subaerial lava capping sequence of delta #3 is substantially thinner at this location (c. 20–25 m) than 0.5 km to the north, where it reaches at least 50 m in thickness (see Figure 5). The evidence for the erosion of the lava-fed delta surfaces suggests that they were modified by wet-based ice.

capping ʻaʻā lavas, and their proportion often exceeds 90% in the uppermost several meters, corresponding to a passage zone, that is, a transition zone separating subaqueous from subaerial lithofacies (see Jones, 1969; Smellie and Edwards, 2016). Passage zones in ʻaʻā lava-fed deltas are characteristically crudely defined.

5 Geochronology

We present 22 new ^{40}Ar/^{39}Ar ages for volcanic units at 19 localities, most dated for the first time (Figure 3; Table 2; Supplementary Figure S1). The new ages vary from 4.10 ± 0.12 to 0.063 ± 0.020 Ma. Lava-fed deltas at Cape Washington are stratigraphically consistent and range from 4.10 ± 0.12 Ma (delta #1) through 3.271 ± 0.039 Ma (delta #2) to 3.161 ± 0.011 Ma (delta #4). An additional ^{40}Ar/^{39}Ar step-heating analysis obtained on delta #4 at a different locality (Figure 11) proved to be slightly but significantly younger, at 2.903 ± 0.037 Ma, which is unexplained and might cast doubt on the mapped correlation, although the units look identical and their elevations (including the passage zone) are comparable. The lava-fed delta that dominates the separate small shield volcano outcrop on the east side of the Cape Washington peninsula yielded an imprecise age of c. 1.8 Ma, whereas the lava-fed delta northwest of Edmonson Point is dated as 1.027 ± 0.006 Ma. The tuff cones show a wide age range, from 2.951 ± .050 Ma (northeast of Baker Rocks) to 0.063 ± 0.020 Ma (summit lava at Shield Nunatak), but most are of Pleistocene age (≤ c 1.74 Ma). The megapillow complexes range in age from 0.907 ± 0.005 (southwest of Edmonson Point) to 0.128 ± 0.007 Ma and 0.127 ± 0.003 Ma (north of Edmonson Point). However, with an age for the megapillow complex outcrop at southern Edmonson Point published by Giordano et al. (2012) (0.298 ± 0.055 Ma), the ages collectively indicate that megapillow complexes in the MMVF were emplaced in multiple episodes at c. 0.91, c. 0.30, and c. 0.13 Ma. Scoria cones and associated intrusions (necks) and lava fields yielded ages of 2.913 ± 0.012 Ma and 1.657 ± 0.010 Ma (both near Cape Washington), 1.629 ± 0.013 Ma (lava underlying

Shield Nunatak), and 0.088 ± 0.004 Ma (young lava unconformably draping trachytic ignimbrite at Edmonson Point; Figure 8). The latter age is indistinguishable within uncertainties from those of 0.091 ± 0.019 Ma (Edmonson Point) and 0.112 ± 0.084 Ma (nunatak northwest of Edmonson Nunatak) obtained on likely correlative units by Giordano et al. (2012). There is no obvious association between the different eruptive types and any narrow time periods. All types erupted throughout the Late Pliocene and Pleistocene.

Finally, we dated an outcrop of trachytic ignimbrite at Edmonson Point. Its distinctive composition indicates that it was derived from the summit of Mount Melbourne. It has an age of 114.7 ± 2.8 ka. Our new age is close to but slightly younger than the mean age reported by Giordano et al. (2012) (124.3 ± 6.1 ka). Taking into account the slight increase in ages, if the most recent values for the reference minerals used by Giordano et al. (2012) are considered, our determination is not greatly dissimilar. We consider the c. 115 ka age a reliable estimate for the emplacement of the ignimbrite at Edmonson Point.

6 Discussion

6.1 Environmental conditions during eruptions in the Mount Melbourne Volcanic Field

The size, lithofacies, compositional uniformity, and internal architectures of the individual low-elevation outcrops in the MMVF examined in this study indicate that they are the products of small volcanoes (sensu White and Ross, 2011). They might also be called monogenetic, but for ancient eruptive centers, it is often impossible to distinguish the products of multiple eruptions in a single edifice. Studies of similar-sized centers often show that they had long histories of multiple eruptions separated by short breaks in activity. However, the lack of obvious internal erosional surfaces that could have been caused by an eruptive hiatus suggests that they are likely to be monogenetic. The construction and morphology of small volcanic centers are determined by internal and external factors. Internal factors include the composition and physical properties of the erupting magma (e.g., viscosity and volatile content). External factors include tectonic setting (differential stress) and magma input (production) rate, but these factors simply affect the size of an edifice [polygenetic (large) *versus* monogenetic (small)] (Takada, 1994). They do not determine the style of eruption or type of monogenetic edifice (e.g., scoria cone *versus* tuff cone). Other external factors are essentially environmental and include the presence and recharge rate of groundwater and surface water (lake, sea). The influence of environmental factors is reflected in the sequence architecture and features of the lithofacies (e.g., clast grading and morphology, clast types, joint patterns, and relative crystallinity).

6.1.1 Scoria cones

The lithofacies that form the small isolated scoria cones (i.e., oxidized scoria, agglutinate, and clastogenic lavas) and the association of some containing ʻaʻā lavas with oxidized autobreccias, or rarely pāhoehoe, are diagnostic of "dry" magmatic eruptions in the absence of surface water or groundwater. Given the polar setting (74°S–75°S), the region need not be entirely ice-free. However, it is possible, given the low elevation and coastal location of the MMVF (<1,500 m asl; mostly <500 m). Despite the widespread extent of snow and ice affecting the MMVF today, the locations of the scoria cone outcrops consist of bedrock with a snow cover probably too thin to interact significantly with the erupting magmas. Likely, modern eruptions at many sites would also produce scoria cones with magmatic or "dry" lithofacies. Therefore, the eruption of the scoria cones indicates environmental conditions comparable with today or with less snow and ice. However, lavas that flow across the snow- or ice-covered ground should show signs of interaction, resulting in distinctive cooling joint patterns (Mee et al., 2006), although the evidence may be difficult to detect (Edwards et al., 2012). However, the apparent absence of such evidence at the localities visited implies that snow- and ice-free conditions probably prevailed at those localities.

6.1.2 Tuff cones

After scoria cones, tuff cones (Surtseyan) are the next most common edifice type. They are not diagnostic of the environment but are formed by the interaction of magma with surface water, either seawater or glacial meltwater, rather than groundwater. The topography surrounding the tuff cone outcrops is unable to pond freshwater, and pluvial lakes are, therefore, unlikely. From our argument earlier, the tuff cones were surrounded by water with a surface at a high elevation (elevations mainly varying between c. 200 m and c. 300 m above modern datum). If the source of the water was marine, it implies that the sea level was at a similar elevation. The Holocene marine limit in the Terra Nova region is c. 30 m asl (Baroni and Orombelli, 1991; Baroni and Hall, 2004; Rhee et al., 2020), similar to that in southern Victoria Land (Hall et al., 2004). Pre-Holocene (age uncertain) raised beaches are also known to be present in southern Victoria Land. However, the marine limit for the few currently described is still within the Holocene marine limit (Gardner et al., 2006). However, Rhee et al. (2020) described undated "very wide and flat benches [also described by the authors as terraces] with minor elevation variations" at elevations up to c. 200 m on Inexpressible Island (southwestern Terra Nova Bay, northern Victoria Land). From the lack of beach deposits and a surface composed of shattered bedrock and erratics, the surfaces were presumed by Rhee et al. (2020) to be glacial in origin. Although they may be a result of structurally controlled glacial erosion (personal communication from C Baroni, June 2022), there is no support from the underlying geology, which is composed of essentially isotropic plutonic rocks lacking horizontal planes of weakness that ice might have preferentially exhumed (Vincenzo and Rocchi, 1999; Rocchi et al., 2004). Alternatively, the flat terrace-like morphology might be relicts of wave-cut platforms that were subsequently overridden, fractured, and otherwise modified by ice. Their interpretation as marine features has not been verified and is therefore speculative; if they have a marine origin and associated uplift, they will increase the likelihood that marine water may have been involved in the eruption of at least some of the tuff cones in the MMVF. An alternative source of water is meltwater created during glaciovolcanic eruptions, a scenario that was assumed by previous workers without supporting evidence (Wörner et al., 1989; Giordano et al., 2012), and we discuss this in the following paragraphs.

Distinguishing between seawater and glacial meltwater can be achieved in favorably exposed instances by examining the lithofacies and architecture of tuff cones. Because of the buttressing effects of coeval ice during glaciovolcanic eruptions, the tephra products rapidly infill the englacial (meltwater-filled) vault and bank up against the enclosing ice walls (Smellie, 2018, in press; Edwards et al., 2022). This leads to a distinctive edifice morphology with a high aspect ratio

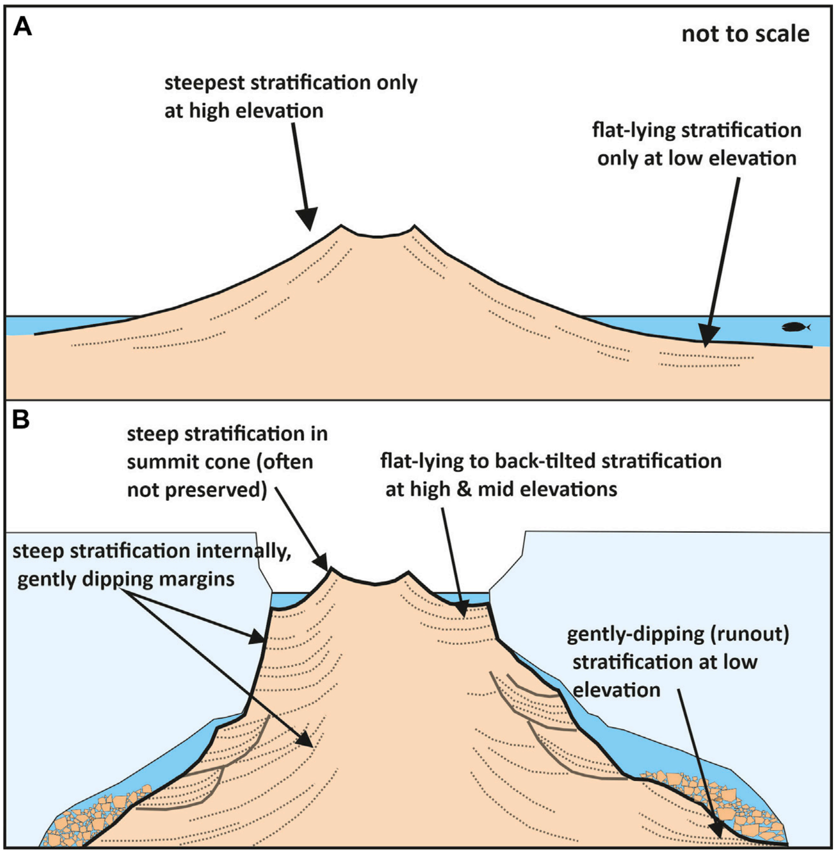

FIGURE 14
Schematic diagrams illustrating the contrasting morphologies and internal architectures of tuff cones erupted under **(A)** non-glacial, unconfined conditions (in the sea or a pluvial lake) and **(B)** glacial, confined conditions (i.e., under an ice sheet). **(A)** omits the effects of undercutting of tuff cones erupted in exposed locations, which can cause slumping and shear surfaces (illustrated in Figure 16), sometimes associated with beach deposits (White, 1996). Note how tuff cones constructed in ice also have higher aspect ratios (height:basal width; Smellie, 2013).

(i.e., limited lateral extent) and an internal architecture comprising gently dipping strata at all elevations around the margins of englacial tuff cones. As volcanic heat is transferred to the enclosing ice, the walls recede, thus removing their buttressing support and leading to repeated sector collapses of the tuff cone flanks. Glaciovolcanic tuff cones are characterized by prominent slump-scar surfaces (Smellie, 2001; Smellie, 2018). By contrast, eruptions in the sea (or in pluvial lakes) are unconfined, and the strata are laterally extensive and asymptotic, declining from c. 20° to 45° around the summit crater to almost horizontal in the subaqueous ring plain (Sohn, 1996; Smellie et al., 2018). These relationships are illustrated in Figure 14. Of course, marine-emplaced tuff cones constructed in exposed locations can also be undercut by wave activity and may collapse similarly to collapses that affect larger volcanic arc edifices (Moorhouse and White, 2016; Romero et al., 2021). The scarcity of descriptions of collapse features in small marine tuff cones suggests that they are seldom preserved (marine-emplaced tuff cones are typically short-lived features; Sohn, 1996; Kano, 1998; Cole et al., 2001; Solgevik et al., 2007; Cavallero and Cortelli, 2019; Garvin et al., 2018).

Tuff cone outcrops at Harrow Peaks, Baker Rocks (south), east of Willows Nunatak, and Shield Nunatak have features that appear to have been determined by eruptions through a glacial cover. The Harrow Peaks outcrop is inland and sits astride a sharp-crested, steep bedrock ridge with an elevation of c. 360–400 m asl. There is abundant evidence for water saturation of the tephra pile, including the presence of coeval water-cooled hypabyssal intrusions with fluidal margins. The characteristics have been interpreted as diagnostic of eruption in a meltwater lake perched atop the ridge, which was covered by cold-based ice during the eruption to confine the meltwater in a vault on top of a steeply dipping (50–70°) bedrock (Smellie et al., 2018). The other three outcrops show lapilli tuff strata that are essentially flat-lying at high elevations in the outcrops, and strata at Shield Nunatak also frequently dip in toward the center of the nunatak (Figures 6, 7). These observations are inconsistent with unconfined eruption and suggest that the tephra piles occupied and infilled an englacial vault, with the tephra banked against the ice walls (Figure 14B). Moreover, water-cooled (entablature) jointing affects coeval hypabyssal intrusions up to high elevations, and one outcrop (Baker Rocks, south) has intrusive pillow lava between 400 and 600 m asl. Hence, the tephra piles were water saturated to similar heights. All three outcrops are also associated with coarse grey scoria lapillistones. The scoria deposits occur at the top (Baker Rocks south; Shield Nunatak), within (Shield Nunatak), and at the exposed base (east of Willows Nunatak; Figures 6, 7) of the outcrops. The summit of Baker Rocks (south) is a small scoria cone. It is draped by a thin cover of fine lapilli tuffs that were probably sourced from the crater responsible for the adjacent outcrop at Baker Rocks (north), consistent with the c. 1 Myr age difference between the two centers

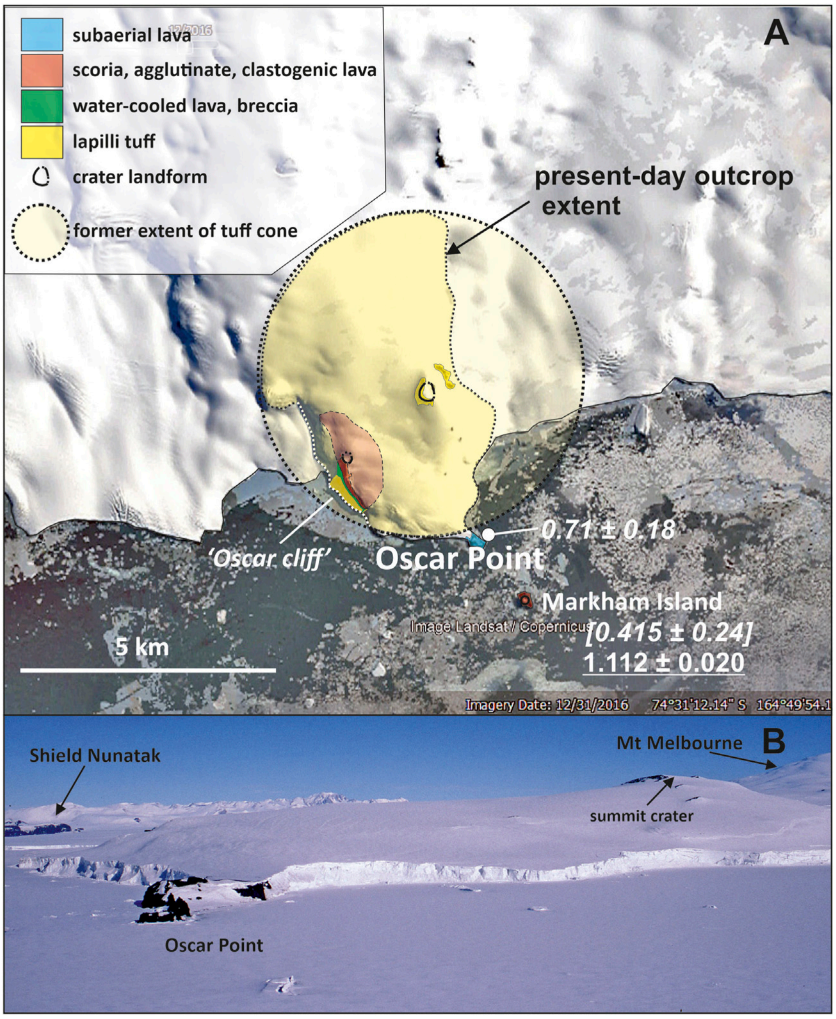

FIGURE 15
(A) Map of Oscar Point showing the inferred original extent of the tuff cone that forms most of the locality. **(B)** Photo of Oscar Point looking northwest, showing the very low gradient of the tuff cone flanks compared with steeper gradients rising to the cratered summit area. Evidence for pervasive water-cooling of coeval intrusions occurs up to c. 180 m asl in "Oscar cliff," suggesting that the contemporary sea level reached a similar elevation. See Figure 16 for a view of the tuff cone strata and syn-eruptive deformation at "Oscar cliff." Satellite image courtesy of Google Earth (data provider Landsat/Copernicus, 2016).

(Supplementary Figure S1). Summit scoria cones are a common feature of tuff cones and form as the vents dry out (Wohletz and Sheridan, 1983; Sohn, 1996; Cole et al., 2001; Solgevik et al., 2007; Smellie et al., 2018). However, the prominent necks intruding scoria lapillistones at northeast Shield Nunatak and the outcrop east of Willows Nunatak are entablature jointed, indicating that the scoria deposits were water-saturated by the time the necks intruded. We concur with Wörner et al. (1989) that the occurrence of "dry" scoria deposits within lapilli tuff successions in the MMVF was due to variable water levels within the englacial cavities during eruptions. They are incompatible with an origin by eruptions in an unconfined setting.

By contrast, the tuff cone at Oscar Point (Figure 15) has a broad shield morphology with low flank gradients steepening up to a small summit cone, suggesting eruption in an unconfined setting. The outcrop also shows spectacular syn-eruptive deformation, comprising disturbed bedding and numerous shear surfaces along which strata have slipped (Figure 16). The features are consistent with undercutting and slope collapses (slides, slumps) triggered by contemporary marine erosion, or else collapses of bedding over-steepened in the summit region of the tuff cone followed by redeposition at lower elevations (Sohn, 1996). Water-cooled intrusive sheets also occur at c. 180 m asl (estimated; Figure 15A) and extend to lower levels as irregular masses, indicating a high coeval sea level. By contrast, it is difficult to assign an eruptive setting unambiguously to tuff cone outcrops northeast of Baker Rocks and north of Willows Nunatak. Both appear to fit well with a model of unconfined eruptions, presumably in seawater, as a lacustrine setting is excluded (lack of suitable palaeotopography to pond water). They contain strata with variable dips (<5–24) that appear to extend laterally 750 m to more than 1 km. Bed orientations in the outcrop northeast of Baker Rocks indicate that at least two eruptive centers were active, probably simultaneously, and a crater-rim unconformity is preserved in high elevation exposures (above c. 350 m asl) of the more southwesterly center. The age of the Oscar Point tuff cone is unknown, but the ages of the other two (2.951 ± 0.050 Ma, 0.756 ± 0.023 Ma; Table 2) correspond to relatively low $\delta^{18}O$ values consistent

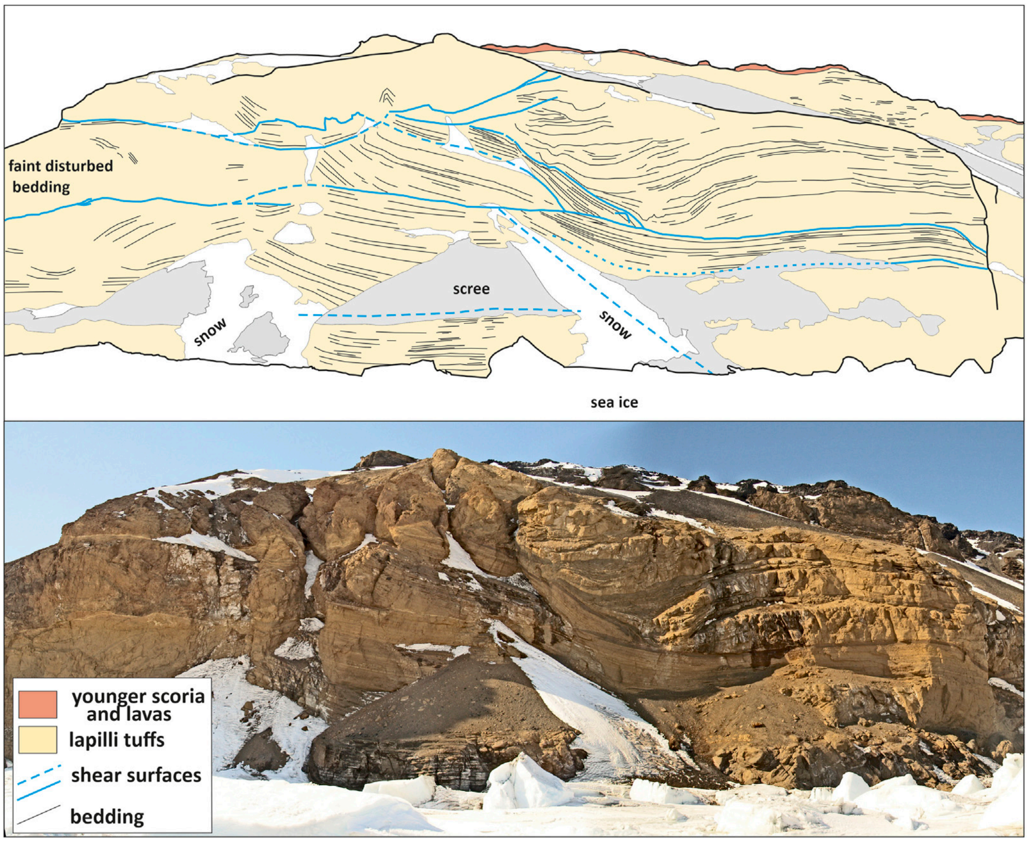

FIGURE 16
Sketch and photograph of "Oscar cliff" showing gently dipping bedding with multiple shear surfaces and associated localized folding caused by contemporary marine undercutting causing instability or over-steepened bedding in the summit region that collapsed and was redeposited near the toe of the tuff cone. The capping unit of scoria and lavas shown is unrelated to the tuff cone. The height to the skyline is c. 180 m.

with an interglacial period (Figure 17). All three localities are also situated on the coast. The evidence is most consistent with eruptions that were unconfined and affected by seawater that extended over each of the sites. However, as indicated earlier, there is currently no unambiguous corroborating evidence for substantially higher sea levels (up to c. 200 m asl) during the eruption of the tuff cones. The environment during the eruption of the outcrop at Baker Rocks (north) is also equivocal. It shows steeply dipping (28) strata where a crater-rim unconformity is exposed high in the outcrop. Ash-coated lapilli are also present in the lapilli tuffs above c. 500 m asl. The age of the outcrop is not well defined, with two options of 0.33 ± 0.03 or 0.20 ± 0.01 Ma (by K-Ar; Supplementary Figure S1). Both possible ages have high errors but correspond to periods of relatively low $\delta^{18}O$ values, likely interglacial (Figure 17; and see Section 6.3). The outcrop location is further inland than the other three tuff cones. In the absence of a palaeotopography suitable for ponding a pluvial lake, the source of contemporaneous water would have to be either the sea or a free-flowing aquifer readily recharged by seawater (Sohn, 1996). The bedrock underneath the outcrop is likely composed of Palaeozoic granitoids or siliceous Beacon Supergroup sedimentary strata, neither of which appear to be good candidates for a free-flowing aquifer (Nathan and Schulte, 1968). However, an unknown fault zone could act as a proxy aquifer. Thus, the environment is equivocal, and with so little lateral extent of the outcrop preserved, a glacial setting is not precluded.

6.1.3 Megapillow complexes

The topography surrounding the megapillow complexes in the MMVF is incapable of ponding water in a pluvial lake. From our discussion above, if the sea level was substantially higher in the past, eruptions might thus have been submarine. The suggestion is unverified at present, but a marine setting during the emplacement of the megapillow complexes is thought to be unlikely for the reasons presented below. Conversely, eruption beneath ice could also create a meltwater lake into which the megapillow complexes were emplaced, and the polar location of the MMVF (74°S) makes a glacial setting a plausible option. Pillow mounds and ridges are well-known as glaciovolcanic edifices (Höskuldsson et al., 2006; Edwards et al., 2009; Smellie, 2013; Pollock et al., 2014) and also in submarine settings (Schmincke and Bednarz, 1990; Goto and McPhie, 2004), but megapillow complexes like those in the MMVF have not yet been described. Megapillows were described in a subglacial lava field in British Columbia, but they are volumetrically minor. They were regarded as feeder tubes for associated pillow lavas (Hungerford et al., 2014). However, that outcrop also contains lithofacies called massive lavas, comprising low oblate lava lobes up to 3 m thick and 2–15 m long showing entablature prismatic jointing overlying suppressed colonnades and locally with hackly jointed upper surfaces. The features closely resembled our lava lobes and were similarly attributed to enhanced magma discharge rates. However, they occur in a geographically restricted part of a lava field rather than

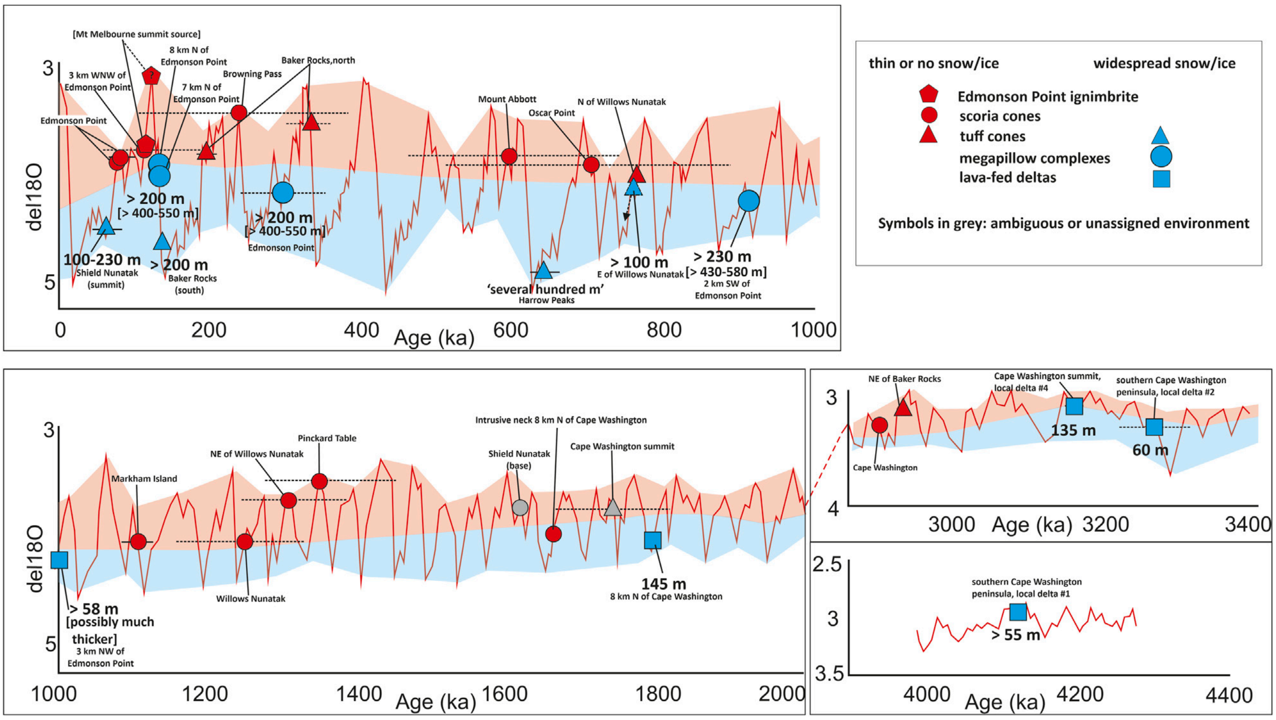

FIGURE 17
Marine isotope curve (after Lisiecki and Raymo, 2005) with the ages of dated volcanic units in the MMVF superimposed. Error bars are also shown (horizontal lines); where absent, the errors are less than the width of the data point shown. There is a striking dichotomy in the environmental conditions assigned to each dated unit. Those showing evidence for glacial conditions are characterized by significantly higher $\delta^{18}O$ values compared with units showing evidence for ice-poor or ice-free conditions. The errors on the ages of many of the samples from the latter localities are very large (obtained by K-Ar), but it may be significant that the mean ages correspond to low $\delta^{18}O$ values, and several coincide with $\delta^{18}O$ minima. Calculated minimum palaeo-ice thicknesses are also shown for the glacially emplaced units; values given within square brackets are more realistic estimates. See text for further explanation.

as a major constituent of several prominent glaciovolcanic mounds composed of a plexus of megapillows, lava lobes, and lava sheets.

The unusual, irregular glass-lined cavities observed in the MMVF outcrops are interpreted here as ice-block melt-out cavities (Figure 9D), formed by the incorporation of ice blocks trapped by advancing lava (Skilling, 2009). Although a rare occurrence, their presence is highly significant as it argues against a submarine or pluvial lake in favor of a subglacial setting. Since ice floats, it implies that the meltwater did not form a deep lake but was at least partly drained to allow the ice block(s) to accumulate. This is also consistent with the presence of pumice lapillistones and stratified pumiceous lapilli tuffs. Pumice is likely to float and would be reworked by traction currents only if the vault meltwater was largely drained. However, the frequent occurrence of entablature jointing also indicates that the lava surfaces were rapidly chilled by water, here assumed to be meltwater. This conundrum may be explained if emplacement was within a subglacial vault that was largely drained but continually replenished by melting the ice roof and walls. The vault is envisaged actively draining basally; it was not entirely filled by meltwater. The higher magma discharge rates inferred for the complexes may have exerted positive pressures on the overlying ice, causing it to lift and facilitating basal meltwater drainage. The lavas were chilled by contact with ice and washed with water, but they were probably only partially immersed. Radiant heat from the cooling lava would cause the melting of the ice roof, and meltwater would flow freely over the lava surfaces. A similar scenario was proposed by Hodgetts et al. (2021) for subglacially emplaced, water-cooled sheet lavas in an unusual tuya in Iceland. The tuya was constructed on a sloping bedrock surface, which promoted efficient subglacial drainage and a wet but not water-filled englacial vault. The colonnades in the megapillow complexes in the MMVF represent a slower, conductive cooling regime at the base of the thicker lava sheets, where they were in contact with earlier-emplaced lava, possibly still warm, and water was excluded (displaced). In places, lava overrode water-filled hollows in the underlying surface, causing breakouts and generating localized clusters of small lava pillows. Local minor instability of the pile was probably responsible for the generation of hyaloclastite, although the hyaloclastite was often reworked and redeposited by traction currents and occasional mass flows. The formation of minor interbedded pumice and lapilli tuffs in the megapillow complex at Edmonson Point, apparently deposited at different times during its growth, implied that explosivity was also sometimes achieved, with the explosively generated products reworked through the vault by currents and minor collapses of the tephra pile. Although explosivity can occur at high ambient pressures (by IFCI; Dürig et al., 2020), it is an unlikely explanation for the pumiceous lapilli tuffs at Edmonson Point, which contain abundant highly inflated pumices and lack the distinctive curviplanar ash-size shards that characterize IFCI deposits. The thickest tephra deposit (>20 m) caps the complex on top of the ridge on the west side of Edmonson Point, implying that explosivity may ultimately have succeeded effusion in the final stages of the eruption of that complex. Similar deposits are absent from the other megapillow complexes in the MMVF, which presumably remained wholly effusive. However, the evidence for only partial immersion of the lava masses in water argues against a submarine (wholly drowned) origin. A glaciovolcanic origin is the most plausible explanation for the eruptive setting.

6.1.4 Lava-fed deltas

Although lava-fed deltas are not environment-specific, there are clear indications that they formed in association with ice in the MMVF. The passage zones in the lava-fed deltas on the Cape Washington peninsula have an overall gentle southerly or southwesterly dip. As water levels in the sea and pluvial lakes are horizontal, the presence of dipping passage zones in the Cape Washington peninsula deltas is diagnostic of emplacement on the flanks of volcanoes draped by ice (Smellie et al., 2011b; Smellie, 2018). The gentle dips also indicate that the original volcanoes were shield-like in morphology, and the craters that fed the deltas were situated to the east of the Cape Washington peninsula but have since been lost by a combination of glacial and marine erosion. Because the isolated delta outcrop north of Edmonson Point is small and its capping lavas were removed by erosion, the orientation of the delta and its passage zone is unclear. Although the delta prograded to the east, indicating a source vent somewhere to the west, it may have erupted in a glacial, pluvial lake or marine setting. However, the two prominent subhorizontal bands of pervasive alteration observed in the associated lithic breccias close to the passage zone (Figure 9H) are likely to have formed due to prolonged immersion in water that underwent a change in surface elevation at least once. Delta advancement in a pluvial lake or into the sea would show only a single horizontal alteration front reflecting a sea or lake surface that would have been invariable during the eruption. The presence of two alteration zones, interpreted as two different former water levels, suggests that the water responsible for the alteration was dynamic, and its surface fluctuated with time due to subglacial meltwater discharge (Smellie, 2006). The likeliest eruptive scenario, therefore, is glaciovolcanic, with emplacement in wet-based ice. The former presence of wet-based ice during the eruption of the Cape Washington peninsula deltas is also supported by eroded surfaces between at least two of those deltas (deltas #1 and #3; Figures 13A, B).

6.1.5 Edmonson Point ignimbrite

Although not part of our study of the satellite and flank vents, the Edmonson Point ignimbrite, which erupted from Mount Melbourne summit, is an *in situ* pumiceous magmatic deposit that shows no evidence of water or ice interaction. Its presence, low elevation (essentially at sea level), and lack of evidence for subsidence had it been deposited on snow or ice indicate that it was deposited at an ice-free location, and the period was thus ice-poor or possibly ice-free (Figure 17; see section 7.3).

6.2 Effect of eruptive environment on eruptive style and edifice construction

The range of compositions overlaps for each of the edifice types in the MMVF and, apart from a bias to tephrite/basanites for the lava-fed deltas (Figure 2), there are no obvious compositional differences that explain the markedly different styles of eruption represented. Although many of the scoria cones are at relatively high elevations (e.g., above 1,200 m in Random Hills; Figure 3), they also occur close to sea level. The other types of flank and satellite vents occur at similar elevations to the scoria cones (i.e., mostly <600 m asl), and relative elevation (with respect to potential interaction with marine water) is not the dominant determining factor for eruptive style. A major conclusion of our study is that the principal determinant for volcanic eruptions and edifice construction in the MMVF is environmental, specifically the presence at the eruptive sites of water in all its forms (snow, ice, meltwater, and surface water). Figure 18 schematically shows the relationships between the principal lithofacies, internal architectures, and edifice construction for centers that erupted in various environmental settings. For example, an absence of water or insufficient snow/ice at eruptive sites in the MMVF resulted in scoria cones and their associated lava fields. Most of the tuff cone outcrops visited show strong evidence for eruption within the ice, including gently and sometimes inward-dipping summit strata at high elevations and evidence for water saturation of the tephra piles at high elevations. However, the characteristics of a few tuff cone outcrops are more ambiguous and possibly fit better with eruptions in an unconfined setting (i.e., laterally continuous strata, steep-dipping in summit areas), with a water source potentially provided by the sea. This is particularly true for the Oscar Point tuff cone (Figure 15). Moreover, their ages appear to correspond to warmer periods compared with the marine $\delta^{18}O$ curve (Figure 17; and see Section 6.3) when ice extent would have been reduced and sea levels higher than today. However, independent corroborating evidence for the substantially higher sea levels required is currently lacking. Distinguishing between glacial and non-glacial settings reliably for tuff cones depends on reconstructing the internal architecture and, ideally, the original morphology of the tephra piles, which are not always possible for outcrops that are highly eroded or largely obscured by snow and ice. Effusive eruptions associated with a thin slope-draping glacial cover (<c. 150 m thick for the MMVF) created several small shield volcanoes constructed from multiple ʻaʻā lava-fed deltas, mainly in the Cape Washington peninsula area. Similar examples also crop out extensively elsewhere in Victoria Land (Smellie et al., 2011a; Smellie et al., 2011b; Smellie et al., 2013; Smellie, 2021). By contrast, effusive eruptions associated with high magma discharge rates and a much thicker glacial cover (several to many hundreds of meters; see Section 6.4) created the distinctive megapillow complexes. Under similarly thick ice but lower magma discharge rates, pillow lava mounds would be formed.

6.3 Comparison with the marine oxygen isotope record

The arguments given above for eruptive settings are based solely on interpretations of the lithofacies present and their architecture. However, considerable ancillary support is also provided by the ages of the outcrops when they are plotted on the marine $\delta^{18}O$ isotope curve (Figure 17). Only two outcrops we visited have no eruptive environment currently assigned due to inconclusive lithofacies and architectures. The remaining outcrops are designated as "glacial" (lava-fed deltas; megapillow complexes; several tuff cones) and "non-glacial" (scoria cones and associated lava fields; possibly some other tuff cones). It is probably significant that despite the high errors on some of the published ages (most determined by imprecise K-Ar), all of the unambiguously "glacial" outcrops have ages corresponding to

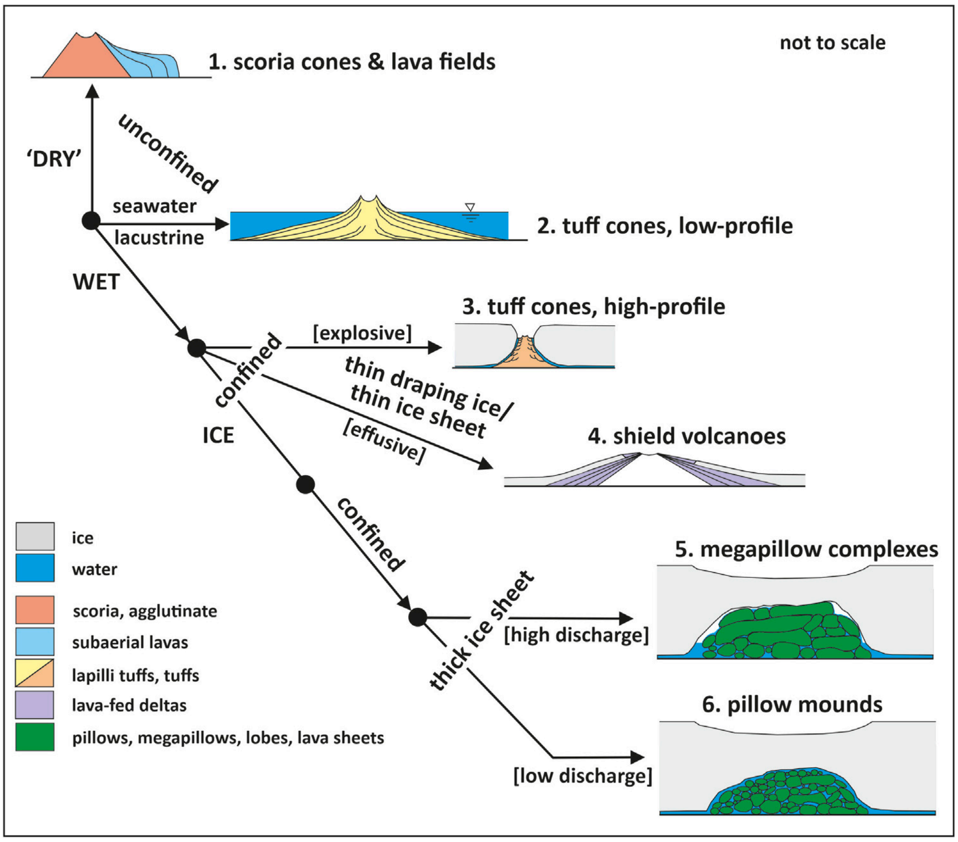

FIGURE 18
Schematic diagrams illustrating the impact of water on resulting edifice type under a range of environmental conditions. The presence or absence of water, including ice and its thickness, is the principal determinant of edifice construction. Note that glaciovolcanic (i.e., high-profile) tuff cones (category 3) can probably evolve into shield volcanoes draped by lava-fed deltas (category 4). The diagram also includes pillow mounds (category 6). Although not present in the MMVF, they are more common in glaciovolcanic settings generally and are likely to form under lower magma discharge rates than those that yield megapillow complexes.

relatively high δ^{18}O values on the marine isotope curve, whereas the "non-glacial" outcrops correspond in age to significantly lower δ^{18}O values. Only one outcrop conflicts with this conclusion: an intrusive neck c. 8 km north of Cape Washington (Figure 17). The constituent "lithofacies unequivocally indicate "dry' magmatic eruptions and a non-glacial or at least ice-poor setting, but the equivalent value on the δ^{18}O curve is relatively high (Figure 17). However, the outcrop age corresponds to a steep section of the δ^{18}O curve. Thus, the simplest explanation is that even a slight change in the age (by only a few ka) could displace it to substantially lower δ^{18}O values on the curve and remove the conflict. For the few tuff cones in the MMVF that might have erupted within the sea, a similar argument applies, thus emphasizing the ambiguity of the interpretation currently assigned to those outcrops. Finally, it is noticeable that within the constraints of the errors attached to the ages [which are very small (mainly 20–30 Kyr) in our new age dataset], the eruptions of units that experienced "glacial" conditions fall on the steep rising limbs of the δ^{18}O curve corresponding to periods of rapid ice melt, either glacial to interglacial transitions or a change to interstadials (Figure 17). Such a trend is a predicted consequence of the warmer climatic conditions lowering the superimposed glaciostatic load and triggering eruptions (Jull and McKenzie, 1996; Maclennan et al., 2002; Jellinek et al., 2004; Watt et al., 2013; Wilson and Russell, 2020).

6.4 Contemporaneous ice thicknesses

Empirical estimates for contemporaneous ice thicknesses are also shown in Figure 17. For each of the Cape Washington peninsula lava-fed deltas near Cape Washington, calculated ice thicknesses are >55, 55, 60, and 135 m (oldest delta to youngest, respectively). The additional younger delta 9 km north of Cape Washington was associated with ice c. 145 m thick, whereas the isolated delta relict north of Edmonson Point is too poorly exposed for an estimate. Calculations for the deltas are based on the observed thickness of subaqueous lithofacies to which is added c. 30 m to allow for any superimposed snow, firn, or crevassed ice (see Smellie et al. 2011b). The calculated thicknesses are minima as no allowance is made for ice surface sagging, but any sagging would be confined principally to the vicinity of the edifice; see Smellie et al. (2011b) for details of assumptions used in calculations. Other putative ice thicknesses at the eruptive sites are as follows:

1) Megapillow complexes: >200 m (i.e., the individual thickness of most of the megapillow complexes) but probably much thicker; for example, the coeval ice surface for the highest outcrop (west-northwest of Edmonson Point) must have substantially exceeded 400 m asl, which is the elevation of its preserved surface. The

thicknesses shown in Figure 17 are minima and based on the maximum elevation reached by the individual outcrops (but see further comments below).

2) Tuff cones: thicknesses calculated for glacially emplaced tuff cones vary between >100 m (east of Willows Nunatak) and several hundred meters (Harrow Peaks; see Smellie et al., 2018).

The estimates calculated for the lava-fed deltas and Shield Nunatak are the most accurate and are unlikely to be incorrect by more than a few tens of meters because the bases and original tops of most of the outcrops are exposed and the outcrops are capped by lavas that were emplaced subaerially. Hence, the coeval ice was melted through completely.

Estimates for the other landforms are probably less accurate, particularly for the megapillow complexes emplaced entirely subglacially. Two scenarios are possible for the complexes. (1) In undegassed magmas, the coeval ice thicknesses would have been substantial [i.e., much greater than the preserved thicknesses (mainly c. 200 m) of the individual complexes] to suppress runaway vesiculation triggering explosivity, whether magmatic or hydrovolcanic. Thus, for a complex 200 m thick, the minimum thickness of contemporary ice would have been c. 550 m (comprising 200 m of magma and 200 m of superimposed ice plus c. 150 m to account for ice surface sag toward the complex; see Gudmundsson, 2003; Smellie et al., 2011b). The elevation of the highest megapillow complex surface is c. 400 m asl (nunatak west-northwest of Edmonson Point). It is an eroded surface; hence, it must have been higher originally. Similar reasoning suggests that the coeval ice surface would have had a minimum elevation of c. 750 m asl (i.e., 400 + 200 + 150 m). This is the thickest ice sheet for which volcanic rocks in the MMVF provide evidence. However, for that example, if uplift has subsequently occurred (although undocumented at present), the deduced surface elevation and associated ice sheet thickness would need to be reduced. Since the megapillow complex at Edmonson Point shows an upward transition to explosive activity, the coeval ice thickness is better defined and any overlying ice would not be greater than c. 200 m thick. The exposed thickness of the complex at the locality is c. 200 m; hence, the maximum ice thickness there during effusion was ≤ 550 m.

Alternatively, (2) if the magmas were degassed and emplaced in a partially drained vault, the ambient pressures would have been much less than those imposed by the superimposed ice and might even have been atmospheric if the vault drained to the ice sheet margins (*cf.* Schopka et al., 2006; Wilson et al., 2013). Low vault pressures (equivalent to less than c. 200 m of superimposed ice) would have promoted pervasive vesiculation and a rapid transition to explosive (hydrovolcanic) activity at an early stage, which is not observed. Hence, some of the magmas (not Edmonson Point) might have been degassed when emplaced. However, the presence of vesicle zones signifying inflation, together with megavesicles, suggest that the magmas were not degassed.

Even if it was assumed (1) that the magmas were degassed and that c. 50 m of ice remained above the cooling complex (to avoid subaerial exposure) and (2) that the ice also sagged toward the cooling magma mass, the megapillow complexes that were c. 200 m thick would have been emplaced below the ice that was at least 400 m thick (i.e., 200 + 50 + 150 m). Whichever assumptions are used, the estimates indicate that substantially thicker ice conditions existed during the emplacement of the megapillow complexes than occurs at those locations today (see also Smellie et al., 2018). However, even the maximum calculated ice thicknesses would be unable to completely drown the topography of the region (Random Hills rise to >1,500 m asl, and the summit of Mount Melbourne is at 2,732 m). The ice cover indicated is, therefore, relatively thin overall, suggesting that it was mainly an icefield during the past 4 Myr. This does not preclude transient episodes of greater ice thicknesses at times when the ice overrode much of the topography (see Smellie et al., 2018), but those episodes are not represented by the volcanic record, and they were atypical for the bulk of the period represented.

7 Conclusions

The Late Pliocene to present Mount Melbourne Volcanic Field has a diversity of flank and satellite volcanic centers unrivaled anywhere else in the West Antarctic Rift System. Based on the lithofacies and internal architectures, several discrete groups of volcanic edifices are present, comprising scoria cones (together with their associated lava fields), possibly two types of tuff cones, megapillow complexes, and shield volcanoes constructed from lava-fed deltas. The diversity of edifice types is not related to compositional differences, which overlap completely (tephrite/basanite/alkali basalt–benmoreite) or due to elevation differences relative to any putative source of surface water (e.g., the sea) as the edifices crop out over a similar range of elevations. However, contemporary environmental conditions appear to have exerted the strongest control on eruptive style and, thus, edifice construction, specifically the presence or absence of water, including ice and its thickness. Eruptions under "dry" conditions created scoria cones and associated small lava fields (mainly ʻaʻā lavas). Conversely, if some eruptions occurred under wet unconfined (e.g., submarine) conditions, tuff cones would be constructed composed of laterally extensive lapilli tuff strata with low-gradient flanks. However, the unconfined tuff cone eruptions, which appear to be unequivocal for the low-profile, shield-like Oscar Point tuff cone, require a high marine limit (at least 200 m above present datum), probably linked to local uplift, which is currently unverified. The suggestion thus requires independent validation. Three categories of glaciovolcanic edifices were also created depending on whether the eruptions occurred under thin (≤ c. 200 m) or much thicker ice. Under conditions of thin draping ice, effusive eruptions formed glaciovolcanic shield volcanoes composed of multiple ʻaʻā lava-fed deltas, whereas explosive eruptions formed tuff cones with distinctive gently or inward-dipping strata at high elevations in flooded tephra piles due to banking of the strata against surrounding buttressing ice walls. One of the glaciovolcanic tuff cones (Shield Nunatak) has a weakly developed cap of sheet-like ʻaʻā lavas, and it is transitional to a tuya. Eruptions under ice that was thick enough to suppress explosivity in undegassed magmas created sizeable megapillow complexes, a distinctive category of glaciovolcanic edifice that has not been described previously. They probably erupted into partially drained englacial vaults at moderately high discharge and relatively slow cooling rates. Thus, our study demonstrates that other than the abundant scoria cones and associated small lava fields, the Plio-Pleistocene centers in the MMVF are mainly glaciovolcanic, but they were constructed under a range of environmental conditions.

The volcanic units indicate that contemporary ice thicknesses at times were <55 m, but ice surfaces reached 750 m asl at one site, at least, at other times, much higher (therefore thicker ice) than at that site today. Eruptions of the glacially emplaced units are mostly biased to periods of rapid ice thinning during deglaciation. The glacial thermal regime varied between wet-based (megapillow complexes and at least some lava-fed deltas; with evidence for basal meltwater discharge or erosion) and cold-based (tuff cone at Harrow Peaks, with an absence of basal meltwater discharge). With the much-improved dating precision, it appears that several glaciovolcanic edifices erupted at or close to glacial maxima. In the absence of other data, they are our best guide to past terrestrial palaeo-ice thicknesses and glacial thermal regime in the Terra Nova Bay region of northern Victoria Land. They indicate that the Late Pliocene and Pleistocene ice was generally quite thin and would have draped the landscape as an icefield rather than completely or largely drowning the topography as an expansive ice sheet. Although transient thicker ice probably occurred at times, it is not well represented. It is also noticeable that the ice became significantly thicker as $\delta^{18}O$ values increased toward the present. Finally, even during the earliest volcanic eruptions, at c. 4.1 Ma, when $\delta^{18}O$ variations were very limited and $\delta^{18}O$ values were slightly lower than today, the evidence indicates that an ice cover was present in the MMVF, although probably very thin at that time (just a few tens of meters at the coast). Thus, the volcanic record suggests that ice was probably never completely absent throughout the period investigated.

Data availability statement

The datasets presented in this study can be found in online repositories (see Supplementary Material).

Author contributions

JS: conceptualization (lead), data acquisition (lead), data curation (equal), formal analysis (lead), investigation (lead), writing—original draft (lead), writing—review and editing (lead). SR: funding acquisition (lead), conceptualization (supporting), data acquisition (equal), data curation (equal), formal analysis (supporting), investigation (supporting), writing—original draft (supporting), writing—review and editing (supporting). GD: conceptualization (supporting), data acquisition (equal), data curation (equal), formal analysis (supporting), investigation (supporting), writing—original draft (supporting), writing—review and editing (equal).

Funding

This study was funded by the Programma Nazionale di Recherche in Antartide (Italy; Grant PNRA 2018_00037 awarded to Sergio Rocchi, Pisa).

Acknowledgments

This investigation was inspired by the seminal pioneering study of the MMVF by Gerhardt Wörner and Lothar Viereck, which the authors wish to acknowledge publicly. The authors also gratefully acknowledge the support of the Programma Nazionale di Recherche in Antartide (PNRA) of Italy, which provided the logistics involved and supported the research (Project PNRA 2018_00037; awarded to SR). The authors are also grateful to the Expedition Leaders and all the station support personnel at the Italian Mario Zuchelli Station, who made them very welcome during their stay in 2005–2006, 2011–2012, and 2014, when the fieldwork for this study took place, and to the pilots (Mark Read, Jeff McLintock, Giles de Garnham, Bob McElhinney, Carl Manion, Dominic O'Rourke, Lee Armstrong and Jamie Henery) of Helicopters New Zealand who flew them during the fieldwork. They are also grateful to Samuele Agostini, who participated in some of the fieldwork in 2014; Carlo Baroni for the helpful comments on the interpretation of putative high-elevation pre-Holocene raised marine surfaces in the region; Maurizio Gemelli and Irene Rocchi for processing samples for Ar dating; and the three anonymous reviewers of this study. Finally, JS is grateful to Annika Burns (Leicester University) for making the numerous thin sections from often challenging samples that are also at the heart of this study and to the Trans-Antarctic Association (United Kingdom) for financial support. This study is a contribution to the aims and objectives of AntVolc (SCAR Expert Group on Antarctic volcanism: https://scar.org/science/antvolc/home/).

Conflict of interest

The authors declare that the research was conducted in the absence of any commercial or financial relationships that could be construed as a potential conflict of interest.

Publisher's note

Supplementary material

The Supplementary Material for this article can be found online at: https://www.frontiersin.org/articles/10.3389/feart.2022.1061515/full#supplementary-material

SUPPLEMENTARY FIGURE S1
Satellite image of the Mount Melbourne Volcanic Field with all isotopic ages.

SUPPLEMENTARY FIGURE S2
Map showing the localities visited.

SUPPLEMENTARY FIGURE S3
Dating methods and results.

References

Allen, C. C. (1980). Icelandic subglacial volcanism: Thermal and physical studies. *J. Geol.* 88, 108–117. doi:10.1086/628478

Armienti, P., Civetta, L., Innocenti, F., Manetti, P., Tripodo, A., Villari, L., et al. (1991). New petrological and geochemical data on Mt. Melbourne volcanic field, northern Victoria Land, Antarctica. (II Italian antarctic expedition). *Mem. della Soc. Geol. Ital.* 46, 397–424.

Armstrong, R. L. (1978). K–Ar dating: Late cenozoic McMurdo volcanic group and dry valley glacial history, Victoria Land, Antarctica. *N. Z. J. Geol. Geophys.* 21, 685–698. doi:10.1080/00288306.1978.10425199

Baroni, C., and Hall, B. L. (2004). A new Holocene relative sea-level curve for Terra Nova Bay, Victoria Land, Antarctica. *J. Quat. Sci.* 19, 377–396. doi:10.1002/jqs.825

Baroni, C., and Orombelli, G. (1991). Holocene raised beaches at Terra Nova Bay, Victoria Land, Antarctica. *Quat. Res.* 36, 157–177. doi:10.1016/0033-5894(91)90023-x

Batiza, R., Smith, T. L., and Niu, Y. (1989). Geological and petrologic evolution of seamounts near the EPR based on submersible and camera study. *Mar. Geophys. Res.* 11, 169–236.

Batiza, R., and White, J. D. L. (2000). "Submarine lavas and hyaloclastite," in *Encyclopedia of volcanoes*. Editor H. Sigurdsson 1st edition (Sand Diego: Academic Press), 361–381.

Beccaluva, L., Coltorti, M., Orsi, G., Saccani, E., and Siena, F. (1991). Basanite to tephrite lavas from Melbourne volcanic province, Victoria Land, Antarctica. *Mem. della Soc. Geol. Ital.* 46, 383–395.

Bondre, N. R., Duraiswami, R. A., and Dole, G. (2004). Morphology and emplacement of flows from the deccan volcanic province, India. *Bull. Volcanol.* 66, 29–45. doi:10.1007/s00445-003-0294-x

Bonnichsen, B., and Kauffmann, D. F. (1987). "Physical features of rhyolite lava flows in the Snake River Plain volcanic province, southwestern Idaho," in *The emplacement of silicic domes and lava flows*. Editor J. H. Fink (Washington, DC: Geological Society of America Special Paper), 212, 119–145.

Brand, B. D., and Clarke, A. B. (2009). The architecture, eruptive history, and evolution of the Table Rock Complex, Oregon: From a Surtseyan to an energetic maar eruption. *J. Volcanol. Geotherm. Res.* 180, 203–224. doi:10.1016/j.jvolgeores.2008.10.011

Branney, M. J., and Kokelaar, P. (2002). *Pyroclastic density currents and the sedimentation of ignimbrites*, 27. London, Memoirs: Geological Society, 143.

Brown, R. J., Bonadonna, C., and Durant, A. J. (2012). A review of volcanic ash aggregation. *Phys. Chem. Earth* 45-46, 65–78. doi:10.1016/j.pce.2011.11.001

Cas, R. A. F., and Simmons, J. M. (2018). Why deep-water eruptions are so different from subaerial eruptions. *Frontiers in Earth Science*, 6, 198. doi:10.3389/feart.2018.00198

Cavallaro, D., and Coltelli, M. (2019). The Graham volcanic field offshore southwestern Sicily (Italy) revealed by high-resolution seafloor mapping and ROV images. *Front. Earth Sci.* 7, 311. doi:10.3389/feart.2019.00311

Chadwick, W. W., Cashman, K. V., Embley, R. W., Matsumoto, H., Dziak, R. P., de Ronde, C. E. J., et al. (2008). Direct video and hydrophone observations of submarine explosive eruptions at NW Rota-1 volcano, Mariana arc. *J. Geophys. Res.* 113, B08S10. doi:10.1029/2007JB005215

Clague, D. A., and Paduan, J. B. (2009). "Submarine basaltic volcanism," in *Submarine volcanism and mineralization: Modern through ancient* (Quebec City, Canada: Geological Association of Canada), 41–60. Short Course 29-30 May 2008.

Cole, P. D., Guest, J. E., Duncan, A. M., and Pacheco, J.-M. (2001). Capelinhos 1957-1958, faial, azores: Deposits formed by an emergent surtseyan eruption. *Bull. Volcanol.* 63, 204–220. doi:10.1007/s004450100136

Del Carlo, P., Di Roberto, A., Di Vincenzo, G., authors, 5, Landi, P., Pompilio, M., et al. (2015). Late pleistocene–holocene volcanic activity in northern Victoria Land recorded in Ross Sea (Antarctica) marine sediments. *Bull. Volcanol.* 77, 36. doi:10.1007/s00445-015-0924-0

Dürig, T., White, J. D. L., Murch, A. P., authors, 7, Buttner, R., Mele, D., et al. (2020). Deep-sea eruptions boosted by induced fuel-coolant explosions. *Nat. Geosci.* 13, 498–503. doi:10.1038/s41561-020-0603-4

Edwards, B., Magnússon, E., Thordarson, T., Guðmundsson, M. T., Höskuldsson, A., Oddson, B., et al. (2012). Interactions between lava and snow/ice during the 2010 Fimmvörðuháls eruption, south-central Iceland. *J. Geophys. Res.* 117, B04302. doi:10.1029/2011JB008985

Edwards, B. R., Russell, J. K., and Pollock, M. (2022). Cryospheric impacts on volcano-magmatic systems. *Front. Earth Sci.* 10. doi:10.3389/feart.2022.871951

Edwards, B. R., Skilling, I. P., Cameron, B., Haynes, C., Lloyd, A., and Hungerford, J. H. D. (2009). Evolution of an englacial volcanic ridge: Pillow Ridge tindar, Mount Edziza volcanic complex, NCVP, British Columbia, Canada. *J. Volcanol. Geotherm. Res.* 185, 251–275. doi:10.1016/j.jvolgeores.2008.11.015

Fisher, R. V., and Schmincke, H.-U. (1984). *Pyroclastic rocks*. Berlin: Springer-Verlag, 465.

Forbes, A. E. S., Blake, S., McGarvie, D. W., and Tuffen, H. (2012). Pseudopillow fracture systems in lavas: Insights into cooling mechanisms and environments from lava flow fractures. *J. Volcanol. Geotherm. Res.* 245-246, 68–80. doi:10.1016/j.jvolgeores.2012.07.007

Forbes, A. E. S., Blake, S., and Tuffen, H. (2014). Entablature: Fracture types and mechanisms. *Bull. Volcanol.* 76, 1–13. doi:10.1007/s00445-014-0820-z

Fox, C. G., Murphy, K. M., and Embley, R. W. (1987). Automated display and statistical analysis of interpreted deep-sea bottom photographs. *Mar. Geol.* 78, 199–216. doi:10.1016/0025-3227(88)90109-0

Gambino, S., Armienti, P., Cannata, A., and authors, 5 (2021). *Mount Melbourne and mount rittmann*, 55. London, Memoirs: Geological Society, 741–758.

Gardner, N., Hall, B., and Wehmiller, J. (2006). Pre-holocene raised beaches at Cape Ross, southern Victoria Land, Antarctica. *Mar. Geol.* 229, 273–284. doi:10.1016/j.margeo.2006.01.006

Garvin, J. B., Slayback, D. A., Ferrini, V., 4 authorsGiguere, C., Asrar, G. R., et al. (2018). Monitoring and modelling the rapid evolution of Earth's newest volcanic island: *Hunga Tonga Hunga Ha'apai* (Tonga) using high spatial resolution satellite observations. *Geophys. Res. Lett.* 45, 3445–3452. doi:10.1002/2017gl076621

Giordano, G., Lucci, F., Phillips, D., Cozzupoli, D., and Runci, V. (2012). Stratigraphy, geochronology and evolution of the Mt. Melbourne volcanic field (north Victoria Land, Antarctica). *Bull. Volcanol.* 74, 1985–2005. doi:10.1007/s00445-012-0643-8

Go, S. Y., Kim, G. B., Jeong, J. O., and Sohn, Y. K. (2017). Diatreme evolution during the phreatomagmatic eruption of the Songaksan tuff ring, Jeju Island, Korea. *Bull. Volcanol.* 79, 23. doi:10.1007/s00445-017-1103-2

Goehring, L., and Morris, S. W. (2008). Scaling of columnar joints in basalt. *J. Geophys. Res.* 113, B10203. doi:10.1029/2007JB005018

Goto, Y., and McPhie, J. (2004). Morphology and propagation styles of Miocene submarine basanite lavas at Stanley, northwestern Tasmania, Australia. *J. Volcanol. Geotherm. Res.* 130, 307–328. doi:10.1016/s0377-0273(03)00311-1

Granot, R., and Dyment, J. (2018). Late cenozoic unification of east and west Antarctica. *Nat. Commun.* 9, 3189. doi:10.1038/s41467-018-05270-w

Gregg, T. K. P., and Fink, J. H. (1995). Quantification of submarine lava-flow morphology through analog experiments. *Geology* 23, 73–76. doi:10.1130/0091-7613(1995)023<0073:qoslfm>2.3.co;2

Griffiths, R. W., and Fink, J. H. (1992). Solidification and morphology of submarine lavas: A dependence on extrusion rate. *J. Geophys. Res.* 97, 19729–19737. doi:10.1029/92jb01594

Grossenbacher, K. A., and McDuffie, S. M. (1995). Conductive cooling of lava: Columnar joint diameter and stria width as functions of cooling rate and thermal gradient. *J. Volcanol. Geotherm. Res.* 69, 95–103. doi:10.1016/0377-0273(95)00032-1

Gudmundsson, M. T. (2003). Melting of ice by magma-ice-water interactions during subglacial eruptions as an indicator of heat transfer in subaqueous eruptions. *Am. Geophys. Union Geophys. Monogr.* 140, 61–72.

Hall, B. L., Baroni, C., and Denton, G. H. (2004). Holocene relative sea-level history of the southern Victoria Land coast, Antarctica. *Glob. Planet. Change* 42, 241–263. doi:10.1016/j.gloplacha.2003.09.004

Hamilton, W. (1972). The hallett volcanic province, Antarctica. Geological Survey Professional Paper 456-C, 59.

Hodgetts, A. G. E., McGarvie, D., Tuffen, H., and Simmons, I. C. (2021). The Thórólfsfell tuya, South Iceland – a new type of basaltic glaciovolcano. *J. Volcanol. Geotherm. Res.* 411, 107175. doi:10.1016/j.jvolgeores.2021.107175

Höskuldsson, A., Sparks, R. S. J., and Carroll, M. R. (2006). Constraints on the dynamics of subglacial basalt eruptions from geological and geochemical observations at Kverkfjöll, NE Iceland. *Bull. Volcanol.* 68, 689–701. doi:10.1007/s00445-005-0043-4

Houghton, B. F., and Hackett, W. R. (1984). Strombolian and phreatomagmatic deposits of ohakune craters, ruapehu, New Zealand: A complex interaction between external water and rising basaltic magma. *J. Volcanol. Geotherm. Res.* 21, 207–231. doi:10.1016/0377-0273(84)90023-4

Hungerford, J. D. G., Edwards, B. R., Skilling, I. P., and Cameron, B. I. (2014). Evolution of a subglacial basaltic lava flow field: Tennena volcanic center, Mount Edziza Volcanic Complex, British Columbia, Canada. *J. Volcanol. Geotherm. Res.* 272, 39–58. doi:10.1016/j.jvolgeores.2013.09.012

Jellinek, A. M., Manga, M., and Saar, M. O. (2004). Did melting glaciers cause volcanic eruptions in eastern California? Probing the mechanics of dike formation. *J. Geophys. Res.* 109. doi:10.1029/2004JB002978

Jones, J. G. (1969)., 124. London, 197–211. doi:10.1144/gsjgs.124.1.0197Intraglacial volcanoes of the laugarvatn region, south-west Iceland—IQ. *J. Geol. Soc.*

Jones, J. G. (1970). Intraglacial volcanoes of the laugarvatn region, southwest Iceland, II. *J. Geol.* 78, 127–140. doi:10.1086/627496

Jordan, T. A., Riley, T. R., and Siddoway, C. S. (2020). The geological history and evolution of West Antarctica. *Nat. Rev. Earth Environ.* 1, 117–133. doi:10.1038/s43017-019-0013-6

Jull, M., and McKenzie, D. (1996). The effect of deglaciation on mantle melting beneath Iceland. *J. Geophys. Res.* 101, 21815–21828. doi:10.1029/96jb01308

Kano, K. (1998). A shallow-marine alkali-basalt tuff cone in the Middle Miocene jinzai formation, izumo, SW Japan. *J. Volcanol. Geotherm. Res.* 87, 173–191. doi:10.1016/s0377-0273(98)00098-5

Kokelaar, B. P. (1983)., 140. London, 939–944. doi:10.1144/gsjgs.140.6.0939The mechanism of Surtseyan volcanism*J. Geol. Soc.*

Kokelaar, P. (1986). Magma-water interactions in subaqueous and emergent basaltic. *Bull. Volcanol.* 48, 275–289. doi:10.1007/bf01081756

Kuiper, K. F., Deino, A., Hilgen, F. J., Krijgsman, W., Renne, P. R., and Wijbrans, J. R. (2008). Synchronizing rock clocks of Earth history. *Science* 320, 500–504. doi:10.1126/science.1154339

Latutrie, B., and Ross, P.-S. (2020). What lithic clasts and lithic-rich facies can tell us about diatreme processes: An example at round butte, Hopi buttes volcanic field, Navajo nation, Arizona. *J. Volcanol. Geotherm. Res.* 411, 107150. doi:10.1016/j.jvolgeores.2020.107150

Le Maitre, R. W., Streckeisen, A., Zanettin, B., and 12 authors (2002), Igneous rocks. A classification and glossary of terms. *Recommendations of the international union of geological sciences subcommission on the systematics of igneous rocks*. Cambridge: Cambridge University Press, 236.

Lee, M. J., Lee, J. I., Kim, T. H., Lee, J., and Nagao, K. (2015). Age, geochemistry and Sr-Nd-Pb isotopic compositions of alkali volcanic rocks from Mt. Melbourne and the Western Ross Sea, Antarctica. *Geosciences J.* 19, 681–695. doi:10.1007/s12303-015-0061-y

LeMasurier, W. E. (2008). Neogene extension and basin deepening in the West Antarctic rift inferred from comparisons with the East African rift and other analogs. *Geology* 36, 247–250. doi:10.1130/g24363a.1

Lescinsky, D. T., and Fink, J. H. (2000). Lava and ice interaction at stratovolcanoes—Use of characteristic features to determine past glacial extents and future volcanic hazards. *J. Geophys. Res.* 105, 23711–23726. doi:10.1029/2000jb900214

Lisiecki, L. E., and Raymo, M. E. (2005). A Pliocene-Pleistocene stack of 57 globally distributed benthic δ18O records. *Paleoceanography* 20, PA1003. doi:10.1029/2004PA001071

Long, P. E., and Wood, B. J. (1986). Structures, textures and cooling histories of Columbia River basalt flows. *Geol. Soc. Am. Bull.* 97, 1144–1155. doi:10.1130/0016-7606(1986)97<1144:stacho>2.0.co;2

Lyon, G. L. (1986). Stable isotope stratigraphy of ice cores and the age of the last eruption at Mount Melbourne, Antarctica. *N. Z. J. Geol. Geophys.* 29, 135–138. doi:10.1080/00288306.1986.10427528

Lyon, G. L., and Giggenbach, W. F. (1974). Geothermal activity in Victoria Land, Antarctica. *N. Z. J. Geol. Geophys.* 17, 511–521. doi:10.1080/00288306.1973.10421578

Maclennan, J., Jull, M., McKenzie, D., Slater, L., and Grönvold, K. (2002). The link between volcanism and deglaciation in Iceland. *Geochem. Geophys. Geosystems* 3, 1–25. doi:10.1029/2001gc000282

Martin, A. P., Cooper, A. F., Price, R. C., Kyle, P. R., and Gamble, J. A. (2021). *Erebus volcanic province: Petrology*, 55. London, Memoirs: Geological Society, 447–489.

Mee, K., Tuffen, H., and Gilbert, J. S. (2006). Snow-contact volcanic facies and their use in determining past eruptive environments at Nevados de Chillán volcano, Chile. *Bull. Volcanol.* 68, 363–376. doi:10.1007/s00445-005-0017-6

Moorhouse, B. L., and White, J. D. L. (2016). Interpreting ambiguous bedforms to distinguish subaerial base surge from subaqueous density current deposits. *Depositional Rec.* 2, 173–195. doi:10.1002/dep2.20

Mulder, T., and Alexander, J. (2001). The physical character of subaqueous sedimentary density flows and their deposits. *Sedimentology* 48, 269–299. doi:10.1046/j.1365-3091.2001.00360.x

Narcisi, B., and Petit, J. R. (2021). *Englacial tephras of east Antarctica*, 55. London, Memoirs: Geological Society, 649–664.

Nathan, S., and Schulte, F. J. (1968). Geology and petrology of the campbell–aviator divide, northern Victoria Land, Antarctica. *N. Z. J. Geol. Geophys.* 11, 940–975. doi:10.1080/00288306.1968.10420762

Niespolo, E. M., Rutte, D., Deino, A. L., and Renne, P. R. (2017). Intercalibration and age of the Alder Creek sanidine ^{40}Ar/^{39}Ar standard. *Quat. Geochronol.* 39, 205–213. doi:10.1016/j.quageo.2016.09.004

Ort, M. H., Lefebvre, N. S., Neal, C. A., McConnell, V. S., and Wohletz, K. H. (2018). Linking the Ukinrek 1977 maar-eruption observations to the tephra deposits: New insights into maar depositional processes. *J. Volcanol. Geotherm. Res.* 360, 36–60. doi:10.1016/j.jvolgeores.2018.07.005

Panter, K. S., Castillo, P., Krans, S., authors, 7, McIntosh, W., Valley, J. W., et al. (2018). Melt origin across a rifted continental margin: A case for subduction-related metasomatic agents in the lithospheric source of alkaline basalt, NW Ross Sea, Antarctica. *J. Petrology* 59, 517–558. doi:10.1093/petrology/egy036

Panter, K. S., Wilch, T. I., Smellie, J. L., Kyle, P. R., and McIntosh, W. C. (2021). *Marie Byrd Land and Ellsworth Land: petrology*, 55. London, Memoirs: Geological Society, 577–614.

Pedersen, G. B. M., Grosse, P., and Gudmundsson, M. T. (2020). Morphometry of glaciovolcanic edifices from Iceland: Types and evolution. *Geomorphology* 368, 107334. doi:10.1016/j.geomorph.2020.107334

Pollock, M., Edwards, B. R., Hauksdottir, S., Alcorn, R., and Bowman, L. (2014). Geochemical and lithostratigraphic constraints on the formation of pillow-dominated tindars from Undirhlíðar quarry, Reykjanes Peninsula, southwest Iceland. *Lithos* 200-201, 317–333. doi:10.1016/j.lithos.2014.04.023

Resing, J. A., Rubin, K. H., Embley, R. W., 20 authorsBaker, E. T., Dziak, R. P., et al. (2011). Active submarine eruption of boninite in the northeastern Lau Basin. *Nat. Geosci.* 4, 799–806. doi:10.1038/ngeo1275

Rhee, H. H., Lee, M. K., Seong, Y. B., Lee, J. I., Yoo, K.-C., and Yu, B. Y. (2020). Post-LGM dynamic deglaciation along the Victoria Land coast, Antarctica. *Quat. Sci. Rev.* 247, 106595. doi:10.1016/j.quascirev.2020.106595

Rocchi, S., Di Vincenzo, G., and Armienti, P. (2005). No plume, no rift magmatism in the West Antarctic rift. *Geol. Soc. Am. Special Pap.* 388, 435–447.

Rocchi, S., Di Vincenzo, G., and Ghezzo, C. (2004). The Terra Nova intrusive complex (Victoria Land, Antarctica). *Terra Antartica Rep.* 10, 1–50.

Rocchi, S., and Smellie, J. L. (2021). *Northern Victoria Land: Petrology*, 55. London, Memoirs: Geological Society, 383–413.

Rocchi, S., Storti, F., Di Vincenzo, G., and Rossetti, F. (2003). Intraplate strike-slip tectonics as an alternative to mantle plume activity for the Cenozoic rift magmatism in the Ross Sea region, Antarctica. *Geol. Soc. Lond. Spec. Publ.* 210, 145–158. doi:10.1144/gsl.sp.2003.210.01.09

Romero, J. E., Polacci, M., Watt, S., Tormey, D., Sielfeld, G., Arzilli, F., et al. (2021). Volcanic lateral collapse processes in mafic arc edifices: A review of their driving processes, types and consequences. *Front. Earth Sci.* 9, 639825. doi:10.3389/feart.2021.639825

Russell, J. K., Edwards, B. R., and Porritt, L. A. (2013). Pyroclastic passage zones in glaciovolcanic sequences. *Nat. Commun.* 4, 1788. doi:10.1038/ncomms2829

Salvini, F., Brancolini, G., Busetti, M., Storti, F., Mazzarini, F., and Coren, F. (1997). Cenozoic geodynamics of the Ross Sea region, Antarctica: Crustal extension, intraplate strike-slip faulting, and tectonic inheritance. *J. Geophys. Res.* 102, 24669–24696. doi:10.1029/97jb01643

Schmincke, H.-U., and Bednarz, U. (1990). “Pillow, sheet-flow and breccia volcanoes and volcano-tectonic cycles in the Extrusive Series of the northeastern Troodos ophiolite (Cyprus),” in *Ophiolites: Oceanic crustal analogues*. Editors J. Malpas, E. M. Moores, A. Panayiotou, and C. Xenophontos (Nicosia, Cyprus: Geological Survey Department), 185–206.

Schopka, H. H., Gudmundsson, M. T., and Tuffen, H. (2006). The formation of helgafell, southwest Iceland, a monogenetic subglacial hyaloclastite ridge: Sedimentology, hydrology and volcano-ice interaction. *Bull. Volcanol.* 152, 359–377. doi:10.1016/j.jvolgeores.2005.11.010

Self, S., Keszthelyi, L., and Thordarson, Th. (1998). The importance of pāhoehoe. *Annu. Rev. Earth Planet. Sci.* 26, 81–110. doi:10.1146/annurev.earth.26.1.81

Self, S., Thordarson, Th., Keszthelyi, L., authors, 5, Hon, K., Murphy, M. T., et al. (1996). A new model for the emplacement of Columbia River basalts as large, inflated pahoehoe lava flow fields. *Geophys. Res. Lett.* 23, 2689–2692. doi:10.1029/96gl02450

Siddoway, C. S. (2021). “The geology of West Antarctica,” in *Geology of the antarctic continent*. Editor G. Kleinschmidt (Stuttgart: Gebrüder Borntraeger Verlagsbuchhandlung), 87–131.

Skilling, I. P. (1994). Evolution of an englacial volcano: Brown bluff, Antarctica. *Bull. Volcanol.* 56, 573–591. doi:10.1007/bf00302837

Skilling, I. P. (2009). Subglacial to emergent basaltic volcanism at hlöðufell, south-west Iceland: A history of ice-confinement. *J. Volcanol. Geotherm. Res.* 186, 276–289. doi:10.1016/j.jvolgeores.2009.05.023

Smellie, J. L. (2021). *Antarctic volcanism: volcanology and palaeoenvironmental overview*, 55. London, Memoirs: Geological Society, 19–42.

Smellie, J. L., and Edwards, B. E. (2016). *Glaciovolcanism on Earth & Mars. Products, processes and palaeoenvironmental significance*. Cambridge University Press, 483.

Smellie, J. L. (2018). “Glaciovolcanism – A 21st century proxy for palaeo-ice,” in *Past Glacial Environments (sediments, forms and techniques)*. Editors J. Menzies and J. J. M. van der Meer 2nd edition (Amsterdam, Netherlands: Elsevier), 335–375.

Smellie, J. L. (2001). “Lithofacies architecture and construction of volcanoes erupted in englacial lakes: Icefall nunatak, mount murphy, eastern marie byrd Land, Antarctica,”in *Volcaniclastic sedimentation in lacustrine settings*. Editors J. D. L. White and N. Riggs *International Association of Sedimentologists Special Publications* (Oxford: Blackwell Science), 30, 9–34.

Smellie, J. L., and Martin, A. P. (2021). *Erebus volcanic province: Volcanology*, 55. London, Memoirs: Geological Society, 415–446.

Smellie, J. L. (2013). “Quaternary vulcanism: Glaciovolcanic landforms,” in *The encyclopedia of Quaternary science*. Editor S. A. Elias 3rd edition (Amsterdam: Elsevier), Vol. 1. (In press).

Smellie, J. L., Rocchi, S., and Armienti, P. (2011a). Late Miocene volcanic sequences in northern Victoria Land, Antarctica: Products of glaciovolcanic eruptions under different thermal regimes. *Bull. Volcanol.* 73, 1–25. doi:10.1007/s00445-010-0399-y

Smellie, J. L., Rocchi, S., Gemelli, M., Di Vincenzo, G., and Armienti, P. (2011b). A thin predominantly cold-based Late Miocene East Antarctic ice sheet inferred from glaciovolcanic sequences in northern Victoria Land, Antarctica. *Palaeogeogr. Palaeoclimatol. Palaeoecol.* 307, 129–149. doi:10.1016/j.palaeo.2011.05.008

Smellie, J. L., Rocchi, S., Johnson, J. S., Di Vincenzo, G., and Schaefer, J. M. (2018). A tuff cone erupted under frozen-bed ice (northern Victoria Land, Antarctica): Linking glaciovolcanic and cosmogenic nuclide data for ice sheet reconstructions. *Bull. Volcanol.* 80, 12. doi:10.1007/s00445-017-1185-x

Smellie, J. L., and Rocchi, S. (2021). *Northern Victoria Land: Volcanology*, 55. London, Memoirs: Geological Society, 347–381.

Smellie, J. L. (2006). The relative importance of supraglacial versus subglacial meltwater escape in basaltic subglacial tuya eruptions: An important unresolved conundrum. *Earth-Science Rev.* 74, 241–268. doi:10.1016/j.earscirev.2005.09.004

Smellie, J. L., Wilch, T., and Rocchi, A. (2013). ʻAʻā lava-fed deltas: A new reference tool in paleoenvironmental studies. *Geology* 41, 403–406. doi:10.1130/g33631.1

Sohn, C., and Sohn, Y. K. (2019). Distinguishing between primary and secondary volcaniclastic deposits. *Sci. Rep.* 9, 12425. doi:10.1038/s41598-019-48933-4

Sohn, Y. K., and Chough, S. K. (1992). The ilchulbong tuff cone, cheju island, South Korea: Depositional processes and evolution of an emergent, surtseyan-type tuff cone. *Sedimentology* 39, 523–544. doi:10.1111/j.1365-3091.1992.tb02135.x

Sohn, Y. K. (1996). Hydrovolcanic processes forming basaltic tuff rings and cones on Cheju Island, Korea. *Geol. Soc. Am. Bull.* 108, 1199–1211. doi:10.1130/0016-7606(1996)108<1199:hpfbtr>2.3.co;2

Sohn, Y. K., Park, K. H., and Yoon, S. H. (2008). Primary versus secondary and subaerial versus submarine hydrovolcanic deposits in the subsurface of Jeju Island, Korea. *Sedimentology* 55, 899–924. doi:10.1111/j.1365-3091.2007.00927.x

Solgevik, H., Mattsson, H. B., and Hermelin, O. (2007). Growth of an emergent tuff cone: Fragmentation and depositional processes recorded in the capelas tuff cone, são miguel, azores. *J. Volcanol. Geotherm. Res.* 159, 246–266. doi:10.1016/j.jvolgeores.2006.06.020

Storti, F., Salvini, F., Rossetti, F., and Phipps Morgan, J. (2007). Intraplate termination of transform faulting within the Antarctic continent. *Earth Planet. Sci. Lett.* 260, 115–126. doi:10.1016/j.epsl.2007.05.020

Takada, A. (1994). The influence of regional stress and magmatic input on styles of monogenetic and polygenetic volcanism. *J. Geophys. Res.* 99, 13563–13573. doi:10.1029/94jb00494

Valentine, G. A., Graettinger, A. H., and Sonder, I. (2014). Explosion depths for phreatomagmatic eruptions. *Geophys. Res. Lett.* 41, 3045–3051. doi:10.1002/2014gl060096

Vespermann, D., and Schmincke, H.-U. (2000). “Scoria cones and tuff rings,” in *Encyclopedia of volcanoes*. Editor H. Sigurdsson (San Diego: Academic Press), 683–694.

Vincenzo, G. D., and Rocchi, S. (1999). Origin and interaction of mafic and felsic magmas in an evolving late orogenic setting: The early paleozoic Terra Nova intrusive complex, Antarctica. *Contributions Mineralogy Petrology* 137, 15–35. doi:10.1007/s004100050579

Walker, G. P. L. (1992). Morphometric study of pillow-size spectrum among pillow lavas. *Bull. Volcanol.* 54, 459–474. doi:10.1007/bf00301392

W. E. LeMasurier and J. W. Thomson (Editors) (1990). “Volcanoes of the Antarctic plate and southern oceans,”, 48, 487.*Am. Geophys. Union, Antarct. Res. Ser.*

Watt, S. F. L., Pyle, D. M., and Mather, T. A. (2013). The volcanic response to deglaciation: Evidence from glaciated arcs and a reassessment of global eruption records. *Earth-Science Rev.* 122, 77–102. doi:10.1016/j.earscirev.2013.03.007

White, J. D. L., and Houghton, B. F. (2006). Primary volcaniclastic rocks. *Geology* 34, 677–680. doi:10.1130/g22346.1

White, J. D. L. (1996). Pre-emergent construction of a lacustrine basaltic volcano, Pahvant Butte, Utah (USA). *Bull. Volcanol.* 58, 249–262. doi:10.1007/s004450050138

White, J. D. L., and Ross, P. S. (2011). Maar-diatreme volcanoes: A review. *J. Volcanol. Geotherm. Res.* 201, 1–29. doi:10.1016/j.jvolgeores.2011.01.010

White, J. D. L., Smellie, J. L., and Clague, D. (2003). *Introduction: A deductive outline and topical overview of subaqueous explosive volcanism*, 140. American Geophysical Union Geophysical Monographs, 1–23.

White, J. D. L. (2000). Subaqueous eruption-fed density currents and their deposits. *Precambrian Res.* 101, 87–109. doi:10.1016/s0301-9268(99)00096-0

Wilch, T. I., McIntosh, W. C., and Panter, K. S. (2021). Marie Byrd Land and Ellsworth Land: volcanology. *Geological Society, London, Memoirs*, 55, 515–576.

Wilson, A. M., and Russell, J. K. (2020). Glacial pumping of a magma-charged lithosphere: A model for glaciovolcanic causality in magmatic arcs. *Earth Planet. Sci. Lett.* 548, 116500. doi:10.1016/j.epsl.2020.116500

Wilson, L., Smellie, J. L., and Head, J. W. (2013). “Volcano-ice interaction,” in *Modeling of volcanic processes: The physics and mathematics of volcanism*. Editors S. A. Fagents, T. K. P. Gregg, and R. M. C. Lopes (Cambridge: Cambridge University Press), 275–299.

Witham, A. G., and Sparks, R. S. J. (1986). Pumice. *Bull. Volcanol.* 48, 209–223. doi:10.1007/bf01087675

Wohletz, K. H., and Sheridan, M. F. (1983). Hydrovolcanic explosions II. Evolution of basaltic tuff rings and tuff cones. *Am. J. Sci.* 283, 385–413. doi:10.2475/ajs.283.5.385

Wohletz, K. H. (2003). *Water/magma interaction: Physical considerations for the deep submarine environment*, 140. American Geophysical Union Geophysical Monographs, 25–49.

Wörner, G., Niephaus, H., Hertogen, J., and Viereck, L. (1989). The Mt. Melbourne volcanic field (Victoria Land, Antarctica), II. Geochemistry and magma Genesis. *Geol. Jahrb.* E38, 395–433.

Wörner, G., and Orsi, G. (1990). Volcanic geology of Edmonson point, Mt. Melbourne volcanic field, north Victoria Land, Antarctica. *Polarforschung*. Bremerhaven: Alfred Wegener Institut 60, 84–86.

Wörner, G., and Viereck, L. (1990). *Mount Melbourne*, 48. American Geophysical Union, Antarctic Research Series, 72–78.

Wörner, G., and Viereck, L. (1987). Subglacial to emergent volcanism at shield nunatak, Mt. Melbourne volcanic field, Antarctica. *Polarforschung* 57, 27–41.

Wörner, G., and Viereck, L. (1989). The Mt Melbourne volcanic field (Victoria Land, Antarctica). I. Field observations. *Geol. Jahrb.* E38, 369–393.

Zimanowski, B., and Büttner, R. (2003). *Phreatomagmatic explosions in subaqueous volcanism*, 140. American Geophysical Union Geophysical Monographs, 51–60.

frontiers | Frontiers in Earth Science

TYPE Original Research
PUBLISHED 27 February 2023
DOI 10.3389/feart.2023.1116157

A kitchen experiment for replicating lava-ice interaction on stratovolcanoes

Chris E. Conway[1,2]*, Kenichiro Tani[2], Takashi Sano[2], Keiko Matsumoto[1] and Osamu Ishizuka[1]

[1]Research Institute of Earthquake and Volcano Geology, Geological Survey of Japan, National Institute of Advanced Industrial Science and Technology, Tsukuba, Japan, [2]Department of Geology and Paleontology, National Museum of Nature and Science, Tsukuba, Japan

OPEN ACCESS

EDITED BY
John Smellie,
University of Leicester, United Kingdom

REVIEWED BY
Adelina Geyer,
Institute of Earth Sciences Jaume Almera (CSIC), Spain
Jennie Gilbert,
Lancaster University, United Kingdom

*CORRESPONDENCE
Chris E. Conway,
✉ c.conway@aist.go.jp

SPECIALTY SECTION
This article was submitted to Volcanology, a section of the journal Frontiers in Earth Science

RECEIVED 05 December 2022
ACCEPTED 15 February 2023
PUBLISHED 27 February 2023

CITATION
Conway CE, Tani K, Sano T, Matsumoto K and Ishizuka O (2023), A kitchen experiment for replicating lava-ice interaction on stratovolcanoes.
Front. Earth Sci. 11:1116157.
doi: 10.3389/feart.2023.1116157

Many Quaternary stratovolcanoes host (or hosted) glacial ice with volumes that have fluctuated in response to long-term global climate cycles. The repeated advance and retreat of ice in valleys on the flanks of volcanoes throughout their eruptive histories has impacted how and where lava flows are emplaced and preserved. Understanding the dynamics of lava-ice interaction is a vital part of reconstructing the growth histories of many stratovolcanoes and can provide valuable clues about the evolution of Earth's climate. We have constructed a basic experiment, using common kitchen ingredients and utensils, to replicate the interaction between lava flows and glaciers on stratovolcanoes. This article outlines the ingredients and recipes for soda bread (stratovolcano analogy), ice cream (glacier analogies), and sauce (lava flow analogies), and describes exercises that provide qualitative lessons about the morphology of volcanoes, natural hazards, and paleoclimate. As such, the experiment can be used in geoscience outreach demonstrations for students and will assist non-specialist scientists with undertaking field identification of ice-bounded lava flows.

KEYWORDS

glaciovolcanism, stratovolcano, lava-ice interaction, climate change, geoscience outreach

Introduction

Glaciovolcanism

Many volcanoes are sites of interaction between the hottest (magma) and coldest (ice) natural materials on Earth's surface. Magmatic and volcanic activity in the presence of ice or snow gives rise to eruptive activity defined under the term of glaciovolcanism (Kelman et al., 2002; Smellie, 2006). In addition to the obvious candidates of Antarctica and Iceland, glaciovolcanism has also occurred extensively at volcanoes that line the edges of continents around the Pacific Ocean (e.g., Mee et al., 2009; Cole et al., 2018; Wilson et al., 2019; Kataoka et al., 2021; Loewen et al., 2021; Figure 1). Subduction zone volcanism throughout Japan, Kamchatka, north-western United States, Central and South America, New Zealand, Papua New Guinea, Indonesia, and the Philippines has typically produced tall composite cones that form as a result of frequent eruptions over long time periods (Davidson and de Silva, 2000). The lofty heights of these volcanic features mean that many of them experience seasonal snowfall under current climate conditions, and ones that are located in the high-latitudes host permanent ice caps and glaciers (e.g., Mount Veniaminof, Alaska). In this "Pacific ring of fire and ice", even volcanoes in tropical regions such as Papua New Guinea (e.g., Mount

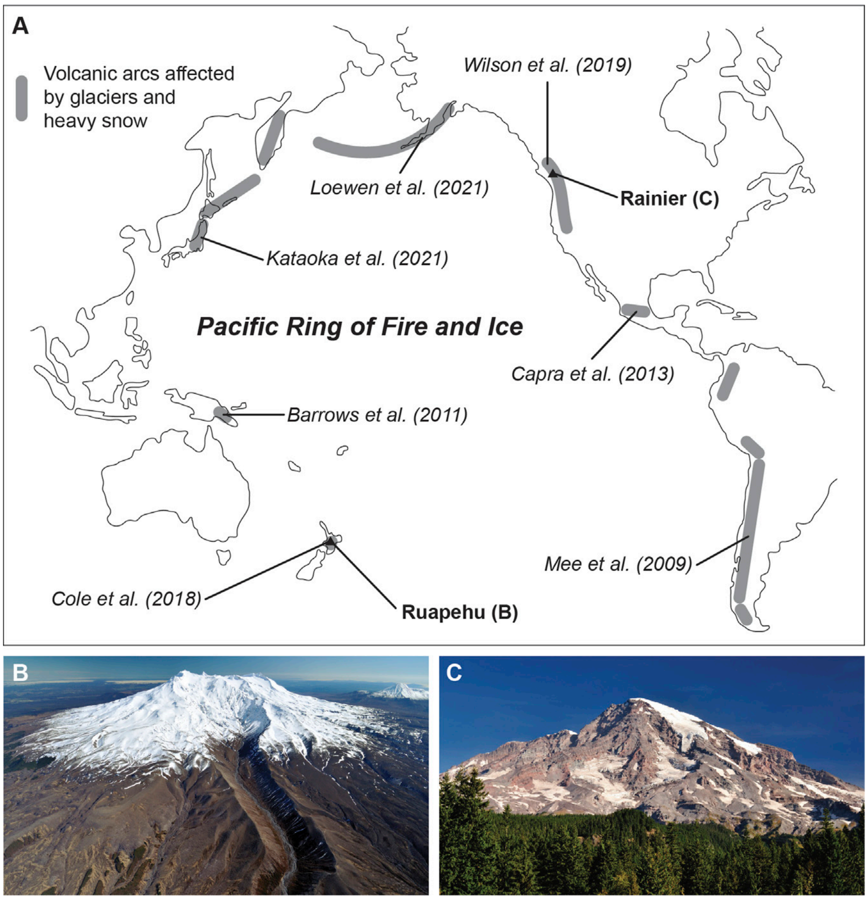

FIGURE 1
Locations and examples of arc stratovolcanoes where glaciovolcanism has occurred during the last ~250,000 years. **(A)** Map of volcanic arcs (grey lines) around the Pacific Ocean that have been affected by glaciers and heavy snow. Locations are noted for Rainier and Ruapehu volcanoes, and for representative study sites mentioned in the text. **(B)** Photograph of a glacial valley (Wahianoa River) on the southeast flank of snow-covered Mount Ruapehu in New Zealand. **(C)** Photograph of the southeast flank of Mount Rainier in Washington, United States, which comprises glaciers and steep ridges of lava. Photographs were provided by Dougal Townsend.

Giluwe; Barrows et al., 2011) and Mexico (e.g., Nevado de Toluca; Capra et al., 2013) have experienced glaciation and therefore may have been affected by glaciovolcanism.

The abundance and extent of glaciers on volcanoes have fluctuated in response to 100,000 years-long global climate cycles over the last ~700,000 years (Goñi et al., 2019; Coombs and Jicha, 2020). During the Last Glacial Maximum (LGM), around 25,000–20,000 years ago, when the average global temperature was 6°C colder than today (Tierney et al., 2020), large glaciers were present on many volcanoes, including ones that are currently free of permanent ice (Eaves et al., 2016). Signs of past glaciation exist as u-shaped valleys, moraines, and striated lavas (Figure 1B). Within the traditional view of the evolution of stratovolcanoes affected by glaciers (e.g., Hobden et al., 1996), these features record periods of erosion (during relatively cold climate stages) that were distinct in timing from periods of volcanic growth (during relatively warm climate stages). Under this paradigm, ridges of lava on the sides of valleys are inferred to have been carved out by glaciers. This has certainly occurred at numerous volcanoes (e.g., Singer et al., 1997); however, $^{40}Ar/^{39}Ar$ and K-Ar dating of lavas has also shown that eruptions have occurred during periods when glaciers were extensive in many cases (Fiertsein et al., 2011; Conway et al., 2016; Calvert et al., 2018; Pure et al., 2020). These examples challenge the dichotomy between volcanic growth and glacial erosion and present a key question: what happens when lava is erupted at a stratovolcano that is covered in ice?

Building on pioneering work by Mathews (1952) in British Columbia, a landmark publication by Lescinsky and Sisson (1998) showed that thick lavas located on the tops and sides of ridges at Mount Rainier in Washington, United States (Figure 1C), formed when they flowed down the flanks of the volcano and were confined along the margins of valley-filling glaciers during past cold periods of Earth's history. The ice deflected the lavas from flowing into valleys, forcing them to pond into thick units along high-elevation parts of the volcano. The glaciers retreated after thousands of years, and left the lavas "perched" on the tops and sides of ridges. Similar landforms have been described at Mount Ruapehu in New Zealand (Figures 1, 2; Spörli and Rowland, 2006; Conway et al., 2015). The steep

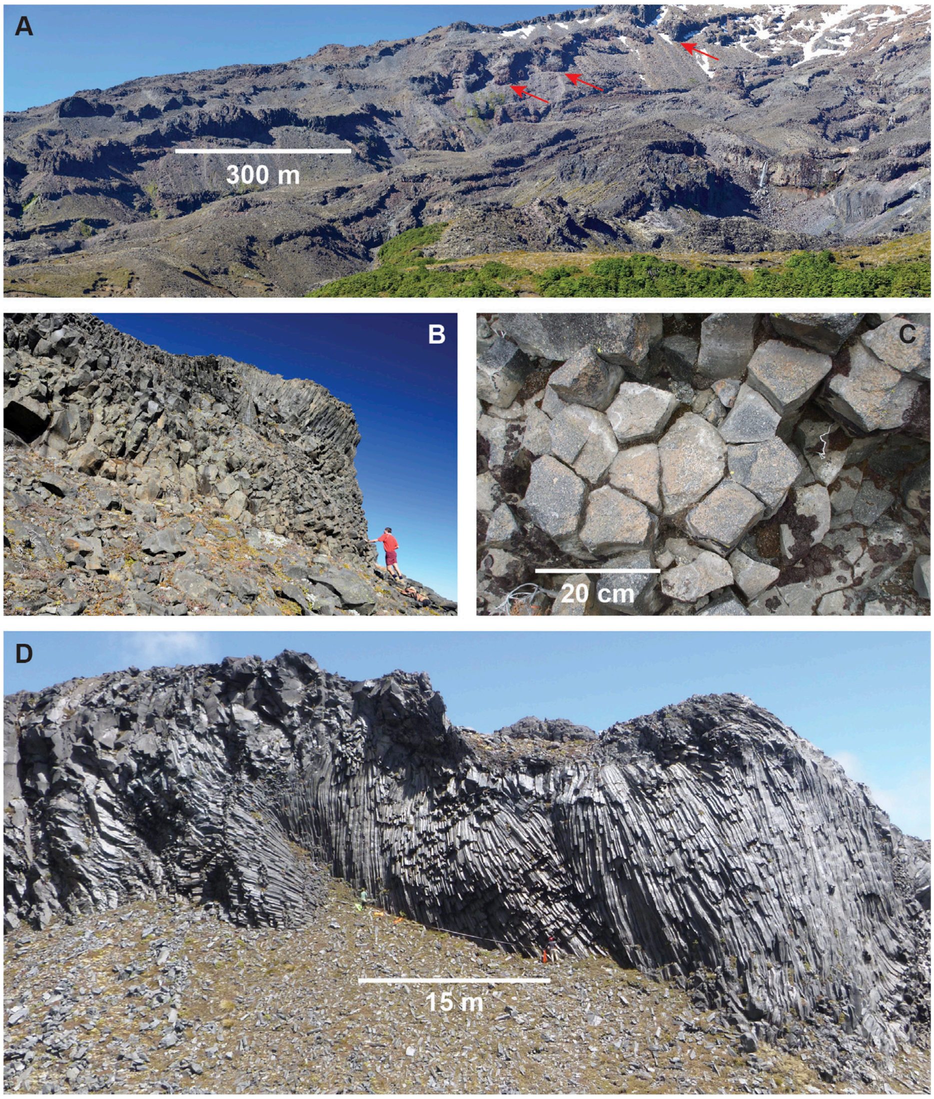

FIGURE 2
Examples of ice-bounded lava flows at Mount Ruapehu, New Zealand. **(A)** Thick lavas on the northern ridge of the Mangaturuturu valley on the southwestern flank, which were emplaced next to glacial ice between ~45–20 ka. Red arrows point to "knuckles" of lava. Photograph provided by Dougal Townsend. **(B)** Column-forming joints on the margin of an ice-bounded lava flow on the western flank. Photograph provided by Dougal Townsend. **(C)** Cross-section view of "columns" with diameters of ca. 10 cm on an ice-bounded lava flow on the southeastern flank. **(D)** Fanning column-forming joints in an ice-bounded lava flow on the northwest flank. People are standing 15 m apart.

sides of such outcrops display glassy textures and characteristic fractures that indicate they cooled quickly against water and steam produced by melting of the ice (Figure 2C). Rapid cooling against vertical walls of ice has produced horizontal or curved "columns" on many ice-bounded lavas (Figure 2D), which are formed by the propagation of fractures away from (often complex) cooling surfaces (Lodge and Lescinsky, 2009). The intersection of the fractures at angles of ~60° forms the characteristic cross-sectional polygons with diameters of ~10–20 cm (Figure 2C).

As forecast by Lescinsky and Sisson (1998), ice-bounded lavas have now been identified at several stratovolcanoes around the Pacific (e.g., Mee et al., 2009; Conway et al., 2015; Lachowycz et al., 2015; Coombs and Jicha, 2020; Mixon et al., 2021). Although the mechanism of their formation is well-defined in theory, it remains difficult to grasp the dynamics of lava-ice interaction without direct observation of such an eruption. Emplacement of lava flows onto snow (Edwards et al., 2015) and ice caps (Loewen et al., 2021) has been documented, and large-scale experiments using basaltic melt have been undertaken in the last decade (Edwards et al., 2013). Even with these reference points, identification of ice-bounded lava flows during field surveys requires a certain level of intuitive assessment *via* real-time reconstruction of past environments. There are many circum-Pacific stratovolcanoes with overlapping eruption and glacial histories where lava-ice interaction has not been documented. The experiment described in this contribution is designed to convey the stratigraphic and morphological

TABLE 1 List of ingredients and equipment required for the experiment.

Bread volcano	
Flour	3 cups (360 g)
Baking powder	3 teaspoons (12 g)
Soda (sparkling) water	150 ml
Melted butter	1 tablespoon
Sauce lava flows	
Dark chocolate	25 g
White chocolate	15 g
Hot water	25 ml
Thickener	10 g
Ice cream glacier	
Vanilla ice cream	100 ml
Equipment	
Large bowl	Sifter
Measuring cup	Teaspoon
Mixing spoon	Plate (oven-safe)
Cup (oven-safe)	Oven/microwave
Syringe	Knife

characteristics of ice-bounded lavas, which will assist field geologists with identifying these features in such settings.

Kitchen experiments in geoscience outreach

Active learning methods have been shown to be a successful teaching tool for secondary and tertiary school science subjects (Hake, 1998). Food-based experiments have been particularly popular within this approach, likely because they use inexpensive items and kitchens can be portrayed as accurate representations of scientific laboratories, where hypotheses are tested by carrying out reproducible methods. In Japan, the recipes of “Volcano Kitchen” have been a popular source for outreach activities that utilize common ingredients to teach lessons in volcanology (Hayashi, 2006). A recently published children’s book based on the August 2021 eruption of Fukutoku-Okanoba volcano has also incorporated cooking to introduce primary school students to the petrology of volcanic rocks (Maruya, 2022). Baked goods and candies that look like rocks and minerals are commonly found at geopark visitor centres throughout Japan, and have been successful for introducing domestic and foreign tourists to the textures of rocks in the geologically diverse country. Other examples from around the world include the M&M® magma chamber for simulating fractional crystallization (Wirth, 2003) and the use of fudge and syrup for explaining lava flow rheology (Rust et al., 2008). Whereas precise scaling of natural phenomena is required for analogue modelling (Galland et al., 2006), analogy experiments (after Ichihara, 2023), including the one presented in this contribution, can still convey valuable information with approximate scaling of physical parameters.

Providing a pathway for students to see geoscience as an option for further study and work is indeed a worthwhile activity. Building sustainable and resilient societies will rely on future generations tackling the major issues of climate change mitigation, renewable energy generation, mineral extraction, and natural hazard assessment. Introducing geoscience research to primary and secondary school students (ages 5–18 years) may encourage them to pursue further study of science, technology, engineering, and mathematics (STEM) subjects at university and a career aimed at tackling these challenges. The aim of this contribution is to showcase an analogy experiment of a common glaciovolcanic process (i.e., lava-ice interaction), that can be utilized to introduce the topics of climate change and volcanic hazards to students and non-specialist audiences. The common ingredients and basic kitchen tools make this exercise widely applicable, and the hands-on format is designed to encourage laboratory research *via* active participation in school classrooms and outreach demonstrations for all ages.

Methods and materials

The ingredients and equipment required to make the analogy experiment materials are listed in Table 1, and described herein. Instructions for the experiment are outlined in this section and are also provided in the Supplementary Material.

Stratovolcano analogy

A basic soda bread is used as the stratovolcano analogy (hereafter, Volcano) in the experiment. Sift 3 cups (360 g) of wheat flour and 3 teaspoons (12 g) of baking powder into a large bowl and mix. Pour 100 mL of soda water (also known as sparkling water) into the bowl at first, and stir into the dry ingredients. Add more soda water by increments of 10 mL until the mixture becomes flaky. Push the flaky parts together with your hands to form a dough, and knead by pressing and folding it over repeatedly. If the dough is not sticking together when you fold it, add some more soda water until it becomes a cohesive ball. If the dough is sticking to your hands, add some more flour until you can handle it easily. Spread the dough out into a broad cone, by pushing down the edges. Place the dough on a lightly greased oven-proof plate. Score the top of the dough by making four ~1 cm-deep incisions from near the edges to within 2 cm of the centre, at 90° to each other. Melt the butter and rub it over the top of the dough. The oven or microwave (using the oven setting) should be pre-heated to 200°C, prior to putting in the plate with the dough to bake for 30 min at 200°C. Take out the bread and leave to cool for approximately 10 min. Cut around the score marks to form “valleys” that are 2–3 cm-wide and ~5 cm-long.

Lava flow analogies

Two gelatinous chocolate sauces are used as lava flow analogies in the experiment. To make the first lava flow analogy (hereafter, Lava 1), place 5 g of thickener (powdered collagen gelatine) in a cup

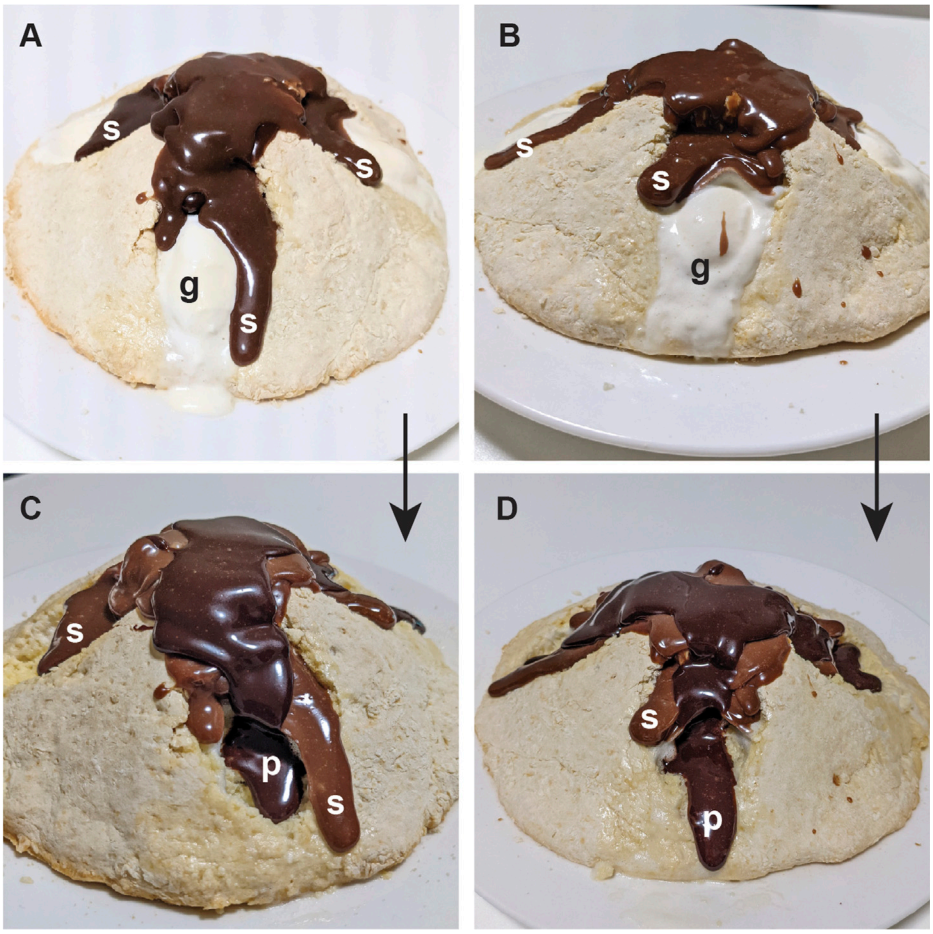

FIGURE 3
The experiment. **(A,B)** Syn-glacial lava flows (s) were deflected by glaciers (g) and emplaced along ridges during the glacial stage. **(C,D)** Post-glacial lavas (p) flowed over older lavas and into ice-free valleys after deglaciation.

and add ~10 mL of hot water, plus 5 g of dark chocolate and 15 g of white chocolate. Heat in a microwave for 40 s (~700 W power), then stir thoroughly to form a thick sauce with even consistency. Repeat the steps using 20 mg of dark chocolate, 5 g of thickener and 10–15 mL of hot water to make Lava 2 in a separate cup. Lava 2 should be slightly less viscous than Lava 1 for the purposes of the experiment.

Glacier analogies

Buy a small container of light-colored plain milk-based ice cream (e.g., vanilla) to use as the glacier analogies (hereafter, Glaciers) in the experiment.

Alternative ingredients and dietary notes

Any carbonated drink can be used as an alternative to soda water. The authors have successfully made the bread volcano using ginger ale, cola, and beer (including non-alcoholic beer). To modify the taste of the bread, add 1–2 teaspoons of salt, and/or 1–2 tablespoons of sugar to the dry ingredients. Milk can be used as an alternative to water when making the sauces.

The ingredients contain gluten, dairy, and sugar. Please check the dietary restrictions of participants if you choose to share the bread, ice cream and chocolate as snacks to eat after the experiment. We do not recommend eating the sauce or ice cream used during the experiment. Instead, consume the remaining chocolate and ice cream ingredients.

The experiment

The experiment can be undertaken after the analogy materials have been constructed (Volcano, Lava 1 and Lava 2, and Glaciers). There are 3 main steps within the experiment, each representing a key stage in the evolution of a glaciated stratovolcano: 1) Syn-glacial; 2) deglacial; and 3) post-glacial.

The aim of syn-glacial stage of the experiment is to reproduce lava flow eruptions that occurred during glacial stages when ice extent was advanced on stratovolcanoes (e.g., during the LGM). Add

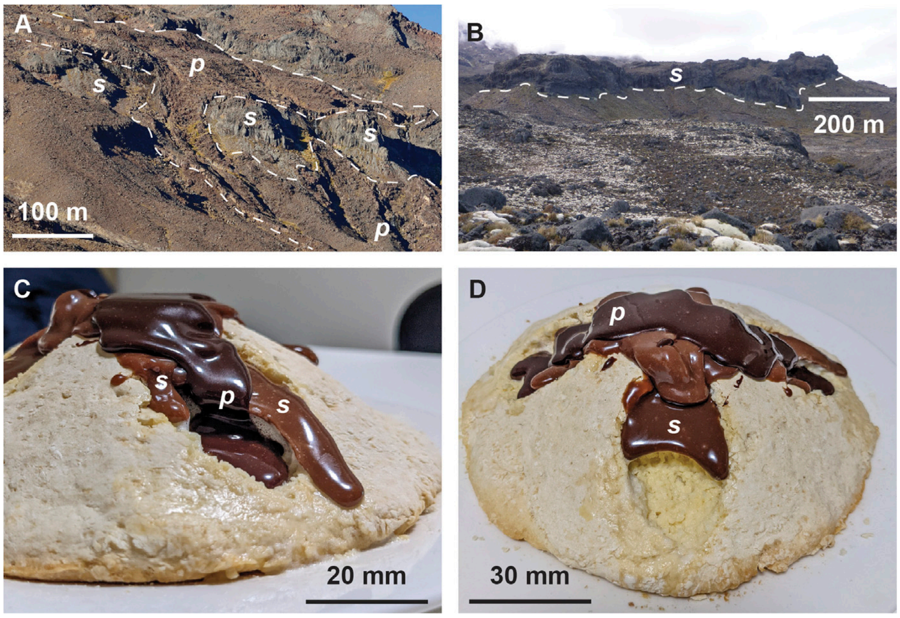

FIGURE 4
Comparison of real lava flows at Mount Ruapehu and experimental products. **(A,C)** Post-glacial lavas (p) flowed over and around older syn-glacial lavas (s). **(B,D)** Thick and wide syn-glacial lavas (s) were impounded by glaciers within valleys. Photograph **(A)** was provided by Dougal Townsend.

Glaciers to the valleys on the Volcano. The Glaciers should be thickest in the middle of the valleys, and sit just below the height of the flanks at the heads and sides of the valleys. Leave an area with no Glaciers on the top of the Volcano to represent the summit vent area. Pour Lava 1 onto this summit area at an approximate rate of 2–4 mL s^{-1}, from a height of 2 cm. Vary the starting point of these lava flows on the summit so that Lava 1 moves down onto different sides of the Volcano. Lava 1 should flow down along the ice-free parts of the Volcano, and into the gap between the sides of the valleys and their Glaciers (Figures 3A, B). Leave the Lava 1 flows to cool down and harden.

Whilst making Lava 2, leave the Glaciers to melt and then scoop away the remainder carefully from the valleys. This represents the deglacial stage of the experient. Try not to disturb the Lava 1 flows that have set along the tops and sides of the valleys.

The post-glacial stage of the experiment is designed to replicate the effusion of lava flows on an ice-free stratovolcano following deglaciation. Pour Lava 2 at the same rate onto the top of the volcano in increments and from different starting points again. This time, Lava 2 flows should travel over the syn-glacial stage Lava 1 flows and move into the bottom of the valleys (Figures 3C, D).

Results

Herein, we highlight the similarities between the experimental products and real examples of ice-bounded lava flows, and note aspects of lava-ice interaction at volcanoes that are not captured by the experiment, and *vice versa*. Eruptions that have produced ice-bounded lava flows at Ruapehu and Rainier volcanoes started from vents that were covered by ice at their summits. It is envisioned that such vents eventually became ice-free as eruptive products piled up during the onset of an eruption, allowing lavas to travel through or beside glaciers *via* meltwater channels created by lava-ice interaction (Lescinsky and Fink, 2000). In the experiment, Lava 1 was poured onto the ice-free summit part of the Volcano for simplicity during the syn-glacial stage, rather than being pushed up from beneath the Glaciers. Similarly, Lava 2 was poured onto the top of the Volcano during the post-glacial stage, after the Glaciers had been removed.

Lava 1, which flowed along the margins of the Glaciers, remained perched on the sides of valleys after the Glaciers were removed during the deglacial stage (Figure 3). These features are close replicants of ice-bounded lava flows at Mount Ruapehu, New Zealand (Figures 2, 4). At Ruapehu, and other stratovolcanoes around the margins of the Pacific Ocean (Figure 1A), ice-bounded lavas stand out as thick (>20 m-thick) and steep-sided units on the tops and sides of ridges adjacent to glacial valleys (Figures 4A, C; Lescinsky and Sisson, 1998), and as broad ice-dammed lavas within valleys (Figures 4B, D; Conway et al., 2015). They can show local variations in thickness along ridges, as their morphology was governed by the shape of the ice wall against which they were impounded. This can be seen in some examples at Ruapehu where lavas are relatively thin along the crest of ridges and thicken considerably into “knuckles” toward the valley (Figure 2A). These intricacies are not reproduced by the small-scale experiment, nor are the fine-scale cooling fractures, such as decimetre-scale column-forming joints, that are produced by rapid quenching of lava against meltwater and steam at the edges of glaciers (Figure 2C; Lescinsky and Fink, 2000; Mee et al., 2009; Lodge and Lescinsky, 2009; Conway et al.,

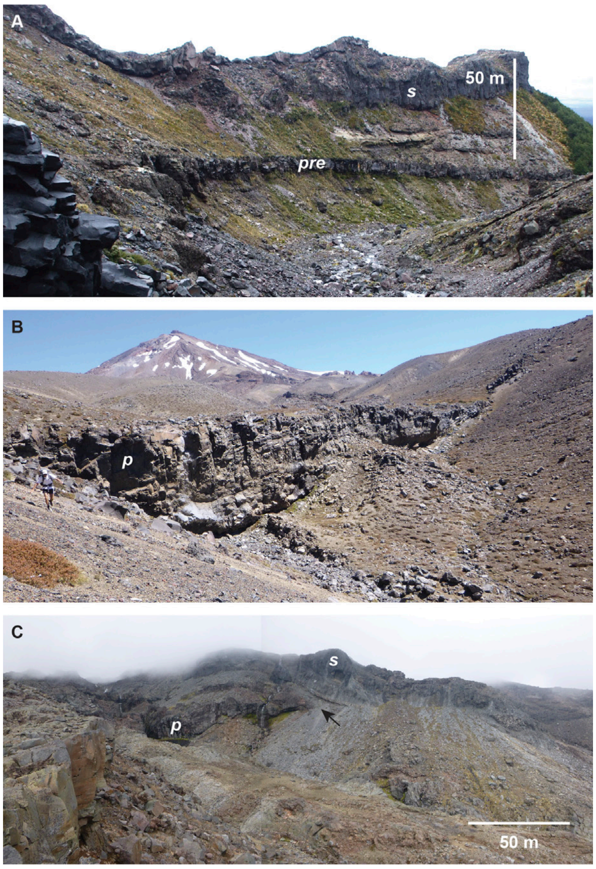

FIGURE 5
Stratigraphic features of pre-, syn-, and post-glacial lava lavas (pre, s, p) at Mount Ruapehu, New Zealand. **(A)** The syn-glacial lava exhibits a thick and uneven morphology, and is younger than the lower pre-glacial lava, which is a uniformly thin unit that has been eroded by glacial (and fluvial) action. **(B)** This post-glacial lava flowed into the valley and was not ponded along the ridge. **(C)** The post-glacial lava is younger than the syn-glacial lava in this photo. Although it looks like (p) is outcropping from beneath (s) at the location marked by the arrow, the post-glacial lava flowed into the valley after retreat of the ice that buttressed the syn-glacial lava.

2015). While fracturing and fragmentation of Lava 1 will not occur in the experiment, one might see mixing of melted ice cream and the lavas. Such features resemble ice-melt lahars generated by lava-ice interaction, which can be fatal phenomena produced at ice-capped stratovolcanoes (Pierson et al., 1990; Smellie, 2022). Ice-bounded lavas on volcanoes may undergo erosion through rockfall, because their steep and finely fractured margins are vulnerable to collapse. They may also be affected by subsequent re-advance of glaciers. These aspects are not captured by the experiment; following the removal of the Glaciers, Lava 1 flows will remain in-place where they hardened along the sides of the valleys.

After removal of the Glaciers, Lava 2 flowed over and around the syn-glacial Lava 1 to build up the top of the Volcano and moved into the valleys during the post-glacial stage of the experiment (Figures 3C, D). These characteristics are commonly observed for Holocene lavas on volcanoes that erupted during the current interglacial period. Such flows often appear thin and rubbly on the tops of ridges because they were not contained or impounded by obstacles, as opposed to ice-bounded flows (Figures 4A, C). This feature was emphasized in the experiment by using a greater amount of water to ensure that Lava 2 was less viscous than Lava 1.

Discussion

The importance of recognizing ice-bounded lava flows

There are 138 active arc stratovolcanoes with glaciers on Earth (Edwards et al., 2020). Many more stratovolcanoes hosted glaciers during past cold periods such as the LGM, but are currently free of permanent ice (e.g., Eaves et al., 2016). Glaciers have therefore been a key part of the life cycles of many volcanoes, and will continue to impact eruptions in the future. As fluctuations in the volumes of glaciers on human timescales become apparent (Vargo et al., 2020), it is pertinent to be aware of how glacier extents have changed over longer timescales in the past. Examining the links between volcanism and the cryosphere that arose from these past changes is important for forecasting future eruptive activity.

Stratovolcanoes grow into large constructional structures over time periods of several 10^2 to 10^5 years due to the repetitive emplacement of lava and tephra onto their flanks (Davidson and de Silva, 2000; Yamamoto et al., 2018; Christiansen et al., 2020). Whereas symmetrical cones such as Mount Fuji are often presented as icons of arc stratovolcanoes, many are in fact asymmetrical and complex structures (Figures 1B, C). The latter types exist because volcanoes also undergo destruction throughout their lifetimes, *via* sector collapse and erosion. Ice is a key agent for both collapse and erosion at volcanoes that have been affected by glaciers. Retreating glaciers promote edifice collapse by destabilising steep and weak units of volcanic rock (Capra, 2006), whereas advancing glaciers scour out valleys and push eroded material onto the ring plains that surround volcanoes (Eaves et al., 2016). Ice also acts to modify the preservation and distribution of volcanic rocks on stratovolcanoes during eruptions, as shown by the experiment (Figure 3). Understanding how glaciers have affected the preservation of volcanic deposits is vital, because these deposits provide a necessary record of past volcanic activity and, therefore, a framework for the possible timing and types of future eruptions at active volcanoes.

The most important message conveyed by the experiment is that many of the lavas observed on the sides of valleys exist because glaciers deflected them onto those locations during eruptions, rather than having exposed them *via* erosion after they were emplaced onto ice-free flanks. Syn-glacial lavas exhibit an increase in thickness towards the valley and characteristic cooling fractures on their margins that indicate they were impounded and chilled by valley-filling ice (Figure 2; Figure 5A). Post-glacial lavas generally exhibit more uniform thicknesses, with no evidence for impedance of their flow towards lower elevations by a morphological barrier, and will lack evidence for rapid cooling (Figure 5A). A major implication of identifying ice-bounded lavas is that stratovolcanoes can be continuously active during their lifetimes. This differs from the traditional model of stratovolcano evolution that states that eruptions and edifice growth occur during interglacial stages and relative inactivity and erosion occur during glacial stages.

Age data for ice-bounded lava flows record more than just the timing of an eruption; they provide *in situ* constraints of the past presence and extent of ice in alpine settings (Lescinsky and Fink, 2000). Conversely, ages for post-glacial lavas that flowed into valleys provide constraints for the timing of glacier retreat (Figure 5B; Conway et al., 2015). These constraints are valuable for reconstructing the past climate and environments of Earth. Despite these useful products, the influence of ice on the distribution of lava flows during eruptions also produces complex stratigraphic relationships that can be difficult to unravel. Post-glacial lava flows may appear to be stratigraphically lower than syn-glacial ice-bounded lavas in the field, although they are younger in age (Figure 5C). This apparent inversion of stratigraphy is important to recognize when documenting the eruptive history of a stratovolcano, and using geochronology to measure absolute ages for volcanic units is useful for testing such stratigraphic relationships in the field.

Studying the differences in volumes and compositions of syn- versus post-glacial lavas and tephras (explosive eruption deposits) also offers the opportunity to investigate whether the addition/removal of ice masses on volcanoes affect their underlying magmatic systems. Geological and geochemical evidence from Iceland indicates that deglaciation after the LGM resulted in an increase in rates of volcanism because the removal of ice on the crust resulted in increased production and eruption of new magma (Maclennan et al., 2002). It remains unclear whether deglaciation leads to increased eruption rates at arc stratovolcanoes (Watt et al., 2013; Conway et al., 2016; Pure et al., 2020), although a few studies have interpreted that eruption dynamics at some volcanoes were influenced by the retreat of ice following the LGM in Chile (Rawson et al., 2016). With glacier volumes in many locations currently decreasing in response to anthropogenic climate change (Vargo et al., 2020), it is critical to understand the links between deglaciation and volcanism in more detail so that we can forecast how the melting of glaciers and ice sheets will affect eruptive activity in the future (Tuffen, 2010).

Additional hazards related to volcano-ice interaction include sector collapses and lahars. A large landslide in 2010 at Mount Meager in southwest Canada was prompted by glacial retreat and melting of snow (Roberti et al., 2018). Meltwater lahars are an extremely hazardous phenomenon produced at snow- and ice-clad stratovolcanoes (Pierson et al., 1990; Uesawa, 2014; Smellie, 2022). Snowy volcanoes are popular tourist locations for winter activities, so constraining rates of meltwater production (Cole et al., 2021) and modelling the travel pathways for lahars (Kataoka et al., 2021) represent vital research objectives and hazard mitigation tools in volcanology.

Key points for educators and experimenters

The coexistence of magma and ice at glaciated stratovolcanoes make them hotspots to learn about cool geological ideas. Lava-ice interaction has produced stunning outcrops of volcanic rock (Figure 2), which record valuable information about the evolution of volcanoes and Earth's climate. These visually striking features can serve as icons for geoscience education, to increase future generations' interest in mitigating climate change and natural hazards. Background information and the key lessons about volcanoes and glaciers that the experiment highlights are summarized below.

1 Global climate variability has produced repetitive 100,000 years-long cycles of glacial advance and retreat over the last ~700,000 years. Ice sheets and glaciers grew during the last glacial period, and had well-advanced extents during the LGM around 20 ka, when the average global temperature was 6°C lower than today.

2 As glaciers have advanced and retreated due to these long-term climate cycles, they have repeatedly carved out valleys on many long-lived arc stratovolcanoes with high summit elevations, such as many of those located around the margins of the Pacific Ocean.

3 If effusive eruptions occur when valleys are filled with ice, lava is deflected toward the sides of the valleys and becomes ponded and chilled along ridges adjacent to glaciers. This process creates thick lava flows that remain perched on the tops and sides of ridges after the glaciers retreat. Ice-bounded lava flows often exhibit horizontally oriented column-forming joints that indicate that the lava cooled quickly next to the vertical margins of glaciers.

4 If eruptions occur when valleys are not filled with ice, lava will flow into valleys and become emplaced at lower elevations on volcanoes. These lavas will be thinner along ridges than ice-bounded lavas.

5 Measuring the ages, volumes, and compositions of syn- and post-glacial lava flows and tephras (explosive eruption products) has several major implications for understanding the evolution of our planet. Ages for ice-bounded and valley-filling lavas provide valuable constraints on the timing of past glacial advance and retreat, respectively. Comparing the volumes and composition of syn-glacial lavas and tephras with those of post-glacial lavas and tephras allows investigation of whether the addition and removal of ice masses on top of volcanoes affects the behaviour of the underlying magma systems.

6 Interactions between volcanoes and ice/snow pose major risks for nearby populations. Explosive eruptions, landslides, and lahars are examples of hazardous phenomena produced at ice- and snow-clad volcanoes. Further research is required to understand how eruptive activity will be affected by ice sheet and glacier decay associated with climate change in the future, and how society can build resilience to volcanic hazards at ice- and snow-clad volcanoes.

Conclusion

This article has described a classroom exercise that conveys lessons about the morphology of volcanoes, natural hazards, and paleoclimate by using a small-scale kitchen experiment with easily accessible ingredients and apparatus. Simple recipes for soda bread (stratovolcano analogy), ice cream (glacier analogies), and sauce (lava analogies) are outlined along with instructions for how to use them to replicate the interaction between lava flows and ice on stratovolcanoes. The experiment conveys the process of lava-ice interaction, whereby effusive eruptions during glacial periods lead to the deflection and ponding of lava flows on the ridges adjacent to ice-filled valleys. Recognition of the products of this process is vital for understanding the eruption histories of glaciated stratovolcanoes, and can inform paleoclimate reconstructions by providing valuable constraints on the past extent and timing of glacial advances. This is a qualitative experiment designed to equip students and non-specialist scientists with the understanding to undertake field identification of ice-bounded lava flows. Moreover, we hope that this exercise generates interest in the related themes of climate change and volcanic hazards, and encourages students to consider careers in science.

Data availability statement

The datasets presented in this study can be found in online repositories. The names of the repository/repositories and accession numbers can be found in the article/Supplementary Material.

Author contributions

CC conceptualized the experiment. It was first trialled by CC, KT, and TS at the National Museum of Nature and Science in Tsukuba, Japan, and first utilized in a classroom experiment conducted by CC at Utsunomiya Girls' High School in 2017. CC and KM carried out the recorded version of the experiment. All authors contributed to trialling and refining the recipes and experiment, and to the writing of the manuscript.

Funding

CC and OI were supported by JSPS-RSNZ bilateral research grant JPJSBP120211003. National Geographic Society Explorer Grant CP-114R-17 helped CC, KT, and OI to pursue glaciovolcanism research activities in Japan.

Acknowledgments

The bread recipe described in this article was modified from one provided to CC by Patsy Sziranyi and Esther Conway, with additional baking advice from Patrick Conway. We are very grateful to Dougal Townsend (GNS Science) for providing photographs. CC thanks Andrew Calvert, Rosie Cole, Carolyn Driedger, Shaun Eaves, John Gamble, Graham Leonard, Leo Pure, Thomas Sisson, Dougal Townsend, James Vallance, James White, and Colin Wilson for valuable discussions during field surveys at Ruapehu and Rainier volcanoes. Thank you to John Smellie, Valerio Acocella, and the two reviewers for very helpful comments.

Conflict of interest

The authors declare that the research was conducted in the absence of any commercial or financial relationships that could be construed as a potential conflict of interest.

Publisher's note

Supplementary material

The Supplementary Material for this article can be found online at: https://www.frontiersin.org/articles/10.3389/feart.2023.1116157/full#supplementary-material

References

Barrows, T. T., Hope, G. S., Prentice, M. L., Fifield, L. K., and Tims, S. G. (2011). Late pleistocene glaciation of the Mt Giluwe volcano, Papua New Guinea. *Quat. Sci. Rev.* 30, 2676–2689. doi:10.1016/j.quascirev.2011.05.022

Calvert, A. T., Fierstein, J., and Hildreth, W. (2018). Eruptive history of middle sister, Oregon cascades, USA–product of a late pleistocene eruptive episode. *Geosphere* 14, 2118–2139. doi:10.1130/GES01638.1

Capra, L. (2006). Abrupt climatic changes as triggering mechanisms of massive volcanic collapses. *J. Volcanol. Geotherm. Res.* 155, 329–333. doi:10.1016/j.jvolgeores.2006.04.009

Capra, L., Bernal, J. P., Carrasco-Núñez, G., and Roverato, M. (2013). Climatic fluctuations as a significant contributing factor for volcanic collapses. Evidence from Mexico during the Late Pleistocene. *Glob. Planet. Change.* 100, 194–203. doi:10.1016/j.gloplacha.2012.10.017

Christiansen, R. L., Calvert, A. T., Champion, D. E., Gardner, C. A., Fierstein, J. E., and Vazquez, J. A. (2020). The remarkable volcanism of Shastina, a stratocone segment of Mount Shasta, California. *Geosphere* 16, 1153–1178. doi:10.1130/GES02080.1

Cole, R. P., White, J. D. L., Conway, C. E., Leonard, G. S., Townsend, D. B., and Pure, L. R. (2018). The glaciovolcanic evolution of an andesitic edifice, South Crater, Tongariro volcano, New Zealand. *J. Volcanol. Geotherm. Res.* 352, 55–77. doi:10.1016/j.jvolgeores.2017.12.003

Cole, R. P., White, J. D. L., Dürig, T., Büttner, R., Zimanowski, B., Bowman, M. H., et al. (2021). Controls on andesitic glaciovolcanism at ice-capped volcanoes from field and experimental studies. *Geology* 49, 1069–1073. doi:10.1130/G48735.1

Conway, C. E., Townsend, D. B., Leonard, G. S., Wilson, C. J. N., Calvert, A. T., and Gamble, J. A. (2015). Lava-ice interaction on a large composite volcano: A case study from Ruapehu, New Zealand. *Bull. Volcanol.* 77 (21), 21. doi:10.1007/s00445-015-0906-2

Conway, C. E., Leonard, G. S., Townsend, D. B., Calvert, A. T., Wilson, C. J. N., Gamble, J. A., et al. (2016). A high-resolution $^{40}Ar/^{39}Ar$ lava chronology and edifice construction history for Ruapehu volcano, New Zealand. *J. Volcanol. Geotherm. Res.* 327, 152–179. doi:10.1016/j.jvolgeores.2016.07.006

Coombs, M. L., and Jicha, B. R. (2020). The eruptive history, magmatic evolution, and influence of glacial ice at long-lived Akutan volcano, eastern Aleutian Islands, Alaska, USA. *Geol. Soc. Amer. Bull.* 133, 963–991. doi:10.1130/B35667.1

Davidson, J., and de Silva, S. (2000). "Composite volcanoes," in *Encyclopedia of volcanoes*. Editor H. Sigurdsson (London: Academic Press), 663–682.

Eaves, S. R., Mackintosh, A. N., Anderson, B. M., Doughty, A. M., Townsend, D. B., Conway, C. E., et al. (2016). The last glacial Maximum in the central north island, New Zealand: Palaeoclimate inferences from glacier modelling. *Clim. Past.* 12, 943–960. doi:10.5194/cp-12-943-2016

Edwards, B. R., Karson, J., Wysocki, R., Lev, E., Bindeman, I., and Kueppers, U. (2013). Insights on lava–ice/snow interactions from large-scale basaltic melt experiments. *Geology* 41, 851–854. doi:10.1130/G34305.1

Edwards, B. R., Belousov, A., Belousova, M., and Melniko, D. (2015). Observations on lava, snowpack and their interactions during the 2012–13 Tolbachik eruption, Klyuchevskoy Group, Kamchatka, Russia. *J. Volcanol. Geotherm. Res.* 307, 107–119. doi:10.1016/j.jvolgeores.2015.08.010

Edwards, B. R., Kochtitzky, W., and Battersby, S. (2020). Global mapping of future glaciovolcanism. *Glob. Planet. Change* 195, 103356. doi:10.1016/j.gloplacha.2020.103356

Fiertsein, J., Hildreth, W., and Calvert, A. T. (2011). Eruptive history of South sister, Oregon cascades. *J. Volcanol. Geotherm. Res.* 207, 145–179. doi:10.1016/j.jvolgeores.2011.06.003

Galland, O., Cobbold, P. R., Hallot, E., de Bremond d'Ars, J., and Delavaud, G. (2006). Use of vegetable oil and silica powder for scale modelling of magmatic intrusion in a deforming brittle crust. *Earth Planet. Sci. Lett.* 3, 786–804. doi:10.1016/j.epsl.2006.01.014

Goñi, M. F. S., Ferretti, P., Polanco-Martínez, J. M., Rodrigues, T., Alonso-García, M., Rodríguez-Tovar, F. J., et al. (2019). Pronounced northward shift of the westerlies during MIS 17 leading to the strong 100-kyr ice age cycles. *Earth Plan. Sci. Lett.* 511, 117–129. doi:10.1016/j.epsl.2019.01.032

Hake, R. R. (1998). Interactive-engagement versus traditional methods: A six-thousand-student survey of mechanics test data for introductory physics courses. *Amer. J. Phys.* 66, 64–74. doi:10.1119/1.18809

Hayashi, S. (2006). The world's most delicious book on volcanoes: Eruption experiments using chocolate and cocoa powder. *Komine Shoten* 127. (in Japanese). ISBN-13:978-4338186087.

Hobden, B. J., Houghton, B. F., Lanphere, M. A., and Nairn, I. A. (1996). Growth of the tongariro volcanic complex: New evidence from K-Ar age determinations. *New zeal. J. Geol. geophys.* 39, 151–154. doi:10.1080/00288306.1996.9514701

Ichihara, M. (2023). Understanding the flow-to-fracture transition of volcanic fluids through analogy experiments. *Sci. Assembly Int. Assoc. Volcanol. Chem. Earth's Interior*. Abstract number 1489.

Kataoka, K. S., Tsunematsu, K., Matsumoto, T., Urabe, A., and Kawashima, K. (2021). Crisis hazard assessment for snow-related lahars from an unforeseen new vent eruption: The 2018 eruption of kusatsu-shirane volcano, Japan. *Earth Planets Space* 73 (220), 220. doi:10.1186/s40623-021-01522-0

Kelman, M. C., Russell, J. K., and Hickson, C. J. (2002). Effusive intermediate glaciovolcanism in the garibaldi volcanic belt, southwestern British Columbia, Canada. *Chapman. Geol. Soc. Lond. Spec. Pub* 202, 195–211. Volcano-ice interaction on Earth and Mars. Edited by J. L. Smellie and M. G. doi:10.1144/GSL.SP.2002.202.01.10

Lachowycz, S. M., Pyle, D. M., Gilbert, J. S., Mather, T. A., Mee, K., Naranjo, J. A., et al. (2015). Glaciovolcanism at volcán sollipulli, southern Chile: Lithofacies analysis and interpretation. *J. Volcanol. Geotherm. Res.* 303, 59–78. doi:10.1016/j.jvolgeores.2015.06.021

Lescinsky, D. T., and Fink, J. H. (2000). Lava and ice interaction at stratovolcanoes: Use of characteristic features to determine past glacial extents and future volcanic hazards. *J. Geophys. Res. Sol. Earth* 105, 23711–23726. doi:10.1029/2000JB900214

Lescinsky, D. T., and Sisson, T. W. (1998)., 26. Washington, 351–354. doi:10.1130/0091-7613(1998)026<0351:RFIBLF>2.3.CO;2Ridge-forming, ice-bounded lava flows at Mount Rainier, Washington*Geology*

Lodge, R. W. D., and Lescinsky, D. T. (2009). Fracture patterns at lava–ice contacts on Kokostick Butte, OR, and Mazama Ridge, Mount Rainier, WA: Implications for flow emplacement and cooling histories. *J. Volcanol. Geotherm. Res.* 185, 298–310. doi:10.1016/j.jvolgeores.2008.10.010

Loewen, M. W., Dietterich, H. R., Graham, N., and Izbekov, P. (2021). Evolution in eruptive style of the 2018 eruption of Veniaminof volcano, Alaska, reflected in groundmass textures and remote sensing. *Bull. Volcanol.* 83 (72), 72. doi:10.1007/s00445-021-01489-6

Maclennan, J., Jull, M., McKenzie, D., Slater, L., and Grönvold, K. (2002). The link between volcanism and deglaciation in Iceland. *Geochem. Geophys. Geosyst.* 3, 1–25. doi:10.1029/2001GC000282

Maruya, Y. (2022). The adventures of pumice. *Ishida Bookbind.*, 40. pages (in Japanese).

Mathews, W. H. (1952). Ice-dammed lavas from clinker mountain, southwestern British Columbia. *Amer. J. Sci.* 250, 553–565. doi:10.2475/ajs.250.8.553

Mee, K., Gilbert, J. S., McGarvie, D. W., Naranjo, J. A., and Pringle, M. S. (2009). Palaeoenvironment reconstruction, volcanic evolution and geochronology of the Cerro Blanco subcomplex, Nevados de Chillán volcanic complex, central Chile. *Bull. Volcanol.* 71, 933–952. doi:10.1007/s00445-009-0277-7

Mixon, E. E., Singer, B. S., Jicha, B. R., and Ramirez, A. (2021). Calbuco, a monotonous andesitic high-flux volcano in the Southern Andes, Chile. *J. Volcanol. Geotherm. Res.* 416, 107279. doi:10.1016/j.jvolgeores.2021.107279

Pierson, T. C., Janda, R. J., Thouret, J.-C., and Borrero, C. A. (1990). Perturbation and melting of snow and ice by the 13 November 1985 eruption of Nevado del Ruiz, Colombia, and consequent mobilization, flow and deposition of lahars. *J. Volcanol. Geotherm. Res.* 41, 17–66. doi:10.1016/0377-0273(90)90082-Q

Pure, L. R., Leonard, G. S., Townsend, D. B., Wilson, C. J. N., Calvert, A. T., Cole, R. P., et al. (2020). A high resolution ^{40}Ar/^{39}Ar lava chronology and edifice construction history for Tongariro volcano, New Zealand. *J. Volcanol. Geotherm. Res.* 403, 106993. doi:10.1016/j.jvolgeores.2020.106993

Rawson, H., Pyle, D. M., Mather, T. A., Smith, V. C., Fontijn, K., Lachowycz, S. M., et al. (2016). The magmatic and eruptive response of arc volcanoes to deglaciation: Insights from southern Chile. *Geology* 44, 251–254. doi:10.1130/G37504.1

Roberti, G., Ward, B., van Wyk de Vries, B., Friele, P., Perotti, L., Clague, J. J., et al. (2018). Precursory slope distress prior to the 2010 Mount Meager landslide, British Columbia. *Landslides* 15, 637–647. doi:10.1007/s10346-017-0901-0

Rust, A., Cashman, K., and Wright, H. (2008). Fudge factors in lessons on crystallization, rheology and morphology of basalt lava flows. *J. Geosci. Educ.* 56, 73–80. doi:10.5408/1089-9995-56.1.73

Singer, B. S., Thompson, R. A., Dungan, M. A., Feeley, T. C., Nelson, S. T., Pickens, J. C., et al. (1997). Volcanism and erosion during the past 930 k.y. at the Tatara–San Pedro complex, Chilean Andes. *Geol. Soc. Bull. Amer.* 109, 127–142. doi:10.1130/0016-7606(1997)109<0127:VAEDTP>2.3.CO;2

Smellie, J. L. (2022). "Sedimentation associated with glaciovolcanism: A review. Volcanic processes in the sedimentary record: When volcanoes meet the environment, *Geol. Soc. Lond. Spec. Pub*, 520, 1–43. doi:10.1144/SP520-2021-135

Smellie, J. L. (2006). The relative importance of supraglacial versus subglacial meltwater escape in basaltic subglacial tuya eruptions: An important unresolved conundrum. *Earth-Sci. Rev.* 74, 241–268. doi:10.1016/j.earscirev.2005.09.004

Spörli, K. B., and Rowland, J. V. (2006). 'Column on column' structures as indicators of lava/ice interaction, Ruapehu andesite volcano, New Zealand. *J. Volcanol. Geotherm. Res.* 157, 294–310. doi:10.1016/j.jvolgeores.2006.04.004

Tierney, J. E., Zhu, J., King, J., Malevich, S. B., Hakim, G. J., and Poulsen, C. J. (2020). Glacial cooling and climate sensitivity revisited. *Nature* 584, 569–573. doi:10.1038/s41586-020-2617-x

Tuffen, H. (2010). How will melting of ice affect volcanic hazards in the twenty-first century? *Phil. Trans. Roy. Soc. A* 368, 2535–2558. doi:10.1098/rsta.2010.0063

Uesawa, S. (2014). A study of the Taisho lahar generated by the 1926 eruption of Tokachidake Volcano, central Hokkaido, Japan, and implications for the generation of cohesive lahars. *J. Volcanol. Geotherm. Res.* 270, 23–34. doi:10.1016/j.jvolgeores.2013.11.002

Vargo, L. J., Anderson, B. M., Dadíc, R., Horgan, H. J., Mackintosh, A. N., King, A. D., et al. (2020). Anthropogenic warming forces extreme annual glacier mass loss. *Nat. Clim. Change* 10, 856–861. doi:10.1038/s41558-020-0849-2

Watt, S. F. L., Pyle, D. M., and Mather, T. A. (2013). The volcanic response to deglaciation: Evidence from glaciated arcs and a reassessment of global eruption records. *Earth-Sci. Rev.* 122, 77–102. doi:10.1016/j.earscirev.2013.03.007

Wilson, A. M., Russell, J. K., and Ward, B. C. (2019). Paleo-glacier reconstruction in southwestern British Columbia, Canada: A glaciovolcanic model. *Quat. Sci. Rev.* 218, 178–188. doi:10.1016/j.quascirev.2019.06.024

Wirth, K. R. (2003). Using an M&M® magma chamber to illustrate magmatic differentiation. *Geol. Soc. Amer. Ann. Meet.*, 120–218.

Yamamoto, T., Kudo, T., and Ishizuka, O. (2018). Temporal variations in volumetric magma eruption rates of Quaternary volcanoes in Japan. *Earth Planets Space* 70 (65), 65. doi:10.1186/s40623-018-0849-x

Frontiers | Frontiers in Earth Science

TYPE Original Research
PUBLISHED 07 March 2023
DOI 10.3389/feart.2023.1095135

OPEN ACCESS

EDITED BY
Alison Hollomon Graettinger,
University of Missouri–Kansas City,
United States

REVIEWED BY
James D. L. White,
University of Otago, New Zealand
Chris Conway,
National Institute of Advanced Industrial Science and Technology (AIST), Japan

*CORRESPONDENCE
Meagen Pollock,
✉ mpollock@wooster.edu

SPECIALTY SECTION
This article was submitted to Volcanology,
a section of the journal
Frontiers in Earth Science

RECEIVED 10 November 2022
ACCEPTED 15 February 2023
PUBLISHED 07 March 2023

CITATION
Pollock M, Edwards BR, Judge S, Wallace C, Hiatt A, Perpalaj A, Was E and Hauksdóttir S (2023), The complex construction of a glaciovolcanic ridge with insights from the 2021 Fagradalsfjall Eruption (Iceland).
Front. Earth Sci. 11:1095135.
doi: 10.3389/feart.2023.1095135

The complex construction of a glaciovolcanic ridge with insights from the 2021 Fagradalsfjall Eruption (Iceland)

Meagen Pollock[1]*, Benjamin R. Edwards[2], Shelley Judge[1], Chloe Wallace[1], Alex Hiatt[1], Aleksander Perpalaj[2], Ellie Was[2] and Steinunn Hauksdóttir[3]

[1]Department of Earth Sciences, The College of Wooster, Wooster, OH, United States, [2]Department of Earth Sciences, Dickinson College, Dickinson, PA, United States, [3]ÍSOR, Iceland GeoSurvey, Reykjavik, Iceland

Glaciovolcanic landforms provide global-scale records of paleoenvironmental conditions and yield insights into subglacial eruption processes. Models for the formation of glaciovolcanic ridges, or tindars, are relatively simple, proposing a monogenetic eruption and a fairly uniform stratigraphy with or without a single transition from effusive pillow lavas to explosive fragmental deposits. Others have suggested that tindars are more complicated. To build a more robust model for tindar formation, we conducted a field and geochemical study of Undirhlíðar ridge on the Reykjanes Peninsula in southwestern Iceland. We show that the ridge was built through a complex sequence of eruptive and intrusive events under dynamically changing ice conditions. Quarry walls expose a continuous cross-section of the ridge, revealing multiple pillow and fragmental units. Pillow lava orientations record the emplacement of discrete pillow-dominated lobes and the migration of volcanic activity between eruptive vents. Volatile contents in glassy pillow rinds show repeated pulses of pillow lava emplacement under glaciostatic conditions, with periods of fragmentation caused by depressurization. Variations in major elements, incompatible trace element ratios, and Pb-isotopes demonstrate that the eruption was fed from separate crustal melt reservoirs containing melts from a compositionally heterogeneous mantle source. A shift in mantle source signature of pillow lavas suggests that the primary ridge-building phase was triggered by the injection of magma into the crust. Within the growing edifice, magma was transported through dykes and irregularly shaped intrusions, which are up to 20% by area of exposed stratigraphy sequences. The model for tindar construction should consider the significant role of intrusions in the growth of the ridge, a detail that would be difficult to identify in natural erosional exposures. The 2021–22 eruptions from the adjacent Fagradalsfjall vents allow us to draw parallels between fissure-fed eruptions in subaerial and ice-confined environments and test hypotheses about the composition of the mantle underlying the Reykjanes Peninsula. Both Fagradalsfjall and Undirhlíðar ridge eruptions may have occurred over similar spatial and temporal scales, been triggered by mixing events, erupted lavas with varying mantle source signatures, and focused volcanic activity along migrating vents. Differences in composition between the two locations are not related to systematic lateral variations in the underlying mantle. Rather, the Undirhlíðar ridge and Fagradalsfjall eruptions capture complex interactions among the crustal magma plumbing system, mantle source heterogeneity, and melting conditions for a moment in time.

KEYWORDS

glaciovolcanism, Iceland, Fagradalsfjall, geochemistry, volcano-ice interaction

1 Introduction

Glaciovolcanism creates global-scale records of paleoenvironmental conditions (Smellie and Edwards, 2016; Smellie, 2018) and magmatic-climatic system interactions. Dramatic glaciovolcanic eruptions in Iceland (Gjálp in 1996 and Eyjafjallajökull in 2010) have driven research on glaciovolcanism over the past 2 decades (Smellie and Edwards, 2016), yielding first-hand observations of the effects of the cryosphere on volcanic products (Edwards et al., 2022). Those products are used in paleoclimate studies to constrain the extent and thickness of past glaciers and ice sheets on Earth (e.g., Lescinsky and Fink, 2000; Smellie, 2008; Tuffen et al., 2010; Edwards et al., 2011) and on Mars (cf. Smellie and Edwards, 2016), and they provide critical insights into subglacial eruption dynamics, with implications for understanding flash flooding caused by rapid ice-melt (jökulhlaups) and other hazards related to volcano-ice interaction (Gudmundsson et al., 2008; Oddsson et al., 2016).

While globally significant, the details of glaciovolcanic eruptive processes are obscured by limited accessibility during active eruptions (Gudmundsson et al., 1997; Gudmundsson et al., 2004; Gudmundsson et al., 2012; Gudmundsson, 2005; Edwards et al., 2012; Oddsson et al., 2016). Much of our understanding derives from the parts of the eruption that break through the ice or from glaciovolcanic landforms that have been exposed by Holocene ice retreat, especially in Antarctica, Canada, and Iceland (e.g., Jones, 1969; Jones, 1970; Höskuldsson et al., 2006; Smellie et al., 2008; Edwards et al., 2009; Edwards et al., 2020). Even these insights are limited by the variability of erosion processes, which frequently provide limited views into edifice interiors and effectively restrict access to stratigraphic information.

Tindars are elongate glaciovolcanic ridges not capped by flat-lying lava flows (Jones, 1969; Smellie, 2007; Smellie, 2013; Jakobsson and Gudmundsson, 2008). Analogous to linear tuyas of Russell et al. (2014), tindars have a length to width ratio greater than 2:1 and consist of some combination of pillow lavas and tephra, depending on magmatic and ice conditions (Jakobsson and Gudmundsson, 2008; Russell et al., 2014). Most tindar formation models propose a monogenetic eruption under ice, with an initial pillow-building phase followed by a transition to explosive volcanic activity as water depth decreases (e.g., Jakobsson and Johnson, 2012). However, the complexity of pillow-dominated tindars has been demonstrated by detailed investigations of edifices that have been deeply dissected by erosion or other processes, such as mining (Jones, 1969; Jones, 1970; Höskuldsson et al., 2006; Edwards et al., 2009; Hungerford et al., 2014; Pollock et al., 2014). Lithofacies variations have been attributed to changes in lava effusion rate, shifts in the magma source region, and fluctuating lake levels caused by ice melt and the development of drainage systems (Moore et al., 1995; Höskuldsson et al., 2006; Edwards et al., 2009; Hungerford et al., 2014; Pollock et al., 2014; Oddsson et al., 2016). Some complex pillow-dominated tindars show sustained hydrostatic conditions and short-lived (e.g., weeks to months) eruptive activity (Hungerford et al., 2014; Wilson and Russell, 2017), yet others are constructed by repeated eruptive events over longer time scales (e.g., years to decades) (Edwards et al., 2009; Pollock et al., 2014). Edifice architecture can be further complicated by the migration of the eruptive vent during ridge formation and the emplacement of subglacial lava flows in ice tunnels (Hungerford et al., 2014; Oddsson et al., 2016).

To better understand the construction of pillow-dominated tindars, we conducted a comprehensive lithostratigraphic and geochemical study of Undirhlíðar ridge in southwestern Iceland. Quarries along the ridge provide exceptional views of the internal tindar architecture. Recent effusive activity at Fagradalsfjall, which is located adjacent to Undirhlíðar ridge, has provided a modern subaerial analogue for fissure eruptions in the region. Our results include maps of lateral and vertical stratigraphic variations, measurements of individual pillow lava orientations, geochemical (major, trace, volatiles, limited isotopes) characterization of all mappable lithologies, and models of magma evolution and paleo-ice conditions. We describe the formation of Undirhlíðar from magma source to volcanic edifice, exploring the complex relationships among paleo-ice conditions, the underlying magmatic system, and eruptive dynamics. Our findings reveal the emplacement mechanisms for a growing pillow lava pile and the effects of magmatic processes on the composition of the resulting edifice. We compare our model to the 2021–22 activity at nearby Fagradalsfjall, drawing new contrasts and parallels between fissure-fed eruptions in subaerial and ice-confined environments. Our work presents one of the most comprehensive geochemical and physical investigations of a single pillow-dominated tindar to date.

2 Geologic setting

The Reykjanes Peninsula in southwestern Iceland links the submarine Reykjanes Ridge to Iceland's Western Volcanic Zone through five en echelon NE-SW trending volcanic systems (Figure 1; Jakobsson et al., 1978; Saemundsson, 1979; Sæmundsson et al., 2020). The volcanic systems are delineated by geophysical patterns and structural features that show elongated swarms of dykes, fissures, faults, and craters that extend from central zones of magma upwelling and storage (Sæmundsson et al., 2020). Holocene volcanic activity has generally migrated from east to west across the volcanic systems, occurring periodically every ~800–1,000 years (Sæmundsson et al., 2020). Eruptions along the volcanic systems during the last glacial maximum (26.5–19 ka Late Weichselian glaciation; Patton et al., 2017) produced NE-trending glaciovolcanic tindar ridges that stand out in relief among younger, post-glacial lava flows (<15 ka) emplaced in ice-free environments (Figure 1). Our study area is at the northern end of the Krýsuvík system.

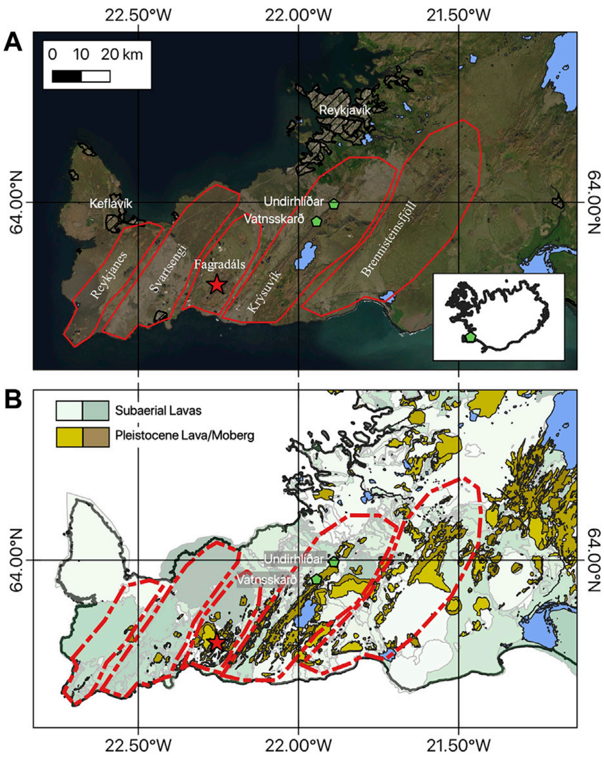

FIGURE 1
Location of field area. **(A)** Satellite image (ESRI Satellite plugin for QGIS) showing relevant parts of the Reykjanes Peninsula, including the 5 main fissures zones (Sæmundsson et al., 2020), the Fagradals eruption site, and the two quarries that bound the field area. **(B)** Same map elements as **(A)** but using geological mapping from ÍSOR to highlight glaciovolcanic (brown shades) versus subaerial units.

After ~800 years of volcanic inactivity on the Reykjanes Peninsula (Sæmundsson et al., 2020), eruptions recently occurred at Fagradalsfjall, which is immediately west of and adjacent to Krýsuvík. In February 2021, elevated seismicity and ground surface deformation suggested the migration of magma and magmatic fluids in the subsurface (Cubuk-Sabuncu et al., 2021; Geirsson et al., 2021; Flóvenz et al., 2022; Sigmundsson et al., 2022). Intense earthquake swarms and changes in ground deformation patterns indicated the intrusion of a NE-SW-trending vertical segmented dyke with sustained magma inflow (Sigmundsson et al., 2022). On 19 March 2021, a fissure eruption began as an effusive outpouring of basaltic lava from closely-spaced vents (Bindeman et al., 2022; Halldórsson et al., 2022). After about a month of activity, five additional vents opened along a 1 km-long segment extending to the northeast (Bindeman et al., 2022; Pedersen et al., 2022). During this first eruptive phase, effusion rates were low to moderate (Pedersen et al., 2022) and periodic fire fountaining from multiple vents built spatter cones and fed lava flows (Bindeman et al., 2022; Halldórsson et al., 2022). After about 3 months of activity, the eruption focused to one vent and effusion rates increased with more intense fire fountaining (Halldórsson et al., 2022; Pedersen et al., 2022). The expansion of the lava field was constrained by the topography of the surrounding ridges. Lava flows filled valleys by inflation and successive emplacement of later flows, then spilled into adjacent valleys (Pedersen et al., 2022). The eruption entered its final phase in September, forming a lava pond that partially drained before the eruption ceased on 18 September 2021 (Pedersen et al., 2022). On 3 August 2022, a second short-lived eruption began in Meradalir about 1 km northeast of the 2021 main eruptive vent (Global Volcanism Program, 2022a). This eruption was preceded by a pattern of increased seismicity and ground deformation similar to the previous eruption (Global Volcanism Program, 2022c). Lasting about 2 weeks, this eruption began as weak lava fountaining along a fissure, followed by a decrease in lava effusion rate and the development of a central cone that contained a lava pond and fed lava flows to the surrounding Meradalir valley (Global Volcanism Program, 2022b).

Krýsuvík, the volcanic system of which Undirhlíðar ridge is the northernmost section, is distinct among the volcanic systems on the Reykjanes Peninsula (Figure 1). It is the only volcanic system to host a buried caldera, identified by circular geophysical anomalies at depth and the remnant at Lake Kleifarvatn (Eysteinsson, 2001; Hersir et al., 2020; Sæmundsson et al., 2020). The ancient central volcano may have been rooted by an intrusive complex, evidenced by layered gabbroic xenoliths in volcanic ejecta and the eruption of evolved tholeiitic basalts (Jónsson, 1978; Sæmundsson et al., 2020). The Krýsuvík geothermal area, in the southern part of the system, covers ~60 km^2 and is bound by two NE-SW trending tindar complexes, Núphlíðarháls-Vesturháls to the west and Sveifluháls to the east (Hersir et al., 2020). Along strike with Sveifluháls to the northeast is Undirhlíðar ridge, an early Weischelian (118–80 kyr; Lambeck et al., 2006; Sæmundsson et al., 2016) pillow-dominated tindar. Undirhlíðar ridge is ~7 km long and has been excavated at its northern extent in Undirhlíðar and Vatnsskarð quarries, which are separated by ~3 km and have walls ~100 m high, exposing both longitudinal and across-axis cross sections of the ridge.

In a previous paper (Pollock et al., 2014), we presented the lithostratigraphic and compositional variations exposed in Undirhlíðar quarry. We proposed a model for the construction of the northern part of Undirhlíðar ridge that comprises at least three eruptive phases ranging in style from explosive to effusive (Figure 10 in Pollock et al., 2014). The pillow lava units comprising the core of the ridge were formed in an initial effusive phase that erupted magma from an incompatible element-enriched mantle source. This was followed by intrusions of a less-enriched magma and a second effusive phase that began with an explosive event. Because the first and second eruptive phases were fed by magmas from slightly different mantle sources, we hypothesized that magma resided in discrete melt bodies that experienced separate evolutionary histories, consistent with evidence for a local intrusive complex and the sheeted sill model for volcanic systems (Gee et al., 1998; Maclennan et al., 2003; Eason and Sinton, 2009; Peate et al., 2009). Lithologically, the boundary between the first and second eruptive phases is marked with deposits of vitric tuff-breccia, interpreted as products of subaqueous fire-fountaining, suggesting that pillow-forming eruptions may have been initiated by mild explosive activity. A final effusive phase produced a capping layer of pillow lavas that are geochemically related to the pillow lavas from the preceding effusive phase. While intrusions were also documented in this study, their importance to the overall ridge formation was not as well understood.

The Undirhlíðar study modified the existing model for subglacial pillow-forming eruptions (Jones, 1969; Jones, 1970; Moore et al., 1995; Höskuldsson et al., 2006) by documenting multiple episodes of pillow lava emplacement and transitions in eruptive style that coincided with shifts in the underlying magmatic system. Here, we examine whether the model applies to the rest of the ridge by extending our work to Vatnsskarð quarry and the ~3 km length of the ridge between the quarries. Along the ridge, water-carved gullies offer ~100 m high exposures of fragmental volcanic material, intrusions, pillow lavas, and glacial diamict. Vatnsskarð quarry is ~750 m long and exposes ~80 m high walls that show several distinct pillow lava units, volcaniclastic units, and intrusions. Where Undirhlíðar quarry revealed glaciovolcanic processes at the margins of a tindar ridge, Vatnsskarð quarry provides insights into glaciovolcanic processes nearer to the center of magma upwelling and storage within a volcanic system. Since our original model at Undirhlíðar in 2014, the adjacent Fagradalsfjall volcanic system erupted in 2021–22, allowing us to draw parallels and observe contrasts between fissure eruptions in subaerial and ice-confined environments.

3 Materials and methods

3.1 Field mapping and sample collection

Field mapping at the quarries and along the ridge that connects them has been ongoing since 2009. We sampled and made measurements at a variety of scales. We measured >100 individual pillow lava sizes and orientations using meter tape measures and Brunton compasses with clinometers. Trend and plunge data of pillow basalts for each locality were plotted using Stereonet (v. 11.4.5 Allmendinger et al., 2013; Cardozo and Allmendinger, 2013). Data were contoured using the Kamb contouring method. The average trend and plunge direction for pillows at each locality was calculated based on the center of the contoured pi-maxima. Data from localities close to each other were compared; if averages were similar, then the data were merged into one plot that represented a larger area.

A variety of approaches have been used to map vertical faces in the quarries, including laser range-finding, Gigapan technology, Structure-from-Motion, and drones. Sample and data collection sites were located using standard handheld GPS units, which are generally considered to have non-corrected positional errors of ± 5 m or less. For samples where accurate elevations are critical, we used the Arctic DEM subsampled to 1.8 m resolution to subsequently correct sample elevations to a consistent elevation model.

We note here that quarries, while providing unparalleled exposures and access to fresh samples, can have inherent disadvantages. For example, our field observations are largely centered on pillow lava units, which now dominate the stratigraphy at both quarries. It is possible that the unconsolidated tuff-breccia units originally occupied a larger proportion of the quarries but have been preferentially removed due to ease of mining.

3.2 Major and trace element analyses

Major and trace elements were measured on a total of 89 whole-rock samples, including 6 bombs from fragmental units, 57 pillow lavas, and 26 intrusions (Table 1; Supplementary Table SA1). Whole-rock powders from fresh samples were prepared in alumina grinding containers and sieved through 325 mesh. Loss on ignition (LOI) was determined by heating the powders for 1 h at 950°C following Boyd and Mertzman (1987). Most samples were analyzed for major elements by X-ray fluorescence spectroscopy (XRF; 86 samples) at the College of Wooster following the methods of Pollock et al. (2014). The XRF was drift corrected prior to each run and repeat analyses of standards shows reproducibility <2%. Most trace elements were measured by inductively coupled plasma mass spectrometry (ICP-MS; 71 samples) at the Peter Hooper Lab, Washington State University, United States following standard methods (Lichte et al., 1987; Jarvis, 1988; Doherty, 1989; Jenner et al., 1990; Longerich et al., 1990). Analytical runs consisted of unknowns, standards, and drift correction solutions. Reproducibility is <5% for rare Earth elements and <10% for all other elements. Full analytical precision and accuracy details for XRF and ICP-MS analyses are provided in the Supplementary Tables SA2–SA4). A few samples (3) were analyzed at Duke University by directly coupled plasma atomic emission spectroscopy (DCP-AES) and ICP-MS following the methods of Klein et al. (1991); Cheatham et al. (1993), respectively. DCP-AES analyses show reproducibility of 1%–2% for all major elements with the exception of K_2O (~10%) and P_2O_5 (< 8%). ICP-MS analyses at Duke show reproducibility of 1%–5% for trace elements. Full quality assurance data for the Duke analyses are provided in the Supplementary Material to Pollock et al. (2014). Interlab comparison of duplicate samples analyzed by ICP-MS at Duke and Washington State Universities shows good agreement between methods (Supplementary Table SA5).

3.3 Sr-Nd-Pb isotope analyses

Sr-Nd-Pb isotope ratios were measured on seven whole-rock powders from Undirhlíðar and Vatnsskarð quarries by thermal ionization mass spectrometry (TIMS) at the University of North Carolina at Chapel Hill (Table 2). Samples were dissolved and cations were separated following the methods of (Miller and Glazner, 1995). Measurements were made on a VG Sector 54 mass spectrometer. Sr isotopes are referenced to $^{87}Sr/^{86}Sr$ = 0.710231 ± 9 (NBS 987, n = 9). Nd isotopes are referenced to $^{146}Nd/^{144}Nd$ = 0.512102 ± 10 (JNdi, n = 20).

3.4 Volatile analyses

Volatiles (H_2O and CO_2) were measured on pristine glassy rims from 38 pillow lavas. In Undirhlíðar quarry, seven samples were collected from a cluster of adjacent pillows, four of which were collected from a single pillow (Table 3). For most samples, three glass chips were selected for analysis. Glass chips ranged in size from <1 mm to 7 mm in diameter and were chosen to avoid significant weathering, alteration, phenocrysts, and vesicles. Chips

TABLE 1 Geochemistry of selected Undirhlíðar ridge samples. Major elements (in wt. %) and select trace elements (bold) measured by XRF. All other trace elements measured by ICP-MS. Details of analytical methods are described in the text. All samples are whole-rock pillow lavas except 16MP03 (dyke). Location describes sample sites in Undirhlíðar quarry (UND), Vatnsskarð quarry (VAT), or along the ridge between the quarries. Compositional group defined by La_N/Sm_N value as described in the text. The full geochemical dataset and quality data are available in the (Supplementary Material).

Sample ID	16CW08	16MP02	VAT-NA-13-09	VAT-SA-13-19	VAT-SA-13-07	16RH02	16MP03
Location	Ridge	UND	VAT	VAT	VAT	Ridge	Ridge
Compositional group	More-enriched	Less-enriched	Less-enriched	Less-enriched	Mixed	Mixed	Mixed
Major Elements (wt.%)							
SiO_2	49.08	47.76	47.74	48.14	47.95	49.01	49.25
TiO_2	1.74	1.49	1.82	1.72	1.59	1.85	2.01
Al_2O_3	15.30	16.54	15.34	15.60	15.96	15.10	14.48
FeO*	11.76	10.94	12.16	11.98	11.67	12.71	13.15
MnO	0.20	0.18	0.20	0.20	0.19	0.21	0.22
MgO	7.38	8.88	8.35	8.10	8.65	7.16	6.96
CaO	11.79	11.83	11.88	11.71	11.50	11.12	11.21
Na_2O	2.32	2.11	2.17	2.22	2.19	2.38	2.23
K_2O	0.25	0.12	0.16	0.17	0.16	0.26	0.28
P_2O_5	0.19	0.13	0.17	0.15	0.14	0.19	0.21
Sum	100.00	100.00	99.99	100.00	99.99	100.00	100.00
LOI	—	—	0.43	0.32	0.47	—	—
Trace Elements (ppm)							
Sc	41.4	35.7	41.1	40.4	41.2	40.8	42.7
V	**342**	**297**	**308**	**325**	**315**	**373**	**394**
Cr	**130**	**373**	**368**	**279**	**270**	**251**	**160**
Ni	**82**	**162**	**120**	**136**	**109**	**94**	**74**
Cu	**135**	**146**	**126**	**132**	**133**	**142**	**179**
Zn	**93**	**87**	—	—	—	**104**	**107**
Rb	4.0	1.5	2.4	2.8	4.0	4.7	5.3
Sr	205	217	211	209	203	175	168
Y	24.77	20.76	24.68	24.38	25.14	28.58	30.76
Zr	94	68	83	79	89	99	107
Nb	12.95	8.22	**12**	**10**	**10**	12.56	13.51
Cs	0.05	0.03	0.03	0.03	0.05	0.05	0.07
Ba	72	37	47	48	63	71	75
La	9.38	6.08	7.47	7.06	8.58	9.38	10.03
Ce	21.89	15.01	18.41	17.29	20.55	22.22	23.88
Pr	3.07	2.22	2.70	2.56	2.95	3.21	3.41
Nd	13.97	10.51	12.85	12.35	13.71	14.54	15.79
Sm	3.86	3.11	3.75	3.60	3.84	4.18	4.49
Eu	1.44	1.21	1.38	1.36	1.46	1.55	1.62
Tb	0.79	0.63	0.77	0.76	0.78	0.88	0.93
Gd	4.46	3.67	4.44	4.29	4.56	4.92	5.33
Dy	5.01	4.04	4.81	4.77	4.92	5.53	5.89
Ho	1.01	0.84	1.00	0.98	1.02	1.16	1.22
Er	2.69	2.23	2.64	2.68	2.78	3.15	3.32
Tm	0.39	0.32	0.38	0.39	0.40	0.45	0.49
Yb	2.36	1.95	2.27	2.34	2.40	2.83	3.01
Lu	0.36	0.30	0.36	0.37	0.38	0.44	0.46
Hf	2.53	1.87	2.27	2.22	2.42	2.69	2.88
Ta	0.80	0.51	0.68	0.67	0.81	0.80	0.85
Pb	0.69	0.46	0.51	0.62	0.73	0.76	0.89
Th	0.67	0.25	0.40	0.42	0.58	0.66	0.71
U	0.21	0.08	0.13	0.13	0.17	0.20	0.22

were doubly polished into 100–200 micron-thick wafers. Thickness of each glass wafer was measured three times and averaged for each chip for a precision of ± 5 microns. Wafers were analyzed by Fourier Transform Infrared Spectroscopy (FTIR) at the University of Massachusetts Amherst on a Bruker Tensor 27 FTIR with attached Hyperion 3000 microscope. FTIR spectra were obtained

TABLE 2 Radiogenic isotope data for whole-rock samples from Undirhlíðar ridge. Location describes sample site in Undirhlíðar (UND) or Vatnsskarð (VAT) quarries. Compositional group defined by La_N/Sm_N value as described in the text. Major and trace element data for UND samples are reported in Pollock et al., 2014. All samples are pillow lavas except for S-10-21 (dyke). Details of analytical methods are described in the text. Error is 2 σ standard deviation.

Sample ID	Location	Compositional group	$^{206}Pb/^{204}Pb$	2σ	$^{207}Pb/^{204}Pb$	2σ	$^{208}Pb/^{204}Pb$	2σ	$^{208}Pb/^{204}Pb$	2σ	$^{143}Nd/^{144}Nd$	2σ
VAT-NA-13–09	VAT	less-enriched	18.8573	0.0029	15.5294	0.0026	38.4810	0.0067	0.703189	0.000004	0.513022	0.0000041
VAT-SA-13-10	VAT	less-enriched	18.7983	0.0016	15.5092	0.0014	38.3571	0.0039	0.703161	0.000010	0.513025	0.0000062
W-08-01	UND	less-enriched	18.8316	0.0032	15.5181	0.0028	38.4313	0.0076	0.703181	0.000004	0.513025	0.0000051
S-10-23	UND	less-enriched	18.8352	0.0033	15.5241	0.0029	38.4579	0.0070	0.70328	0.000004	0.512999	0.0000041
S-10-21	UND	less-enriched	18.8216	0.0012	15.5105	0.0011	38.4034	0.0031	0.70317	0.000004	0.513026	0.0000041
S-10-25	UND	more-enriched	18.8772	0.0014	15.5075	0.0011	38.4229	0.0026	0.703165	0.000004	0.51302	0.0000092
S-10-04	UND	less-enriched	18.8709	0.0012	15.5122	0.0011	38.4239	0.0027	0.703163	0.000004	0.513034	0.0000072

for a 10 × 10 micron area using OPUS (version 7.2) software. Care was taken to avoid measuring sites adjacent to fractures, vesicles, crystals, and margins. At least three sites were measured for each chip, so each value reported represents the average of 3–12 spectra. Individual FTIR measurements are presented in the (Supplementary Table SA7).

IR peak absorbance at ~3529 cm^{-1} was used to calculate total water (H_2O_t) concentration using the Beer-Lambert Law (Stolper, 1982). Glass density was 2,750 ± 55 g/L, estimated using Bottinga and Weill (1972) and based on average composition of the sample suite. The molar absorption coefficient for H_2O in basalt was 63 ± 3 L/mol-cm (Dixon et al., 1995). Water speciation was not determined for most samples because spectra did not show measurable peaks at the 4,500 cm^{-1} and 5,200 cm^{-1} bands (Mcintosh et al., 2017). For the few samples with peaks detected at 1,630 cm^{-1}, spectra were analyzed using Spectragryph (v.1.2.16.1). Peak absorbance was determined on spectra corrected with adaptive baselines. Molecular water (H_2O_m) concentrations were calculated the Beer-Lambert law and the same parameters described above with a molar absorption coefficient of 25 ± 3 L/mol-cm (Dixon et al., 1995). Uncertainty was estimated by propagating errors through the Beer Lamber Law for sample thickness, density, absorption coefficient, and absorbance based on repeated analyses of the same site. Average precision (1-θ) for H_2O_t concentrations is 10%, which is consistent with previous studies of total water measurements made by FTIR (Dixon and Clague, 2001). Error for H_2O_m concentrations is higher because of additional uncertainty in absorbance intensity measured from adaptive baselines (McIntosh et al., 2022).

Most samples did not show a measurable CO_2 peak at ~2,360 cm^{-1}, and the CO_2 peaks that were observed did not consistently appear in the spectra, even within the same chip. Therefore, CO_2 values are interpreted to be below the lower limit of quantification (20 ppm). The Supplementary Material contains the data for the few CO_2 peaks that were detected. The Beer-Lambert Law was used to calculate the CO_2 concentration using the same parameters described above and a molar absorption coefficient of 945 L/mol-cm for CO_2 (Fine and Stolper, 1985).

After FTIR analysis, 11 glass samples were carbon coated and analyzed for major elements by electron probe microanalysis (EPMA) at the University of Massachusetts Amherst. The Cameca SX 50 microprobe was operated under an acceleration voltage of 15 keV, a beam current of 20 nA, and a spot size of 30 μm. Full compositional data for the glass chips are provided in the (Supplementary Table SA1).

3.5 Geochemical models

The alphaMELTS program (v. 1.9) was used to model crystallization and melting (Smith and Asimow, 2005). Using the MELTS thermodynamic model (Ghiorso and Sack, 1995), liquid lines of descent (LLD) were calculated for isobaric fractional crystallization at 1 kb and 1,200°C with 3°C steps. A primitive aphyric lava was used for the parent magma (VAT-SA-13-07, MgO 8.6 wt.%, La_N/Sm_N 1.44) with the addition of 0.5 wt.% H_2O. Initial Fe_2O_3 was calculated from FeO in alphaMELTS at the FMQ buffer. The same conditions were used to calculate the liquidus phase for two additional parent magma compositions (16MP02 and S-10-18 from Pollock et al., 2014). Using the pMELTS thermodynamic model (Ghiorso et al., 2002), mantle melts were generated through isentropic decompression melting starting at 4 GPa and 1,500°C with 0.01 GPa steps. Melting was continuous with 0.05% residual porosity. Two mantle source compositions were modeled: Depleted MORB mantle (Workman and Hart, 2005) and enriched mantle comprising 95% DMM and 5% pyroxenite from Koornneef et al. (2012). Trace element partition coefficients from McKenzie and O'Nions (1991), McKenzie and O'Nions (1995) remained constant during melting. Melts were aggregated using the 1D aggregation model and extracted at 2.17 GPa for both mantle sources.

VolatileCalc (v. 2.0) was used to calculate volatile saturation pressures (Newman and Lowenstern, 2002). Liquid temperatures were determined with alphaMELTS using glass or whole-rock compositions under the same conditions as the LLD models. Water concentrations were determined by FTIR. Because CO_2 solubility affects H_2O saturation pressures, pressures were

TABLE 3 Water contents, elevations, and saturation pressures of Undirhlíðar ridge samples. Location describes sample sites in Undirhlíðar quarry (UND), Vatnsskarð quarry (VAT), or along the ridge between the quarries. Compositional group defined by La_N/Sm_N value as described in the text. H_2O_t and H_2O_m concentrations (in wt.%) are calculated averages of n number of FTIR spectra. Error is 2 σ standard deviation of uncertainty propagated through the Beer-Lambert Law. n.d. indicates values that were not determined. Elevations (in m) determined from a digital elevation model as described in the text. Ce (in ppm) determined on whole-rock samples. Pressure (in MPa) is H_2O saturation pressure calculated using VolatileCalc (v. 2.0) assuming complete CO_2 degassing (i.e., $CO_2 = 0$ ppm) as described in text. Full compositional data and pressure calculations are available in Supplementary Material. Four samples from the same pillow lava and seven samples from the cluster of adjacent pillows as shown in Figure 11D are indicated with superscripts a and b, respectively.

Sample ID	Location	Compositional group	H_2O_t (wt.%)	2σ	n	H_2O_m (wt.%)	2σ	n	Elevation (m)	H_2O_m/ H_2O_t	Ce (ppm)	H_2O/ Ce	Pressure (MPa)
[a]0613UAH06-gl	UND	more-enriched	0.36	0.06	9	n.d.	—	—	98	—	n.d.	—	1.6
[a]0613UAH07-gl	UND	more-enriched	0.39	0.08	9	n.d.	—	—	98	—	n.d.	—	1.6
[a]0613UAH08-gl	UND	more-enriched	0.35	0.06	6	n.d.	—	—	98	—	n.d.	—	1.4
[a]0613UAH09-gl	UND	more-enriched	0.39	0.04	3	n.d.	—	—	98	—	n.d.	—	1.4
[b]0613UAH01-gl	UND	more-enriched	0.39	0.08	9	n.d.	—	—	98	—	n.d.	—	1.6
[b]0613UAH04-gl	UND	more-enriched	0.4	0.02	3	n.d.	—	—	98	—	n.d.	—	1.3
[b]0613UAH05-gl	UND	more-enriched	0.37	0.08	9	0.05	0.02	2	98	0.14	n.d.	—	1.6
0613UAH11-gl	UND	more-enriched	0.36	0.04	6	n.d.	—	—	103	—	n.d.	—	1.4
0613UAH12-gl	UND	more-enriched	0.38	0.02	3	n.d.	—	—	100	—	n.d.	—	1.5
0613UAH13-gl	UND	less-enriched	0.28	0.06	11	n.d.	—	—	126	—	n.d.	—	0.9
0613UAH15-gl	UND	more-enriched	0.36	0.08	3	n.d.	—	—	143	—	n.d.	—	1.4
0613UAH16-gl	UND	less-enriched	0.24	0.04	9	n.d.	—	—	142	—	n.d.	—	0.7
0613UAH17-gl	UND	more-enriched	0.34	0.04	9	n.d.	—	—	104	—	n.d.	—	1.3
16BRE07	Ridge	less-enriched	0.29	0.02	3	n.d.	—	—	165	—	15.13	192	1.0
16CW01	Ridge	less-enriched	0.28	0.08	8	n.d.	—	—	167	—	14.84	189	0.9
16CW02	Ridge	less-enriched	0.19	0.12	21	n.d.	—	—	145	—	16.13	118	0.4
16CW03	UND	less-enriched	0.16	0.04	9	n.d.	—	—	156	—	n.d.	—	0.3
16CW04	UND	less-enriched	0.22	0.1	12	n.d.	—	—	152	—	18.88	117	0.5
16CW05	UND	less-enriched	0.23	0.1	12	0.02	0.01	3	144	0.09	15.78	146	0.5
16CW07	Ridge	mixed	0.33	0.1	8	n.d.	—	—	183	—	21.95	150	1.2
16CW08	Ridge	more-enriched	0.29	0.08	9	0.03	0.01	2	120	0.10	21.89	132	0.9
16CW09	Ridge	less-enriched	0.23	0.08	12	n.d.	—	—	210	—	17.17	134	0.6
16MP04	VAT	less-enriched	0.16	0.08	10	n.d.	—	—	177	—	15.45	104	0.3
16MP06	VAT	less-enriched	0.22	0.08	12	n.d.	—	—	138	—	16.81	131	0.6
16MP13	Ridge	less-enriched	0.23	0.06	10	n.d.	—	—	163	—	15.75	146	0.6
16MP14	Ridge	less-enriched	0.25	0.12	10	0.04	0.02	5	131	0.16	16.33	153	0.7
VAT-N-09-03	VAT	less-enriched	0.29	0.06	4	n.d.	—	—	136	—	—	—	0.9
VAT-N-09-04	VAT	less-enriched	0.31	0.04	4	n.d.	—	—	148	—	—	—	1.1

(Continued on following page)

TABLE 3 (*Continued*) **Water contents, elevations, and saturation pressures of Undirhlíðar ridge samples. Location describes sample sites in Undirhlíðar quarry (UND), Vatnsskarð quarry (VAT), or along the ridge between the quarries. Compositional group defined by La_N/Sm_N value as described in the text. H_2O_t and H_2O_m concentrations (in wt.%) are calculated averages of n number of FTIR spectra. Error is 2 σ standard deviation of uncertainty propagated through the Beer-Lambert Law. n.d. indicates values that were not determined. Elevations (in m) determined from a digital elevation model as described in the text. Ce (in ppm) determined on whole-rock samples. Pressure (in MPa) is H_2O saturation pressure calculated using VolatileCalc (v. 2.0) assuming complete CO_2 degassing (i.e., CO_2 = 0 ppm) as described in text. Full compositional data and pressure calculations are available in Supplementary Material. Four samples from the same pillow lava and seven samples from the cluster of adjacent pillows as shown in Figure 11D are indicated with superscripts a and b, respectively.**

Sample ID	Location	Compositional group	H_2O_t (wt.%)	2σ	n	H_2O_m (wt.%)	2σ	n	Elevation (m)	H_2O_m/ H_2O_t	Ce (ppm)	H_2O/ Ce	Pressure (MPa)
VAT-NA-13-03	VAT	less-enriched	0.3	0.08	4	n.d.	—	—	183	—	17.22	174	1.0
VAT-NA-13-06	VAT	less-enriched	0.28	0.04	4	n.d.	—	—	140	—	17.64	159	0.9
VAT-NA-13-07	VAT	less-enriched	0.29	0.08	12	n.d.	—	—	140	—	17.25	168	0.9
VAT-NA-13-09	VAT	less-enriched	0.29	0.12	3	n.d.	—	—	228	—	18.41	158	1.0
VAT-NA-13-16	VAT	less-enriched	0.31	0.06	12	n.d.	—	—	204	—	17.66	176	1.1
VAT-SA-13-02	VAT	less-enriched	0.25	0.12	12	n.d.	—	—	146	—	17.05	147	1.2
VAT-SA-13-04	VAT	less-enriched	0.24	0.08	4	0.03	0.01	2	147	0.13	15.56	154	0.7
VAT-SA-13-10	VAT	less-enriched	0.29	0.04	12	n.d.	—	—	140	—	17.29	168	0.9
VAT-SA-13-21	VAT	less-enriched	0.28	0.06	13	n.d.	—	—	139	—	17.86	157	0.9
VAT-SA-13-24	VAT	less-enriched	0.26	0.06	4	n.d.	—	—	132	—	14.25	182	0.8

calculated at 0 ppm and 15 ppm CO_2, representing complete and partial degassing. Full calculation data are provided in the (Supplementary Table SA8).

4 Results

4.1 Lithostratigraphy

We have broken out several different lithofacies, including: 1) Pillow lava, 2) tuff, 3) lapilli tuff, 4) tuff-breccia, 5) dykes, 6) massive, columnar-jointed basaltic intrusions, 7) and diamict (Figures 2, 3). These lithofacies are essentially the same as those described in Pollock et al. (2014), and so are not described in detail here. The most common pillow-dominated units comprise stacked pillow lavas with very little intra-pillow material (Figure 4A). Tuff and lapilli tuff are limited to relatively thin interbeds between pillow units (Figure 4B), although they are more extensive locally on the eastern side of the ridge. Tuff-breccia is present in larger masses (Figures 3, 4C). Since the basic stratigraphy for Undirhliðar quarry was described by Pollock et al. (2014), here we focus on describing Vatnsskarð quarry and the ridge between the quarries.

Undirhliðar ridge is the northern extension of a much larger composite tindar ridge complex that extends for more than 20 km in total length (Figure 1). The northern half of the Undirhliðar segment is dominated by intact pillow lavas and pillow lava rubble (Figure 2C), which is sporadically directly overlain by a tan-brown, variably indurated diamicton interpreted to be of glacial origin. Approximately 1.5 km south of Undirhliðar quarry, the east side of the ridge abruptly shifts from pillow rubble to variably palagonitized lapilli tuff and tuff-breccia. Where they are in contact, the fragmental materials appear to directly overlie pillow lava units; however, the palagonitized tephra deposits are absent from either of the quarries. In several places small dykes (< 1 m thick) cut through the tephra-rich east side deposits and appear to be less common, although still present, in pillow units along the west-central part of the ridge (Figure 2C). Vatnsskarð quarry marks the southern end of the study area, where mining operations as of 2021 have bisected approximately half of the ridge width.

Vatnsskarð quarry, which is still active and expanding, is approximately 1 km long and up to 80 m from the quarry floor to the top of the ridge. Most of the Vatnsskarð quarry walls expose longitudinal sections of the ridge, but the northern end exposes a cross section that is perpendicular to the length of the ridge. We have identified 7 different pillow lava units based on stratigraphy and location, 4 different primary fragmental units (tuff, lapilli tuff, tuff-breccia), and overlying glaciofluvial deposits (tuff-breccia/diamict Figure 3). The north wall is dominated by pillow lavas, and because of their plunge orientations (see below), we have designated these pillows as a distinct unit (LpN; Figure 3).

The walls of Vatnsskarð quarry expose a continuous longitudinal section of the ridge, from the basal contact, through

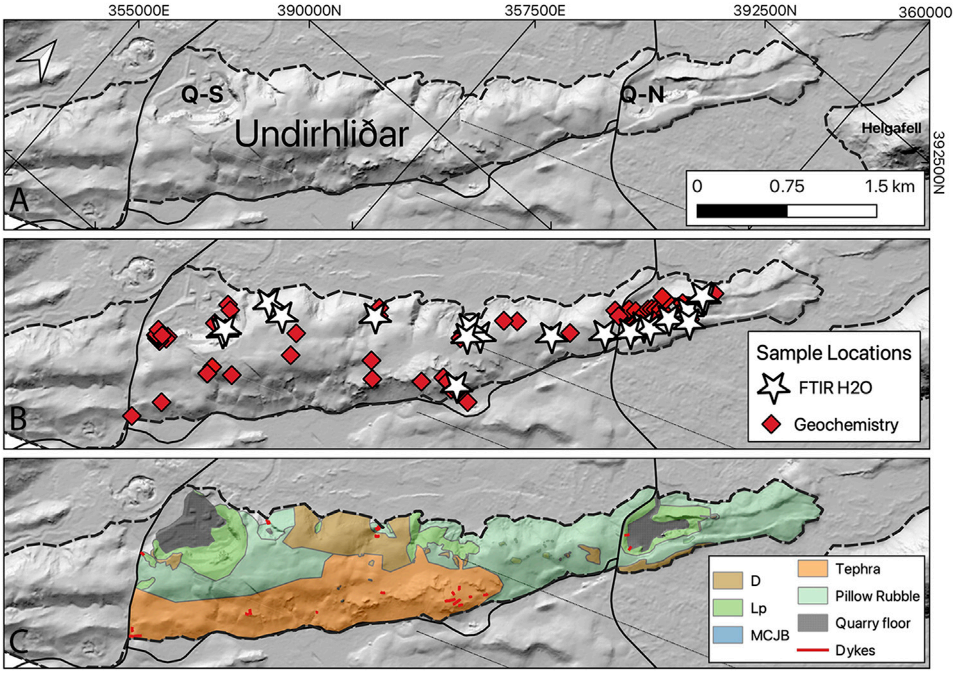

FIGURE 2
Maps showing the morphology, sample locations, and geology of Undirhliðar ridge between Undirhliðar (Q–N) and Vatnsskarð (Q–S) quarries. **(A)** Digital elevation model (DEM) showing the overall ridge morphology; data for the DEM from the ArcticDEM website, sampled at 1.0 m resolution. **(B)** Locations of samples used in this study. **(C)** Geology of the ridge based on new mapping.

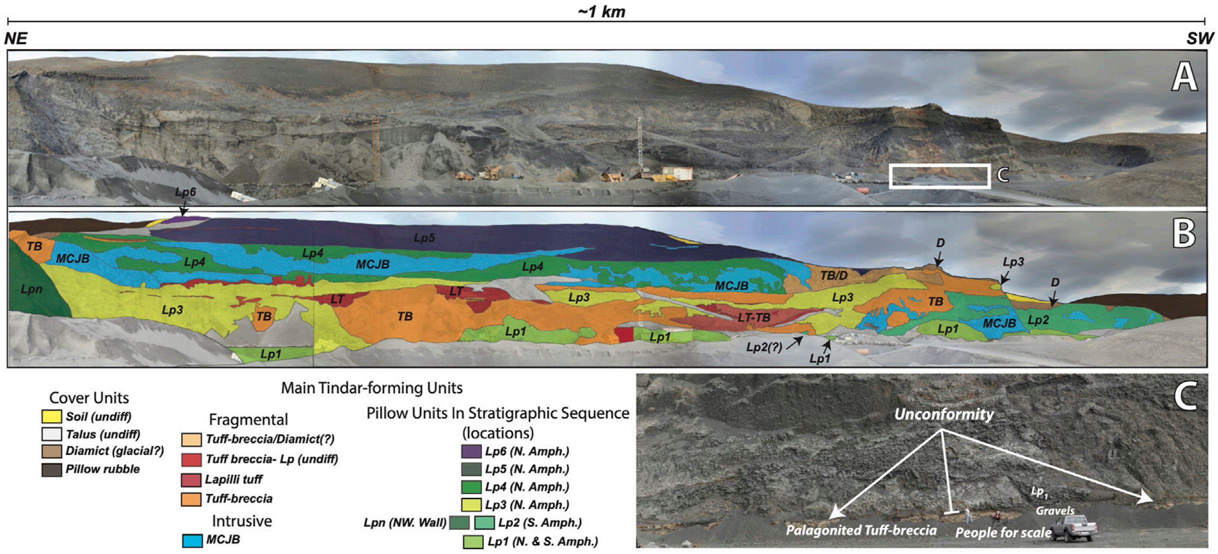

FIGURE 3
Stratigraphy of units at Vatnsskarð quarry. **(A)** Composited image of the quarry with interpreted distribution of units below **(B)**. **(C)** Close-up view of the palagonitized tuff-breccia that forms the bedrock to the ridge and is unconformably overlain by quarry units.

volcanic stratigraphy with multiple pillow and fragmental units, to capping sedimentary units (Figure 3). The basal contact is exposed near the center of the walls, where the lowest pillows (Lp1) appear in lenses that lie unconformably over sedimentary layers of yellow diamict containing cobble-sized clasts of vesicular basalt. The upper contact of the basal pillows lavas (Lp1) is marked by a thin (cm-scale) layer of vitric tuff and a sharp contact with overlying pillows (Lp2). Lp2 comprises the bulk of the central and southern quarry walls. Within the pillows are isolated lenses of lapilli tuff and vitric tuff-breccia that include glassy basaltic bombs. Above Lp2 is a dark

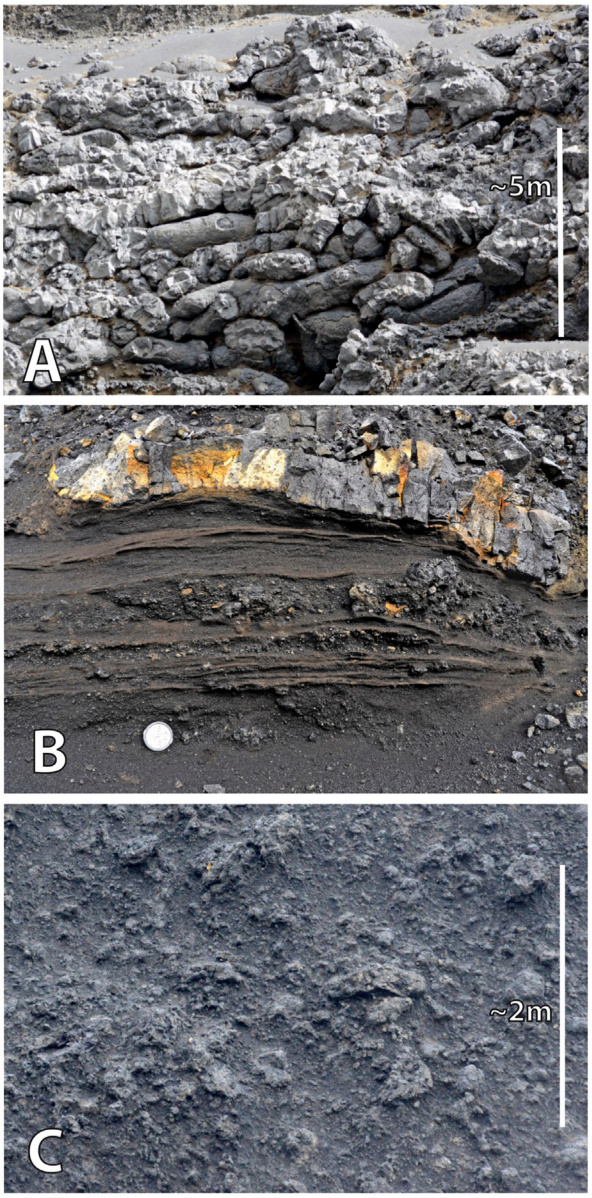

FIGURE 4
Field images of critical lithofacies. **(A)** Shallowly plunging pillow lava tubes from Lp2 in the central wall of Vatnsskarð quarry. View is approximately 30 m across horizontally. **(B)** Thinly laminated beds of tuff and lapilli tuff in the northeastern wall of Vatnsskarð quarry (lens cap for scale). **(C)** View of tuff-breccia unit between Lp2 and Lp3 in the central wall of Vatnsskarð quarry. Largest bombs/pillow fragments are approximately 50 cm in diameter (outcrop was unreachable).

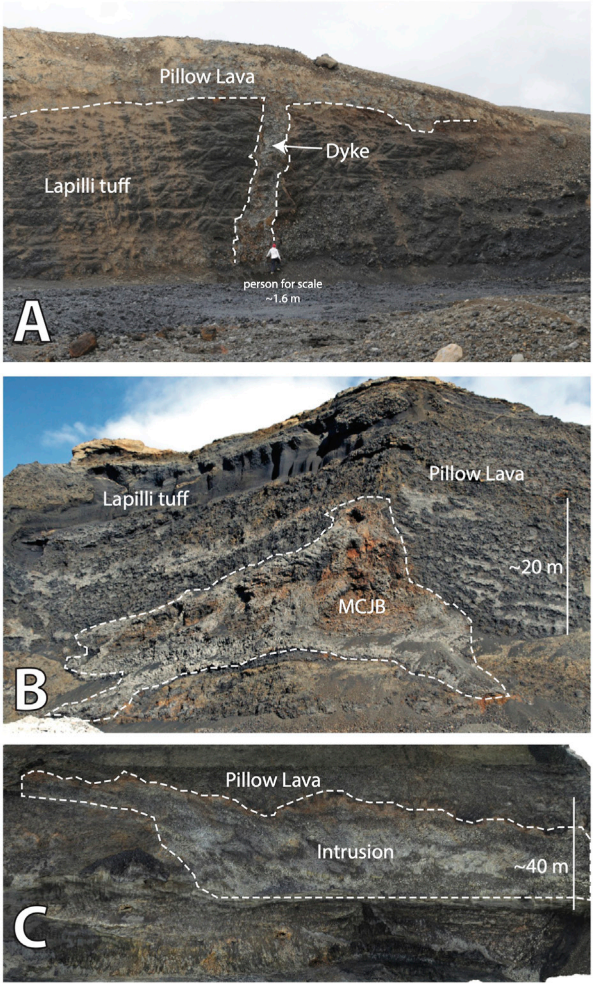

FIGURE 5
Field images showing intrusions. **(A)** Dyke feeding overlying pillow lavas, Undirhliðar quarry. Person for scale. **(B)** Irregular intrusion into pillow lavas, Vatnsskarð quarry. Maximum vertical dimension is 17 m. **(C)** Sill-like intrusion, northern walls, Vatnsskarð quarry. The intrusion is ~300 m long and 38 m tall.

black vitric tuff breccia (TB) that dips downward and thickens to the northeast. This fragmental unit consists of a vitric lapilli tuff (LT) with some highly vesicular glassy fragments that gradually coarsens to bomb-dominated, with glassy bombs that are mostly vesiculated throughout (LT-TB). The TB unit contains lobes of a third pillow unit (Lp3). The upper portion of the Lp3-TB complex is marked by a relatively flat-lying contact with a fourth pillow unit (Lp4) that hosts irregularly shaped intrusions, which are described in detail below. Capping the Lp4-intrusion complex is another pillow unit (Lp5). We lose stratigraphic control above this pillow unit and find one more isolated pillow exposure (Lp6) in a roadcut at the top of the mine. Laterally to the south, the volcanic stratigraphy is capped by a sequence of sedimentary units that lies unconformably over the exposures in the central and southern walls. Most of the sedimentary unit comprises a clast-rich sandy diamict that stands out in relief, containing ~60% gravel-sized fragments and with weathered yellow to red appearance. Cobbles are rounded and striated. The matrix comprises glass and palagonitized sand-size grains. Within the sandy diamict is a 3 m-thick unit of gray muddy diamict with sparse interbedded sandy lenses.

Pillow units are distinguished based on their appearance and orientations. For example, Lp1 and Lp2 show a sharp contrast in appearance: Pillow lavas in Lp1 are aphyric, variably fractured, and weathered brown-yellow, whereas Lp2 pillows are darker, fresher-looking, olivine-bearing and have fresh glassy rinds with corrugated textures. Pillow orientations differ among the quarry walls (Figure 6). Lp2 pillows in the south wall plunge steeply to the

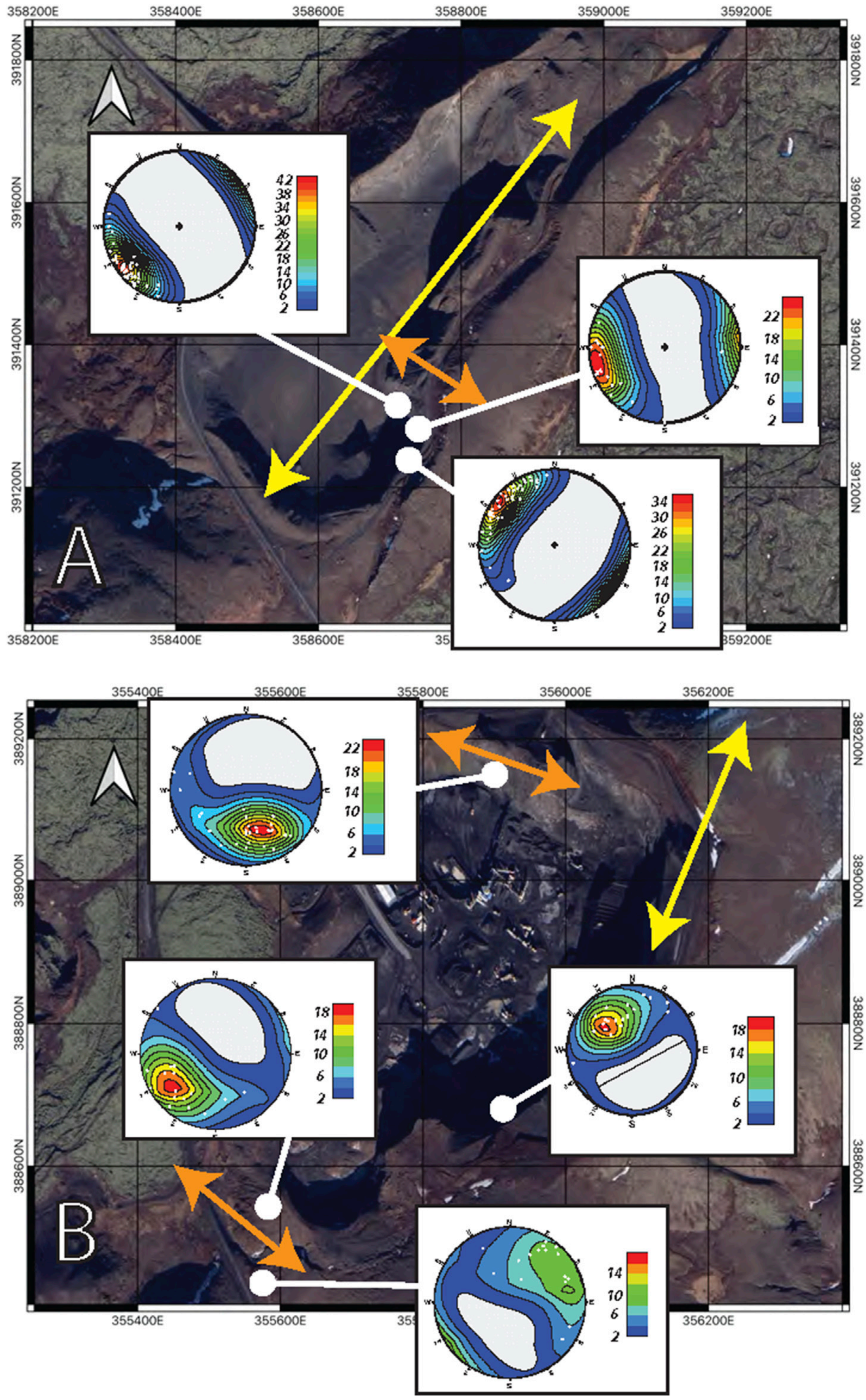

FIGURE 6
Quantification of pillow orientations. **(A)** Satellite image of the Central Wall of Undirhlíðar showing populations of pillow plunges. **(B)** Satellite image of the central and southern walls at Vatnsskarð quarry showing populations of pillow plunges. In **(A, B)** yellow arrows show the general trend of the overall ridge, and orange arrows show fissure trends inferred from pillow plunge directions.

southwest. Pillow units in the main quarry walls plunge to northwest. The north wall exposes a pillow unit (LpN) that plunges steeply to the south.

Irregular subhorizontal intrusions are present in all of the quarry walls (Figures 3, 5). They appear as laterally extensive massive columnar jointed basalts that are irregular in shape with complex jointing patterns. Many of the irregular intrusions show chilled margins and glassy contacts with the surrounding pillow lavas. The intrusions are holocrystalline with visible plagioclase, olivine, and clinopyroxene phenocrysts and crystal size increasing toward the interior. Some parts of the intrusions are slightly vesiculated (< 3%), although other locations along the margin have 10%–15% vesicularity, showing mm-scale vesicles, and sparse larger (4–5 mm) pipe vesicles. These irregular intrusions also contain gabbroic and troctolitic xenoliths. The xenoliths tend to appear at the base of the intrusions.

Ridge-parallel dykes cut through the pillow units on the southernmost and northernmost walls that expose cross-sections perpendicular to the ridge (Figure 3). The dykes are ~1–1.5 m wide with chilled margins. They display well developed columnar joints and patterns in vesicularity (pipe vesicles perpendicular to margins and vesicle bands parallel to margins). The cores of some dykes are glassy, vesiculated, and fragmented. Ridge-perpendicular dykes are less abundant but also present.

In Undirhlíðar quarry, pillows in the central part of the quarry generally have southwest trends (236°–256°) with low plunges (Figure 6). These data are consistent with eruption from a vent trending perpendicular to the main ridge axis. However, pillows in the area to the south (pw07-pw10), have northwest trends (307°) with low plunges, suggesting an eruptive vent to the southeast. In Vatnsskarð quarry, a number of areas show pillows with plunge orientations that are also consistent with eruption from small fissures with a variety of orientations with respect to the main ridge axis (Figure 6). For example, pillows in the south wall (Lp2) show plunge directions opposite to pillows exposed in an erosional gully adjacent and south to the quarry.

4.2 Major and trace element geochemistry

Within the Undirhlíðar ridge suite, samples form distinct geochemical clusters defined by Rare Earth Element (REE) patterns (Figure 7). Based on relative light REE (LREE) enrichment, we divide the Undirhlíðar ridge samples into three compositional groups. Most of the suite comprises the "less-enriched" group with chondrite-normalized (McDonough and Sun, 1995) La_N/Sm_N less than 1.31. The "more-enriched" group overlaps the less-enriched group in REE abundance but has La_N/Sm_N ratios greater than 1.50. The "mixed" group has La_N/Sm_N ratios between 1.37 and 1.49 and shows the highest REE abundances in the suite. All of the Undirhlíðar ridge samples have smooth REE patterns with no or slightly positive Eu anomalies.

Undirhlíðar ridge REE data overlap with enriched lavas from the Reykjanes Peninsula but show a more restricted range in LREE enrichment (Figure 7). Reykjanes Peninsula lavas show La_N/Sm_N ranging from 1.20 to 1.67 (Kokfelt et al., 2006; Peate et al., 2009; Koornneef et al., 2012; Eason and Sinton, 2015; Halldórsson et al., 2016). Fagradalsfjall lavas show a wider range in La_N/Sm_N (1.24–2.74) and extend to lower REE abundances (Bindeman et al., 2022; Halldórsson et al., 2022). Using incompatible trace element ratios, Gee et al. (1998) divided Reykjanes Peninsula samples into "depleted" (Nb/Zr < 0.08) and "enriched" (Nb/Zr > 0.08) groups. Peate et al. (2009) further subdivided enriched historical Reykjanes Peninsula lavas into "less-enriched" (Nb/Zr 0.10–0.13, La_N/Sm_N 1.21–1.36) and "more-enriched" (Nb/Zr 0.13–0.14, La_N/Sm_N 1.38–1.48) groups based on incompatible trace element ratios and LREE enrichment. By these definitions, all of the Undirhlíðar ridge samples are enriched. Like Peate et al. (2009), we observe more-enriched and less-enriched subdivisions within the Undirhlíðar ridge dataset. Our more-enriched group shows higher La_N/Sm_N values than the more-enriched group of Peate et al. (2009). Our mixed group would have been classified by Peate et al. (2009) as "more-enriched," but we choose to separate the mixed samples because of compositional differences.

The three compositional groups show variations that are distinguishable in major element space (Figure 8). In general, with decreasing MgO, the Undirhlíðar ridge suite shows decreasing Al_2O_3 and CaO, increasing FeO^T, TiO_2, and Na_2O, and relatively flat SiO_2 values. The less-enriched group encompasses the entire range of MgO found in the dataset, extending to the highest MgO values (MgO >9.0 wt.%). The high-MgO samples are dominated by olivine-phyric intrusions and pillow lavas. At a given value of MgO, some less-enriched samples show elevated Al_2O_3 and CaO and lower FeO^T and K_2O. These samples are plagioclase-phyric pillow lavas. The mixed and more-enriched groups are distinguished by where they overlap with the less-enriched group. Mixed group samples dominate the low-MgO range of the Undirhlíðar ridge dataset. More-enriched samples fall toward the lower edges of TiO_2, FeO^T, and Al_2O_3 fields and the higher edges of CaO field defined by the less-enriched samples. The most notable distinction among the three compositional groups is in K_2O. For a given value of MgO, the more-enriched group shows the greatest variability in K_2O and extends to higher values. This distinction is clearly observed in the ratio of K_2O/TiO_2, where the more-enriched group shows the highest values (avg. 0.18 ± 0.04, $n = 25$), the less-enriched group shows the lowest values (avg. 0.10 ± 0.03, $n = 107$), and the mixed group spans the range of the suite.

Overall, the Undirhlíðar ridge samples are tholeiitic basalts similar in major element composition to other lavas from the Reykjanes Peninsula (Jakobsson et al., 1978; Condomines et al., 1983; Hemond et al., 1988; Hemond et al., 1993; Gee et al., 1998; Kempton et al., 2000; Skovgaard et al., 2001; Fitton et al., 2003; Momme et al., 2003; Kokfelt et al., 2006; Maclennan, 2008; Peate et al., 2009; Jakobsson and Johnson, 2012; Koornneef et al., 2012; Eason and Sinton, 2015; Halldórsson et al., 2016). Reykjanes Peninsula samples span a slightly wider range in MgO compared to Undirhlíðar ridge (Figure 8). Like the Undirhlíðar compositional groups, the less- and more-enriched compositional groups of Peate et al. (2009) are distinct in major elements. Namely, the less-enriched group shows lower MgO, K_2O, and TiO_2 and higher SiO_2 and Fe_2O_3 than the more-enriched group (Peate et al., 2009). Although we observe that our less-enriched samples are lower in K_2O than our more-enriched samples, the other patterns identified by Peate et al. (2009) do not apply to the Undirhlíðar ridge data. Our less-enriched samples are higher in TiO_2 and lower in SiO_2 compared to our more-enriched samples (Figure 8). Our compositional groups span most of the range of MgO values (Figure 9A) and show no correlation with FeO^T (Figure 9B).

The Undirhlíðar ridge dataset shows positive correlations between LREE and incompatible trace element enrichment

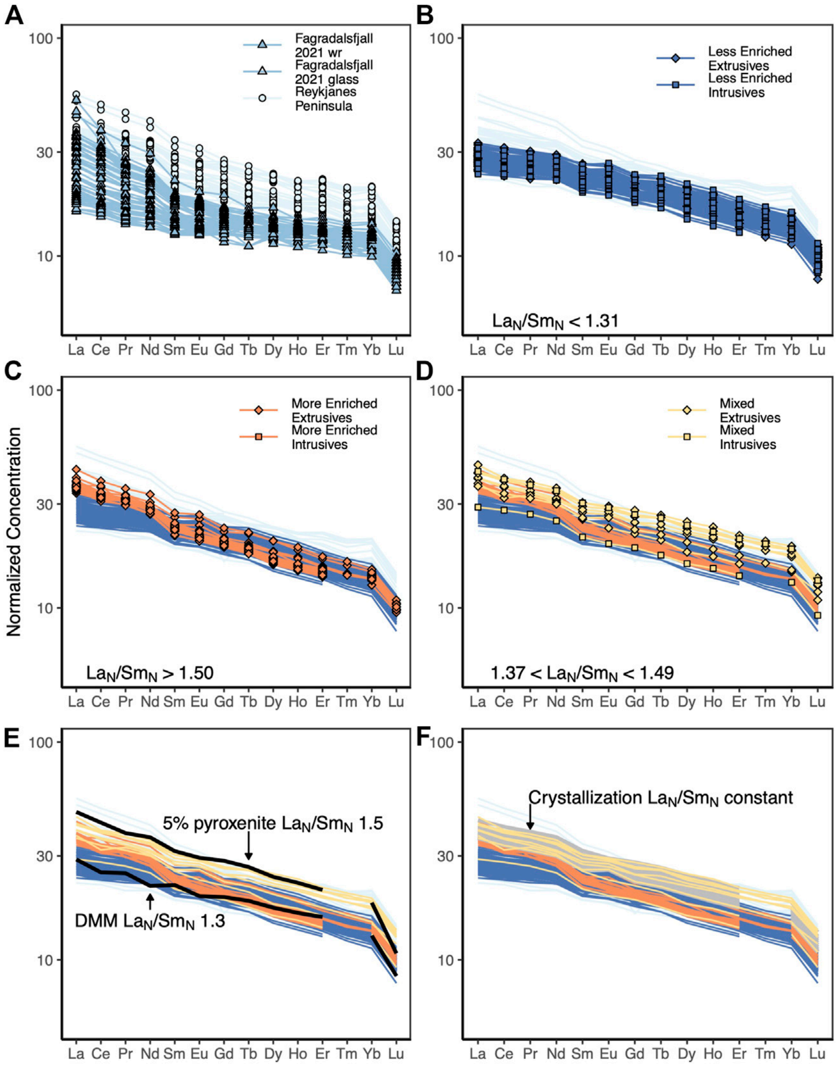

FIGURE 7
Rare Earth element (REE) concentrations normalized to chondrite values from McDonough and Sun (1995). **(A)** Reykjanes Peninsula (light blue circles), including the Fagradalsfjall 2021 eruption (medium blue triangles). Undirhlíðar ridge extrusive (diamonds) and intrusive (squares) samples shown in **(B–D)**, grouped by La_N/Sm_N values: **(B)** $La_N/Sm_N < 1.31$ (less enriched), **(C)** $La_N/Sm_N > 1.50$ (more enriched), **(D)** $1.37 < La_N/Sm_N < 1.49$ (mixed). **(E)** Black lines show alphaMELTS model melt compositions for depleted (DMM) and enriched (5% pyroxenite) mantle sources, illustrating how mixing between two mantle source compositions can generate the Undirhlíðar ridge data. **(F)** Gray field show alphaMELTS model liquid compositions for up to 30% fractional crystallization illustrating how variable extents of crystallization affect REE abundance. See text for model details. Undirhlíðar ridge data from this study and (Pollock et al., 2014). Reykjanes Peninsula data (light blue circles), excluding picrites, from (Kokfelt et al., 2006; Peate et al., 2009; Koornneef et al., 2012; Eason and Sinton, 2015; Halldórsson et al., 2016). Fagradalsfjall data (triangles) from (Bindeman et al., 2022; Halldórsson et al., 2022).

(Figure 9). The more-enriched samples have higher incompatible trace element ratios (Zr/Y 3.6-4.0) compared to the less-enriched group (Zr/Y 3.1-3.6). The mixed samples have incompatible trace element ratios that fall between the more- and less-enriched groups. Undirhlíðar ridge samples overlap with enriched samples from the Reykjanes Peninsula, which encompass greater ranges in incompatible trace element ratios (Wood et al., 1979; Chauvel and Hémond, 2000; Peate et al., 2009; Koornneef et al., 2012; Eason and Sinton, 2015; Halldórsson et al., 2016).

The three compositional groups are correlated with spatial location along the ridge. Almost all of the more-enriched samples are found in the basal stratigraphic units at lower elevations in Undirhlíðar quarry. Mixed samples are the least abundant in the suite and most are located along the ridge between the quarries. The less-enriched group is the most abundant in the suite, found in the dykes and upper units in Undirhlíðar quarry, along the ridge, and heavily concentrated in Vatnsskarð quarry. The single sample from the basal, weathered unit in Vatnsskarð quarry is compositionally distinct from the rest of the suite with a much higher Nb/Zr ratio (Figure 9).

Within the quarries, we observe patterns in trace element compositions related to lithostratigraphic units. Almost all of the Vatnsskarð quarry extrusive samples belong to the less-enriched group; the exceptions are two mixed-group samples (a bomb from a

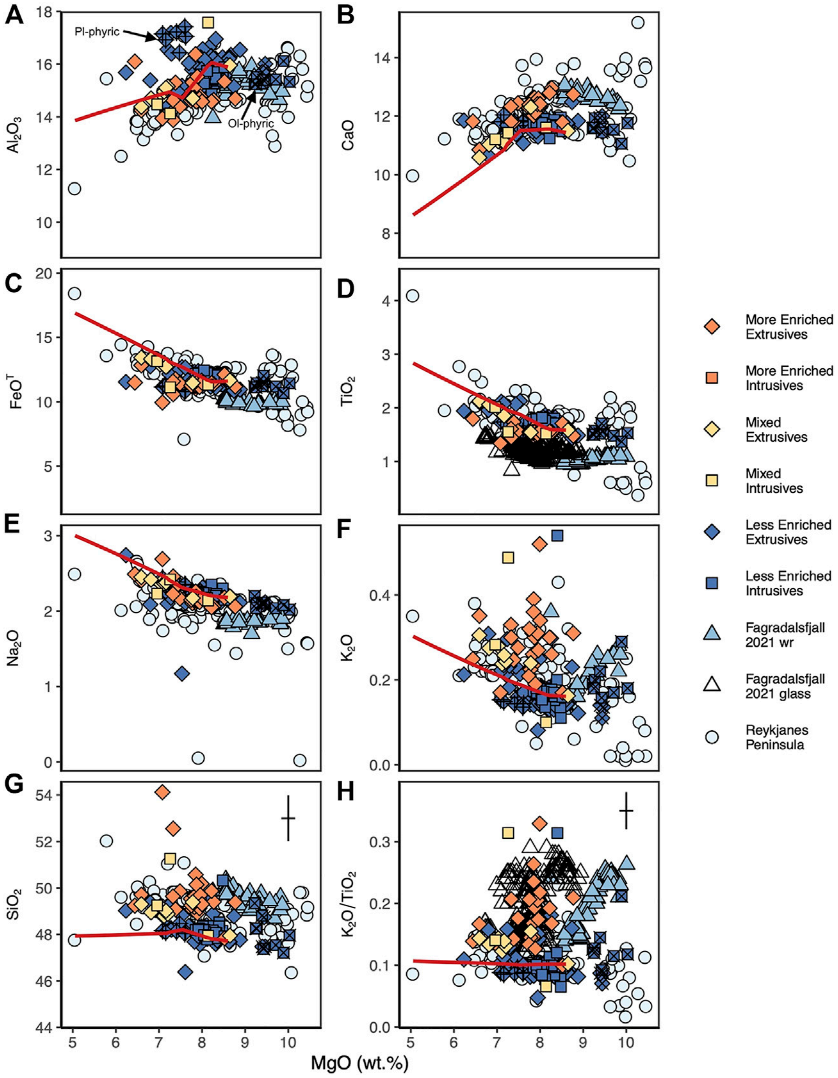

FIGURE 8
Major elements vs. MgO in wt% with symbols and colors as in Figure 7. **(A)** Al_2O_3, **(B)** CaO, **(C)** FeO^T, **(D)** TiO_2, **(E)** Na_2O, **(F)** K_2O, **(G)** SiO_2, **(H)** K_2O/TiO_2. All iron is recalculated as total FeO (FeO^T). Data have been normalized to 100% on an anhydrous basis. Error bars show 2 σ standard deviation on panels **(G, H)**. On all other panels, symbols are larger than 2 σ standard deviation. Symbols with (+) are plagioclase phyric and (x) are olivine phyric. Red line shows alphaMELTS model liquid line of descent of 1 kbar fractional crystallization. See text for model details. Undirhlíðar ridge data from this study and Pollock et al. (2014). Reykjanes Peninsula data (light blue circles), excluding picrites, from (Jakobsson et al., 1978; Condomines et al., 1983; Hemond et al., 1988; Hemond et al., 1993; Gee et al., 1998; Kempton et al., 2000; Skovgaard et al., 2001; Fitton et al., 2003; Momme et al., 2003; Kokfelt et al., 2006; Maclennan, 2008; Peate et al., 2009; Jakobsson and Johnson, 2012; Koornneef et al., 2012; Eason and Sinton, 2015; Halldórsson et al., 2016). Fagradalsfjall whole rock (medium blue triangles) and glass (open triangles) data from Bindeman et al., 2022 and Halldórsson et al., 2022.

tuff breccia unit and a single pillow lava). Within the less-enriched extrusive units, we observe a shift in trace element ratios that correlates with a stratigraphic break between exposures from north to south. Pillow lavas in the north wall show identically low values of La_N/Sm_N (1.20). Pillow lavas in the other Vatnsskarð quarry exposures show a range of La_N/Sm_N values that encompasses most of the range of the less-enriched suite (1.21–1.27). The transition between north wall and the rest of the Vatnsskarð quarry occurs over a distance of tens of meters. In general, Vatnsskarð quarry intrusions show similar REE patterns and abundances to the pillows into which they intrude. However, in Undirhlíðar quarry, less-enriched dykes intrude through more-enriched pillow lavas in the lower stratigraphic units.

4.3 Sr-Nd-Pb isotopes

Undirhlíðar ridge radiogenic isotope compositions (Sr-Nd-Pb) encompass a narrow range that overlaps with isotopically enriched lavas from the Reykjanes Peninsula (Table 2; Figure 10; Schilling, 1973; Sun and Jahn, 1975; Condomines et al., 1983; Hemond et al., 1993; Gee et al., 1998; Kempton et al., 2000; Fitton et al., 2003; Thirlwall et al., 2004; Kokfelt et al., 2006; Peate et al., 2009). Within dataset limits, Undirhlíðar ridge is consistent with several isotopic relationships observed in other lavas from the Reykjanes Peninsula. First, radiogenic isotopes show positive correlations with trace element ratios (Peate et al., 2009). Although six of the seven Undirhlíðar ridge samples are from the less-enriched

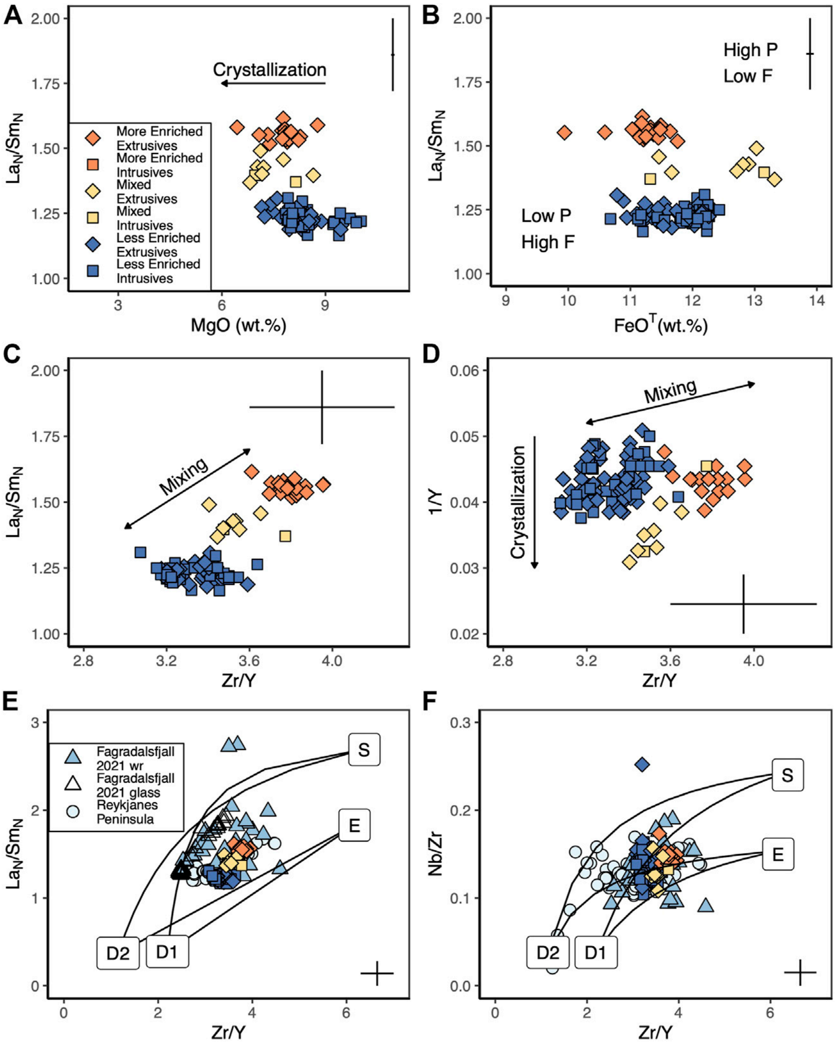

FIGURE 9

Trace element variations with symbols and colors as in Figure 7. **(A)** La_N/Sm_N vs. MgO, **(B)** La_N/Sm_N vs. FeO^T, **(C)** La_N/Sm_N vs. Zr/Y, and **(D)** 1/Y vs. Zr/Y for Undirhlíðar ridge. **(E)** La_N/Sm_N vs. Zr/Y and **(F)** Nb/Zr vs. Zr/Y for Undirhlíðar ridge, Reykjanes Peninsula, and the 2021 eruption of Fagradalsfjall. Arrows in **(A)** through **(D)** indicate the direction of trends caused by mixing and crystallization. Scatter in the data in **(A, C)** indicates variable extents of crystallization. The lack of correlation between trace element ratios and major element indicators of melting in **(D)** suggests mixing. Curves in **(E, F)** show mixing between two depleted mantle components (D1 and D2), the main basaltic plume component ("E" for Eldgjá), and the alkalic component ("S" for Snæfellsnes) after (Murton et al., 2002; Bindeman et al., 2022). Mantle compositions from (Kempton et al., 2000; Murton et al., 2002). Reykjanes Peninsula data (light blue circles), excluding picrites, from (Wood et al., 1979; Chauvel and Hémond, 2000; Peate et al., 2009; Koornneef et al., 2012; Eason and sinton, 2015; Halldórsson et al, 2016). Fagradalsfjall data (triangles) from Bindeman et al. (2022) and Halldórsson et al. (2022). Error bars show 2 σ standard deviation.

compositional group, the single more-enriched sample shows greater $^{206}Pb/^{204}Pb$ (Figure 10). Second, in their suite of historical Reykjanes Peninsula lavas, Peate et al. (2009) observed that their less- and more-enriched compositional groups were nearly identical in radiogenic Nd and Sr compositions and showed linear correlations in Pb-Pb isotope space. With the exception of a pillow lava from the upper units at Undirhlíðar quarry (S-10-23), the Undirhlíðar ridge samples also overlap in $^{143}Nd/^{144}Nd$ and $^{87}Sr/^{86}Sr$ compositions and show linear Pb-Pb isotope patterns (Figure 10). Third, Peate et al. (2009) observed that the Reykjanes Peninsula data plot below the Northern Hemisphere Reference Line (NHRL) for $^{207}Pb/^{204}Pb$ (negative $\Delta^{207}Pb$) and above the NHRL for $^{208}Pb/^{204}Pb$ (positive $\Delta^{208}Pb$). All of the Undirhlíðar ridge samples show negative $\Delta^{207}Pb$ values, forming a linear trend that extends toward more positive values. The Undirhlíðar ridge samples also show $\Delta^{208}Pb$ values that are positive or near zero.

On Pb-Pb isotope plots, the less-enriched Undirhlíðar ridge samples create a linear array (Figure 10). The ends of the linear array are bracketed by samples from Vatnsskarð quarry, with the least isotopically enriched sample from the southern end and the most isotopically enriched sample from <1 km away in the northern end. Samples from the upper stratigraphic units of Undirhlíðar quarry fall between the Vatnsskarð quarry samples. The single sample from the more-enriched group represents the lower stratigraphic units in Undirhlíðar quarry. Although this sample clusters with the less-

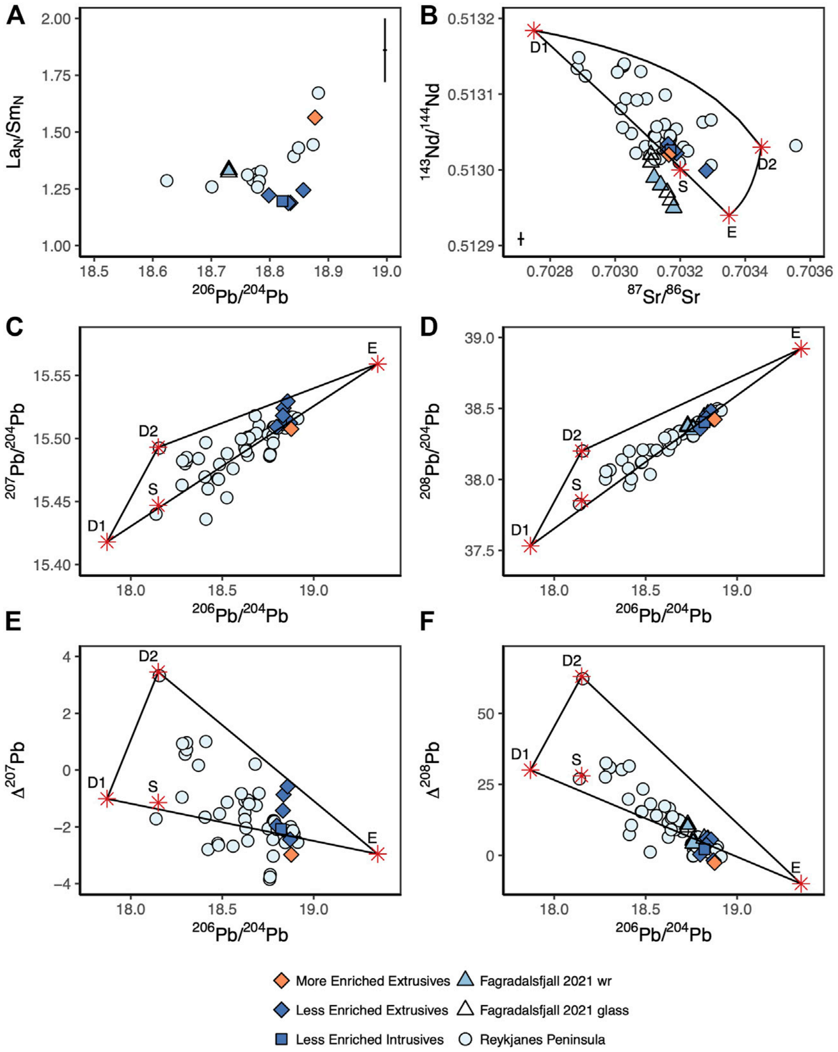

FIGURE 10
Isotope compositions with symbols and colors as in Figure 7. **(A)** La_N/Sm_N vs. $^{206}Pb/^{204}Pb$, **(B)** $^{143}Nd/^{144}Nd$ vs. $^{87}Sr/^{86}Sr$, **(C)** $^{207}Pb/^{204}Pb$ vs. $^{206}Pb/^{204}Pb$, **(D)** $^{208}Pb/^{204}Pb$ vs. $^{206}Pb/^{204}Pb$, **(E)** $\Delta^{207}Pb$ vs. $^{206}Pb/^{204}Pb$, **(F)** $\Delta^{208}Pb$ vs. $^{206}Pb/^{204}Pb$. The more enriched Undirhlíðar ridge sample shows higher $^{206}Pb/^{204}Pb$ than the less enriched samples. Curves in **(B)** through **(F)** show mixing between mantle components defined in Figure 9 (Murton et al., 2002; Bindeman et al., 2022). Mantle compositions from (Thirlwall et al., 2004). $\Delta^{207}Pb$ and $\Delta^{208}Pb$ are 100 x the vertical deviations from the Northern Hemisphere Reference Line (after Hart, 1984; Thirlwall et al., 2004). Undirhlíðar ridge data fall within the fields defined by the mixing curves, forming linear trends on Pb-isotope plots **(C–F)**. Undirhlíðar ridge samples overlap with the more isotopically-enriched Reykjanes Peninsula data. Reykjanes Peninsula data (light blue circles), excluding picrites, from (Schilling, 1973; Sun and Jahn, 1975; Condomines et al., 1983; Hemond et al., 1993; Gee et al., 1998; Kempton et al., 2000; Fitton et al., 2003; Thirlwall et al., 2004; Kokfelt et al., 2006; Peate et al., 2009). Fagradalsfjall data (triangles) from (Bindeman et al., 2022; Halldórsson et al., 2022). Error bars show 2 σ standard deviation. Where no error bars are plotted, symbols are larger than 2 σ error.

enriched samples on a plot of $^{143}Nd/^{144}Nd$ vs. $^{87}Sr/^{86}Sr$, it falls below the linear trend defined by the Vatnsskarð endmembers Pb-Pb isotope plots. The more-enriched sample also has the most negative $\Delta^{207}Pb$ and lowest $\Delta^{208}Pb$ values in the sample suite.

4.4 Volatile concentrations

Water concentrations for Undirhlíðar ridge were analyzed from fresh glass chips that showed vitreous surface textures, sparse plagioclase microlites, and vesicularity <20% (Table 3; Figure 11). Water speciation was not determined for most samples, so measurements represent total water (H_2O_t) concentration. FTIR mapping reveals homogeneous water concentrations within the glass. Highest water concentrations are observed around fractures and vesicles, which were avoided during data acquisition (Supplementary Figure SA1). Only five of the 22 samples produced a detectable peak CO_2 peak at the 2,360 cm^{-1} position, indicating that measured CO_2 values are at or below detection limits (< 20 ppm).

To check if water concentrations represent magmatic conditions, we measured water speciation when possible. Only five samples produced measurable H_2O_m peaks at the 1,630 cm^{-1} band (Table 3). Secondary hydration enriches volcanic glasses in H_2O_m (e.g., Mcintosh et al., 2017). Most samples did not show

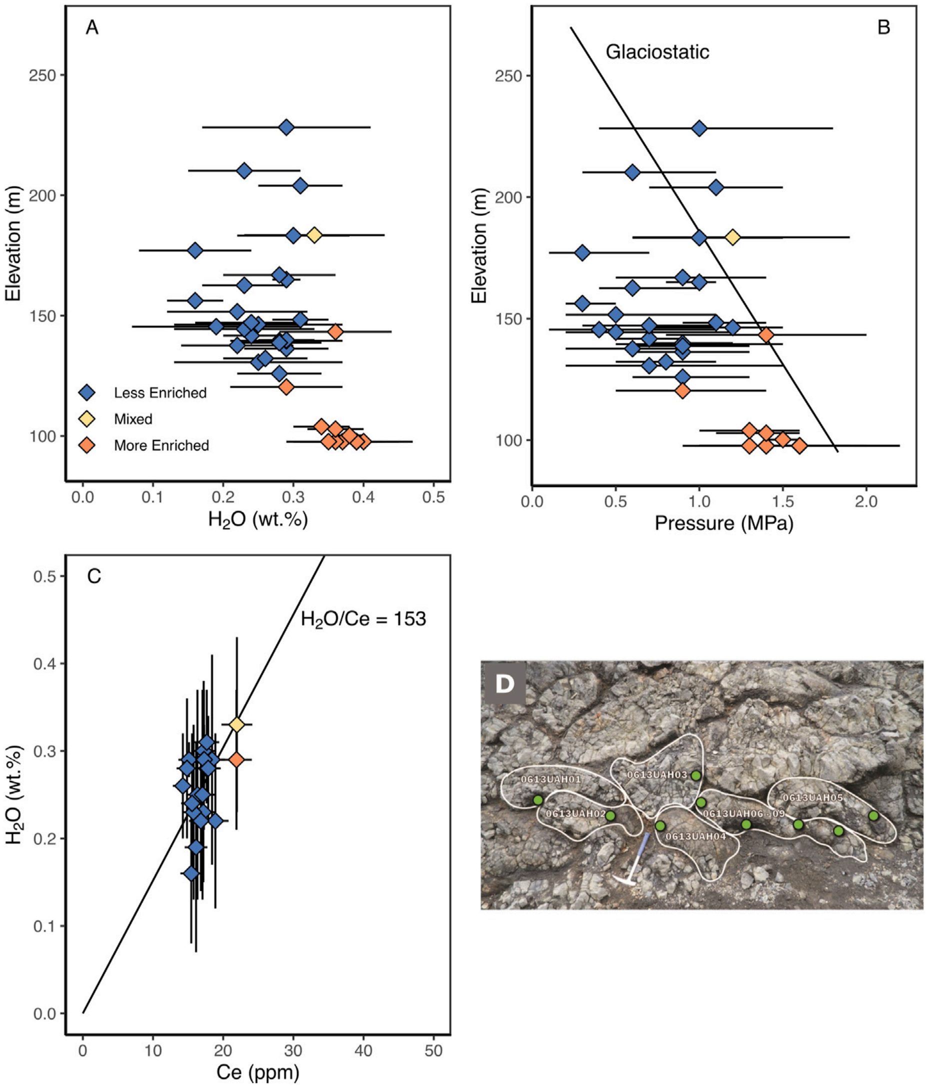

FIGURE 11
Water concentrations in glass samples from Undirhlíðar ridge. Symbols and colors as in Figure 7. **(A)** Elevation vs. H_2O (wt.%) for pillow lavas from this study. H_2O generally decreases with increasing elevation. More-enriched samples show higher H_2O concentrations than less-enriched samples. Error bars show 2 σ standard deviation. Elevations determined from DEM as described in text. **(B)** Calculated H_2O saturation pressures (MPa) assuming complete CO_2 degassing. Error bars based on 2 σ H_2O values. Solid line shows glaciostatic pressures for 200 m thick ice. **(C)** H_2O (wt.%) vs. Ce (ppm). Solid line shows H_2O/Ce ratio for less-enriched samples (153 ± 24) **(D)** Location of nine glassy rims sampled from a cluster of adjacent pillows in Undirhlíðar quarry. Four samples (0613UAH06-09) were collected from the same pillow. Hammer is 42 cm long. Samples shown in **(D)** overlap at the lowest elevations on **(A)**.

measurable H_2O_m. For the few samples that showed measurable peaks, H_2O_m/H_2O_t ratios are less than the values found in experiments of basaltic glasses quenched at high temperatures (Dixon et al., 1995), suggesting that the analzyed glasses in this study did not experience secondary hydration (e.g., Sano and Yamashita, 2019). To determine if water concentrations from a single pillow represent the conditions for surrounding lavas, we conducted detailed sampling of adjanced pillow lavas and assessed small-scale (< 1 m) spatial variations in H_2O_t concentrations (Figure 11). The four samples taken from the same pillow in Undirhlíðar quarry have measured H_2O_t concentrations that are similar within analytical error (Table 3). Likewise, the samples from the cluster of adjacent pillows are within analytical error of one another. Therefore, we find that the H_2O_t data measured by FTIR on individual pillow lavas are reproducible and representative of the unit in which the pillow lava was erupted.

Water concentrations for Undirhlíðar ridge span a wide range (0.16–0.40 wt.%) and generally decrease with increasing elevation (Figure 11). We observe the greatest range of water contents (0.19–0.36 wt.%) at ~145 m elevation. Water concentrations are most variable over the smallest spatial scales in Undirhlíðar quarry, where contents change from 0.23–0.40 wt.% H_2O over walls that are ~50 m high and ~150 m long. Conversely, Vatnsskarð quarry is dominated by less-enriched samples and shows a narrower range of H_2O concentrations (0.24–0.31 wt.%), despite exposing walls that are taller (~80 m) and longer (~750 m).

Calculated water saturation pressures mimic the pattern of water concentrations (Figure 11). Assuming complete CO_2 degassing, saturation pressures range from 0.3 MPa to 1.6 MPa. Using densities of 0.917 g/cm^3 for ice and 1.000 g/cm^3 for water, saturation pressures correspond to ice thicknesses up to 178 ± 33 m and water depths up to 163 ± 31 m. The decrease in saturation pressure with elevation generally follows a linear trend predicted by glaciostatic conditions under 200 m-thick ice. However, most less-enriched samples between ~120 m and ~180 m in elevation fall below the glaciostatic curve.

The significant decrease in water contents starting at ~120 m in elevation is correlated with a shift in trace element ratios (Figure 11). More-enriched samples show greater H_2O concentrations (average 0.37 ± 0.03 wt.%, $n = 12$) and less-enriched samples show lower H_2O concentrations (average 0.25 ± 0.04 wt.%, $n = 25$). To examine the influence of degassing and magma differentiation on water contents, we compared H_2O to Ce, a trace element that behaves similarly during magmatic processes (e.g., Sano and Yamashita, 2019). Water contents show a positive linear correlation with Ce. Less-enriched samples show a wide range in H_2O/Ce ratios (average 153 ± 24, $n = 20$). Samples from the mixed and more-enriched groups fall along a line with a slope that matches the H_2O/Ce ratio of the less-enriched group.

5 Discussion

5.1 Magma generation and evolution

Compositional data indicate that mantle source and crustal processes both play essential roles in the formation and evolution of magma at Undirhlíðar ridge. Some variability in major element and REE patterns is consistent with the effects of crystallization and crystal accumulation (Figures 7, 8). This is demonstrated in the major element trends of increasing FeO^T, TiO_2, and Na_2O and decreasing Al_2O_3 and CaO with decreasing MgO. The most evolved samples in the suite show the greatest REE abundances. The effects of crystal accumulation are apparent in olivine-phyric lavas that show elevated MgO and plagioclase-phyric lavas that show elevated Al_2O_3 and positive Eu anomalies.

The observed compositional variations are consistent with thermodynamic models of fractional crystallization (Figures 7, 8). Isobaric shallow fractional crystallization of a primitive parent magma from the mixed group shows a typical basaltic crystallization sequence of ol, ol + pl, and ol + pl + cpx. The resulting LLD forms downward curving paths in Al_2O_3 and CaO and linear upward paths in FeO^T, TiO_2, and Na_2O that follow major element patterns. REE abundances can also be explained by varying degrees of crystallization, which do not affect the slope of REE patterns but cause relative REE abundances to increase in more evolved lavas. The higher REE abundances of the mixed samples can be generated by up to 30% crystallization. Much of the scatter in major element and REE patterns can be explained by variable degrees of crustal-level crystallization.

While all of the Undirhlíðar ridge magmas evolved in the crust, the samples cannot be related to each other by cooling of a single parent magma. This is demonstrated by the scatter in major and trace elements, particularly in SiO_2, K_2O, K_2O/TiO_2, and La_N/Sm_N at a given value of MgO (Figures 8, 9). More-enriched samples follow major element trends that parallel the modeled LLD at lower values of TiO_2, FeO^T, and Al_2O_3 and higher values of CaO, suggesting a different parent magma composition. Separate parent magmas are also indicated by modeled liquidus phases. For parent magmas from the from the mixed group (VAT-SA-13-07) and the less-enriched group (16MP02), the modeled liquidus phase is olivine; for a parent magma from the more-enriched group (S-10-18), the liquidus phase is clinopyroxene. In Pollock et al. (2014), we argued that the less-enriched and more-enriched groups follow separate LLD and proposed a model for crystallization in separate crustal reservoirs. At that time, we had not identified the mixed samples from the ridge. Our expanded dataset confirms that the Undirhlíðar ridge magmas cannot be derived from crystallization of a single parent magma in the same melt reservoir. The major and trace element variability are consistent with variations in mantle melting or source composition underlying Undirhlíðar ridge.

In Pollock et al. (2014), we argued that the compositional variations in Undirhlíðar quarry could be explained by mixing of mantle melts extracted from over a range of depths, but our expanded study shows that the compositional groups are likely related to mantle heterogeneity. In our expanded dataset, we observe no correlation between La_N/Sm_N and FeO^T (Figure 9), a major element indicator of degree and pressure of melting. Undirhlíðar ridge samples also have smooth REE patterns with no difference in degree of HREE fractionation between the compositional groups (Figure 7), suggesting a relatively constant degree of melting from shallow depths. Instead of variations in melting of a homogeneous mantle source, the variability in Pb isotopes in our expanded dataset demonstrate that the source mantle cannot be a single homogeneous composition.

Mantle source heterogeneity must influence the compositional variability in the Undirhlíðar ridge magmas. Variable enrichment in incompatible elements and radiogenic isotopes in Iceland have been attributed to aggregation of melts from heterogeneous mantle that are extracted over a range of depths (Hanan and Schilling, 1997; Chauvel and Hémond, 2000; Hanan et al., 2000; Kempton et al., 2000; Stracke et al., 2003; Thirlwall et al., 2004; Thirlwall et al., 2006; Kokfelt et al., 2006; Peate et al., 2009; Koornneef et al., 2012). On the Reykjanes Peninsula, linear isotopic trends and correlations between isotopes and trace element indicators of enrichment have been interpreted as near-binary mixing between mantle sources (Thirlwall et al., 2004; Kokfelt et al., 2006; Peate et al., 2009). The presence of up to six mantle endmembers has been suggested by previous workers (Murton et al., 2002; Thirlwall et al., 2004; Kokfelt et al., 2006; Peate et al., 2009). The nature and origin of the mantle heterogeneity is discussed by numerous workers, but many posit that there are enriched components related to the plume and the alkalic source and depleted components related to the ambient mantle (Kempton et al., 2000; Murton et al., 2002; Thirlwall et al., 2004; Kokfelt et al., 2006). Here, we use simple binary mixing equations (Langmuir et al., 1978) to calculate mixing curves among four endmembers: two enriched mantle compositions are defined by the enriched plume (represented by Eldgja (E) and alkalic Snaefellsnes (S) lavas) and two depleted mantle sources that are similarly depleted in trace elements but show different isotopic compositions (Murton et al., 2002; Thirlwall et al., 2004; Kokfelt et al., 2006).

The Undirhlíðar Pb-Pb isotope data create a linear array that we interpret as mixing between two mantle source compositions. The mixing trends are best seen on the $\Delta^{207}Pb$ and $^{207}Pb/^{204}Pb$ plots, where the mixing lines between the Eldgjá and depleted endmembers are most distinct (Figure 10). The Undirhlíðar data form a binary mixing line between two mantle compositions that are intermediate between the endmembers. The less-enriched samples trend toward one endmember that is a mix of Eldgjá and D2. The more-enriched sample trends toward the second endmember that is a mix between Eldgjá and D1. Because the Snæfellsnes endmember is itself intermediate between Eldgjá and D1, it is difficult to determine the role of the Snæfellsnes source using the isotope data. The location of Snæfellsnes on a mixing line between Eldgja and D1 suggests that the alkalic source may make a bigger contribution to the more-enriched samples. This is consistent with observations on plots of trace element ratios, where binary mixing creates hyperbolas whose curvatures are determined by a ratio of the endmember denominators (Figure 9). On plots of La_N/Sm_N versus Zr/Y and Nb/Zr versus Zr/Y, all of the Undirhlíðar ridge data fall within a multi-component mixing array defined by the Eldgjá, Snæfellsnes, and depleted mantle components. The more-enriched samples fall toward an enriched endmember that is intermediate between Snæfellsnes and the depleted endmembers. The less-enriched samples fall toward an endmember that is intermediate between the Eldgjá and depleted endmembers.

To test whether a heterogeneous mantle source can produce the range of La_N/Sm_N values that we observe in the Undirhlíðar ridge data, we modeled polybaric continuous melting for two mantle sources under the same conditions using AlphaMelts. One mantle source is the depleted mantle (DMM) from Workman and Hart (2005). The other mantle source is DMM that has been enriched in pyroxenite (Koornneef et al., 2012). Melts from the two mantle sources reproduce REE patterns observed at Undirhlíðar ridge (Figure 7). The depleted mantle melt overlaps with REE for the less-enriched group. The melt from the DMM enriched with pyroxenite overlaps with REE for the more-enriched group. This suggests that the difference in La_N/Sm_N ratio can be generated by different mantle source compositions that melt under similar conditions. To generate the trace element trends with comparatively constant degrees of melting, the more-enriched samples require a higher amount of the enriched mantle component, which we also observe in our isotopic and trace element ratio data.

Our understanding of the nature of the magma plumbing system can be informed by the relationship between crystallization and mixing of heterogeneous mantle melts. Because the curvature of a mixing hyperbola in plots of incompatible trace element ratios depends on the denominators of the endmembers, mixing should result in a linear array on a plot of 1/Y versus Zr/Y (Langmuir et al., 1978). Undirhlíðar ridge data fall off a linear array as a result of variable degrees of crystallization, with the most evolved lavas extending to the lowest values of 1/Y (Figure 9D). Mixing must have occurred prior to crystallization. This is consistent with major elements trends, where the compositional groups must have had parent magma compositions that differed in CaO, SiO_2, and K_2O (Figure 8). The magma plumbing system preserves mantle source signatures on small spatial scales. Within the area exposed by Undirhlíðar quarry, we observe more-enriched lavas intruded by less-enriched magmas. Vatnsskarð quarry is dominated by the less-enriched group but shows geographic shifts in LREE enrichment within the northernmost exposures. The mixed group is the most evolved, suggesting that it was cooled to greater degrees. Because this compositional variability is preserved, even at the local scale, there must be no large-scale efficient mixing processes to homogenize the magma. We propose that the magmatic plumbing system consisted of separately evolving crustal melt bodies and that original model from Pollock et al. (2014) extends to the entire ridge.

5.2 Paleo-ice conditions

Paleo-ice conditions for Undirhlíðar ridge are constrained by the measurements of water in quenched glassy pillow rims. Glass textures and variations in volatile content show evidence of volatile saturation and degassing. The glasses show abundant vesicles, suggesting degassing of a volatile saturated magma (Tuffen et al., 2010). Because CO_2 degasses more readily than H_2O, and measured CO_2 concentrations are at or below the detection limits, CO_2 was essentially entirely degassed when the glasses were quenched (Dixon and Stolper, 1995). Although it is possible that vesicles represent predominately CO_2 bubbles that formed before H_2O degassing, samples with low H_2O/Ce ratios indicate that H_2O degassing has occurred in the Undirhlíðar suite. Post-emplacement hydration has not affected H_2O contents presented in this study. Although higher H_2O concentrations were observed in the fractures, we avoided fractures while measuring. The lack of measurable H_2O_m peaks and low H_2O_m/H_2O_t ratios suggest that molecular water was not enriched by secondary hydration. Thus, we infer that the Undirhlíðar ridge magmas degassed prior to quenching and that H_2O concentrations are indicative of pressures during emplacement.

Calculated saturation pressures suggest that Undirhlíðar ridge formed within ice at least 200 m thick. The range of water contents and emplacement pressures at Undirhlíðar ridge is similar to those observed in other subglacial edifices on the Reykjanes Peninsula (Nichols et al., 2002; Schopka et al., 2006). At Helgafell, a Pleistocene-age hyaloclastite ridge ~1 km east of this study, ice thickness was estimated to be ~500 m at the time of eruption, although volatile contents indicated lower emplacement pressures caused by meltwater drainage and ice subsidence (Schopka et al., 2006). Estimates of ice thickness on the Reykjanes Peninsula during the last glacial maximum range from 250 m to 500 m (Einarsson et al., 1988; Licciardi et al., 2007; Le Breton et al., 2010; Patton et al., 2017).

A major change in water contents at Undirhlíðar ridge correlates with a shift in the magmatic system. The more-enriched lavas show higher H_2O contents than the less-enriched lavas, which is likely due to differences in magma composition. The geochemical groups have similar H_2O/Ce ratios, indicating that the mixed and more-enriched samples have not experienced more degassing than the less-enriched samples. The positive linear correlation between H_2O and Ce suggests that water is behaving as an incompatible element. We interpret the shift from wetter, more-enriched lavas to less-wet, less-enriched lavas as a result of a shift in melts from a more enriched mantle to a more depleted mantle.

However, within the less-enriched group, lavas show variable extents of degassing. Less-enriched lavas with lower H_2O/Ce ratios have undergone more degassing than those with higher values. Many of the less-enriched samples show saturation pressures lower than expected for glaciostatic conditions. These less-enriched lavas show wide variations in water contents, saturation pressures, and H_2O/Ce ratios over short distances (~100 s of m) at mid-elevations along the ridge. For this group of less-enriched lavas, hydrologic conditions were dynamic during emplacement.

Ice conditions varied during construction of Undirhlíðar ridge. Saturation pressures suggest that Undirhlíðar ridge erupted under thin ice, similar to conditions at Grímsvötn and Eyjafjallajökull (Magnússon et al., 2012). The initial summit eruption in the 2010 Eyjafjallajökull event occurred under ~200 m thick ice, leading to high subglacial water pressures associated with localized glacier uplift and accumulation of meltwater in an ice cauldron (Magnússon et al., 2012). Accumulated water was released in supraglacial flooding that lowered water levels and reduced emplacement pressures (Magnússon et al., 2012). Within days, flank eruptions extending ~1 km from the summit experienced different hydrologic conditions. Flank eruptions occurred on steeper slopes under thinner (50–100 m thick) ice, resulting in rapid drainage of meltwater through high volume, short duration flood events (Magnússon et al., 2012) that created localized water-drained areas with low emplacement pressures (Woodcock et al., 2016). The dynamic variability in hydrologic conditions at Eyjafjallajökull over km-long spatial scales and days-long temporal scales is consistent with the variable extents of degassing observed in the less-enriched lavas that comprise the bulk of the ridge at Undirhlíðar. Saturation pressures return to values consistent with glaciostatic conditions in the upper elevations of Undirhlíðar ridge, suggesting that the upper portions of the edifice were emplaced beneath ice or in a stable englacial lake. The presence of ice at the upper reaches of the ridge is also illustrated by the diamict that drapes over Vatnsskarð quarry, which is consistent with a recovery or return of ice after eruptions ceased.

5.3 Model for undirhlíðar ridge construction

Our detailed study of the compositions and lithostratigraphic relationships allows us to propose several revisions to the existing models for the construction of glaciovolcanic fissure-fed eruptions. We observe a full vertical section of Undirhlíðar ridge in Vatnsskarð quarry. The basal contact of the ridge lies uncomformably over older palagonitized tuff-breccia, pillow lavas and local glaciofluvial deposits. The sandy and muddy diamict units draping over the central and southern walls of the quarry, in addition to the remnant till deposits scattered along the length of the ridge top, suggest that the pillow ridge was covered by a glacier after the eruption. We infer that the ~3 km length of the ridge was emplaced in an ice-confined environment through a series of fissure eruptions.

Eruptions were fed by multiple vents (Figure 12). Plunges reveal that many of the pillows were erupted from vents that parallel the strike of the ridge, but exposures in quarry walls also show eruptive vents and pillow emplacement that were ridge-perpendicular (Figure 6). An example of this is the north wall of the Vatnsskarð quarry, in which the plunge directions in the north wall pillows suggest that this is an isolated "nose" of pillows that erupted off the main ridge axis. The north wall pillow lavas are also compositionally distinct from the other eruptive units in Vatnsskarð quarry, suggesting that the north wall pillows form their own distinct pillow mound within the broader ridge structure.

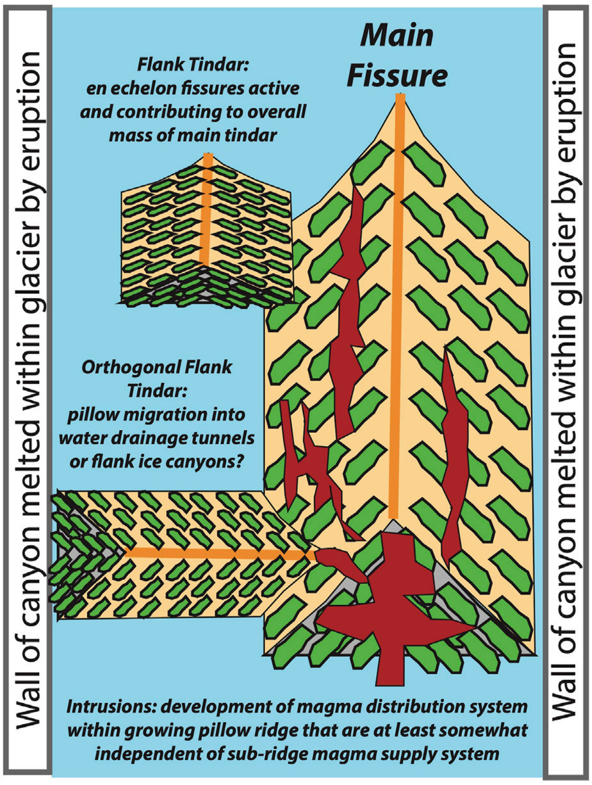

FIGURE 12
Schematic cartoon showing the important, newly identified components of tindar ridge construction. The main fissure system produces pillow lavas (green) that generally plunge downslope perpendicular to the axis of the fissure. Subsidiary, smaller fissures parallel but adjacent to main fissure produce flank pillow mounds that are eventually incorporated into the overall ridge structure. Locally fissures open orthogonal to the main fissure and produce secondary pillow ridges that form perpendicular to the overall fissure structure. Intrusions (red) within the ridge system are part of the lava distributary system within the ridge.

Within the growing edifice, magma was transported in a complex intrusive system (Figure 12). Some dykes are ridge-parallel and cut through pillows that belong to a different compositional group, suggesting that dykes played an important role in transporting magma along-axis. Irregular intrusions are exposed in both Undirhlíðar ridge and in Vatnsskarð quarry. Some have open tube structures and others show evidence of collapsed tube structures, such as shelves and lava drips that are typical of lava tubes in subaerial and glaciovolcanic systems (Hungerford et al., 2014). The irregular and massive intrusions frequently are the same composition as the lavas into which they intrude. We interpret these to be part of the shallow plumbing system of the growing pillow edifice, which were important for distributing magma locally.

Emplacement conditions and the magma source changed as the edifice grew. Eruptions forming the lowermost units were fed by more-enriched mantle melts emplaced into a ~200 m thick ice sheet under glaciostatic conditions. Eruptions forming the bulk of the ridge were fed by less-enriched mantle melts. These less-enriched lavas degassed to variable extents under dynamically shifting hydrologic conditions along the length of the ridge. Less-enriched melts continued to feed eruptions forming the uppermost units, where emplacement conditions were glaciostatic.

We originally proposed a sequence of events for the construction of the volcanic succession exposed at Undirhlíðar quarry that included multiple eruptive and intrusive phases (Pollock et al., 2014). This study expands on previous work by adding detailed lithostratigraphic mapping of Vatnskarð quarry, additional major and trace element data, and new volatile and isotope analyses. Using the field relationships and geochemical findings from this study, we extend the model to the formation of Undirhlíðar ridge that is summarized as follows (Figure 13):

1. The entire ridge was emplaced upon a glaciated surface of pre-existing glaciovolcanic deposits, presumably from an early glaciation. Limited exposures show palagonitized tuff-breccia unconformably overlain by discontinuous gravels.
2. The lower units at the northern extent of Undirhlíðar ridge were emplaced in an initial eruptive phase under ice at least ~200 m thick. These lavas (Lp1-2) were fed from a cooling crustal magma reservoir supplied by melts from a more-enriched mantle source. The eruptive events were mainly effusive, punctuated by pauses and collapse events that deposited stratified layers of vitric tuff and tuff-breccia at the fronts of advancing pillow mounds. At both quarries the lower two pillow units show similar relationships (Pollock et al., 2014; Figure 10) and are overlain locally by lapilli tuff and tuff-breccia. Intrusions are also present in Lp2 at both quarries, although in Vatnskarð the within ridge plumbing is better exposed.
3. The bulk of the ridge was emplaced in subsequent eruptive phases under dynamically changing ice conditions. At Undirlhiðar quarry this phase is mainly preserved as Lp3 (Pollock et al., 2014) but in Vatnskarð quarry the ridge is higher and shows the emplacement of three more pillow units (Lp3-Lp5). This phase was triggered by the injection of melts from a less-enriched mantle source into the crust. In this primary ridge-building phase, separate crustal melt reservoirs fed multiple eruptive vents along the fissure. Draining melt channels and an ephemeral englacial lake created rapidly changing emplacement pressures along the length of the ridge. Eruption style shifted between effusive and explosive, combining with localized pauses in volcanic activity to deposit lenses of tephra between growing pillow mounds. Magma was transported to the margins of the growing edifice through an internal plumbing system of shallow, irregularly shaped intrusions.
4. A final eruptive phase smaller than the others emplaced the final pillow lava unit (Lp6) as well as dykes near the center of the ridge. These lavas were fed by a crustal melt reservoir containing mixed magma that had cooled and crystallized to a greater degree in the crust.
5. The eruption ceased and the edifice was covered by ice, producing the capping layer of glaciofluvial diamict.

By sampling and mapping Undirhlíðar ridge at a high-resolution, we are able to test general models for the construction of tindar ridges. Our study confirms some aspects of the theoretical models, namely, that 1) pillow-dominated tindar ridges are built through a complex sequence of eruptive phases from multiple eruptive vents that show changing eruptive styles (effusive vs. explosive) and 2) hydrologic conditions are dynamic on small spatial scales. Our study also adds new insights into the enigmatic aspects of the theoretical models, namely, that shallow-level intrusions are important to distributing lava within the growing pillow edifice.

5.4 Comparison to subaerial Fagradalsfjall eruption

The 2021–22 eruptions at Fagradalsfjall, which is located on the volcanic system adjacent to the western side of Krýsuvík, allows us to use direct observations of a subaerial fissure eruption to surmise details that cannot be observed in subglacial environments. At Undirhlíðar ridge, pillow orientations and compositions provide evidence for multiple eruptive vents, but it is not possible to know the number or spacing of active vents. Variations in stratigraphic packages are consistent with numerous eruptive pulses, but it is difficult to determine the duration of the Undirhlíðar ridge eruption. Volcanic activity at Fagradalsfjall lasted for ~6 months, followed by a ~2-week eruption nearly a year later (Pedersen et al., 2022). At least five eruptive vents opened along a ~2 km long fissure segment (Bindeman et al., 2022; Pedersen et al., 2022). Volcanic activity pulsated and eruption style shifted between effusive lava extrusion and more explosive fire fountaining (Bindeman et al., 2022; Halldórsson et al., 2022). The resulting lava field covers an area of ~5 km^2 with a DRE volume of ~0.1 km^3 (Bindeman et al., 2022) and an average estimated thickness of 30 m (Pedersen et al., 2022) Like Fagradalsfjall, Undirhlíðar ridge was built by a moderately-sized eruption that occurred along a fissure segment on the order of 3–4 km long, and has an area of about 4.3 km^2. Pillow-dominated tindars like Undirhlíðar ridge are interpreted to be the result of short-duration, small-volume monogenetic events (Jakobsson and Johnson, 2012). Such events have been observed in modern glaciovolcanic eruptions at Eyjafjallajökull (2010) and Gjalp (1996) (Thordarson and Larsen, 2007; Gudmundsson et al., 2012). Despite the difference in eruptive environments, the spatial and temporal scales of the Fagradalsfjall eruption may be similar to the tindar-building fissure eruption that constructed Undirhlíðar ridge.

Direct geophysical and petrological observations at Fagradalsfjall yield insights into the processes that initiated the Undirhlíðar ridge eruption. At Undirhlíðar ridge, lavas with different mantle source signatures were erupted sequentially from separate crustal melt reservoirs, suggesting that the main ridge-building event was triggered by injection of magma into the crustal plumbing system. At Fagradalsfjall, the eruption was fed from a lower crustal magma reservoir at near-Moho (~15–20 km) depths, supplied with chemically variable melts from a heterogeneous mantle (Bindeman et al., 2022; Halldórsson et al., 2022). Erupted lava compositions at Fagradalsfjall progressively transitioned to more enriched mantle melts (Bindeman et al., 2022; Halldórsson et al., 2022). The addition of enriched melts to a deep crustal magma reservoir may have

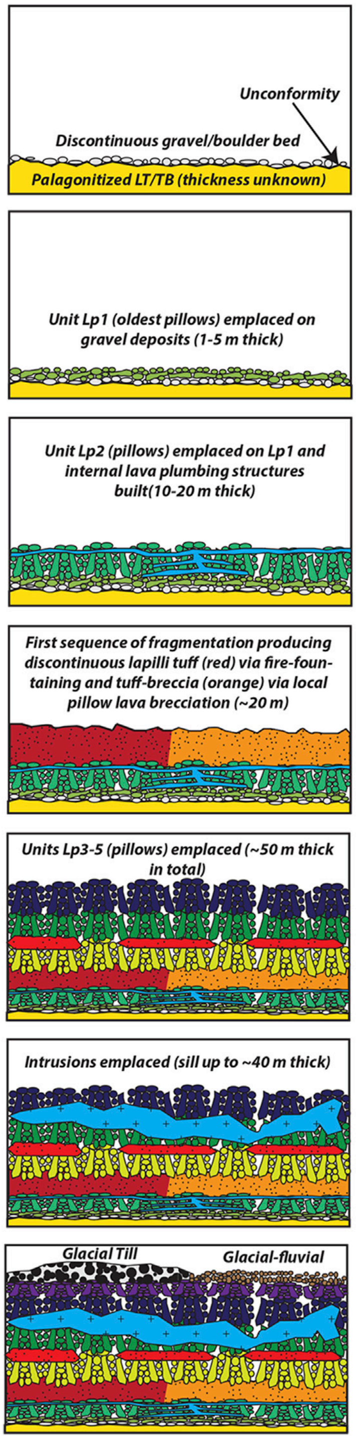

Pre-eruption surface is an eroded, older palagonitized tuff-breccia unit locally overlain by gravel-sized sediment

Phase 1: eruption of Lp1 as relatively thin but laterally extensive pillow sheet(?)

Phase 2: eruption of Lp2 and development of within ridge lava distributory system (lava tubes)

Phase 3: production of vitric tuff-breccia and lapilli tuff via subaqueous fire-fountaining and local pillow pile collapse

Phases 4-6: emplacement of pillow lava units Lp3-5 with local, minor tuff-breccia mainly between Lp3 and Lp4

Phase 7: major intrusions emplaced into mainly Lp4

Phase 8: last discernable pillow unit emplaced (Lp6) with subsequent deposition of glacial-fluvial sediments and glacial till

FIGURE 13
Formation sequence for Undirhlíðar tindar based on exposures in Vatnskarð quarry. Panels are labeled with main eruption events. Unit colors are the same as in the legend for Figure 3.

caused a mixing event that initiated magma ascent and eruption (Halldórsson et al., 2022). In the months leading up to the Fagradalsfjall eruption, seismic swarms and surface inflation were attributed to subsurface magma migration (Cubuk-Sabuncu et al., 2021; Geirsson et al., 2021; Sigmundsson et al., 2022). At least a year prior to the geophysical signals of volcano-tectonic unrest, the deep magma chamber experienced a disequilibrium event (Kahl et al., 2022). Diffusion modeling of olivine and plagioclase crystals suggests that the onset of disequilibrium in the deep magma chamber was related to magma injection and mush disaggregation (Kahl et al., 2022). At both Fagradalsfjall and Undirhlíðar ridge, the supply of heterogeneous mantle melts to the deep parts of the magmatic system played a critical role in initiating eruptions (e.g., Kahl et al., 2022).

The relative locations of the Krýsuvík andFagradalsfjall volcanic systems allows us to comment on spatial variations in mantle composition under the Reykjanes Peninsula. Bindeman et al. (2022) identified at least three different mantle components in the Fagradalsfjall lavas and proposed a lateral gradient in degree of mantle enrichment, in the context of the “plume sheath” suggested by previous researchers (Fitton et al., 1997; Kempton et al., 2000; Murton et al., 2002). The laterally variable plume sheath model predicts that Krýsuvík should erupt lavas more enriched in incompatible trace elements and radiogenic isotopes (Fitton et al., 1997; Kempton et al., 2000; Murton et al., 2002; Bindeman et al., 2022). We find no evidence for a systematic change in mantle composition between Fagradalsfjall and Undirhlíðar ridge. Undirhlíðar ridge has more radiogenic $^{206}Pb/^{204}Pb$ and $^{208}Pb/^{204}Pb$ than Fagradalsfjall, but Sr-Nd isotopes do not show the same enrichment. Fagradalsfjall incompatible trace element ratios overlap with and extend beyond the Undirhlíðar ridge data. The Undirhlíðar ridge and Fagradalsfjall eruptions capture magmatic conditions for moments in time, reflecting complex interactions among the scale of mantle source heterogeneity, the region of melt generation, and the mechanism of melt extraction (e.g., Peate et al., 2009). A more appropriate evaluation of the lateral plume sheath model should examine the full range of trace element and isotope compositions erupted at each of the volcanic systems on the Reykjanes Peninsula over the longest available time frames (e.g., Gee et al., 1998; Peate et al., 2009).

6 Conclusion

Our work presents one of the most comprehensive geochemical and physical investigations of a single pillow-dominated tindar to date. We add to existing models for tindar formation by addressing details not easily identified in natural erosional exposures. We provide evidence for magmatic processes that produce geochemical diversity within the ridge stratigraphy and intrusions that play a significant role in ridge growth. The nearby eruption at Fagradalsfjall provides a modern analogue that is useful for understanding the events at Undirhlíðar ridge. Despite the difference in eruption environment, the Fagradalsfjall and Undirhlíðar ridge eruptions may have been triggered by similar mixing events and occurred over comparable spatial and temporal scales. Overall, we confirm that tindar ridges are built through a complex series of extrusive and intrusive events under changing hydrologic conditions.

Data availability statement

The original contributions presented in the study are included in the article/Supplementary Material, further inquiries can be directed to the corresponding author.

Author contributions

MP: Conceptualization, methodology, investigation, analysis, writing (all phases), visualization, supervision, project administration, funding acquisition. BE: Conceptualization, methodology, investigation, analysis, writing (all phases), visualization, supervision, project administration, funding acquisition. SJ: Analysis, data curation, visualization. CW, AH, AP, and EW: Investigation, visualization. SH: Resources, visualization.

Funding

This work was supported by The College of Wooster Luce Fund, the Keck Geology Consortium (NSF EAR 2050697-MP), NSF EAR 0958928 (MP), NSF EAR 1220176 (MP), the Dickinson College Research and Development Committee, and NSF EAR 1220403 (BE).

Acknowledgments

We thank G. Dwyer for ICP-MS and DCP analyses, D. Coleman and R. Mills for isotope analyses, and S. Seaman for FTIR analyses. Thanks to GAIN for help with manuscript preparation and G. Einarsson (ÍSOR) for supplying information for Figure 1. For their assistance in the field and lab, we thank J. Ciarrocca, J. Franceschi, W. Kochtitzky, B. Kumpf, E. Plascencia, M. Reinthal, A. Silverstein, T. Spillman, M. Williams, and the 2016 Keck Iceland Team. This paper benefited from inspiring discussions with K. Sæmundsson and M.T. Gudmundsson.

Conflict of interest

The authors declare that the research was conducted in the absence of any commercial or financial relationships that could be construed as a potential conflict of interest.

Publisher’s note

Supplementary material

The Supplementary Material for this article can be found online at: https://www.frontiersin.org/articles/10.3389/feart.2023.1095135/full#supplementary-material

References

Allmendinger, R. W., Cardozo, N. C., and Fisher, D. (2013). *Structural Geology Algorithms: Vectors and Tensors*. Cambridge, England: Cambridge University Press.

Bindeman, I. N., Deegan, F. M., Troll, V. R., Thordarson, T., Höskuldsson, Á., Moreland, W. M., et al. (2022). Diverse mantle components with invariant oxygen isotopes in the 2021 Fagradalsfjall eruption, Iceland. *Nat Commun* 13, 3737. doi:10.1038/s41467-022-31348-7

Bottinga, Y., and Weill, D. F. (1972). The viscosity of magmatic silicate liquids; a model calculation. *American Journal of Science* 272, 438–475. doi:10.2475/ajs.272.5.438

Boyd, F. R., and Mertzman, S. A. (1987). *Composition and structure of the Kaapvaal lithosphere, Southern Africa*, 1. University Park, PA: Special Publication - Geochemical Society, 13–24.

Cardozo, N. C., and Allmendinger, R. W. (2013). Spherical projections with OSXStereonet. *Computers and Geosciences* 51, 193–205. doi:10.1016/j.cageo.2012.07.021

Chauvel, C., and Hémond, C. (2000). Melting of a complete section of recycled oceanic crust: Trace element and Pb isotopic evidence from Iceland. *Geochemistry, Geophysics, Geosystems* 1. doi:10.1029/1999GC000002

Cheatham, M. M., Sangrey, W. F., and White, W. M. (1993). Sources of error in external calibration ICP-MS analysis of geological samples and an improved non-linear drift correction procedure. *Spectrochimica Acta Part B: Atomic Spectroscopy* 48, 487–506. doi:10.1016/0584-8547(93)80054-X

Condomines, M., Grönvold, K., Hooker, P. J., Muehlenbachs, K., O'Nions, R. K., Óskarsson, N., et al. (1983). Helium, oxygen, strontium and neodymium isotopic relationships in Icelandic volcanics. *Earth and Planetary Science Letters* 66, 125–136. doi:10.1016/0012-821X(83)90131-0

Cubuk-Sabuncu, Y., Jónsdóttir, K., Caudron, C., Lecocq, T., Parks, M. M., Geirsson, H., et al. (2021). Temporal Seismic Velocity Changes During the 2020 Rapid Inflation at Mt. Þorbjörn-Svartsengi, Iceland, Using Seismic Ambient Noise. *Geophysical Research Letters* 48, e2020GL092265. doi:10.1029/2020GL092265

Dixon, J. E., and Clague, D. A. (2001). Volatiles in basaltic glasses from Loihi Seamount, Hawaii: Evidence for a relatively dry plume component. *Journal of Petrology* 42, 627–654. doi:10.1093/petrology/42.3.627

Dixon, J. E., and Stolper, E. M. (1995). An experimental study of water and carbon dioxide solubilities in mid-ocean ridge basaltic liquids. Part II: Applications to degassing. *Journal of Petrology* 36, 1633–1646. doi:10.1093/oxfordjournals.petrology.a037268

Dixon, J. E., Stolper, E. M., and Holloway, J. R. (1995). An experimental study of water and carbon dioxide solubilities in mid-ocean ridge basaltic liquids. Part I: Calibration and solubility models. *Journal of Petrology* 36, 1607–1631. doi:10.1093/oxfordjournals.petrology.a037267

Doherty, W. (1989). An internal standardization procedure for the determination of yttrium and the rare earth elements in geological materials by inductively coupled plasma-mass spectrometry. *Spectrochimica Acta Part B: Atomic Spectroscopy* 44, 263–280. doi:10.1016/0584-8547(89)80031-X

Eason, D. E., Sinton, J., Gronvold, K., and Kurz, M. D. (2015). Effects of deglaciation on the petrology and eruptive history of the Western Volcanic Zone, Iceland. *Bulletin of Volcanology* 77, 47. doi:10.1007/s00445-015-0916-0

Eason, D. E., and Sinton, J. M. (2009). Lava shields and fissure eruptions of the Western Volcanic Zone, Iceland: Evidence for magma chambers and crustal interaction. *Journal of Volcanology and Geothermal Research* 186, 331–348. doi:10.1016/j.jvolgeores.2009.06.009

Edwards, B., Magnússon, E., Thordarson, T., Guðmundsson, M. T., Höskuldsson, A., Oddsson, B., et al. (2012). Interactions between lava and snow/ice during the 2010 Fimmvörðuháls eruption, south-central Iceland. *Journal of Geophysical Research: Solid Earth* 117. doi:10.1029/2011JB008985

Edwards, B. R., Russell, J. K., Jicha, B., Singer, B. S., Dunnington, G., and Jensen, R. (2020). "A 3 million year record of volcanism and glaciation in northern British Columbia, Canada," *Geological Society of America Special Paper, Untangling the Quaternary Period: A Legacy of Stephen C. Porter*. Editors R. B. Waitt, G. D. Thackray, and A. R. Gillespie doi:10.1130/2020.2548

Edwards, B. R., Russell, J. K., and Simpson, K. (2011). Volcanology and petrology of Mathews Tuya, northern British Columbia, Canada: glaciovolcanic constraints on interpretations of the 0.730 Ma Cordilleran paleoclimate. *Bull Volcanol* 73, 479–496. doi:10.1007/s00445-010-0418-z

Edwards, B. R., Russell, J. K., and Pollock, M. (2022). Cryospheric forcing on volcano-magmatic systems. *Front. Earth Sci.* 10, 871951. doi:10.3389/feart.2022.871951

Edwards, B. R., Skilling, I. P., Cameron, B., Haynes, C., Lloyd, A., and Hungerford, J. H. D. (2009). Evolution of an englacial volcanic ridge: Pillow Ridge tindar, Mount Edziza volcanic complex, NCVP, British Columbia, Canada. *Journal of Volcanology and Geothermal Research* 185, 251–275. doi:10.1016/j.jvolgeores.2008.11.015

Einarsson, T., Albertsson, K. J., Shackleton, N. J., West, R. G., and Bowen, D. Q. (1988). The glacial history of Iceland during the past three million years. *Philosophical Transactions of the Royal Society of London. B, Biological Sciences* 318, 637–644. doi:10.1098/rstb.1988.0027

Eysteinsson, H. (2001). *Resistivity measurements around Trölladyngja and Núpshlíðarháls, Reykjanes Peninsula*. NEA Report OS-2001/038.

Fine, G., and Stolper, E. (1985). The speciation of carbon dioxide in sodium aluminosilicate glasses. *Contr. Mineral. and Petrol.* 91, 105–121. doi:10.1007/BF00377759

Fitton, J. G., Saunders, A. D., Kempton, P. D., and Hardarson, B. S. (2003). Does depleted mantle form an intrinsic part of the Iceland plume? *Geochemistry, Geophysics, Geosystems* 4. doi:10.1029/2002GC000424

Fitton, J. G., Saunders, A. D., Norry, M. J., Hardarson, B. S., and Taylor, R. N. (1997). Thermal and chemical structure of the Iceland plume. *Earth and Planetary Science Letters* 153, 197–208. doi:10.1016/S0012-821X(97)00170-2

Flóvenz, Ó. G., Wang, R., Hersir, G. P., Dahm, T., Hainzl, S., Vassileva, M., et al. (2022). Cyclical geothermal unrest as a precursor to Iceland's 2021 Fagradalsfjall eruption. *Nat. Geosci.* 15, 397–404. doi:10.1038/s41561-022-00930-5

Gee, M. A. M., Thirlwall, M. F., Taylor, R. N., Lowry, D., Murton, B. J., and Bohrson, W. A. (1998). Crustal processes; major controls on Reykjanes Peninsula lava chemistry, SW Iceland. *J.Petrol.* 39, 819–839. doi:10.1093/petroj/39.5.819

Geirsson, H., Parks, M., Vogfjörd, K., Einarsson, P., Sigmundsson, F., Jónsdóttir, K., et al. (2021). The 2020 volcano-tectonic unrest at Reykjanes Peninsula, Iceland: stress triggering and reactivation of several volcanic systems. EGU21-7534. doi:10.5194/egusphere-egu21-7534

Ghiorso, M. S., Hirschmann, M. M., Reiners, P. W., and Kress, V. C. (2002). The pMELTS; a revision of MELTS for improved calculation of phase relations and major element partitioning related to partial melting of the mantle to 3 GPa. *Geochemistry Geophysics Geosystems* 3, 1–35. doi:10.1029/2001gc000217

Ghiorso, M. S., and Sack, R. O. (1995). Chemical mass transfer in magmatic processes IV. A revised and internally consistent thermodynamic model for the interpolation and extrapolation of liquid-solid equilibria in magmatic systems at elevated temperatures and pressures. *Contributions to Mineralogy and Petrology* 119, 197–212. doi:10.1007/bf00307281

Global Volcanism Program (2022a). Report on Fagradalsfjall (Iceland) — 3 August-9 August 2022. Available at: https://volcano.si.edu/ShowReport.cfm?wvar=GVP.WVAR20220803-371032 (Accessed September 26, 2022).

Global Volcanism Program (2022b). Report on Fagradalsfjall (Iceland) — 17 August-23 August 2022). Available at: https://volcano.si.edu/ShowReport.cfm?wvar=GVP.WVAR20220817-371032 (Accessed September 26, 2022).

Global Volcanism Program (2022c). Report on Fagradalsfjall (Iceland) — 27 July-2 August 2022. Available at: https://volcano.si.edu/ShowReport.cfm?wvar=GVP.WVAR20220727-371032 (Accessed September 26, 2022).

Gudmundsson, M., Larsen, G., Höskuldsson, Á., and Gylfason, Á. G. (2008). Volcanic hazards in Iceland. *Jökull* 58, 251–268.

Gudmundsson, M., Sigmundsson, F., and Björnsson, H. (1997). Ice–volcano interaction of the 1996 Gjálp subglacial eruption, Vatnajökull, Iceland. *Nature* 389, 954–957. doi:10.1038/40122

Gudmundsson, M. T. (2005). "6. Subglacial volcanic activity in Iceland," in *Developments in Quaternary Sciences Iceland — Modern Processes and Past Environments*. Editors C. Caseldine, A. Russell, J. Harðardóttir, and Ó. Knudsen (Amsterdam, Netherlands: Elsevier), 127–151. doi:10.1016/S1571-0866(05)80008-9

Gudmundsson, M. T., Sigmundsson, F., Björnsson, H., and Högnadóttir, T. (2004). The 1996 eruption at Gjalp, Vatnajokull ice cap, Iceland: efficiency of heat transfer, ice deformation and subglacial water pressure. *Bulletin of Volcanology* 66, 46–65. doi:10.1007/s00445-003-0295-9

Gudmundsson, M. T., Thordarson, T., Höskuldsson, Á., Larsen, G., Björnsson, H., Prata, F. J., et al. (2012). Ash generation and distribution from the April-May 2010 eruption of Eyjafjallajökull, Iceland. *Sci Rep* 2, 572. doi:10.1038/srep00572

Halldórsson, S. A., Barnes, J. D., Stefánsson, A., Hilton, D. R., Hauri, E. H., and Marshall, E. W. (2016). Subducted lithosphere controls halogen enrichments in the Iceland mantle plume source. *Geology* 44, 679–682. doi:10.1130/G37924.1

Halldórsson, S. A., Marshall, E. W., Caracciolo, A., Matthews, S., Bali, E., Rasmussen, M. B., et al. (2022). Rapid shifting of a deep magmatic source at Fagradalsfjall volcano, Iceland. *Nature* 609, 529–534. doi:10.1038/s41586-022-04981-x

Hanan, B. B., Blichert-Toft, J., Kingsley, R., and Schilling, J.-G. (2000). Depleted Iceland mantle plume geochemical signature: Artifact of multicomponent mixing? *Geochemistry, Geophysics, Geosystems* 1. doi:10.1029/1999GC000009

Hanan, B. B., and Schilling, J.-G. (1997). The dynamic evolution of the Iceland mantle plume: the lead isotope perspective. *Earth and Planetary Science Letters* 151, 43–60. doi:10.1016/S0012-821X(97)00105-2

Hemond, C., Arndt, N. T., Lichtenstein, U., Hofmann, A. W., Oskarsson, N., and Steinthorsson, S. (1993). The heterogeneous Iceland plume: Nd-Sr-O isotopes and trace element constraints. *Journal of Geophysical Research: Solid Earth* 98, 15833–15850. doi:10.1029/93JB01093

Hemond, Ch., Condomines, M., Fourcade, S., Allègre, C. J., Oskarsson, N., and Javoy, M. (1988). Thorium, strontium and oxygen isotopic geochemistry in recent tholeiites from Iceland: crustal influence on mantle-derived magmas. *Earth and Planetary Science Letters* 87, 273–285. doi:10.1016/0012-821X(88)90015-5

Hersir, G. P., Árnason, K., Vilhjálmsson, A. M., Saemundsson, K., Ágústsdóttir, Þ., and Friðleifsson, G. Ó. (2020). Krýsuvík high temperature geothermal area in SW Iceland: Geological setting and 3D inversion of magnetotelluric (MT) resistivity data. *Journal of Volcanology and Geothermal Research* 391, 106500. doi:10.1016/j.jvolgeores.2018.11.021

Höskuldsson, A., Sparks, R. S. J., and Carroll, M. R. (2006). Constraints on the dynamics of subglacial basalt eruptions from geological and geochemical observations at Kverkfjoll, NE-Iceland. *Bull. Volc.* 68, 689–701. doi:10.1007/s00445-005-0043-4

Hungerford, J. D. G., Edwards, B. R., Skilling, I. P., and Cameron, B. I. (2014). Evolution of a subglacial basaltic lava flow field: Tennena volcanic center, Mount Edziza volcanic complex, British Columbia, Canada. *Journal of Volcanology and Geothermal Research* 272, 39–58. doi:10.1016/j.jvolgeores.2013.09.012

Jakobsson, S. P., and Gudmundsson, M. T. (2008). Subglacial and intraglacial volcanic formations in Iceland. *Jökull* 58, 179–196.

Jakobsson, S. P., and Johnson, G. L. (2012). Intraglacial volcanism in the Western Volcanic Zone, Iceland. *Bull Volcanol* 74, 1141–1160. doi:10.1007/s00445-012-0589-x

Jakobsson, S. P., Jonsson, J., and Shido, F. (1978). Petrology of the western Reykjanes Peninsula, Iceland. *J.Petrol.* 19, 669–705. doi:10.1093/petrology/19.4.669

Jarvis, K. E. (1988). Inductively coupled plasma mass spectrometry: A new technique for the rapid or ultra-trace level determination of the rare-earth elements in geological materials. *Chemical Geology* 68, 31–39. doi:10.1016/0009-2541(88)90084-8

Jenner, G. A., Longerich, H. P., Jackson, S. E., and Fryer, B. J. (1990). ICP-MS — A powerful tool for high-precision trace-element analysis in Earth sciences: Evidence from analysis of selected U.S.G.S. reference samples. *Chemical Geology* 83, 133–148. doi:10.1016/0009-2541(90)90145-W

Jones, J. G. (1969). Intraglacial volcanoes of the Laugarvatn region, south-west Iceland, I. *Quarterly Journal of the Geological Society* 124, 197–211. doi:10.1144/gsjgs.124.1.0197

Jones, J. G. (1970). Intraglacial volcanoes of the Laugarvatn region, southwest Iceland, II. *J.Geol.* 78, 127–140. doi:10.1086/627496

Jónsson, J. (1978). *Jarðfræðikort af Reykjanesskaga (Geological map of Reykjanes Peninsula).* Orkustofnun JHD, Reykjavik: Iceland Energy Authority.

Kahl, M., Mutch, E. J. F., Maclennan, J., Morgan, D. J., Couperthwaite, F., Bali, E., et al. (2022). Deep magma mobilization years before the 2021 CE Fagradalsfjall eruption, Iceland. *Geology* 51, 184–188. doi:10.1130/G50340.1

Kempton, P. D., Fitton, J. G., Saunders, A. D., Nowell, G. M., Taylor, R. N., Hardarson, B. S., et al. (2000). The Iceland plume in space and time: a Sr–Nd–Pb–Hf study of the North Atlantic rifted margin. *Earth and Planetary Science Letters* 177, 255–271. doi:10.1016/S0012-821X(00)00047-9

Klein, E. M., Langmuir, C. H., and Staudigel, H. (1991). Geochemistry of basalts from the southeast Indian Ridge, 115°E–138°E. *Journal of Geophysical Research: Solid Earth* 96, 2089–2107. doi:10.1029/90JB01384

Kokfelt, T. F., Hoernle, K., Hauff, F., Fiebig, J., Werner, R., and Barge-Schonberg, G. (2006). Combined trace element and Pb-Nd–Sr-O isotope evidence for recycled oceanic crust (upper and lower) in the Iceland mantle plume. *Journal of Petrology* 47, 1705–1749. doi:10.1093/petrology/egl025

Koornneef, J. M., Stracke, A., Bourdon, B., Meier, M. A., Jochum, K. P., Stoll, B., et al. (2012). Melting of a Two-component Source beneath Iceland. *Journal of Petrology* 53, 127–157. doi:10.1093/petrology/egr059

Langmuir, C. H., Vocke, R. D., Hanson, G. N., and Hart, S. R. (1978). A general mixing equation with applications to Icelandic basalts. *Earth and Planetary Science Letters* 37, 380–392. doi:10.1016/0012-821X(78)90053-5

Le Breton, E., Dauteuil, O., and Biessy, G. (2010). Post-glacial rebound of Iceland during the Holocene. *Journal of the Geological Society* 167, 417–432. doi:10.1144/0016-76492008-126

Lescinsky, D. T., and Fink, J. H. (2000). Lava and ice interaction at stratovolcanoes: Use of characteristic features to determine past glacial extents and future volcanic hazards. *Journal of Geophysical Research: Solid Earth* 105, 23711–23726. doi:10.1029/2000JB900214

Licciardi, J. M., Kurz, M. D., and Curtice, J. M. (2007). Glacial and volcanic history of Icelandic table mountains from cosmogenic 3He exposure ages. *Quaternary Science Reviews* 26, 1529–1546. doi:10.1016/j.quascirev.2007.02.016

Lichte, F. E., Meier, A. L., and Crock, J. G. (1987). Determination of the rare-earth elements in geological materials by inductively coupled plasma mass spectrometry. *Analytical Chemistry* 59, 1150–1157. doi:10.1021/ac00135a018

Longerich, H. P., Jenner, G. A., Fryer, B. J., and Jackson, S. E. (1990). Inductively coupled plasma-mass spectrometric analysis of geological samples: A critical evaluation based on case studies. *Chemical Geology* 83, 105–118. doi:10.1016/0009-2541(90)90143-U

Maclennan, J. (2008). Concurrent mixing and cooling of melts under Iceland. *Journal of Petrology* 49, 1931–1953. doi:10.1093/petrology/egn052

Maclennan, J., McKenzie, D., Hilton, F., Gronvöld, K., and Shimizu, N. (2003). Geochemical variability in a single flow from northern Iceland. *Journal of Geophysical Research: Solid Earth* 108, ECV 4-1–ECV 4-21. doi:10.1029/2000JB000142

Magnússon, E., Gudmundsson, M. T., Roberts, M. J., Sigurðsson, G., Höskuldsson, F., and Oddsson, B. (2012). Ice-volcano interactions during the 2010 Eyjafjallajökull eruption, as revealed by airborne imaging radar. *Journal of Geophysical Research: Solid Earth* 117. doi:10.1029/2012JB009250

McDonough, W. F., and Sun, S. -S. (1995). The composition of the Earth. *Chemical Geology* 120, 223–253. doi:10.1016/0009-2541(94)00140-4

Mcintosh, I. M., Nichols, A. R. L., Tani, K., and Llewellin, E. W. (2017). Accounting for the species-dependence of the 3500 cm−1 H2Ot infrared molar absorptivity coefficient: Implications for hydrated volcanic glasses. *American Mineralogist* 102, 1677–1689. doi:10.2138/am-2017-5952CCBY

McIntosh, I. M., Tani, K., Nichols, A. R. L., Chang, Q., and Kimura, J.-I. (2022). Past eruptions of a newly discovered active, shallow, silicic submarine volcano near Tokyo Bay, Japan. *Geology* 50, 1111–1115. doi:10.1130/G50148.1

McKenzie, D., and O'Nions, R. K. (1991). Partial melt distributions from inversion of rare earth element concentrations. *Journal of Petrology* 32, 1021–1091. doi:10.1093/petrology/32.5.1021

McKenzie, D., and O'Nions, R. K. (1995). The source regions of ocean island basalts. *Journal of Petrology* 36, 133–159. doi:10.1093/petrology/36.1.133

Miller, J. S., and Glazner, A. F. (1995). Jurassic plutonism and crustal evolution in the central Mojave Desert, California. *Contr. Mineral. and Petrol.* 118, 379–395. doi:10.1007/s004100050021

Momme, P., Óskarsson, N., and Keays, R. R. (2003). Platinum-group elements in the Icelandic rift system: melting processes and mantle sources beneath Iceland. *Chemical Geology* 196, 209–234. doi:10.1016/S0009-2541(02)00414-X

Moore, J. G., Hickson, C. J., and Calk, L. C. (1995). Tholeiitic-alkalic transition at subglacial volcanoes, Tuya region, British Columbia, Canada. *Journal of Geophysical Research* 100, 24577–24592. doi:10.1029/95jb02509

Murton, B. J., Taylor, R. N., and Thirlwall, M. F. (2002). Plume–ridge interaction: a geochemical perspective from the Reykjanes Ridge. *Journal of Petrology* 43, 1987–2012. doi:10.1093/petrology/43.11.1987

Newman, S., and Lowenstern, J. B. (2002). VolatileCalc: a silicate melt–H2O–CO2 solution model written in Visual Basic for excel. *Computers and Geosciences* 28, 597–604. doi:10.1016/S0098-3004(01)00081-4

Nichols, A. R. L., Carroll, M. R., and Hoskuldsson, A. (2002). Is the Iceland hot spot also wet? Evidence from the water contents of undegassed submarine and subglacial pillow basalts. *Earth and Planetary Science Letters* 202, 77–87. doi:10.1016/S0012-821X(02)00758-6

Oddsson, B., Gudmundsson, M. T., Edwards, B. R., Thordarson, T., Magnússon, E., and Sigurðsson, G. (2016). Subglacial lava propagation, ice melting and heat transfer during emplacement of an intermediate lava flow in the 2010 Eyjafjallajökull eruption. *Bull Volcanol* 78, 48–17. doi:10.1007/s00445-016-1041-4

Patton, H., Hubbard, A., Bradwell, T., and Schomacker, A. (2017). The configuration, sensitivity and rapid retreat of the Late Weichselian Icelandic ice sheet. *Earth-Science Reviews* 166, 223–245. doi:10.1016/j.earscirev.2017.02.001

Peate, D. W., Baker, J. A., Jakobsson, S. P., Waight, T. E., Kent, A. J. R., Grassineau, N. V., et al. (2009). Historic magmatism on the Reykjanes Peninsula, Iceland; a snap-shot of melt generation at a ridge segment. *Contributions to Mineralogy and Petrology* 157, 359–382. doi:10.1007/s00410-008-0339-4

Pedersen, G. B. M., Belart, J. M. C., Óskarsson, B. V., Gudmundsson, M. T., Gies, N., Högnadóttir, T., et al. (2022). Volume, Effusion Rate, and Lava Transport During the 2021 Fagradalsfjall Eruption: Results From Near Real-Time Photogrammetric Monitoring. *Geophysical Research Letters* 49, e2021GL097125. doi:10.1029/2021GL097125

Pollock, M., Edwards, B., Hauksdóttir, S., Alcorn, R., and Bowman, L. (2014). Geochemical and lithostratigraphic constraints on the formation of pillow-dominated tindars from Undirhlíðar quarry, Reykjanes Peninsula, southwest Iceland. *Lithos* 200– 201, 317–333. doi:10.1016/j.lithos.2014.04.023

Russell, J. K., Edwards, B. R., Porritt, L., and Ryane, C. (2014). Tuyas: a descriptive genetic classification. *Quaternary Science Reviews* 87, 70–81. doi:10.1016/j.quascirev.2014.01.001

Saemundsson, K. (1979). Outline of the geology of Iceland. *Jökull* 29, 7–28.

Sæmundsson, K., Sigurgeirsson, M. Á., and Friðleifsson, G. Ó. (2020). Geology and structure of the Reykjanes volcanic system, Iceland. *Journal of Volcanology and Geothermal Research* 391, 106501. doi:10.1016/j.jvolgeores.2018.11.022

Sæmundsson, K., Sigurgeirsson, M. Á., Hjartarson, Á., Kaldal, I., and Kristinsson, S. G. (2016). Geological Map of of Southwest Iceland. Available at: https://en.isor.is/geological-maps-geological-web-map.

Sano, T., and Yamashita, S. (2019). Evolution, hydrothermal assimilation, and ascent of magma inferred from volatile contents in MORB glasses: An example from thick lava pile at IODP Site 1256. *Lithos* 346–347, 105143. doi:10.1016/j.lithos.2019.07.010

Schilling, J.-G. (1973). Iceland mantle plume: Geochemical study of Reykjanes Ridge. *Nature* 242, 565–571. doi:10.1038/242565a0

Schopka, H. H., Gudmundsson, M. T., and Tuffen, H. (2006). The formation of Helgafell, southwest Iceland, a monogenetic subglacial hyaloclastite ridge; sedimentology, hydrology and volcano-ice interaction. *J.Volcanol.Geotherm.Res.* 152, 359–377. doi:10.1016/j.jvolgeores.2005.11.010

Sigmundsson, F., Parks, M., Hooper, A., Geirsson, H., Vogfjörd, K. S., Drouin, V., et al. (2022). Deformation and seismicity decline before the 2021 Fagradalsfjall eruption. *Nature* 609, 523–528. doi:10.1038/s41586-022-05083-4

Skovgaard, A. C., Storey, M., Baker, J., Blusztajn, J., and Hart, S. R. (2001). Osmium–oxygen isotopic evidence for a recycled and strongly depleted component in the Iceland mantle plume. *Earth and Planetary Science Letters* 194, 259–275. doi:10.1016/S0012-821X(01)00549-0

Smellie, J. L. (2007). “Glacial landforms, Quaternary vulcanism, subglacial landforms,” in *Encyclopedia of Quaternary Science*. Editor S. A. Elias (Oxford: Elsevier), 784–798. doi:10.1016/B0-44-452747-8/00101-0

Smellie, J. L. (2008). Basaltic subglacial sheet-like sequences: Evidence for two types with different implications for the inferred thickness of associated ice. *Earth-Science Reviews* 88, 60–88. doi:10.1016/j.earscirev.2008.01.004

Smellie, J. L. (2013). “Quaternary vulcanism: subglacial landforms,” in *Reference module in Earth Systems and Environmental Sciences The Encyclopedia of Quaternary Science* (Amsterdam: Elsevier), 780–802.

Smellie, J. L. (2018). “Chapter 10 - Glaciovolcanism: A 21st Century Proxy for Palaeo-Ice,” in *Past Glacial Environments*. Editors J. Menzies and J. J. M. van der Meer Second Edition (Amsterdam: Elsevier), 335–375 doi:10.1016/B978-0-08-100524-8.00010-5

Smellie, J. L., and Edwards, B. R. (2016). *Glaciovolcanism on Earth and Mars*. Cambridge, United Kingdom: Cambridge University Press.

Smellie, J. L., Johnson, J. S., McIntosh, W. C., Esser, R., Gudmundsson, M. T., Hambrey, M. J., et al. (2008). Six million years of glacial history recorded in volcanic lithofacies of the James Ross Island Volcanic Group, Antarctic Peninsula. *Palaeogeography, Palaeoclimatology, Palaeoecology* 260, 122–148. doi:10.1016/j.palaeo.2007.08.011

Smith, P. M., and Asimow, P. D. (2005). Adiabat_1ph: A new public front-end to the MELTS, pMELTS, and pHMELTS models. *Geochemistry, Geophysics, Geosystems* 6. doi:10.1029/2004GC000816

Stolper, E. (1982). The speciation of water in silicate melts. *Geochimica et Cosmochimica Acta* 46, 2609–2620. doi:10.1016/0016-7037(82)90381-7

Stracke, A., Bizimis, M., and Salters, V. J. M. (2003). Recycling oceanic crust: Quantitative constraints. *Geochemistry, Geophysics, Geosystems* 4. doi:10.1029/2001GC000223

Sun, S.-S., and Jahn, B. (1975). Lead and strontium isotopes in post-glacial basalts from Iceland. *Nature* 255, 527–530. doi:10.1038/255527a0

Thirlwall, M. F., Gee, M. A. M., Lowry, D., Mattey, D. P., Murton, B. J., and Taylor, R. N. (2006). Low δ18O in the Icelandic mantle and its origins; evidence from Reykjanes Ridge and Icelandic lavas. *Geochim.Cosmochim.Acta* 70, 993–1019. doi:10.1016/j.gca.2005.09.008

Thirlwall, M. F., Gee, M. A. M., Taylor, R. N., and Murton, B. J. (2004). Mantle components in Iceland and adjacent ridges investigated using double-spike Pb isotope ratios. *Geochim.Cosmochim.Acta* 68, 361–386. doi:10.1016/s0016-7037(03)00424-1

Thordarson, T., and Larsen, G. (2007). Volcanism in Iceland in historical time: Volcano types, eruption styles and eruptive history. *Journal of Geodynamics* 43, 118–152. doi:10.1016/j.jog.2006.09.005

Tuffen, H., Owen, J., and Denton, J. (2010). Magma degassing during subglacial eruptions and its use to reconstruct palaeo-ice thicknesses. *Earth-Science Reviews* 99, 1–18. doi:10.1016/j.earscirev.2010.01.001

Wilson, A. M., and Russell, J. K. (2017). Lillooet Glacier basalts, southwestern British Columbia, Canada: products of Quaternary glaciovolcanism. *Can. J. Earth Sci.* 54, 639–653. doi:10.1139/cjes-2016-0201

Wood, D. A., Joron, J.-L., Trueil, M., Norry, M., and Tarney, J. (1979). Elemental and Sr isotope variations in basic lavas from Iceland and the surrounding ocean floor. *Contributions to Mineralogy and Petrology* 70, 319–339. doi:10.1007/bf00375360

Woodcock, D. C., Lane, S. J., and Gilbert, J. S. (2016). Ice-melt rates during volcanic eruptions within water-drained, low-pressure subglacial cavities. *Journal of Geophysical Research: Solid Earth* 121, 648–662. doi:10.1002/2015JB012036

Workman, R. K., and Hart, S. R. (2005). Major and trace element composition of the depleted MORB mantle (DMM). *Earth and Planetary Science Letters* 231, 53–72. doi:10.1016/j.epsl.2004.12.005

frontiers | Frontiers in Earth Science

TYPE Review
PUBLISHED 12 April 2023
DOI 10.3389/feart.2023.1082342

An assessment of potential causal links between deglaciation and eruption rates at arc volcanoes

Chris E. Conway[1]*, Leo R. Pure[2] and Osamu Ishizuka[1]

[1]Research Institute of Earthquake and Volcano Geology, Geological Survey of Japan, AIST, Tsukuba, Japan, [2]Environment Approvals Division, Department of Climate Change, Energy, the Environment and Water, Canberra, ACT, Australia

OPEN ACCESS

EDITED BY
John Smellie,
University of Leicester, United Kingdom

REVIEWED BY
Luis E. Lara,
Servicio Nacional de Geología y Minería de Chile (SERNAGEOMIN), Chile
Vera Ponomareva,
Institute of Volcanology and Seismology, Russia
Benjamin Edwards,
Dickinson College, United States

*CORRESPONDENCE
Chris E. Conway,
✉ c.conway@aist.go.jp

SPECIALTY SECTION
This article was submitted to Volcanology,
a section of the journal
Frontiers in Earth Science

RECEIVED 28 October 2022
ACCEPTED 27 March 2023
PUBLISHED 12 April 2023

CITATION
Conway CE, Pure LR and Ishizuka O (2023), An assessment of potential causal links between deglaciation and eruption rates at arc volcanoes.
Front. Earth Sci. 11:1082342.
doi: 10.3389/feart.2023.1082342

One of the fundamental questions that underpins studies of the interactions between the cryosphere and volcanism is: do causal relationships exist between the ice volume on a volcano and its eruption rate? In particular, it is critical to determine whether the decompression of crustal magma systems *via* deglaciation has resulted in enhanced eruption rates along volcanic arcs in the middle to high latitudes. Evidence for such a feedback mechanism would indicate that ongoing glacier retreat could lead to future increases in eruptive activity. Archives of eruption frequency, size, and style, which can be used to test whether magma generation and eruption dynamics have been affected by local ice volume fluctuations, exist in the preserved eruptive products of Pleistocene-Holocene volcanoes. For this contribution, we have reviewed time-volume-composition trends for 33 volcanoes and volcanic groups in arc settings affected by glaciation, based on published radiometric ages and erupted volumes and/or compositions of edifice-forming products. Of the 33 volcanic systems examined that have geochronological and volumetric data of sufficient resolution to compare to climatic changes since ~250 ka, increases in apparent eruption rates during post-glacial periods were identified for 4, with unclear trends identified for a further 12. Limitations in the geochronological and eruption volume datasets of the case studies make it difficult to test whether apparent eruption rates are correlated with ice coverage. Major caveats are: 1) the potential for biased preservation and exposure of eruptive materials within certain periods of a volcano's lifespan; 2) the relative imprecision of geochronological constraints for volcanic products when compared with high-resolution climate proxy records; 3) the reliance on data only from immediately before and after the Last Glacial Termination (~18 ka), which are rarely compared with trends throughout the Pleistocene to test the reproducibility of eruptive patterns; and 4) the lack of consideration that eruption rates and magma compositions may be influenced by mantle and crustal processes that operate independently of glacial advance/retreat. Addressing these limitations will lead to improvements in the fields of geochronology, paleoclimatology, and eruption forecasting, which could make valuable contributions to the endeavours of mitigating future climate change and volcanic hazards.

KEYWORDS

volcano-climate, glaciovolcanic, eruption history, arc volcanism, Ar/Ar age dating

Introduction

An important goal at the Frontier of Earth science research is to understand the connections between volcanic plumbing systems and crustal pressurization and depressurization caused by glacial advance and retreat. Advancing this goal will improve the understanding of volcano-climate feedback processes on regional and global scales, which may support the long-term forecasting and mitigation of volcanic activity and hazards, and the use of volcanic deposits as climate records. The idea that enhanced rates of volcanism occur as a result of deglaciation has attracted much attention over the last 30 years (Sigvaldason et al., 1992). Maclennan et al. (2002) showed that the rate of volcanic activity in Iceland during the early post-glacial period (~12.5–10 ka) increased by a factor of up to 50. Based on volumetric and geochronologic data for eruptive deposits, this observation has been attributed to a greater degree of mantle melting and a facilitation of magma ascent pathways through the crust as the overburden pressure imposed by glaciers was reduced (Jull and McKenzie, 1996; Figure 1). Patterns of eruption frequency during the Quaternary in eastern California (Jellinek et al., 2004) and western Europe (Nowell et al., 2006) have also been attributed to post-glacial depressurization of the crust in continental intraplate settings. Studies of the response of volcanoes to glacial retreat in continental arc settings have produced varied conclusions. Distal tephra records in marine cores, which provide high temporal resolution to test causality between volcanism and changes in sea-level and/or ice volume over numerous glacial cycles (e.g., Schindlbeck et al., 2018), indicate that periods of enhanced volcanism occurred following deglaciation (Kutterolf et al., 2019). More proximal terrestrial and marine tephra records have provided compositional and volumetric data for studying magma system response to deglaciation, but only for the time period since ~20 ka (Watt et al., 2013; Praetorius et al., 2016; Rawson et al., 2016). Such records can be hampered by the under-recording of relatively small-scale eruptions (Kiyosugi et al., 2015) and the poor preservation of tephras during glacial periods (Watt et al., 2013).

Constraining volumetric eruption rates and magma chemistry evolution trends for individual Pleistocene volcanic edifices in the context of local ice histories may offer further understanding of the feedbacks between (de)glaciation and eruption dynamics. Some studies that examined relationships between inferred eruption rates, lava compositions, and ice coverage have advocated for a genetic link between ice retreat and eruptive dynamics (e.g., Singer

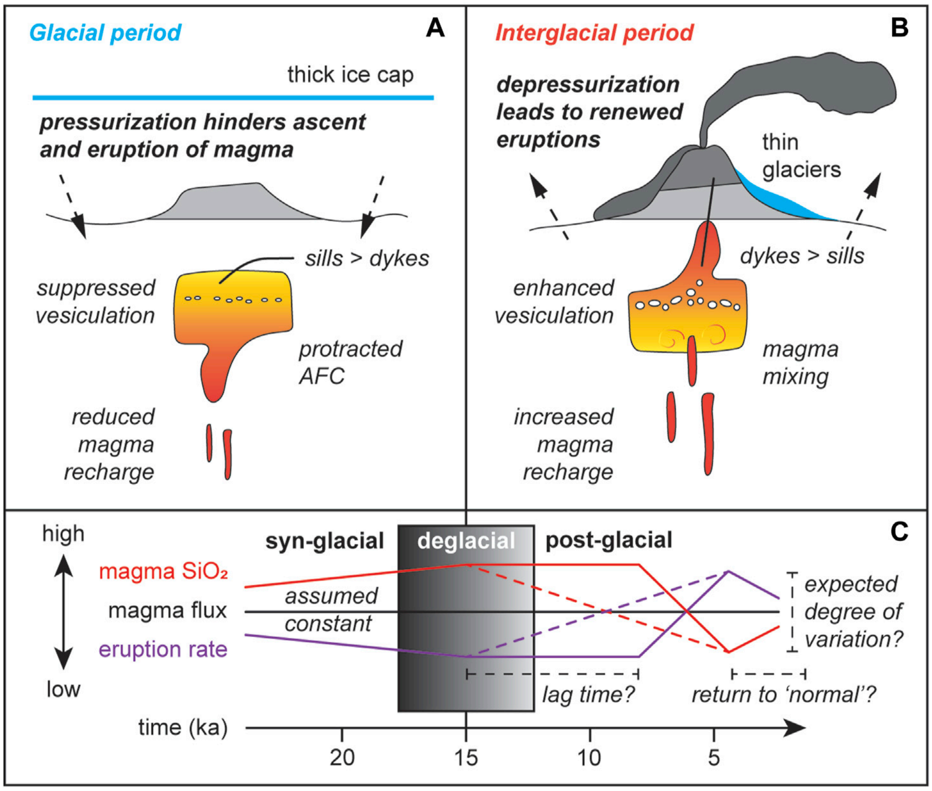

FIGURE 1
Summary of the hypothesis that **(A)** ice loading on volcanoes suppresses volcanic activity and that **(B)** deglaciation causes increased eruption rates at volcanoes for a constant supply of magma into the crust. **(C)** The predicted effects of deglaciation on eruptive rates and whole-rock SiO_2 concentrations for the ~25 to 5 ka interval, which includes the LGM and last deglaciation. Studies have postulated a lag between deglaciation and changes in eruptive rates and compositions due to gradual magma system depressurization (e.g., Jellinek et al., 2004; Rawson et al., 2016; Wilson and Russell, 2020). In **(C)**, the decrease in SiO_2 concentrations after 10 ka represents the transition from the situation in **(A)** where suppressed vesiculation and ascent causes stalled magmas to evolve to elevated SiO_2 concentrations to **(B)** where depressurization after deglaciation allows low-SiO_2 magmas to ascend and erupt more often with less time differentiating in the crust.

TABLE 1 Glaciated volcanoes considered in this paper.

Volcano	Latitude longitude	Age range (ka)	LGM ice setting	Last eruption	Modern summit (m.a.s.l.)	Publication
Alaskan Peninsula and Aleutians, United States						
Akutan (Aleutians)	54.13°N 165.99°W	2360–0	ice sheet	1992 CE	1303	Coombs and Jicha (2020)
Seguam (Aleutians)	52.32°N 172.51°W	318–0	ice cap	1993 CE	1054	Jicha and Singer (2006)
Tanaga (Aleutians)	51.89°N 178.15°W	295–0	ice cap	1914 CE	1806	Jicha et al. (2012)
Fisher, Unimak Island (Aleutians)	54.65°N 164.43°W	600–0	ice sheet	1830 CE	1112	Stelling et al. (2005)
Kaguyak dome field (Alaska)	58.61°N 154.03°W	300–5	ice sheet	3850 BCE	901	Fierstein and Hildreth (2008)
Katmai volcanic cluster (Alaska)	58.28°N 154.96°W	680–0	ice sheet	1912 CE	2047	Hildreth et al. (2003a)
Mount Katmai (Alaska)	58.28°N 154.96°W	89–0	ice sheet	1912 CE	2047	Hildreth and Fierstein (2012)
Cascades, United States						
Mount Mazama	42.93°N 122.12°W	420–5	ice cap	2850 BCE	2487	Bacon and Lanphere (2006)
North Sister	44.16°N 121.77°W	400–55	ice cap	440 CE	3159	Schmidt and Grunder (2009)
Middle Sister	44.13°N 121.78°W	50–1.5	ice cap	440 CE	3159	Calvert et al. (2018)
South Sister	44.10°N 121.77°W	50–2	ice cap	440 CE	3159	Fiertsein et al. (2011)
Kulshan caldera (pre-Mount Baker)	48.78°N 121.81°W	Caldera-forming-eruption at 1.15 Ma		1880 CE (Mount Baker)	3285	Hildreth (1996)
Mount Baker and Black Buttes volcano	48.77°N 121.81°W	495–6.5	ice sheet	1880 CE	3285	Hildreth et al. (2003b)
Mount Adams	46.21°N 121.49°W	520–10	ice sheet	950 CE	3742	Hildreth and Lanphere (1994)
Mount Rainier	46.85°N 121.76°W	1000–0	ice sheet	1450 CE	4392	Lanphere and Sisson (2003)
Mount St. Helens	46.20°N 122.18°W	300–12.8	ice cap	2008 CE	2549	Clynne et al. (2008)
Trans-Mexican Volcanic Belt, Mexico						
Popocatépetl volcanic complex	19.02°N 98.62°W	538–0	ice cap	2022 CE	5393	Gisbert et al. (2021)

(Continued on following page)

TABLE 1 (*Continued*) Glaciated volcanoes considered in this paper.

Volcano	Latitude longitude	Age range (ka)	LGM ice setting	Last eruption	Modern summit (m.a.s.l.)	Publication
Ecuadorian Andes						
Pichincha Volcanic Complex	0.17°S 78.60°W	850–0	ice cap	2002 CE	4784	Robin et al. (2010)
Tungurahua	1.47°S 78.44°W	300–0	ice cap	2016 CE	5023	Bablon et al. (2020)
Antisana	0.48°S 78.14°W	>400–0	ice cap	1802 CE	5753	Hall et al. (2017)
Iliniza	0.66°S 78.72°W	~130–5	ice cap	Pre-Holocene	5162	Santamaría et al. (2022)
Chimborazo	1.47°S 78.82°W	~120–0	ice cap	550 CE	6261	Samaniego et al. (2012)
Cushnirumi, Mojanda, Fuya Fuya, Imbabura, Cubilche, and Cusín volcanoes	0.26°N 78.18°W	~1100–8	ice cap	5550 BCE	4609	Bablon et al. (2020)
Peruvian Andes						
El Misti	16.29°S 71.41°W	833–0	ice cap	1985 CE	5822	Thouret et al. (2001)
Ampato-Sabancaya	15.77°S 71.86°W	450–0	ice cap	2022 CE	5960	Samaniego et al. (2016)
Chilean Andes						
Paniri	22.06°S 68.23°W	1390–100	ice cap	100 ka	5960	Godoy et al. (2018)
Parinacota	18.17°S 69.14°W	163–0	ice cap	290 CE	6336	Hora et al. (2007)
Antuco-Sierra Velluda	37.41°S 71.35°W	430–0	ice sheet	1869 CE	2979	Martínez et al. (2018)
Calbuco	41.33°S 72.62°W	100–0	ice sheet	2015 CE	1974	Mixon et al. (2021)
Tatara-San Pedro	35.99°S 70.85°W	930–0	ice sheet	Pre-Holocene	3621	Singer et al. (1997), Dungan et al. (2001)
Puyehue-Cordón Caulle	40.59°S 72.12°W	314–0	ice sheet	2012 CE	2236	Singer et al. (2008)
Aucanquilcha	21.22°S 68.48°W	1040–200	ice cap	>200 ka	6176	Klemetti and Grunder (2007)
El Cóndor, Falso Azufre, and Incahuasi volcanoes (Chile-Argentina)	25.34°S 68.52°W	~2000–>12	ice cap	Pre-Holocene	5481	Grosse et al. (2018)

(Continued on following page)

TABLE 1 (*Continued*) Glaciated volcanoes considered in this paper.

Volcano	Latitude longitude	Age range (ka)	LGM ice setting	Last eruption	Modern summit (m.a.s.l.)	Publication
Taupō Volcanic Zone, New Zealand						
Ruapehu	39.28°S 175.57°E	200–0	ice cap	2007 CE	2797	Gamble et al. (2003); Conway et al. (2016); Conway et al. (2018)
Tongariro	39.16°S 175.63°E	512–0	ice cap	2012 CE	1978	Pure et al. (2020)

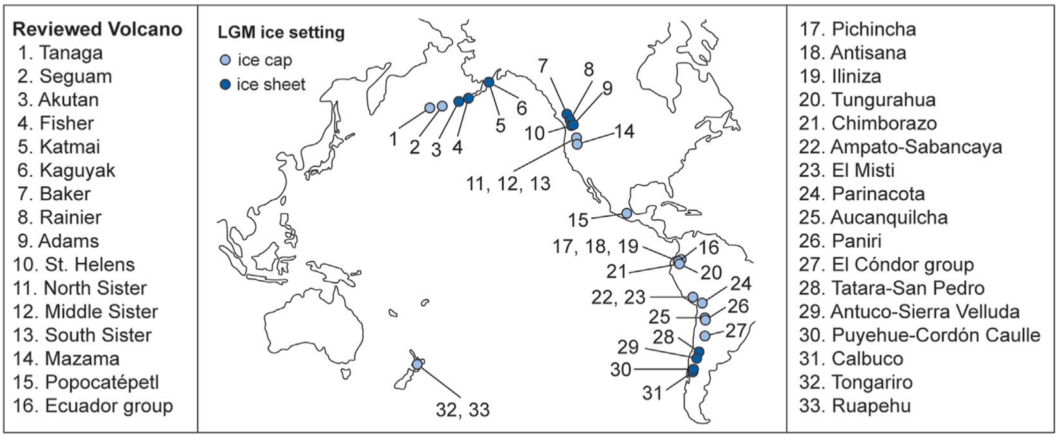

FIGURE 2
Map of circum-Pacific arc volcanoes that are assessed in this paper. The numbers refer to the volcanoes and volcanic systems, and LGM ice thicknesses are shown using light and dark blue dots. See Table 1 for the studies that report data on these volcanoes.

et al., 2008; Figure 1). Other studies have found no clear indication that deglaciation causes enhanced rates of volcanism (e.g., Schmidt and Grunder, 2009). To accompany in-depth analyses of tephra records (e.g., Watt et al., 2013; Kutterolf et al., 2019), a comprehensive review of studies on the proximal eruption records of glaciated volcanic edifices is required to improve our understanding of this topic.

The majority of active volcanoes (i.e., have had eruptions in the Holocene) with coexistent glaciers on Earth are located in subduction zones (190/245; Edwards et al., 2020). In order to investigate whether future eruptive behaviour at these locations may be influenced by current climate warming trends, we have examined the potential influence of (de)glaciation on volcanism during the past ~500 kyr. This assessment focusses on 33 volcanoes or volcanic groups that occur in circum-Pacific continental and oceanic arcs (Table 1; Figure 2). Our review aims to: (1) assess the evidence for causal relationships between glaciation and eruption rates at arc volcanoes based on currently available high-resolution eruptive histories; (2) identify and describe the limitations that may preclude accurate assessments of feedbacks between ice volume changes and volcanic activity; and (3) outline the future outlook of research on potential volcano-cryosphere feedbacks and highlight the benefits that will result from striving for comprehensive studies of these phenomena.

Examination of the hypothesis: Deglaciation leads to increased eruption rates

Surficial changes at volcanoes can impact their magma plumbing systems at depth. Pinel and Jaupart (2000) proposed that edifice construction progressively exerts a load on the crust, meaning that as a volcano grows in height, magmas must become more evolved (i.e., buoyant) if they are to ascend and erupt by overcoming the changing stress field. Conversely, sudden removal of part of an edifice in sector collapses leads to rapidly renewed eruption of primitive, dense magmas as the surface load is removed (Cassidy et al., 2015). In a similar way, the long-term loading of a volcano by prolonged growth of glaciers or ice sheets, and the relatively rapid unloading as ice melts during periods of deglaciation, has been interpreted to impact the rates of volcanism and compositions of erupted magmas in glaciated regions (e.g., Huybers and Langmuir, 2009; Figure 1). In volcanic arc settings, the crust hosts magma systems whose storage and ascent processes can be affected by changes in surficial loading on and around the volcanic edifice (Watt et al., 2013). Accordingly, relationships and feedbacks between ice extent, volcanism and magmatism have also been proposed for arc settings (e.g., Kutterolf et al., 2013).

Subduction zone volcanoes, many of which have been periodically glaciated (Edwards et al., 2020), are responsible for most of Earth's total subaerial magma output (~90% of eruptions since 1900; Siebert, 2002). For this reason, any causative links between ice extent and arc volcanism may be fundamentally connected to the evolution of Earth's climate and the hazard potential of active volcanoes. Studies that have reported such a link propose that magmatic systems become pressurized as ice accumulates on volcanic edifices (or across the continent in some cases) during glacial advance. The associated suppression of vesiculation and favourable formation of sills over dykes is inferred to stifle eruption rates (Jellinek et al., 2004; Mora and Tassara, 2019; Wilson and Russell, 2020; Figure 1A). During glacial retreat, volcanic edifices are depressurized, hence the hypothesis predicts that eruption frequencies and volumes will increase when ice masses disappear as dyke propagation and magma volatile saturation are enhanced (Bindeman et al., 2010; Wilson and Russell, 2020; Figure 1B). The central question underpinning the hypothesis is therefore: are climatically driven changes in ice-loading at volcanoes sufficient to influence eruption rates and/or erupted magma compositions?

While a general hypothesis has been agreed upon (i.e., deglaciation leads to enhanced eruption rates), the assumptions and limitations of studies that test this hypothesis are seldom reported. Testing whether ice loading reduces rates of volcanism implies that eruptible magma ascent is suppressed and/or magma recharge is prevented at the time of ice loading (e.g., Praetorius et al., 2016; Rawson et al., 2016). Such a condition implies that there is a steady-state flux of magma from the mantle to the surface *via* the crust over the ~10–100 kyr time periods of interest (Figure 1C), and that deviations from regular eruptive rates or compositions can be interpreted as being driven by external processes (i.e., ice loading). However, volcanoes in non-glaciated regions also exhibit periods of enhanced growth and relative quiescence (e.g., Yamamoto et al., 2018). In such settings, variable time-volume-composition trends can be explained without oscillations in surface loading and therefore must result from crustal and mantle conditions and processes that control magma generation, storage and eruption, and the regional stress field (Mora and Tassara, 2019). Furthermore, neither the anticipated degree of change to eruption rates and magma compositions nor the expected time lag between ice retreat and volcanic response are outlaid in the framing of studies aiming to test the hypothesis (Figure 1C). As such, statistical tests are not utilized in the way they are for other volcanological studies that examine causality (e.g., Cisneros de León et al., 2022), and time-volume-composition trends may be explained *via* complex, multi-staged, or delayed eruption response models (e.g., Rawson et al., 2016). It is therefore unclear to what degree the erupted magma compositions and volumes are expected to diverge from a baseline due to changes in crustal loading from glacial advance and retreat (Edwards et al., 2002).

Inferences on whether ice loading impacts the volcanic and magmatic system are also entwined with a number of contrasting (but not mutually exclusive) views about how time-volume edifice growth curves should be interpreted. For many volcanic systems it is plausible that glacial erosion, preservation biases, and real eruptive hiatuses have each affected the surviving rock record, but the relative influence from each of these phenomena is debated (e.g., Pure et al., 2020; Mixon et al., 2021). Attempts to assess links between climate and volcanism are often secondary discussion points in studies where the primary objective is to understand the eruption history and hazard potential of a volcano (e.g., Jicha and Singer, 2006; Singer et al., 2008; Conway et al., 2016; Calvert et al., 2018; Pure et al., 2020). Many of the gaps in our knowledge about the links between deglaciation and eruptive dynamics that were identified by Tuffen (2010) are thus yet to be addressed. These include uncertainty in how rapidly arc volcanic systems may react to deglaciation and whether subduction zone volcanoes respond to small changes in ice thickness. Ignoring these complications for the time being, the frequent eruptions and long lifespans of Pleistocene arc volcanoes provide valuable records of evolving eruptive and magmatic activity that can be compared with changes to the regional and global paleoenvironment. The potential causality between deglaciation and eruptive activity at arc volcanoes can therefore be assessed by undertaking extensive field campaigns that establish high-resolution eruptive histories from radiometric age data and detailed mapping work. The approach we have taken for this review is to compile high-fidelity proximal eruptive records for arc volcanoes affected by glaciation and compare them with global (benthic $\delta^{18}O$) and regional (moraine chronology) proxy records for past ice extent.

Time-volume trends for arc volcanoes affected by Pleistocene glaciations

We identified and reviewed studies of arc volcanoes in the middle to high latitudes (plus Mexico and Ecuador) that satisfied the following requirements: (1) the volcano or volcanic cluster has been glaciated at least once in its lifetime; (2) the study reports geochronological data, or an eruptive stratigraphy constrained by radiometric dating; and (3) stratigraphic data are reported with coupled data on erupted magma volumes and/or compositions. Of the 33 volcanoes and volcanic systems that passed these criteria and are considered in this review (Table 1; Figure 2), four are from the oceanic Aleutian arc, two are from the continental Alaskan Peninsula arc, eight are from the continental Cascades arc in the western United States, one is from the continental arc of the Trans-Mexican Volcanic Belt, six are from the Ecuadorian Andes, two are from the Peruvian Andes, eight are from the Chilean Andes, and two are from the Taupō Volcanic Zone in New Zealand. In Table 1; Figure 2, the volcanoes are categorized as those that were affected by ice sheets or ice caps during the Last Glacial Maximum (LGM), according to regional ice thickness reconstructions (Davies et al., 2020; Palacios et al., 2020). The paucity of datasets from the mainland Aleutians, Wrangells, Canadian Cascades, and southern Chile resulted in the inclusion of relatively few (11) volcanoes from areas affected by thick ice (>500 m of ice). The majority (22) of the volcanoes covered in this review were impacted by alpine ice caps

TABLE 2 Summary of geochronological precision, preservation considerations, and time-volume correlations with climatic changes. The radiometric ages and other summarized information are from the references in Table 1, unless otherwise noted.

Volcano	Representative lava ages near the LGM (~20 ka)	Was lava-ice interaction considered or reported?	Was supra-glacial emplacement of eruptives considered?	Do apparent eruptives rates increase during interglacial periods and decrease during glacial periods?
Alaskan Peninsula and Aleutians, USA				
Akutan [Aleutians] (Coombs and Jicha, 2020)	Ar/Ar: 13 ± 7 ka, 9 ± 4 ka (2sd errors)	Yes	Yes	NO: No evidence for correlated edifice growth rates and inferred ice coverage at Akutan
Seguam [Aleutians] (Jicha and Singer, 2006)	Ar/Ar: 22.8 ± 5.1 ka, 12.1 ± 5.1 ka, 8.4 ± 1.5 ka (2sd errors)	No	No	NO: Apparent high and consistent eruption rates occurred throughout MIS 4–2 glaciation
Tanaga volcanic cluster [Aleutians] (Jicha et al., 2012)	Ar/Ar: 19.2 ± 7.6 ka, 7.7 ± 12.1 ka (2sd errors)	Yes	No	NO: Continuous eruptive activity without significant hiatuses (i.e., >10 kyr) has persisted since 150 ka, and only a short apparent eruptive hiatus occurred from 175 to 140 ka (during MIS 6 glaciation)
Fisher, Unimak Island [Aleutians] (Stelling et al., 2005)	Ar/Ar: 26 ± 14 ka (2sd error).	No	No	UNCLEAR: Insufficient data resolution
Kaguyak cluster [Alaska] (Fierstein and Hildreth, 2008)	Ar/Ar: 29 ± 4 ka, 26 ± 5 ka, 6 ± 5 ka (2sd errors)	Yes	No	NO: No observed correlation between dome growth rates (individually or collectively) and climatic changes
Katmai volcanic cluster, and Mount Katmai [Alaska] (Hildreth et al., 2003a; Hildreth and Fierstein, 2012)	K/Ar: 39 ± 12 ka, 21 ± 11 ka, 15 ± 18 ka; Ar/Ar: 22.5 ± 1.6 ka (2sd errors)	Yes	Yes	UNCLEAR: Since 200 ka, there are no gaps in eruptive activity period (outside of analytical uncertainty) greater than ~10 kyr for the arc-front group of the Katmai cluster. There is evidence for both preservation bias (favouring preservation of eruptives in warmer climatic periods) and glacial erosion on Mount Katmai, indicating complex interplay between constructive and destructive forces in shaping the modern edifice
Cascades, United States				
Mount Mazama (Bacon and Lanphere, 2006)	Ar/Ar: 18 ± 4 ka (2sd error)	Yes	Yes	MAYBE: Possible increase in eruption rate following deglaciations after MIS 12, 10, 8, 6, 5.2, and 2, but also reduced volcanism in MIS 7 and increased volcanism in MIS 6
Middle Sister (Calvert et al., 2018)	Ar/Ar: 19.4 ± 3.4 ka, 19.9 ± 12.4 ka, 18.2± 4.4 ka (2sd errors)	Yes	Yes	NO: Middle Sister peak eruptive rate occurred in MIS 2 and ended immediately prior to LGM deglaciation
North Sister (Schmidt and Grunder, 2009)	Ar/Ar: 19.5 ± 11.6 ka, 14.3 ± 11.5 ka (2sd errors)	Yes	No	NO: No evidence that eruption rates increased following deglaciations
South Sister (Fiertsein et al., 2011)	Ar/Ar: 19.1 ± 7.4 ka, 23.5 ± 2.2 ka (2sd errors)	Yes	No	NO: 70% of edifice growth occurred during MIS 3 and 2
Mount Baker and Black Buttes volcano (Hildreth et al., 2003b)	K/Ar: 24 ± 16 ka, 14 ± 9 ka (2sd errors)	Yes	Yes	NO: Although K/Ar ages for Black Buttes volcano and Mount Baker lavas occur predominantly in relatively warm climatic periods at MIS 9, 7, 5 and 1, the volumetric growth rates are greatest over 500–250 and 50–0 ka, which include multiple glacial-interglacial cycles. Eruptive activity was also common during glacial periods and many examples of lava-ice contact textures are in nominal 'interglacial' periods because significant ice masses still persist on Mount Baker today

(Continued on following page)

TABLE 2 (*Continued*) Summary of geochronological precision, preservation considerations, and time-volume correlations with climatic changes. The radiometric ages and other summarized information are from the references in Table 1, unless otherwise noted.

Volcano	Representative lava ages near the LGM (~20 ka)	Was lava-ice interaction considered or reported?	Was supra-glacial emplacement of eruptives considered?	Do apparent eruptives rates increase during interglacial periods and decrease during glacial periods?
Mount Adams (Hildreth and Lanphere, 1994)	K/Ar: 15 ± 8 ka, 28 ± 6 ka (2sd errors)	Yes	No	NO: Generally continuous eruptive activity since 520 ka with major edifice building stages at MIS 13 (~500 ka), MIS 12 to 10 (~450–330 ka) and the MIS 3–2 boundary (~30 ka)
Mount Rainier (Lanphere and Sisson, 2003; age data from T.W. Sisson, pers. comm., 2022)	Ar/Ar: 20.1 ± 4.0 ka, 19.9 ± 1.6 ka, 16.7 ± 4.2 ka (2sd errors) (T.W. Sisson pers. comm., 2022)	Yes	Yes	NO: No correlations between glacial cycles and time-volume trends at Cascade volcanoes (Mount Baker, Mount Rainier, and Mount Adams)
Mount St. Helens (Clynne et al., 2008)	Ar/Ar: 17.8 ± 5.4 ka (2sd error)	Yes	Yes	UNCLEAR: Apparent eruptive hiatuses occurred in MIS 8 and 6–3, but supra-glacial pyroclastic flow deposits were emplaced during MIS 8, and detailed volume data are not reported
Cascades and Alaska-Aleutian arc volcanoes (from compilation by Calvert et al. (2014), Calvert et al. (2018)	See other Cascades and Alaska-Aleutians age data above	N/A	N/A	MAYBE: Age-weighted edifice volumes suggest increased output following MIS 6 and MIS 8, which were the two strongest glaciations since 300 ka. However, sample age distribution may not represent eruptive rates accurately. In contrast, Rainier and South and Middle Sisters primarily grew during glaciations
Trans-Mexican Volcanic Belt, Mexico				
Popocatépetl volcanic complex (Gisbert et al., 2021)	Ar/Ar: 22 ± 8 ka (2sd error)	No	No	UNCLEAR: Time-volume trends not presented
Ecuadorian Andes				
Pichincha volcanic complex (Robin et al., 2010)	Ar/Ar: youngest age is 52 ± 6 ka (2sd error)	Yes	No	NO: Erupted volumes and compositions are not discussed in the context of ice loading or unloading. High eruption rates estimated for period from 60–11 ka (~MIS 3–2)
Tungurahua (Bablon et al., 2020)	K/Ar: 29 ± 4 ka, 7 ± 8 ka (2sd errors)	No	No	UNCLEAR: Erupted volumes and compositions are not discussed in the context of ice loading/unloading and time-volume data is of low resolution. Apparent lacuna from ~80–30 ka (MIS 4–3) and edifice growth rates increase significantly starting from around the LGM (~30 ka)
Antisana (Hall et al., 2017)	No new Ar/Ar ages; existing Ar/Ar ages >165 ka; oldest ^{14}C age reported is 13.9 ± 0.4 ka	No	No	UNCLEAR: Estimated volumes for eruptive stages indicate a slightly higher rate for the post-15 ka period, compared to 400–15 ka period. However, time-volume data before 15 ka are of low resolution and erupted volumes and compositions are not discussed in the context of ice loading/unloading
Iliniza (Santamaría et al., 2022)	K/Ar: 25 ± 6 ka, 6 ± 8 ka (2sd errors). 11 new K/Ar ages in total	No	No	NO: Peak edifice growth occurred in early MIS 5 and MIS 3–2, with no post-LGM eruptive activity

(Continued on following page)

TABLE 2 (*Continued*) Summary of geochronological precision, preservation considerations, and time-volume correlations with climatic changes. The radiometric ages and other summarized information are from the references in Table 1, unless otherwise noted.

Volcano	Representative lava ages near the LGM (~20 ka)	Was lava-ice interaction considered or reported?	Was supra-glacial emplacement of eruptives considered?	Do apparent eruptives rates increase during interglacial periods and decrease during glacial periods?
Chimborazo (Samaniego et al., 2012)	Ar/Ar: youngest age is 37 ± 9 ka (2sd error). 11 new Ar/Ar ages in total	No	No	UNCLEAR: Time-volume data resolution is low and edifice growth rates peaked at 120–35 ka (MIS 5–3), but major explosive activity also occurred in MIS 2 near the LGM
Cushnirumi, Mojanda, Fuya Fuya, Imbabura, Cubilche, and Cusín volcanoes (Bablon et al., 2020)	K/Ar: 25 ± 16 ka, 19 ± 16 ka (2sd errors); not plotted in Figure 7	No	No	UNCLEAR: Insufficient resolution to examine sub-100 kyr changes in eruption rates for these volcanoes
Peruvian Andes				
El Misti (Thouret et al., 2001)	Ar/Ar: youngest reported age is 49 ± 6 ka (2sd error).	Yes	No	UNCLEAR: Erupted volumes and compositions are not discussed in the context of ice loading/unloading and volume estimation methods are unclear
Ampato-Sabancaya (Samaniego et al., 2016)	K/Ar: 34 ± 8 ka, 17 ± 6 ka (2sd errors)	No	No	NO: Edifice growth rates increase in after MIS 6, in MIS 4–2 and in MIS 1. Authors conclude that changes in time-volume trends arose because edifice growth occurred in spurts
Chilean Andes				
Paniri (Godoy et al., 2018)	Ages are >100 ka	No	No	UNCLEAR: Apparent edifice growth rate is greatest in most recent growth stage at ~250–100 ka (~MIS 7–5), and time-volume data resolution is low
Parinacota (Hora et al., 2007)	Ar/Ar: 22.4 ± 7.5 ka, 20.0 ± 4.0 ka (2sd errors)	No	No	NO: Apparent eruptive hiatus from ~117 to 52 ka (MIS 5–4), followed by edifice construction from late MIS 4 and MIS 3–2
Antuco-Sierra Velluda (Martínez et al., 2018)	Ar/Ar: 22.0 ± 6.3 ka (2sd error)	No	No	NO: Edifice growth rates are greatest in late-MIS 6, MIS 5.3, and MIS 4–1 with apparent eruptive hiatuses at ~120–100 ka (MIS 5.5–5.4), 86–77 ka (MIS 5.2–5.1), and 15–10 ka (MIS 1)
Calbuco (Mixon et al., 2021)	Ar/Ar: 22.5 ± 7.4 ka, 11.5 ± 8.0 ka (2sd errors)	Yes	No	NO: Peak edifice growth at 100–55 ka (MIS 5–4), 30–7 ka (MIS 2–1) and 4–0 ka. An apparent eruptive hiatus at ~55–30 ka was interpreted by the authors not be the result of sampling bias, but rather due to glacial erosion or reduced magma supply with no dated lavas in that period
Tatara-San Pedro (Singer et al., 1997)	K/Ar: 25 ± 9 ka, 19 ± 13 ka (2sd errors)	No	No	NO: Although there are at least 8 eruptive hiatuses or unconformities, time-volume data show generally continuous edifice growth from eruptions from MIS 5 to 2 (i.e., ~110 to ~19 ka for dated lavas), which includes potential glacial advances

(Continued on following page)

TABLE 2 (*Continued*) Summary of geochronological precision, preservation considerations, and time-volume correlations with climatic changes. The radiometric ages and other summarized information are from the references in Table 1, unless otherwise noted.

Volcano	Representative lava ages near the LGM (~20 ka)	Was lava-ice interaction considered or reported?	Was supra-glacial emplacement of eruptives considered?	Do apparent eruptives rates increase during interglacial periods and decrease during glacial periods?
Puyehue-Cordón Caulle (Singer et al., 2008)	Ar/Ar: 31.6 + 5.3 ka, 18.7 ± 1.1 ka, 14.9 ± 2.9 ka (2sd errors)	No	No	YES: Increased edifice growth rates at ~131, 69, and 19 ka during deglaciations after MIS 6, 4, and 2, respectively. Average edifice growth in these glacial periods (MIS 6 and 4–2) are lower than in interglacial periods. Authors interpret this to mean that unloading of ice during deglaciations allowed melt to ascend more easily through the crust
Aucanquilcha (Klemetti and Grunder, 2007)	N/A. No relevant ages.	No	No	UNCLEAR: Erupted volumes and compositions are not discussed in the context of ice loading or unloading. There is little evidence for glaciation and no lava dates since 200 ka
El Cóndor, Falso Azufre, Incahuasi volcanoes [Chile-Argentina] (Grosse et al., 2018)	Ar/Ar: 36 ± 12 ka, 23 ± 25 ka (2sd errors); not plotted on Figure 7	No	No	UNCLEAR: Insufficient resolution to examine sub-100 kyr changes in eruption rates for these volcanoes
Taupō Volcanic Zone, New Zealand				
Ruapehu (Conway et al., 2016)	Ar/Ar: 23.0 ± 1.6 ka, 20.9 ± 2.8 ka, 17.8 ± 2. ka (2sd errors)	Yes	Yes	NO: Apparent eruptive rates are consistent from MIS 3 to present
Tongariro (Pure et al., 2020)	Ar/Ar: 28.3 ± 5.2 ka, 12.9 ± 11.8 ka (2sd errors)	Yes	Yes	YES: Edifice growth rates peak in MIS 5, 3 and 1 interglacial periods, but are shown to result from preservation bias (low preservation during glacial periods) because systematic changes in MgO concentrations are decoupled from and uncorrelated with edifice growth rates

and glaciers (~200 m of ice). Volcanoes from Kamchatka, the Kuriles, Japan, Indonesia, Papua New Guinea, and the Philippines were not considered due to a lack of detailed time-volume data for edifice materials and/or ambiguity about glaciation in these settings.

Table 2 summarizes key results and interpretations presented in the studies of these 33 volcanic systems, as relevant to this review. A compilation of apparent growth rates (time-volume curves) from 20 of these volcanoes is presented in Figure 3, which are taken from the preserved, averaged, or minimum volumes reported in the data sources. Time-volume trends reported for the volcanoes are summarized below and considered in the context of time-varied ice coverage throughout repeated climatic cycles. Time-composition data are discussed in the subsequent section, below.

Alaskan Peninsula and the Aleutians

The six volcanoes (or volcanic clusters) considered for the Alaska Peninsula and the Aleutian arc cover the Tanaga volcanic cluster, Seguam, Akutan, Fisher, the Katmai volcanic cluster (including Mount Katmai), and the Kaguyak dome field (Tables 1 and 2; Figure 2). Reported geochronological results for these systems date from before 2 Ma to the Holocene, but most radiometric ages are between 300 and 0 ka, and thus document eruption histories that coincided with glacial advance and retreat from Marine Isotope Stage (MIS) 8 through 1 (see references in Table 1). Kaufman et al. (2011) reported the extent of glacial advances during the late Pleistocene which covered the entire volcanic arc component of the Alaskan Peninsula and most (>90%) of the eastern Aleutian Islands (including Akutan, Unalaska and westward to Vsevidof volcano). However, by 18 ka only areas east of (but excluding) Veniaminof volcano were still glaciated as the continental ice sheet retreated (Dalton et al., 2020). Published research therefore shows that Tanaga and Seguam potentially only supported ice caps during peak glacial advances of the late Pleistocene whereas Akutan and Fisher caldera were wholly or partly covered by the continental ice sheet at such times.

Only the studies of Seguam and the Kaguyak domes report time-volume data with sufficient resolution to compare with climatic changes since ~250 ka (Figure 3; Fierstein and Hildreth, 2008; Jicha and Singer, 2006). During MIS 6 and other nominal glacial periods, some volcanoes display apparent eruptive hiatuses (Tanaga: Jicha et al., 2012; Akutan; Coombs and Jicha, 2020) whereas others underwent persistent edifice growth from new eruptions (Katmai cluster: Hildreth et al., 2003a).

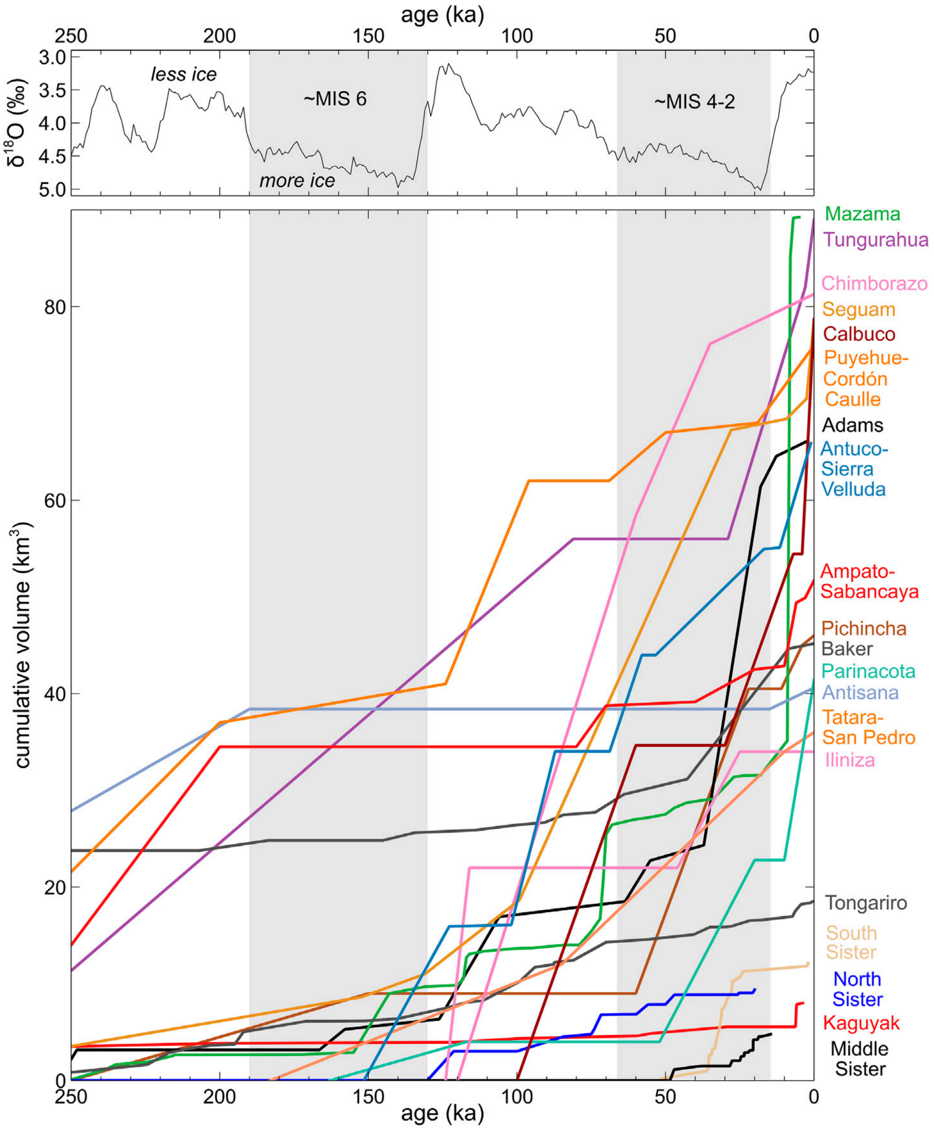

FIGURE 3
Summary of benthic $\delta^{18}O$ climate proxy data (Lisiecki and Raymo, 2005) and edifice growth rates for 20 of the volcanic systems assessed in this review since 250 ka. In upper and lower panels, the approximate positions of glacial MIS stages are shaded in grey, and unshaded regions are interglacial MIS stages. Cumulative volcano edifice growth volumes and ages are from the studies in Table 1, which are compiled in the Supplementary File S1. Of the total 33 volcanic systems considered in this review, 13 are excluded from this figure because they are older than ~100 ka (Paniri, Aucanquilcha), or their time-volume data are of low resolution or absent (Tanaga, Akutan, Fisher, Katmai cluster [including Mount Katmai], Mount Rainier, Mount St. Helens, Mount Hood, Shasta, Lassen, Popocatepétl, El Misti), or their total volumes exceed 100 km^3 (Ruapehu); note that Kulshan caldera is counted with Mount Baker. To fit on the diagram, cumulative volume sums begin from ~0 km^3 for Pichincha and Mazama.

Domes and edifice eruptives commonly display field evidence for syn-glacial lava emplacement, including horizontal column jointing and overthickening of flows (Jicha and Singer, 2006; Fierstein and Hildreth, 2008; Hildreth and Fierstein, 2012; Coombs and Jicha, 2020). Erosion is inferred to have modified the surviving volumes of erupted material. Estimates of eroded volumes are not given for all six volcanic systems but estimates are as high as 50% in the Katmai cluster, based on valley erosion of originally conical edifices (Hildreth et al., 2003a). Of the studies of the six systems, two proposed that variable time-volume trends reflect the incomplete preservation of erupted materials in situations where lavas are erupted onto ice and 'flushed' off the edifice as debris (Hildreth and Fierstein, 2012; Coombs and Jicha, 2020). Evidence for glacial erosion on Aleutian Island volcanoes is generally limited to small volumes of till on ring plain areas and smoothed upper surfaces on lava flows (Jicha and Singer, 2006; Jicha et al., 2012). Smoothed lava surfaces are also observed on the Alaskan Peninsula volcanoes (e.g., Katmai) but till and moraine volumes are much greater (Hildreth and Fierstein, 2012).

Cascades

Quaternary volcanoes of the Cascades arc have morphologies and eruption histories that have been significantly impacted by glaciation. Mounts Baker (including Kulshan caldera), Rainier, St. Helens, Adams, Hood, Mazama, and the Three Sisters are complex volcanic edifices, some of which have likely lost up to 70% of their original material due to glacial erosion (Hildreth, 2007).

There is no evidence for increased eruption rates following major deglaciations at the large and long-lived Baker, Rainier, and Adams volcanoes. Ice-contact textures and morphologies are reported in edifice records since 500 ka at both Baker and Adams (Hildreth and Lanphere, 1994; Hildreth et al., 2003b). No correlation between inferred ice extent and eruptive rate or magma compositions is reported for Rainier, which grew during glacial periods, and time-volume trends were inferred to reflect variable tectonic stress regimes in the crust (Lanphere and Sisson, 2003). An apparent eruptive hiatus from ~250 to 150 ka at St. Helens precludes interpretations about volcanism-glaciation feedbacks for that period (Clynne et al., 2008). However, the absence of notable temporal variations in lava and pyroclast chemistry since ~300 ka suggests that magma generation and eruption dynamics were not impacted by ice loading and unloading (Clynne et al., 2008).

Detailed eruptive histories and volume reconstructions for the Three Sisters volcanoes provided no evidence that eruption rates increased following periods of glacial retreat. At North Sister, Schmidt and Grunder (2009) estimated that half of the erupted volume has been eroded from the volcano. Whilst acknowledging the large uncertainties in calculating the volumes of edifice-forming products, the authors found no correlation between periods of reduced ice coverage and eruption rate over the growth history from ~400 to 55 ka. At Middle Sister (~50–1.5 ka), the peak eruptive episode occurred during increased ice coverage and ended immediately prior to the LGM (Calvert et al., 2018; Figure 3). Similarly, 70% of edifice growth at South Sister (~50–2 ka) occurred in the presence of extensive ice coverage during MIS 3 and 2 (Fiertsein et al., 2011). The evolution of Mazama includes possible increases in eruption rate following deglaciations after MIS 12, 10, 8, 6, 5.2, and 2. However, periods of reduced volcanism in MIS 7 and increased volcanism in MIS 6 show that the pattern is not reproducible (Bacon and Lanphere, 2006).

Mexico

Ice-caps likely covered the summits of Colima, Nevado de Toluca, Pico de Orizaba, Cofre de Perote, and Popocatépetl at ~20 ka (Capra et al., 2013), although only the latter has a high-resolution eruptive history available to study volcano-ice interactions. Popocatépetl volcanic complex of the Trans-Mexican Volcanic Belt has an eruptive history dating back to ~538 ka and is currently one of the most active volcanoes in Mexico. Small summit glaciers have retreated rapidly in historic times (Delgado Granados et al., 2007), but broad valleys on the lower flanks attest to more extensive glaciation in the past.

Despite the likely widespread occurrence of glaciovolcanic products at Popocatépetl, they are not described in a recent overview of its eruptive history that combines new and existing data (Gisbert et al., 2021). This study did not examine the volumes and compositions of erupted magmas within the context of the temporal evolution of the complex and its ice cover. We note here that the Popocatépetl volcanic complex comprises lava flows that show a near-continuous growth history since ~350 ka, which are recorded by 34 radiometric ages, except for an apparent hiatus in major edifice construction that lasted from ~190 to 100 ka (approximately MIS 6). Following a major sector collapse event and explosive eruption, construction of the modern Popocatépetl cone has been ongoing since ~23 ka.

Ecuadorian Andes

We reviewed the eruptive histories of six volcanoes in the Ecuadorian Andes that exhibit evidence for late Pleistocene glacial advances: Pichincha, Antisana, Iliniza, Tungurahua, and Chimborazo. Preserved edifice volumes and ages for Cushnirumi, Mojanda, Fuya Fuya, Imbabura, Cubilche, and Cusín volcanoes in the Ecuadorian Andes were also reported by Bablon et al. (2020) in a multi-volcano study, and are counted as one volcanic system of the total 33 systems considered in this review. For Pichincha, Antisana, Iliniza, Tungurahua, and Chimborazo, the available data on edifice growth histories at these volcanoes are generally of insufficient resolution to draw robust conclusions about volcanism-deglaciation feedbacks, and in some cases the data show contradictory patterns in edifice growth rates at the MIS 6 and 2 (LGM) terminations (Figure 3). Erosion is discussed generally, as it is relevant to estimating eruptive volumes, but syn-glacial edifice construction is not discussed in detail for the studies of these five volcanoes.

Pichincha is characterized by an average eruptive rate of 0.82 km^3/kyr from ~60 to 22 ka (~MIS 4–2) which is followed by an apparent hiatus until 11 ka and then continued growth at 0.25–0.64 km^3/kyr for the rest of the Holocene (Figure 3; Robin et al., 2010). Notably, the apparent hiatus occurs after the LGM. At Antisana only three average growth rates determined since 250 ka are suited for examining potential deglaciation responses following the LGM (Figure 3; Hall et al., 2017). Elevated edifice growth rates after ~15 ka, relative to the apparent hiatus between 190 ± 23 ka and ~15 ka, appear to show increased eruptive rates following deglaciation, but a similar pattern is not seen after the MIS 6 deglaciation (ending at ~130 ka). At Iliniza, the northern edifice was constructed at a rate of 3.5 ± 2.6 km^3/kyr over the period of ~124–116 ka following the MIS 6 glacial termination (Santamaría et al., 2022). After a ~70 kyr-long apparent lacuna during MIS 5 and 4, construction of the South Iliniza edifice recommenced at ~46 ka and continued until ~25 ka (MIS 3–2), with no post-25 lava flows. These time-volume data from Iliniza are of limited resolution and only capture one major deglaciation event (after MIS 6). Over Tungurahua's ~300 kyr growth history, there is an apparent lacuna from ~81 to 29 ka (~MIS 5.1–3) after which edifice growth continued at 1.0–2.3 km^3/kyr from ~29 ka onwards, hence edifice growth appears decoupled from changes in ice coverage (Bablon et al., 2020; Figure 3). Chimborazo's basal edifice formed during ~120–60 ka (~MIS 5), at a rate of 0.7–1.0 km^3/kyr and was followed by a large sector collapse at ~65 ka (Samaniego et al., 2012). Subsequently, the Intermediary edifice was constructed at a rate of 0.4–0.7 km^3/kyr from ~60–35 ka (~MIS 3) which slowed to ~0.1 km^3/kyr when 95% of the Young Cone was constructed between ~30 and 14 ka (MIS 2). These results indicate a progressive decrease of the magmatic output rate during the history of Chimborazo, and no forcing of elevated eruption rates following deglaciation after the LGM. In general, the age data are of insufficient resolution to make meaningful comparisons between edifice growth rates and climatic changes since ~250 ka at Cushnirumi, Mojanda, Fuya Fuya, Imbabura, Cubilche, and Cusín volcanoes. For example, only two growth rates have been determined for Imbabura in the periods from >47 to ~30 ka and ~35 to 0 ka, and the other volcanoes have only a single growth rate reported for the entire eruptive histories.

Peruvian Andes

The eruptive histories of the long-lived volcanic complex of Ampato-Sabancaya (since ~450 ka) and modern cone of El Misti (since ~112 ka) contain limited evidence for volcanism-deglaciation feedback processes. Major growth periods at Ampato-Sabancaya occurred at ~450–400 ka, ~250–200 ka, and ~80–70 ka, and appear to be separated by ≥100 kyr lacunae (Figure 3; Samaniego et al., 2016). The resolution of the post-80 ka record is of much higher resolution than the earlier history and shows periodically higher growth rates at ~80–70 ka (~MIS 5.1), ~40–20 ka (~MIS 4–2), and after 10 ka (MIS 1). These variations in edifice growth rates occur in both periods of elevated and reduced ice coverage as inferred from $\delta^{18}O$ climate proxy data.

Edifice construction of the ~70–83 km^3 El Misti volcano (Misti stages 2, 3, and 4) since ~112 ka occurred during five main periods of increased eruption rates with intervening periods of erosion at ~45, ~35, ~28, and ~12 ka (Thouret et al., 2001). These periods of edifice growth continued through glacial stages at relatively high rates compared with MIS 5, however, the trends were constrained by only five absolute ages for lavas and volume estimates with large analytical uncertainties. The authors noted that the time-volume trends should be treated as preliminary findings. There are no strong trends when erupted magma compositions are plotted against their age for El Misti (Rivera et al., 2017), and the mapping and geochemical studies indicate ice loading/unloading has not impacted the rates and compositions of volcanism at El Misti.

Chilean Andes

We assessed studies for eight volcanoes from the Chilean Andes that span a latitudinal range of ~18–41°S. The southernmost cones of Tatara-San Pedro, Antuco-Sierra Velluda, Puyehue-Cordón Caulle and Calbuco experienced advance of the Patagonian Ice Sheet during late Pleistocene glaciations (Davies et al., 2020), whereas the more northerly Parinacota, Aucanquilcha, Paniri, and the El Cóndor group (including Falso Azufre, and Incahuasi: Grosse et al., 2018) were impacted by ice caps and flank glaciers (Figure 2).

Following inception at ~163 ka, the growth of Parinacota volcano was interrupted by an apparent hiatus in eruptive activity from ~117 to 52 ka (~MIS 5–4), which was followed by cone construction throughout MIS 3 and 2 (Hora et al., 2007; Figure 3). Construction of the long-lived Paniri volcano since ~1.4 Ma is typified by its highest growth rates during the most recent constructional stage from ~250 to 100 ka (Godoy et al., 2018). Relatively scarce radiometric age data preclude the assessment of temporal variations in eruptions rates on shorter time scales, and as such there is no evidence that glacial loading and unloading of the edifice impacted the rates of volcanism. The eruptive history of Aucanquilcha (since ~1 Ma) was divided into four stages by Klemetti and Grunder (2007) based on eleven $^{40}Ar/^{39}Ar$ ages, with most of the edifice growth attributed to effusive activity prior to 800 ka and no apparent activity since 200 ka. Similar to Paniri, Aucanquilcha's edifice growth rates could not be assessed with respect to sub-100 kyr climatic changes because of the resolution of age data, and the lack of eruptions during the late Pleistocene precluded evaluation of rates of volcanism during recent glaciations.

With an inception age of ~930 ka, the Tatara-San Pedro volcanic complex preserves ~55 km^3 of lavas within unconformity-bound sequences, which have basal lava ages that generally indicate that the minimum upper limits of lacunae correlate with global ice-volume peak advances. Repeated glacial advances are therefore inferred to have provided a punctuated growth record for the edifice, due to major erosional episodes that removed up to 50%–95% of material during the period from 930 to 200 ka (Singer et al., 1997). Time-volume trends for the Tatara-San Pedro volcanic complex are shown since 250 ka in Figure 3 (Singer et al., 1997).

Volcanism has been near-continuous since ~100 ka to form the Antuco-Sierra Velluda volcanic complex, at an average growth rate of 0.43 km^3/kyr (Martínez et al., 2018; Figure 3). Divided into stages, the minimum flux rates for the periods from 150 to 17 ka, 17–6.2 ka, and 6.2 ka to present were 0.28 km^3/kyr, 0.27 km^3/kyr, and 0.65 km^3/kyr. The authors stated that main growth of the volcano occurred following major deglaciation from MIS 6 and 2, however, there is only one dated lava during early MIS 5 compared with the twelve that coincide with MIS 4-2 that indicate steady growth through the last glacial period. The authors imply that deglaciation induced a stress drop of ~3–5 MPa, which promoted easier ascent of basaltic magma that was erupted after ~17 ka. Although a notable increase in eruption rate is reported after the ~6.2 ka sector collapse event, the effect of this rapid edifice unloading mechanism on the magma system was not discussed by Martínez et al. (2018).

The Puyehue-Cordón Caulle volcanic complex preserves ~131 km^3 of lavas and tephras that have amassed since 314 ka (Singer et al., 2008; Figure 3). Eruptive rates were non-uniform over this time period, with notable cone growth episodes occurring at ~131, 69, and 19 ka, which coincide with ice retreat at the terminations of MIS 6, 4, and 2. Singer et al. (2008) interpreted this as evidence that unloading of ice during deglaciations allowed magma to ascend more easily through the crust at these times.

Construction of the Calbuco volcano since 100 ka was recently constrained by Mixon et al. (2021), who reported edifice growth rates of 0.43 km^3/kyr for the period from ~100 to 55 ka, 2.2 km^3/kyr for the period from ~30 to 7 ka, and 4.8 km^3/kyr from 4 ka to present (Figure 3). The authors suggest that the lacuna between ~55 and 30 ka may represent elevated glacial erosion or reduced magma supply during the last glacial period, whereas the increased Holocene eruption rate may reflect a delayed response of the magma system to ice unloading during the Last Termination. However, the contribution of sector collapse events at ~18 and ~9 ka to post-glacial modifications of the crustal magma system were not considered in this study, and the lack of a marked shift in erupted compositions during the Holocene make it difficult to assess whether ice unloading impacted magma storage and eruption dynamics at Calbuco.

A multi-volcano study from Grosse et al. (2018) presents data for El Cóndor, Falso Azufre, and Incahuasi volcanoes in the

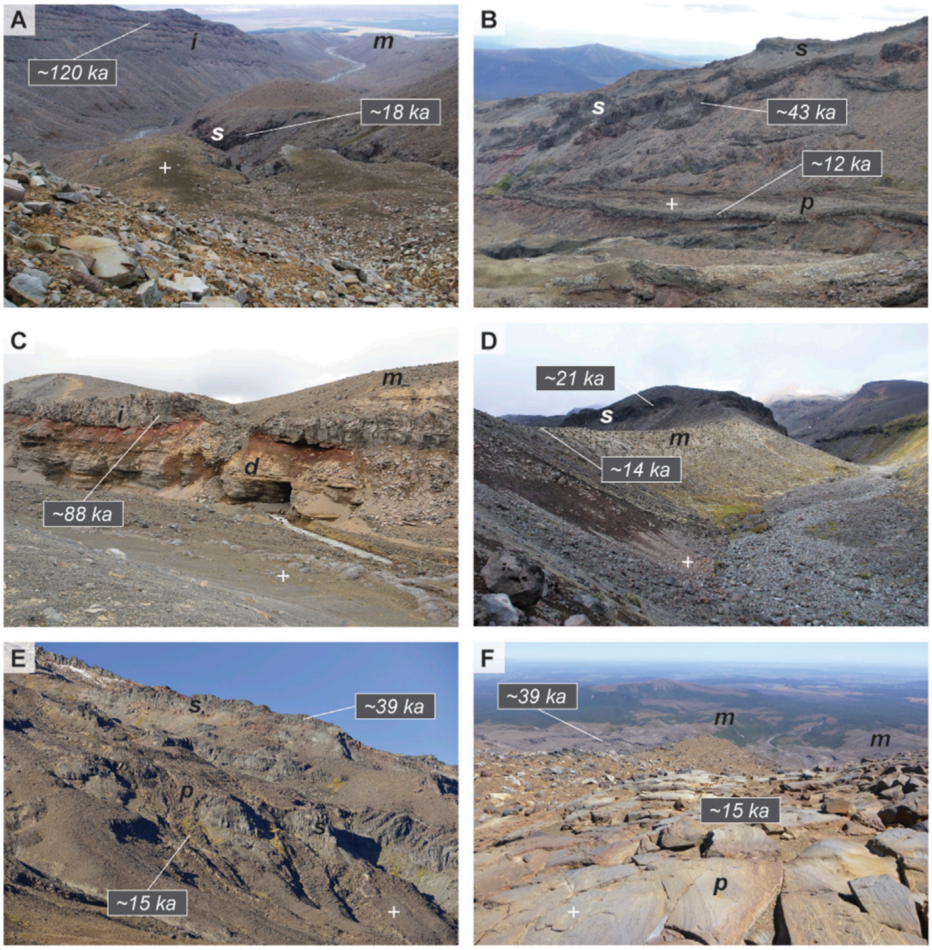

FIGURE 4
Examples of glaciovolcanic landforms at Ruapehu, New Zealand. Lava age constraints are from Gamble et al. (2003) and Conway et al. (2016); moraine age constraint in **(D)** is from Eaves et al. (2019). Key labelled features are: interglacial lava (i); syn-glacial lava (s); post-glacial lava (p); debris flow deposits (d); moraine (m). Location markers for photos (+) are given in degree decimals for each panel. **(A)** View towards the southeast down the Wahianoa valley, with MIS 5 interglacial stage lavas exposed on the top left and LGM moraines visible at top right. A lobe of syn-glacial lava was emplaced in a glacial cavity prior to post-LGM glacial retreat (–39.301, 175.590). **(B)** View to the northwest of ice-bounded syn-glacial lavas and post-glacial valley-filling lavas in the Mangaturuturu valley (–39.282, 175.534). **(C)** Outcrop of a MIS 5 interglacial stage lava flow with underlying baked debris flow deposits and overlying moraine in the lower Whangaehu valley (–39.287, 175.630). **(D)** View towards the northeast of syn-glacial lava that was bounded by an LGM glacier, which later retreated to form ~14 ka moraines in the Mangaehuehu valley (–39.317, 175.538). **(E)** View to the south of the northwest flank of Ruapehu volcano. Ice-bounded lavas outcrop as grey bluffs in the centre of the photo and along the skyline ridge, with thinner red-brown post-glacial lavas that flowed around them after glaciers had retreated (–39.259, 175.533). **(F)** View towards the northwest with moraines bordering the Whakapapaiti valley in the mid-ground and glacially striated post-glacial lavas on the upper flank (–39.263, 175.549).

southern Central Volcanic Zone of Chile that borders with Argentina. These volcanoes are predominantly older than 250 ka, and the resolution of age and precision of age data in the 250–0 ka period is low (e.g., El Cóndor K/Ar ages of 128 ± 46 ka, 90 ± 30 ka, 36 ± 24 ka, and 23 ± 50 ka) which makes it challenging to compare eruptive outputs to deglaciation events. For these reasons the data are not shown in Figure 3.

New Zealand

Ruapehu and Tongariro are active andesite-dacite volcanoes of the Taupō Volcanic Zone, New Zealand, with inception ages of ~230 a and ~350 ka, respectively (Leonard et al., 2021). The edifices are predominantly composed of andesitic lava flows and breccias, and display clear evidence of late Pleistocene lava-ice interaction and glacial erosion, although only small glaciers remain on Ruapehu's upper flanks today and none remain on Tongariro (Eaves and Brook, 2020). The recent integration of the eruptive and glacial histories for these volcanoes has led to edifice growth models of 'edifice growth adjacent to glaciers' (Conway et al., 2016; Pure et al., 2020) that deviate from the past ones of 'volcano growth spurts separated by erosion during quiescence' (Hobden et al., 1999; Gamble et al., 2003).

Glaciation of the Tongariro edifice during MIS 8 and 6 is indicated by ridge-forming lava and till on the southern and eastern flanks (Pure et al., 2020), whereas evidence for MIS 6 glaciation of the early Ruapehu edifice exists as hyaloclastite

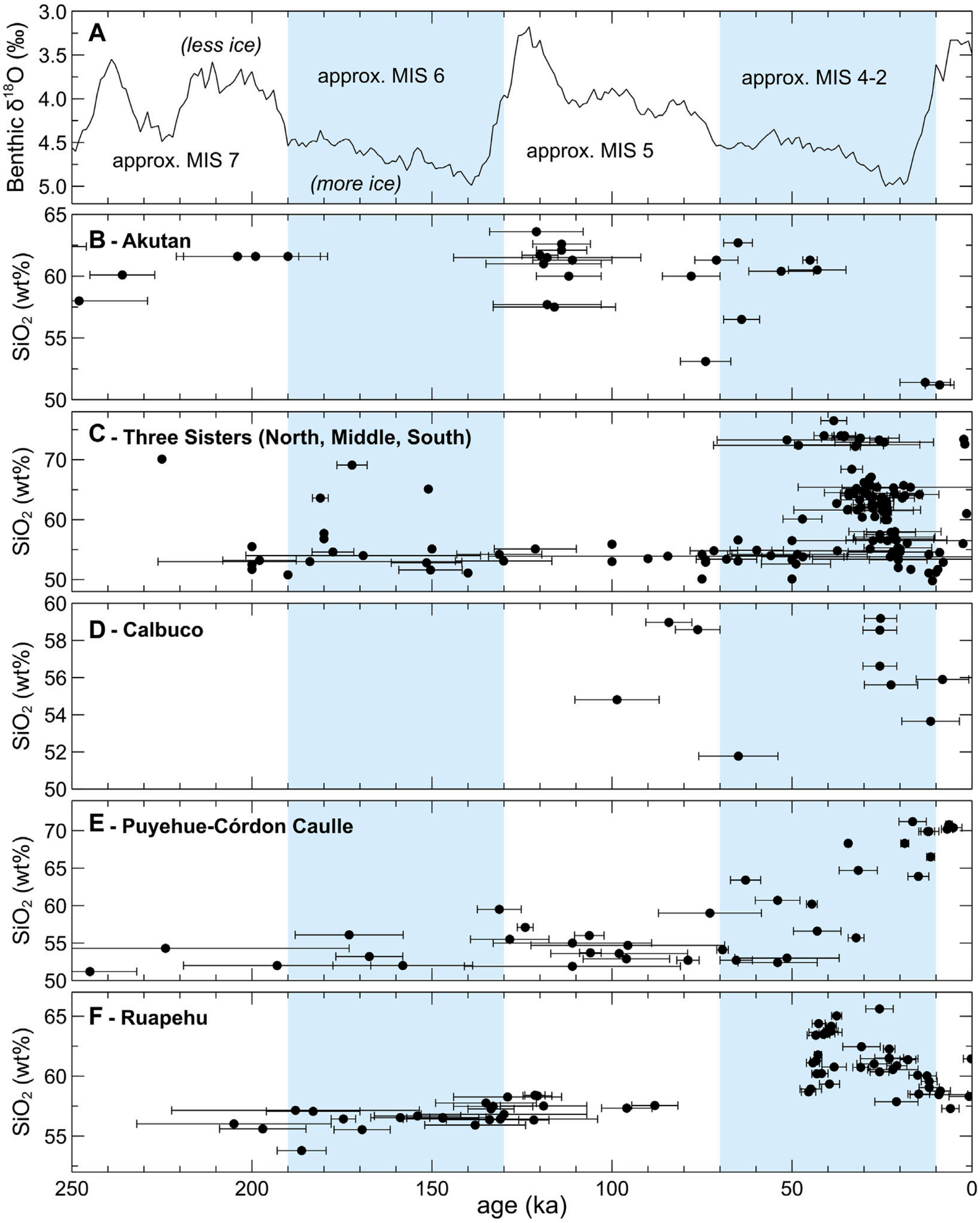

FIGURE 5
Summary of benthic $\delta^{18}O$ climate proxy data **(A)** (Lisiecki and Raymo, 2005) and whole-rock SiO_2 contents for dated samples from the following volcanoes: **(B)** Akutan, Aleutians (Coombs and Jicha, 2020); **(C)** the Three Sisters (North, Middle and South), Cascades (Calvert et al., 2018)—note that some samples lack age errors; **(D)** Calbuco, Chile (Mixon et al., 2021); **(E)** Puyehue-Córdon Caulle, Chile (Singer et al., 2008); **(F)** Ruapehu, New Zealand (Gamble et al., 2003; Conway et al., 2016; Conway et al., 2018). Compositional diversity is generally greatest in MIS 4–2 (all volcanoes shown), but similar diversity also occurs in MIS 6 (Three Sisters) and MIS 5 (Akutan and Calbuco).

(subglacial) breccias that underlie ~180 ka lavas and ~160 ka lavas on the northern and southern flanks, respectively (Gamble et al., 2003; Conway et al., 2016; Cole et al., 2020). Widespread till, u-shaped valleys bounded by moraines, striated lava flows, subglacial tephra deposits, and ice-impounded lavas indicate that summit ice caps and flank glaciers persisted on both edifices throughout MIS 4–2, with significant advances at ~60 ka and ~20 ka (Figure 4; Conway et al., 2015; Conway et al., 2016; Eaves et al., 2016; Cole et al., 2018; Pure et al., 2020).

Both volcanoes show near-continuous growth histories since ~200 ka, however, there are no dated lavas at Ruapehu with ages between ~80 and 50 ka, which coincides with the New Zealand peak glacial advance (66–61 ka: Williams et al., 2015). The wide compositional variation during MIS 3 and a steady edifice growth rate since 50 ka (Conway et al., 2016; Conway et al., 2018) indicate that Ruapehu's magma system was likely not impacted by glacial loading and unloading. At Tongariro, significantly lower edifice growth rates during glacial periods relative to interglacial periods (Figure 3) and the lack of corresponding changes in lava chemistry indicates that deglaciation did not result in pulses of eased ascent of stored magmas (Pure et al., 2020). The reduced preservation of lavas during MIS 6 and 4–2 at Tongariro may be partly attributed to the 'flushing' of lavas onto the ring plain following their eruption onto ice. This lost material may be contained within the substantial volcaniclastic sequences that surround the edifice. The preservation of lavas erupted during MIS 3 and 2 at Ruapehu may have been due to the availability of emergent ridges where ice-bounded lava flows were emplaced (Conway et al., 2016). At Ruapehu, collapse events may have been assisted by de-buttressing of steep, fractured, and altered upper flanks during periods of ice retreat (Tost and Cronin, 2015), including the collapse that led to the emplacement of the ~10.5 ka Murimotu Formation debris flow deposits on the north-western flank (Palmer and Neall, 1989).

The long-term evaluation of time-volume and time-composition trends at Tongariro was interpreted to show that edifice-building rates during glacial periods were only ~20% of growth rates during periods of lower ice coverage (Pure et al., 2020; Figure 3). Tongariro's post-230 ka lifespan therefore comprises subequal time in periods of reduced and heightened ice coverage, which equates to a long-term edifice growth rate that is ~60% of interglacial growth rates. By difference, up to ~40% of erupted material has been transported to the ring plain by "flushing". In terms of volumes, the amount of erupted material that was emplaced onto ice masses and flushed to the ring plain was therefore ~36 km^3, relative to the ~60 km^3 ring plain total, but noting that the ring plain contains materials up to ~1 Ma (Cameron et al., 2010). The remaining ~24 km^3 may represent airfall deposits and/or pre-230 ka volcaniclastic materials.

Time-composition trends for arc volcanoes affected by Pleistocene glaciations

To supplement the assessment of variable edifice growth rates provided above, we briefly review time-composition trends (where the data are available) in the context of climatic changes for the 33 volcanoes in this section. Volcanoes showing similar patterns are grouped and discussed together below. Whole-rock SiO$_2$ contents for dated volcanic products from five representative circum-Pacific arc volcanoes are presented in Figure 5, in order to compare magma chemistry evolution trends with the climate record.

Time-varied pressurization of magmatic systems caused by glacial advance and retreat may be connected to contemporaneous changes in erupted magma compositions (Figure 1). During glacial periods, it is hypothesized that the impedance of magma ascent leads to extended crustal residence, thus resulting in crystal fractionation and assimilation that would increase the SiO$_2$ content of magma batches (Edwards et al., 2002; Wilson and Russell, 2020). Conversely, erupted magmas are expected to be relatively mafic following deglaciation because denser magmas may ascend more easily following depressurization of the crust (Pinel and Jaupart, 2000), although there are examples of mafic magmas that are more buoyant than coexisting felsic magmas (e.g., Eichelberger, 1980). Demonstrating causal connections between ice loading and the compositions of erupted magmas would require strong (and perhaps reproducible) correlations between eruptive compositions and climatic changes.

The time-composition trends in Figure 5 show some patterns that coincided with climatic changes. However, it appears that the range of compositional diversity, rather than shifts to more silicic compositions (or *vice versa*), are more strongly correlated with climatic changes. Moreover, although the volcanoes in Figure 5 generally display the greatest compositional diversity in MIS 4–2 (e.g., Ruapehu), similar diversity also occurs in MIS 6 (North Sister, Middle Sister and South Sister) and MIS 5 (Akutan and Calbuco). Determining why the amount of compositional diversity at some arc volcanoes is correlated with climatic changes is beyond the scope of this study.

More broadly, there is no reported or evident relationship between glacial loading and erupted magma compositions at the following volcanoes: Mazama, Middle Sister, South Sister, Mount Adams, Mount Baker and Black Buttes volcano, Akutan, the Tanaga cluster, Ruapehu, Tongariro, Paniri, Calbuco, or at Puyehue-Cordón Caulle (references in respective order of listed volcanoes: Bacon and Lanphere, 2006; Calvert et al., 2018; Fiertsein et al., 2011; Hildreth and Lanphere, 1994; Hildreth et al., 2003b; Coombs and Jicha, 2020; Jicha et al., 2012; Conway et al., 2016; Conway et al., 2018; Pure et al., 2020; Godoy et al., 2018; Mixon et al., 2021; Singer et al., 2008). These volcanic systems have age ranges from >500 ka to the Holocene, and most cover multiple glacial-interglacial cycles (Table 1). Furthermore, no correlations between eruptive rates and compositions are observed at Mount Baker and Black Buttes volcano, Mount Rainier, or at Tongariro (Hildreth et al., 2003b; Lanphere and Sisson, 2003; Pure et al., 2020).

Elsewhere, a lack of correlation between eruptive compositions and ages precludes a connection between eruptive compositions and ice-loading, such as at Tatara-San Pedro, Mount St. Helens, Seguam, the Kaguyak domes, and Antuco-Sierra Velluda (Dungan et al., 2001; Jicha and Singer, 2006; Clynne et al., 2008; Fierstein and Hildreth, 2008; Martínez et al., 2018). At Seguam, SiO$_2$ concentrations in lavas and pyroclastic materials are also uncorrelated with the inferred amount of ice coverage on the edifice through time (Jicha and Singer, 2006).

For some of the volcanoes considered in this review, neither erupted volumes nor eruptive compositions are discussed in the context of ice loading or climatic changes through time, even if the data exist, such as at Aucanquilcha (Klemetti and Grunder, 2007), Katmai (Hildreth and Fierstein, 2012), three Chilean-Argentinian volcanoes (Grosse et al., 2018), and six Ecuadorian Andes volcanoes (Bablon et al., 2020). For some volcanoes, such as Tungurahua, Antisana, and the Pichincha complex, magmas became more silicic with time, but no clear changes can be linked to glacial cycles (Robin et al., 2010; Hall et al., 2017; Bablon et al., 2020). At Iliniza, the reverse is observed where magmas became less silicic and more magnesian with time,

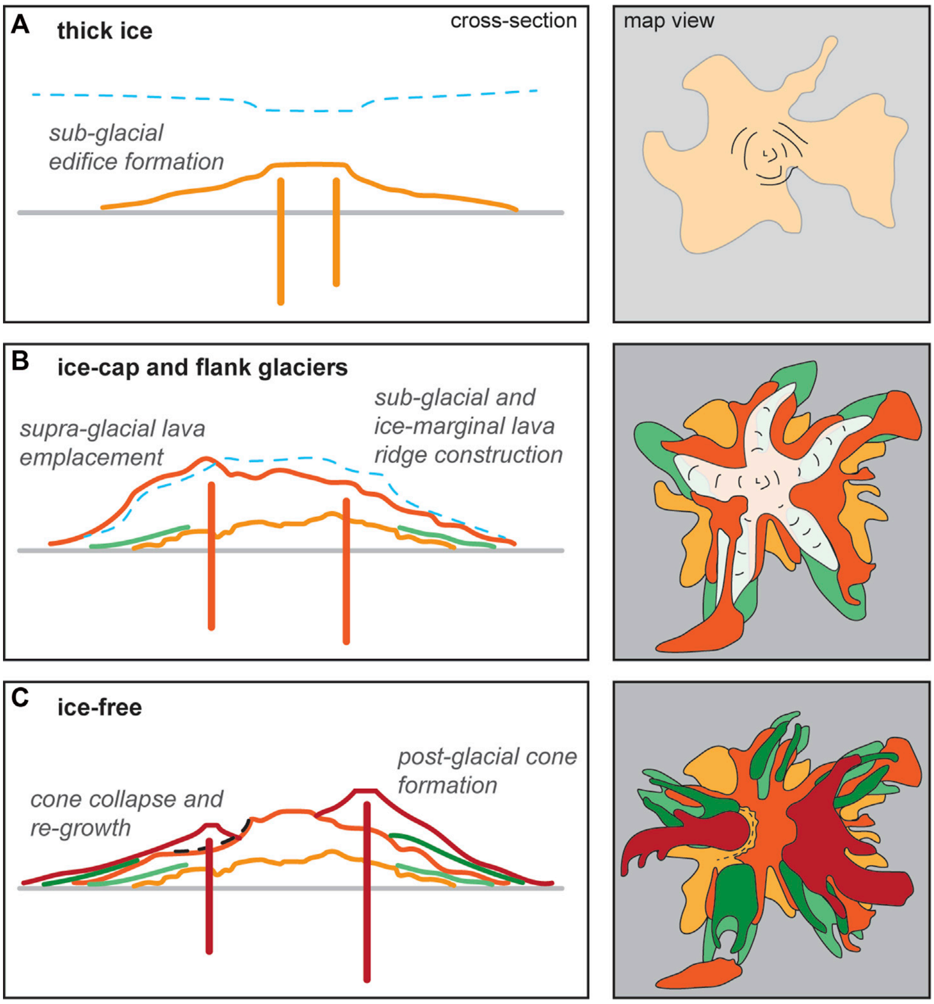

FIGURE 6
Evolution of a volcano that grew with changing ice cover over time (dashed blue line). Cross sections on the left correspond to map views on the right. **(A)** Tuya-like landform develops under a continental ice sheet. **(B)** The edifice continues to grow with reduced ice coverage beneath an ice-cap and around valley glaciers (dark orange and green units) that overlie older glacially eroded lavas [light orange units, as in panel **(A)**]. Irregular and asymmetric landforms in summit areas are constructed subglacially, as shown in the cross section. Flank areas also grow where erupted materials are deposits around glaciers and onto existing flank bedrock (light green and dark orange units). Supra-glacial lavas are only preserved where they are emplaced on bedrock, which results in distal flow areas from being disconnected from high summit areas [compare the bottom-left dark orange unit between panels **(B, C)**]. **(C)** Ice-free growth (dark red units) construct 'perfect' cone vents that erupt young lavas and pyroclastic deposits into vacant valleys, as also shown in field photos (Figures 4B, E). Irregular summit landforms constructed in the presence of ice may undergo collapse [black dashed line in panel **(C)**] and be replaced by new cones [compare dark orange unit profiles in the cross sections of panels **(B, C)**]. Glacial erosion of older units may excavate valley-floor units and widen valleys [compare light and dark green units between panels **(B, C)**].

but changes are also not discussed in relation to changing ice coverage (Santamaría et al., 2022). In other cases, correlations between eruptive rate and compositions occur but they are not causally connected with time-varied ice coverage. An example is North Sister, where apparent eruptive rates decline between ~300 and ~100 ka by ~30% which coincides with a decrease in Ni and MgO concentrations in eruptives and was interpreted to show olivine-dominated fractionation as the magmatic system waned (Schmidt and Grunder, 2009).

For some of the systems the time-composition data is not reported or discussed. Such is the case for El Misti, the Katmai cluster, Chimborazo, Ampato-Sabancaya, and Popocatépetl (Thouret et al., 2001; Hildreth et al., 2003a; Samaniego et al., 2012; Samaniego et al., 2016; Gisbert et al., 2021). At other volcanoes where time-volume-composition data are available, the resolution of geochronological ages is too low to examine magma composition-deglaciation feedbacks, such as for Fisher volcano in the Aleutians (Stelling et al., 2005).

At some volcanoes, sector collapses have been correlated with changes in erupted magma compositions (e.g., Parinacota: Hora et al., 2007), which represent a similar yet more rapid change in lithostatic load on the magmatic system than typically occurs *via* glacial retreat. Despite this, none of the 33 volcanoes and volcanic systems (and two multi-volcano studies: Grosse et al., 2018; Bablon et al., 2020) examined above show any reproducible correlations between the compositions of erupted materials and ice coverage.

Discussion

In this section we introduce and explain four major caveats that were identified in the review. The discussion is intended to aid interpretation of published results, and to help direct future studies of the causal relationships between deglaciation and volcanism. The outcomes and benefits of addressing these limitations, which currently hamper the reconstructions of complex volcanic histories, are summarized at the end of the discussion section.

Biased preservation and exposure of eruptive products

An important consideration when interpreting time-volume data (e.g., Figure 3) is as follows: do smaller volumes of preserved eruptives in glacial periods indicate reduced eruption rates (i.e., evidence of absence), or do they reflect erosion and/or lack of preservation of syn-glacial eruptives (i.e., absence of evidence)? The degree to which eruptive records at a given volcano are affected and modified by erosion, incomplete preservation, and magma system depressurization depend on specific local and regional contexts. For this reason, it is essential to determine what the estimated volumes of preserved material at a given volcano actually represent when interpreting time-volume data. In many cases, erosion and a lack of preservation can lead to confusing and inaccurate pictures of edifice growth rates because estimated volumes may differ from the original eruptive volumes (Singer et al., 1997; Edwards et al., 2015).

Figure 6 shows three scenarios of ice coverage at a volcano and the associated styles of edifice growth. In these examples, the surviving edifice structure ultimately depends on the interplay between edifice growth, erosion, and the supra-glacial emplacement of eruptives. Subglacial eruptions (Figure 6A) may produce lapilli tuffs, hyaloclastites, and pillow lavas that construct tuyas and asymmetric landforms, which may be associated with outbursts from subglacial lakes known as "jökulhlaups" (e.g., Lachowycz et al., 2015; Cole et al., 2018; Russell et al., 2021). Whether such materials get preserved depends on whether eruptions were explosive or effusive, whether eruptions discharged into subglacial water bodies, the geometries and post-eruptive landforms, the subsequent action of erosion, and whether jökulhlaup events transported syn-eruptive material off the edifice (Smellie, 2021). Alternatively, when volcanoes support ice-caps and flank glaciers (Figure 6B), eruptions may build ridges along the sides of glaciers, as indicated by lava-ice interaction features (see dark orange and green units in Figure 6B), and erupted materials may be emplaced onto glaciers and then flushed off the edifice as debris when glaciers melt (e.g., Lescinsky and Sisson, 1998). Concurrently, glaciers may erode valley floor material where the abrasive force is the greatest (see green units in Figure 6C) whilst also removing subequal or lesser volumes of valley wall material (e.g., Singer et al., 1997; Pure et al., 2020). Subsequent edifice growth in an ice-free environment (Figure 6C) is commonly associated with young lavas flowing into ice-free valley floors and with the construction of "perfect" cone vents (Figures 4B, E, 6C; see also Hobden et al., 1999).

Additionally, contrasting methods for estimating volumes can make it difficult to compare time-volume datasets from different studies. In cases where high-resolution time-volume datasets exist, the sum total of estimated lava flow volumes (based on observable surficial distributions and thicknesses) may be much smaller than the total volume between the volcano's surface and its pre-volcanic datum, because significant volumes of buried material may have poorly constrained age and provenance (e.g., Godoy et al., 2018; Pure et al., 2020). Such obstacles are variably acknowledged in the studies considered by this assessment, and we expand on these ideas below.

Volume estimation methods

A range of methods have been used to estimate the volumes of volcanoes and individual eruptive units. For whole edifices these methods include finding the area between a pre-volcanic datum and a digital elevation model of the volcano's surface (often with a GIS program: e.g., Samaniego et al., 2016), and using a 3-dimensional shape to approximate the geometry of the edifice (e.g., Godoy et al., 2018). For individual eruptive units, volume estimation methods include taking field thicknesses and multiplying by the areal distribution of lava flows that are either observable, or buried and inferred (e.g., Mazama, Cascades: Bacon and Lanphere, 2006; Three Sisters, Cascades; Fiertsein et al., 2011; Calvert et al., 2018; Tongariro, New Zealand; Pure et al., 2020). Methods for individual eruptive units also include subdividing sectors of a volcano using 3-dimensional shape approximations to estimate volume, based on where each major eruptive sequence occurs (e.g., Parinacota, Chile: Hora et al., 2007; Ruapehu, New Zealand; Conway et al., 2016).

Reconstructed volumes of eroded material

To accurately reconstruct the long-term shifts in eruptive rates at a Pleistocene-age volcano, the volumes of lost materials need to be estimated. In undertaking this exercise, the most common approaches are (1) to assume that each eruptive vent had a perfect cone geometry (Thouret et al., 2001) and/or (2) to assume that valleys were previously filled with erupted deposits and were subsequently eroded (Singer et al., 1997). However, sometimes the surviving edifice volume is simply assumed to represent the total amount of erupted material, even where glacial unconformities are reported (e.g., Samaniego et al., 2012; Samaniego et al., 2016), which may be inaccurate at volcanoes that have experienced glacial advances and sector collapses.

Approaches (1) and (2) noted above are justified for vents and flanks that grew in ice-free environments (e.g., Figure 6C). In such cases, the existence of laterally excavated sequences of planar lava flows (e.g., Figure 4A; green units in Figure 6C) and valley-bounding moraines (e.g., see "m" in Figures 4A, C, D, F) may be used to infer distinct periods of edifice growth and erosion. In applying the ice-free growth model, some studies have estimated the amount of denudation by glaciers within valleys to infer eroded volumes (e.g., Mixon et al., 2021). Using this framework, the estimated volume of eroded material at Paniri (Chile) is 4.4 km^3, relative to 79.9 km^3 of surviving edifice material (Godoy et al., 2018). Elsewhere, estimates of the down-cutting rates from glacial erosion have been estimated by assuming that lava ridges perched above glaciers are remnants surviving after glacial erosion on surrounding pre-existing lava. Using this approach, Hildreth et al. (2003b) inferred down-cutting rates of 0.4–1.75 m/kyr at Mount Baker. However, lava ridges may also be primary (constructional) landforms rather than secondary (erosional) landforms because many glaciated volcanoes demonstrably grew in the presence of ice (e.g., Conway et al., 2016). Furthermore, although valleys at most volcanoes were occupied by glaciers, in many cases it is difficult to differentiate whether such valleys were built around ice or were eroded by ice, or both (e.g., Singer et al., 1997; Singer et al., 2008).

Eruptive products with high preservation potential

The estimated volumes of Holocene lava flows and consolidated pyroclastic deposits are relatively likely to represent the actual amount of erupted magma because, in most cases, there has been minimal opportunity for erosion to occur *via* glaciation or through sector collapse events. Evidence for this includes lavas and pyroclastic deposits that have intact carapaces and no glacial striations, and are fully traceable to their source vents, as illustrated by the dark red units in Figure 6C (e.g., the Ngāuruhoe cone of Tongariro, New Zealand: Hobden et al., 1999). In the example shown in Figure 6, the volcano may have had a steady eruptive rate over 200 kyr, but the volume of syn-glacial eruptive products may be under-represented compared with post-glacial products, due to the more complete preservation of the latter.

Eruptive products with low preservation potential

Tephras and unconsolidated pyroclastic deposits are much less likely to be preserved on a volcano's edifice over its long-term record than lavas and some pyroclastic deposits. A study of tephra record completeness in ice-free regions suggests that <1% of products from eruptions with a volcanic explosivity index of ≥2 have been preserved in post-LGM stratigraphic records, although the total volume of preserved, erupted material may be >1% (Watt et al., 2013). Unconsolidated pyroclastic deposits that are not capped by lavas are rare in the edifice records of most glaciated volcanoes (e.g., Hackett and Houghton, 1989). Typically, explosive eruption deposits on volcanoes comprise the minority of preserved edifice material (e.g., p. 732 of Hildreth et al., 2003b; p. 364 of Fierstein and Hildreth, 2008; p. 405 of Martínez et al., 2018). Collectively, these observations show that edifice records on volcanoes are biased towards preserving lavas and pyroclastic deposits capped by lavas, relative to tephras and uncapped pyroclastic deposits.

Although explosive eruptions can represent a significant proportion of a given volcano's eruptive output, the pre-LGM record is usually poor and only preserves the largest-volume events (Kiyosugi et al., 2015). In regions affected by continental glaciation, the ring plain tephra record is often obliterated by glacial erosion (e.g., Hildreth, 1996). Accurate reconstructions of past eruptive rates at glaciated volcanoes may only be possible if ring plain records, which comprise lavas and pyroclastic debris (eroded *via* fluvial or glacial action), tephras, and sector collapse deposits, can be correlated with specific source volcanoes based on radiometric dating, compositional affinity, drainage patterns and detailed stratigraphic mapping (e.g., Tost and Cronin, 2015). Such exercises are extremely resource- and time-intensive and are also undermined by long run-outs of some sector collapse debris flows that can travel hundreds of kilometres from their source volcano (Vallance and Scott, 1997; Waythomas and Wallace, 2002; Tost and Cronin, 2015).

There are also other biases that appear to affect the preservation of erupted materials in the edifice record. The most notable is when eruptives are emplaced onto ice masses but never make contact with bedrock, which prevents them from being preserved because they are flushed away as debris during deglaciation. This has been inferred from eruptive records (e.g., Jicha and Singer, 2006; Conway et al., 2016; Pure et al., 2020) and observed for modern eruptions (e.g., Edwards et al., 2015; Loewen et al., 2021).

The summary in Table 2 shows that of 33 studies, 20 considered lava-ice interaction and 10 of these studies considered or reported evidence of supra-glacial emplacement of erupted materials. Notably, the only studies that considered supra-glacial emplacement were those that also reported evidence or likelihood of lava-ice interaction (Table 2: Akutan, Katmai, Middle Sister, Baker, Rainier, St. Helens, Ruapehu, and Tongariro volcanoes). No studies of Andean volcanoes from Ecuador, Peru, Argentina or Chile considered supra-glacial emplacement of erupted materials, even though the ages of these volcanoes and extents of ice coverage would have made supra-glacial emplacement of eruptives highly likely (Table 2). Lava flows that were emplaced in ice-free valleys during past interglacial periods may also have low preservation and/or exposure potential, because they can be eroded in subsequent glacial advances and buried by younger till and volcanic deposits (e.g., Conway et al., 2016; Figure 4C).

Post-glacial sector collapses of asymmetric landforms that grew in the presence of ice have been reported widely in both northern and southern hemispheres. Capra (2006) identified over 20 post-LGM sector collapse events from Argentina, Bolivia, Chile, Ecuador, Mexico, New Zealand, and the United States, which is not a comprehensive list (*cf.* Osceola Mudflow at Rainier, Cascades: Vallance and Scott, 1997; Murimotu Formation at Ruapehu, New Zealand; Palmer and Neall, 1989). Such sector collapse events remove edifice material of a variety of ages depending on which materials were part of the collapsed landform. The existence of hydrothermally altered material in sector collapse deposits, which may form in subglacial environments *via* interactions with meltwater, show that subglacial materials are commonly removed from the edifice in collapse events (e.g., Vallance and Scott, 1997; Waythomas and Wallace, 2002). Subglacial and syn-glacial eruptives are thus likely to have low preservation potential because of their propensity to be fragmented, altered, buried, collapsed, and eroded. The ability to accurately reconstruct eruptive rates in materials that pre-date sector collapse events may be hampered by mass wasting that removes significant volumes of older material from the edifice, which could therefore lead to underestimates of pre-collapse (i.e., syn-glacial) eruptive rates.

Summary

Estimates of erupted volumes are a major source of uncertainty in studies that seek to address the question: does deglaciation cause increased eruptive rates? There is then a marked contrast between studies that interpret variations in time-volume trends as arising from erosion and eruptive quiescence (e.g., Singer et al., 1997; Singer et al., 2008) and other studies that infer a preservation bias whereby erupted materials were flushed off the edifice to the ring plain (e.g.,

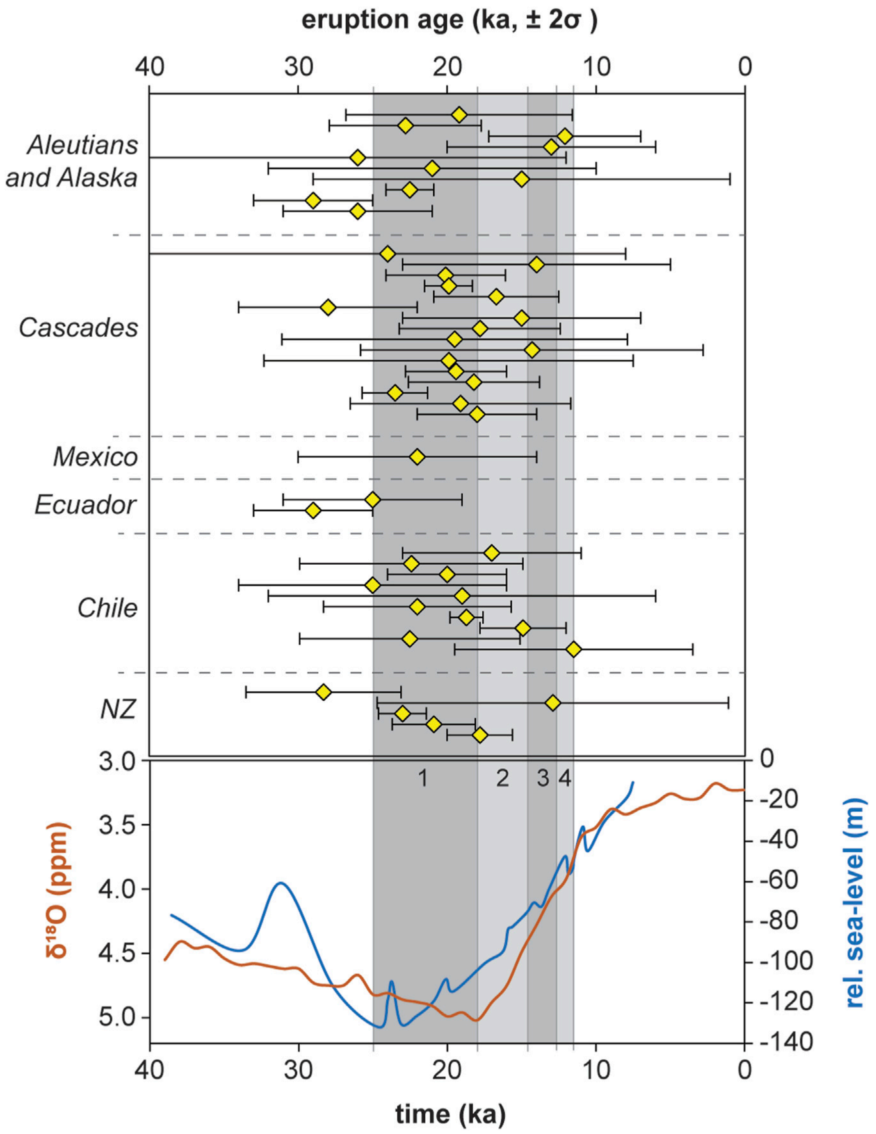

FIGURE 7
Comparison of the precision of radiometric dating constraints for lava eruption ages and the timing of the Last Glacial Termination. $^{40}Ar/^{39}Ar$ and K-Ar data for lavas with preferred ages between 30 and 10 ka were compiled from the reviewed papers (see Table 2). Error bars are 2σ. The stacked benthic $\delta^{18}O$ curve of Lisiecki and Raymo (2005) is plotted in orange, and the reconstructed relative sea-level of Thompson and Goldstein (2006) is plotted in blue in the lower panel. Periods within the Last Termination are labelled with numbers: (1) Last Glacial Maximum; (2) Heinrich Stadial 1; (3) Antarctic Cold Reversal; (4) Younger Dryas.

Pure et al., 2020). In many cases, field records provide strong evidence that 1) glacial and fluvial erosion occurs, 2) greater volumes of erupted materials are preserved in periods of reduced ice coverage because of a preservation bias, 3) volcanoes erupt both explosively and effusively, and 4) Pleistocene-age volcanoes contain significant volumes of unobservable buried material. On the contrary, field records struggle to accurately show 1) how much erosion has occurred because assumptions about pre-erosional geometry cannot be verified, 2) what volume of material that was erupted syn-glacially has been flushed to the ring plain because clast provenance can be difficult to establish and continental glaciation can obliterate ring plain records, 3) how much volume has been erupted effusively *versus* explosively because different lithologies have different likelihoods of being preserved, and 4) the ages and provenance of completely buried edifice materials.

Limitations of geochronological precision

Testing whether causal relationships exist between deglaciation and eruption rates requires chronological data that clearly distinguishes between cause and effect. At arc volcanoes, eruptive records must therefore have sufficient precision and accuracy to make comparisons between the timing of eruptions and fluctuations of ice extent. Geochronological data that constrain fluctuations in ice coverage and eruptive rates should ideally be independent, accurate, and precise. The accuracy and precision of such geochronological data is essential to determining whether the depressurization of arc magmatic systems *via* ice retreat has led to enhanced eruption rates immediately or by delayed mechanisms. Herein, the methods for determining the timing of ice retreat and volcanic events are examined to assess the strength of evidence that may or may not support causal links between deglaciation and increased eruption rates.

Timing of deglaciation

In Figure 3, volcanic growth histories are compared against the stacked benthic $\delta^{18}O$ curve from Lisiecki and Raymo (2005), which largely reflects global ice volume, to assess whether eruption rates at arc volcanoes have been influenced by climate change. Within the reviewed papers, the distinctions between reduced and advanced terrestrial ice cover have generally been taken as those that define each Marine Isotope Stage (MIS). These are sometimes integrated with regional paleoclimate information to confirm the timings of glacial advance and retreat, however, few detailed glacier reconstructions exist for arc volcanoes (*cf.* Eaves et al., 2016; Eaves et al., 2019). When testing whether sea-level changes have affected volcanism (e.g., Wallmann et al., 1988), it can be assumed that rates of lithostatic (un)loading are constant at the scale of an individual volcano or region. On the other hand, ice advance or retreat can occur at different rates within separate valleys of the same volcano due to local morphological and climatological effects (Eaves et al., 2019). The following discussion focusses on the general timing of ice retreat during the Last Termination for the purpose of comparing that timeframe to the precision of eruption age measurements for lava flows, because links between long-term eruptive rates and small-scale glacier mass fluctuations are not well-studied.

The rapid rise in sea-level from 18 to 11.7 ka reflects the wholesale melting of ice sheets and glaciers during the Last Glacial Termination (Denton et al., 2010), which is supported by the stacked record of benthic foraminiferal $\delta^{18}O$ compositions (Lisiecki and Raymo, 2005). For the sea-level record, the average 2σ error on corrected coral ages calculated from published U and Th isotope ratio data over that period is ±0.7 ka (Thompson and Goldstein, 2006). On land, moraine records at or near the volcanoes assessed in this review reflect a period of approximately 10 kyr for the retreat of glaciers from LGM to near-historical extents. Davies et al. (2020) summarized that the Patagonian Ice Sheet in South America started to retreat from greatest extent at ~28 ka and then stabilised at 21–18 ka. Subsequently, the ice sheet underwent rapid deglaciation and separated into disconnected ice masses by 15 ka, followed by readvances or stabilisations of glaciers at 14–13 ka and 11 ka. These conclusions are supported by ^{10}Be exposure ages from moraines near Lago Palena on the border of Chile and Argentina (43.9° S; 71.5° W), which have 2σ errors on mean moraine ages of 0.8–1.4 ka (Sotores et al., 2022). This level of precision is similar to that (2σ values of 0.4–1.8 ka) reported for ^{3}He exposure dating of LGM and late-glacial moraines at Tongariro and Ruapehu volcanoes in New Zealand reported by Eaves et al. (2016), Eaves et al. (2019).

Timing of volcanism

The ^{40}Ar/^{39}Ar and K-Ar geochronometers have been applied extensively to define the eruptive histories of Quaternary volcanoes worldwide, and they are vital tools for constraining ages for late Pleistocene arc volcanic rocks. One or both of the dating methods have been used for each of the studies that are covered in this review. They are best suited to dating the microcrystalline (non-glassy) groundmass material of lava flows (Gamble et al., 2003; Fleck et al., 2014; Calvert et al., 2018; Sisson et al., 2019). In particular, lavas that were emplaced subaerially next to glaciers provide ideal products for dating because they pond into thick flows with slowly cooled interiors that produce coarsely crystalline groundmass textures (groundmass microlites >20 μm; Conway et al., 2016). In contrast, subglacial volcanism can produce glassy (and hydrothermally altered) volcanic products that are difficult to date using these methods (Flude et al., 2010; Guillou et al., 2010). Eruptive activity during interglacial stages at volcanoes may form rubbly, blocky, or thin lava flows over steep flanks or within ice-free valleys that are also characterized by glassy groundmass textures (Pure et al., 2020). Low radiogenic ^{40}Ar yields and high atmospheric ^{40}Ar in low-K and/or young (<20 ka) lavas also presents a major challenge for defining the recent eruption histories at arc volcanoes (Jicha, 2009).

The precision of geochronological data in studies assessed in this review is compared with the duration of the Last Termination in Figure 7. Out of 44 ages between 30 and 10 ka, five have 2σ values of 6%–9% relative to the age (i.e., 2σ values of 1.1–2.2 ka). A further ten age measurements have 2σ values of >9–20% relative to the preferred age. Sixteen lavas have 2σ values between 21% and 42% relative to the preferred age, and the remaining thirteen have 2σ values of 52%–93%. An age of 17.8 ± 2.2 ka reported by Conway et al. (2016) indicates, with 95% confidence, that the lava erupted between 20.0 and 15.6 ka. Despite being a relatively precise age, this ± 2σ range spans the period from full glacial conditions to major ice retreat at Ruapehu volcano. The 17.8 ± 2.2 ka age is however distinct from a re-advance at ~14–11 ka corresponding to the Antarctic Cold Reversal (Eaves et al., 2019). At Calbuco, an age of 11.5 ± 8.0 ka reported by Mixon et al. (2021) spans the period from LGM extent of the Patagonian Ice Sheet at 19.5 ka, through rapid retreat at 17 ka, to re-advances of glaciers at 14–13 ka, 11 ka, and 6–5 ka (Moreno et al., 2015). Combined with field observations, these age constraints are suitable for broadly identifying syn-versus post-glacial eruptive stages, but cannot be directly compared with climatic events on sub-kyr-scales (Figure 7). As such, it is difficult with currently available analytical precision to test the sensitivity of the volcanic response to deglaciation. For example, it would be valuable to know whether eruptions are initiated during large-scale glacier retreat, when a threshold of 70% of ice was lost, or 3 kyr after near-modern glacier extents were reached. Similarly, more precise age data may allow testing of whether minor stabilizations or re-advances of glaciers paused or slowed any potential increases in eruptive rates after the LGM. This has significant implications for understanding whether future glacial retreat under current warming will lead to increased rates of volcanism, and our ability to provide meaningful forecasts for such volcanic activity.

Calibrated ^{14}C ages for organic material underlying, overlying, or included in layers of volcanic material can provide precise geochronological constraints. Analytical uncertainties of ±100 years (2σ) are regularly reported (e.g., Bromley et al., 2019), which are significantly smaller than uncertainties on

TABLE 3 **Summary of changes in edifice growth rates relative to preceding periods as in Figure 3.**

Volcano	Increased km^3/kyr in ~MIS 5 (after MIS 6 deglaciation)?	Increased km^3/kyr in ~MIS 4–2 (during deglaciation)?	Post-LGM increase in km^3/kyr?
Mazama	Yes	No	Yes
Tungurahua	No	Yes	Yes
Calbuco	Yes	Yes	Yes
Puyehue- Cordón Caulle	Yes	Yes, but not much	Yes
Antuco-Sierra Velluda	Yes	No	Yes
Seguam	Yes	Yes	Yes
Adams	Yes	Yes	No
Ampato-Sabancaya	Yes	Yes	Yes
Pichincha	No	Yes	Yes
Antisana	No	No	Yes
Iliniza	Yes	Yes	No
Parinacota	No	Yes	Yes
Tongariro	Yes	No	Yes
Kaguyak	No	No	Yes

typical $^{40}Ar/^{39}Ar$ and K-Ar age determinations, as summarised above. Radiocarbon dating has been successfully used to establish high-resolution eruptive records from post-glacial tephras in studies that investigate potential causality between deglaciation and apparent eruption rates (Watt et al., 2013; Rawson et al., 2016). Radiocarbon dating is not always feasible, however, particularly for eruptives with ages >50 ka and on the upper flanks of volcanoes in middle to high latitudes that have little organic material interbedded or overlain by lavas and pyroclastic units.

Summary

Neither eruptive episodes nor deglaciation are instantaneous events, and establishing causality between them has been, and will continue to be, a challenging endeavour. The limits of analytical precision with the K-Ar and $^{40}Ar/^{39}Ar$ geochronometers provide age estimates within 1–2 kyr ranges for medium-to high-K andesite lavas of Late Glacial age, but often 10 kyr or more for low-K lavas. Such uncertainties hinder meaningful assessments of whether variations in eruption rates were caused by deglaciation, and prevent the identification and measurement of time gaps (i.e., "lag times"; Figure 1C) that may occur between deglaciation and episodes of heightened eruptive activity.

Reproducibility of trends over multiple climate cycles

Post-LGM increases in edifice growth rates at arc volcanoes are a commonly reported feature that has been interpreted in some cases as evidence that deglaciation causes increased eruptive rates (e.g., Singer et al., 2008; see also Parinacota and Antuco-Sierra Velluda in Figure 3). Such a finding may indicate that magma systems at numerous volcanoes were primed for a response to unloading during the Last Termination and, therefore, may have experienced a similar evolution during previous transitions from cold to warm climate stages. Alternatively, the finding may indicate that biases in eruption records have affected numerous volcanoes similarly. Whereas some tephra records only permit investigation of post-LGM volcanic activity (e.g., Praetorius et al., 2016), sampling of Pleistocene volcanic edifices allows longer eruption records to be constructed that may permit investigation of eruption rate changes during older glacial/interglacial transitions. The observation of increased eruptive rates following deglaciation over multiple glacial-interglacial cycles at any given volcano would strengthen support for causality between ice unloading and eruption rates. Notwithstanding the challenges created by volcanic record incompleteness, and the uncertainty about whether edifice growth rates accurately reflect eruptive rates, the following discussion considers whether post-glacial increases in apparent eruptive rates at glaciated arc volcanoes are reproducible.

Reproducibility of edifice growth responses to deglaciation

Of the 20 volcanoes shown in Figure 3, 12 show post-LGM (~20 ka) increases in edifice growth rates (Tables 2, 3). However, only 7 of these 12 volcanoes show increased edifice growth rates after the MIS 6 deglaciation (~130 ka), which was the most substantial deglaciation event in the ~150 kyr preceding the LGM (Singer et al., 2000; Kaplan et al., 2004). Furthermore, of the 7 volcanoes that show post-glacial increases in edifice growth rates after MIS 6 and the LGM, 3 volcanoes show relative increases in edifice growth rates in the MIS 4–2 period as well, which is when ice coverage was generally increasing into the MIS 2 glaciation. Thus only 4 of 20 volcanoes examined (Mazama, Puyehue-Cordón Caulle, Antuco-Sierra Velluda, and Tongariro) show repeated increases in apparent eruptive rates following the MIS 6 glaciation and the LGM without contradictory increased growth rates in the MIS 4–2 period (Bacon and Lanphere, 2006; Singer et al., 2008; Martínez et al., 2018; Pure et al., 2020).

At Mazama, the increased eruptive rate in the Holocene is largely due to a large caldera-forming eruption that ejected ~50 km^3 of magma (Bacon and Lanphere, 2006; Figure 3). Eruptions of this size from Quaternary arc volcanoes are rare in the Cascade arc, with only three caldera-forming eruptions having occurred since 1.15 Ma (Hildreth, 2007). On correlations alone, it appears unlikely that the timing of the caldera-forming Crater Lake eruption at Mazama was triggered by deglaciation, noting also that the Kulshan caldera-forming eruption at 1.15 Ma was subglacial (Hildreth, 1996). In comparison, other Quaternary arcs that experienced similar amounts of ice-loading during Pleistocene glaciations have hosted more caldera-forming eruptions than the Cascade arc, such as eight or more in central Chile and >20 in the Alaska-Aleutian arc (Miller and Smith, 1987; Newhall and Dzurisin, 1988).

In the study of Puyehue-Cordón Caulle, the authors interpreted post-glacial increases in edifice growth rates to be the consequence of ice unloading of the crust, which promoted greater melt ascent from the deep crust than in pre-glacial and glacial periods (Singer et al., 2008). However, time *versus* compositional data from erupted lavas do not provide convincing support for this conclusion because neither edifice growth rates nor $\delta^{18}O$ climate proxy data are correlated with changes in the compositions of erupted lavas. The authors also acknowledge the influence of sector collapses and glacial erosion in modifying the amount of preserved edifice material at Puyehue-Cordón Caulle, which questions whether volcanic records are sufficiently representative of Pleistocene and Holocene eruptive rates.

Eruptive records from Antuco-Sierra Velluda have been interpreted to show potential increases in eruptive rates since ~150 ka, or after the MIS 6 glaciation, with a small decrease in edifice growth rates during 60–17 ka (~MIS 3–2), which the authors consider may be due to less severe glaciation during MIS 4 than in MIS 6 (Martínez et al., 2018; Figure 3). The growth rates since ~150 ka, however, are relatively uniform, and the variations in edifice growth rates since ~150 ka may be due to supra-glacial emplacement of eruptives in MIS 4–2.

At Tongariro, time-volume patterns were interpreted to arise from a preservation bias whereby lavas and pyroclastic deposits were more commonly emplaced onto ice during glacial periods that were subsequently transported to the ring plain as debris upon deglaciation (Pure et al., 2020). Systematic fluctuations in MgO concentrations through time, however, are uncorrelated with climatic cycles. Thus, the correlations between ice coverage and edifice growth rates at Tongariro are unlikely to accurately represent variable eruptive rates that were modulated by ice loading and unloading of the crust. Taken together, the time-volume-composition data from Mazama, Puyehue-Cordón Caulle, Antuco-Sierra Velluda, and Tongariro provide limited support for the idea that deglaciation causes increased eruptive rates at arc volcanoes.

A number of studies have examined potential volcanic responses to deglaciation over multiple glacial-interglacial cycles (e.g., Singer et al., 1997; Edwards et al., 2002; Hildreth et al., 2003b; Lanphere and Sisson, 2003; Bacon and Lanphere, 2006; Jicha and Singer, 2006; Singer et al., 2008; Schmidt and Grunder, 2009; Jicha et al., 2012; Calvert et al., 2014; Conway et al., 2016; Calvert, 2019; Coombs and Jicha, 2020; Pure et al., 2020; Santamaría et al., 2022) whereas other studies only considered or have data for edifice growth rates during and after the last glacial period (e.g., Fiertsein et al., 2011; Calvert et al., 2018). Of the studies that solely consider the MIS 3–1 interval, some show maximum edifice growth rates during the glacial period when ice coverage was greatest (e.g., Middle Sister: Calvert et al., 2018) whereas others show maximum apparent eruptive rates after the LGM (e.g., Calbuco, Chile: Mixon et al., 2021), as in Figure 3. For the former examples with relatively high eruption rates during MIS 3–2, the ages and distributions of ice-affected volcanic products can provide valuable information about the past extents of glaciers on their edifices. Although moraines record outer ice limits during advances, ice-bounded lavas that erupted independently of ice dynamics can provide unique constraints on the presence and thickness of glaciers throughout stages of prior glacial advance and retreat (e.g., Lescinsky and Fink, 2000; Edwards et al., 2002; Conway et al., 2015). Such data from glaciovolcanic deposits can be used to constrain paleoclimate models.

Several studies that examined multiple glacial-interglacial cycles have concluded that the clustering of radiometric ages into interglacial periods does not equate to increases in eruptive rates because time-volume trends do not show post-glacial increases in edifice growth rates (e.g., Hildreth et al., 2003b). Such observations contrast with approaches elsewhere that use the statistical distribution of radiometric ages as a proxy for edifice growth rates in the absence of detailed time-volume data (Calvert et al., 2014; Calvert, 2019). In these cases, although the number of age determinations in interglacial periods is often higher than in glacial periods, as at Mount Rainier, this correlation is not supported by time-volume records from edifice-forming lavas and pyroclastic deposits, because the apparent correlation is an artifact of non-deposition and non-preservation during the periods of abundant ice coverage (Calvert et al., 2014; Sisson and Calvert, 2023).

Progressively increasing edifice growth rates

Preservation and erosion act to reduce the volume of older edifice material, relative to younger edifice material. A potential consequence of this is that reconstructed time-volume data may show ever-increasing edifice growth rates through time. Examples of this pattern are Baker, Adams, and Parinacota (Figure 3), which have upward-facing curves with broadly increasing km^3/kyr rates through time (Hildreth and Lanphere, 1994; Hildreth et al., 2003b; Hora et al., 2007). If arguments are made that apparent eruptive rates increase after the LGM because of deglaciation and magma system depressurization, then the same test should be applied to earlier periods of the volcano's history. For Baker, Adams, and Parinacota, apparent eruptive rates increase during the last glacial period (i.e., ~MIS 4–2) relative to MIS 5, which contradicts the conclusion that deglaciation is the cause of increased eruptive rates.

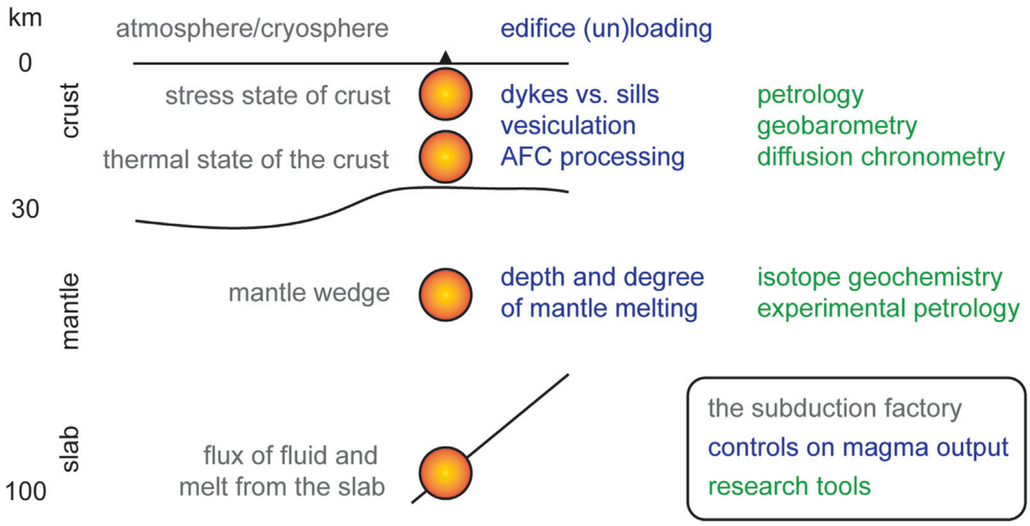

FIGURE 8
A summary of the components and characteristics of glaciated arc systems (grey text) that are influenced by processes controlling magma output (blue text), and some key research tools that can be used to determine how such processes operate (green text). The graphic presents a cross-section of a typical arc with depths and lithologies labelled in black text.

Interpretations from global tephra databases

Using a hybrid dataset of tephra records from 40 ka to present, Huybers and Langmuir (2009) reported that subaerial volcanism increased 2 to 6 times against background levels after the post-LGM deglaciation. The authors interpreted the feature to result from mantle decompression following deglaciation and then predicted that sea level rise would suppress eruption rates at mid-oceanic ridges. We note, however, that the tephra dataset reported Bryson et al. (2006), which was used for the analysis of Huybers and Langmuir (2009), acknowledges that terrestrial tephra records may be incomplete because of irregular preservation.

A comparable but more cautionary result was reported in a separate assessment of tephra records from the Andean southern volcanic zone, the Cascades, and Kamchatka by Watt et al. (2013). This study noted that inferred eruptive rates from the LGM to the late-Holocene varied by no more than a factor of two, and time-volume variations were not statistically significant. Watt et al. (2013) also reported that the extent of tephra record incompleteness in post-LGM records is substantial, and may be as little as 0.005% (1 in 20,000 events preserved), and that under-sampling of small (<0.1 km^3) eruptions prevents meaningful quantification of LGM vs. post-LGM eruption rates. For these reasons and those outlined in the ‘Biased preservation and exposure of eruptive products’ section above, it is unclear whether tephra records in the Holocene are sufficiently complete or free of preservation bias to make interpretations about whether global volcanic activity levels increased after the LGM.

Summary

Out of 20 time-volume datasets from arc volcanoes affected by glaciation (Figure 3), 4 show reproducible increases in edifice growth rates after deglaciation events and 12 provide unclear evidence for enhanced post-glacial volcanic activity. Interpretations for why edifice growth rates increase after deglaciation events vary widely and do not always consider eroded or unpreserved materials. For these reasons, periods of heightened erosion or reduced preservation may be misinterpreted as eruptive hiatuses. Some edifice records show progressive increases in growth rates through time (e.g., Baker, Adams, and Parinacota in Figure 3), but it is difficult to determine whether such trends are real or if they are artefacts of erosion, mass-wasting events, and burial; each of these phenomena may disproportionately reduce the exposed volumes of older edifice materials relative to younger materials. Terrestrial tephra records are likely to be less useful than lavas for testing the reproducibility of potential volcanism-deglaciation feedbacks because pre-Holocene tephra records are highly incomplete (Watt et al., 2013). Even for the last glacial cycle alone, it is disputed whether tephra records provide credible evidence for increased post-glacial eruptive rates because volcanic records are incomplete and time-volume variations are statistically insignificant (e.g., Huybers and Langmuir, 2009; Watt et al., 2013; Rawson et al., 2016). The response of volcanoes to deglaciation is not expected to be uniform in time or space, considering the differences in ice volume for each glacial stage and each arc. The response is also likely to differ based on which stage of a volcano’s magma production history is intersected by any given deglaciation event. Therefore, although reproducible correlations between increased ice volumes and reduced eruption rates, across multiple glacial-interglacial cycles, would therefore support a causal relationship, the opposite is untrue. That is, increases in ice volume that are uncorrelated with changes in eruptive rate would not support a causal connection. Furthermore, if increased edifice growth rates in the Holocene are cited as evidence for deglaciation causing increased eruptive rates, then this same standard of evidence should apply to previous glacial-interglacial cycles. These points may be useful for (re) considering whether feedback mechanisms between climate and volcanism often or seldom impacted eruption rates throughout the past and whether many or few volcanoes will be “primed” to respond to future ice retreat.

TABLE 4 Estimates of volume and the pressure applied by ice masses, a volcanic edifice, and the crust on a magmatic plumbing system at 5, 10, and 20 km below the pre-volcanic datum (surface of the crust).

Mass of ice load in heavily glaciated typical volcano				
radius of volcano footprint (km)	8			
volcano footprint (circular) (km^2)	201			
max. fraction of volcano footprint area covered by valley glaciers	0.2			
max. fraction of summit ice cap area covering volcano footprint	0.1			
max. summit ice cap thickness without full icesheet (km)[a]	0.2			
average valley depth (km)	0.2			
volcano volume (km^3)	70			
volcano density (kg/m^3)	2200			
volume covered by ice cap and valley glaciers (km^3)	12.1			
mass of ice/(mass of volcano + mass of ice)	0.07			
Edifice and crustal load pressure on a magma system at a typical volcano				
volcano height (m)	2000			
volcano density (kg/m^3)[b]	2200			
density of crust between volcano and magma system (kg/m^3)[c]	2600			
pressure on 5 km magma system without ice (MPa)	171			
pressure on 10 km magma system without ice (MPa)	298			
pressure on 20 km magma system without ice (MPa)	553			
Glacial load pressure on typical volcano's magmatic system				
ice cap or ice sheet thickness on volcano summit (m)	100	200	500	1000
pressure of ice cap or ice sheet (MPa)	1.0	2.0	4.9	9.8
increase against background pressure on 5 km deep magma system (%)	0.6	1.1	2.9	5.7
increase against background pressure on 10 km deep magma system (%)	0.3	0.7	1.6	3.3
increase against background pressure on 20 km deep magma system (%)	0.2	0.4	0.9	1.8

[a] Smellie and Skilling (1994); Magnússon et al. (2012); Cole et al. (2018).
[b] Tiede et al. (2005).
[c] Cassidy et al. (2009).

Alternative explanations for eruption rate and magma evolution trends

As noted above, exploring the relationship between deglaciation and volcanism has been hindered by geological record incompleteness (preservation), and our ability to read it in detail (precision) over various temporal and spatial scales (reproducibility). In addition to these challenges, it is also pertinent to consider that trends in long-term eruption rates and magma compositions may be controlled by factors unrelated to surficial ice loading variations at arc volcanoes. Indeed, the traditional paradigm for arc volcanoes is that their life cycles are defined by episodic growth and destruction, and that erupted compositions can vary unsystematically through time (e.g., Hobden et al., 1996; Davidson and de Silva, 2000; Eichelberger et al., 2006; Yamamoto et al., 2018). As such, hypotheses that differ from the one outlined in Figure 1 should also be considered in studies that seek to test causality between deglaciation and volcanism. This section briefly summarizes the processes from the surface to the slab that control magma generation and eruption at arc volcanoes (Figure 8), in order to explore how the potential influence of ice coverage compares with independent petrogenetic processes in the mantle and crust within the context of driving time-volume-composition trends. Firstly, however, we provide some context on glaciostatic loads as a reference for pressure changes that could be associated with deglaciation at typical arc volcanoes, and potential consequences for changed eruptive rates.

Pressurization of a magma system by surficial ice masses

Several studies have modelled crustal stress responses to deglaciation. Jellinek et al. (2004) estimated that a ~1–3 MPa decrease in loading pressure during deglaciation of eastern California may have caused stalled magma to ascend, and earlier estimates for silicic magmas were higher (~10–30 MPa decrease required for magma ascent: Jellinek and DePaolo, 2003). In the southern Chilean Andes at Mocho-Choshuenco, Rawson et al. (2016) estimated that loading pressure on crustal magmas at ~16 km depth decreased by ~6 MPa when continental glaciers melted following the LGM. Martínez et al. (2018) also inferred that a stress decrease of ~3–5 MPa following deglaciation that resulted in a basaltic eruption at 17 ka after the LGM at Antuco-Sierra Velluda. Together, these estimates indicate that pressure changes of about <10 MPa are linked to apparent changes in eruptive rates in arc systems.

Estimates of glaciostatic loads on the magmatic system of a representative, glacierized, arc volcano are given in Table 4, based on the conditions for Tongariro volcano during MIS 4 (Eaves et al., 2016; Cole et al., 2018). For a 70 km^3 volcano that is 20% covered by glaciers (200 m thick, in valleys) and 10% covered by a summit ice cap (200 m thick: e.g., Smellie and Skilling, 1994; Magnússon et al., 2012; Cole et al., 2018), the ice forms 7% of the mass load on the pre-volcanic datum, with the remainder coming from the volcano itself. The lithostatic load on a magmatic system, which includes the mass of a 2,000 m-high volcano, increases with its depth in the crust: 151 MPa at 5 km depth, 259 MPa at 10 km depth, and 475 MPa at 20 km depth. When an ice cap and glaciers of uniform thickness cover the volcano, the ice adds a further 1.0–9.8 MPa of pressure onto the magmatic system for ice thicknesses of 100–1,000 m, respectively. For magma systems at 5–20 km depth, this ice contributes 0.2%–5.7% of the total pressure on the magmatic system. The volcanic responses predicted by Jellinek et al. (2004) and Rawson et al. (2016), above, correspond to the pressure decreases that could be caused by removing ~100–600 m of ice from a glaciated volcano. As a percentage, these changes in glaciostatic loading amount to <3% of the total pressure on a typical continental arc magmatic system (Table 4).

Lithostatic loads and sector collapses

The hypothesis in Figure 1 states that deglaciation leads to increased eruption rates and that glaciation supresses eruption rates. However, testing causality between deglaciation and increased eruptive rates is challenging because major sector collapses can occur during or shortly after glacial retreat (Capra, 2006). It is therefore essential to determine the relative influence of glacial retreat *versus* sector collapse on magma systems when interpreting time-volume data for volcanoes because both phenomena cause magma system depressurization. The opposite situation, whereby rock mass is added to a volcano throughout its lifetime, should also be considered alongside glacial ablation when interpreting changes in apparent eruptive rates because these processes may have cancelling effects on magma system pressurization, especially in cases of rapid edifice growth (e.g., Pinel and Jaupart, 2000).

As noted previously (see 'Biased preservation and exposure of eruptive products' section), Capra (2006) surmised that numerous sector collapses at ice-capped volcanoes were induced by ice retreat, due to glacial de-buttressing, load discharge and fluid circulation as ice retreated. There are likely to be many more sector collapses associated with deglaciation than the 23 examples cited in that review, including the early and middle Holocene collapses of Ruapehu volcano (Palmer and Neall, 1989; Donoghue and Neall, 2001), and the Osceola Mudflow collapse event at Mount Rainier (Vallance and Scott, 1997). Such sector collapses removed rock (and remaining ice) masses from the summits and flanks of many volcanoes in catastrophic events. Sector collapse events are therefore relevant to interpreting time-volume-composition trends because collapse events remove *in situ* portions of the eruptive record (discussed in the "Biased preservation and exposure of eruptive products" section, above), and because collapse events immediately depressurize magma plumbing systems concurrently with gradual depressurization caused by deglaciation.

The response of magmatic systems to sector collapse events has been the topic of numerous studies, and the availability of high-resolution datasets for historical and pre-historical examples has inspired several detailed reviews (e.g., Watt, 2019; Romero et al., 2021). Watt (2019) noted that voluminous effusive eruptions of magma with anomalous compositions have often occurred following large sector collapses at arc volcanoes. Short-lived episodes of more frequent mafic eruptions support the idea that edifice unloading facilitates the ascent of dense, mafic magmas. This presents a challenge for interpreting time-composition-volume trends at deglaciated arc volcanoes: sector collapse events and deglaciation can both occur in the same several-millennia period, but both phenomena lead to magma system depressurization. If changes in time-composition-volume trends are related to magma depressurization, then it may be unclear if these trends were driven by sector collapse (over minutes) or deglaciation (over millennia). Whether magma system pressurization and associated changes in time-composition-volume trends were caused by deglaciation *versus* sector collapse will require high-resolution geochronological constraints that are supported by field evidence. Ultimately, however, if magma systems respond to sector collapse events that were triggered by ice retreat, then glaciation imparts a fundamental control on the evolution of eruptive activity at such volcanoes. This is pertinent for considering future hazards at glacierized edifices that will experience ice retreat in the future. Although magma systems may not directly respond to ice retreat linked to climate change, sector collapses and associated eruptive activity will pose significant threats in the future.

Crustal controls on the volumes and compositions of erupted magma

When interpreting time-volume-composition trends at glaciated arc volcanoes (Figure 3), it is pertinent to note that volcanic regions where glaciation has had no (or minor) impact also display variability in the rates of volcanism and geochemistry of erupted magma on time scales of 1–100 kyr. For example, thin glaciers may have been present only on a few volcanoes with summit elevations above 2,000 m a.s.l. during MIS 2 in Japan (Sawagaki et al., 2004), and thus deglaciation is not considered to have impacted their eruption rates. In a review of the volumetric and geochemical evolution of 29 arc volcanoes in Japan, Yamamoto et al. (2018) showed that renewed input of mafic magma and instances of crustal melting led to increased eruptive rates at several volcanoes. In contrast, volcanoes that displayed minor variability in erupted magma compositions were shown to be generally characterized by decreasing eruption rates.

None of the 33 volcanoes and volcanic systems covered by our review have exhibited any reproducible correlations between erupted magma composition and ice coverage. In keeping with this, several studies additional to those cited in Table 1 have further explained non-systematic trends for the time-sequenced compositions of erupted material at these volcanoes to be the result of complex open-system processes that operate in crustal magma storage regions (TDungan et al., 2001; Gamble et al., 2003; Mangler et al., 2021). There are very studies that have attributed changes in the composition of post-glacial eruptive products to depressurization *via* ice retreat. The most commonly cited of these is the case study of Rawson et al. (2016), who identified post-glacial stages of evacuation (eruption of andesite to rhyolite magma), relaxation (basaltic andesite to andesite) and recovery (basaltic andesite to dacite) in the period since 12 ka at Mocho-Choshuenco volcano in Chile. In contrast, Mangler et al. (2022) showed that the sizes, styles, and compositions of eruptions at Popocatépetl since 14 ka can be explained by magma recharge and mixing processes. Conway et al. (2018) showed that a distinct trend towards the eruption of more mafic lavas at Ruapehu commenced at ~26 ka, prior to deglaciation, and thus was not caused by ice unloading of the magma system. The trend was surmised to reflect changes to the composition of assimilated crustal melts in the plumbing system. The eruption of high-Mg basaltic andesites at ~45–40 ka at Ruapehu also contradicts the idea of suppressing denser magmas during glacial stages (Conway et al., 2020).

The long-term flux of magma from the mantle to the surface affects the thermal and chemical evolution of the crust that hosts magma systems beneath volcanoes in both non-glaciated and glaciated arcs (Sisson et al., 2013). It is well-documented that this internal evolution (as opposed to the external, surficial evolution of varied ice/edifice load over time) impacts the timescales of magma residence, volumes of magma reservoirs, extents of crystal fractionation, and compositions of crustal assimilants (e.g., Bacon and Lanphere, 2006). It is therefore valid to test alternative hypotheses to the one shown in Figure 1, such as those that explain the evolution of crustal magma systems in non-glaciated regions, when interpreting time-volume and time-composition trends at glaciated volcanoes.

Signals from the slab and mantle

Flare-ups of increased magma production at circum-Pacific arcs have occurred in 5–10 Myr-long pulses since 50 Ma, which has been linked to major tectonic plate reorganizations (Jicha et al., 2009). In addition to variations in the rate, composition, temperature and angle of subducting slabs (e.g., Gill, 1981), mantle processes can also influence the productivity of arc magma systems, even over periods of months to years (e.g., Ruprecht and Plank, 2013). Further examples of mantle and slab control on eruptive activity and magmatic production rates follow.

In young lavas from the Alaska-Aleutian arc, George et al. (2003) reported positive correlations between convergence rate, volcano volume, and ^{238}U excesses that were interpreted to show that the volume of magma produced depends on the size of the fluid flux supplied to the wedge <10 kyr prior to eruption. Evidence presented by Taniuchi et al. (2020) further supports this conclusion by showing that a ~7 kyr-period of relatively high eruptive output at Rishiri volcano (northwestern Japan) was driven by the production of hydrous primary magmas *via* aqueous fluid-fluxed melting of mantle peridotite. Geospeedometry data have also provided evidence for fast migration of mantle-derived magmas to the surface. Ruprecht and Plank (2013) reported Ni diffusion time scales for olivine of weeks to months that indicate magma ascent rates of 55–80 m per day through the ~35 km-thick crust beneath Irazú volcano in Costa Rica. Fe-Mg interdiffusion time scales for orthopyroxene phenocrysts in high-Mg andesite and dacite lavas from Ruapehu volcano indicate mantle-derived magmas hybridized with mid-crustal felsic magmas less than 10 days before voluminous lava eruptions during MIS 3 (Conway et al., 2020).

The eruption of high-Mg andesite at volcanoes in the northern Cascade arc also indicates slab and mantle processes have a fundamental control on short-term episodes of mafic volcanism with no apparent linkage to deglaciation (Sas et al., 2017). Wall et al. (2018) noted that the waxing and waning eruptive output of andesitic volcanoes in the Cascades over the Pleistocene reflects variability in the thermal energy delivered from the mantle at subduction zones, rather than cyclic surficial loading and unloading imposed by climate variability. Variability in magma compositions and eruptive rates along the Cascades volcanic arc was also shown by Till et al. (2019) to predominantly be related to variations in the flux of basalt into the crust.

These examples from arc volcanoes indicate that slab and mantle processes influence eruption rates and the compositions of erupted materials, and that such processes can cause variability on time scales comparable with global climate cycles. Such alternative phenomena should be considered when evaluating whether deglaciation has caused increased eruption rates or variations in erupted magma compositions, or whether such trends were fundamentally controlled by crustal and/or mantle and slab processes that have not been affected by lithostatic or glaciostatic loading changes.

Summary

A number of alternative explanations, beyond the deglaciation hypothesis in Figure 1, should be considered and tested before trends in an arc volcano's time-volume-composition evolution are interpreted to result from ice loading and unloading. The timescales of magma production and transfer through the crust range from several millennia to several days, which shows that processes other than glaciation and deglaciation can alter eruption rates and magma compositions throughout the life cycles of arc volcanoes.

Future outlook

This discussion has outlined the issues that have so far hindered comprehensive testing of the hypothesis in Figure 1. New studies will have additional tools to overcome some of these challenges, but new challenges may also appear. We outline some of these below.

Large errors on erupted volume estimates will remain a major limitation for investigating volcano growth histories and magma generation processes in the context of glaciation, however, some ongoing technological developments may help. The application of LiDAR and drone-assisted photogrammetry in vegetated and remote areas will improve delineation of map units and calculation of more accurate volume data, as well as integration of edifice and ring plain records of volcano growth and collapse. Despite this, the age and provenance of older volcanic material that is completely buried under younger eruptives will remain difficult to establish in future geological mapping projects.

Improvements in the precision of the K-Ar and ^{40}Ar/^{39}Ar mass spectrometry will greatly assist investigations of potential causality between deglaciation and increased eruption rates, and will create new opportunities for dating Late Pleistocene and Holocene volcanic rocks with relatively low K_2O contents. Improved sensitivity and wider dynamic range in Faraday cup detector amplifiers, such as for the Isotopx ATONA type, are particularly promising (Cox et al., 2020; Mixon et al., 2022). These developments that improve our ability to measure large sample sizes for rocks that have low yields of radiogenic ^{40}Ar will make significant contributions to geochronological datasets, particularly for low-K_2O and Holocene lavas. Moreover, such advances will benefit related fields in geoscience by providing precise age constraints for volcanic rocks that can be used to reconstruct glacier extents and geomagnetic field characteristics in the past (Ingham et al., 2017; Channell et al., 2020).

Investigations into the reproducibility of eruption trends over multiple glacial cycles and sensitivity of volcanic systems to different unloading scenarios will push forward attempts to carry out long-term forecasting of volcanic activity. Establishing long-term patterns in eruptive behaviour (whether influenced by climate or other factors) should be applicable to understanding and mitigating the risks of future eruptions. Interpretations of time-volume-compositional trends at arc volcanoes will be more accurate if mantle and crustal petrogenetic processes are considered alongside changes in lithostatic and/or glaciostatic loading. Integration between data and models will also lead to an improved understanding of magma genesis, storage, ascent, and eruption at arc volcanoes. Such detailed, multi-disciplinary case studies of target volcanoes are underway and will make significant contributions to our comprehension of arc volcanic systems (Singer et al., 2021).

New focus on the impact of climate change on active volcanoes could bring more urgency to understanding future warming and mitigating volcanic hazards. Volcanic eruptions and sector collapse events have immediate and devastating local to regional consequences relative to other global-scale climate change phenomena (e.g., rising sea level). Future volcanic activity and landslides may be increasingly viewed through the lens of modern-day climate change. To positively affect public and media responses to these potential hazards, a comprehensive understanding of the links between volcanism and the cryosphere should be targeted (Edwards et al., 2022).

Conclusion

The depressurization of a typical arc magmatic system, associated with deglaciation, is approximately 3% but may be up to ~10% depending on the depth of the magma system and the thickness of ice coverage. Noting this, of the 33 arc volcanoes and volcanic systems examined in this review, only 4 show increased edifice growth rates following the MIS 6 glaciation and the LGM, which are Mount Mazama, Puyehue-Cordón Caulle, Antuco-Sierra Velluda, and Tongariro (Bacon and Lanphere, 2006; Singer et al., 2008; Martínez et al., 2018; Pure et al., 2020). Across these four studies, there is limited agreement on why fluctuations in edifice growth rates and ice coverage are correlated. Phenomena that were proposed to explain correlated edifice growth rates and ice coverage in these four studies are: a post-glacial, ~50 km^3 caldera-forming eruption (Mazama); erosion and sector collapses that resulted in volcanic record incompleteness (Puyehue-Cordón Caulle); reduced preservation in periods of increased ice coverage when eruptives were emplaced supra-glacially onto ice and then ‘flushed’ to the ring plain (Tongariro); and crustal depressurization from deglaciation, although without any correlation between erupted compositions and climatic cycles (Puyehue-Cordón Caulle, Mazama, and Antuco-Sierra Velluda). Notably, none of the 33 volcanoes or systems show reproducible correlations between eruptive compositions and climatic cycles (or with apparent eruptive rates).

Although comparisons between edifice growth rates, eruptive compositions, and climatic cycles have been made here and in the 33 studies in Table 1, it is doubtful that edifice growth rates accurately represent actual eruptive rates for the following reasons.

(1) The total volume of erupted material at an arc volcano may be difficult to estimate because of significant volcanic record incompleteness. Lavas are much more likely to be preserved on the edifice because they are less prone to erosion (Hildreth et al., 2003b; Fierstein and Hildreth, 2008; Martínez et al., 2018), and pyroclastic deposits are generally preserved on the edifice only when they form large volumes (e.g., Bacon and Lanphere, 2006), are post-glacial (e.g., the Ngāuruhoe cone of Tongariro: Hobden et al., 1999; Pure et al., 2020), or are capped by lavas (Hackett and Houghton, 1989). On the ring plain, tephra deposits may be poorly preserved (Watt et al., 2013) or obliterated by continental glaciation (Hildreth, 1996).

(2) Significant proportions of a volcanic edifice are buried by surficial geology, and the buried proportion may be as high as ~80% of the total edifice volume (e.g., Tongariro, New Zealand: Pure et al., 2020). The unknown age, stratigraphy, and provenance of buried material limits the ability to interpret time-volume trends at arc volcanoes, whether in glaciated or non-glaciated settings.

(3) The volumes of materials that have been eroded from Pleistocene-Holocene age volcanoes *via* sector collapses, fluvial action, and glaciation are difficult to estimate accurately. Estimates vary widely (5%–50%: Hildreth et al., 2003b; Godoy et al., 2018) and are rarely constrained by volume estimates in drainage systems (e.g., Pure et al., 2020).

(4) Sector collapses are more likely to occur following deglaciation, potentially because unstable, glaciovolcanic landforms can collapse when they are no longer supported by ice masses (Vallance and Scott, 1997; Capra, 2006; Conway et al., 2016). Subsequent edifice growth therefore biases the preserved record to show greater volumes of post-glacial eruptives relative to lesser amounts of old and glacial-age materials that are removed from the edifice during collapse.

(5) Materials that are erupted during periods of high ice coverage, which are emplaced onto ice masses supra-glacially, will be 'flushed' to the ring plain as debris during deglaciation (Hildreth and Fierstein, 2012; Coombs and Jicha, 2020; Pure et al., 2020). This biases the edifice record to show lower edifice growth rates during glacial periods, even though there may be no decrease in actual eruptive rates.

Studies that cannot address the five considerations above, to show that edifice growth rates are representative of actual eruptive rates, may lack the evidence needed to make robust interpretations about deglaciation causing increased eruptive rates or affecting other magmatic processes. Noting this, studies that aim to test whether deglaciation causes increased eruptive rates (or that deglaciation controls the compositions of post-glacial eruptives) should satisfy two other requirements, as follows.

(1) Radiometric age data that establishes the timings of eruptions relative to climatic changes must be sufficiently precise to demonstrate sequencing outside of analytical uncertainty. For lavas erupted in the Last Glacial cycle, the 2σ uncertainties of K-Ar and $^{40}Ar/^{39}Ar$ age determinations (Figure 7) are often ~1–10 kyr larger than 2σ age uncertainties in records of ice extent and sea level that are constrained with ^{14}C ages (2σ of typically ±100 years: Bromley et al., 2019) and U-Th disequilibria coral ages (2σ of typically ±0.7 kyr: Thompson and Goldstein, 2006). Notably, ^{3}He and other cosmogenic nuclide systems applied to boulders in Pleistocene-Holocene moraines often have similar analytical uncertainties to those of $^{40}Ar/^{39}Ar$ age determinations on similar-aged lavas (*cf.*, Eaves et al., 2016; Pure et al., 2020).
(2) Alternative processes that can control eruptive rates should be considered when concluding that increased eruptive rates are (solely) caused by deglaciation and associated crustal depressurization. Fluctuations in time-volume trends at non-glaciated arc volcanoes (e.g., Yamamoto et al., 2018) show that eruptive rates can be controlled by processes other than crustal depressurization. Such processes, including tectonically controlled variations in crustal stress states, can influence eruptives rates at arc volcanoes in both glaciated and non-glaciated settings (e.g., Lanphere and Sisson, 2003; Allan et al., 2012).

Within the context of current anthropogenic climate change, interest in the response of volcanoes to deglaciation will continue to grow. Utilization of new mapping and geochronology tools, integration of geological data and models, comprehensive testing of multiple hypotheses, and clear communication of results, limitations, and interpretations will be primary objectives for future research in this field.

Author contributions

All authors listed have made a substantial, direct, and intellectual contribution to the work and approved it for publication.

Funding

CC and OI were supported by JSPS-RSNZ bilateral grant JPJSBP120211003.

Acknowledgments

The authors gratefully acknowledge valuable discussions with Andrew Calvert, Graham Leonard, Thomas Sisson, Dougal Townsend, James Vallance, and Colin Wilson. Thank you to John Smellie and the 3 reviewers for their detailed and helpful comments.

Conflict of interest

The authors declare that the research was conducted in the absence of any commercial or financial relationships that could be construed as a potential conflict of interest.

Publisher's note

Supplementary material

The Supplementary Material for this article can be found online at: https://www.frontiersin.org/articles/10.3389/feart.2023.1082342/full#supplementary-material

References

Allan, A. S. R., Wilson, C. J. N., Millet, M.-A., and Wysoczanski, R. J. (2012). The invisible hand: Tectonic triggering and modulation of a rhyolitic supereruption. *Geology* 40, 563–566. doi:10.1130/G32969.1

Aubry, T. J., Farquharson, J. I., Rowell, C. R., Watt, S. F. L., Pinel, V., Beckett, F., et al. (2022). Impact of climate change on volcanic processes: Current understanding and future challenges. *Bull. Volcanol.* 84 (58), 58. doi:10.1007/s00445-022-01562-8

Bablon, M., Quidelleur, X., Samaniego, P., Le Pennec, J.-L., Santamaría, S., Liorou, C., et al. (2020). Volcanic history reconstruction in northern Ecuador: Insights for eruptive and erosion rates on the whole Ecuadorian arc. *Bull. Volcanol.* 82 (11), 11. doi:10.1007/s00445-019-1346-1

Bacon, C. R., and Lanphere, M. A. (2006). Eruptive history and geochronology of MountMount Mazama and the Crater Lake region, Oregon. *Geol. Soc. Amer. Bull.* 118, 1331–1359. doi:10.1130/B25906.1

Bindeman, I. N., Leonov, V. L., Izbekov, P. E., Ponomareva, V. V., Watts, K. E., Shipley, N. K., et al. (2010). Large-volume silicic volcanism in Kamchatka: Ar–Ar and U–Pb ages, isotopic, and geochemical characteristics of major pre-holocene caldera-forming eruptions. *J. Volcanol. Geotherm. Res.* 189, 57–80. doi:10.1016/j.jvolgeores.2009.10.009

Bromley, G. R. M., Thouret, J.-C., Schimmelpfennig, I., Mariño, J., Valdivia, D., Rademaker, K., et al. (2019). *In situ* cosmogenic ^{3}He and ^{36}Cl and radiocarbon dating of volcanic deposits refine the Pleistocene and Holocene eruption chronology of SW Peru. *Bull. Volcanol.* 81 (64), 64. doi:10.1007/s00445-019-1325-6

Bryson, R. U., Bryson, R. A., and Ruter, A. (2006). A calibrated radiocarbon database of late Quaternary volcanic eruptions. *eEarth Discuss.* 1, 123–134. doi:10.5194/eed-1-123-2006

Calvert, A. T., Fierstein, J., and Hildreth, W. (2018). Eruptive history of middle sister, Oregon Cascades, USA–product of a late Pleistocene eruptive episode. *Geosphere* 14, 2118–2139. doi:10.1130/GES01638.1

Calvert, A. T. (2019). "Inception ages, growth spurts, and lifespans of Cascade Arc volcanoes," in *American geophysical union, fall meeting*. abstract id. V43G-0170.

Calvert, A. T., Sisson, T. W., Bacon, C. R., and Ferguson, D. J. (2014). "Apparent eruptive response of Cascades and Alaska-Aleutian arc volcanoes to major deglaciations," in *American geophysical union, fall meeting*. abstract id. V11B-4710.

Cameron, E., Gamble, J., Price, R., Smith, I., McIntosh, W., and Gardner, M. (2010). The petrology, geochronology and geochemistry of Hauhungatahi volcano, S.W. Taupo Volcanic Zone. *J. Volcanol. Geotherm. Res.* 190, 179–191. doi:10.1016/j.jvolgeores.2009.07.002

Capra, L. (2006). Abrupt climatic changes as triggering mechanisms of massive volcanic collapses. *J. Volcanol. Geotherm. Res.* 155, 329–333. doi:10.1016/j.jvolgeores.2006.04.009

Capra, L., Bernal, J. P., Carrasco-Núñez, G., and Roverato, M. (2013). Climatic fluctuations as a significant contributing factor for volcanic collapses. Evidence from Mexico during the Late Pleistocene. *Glob. Planet. Change.* 100, 194–203. doi:10.1016/j.gloplacha.2012.10.017

Cassidy, J., Ingham, M., Locke, C. A., and Bibby, H. (2009). Subsurface structure across the axis of the Tongariro volcanic centre, New Zealand. *J. Volcanol. Geotherm. Res.* 179, 233–240. doi:10.1016/j.jvolgeores.2008.11.017

Cassidy, M., Watt, S. F. L., Talling, P. J., Palmer, M. R., Edmonds, M., Jutzeler, M., et al. (2015). Rapid onset of mafic magmatism facilitated by volcanic edifice collapse. *Geophys. Res. Lett.* 42, 4778–4785. doi:10.1002/2015GL064519

Channell, J. E. T., Singer, B. S., and Jicha, B. R. (2020). Timing of Quaternary geomagnetic reversals and excursions in volcanic and sedimentary archives. *Quat. Sci. Rev.* 228, 106114. doi:10.1016/j.quascirev.2019.106114

Cisneros de León, A., Mittal, T., de Silva, S. L., Self, S., Schmitt, A. K., and Kutterolf, S. (2022). On synchronous supereruptions. *Front. Earth Sci.* 10 (827252). doi:10.3389/feart.2022.827252

Clynne, M. A., Calvert, A. T., Wolfe, E. W., Evarts, R. C., Fleck, R. J., and Lanphere, M. A. (2008). "The Pleistocene eruptive history of Mount St. Helens, Washington, from 300,000 to 12,800 years before present," in *A volcano rekindled; the renewed eruption of Mount St. Helens, 2004–2006*. Editor D. R. Sherrod, 1750, 593–627. doi:10.3133/pp175028

Cole, R. P., White, J. D. L., Conway, C. E., Leonard, G. S., Townsend, D. B., and Pure, L. R. (2018). The glaciovolcanic evolution of an andesitic edifice, South Crater, Tongariro volcano, New Zealand. *J. Volcanol. Geotherm. Res.* 352, 55–77. doi:10.1016/j.jvolgeores.2017.12.003

Cole, R. P., White, J. D. L., Townsend, D. B., Leonard, G. S., and Conway, C. E. (2020). Glaciovolcanic emplacement of an intermediate hydroclastic breccia-lobe complex during the penultimate glacial period (190–130 ka), Ruapehu volcano, New Zealand. *Geol. Soc. Amer. Bull.* 132 (9–10), 1903–1913. doi:10.1130/B35297.1

Conway, C. E., Chamberlain, K. J., Harigane, Y., Morgan, D. J., and Wilson, C. J. N. (2020). Rapid assembly of high-Mg andesites and dacites by magma mixing at a continental arc stratovolcano. *Geology* 48, 1033–1037. doi:10.1130/G47614.1

Conway, C. E., Gamble, J. A., Wilson, C. J. N., Leonard, G. S., Townsend, D. B., and Calvert, A. T. (2018). New petrological, geochemical, and geochronological perspectives on andesite-dacite magma Genesis at Ruapehu volcano, New Zealand. *Amer. Mineral.* 103, 565–581. doi:10.2138/am-2018-6199

Conway, C. E., Leonard, G. S., Townsend, D. B., Calvert, A. T., Wilson, C. J. N., Gamble, J. A., et al. (2016). A high-resolution ^{40}Ar/^{39}Ar lava chronology and edifice construction history for Ruapehu volcano, New Zealand. *J. Volcanol. Geotherm. Res.* 327, 152–179. doi:10.1016/j.jvolgeores.2016.07.006

Conway, C. E., Townsend, D. B., Leonard, G. S., Wilson, C. J. N., Calvert, A. T., and Gamble, J. A. (2015). Lava-ice interaction on a large composite volcano: A case study from Ruapehu, New Zealand. *Bull. Volcanol.* 77 (21), 21. doi:10.1007/s00445-015-0906-2

Coombs, M. L., and Jicha, B. R. (2020). The eruptive history, magmatic evolution, and influence of glacial ice at long-lived Akutan volcano, eastern Aleutian Islands, Alaska, USA. *Geol. Soc. Amer. Bull.* 133, 963–991. doi:10.1130/B35667.1

Cox, S. E., Hemming, S. R., and Tootell, D. (2020). The Isotopx NGX and ATONA Faraday amplifiers. *Geochronol* 2, 231–243. doi:10.5194/gchron-2-231-2020

Dalton, A. S., Margold, M., Stokes, C. R., Tarasov, L., Dyke, A. S., Adams, R. S., et al. (2020). An updated radiocarbon-based ice margin chronology for the last deglaciation of the North American Ice Sheet Complex. *Quat. Sci. Rev.* 234 (106223), 106223. doi:10.1016/j.quascirev.2020.106223

Davidson, J., and de Silva, S. (2000). "Composite volcanoes," in *Encyclopedia of volcanoes*. Editor H. Sigurdsson (London: Academic Press), 663–682.

Davies, B. J., Darvill, C. M., Lovell, H., Bendle, J. M., Dowdeswell, J. A., Fabel, D., et al. (2020). The evolution of the Patagonian Ice Sheet from 35 ka to the present day (PATICE). *Earth-Sci. Rev.* 204, 103152. doi:10.1016/j.earscirev.2020.103152

Delgado Granados, H., Julio Miranda, P., Huggel, C., Ortega del Valle, S., and Alatorre Ibargüengoitia, M. A. (2007). Chronicle of a death foretold: Extinction of the small-size tropical glaciers of Popocatépetl volcano (Mexico). *Glob. Planet. Change.* 56, 13–22. doi:10.1016/j.gloplacha.2006.07.010

Denton, G. H., Anderson, R. F., Toggweiller, J. R., Edwards, R. L., Schaeffer, J. M., and Putnam, A. E. (2010). The last glacial termination. *Science* 328, 1652–1656. doi:10.1126/science.1184119

Donoghue, S. L., and Neall, V. E. (2001). Late Quaternary constructional history of the southeastern Ruapehu ring plain, New Zealand. *New zeal. J. Geol. geophys.* 44, 439–466. doi:10.1080/00288306.2001.9514949

Dungan, M. A., Wulff, A., and Thompson, R. (2001). Eruptive stratigraphy of the tatara-san Pedro complex, 36degreesS, southern volcanic zone, Chilean Andes: Reconstruction method and implications for magma evolution at long-lived arc volcanic centers. *J. Petrol.* 42, 555–626. doi:10.1093/petrology/42.3.555

Eaves, S. R., and Brook, M. S. (2020). Glaciers and glaciation of north Island, New Zealand. *New zeal. J. Geol. geophys.* 64, 1–20. doi:10.1080/00288306.2020.1811354

Eaves, S. R., Mackintosh, A. N., Anderson, B. M., Doughty, A. M., Townsend, D. B., Conway, C. E., et al. (2016). The last glacial maximum in the central north Island, New Zealand: Palaeoclimate inferences from glacier modelling. *Clim. Past.* 12, 943–960. doi:10.5194/cp-12-943-2016

Eaves, S. R., Winckler, G., Mackintosh, A. N., Schaefer, J. M., Townsend, D. B., Doughty, A. M., et al. (2019). Late-glacial and Holocene glacier fluctuations in north Island, New Zealand. *Quat. Sci. Rev.* 223, 105914. doi:10.1016/j.quascirev.2019.105914

Edwards, B. R., Belousov, A., Belousova, M., and Melniko, D. (2015). Observations on lava, snowpack and their interactions during the 2012–13 Tolbachik eruption, Klyuchevskoy Group, Kamchatka, Russia. *J. Volcanol. Geotherm. Res.* 307, 107–119. doi:10.1016/j.jvolgeores.2015.08.010

Edwards, B. R., Kochtitzky, W., and Battersby, S. (2020). Global mapping of future glaciovolcanism. *Glob. Planet. Change* 195, 103356. doi:10.1016/j.gloplacha.2020.103356

Edwards, B. R., Russell, J. K., and Anderson, R. (2002). Subglacial, phonolitic volcanism at Hoodoo Mountain volcano, northern Canadian Cordillera. *Bull. Volcanol.* 64, 254–272. doi:10.1007/s00445-002-0202-9

Edwards, B. R., Russell, J. K., and Pollock, M. (2022). Cryospheric impacts on volcano-magmatic systems. *Front. Earth Sci.* 10 (871951). doi:10.3389/feart.2022.871951

Eichelberger, J. C. (1980). Vesiculation of mafic magma during replenishment of silicic magma reservoirs. *Nature* 288, 446–450. doi:10.1038/288446a0

Eichelberger, J. C., Izbekov, P. E., and Browne, B. L. (2006). Bulk chemical trends at arc volcanoes are not liquid lines of descent. *Lithos* 87, 135–154. doi:10.1016/j.lithos.2005.05.006

Fierstein, J., and Hildreth, W. (2008). Kaguyak dome field and its Holocene caldera, Alaska Peninsula. *J. Volcanol. Geotherm. Res.* 177, 340–366. doi:10.1016/j.jvolgeores.2008.05.016

Fiertsein, J., Hildreth, W., and Calvert, A. T. (2011). Eruptive history of South Sister, Oregon Cascades. *J. Volcanol. Geotherm. Res.* 207, 145–179. doi:10.1016/j.jvolgeores.2011.06.003

Fleck, R. J., Hagstrum, J. T., Calvert, A. T., Evarts, R. C., and Conrey, R. M. (2014). ^{40}Ar/^{39}Ar geochronology, paleomagnetism, and evolution of the Boring volcanic field, Oregon and Washington, USA. *Geosphere* 10, 1283–1314. doi:10.1130/GES00985.1

Flude, S., McGarvie, D. W., Burgess, R., and Tindle, A. G. (2010). Rhyolites at kerlingarfjöll, Iceland: The evolution and lifespan of silicic central volcanoes. *Bull. Volcanol.* 72, 523–538. doi:10.1007/s00445-010-0344-0

Gamble, J. A., Price, R. C., Smith, I. E. M., McIntosh, W. C., and Dunbar, N. W. (2003). ^{40}Ar/^{39}Ar geochronology of magmatic activity, magma flux and hazards at Ruapehu volcano, Taupo Volcanic Zone, New Zealand. *J. Volcanol. Geotherm. Res.* 120, 271–287. doi:10.1016/S0377-0273(02)00407-9

George, R., Turner, S., Hawkesworth, C., Morris, J., Nye, C., Ryan, J., et al. (2003). Melting processes and fluid and sediment transport rates along the Alaska-Aleutian arc from an integrated U-Th-Ra-Be isotope study. *J. Geophys. Res.* 108 (B5), 2252. doi:10.1029/2002JB001916

Gill, J. (1981). *Orogenic andesites and plate tectonics*. New York: Springer, 390.

Gisbert, G., Delgado-Granados, H., Mangler, M., Prytulak, J., Espinasa-Pereña, R., and Petrone, C. M. (2021). Evolution of the Popocatépetl volcanic complex: Constraints on periodic edifice construction and destruction by sector collapse. *J. Geol. Soc. Lond.* 179 (3). doi:10.1144/jgs2021-022

Godoy, B., Lazcano, J., Rodríguez, I., Martínez, P., Parada, M. A., Le Roux, P., et al. (2018). Geological evolution of Paniri volcano, central Andes, northern Chile. *J. South Amer. Earth Sci.* 84, 184–200. doi:10.1016/j.jsames.2018.03.013

Grosse, P., Orihashi, Y., Guzmán, S. R., Sumino, H., and Nagao, K. (2018). Eruptive history of Incahuasi, Falso Azufre and El cóndor quaternary composite volcanoes, southern central Andes. *Bull. Volcanol.* 80 (44), 44. doi:10.1007/s00445-018-1221-5

Guillou, H., Scao, V., Nomade, S., van Vliet-Lanoë, B., Liorzou, C., and Guðmunsson, A. (2010). ^{40}Ar/^{39}Ar dating of the Thorsmork ignimbrite and Icelandic sub-glacial rhyolites. *Quat. Sci. Rev.* 209, 52–62. doi:10.1016/j.quascirev.2019.02.014

Hackett, W. J., and Houghton, B. F. (1989). A facies model for a quaternary andesitic composite volcano: Ruapehu, New Zealand. *Bull. Volcanol.* 51, 51–68. doi:10.1007/BF01086761

Hall, M. L., Mothes, P. A., Samaniego, P., Militzer, A., Beate, B., Ramón, P., et al. (2017). Antisana volcano: A representative andesitic volcano of the eastern cordillera of Ecuador: Petrography, chemistry, tephra and glacial stratigraphy. *J. South Amer. Earth Sci.* 73, 50–64. doi:10.1016/j.jsames.2016.11.005

Hildreth, W., and Fierstein, J. (2012). Eruptive history of Mount Katmai, Alaska. *Geosphere* 8, 1527–1567. doi:10.1130/GES00817.1

Hildreth, W., Fierstein, J., and Lanphere, M. A. (2003b). Eruptive history and geochronology of the Mount Baker volcanic field, Washington. *Geol. Soc. Amer. Bull.* 115, 729–764. doi:10.1130/0016-7606(2003)115<0729:EHAGOT>2.0.CO;2

Hildreth, W. (1996). Kulshan caldera: A quaternary subglacial caldera in the north Cascades, Washington. *Geol. Soc. Amer. Bull.* 108, 786–793. doi:10.1130/0016-7606(1996)108<0786:KCAQSC>2.3.CO;2

Hildreth, W., Lanphere, M. A., and Fierstein, J. (2003a). Geochronology and eruptive history of the Katmai volcanic cluster, Alaska Peninsula. *Earth Planet. Sci. Lett.* 214, 93–114. doi:10.1016/S0012-821X(03)00321-2

Hildreth, W., and Lanphere, M. A. (1994). Potassium-argon geochronology of a basalt-andesite-dacite arc system: The Mount Adams volcanic field, Cascade Range of southern Washington. *Geol. Soc. Amer. Bull.* 106, 1413–1429. doi:10.1130/0016-7606(1994)106<1413:PAGOAB>2.3.CO;2

Hildreth, W. (2007). Quaternary magmatism in the Cascades–geological perspectives. *U. S. Geol. Surv. profess. Pap.* 1744, 125.

Hobden, B. J., Houghton, B. F., Davidson, J. P., and Weaver, S. D. (1999). Small and short-lived magma batches at composite volcanoes: Time windows at Tongariro volcano, New Zealand. *J. Geol. Soc. Lond.* 156, 865–868. doi:10.1144/gsjgs.156.5.0865

Hobden, B. J., Houghton, B. F., Lanphere, M. A., and Nairn, I. A. (1996). Growth of the Tongariro volcanic complex: New evidence from K-Ar age determinations. *New zeal. J. Geol. geophys.* 39, 151–154. doi:10.1080/00288306.1996.9514701

Hora, J. M., Singer, B. S., and Wörner, G. (2007). Volcano evolution and eruptive flux on the thick crust of the andean central volcanic zone: ^{40}Ar/^{39}Ar constraints from volcán Parinacota, Chile. *Geol. Soc. Amer. Bull.* 119, 343–362. doi:10.1130/B25954.1

Huybers, P., and Langmuir, C. (2009). Feedback between deglaciation, volcanism, and atmospheric CO_2. *Earth Planet. Sci. Lett.* 286, 479–491. doi:10.1016/j.epsl.2009.07.014

Ingham, E., Turner, G. M., Conway, C. E., Heslop, D., Roberts, A. P., Leonard, G. S., et al. (2017). Volcanic records of the Laschamp geomagnetic excursion from Mt Ruapehu, New Zealand. *Earth Plan. Sci. Lett.* 472, 131–141. doi:10.1016/j.epsl.2017.05.023

Jellinek, A. M., and DePaolo, D. J. (2003). A model for the origin of large silicic magma chambers: Precursors of caldera-forming eruptions. *Bull. Volcanol.* 65, 363–381. doi:10.1007/s00445-003-0277-y

Jellinek, A. M., Manga, M., and Saar, M. O. (2004). Did melting glaciers cause volcanic eruptions in eastern California? Probing the mechanics of dike formation. *J. Geophys. Res.* 109, B09206. doi:10.1029/2004JB002978

Jicha, B. R., Coombs, M. L., Calvert, A. T., and Singer, B. S. (2012). Geology and ^{40}Ar/^{39}Ar geochronology of the medium-to high-K Tanaga volcanic cluster, Western Aleutians. *Geol. Soc. Amer. Bull.* 124, 842–856. doi:10.1130/B30472.1

Jicha, B. R. (2009). Holocene volcanic activity at koniuji Island, Aleutians. *J. Volcanol. Geotherm. Res.* 185, 214–222. doi:10.1016/j.jvolgeores.2009.05.018

Jicha, B. R., Scholl, D. W., and Rea, D. K. (2009). Circum-Pacific arc flare-ups and global cooling near the Eocene-Oligocene boundary. *Geology* 37, 303–306. doi:10.1130/G25392A.1

Jicha, B. R., and Singer, B. S. (2006). Volcanic history and magmatic evolution of Seguam Island, aleutian Island arc, Alaska. *Geol. Soc. Amer. Bull.* 118, 805–822. doi:10.1130/B25861.1

Jull, M., and McKenzie, D. (1996). The effect of deglaciation on mantle melting beneath Iceland. *J. Geophys. Res.* 101, 21815–21828. doi:10.1029/96JB01308

Kaplan, M. R., Ackert, R. P., Jr., Singer, B. S., Douglass, D. C., and Kurz, M. D. (2004). Cosmogenic nuclide chronology of millennial-scale glacial advances during O-isotope stage 2 in Patagonia. *Geol. Soc. Amer. Bull.* 116, 308–321. doi:10.1130/B25178.1

Kaufman, D. S., Young, N. E., Briner, J. P., and Manley, W. F. (2011). Alaska palaeo-glacier atlas (version 2). *Dev. Quat. Sci.* 15, 427–445. doi:10.1016/B978-0-444-53447-7.00033-7

Kiyosugi, K., Connor, C., Sparks, R. S. J., Crosweller, H. S., Brown, S. K., Siebert, L., et al. (2015). How many explosive eruptions are missing from the geologic record? Analysis of the quaternary record of large magnitude explosive eruptions in Japan. *J. App. Volcanol.* 4, 17. doi:10.1186/s13617-015-0035-9

Klemetti, E. W., and Grunder, A. L. (2007). Volcanic evolution of volcán Aucanquilcha: A long-lived dacite volcano in the central Andes of northern Chile. *Bull. Volcanol.* 70, 633–650. doi:10.1007/s00445-007-0158-x

Kutterolf, S., Jegen, M., Mitrovica, J. X., Kwasnitschka, T., Freundt, A., and Huybers, P. J. (2013). A detection of Milankovitch frequencies in global volcanic activity. *Geology* 41, 227–230. doi:10.1130/G33419.1

Kutterolf, S., Schindelbeck, J. C., Jegen, M., Freundt, A., and Straub, S. M. (2019). Milankovitch frequencies in tephra records at volcanic arcs: The relation of kyr-scale cyclic variations in volcanism to global climate changes. *Quat. Sci. Rev.* 204, 1–16. doi:10.1016/j.quascirev.2018.11.004

Lachowycz, S. M., Pyle, D. M., Gilbert, J. S., Mather, T. A., Mee, K., Naranjo, J. A., et al. (2015). Glaciovolcanism at volcán sollipulli, southern Chile: Lithofacies analysis and interpretation. *J. Volcanol. Geotherm. Res.* 303, 59–78. doi:10.1016/j.jvolgeores.2015.06.021

Lanphere, M. A., and Sisson, T. W. (2003). Episodic Volcano growth at Mt. Rainier, Washington: A product of tectonic throttling? *Geol. Soc. Am.* 35 (6), 644.

Leonard, G. S., Cole, R. P., Christenson, B. W., Conway, C. E., Cronin, S. J., Gamble, J. A., et al. (2021). Ruapehu and Tongariro stratovolcanoes: A review of current understanding. *New zeal. J. Geol. geophys.* 64, 389–420. doi:10.1080/00288306.2021.1909080

Lescinsky, D. T., and Fink, J. H. (2000). Lava and ice interaction at stratovolcanoes: Use of characteristic features to determine past glacial extents and future volcanic hazards. *J. Geophys. Res. Solid Earth* 105, 23711–23726. doi:10.1029/2000JB900214

Lescinsky, D. T., and Sisson, T. W. (1998)., 26. Washington, 351–354. Ridge-forming, ice-bounded lava flows at Mount Rainier, Washington*Geology.* doi:10.1130/0091-7613(1998)026<0351:RFIBLF>2.3.CO;2

Lin, J., Svensson, A., Hvidberg, C. S., Lohmann, J., Kristiansen, S., Dahl-Jensen, D., et al. (2022). Magnitude, frequency and climate forcing of global volcanism during the last glacial period as seen in Greenland and Antarctic ice cores (60–9 ka). *Clim. Past.* 18, 485–506. doi:10.5194/cp-18-485-2022

Lisiecki, L. E., and Raymo, M. E. (2005). A Pliocene-Pleistocene stack of 57 globally distributed benthic δ^{18}O records. *Paleoceanog. Paleoclimatol.* 20 (PA1003). doi:10.1029/2004PA001071

Loewen, M. W., Dietterich, H. R., Graham, N., and Izbekov, P. (2021). Evolution in eruptive style of the 2018 eruption of Veniaminof volcano, Alaska, reflected in groundmass textures and remote sensing. *Bull. Volcanol.* 83 (72), 72. doi:10.1007/s00445-021-01489-6

Maclennan, J., Jull, M., McKenzie, D., Slater, L., and Grönvold, K. (2002). The link between volcanism and deglaciation in Iceland. *Geochem. Geophys. Geosyst.* 3, 1–25. doi:10.1029/2001GC000282

Magnússon, E., Gudmundsson, M. T., Roberts, M. J., Sigurðsson, G., Höskuldsson, F., and Oddsson, B. (2012). Ice-volcano interactions during the 2010 Eyjafjallajökull eruption, as revealed by airborne imaging radar. *J. Geophys. Res. Solid Earth* 117, B07405. doi:10.1029/2012JB009250

Mangler, M., Petrone, C. M., Hill, S., Delgado-Granados, H., and Prytulak, J. (2021). A pyroxenic view on magma hybridization and crystallization at Popocatépetl volcano, Mexico. *Front. Earth Sci.* 8 (362). doi:10.3389/feart.2020.00362

Mangler, M., Petrone, C. M., and Prytulak, J. (2022). Magma recharge patterns control eruption styles and magnitudes at Popocatépetl volcano (Mexico). *Geology* 50, 366–370. doi:10.1130/G49365.1

Martínez, P., Singer, B. S., Moreno Roa, H., and Jicha, B. R. (2018). Volcanologic and petrologic evolution of antuco-sierra Velluda, southern Andes, Chile. *J. Volcanol. Geotherm. Res.* 349, 392–408. doi:10.1016/j.jvolgeores.2017.11.026

Miller, T. P., and Smith, R. L. (1987). Late Quaternary caldera-forming eruptions in the eastern Aleutian arc, Alaska. *Geology* 15, 434–438. doi:10.1130/0091-7613(1987)15<434:LQCEIT>2.0.CO;2

Mixon, E. E., Jicha, B. R., Tootell, D., and Singer, B. S. (2022). Optimizing ^{40}Ar/^{39}Ar analyses using an Isotopx NGX-600 mass spectrometer. *Chem. Geol.* 593, 120753. doi:10.1016/j.chemgeo.2022.120753

Mixon, E. E., Singer, B. S., Jicha, B. R., and Ramirez, A. (2021). Calbuco, a monotonous andesitic high-flux volcano in the Southern Andes, Chile. *J. Volcanol. Geotherm. Res.* 416, 107279. doi:10.1016/j.jvolgeores.2021.107279

Mora, D., and Tassara, A. (2019). Upper crustal decompression due to deglaciation-induced flexural unbending and its role on post-glacial volcanism at the Southern Andes. *Geophys. J. Intern.* 216, 1549–1559. doi:10.1093/gji/ggy473

Moreno, P. I., Denton, G. H., Moreno, H., Lowell, T. V., Putnam, A. E., and Kaplan, M. R. (2015). Radiocarbon chronology of the last glacial maximum and its termination in northwestern Patagonia. *Quat. Sci. Rev.* 112, 233–249. doi:10.1016/j.quascirev.2015.05.027

Newhall, C. G., and Dzurisin, D. (1988). Historical unrest at large calderas of the world. *U. S. Geol. Surv. Bull.* 1855, 1108. doi:10.3133/b1855

Nowell, D. A. G., Jones, M. C., and Pyle, D. M. (2006). Episodic quaternary volcanism in France and Germany. *J. Quat. Sci.* 21, 645–675. doi:10.1002/jqs.1005

Palacios, D., Stokes, C. R., Phillips, F. M., Clague, J. J., Alcalá-Reygosa, J., Andrés, N., et al. (2020). The deglaciation of the Americas during the Last Glacial Termination. *Earth-Sci. Rev.* 203, 103113. doi:10.1016/j.earscirev.2020.103113

Palmer, B. A., and Neall, V. E. (1989). The Murimotu Formation–9500 year old deposits of a debris avalanche and associated lahars, Mount Ruapehu, North Island, New Zealand. *New zeal. J. Geol. geophys.* 32, 477–486. doi:10.1080/00288306.1989.10427555

Pinel, V., and Jaupart, C. (2000). The effect of edifice load on magma ascent beneath a volcano. *Phil. Trans. Roy. Soc. A* 358, 1515–1532. doi:10.1098/rsta.2000.0601

Praetorius, S., Mix, A., Jensen, B., Froese, D., Milne, G., Wolhowe, M., et al. (2016). Interaction between climate, volcanism, and isostatic rebound in Southeast Alaska during the last deglaciation. *Earth Planet. Sci. Lett.* 452, 79–89. doi:10.1016/j.epsl.2016.07.033

Pure, L. R., Leonard, G. S., Townsend, D. B., Wilson, C. J. N., Calvert, A. T., Cole, R. P., et al. (2020). A high resolution ^{40}Ar/^{39}Ar lava chronology and edifice construction history for Tongariro volcano, New Zealand. *J. Volcanol. Geotherm. Res.* 403, 106993. doi:10.1016/j.jvolgeores.2020.106993

Rawson, H., Pyle, D. M., Mather, T. A., Smith, V. C., Fontijn, K., Lachowycz, S. M., et al. (2016). The magmatic and eruptive response of arc volcanoes to deglaciation: Insights from southern Chile. *Geology* 44, 251–254. doi:10.1130/G37504.1

Rivera, M., Martin, H., Pennec, J.-L., Thouret, J.-C., Gourgaud, A., and Gerbe, M.-C. (2017). Petro-geochemical constraints on the source and evolution of magmas at El Misti volcano (Peru). *Lithos* 268, 240–259. doi:10.1016/j.lithos.2016.11.009

Robin, C., Samaniego, P., Pennec, J.-L., Fornari, M., Mothes, P., and van der Plicht, J. (2010). New radiometric and petrological constraints on the evolution of the Pichincha volcanic complex (Ecuador). *Bull. Volcanol.* 72, 1109–1129. doi:10.1007/s00445-010-0389-0

Romero, J. E., Polacci, M., Watt, S., Kitamura, S., Tormey, D., Siefeld, G., et al. (2021). Volcanic lateral collapse processes in mafic arc edifices: A review of their driving processes, types and consequences. *Front. Earth Sci.* 9 (639825). doi:10.3389/feart.2021.639825

Ruprecht, P., and Plank, T. (2013). Feeding andesitic eruptions with a high-speed connection from the mantle. *Nature* 500, 68–72. doi:10.1038/nature12342

Russell, J. K., Edwards, B. R., Turnbull, M., and Porritt, L. A. (2021). Englacial lake dynamics within a Pleistocene cordilleran ice sheet at Kima' Kho tuya (British Columbia, Canada). *Quat. Sci. Rev.* 273, 107247. doi:10.1016/j.quascirev.2021.107247

Samaniego, P., Barba, D., Robin, C., Fornari, M., and Bernard, B. (2012). Eruptive history of Chimborazo volcano (Ecuador): A large, ice-capped and hazardous compound volcano in the northern Andes. *J. Volcanol. Geotherm. Res.* 221–222, 33–51. doi:10.1016/j.jvolgeores.2012.01.014

Samaniego, P., Rivera, M., Mariño, J., Guillou, H., Liorzou, C., Zerathe, S., et al. (2016). The eruptive chronology of the Ampato–Sabancaya volcanic complex (Southern Peru). *J. Volcanol. Geotherm. Res.* 323, 110–128. doi:10.1016/j.jvolgeores.2016.04.038

Santamaría, S., Quidelleur, X., Hidalgo, S., Samaniego, P., Le Pennec, J.-L., Liorzou, C., et al. (2022). Geochronological evolution of the potentially active Iliniza Volcano (Ecuador) based on new K-Ar ages. *J. Volcanol. Geotherm. Res.* 424, 107489. doi:10.1016/j.jvolgeores.2022.107489

Sas, M., Debari, S. M., Clynee, M. A., and Rusk, B. G. (2017). Using mineral geochemistry to decipher slab, mantle, and crustal input in the generation of high-Mg andesites and basaltic andesites from the northern Cascade Arc. *Amer. Mineral.* 102, 948–965. doi:10.2138/am-2017-5756

Sawagaki, T., Aoki, T., Hasegawa, H., Iwasaki, S., Iwata, S., and Hirakawa, K. (2004). Late quaternary glaciations in Japan. *Dev. Quat. Sci.* 2, 217–225. doi:10.1016/S1571-0866(04)80127-1

Schindlbeck, J. C., Jegen, M., Freundt, A., Kutterolf, S., Straub, S. M., Mleneck-Vautravers, M. J., et al. (2018). 100-kyr cyclicity in volcanic ash emplacement: Evidence from a 1.1 Myr tephra record from the NW pacific. *Sci. Rep.* 8, 4440. doi:10.1038/s41598-018-22595-0

Schmidt, M. E., and Grunder, A. L. (2009). The evolution of North Sister: a volcano shaped by extension and ice in the central Oregon Cascade arc. *Geol. Soc. Amer. Bull.* 121, 643–662. doi:10.1130/B26442.1

Siebert, S. T. (2002). *Volcanoes of the world: An illustrated catalog of Holocene volcanoes and their eruptions, global volcanism program digital inf. Ser. GVP-3.* Washington, D. C: Smithsonian Institution. Available at: http://www.volcano.si.edu/world.

Sigvaldason, G. E., Annertz, K., and Nilsson, M. (1992). Effect of glacier loading/deloading on volcanism: Postglacial volcanic production rate of the Dyngjufjöll area, central Iceland. *Bull. Volcanol.* 54, 385–392. doi:10.1007/BF00312320

Singer, B. S., Hildreth, W., and Vincze, Y. (2000). ^{40}Ar/^{39}Ar evidence for early deglaciation of the central Chilean Andes. *Geophys. Res. Lett.* 27, 1663–1666. doi:10.1029/1999GL011065

Singer, B. S., Jicha, B. R., Harper, M. A., Naranjo, J. A., Lara, L. E., and Moreno-Roa, H. (2008). Eruptive history, geochronology, and magmatic evolution of the Puyehue-Cordón Caulle volcanic complex, Chile. *Geol. Soc. Bull. Amer.* 120, 599–618. doi:10.1130/B26276.1

Singer, B. S., Marcott, S. A., Ferrier, K., Townsend, M., Edwards, B. R., Huver, C., et al (2021). "An integrated approach to ice forcing in arc magmatic plumbing systems (IF-AMPS)," in *American geophysical union, fall meeting 2021*. abstract id. V14B-01.

Singer, B. S., Thompson, R. A., Dungan, M. A., Feeley, T. C., Nelson, S. T., Pickens, J. C., et al. (1997). Volcanism and erosion during the past 930 k.y. at the Tatara–San Pedro complex, Chilean Andes. *Geol. Soc. Bull. Amer.* 109, 127–142. doi:10.1130/0016-7606(1997)109<0127:VAEDTP>2.3.CO;2

Sisson, T. W., and Calvert, A. C. (2023). "Apparent, but probably false, ice-modulated volcanism at Mt. Rainier, Washington (USA)," in *International association of Volcanology and chemistry of Earth's interior, scientific assembly 2023*. abstract id. 1413.

Sisson, T. W., Salters, V. J. M., and Larson, P. B. (2013). Petrogenesis of Mount Rainier andesite: Magma flux and geologic controls on the contrasting differentiation styles at stratovolcanoes of the southern Washington Cascades. *Geol. Soc. Bull. Amer.* 126, 122–144. doi:10.1130/B30852.1

Sisson, T. W., Schmitt, A. K., Danišík, M., Calvert, A. T., Pempena, N., Huang, C.-Y., et al. (2019). Age of the dacite of sunset amphitheater, a voluminous Pleistocene tephra from Mount Rainier (USA), and implications for cascade glacial stratigraphy. *J. Volcanol. Geotherm. Res.* 376, 27–43. doi:10.1016/j.jvolgeores.2019.03.003

Smellie, J. L. (2021). Sedimentation associated with glaciovolcanism: A review. *Geol. Soc. Lond. Spec. Pub.* 520. doi:10.1144/SP520-2021-135

Smellie, J. L., and Skilling, I. P. (1994). Products of subglacial volcanic eruptions under different ice thicknesses: Two examples from Antarctica. *Sediment. Geol.* 91, 115–129. doi:10.1016/0037-0738(94)90125-2

Sotores, R. L., Sagredo, E. A., Kaplan, M. R., Martini, M. A., Moreno, P. I., Reynhout, S. A., et al. (2022). Glacier fluctuations in the northern Patagonian Andes (44°S) imply wind-modulated interhemispheric in-phase climate shifts during Termination 1. *Sci. Rep.* 12, 10842. doi:10.1038/s41598-022-14921-4

Stelling, P., Gardner, J. E., and Begét, J. (2005). Eruptive history of Fisher caldera, Alaska, USA. *J. Volcanol. Geotherm. Res.* 139, 163–183. doi:10.1016/j.jvolgeores.2004.08.006

Taniuchi, H., Kuritani, T., and Nakagawa, M. (2020). Generation of calc-alkaline andesite magma through crustal melting induced by emplacement of mantle-derived water-rich primary magma: Evidence from Rishiri Volcano, southern Kuril Arc. *Lithos* 354-355, 105362. doi:10.1016/j.lithos.2019.105362

Thompson, W. G., and Goldstein, S. L. (2006). A radiometric calibration of the SPECMAP timescale. *Quat. Sci. Rev.* 25, 3207–3215. doi:10.1016/j.quascirev.2006.02.007

Thouret, J. C., Finizola, A., Fornari, M., Legeley-Padovani, A., Suni, J., and Frechen, M. (2001). Geology of El Misti volcano near the city of arequipa, Peru. *Geol. Soc. Amer. Bull.* 113, 1593–1610. doi:10.1130/0016-7606(2001)113<1593:GOEMVN>2.0.CO;2

Tiede, C., Camacho, A. G., Gerstenecker, C., Fernández, J., and Suyanto, I. (2005). Modeling the density at Merapi volcano area, Indonesia, via the inverse gravimetric problem. *Geochem. Geophys. Geosyst.* 6, Q09011. doi:10.1029/2005GC000986

Till, C. B., Kent, A. J. R., Abers, G. A., Janiszewski, H. A., Gaherty, J. B., and Pitcher, B. W. (2019). The causes of spatiotemporal variations in erupted fluxes and compositions along a volcanic arc. *Nat. Commun.* 10 (1350), 1350. doi:10.1038/s41467-019-09113-0

Tost, M., and Cronin, S. J. (2015). Linking distal volcaniclastic sedimentation and stratigraphy with the development of Ruapehu volcano, New Zealand. *Bull. Volcanol.* 77 (94), 94. doi:10.1007/s00445-015-0977-0

Tuffen, H. (2010). How will melting of ice affect volcanic hazards in the twenty-first century? *Phil. Trans. Roy. Soc. A* 368, 2535–2558. doi:10.1098/rsta.2010.0063

Vallance, J. W., and Scott, K. M. (1997). The Osceola Mudflow from Mount Rainier: Sedimentology and hazard implications of a huge clay-rich debris flow. *Geol. Soc. Amer. Bull.* 109, 143–163. doi:10.1130/0016-7606(1997)109<0143:TOMFMR>2.3.CO;2

Wall, K. T., Grunder, A. L., Miggins, D. P., and Coble, M. A. (2018). Multistage growth and compositional change at the Goat Rocks volcanic complex, a major Pliocene–Pleistocene andesite center in the southern Washington Cascades. *Geol. Soc. Amer. Spec. Pap.* 538, 63–91. doi:10.1130/2018.2538(04

Wallmann, P. C., Mahood, G. A., and Pallard, D. P. (1988). Mechanical models for correlation of ring-fracture eruptions at Pantelleria, Strait of Sicily, with glacial sea-level drawdown. *Bull. Volcanol.* 50, 327–339. doi:10.1007/BF01073589

Watt, S. F. L., Pyle, D. M., and Mather, T. A. (2013). The volcanic response to deglaciation: Evidence from glaciated arcs and a reassessment of global eruption records. *Earth-Sci. Rev.* 122, 77–102. doi:10.1016/j.earscirev.2013.03.007

Watt, S. F. L. (2019). The evolution of volcanic systems following sector collapse. *J. Volcanol. Geotherm. Res.* 384, 280–303. doi:10.1016/j.jvolgeores.2019.05.012

Waythomas, C. F., and Wallace, K. L. (2002). Flank collapse at Mount Wrangell, Alaska, recorded by volcanic mass-flow deposits in the Copper River lowland. *Canad. J. Earth. Sci.* 39, 1257–1279. doi:10.1139/e02-032

Williams, P. W., McGlone, M., Neil, H., and Zhao, J.-X. (2015). A review of New Zealand palaeoclimate from the last interglacial to the global last glacial maximum. *Quat. Sci. Rev.* 110, 92–106. doi:10.1016/j.quascirev.2014.12.017

Wilson, A. M., and Russell, J. K. (2020). Glacial pumping of a magma-charged lithosphere: A model for glaciovolcanic causality in magmatic arcs. *Earth Planet. Sci. Lett.* 548 (116500), 116500. doi:10.1016/j.epsl.2020.116500

Yamamoto, T., Kudo, T., and Ishizuka, O. (2018). Temporal variations in volumetric magma eruption rates of Quaternary volcanoes in Japan. *Earth Planets Space* 70 (65), 65. doi:10.1186/s40623-018-0849-x

frontiers | Frontiers in Earth Science

TYPE Original Research
PUBLISHED 31 May 2023
DOI 10.3389/feart.2023.1137416

OPEN ACCESS

EDITED BY
Kristen Fauria,
Vanderbilt University, United States

REVIEWED BY
Calvin F. Miller,
Vanderbilt University, United States
Sean O'Donnell,
The University of Texas at Austin,
United States
Takeshi Kuritani,
Hokkaido University, Japan

*CORRESPONDENCE
Yoshihiko Tamura,
✉ tamuray@jamstec.go.jp

RECEIVED 04 January 2023
ACCEPTED 09 May 2023
PUBLISHED 31 May 2023

CITATION
Tamura Y, Sato T, Ishizuka O, McIntosh IM, Yoshida K, Maeno F and Chang Q (2023), Genesis and interaction of magmas at Nishinoshima volcano in the Ogasawara arc, western Pacific: new insights from submarine deposits of the 2020 explosive eruptions.
Front. Earth Sci. 11:1137416.
doi: 10.3389/feart.2023.1137416

Genesis and interaction of magmas at Nishinoshima volcano in the Ogasawara arc, western Pacific: new insights from submarine deposits of the 2020 explosive eruptions

Yoshihiko Tamura[1]*, Tomoki Sato[1], Osamu Ishizuka[2], Iona M. McIntosh[1], Kenta Yoshida[1], Fukashi Maeno[3] and Qing Chang[1]

[1]Research Institute for Marine Geodynamics (IMG), Japan Agency for Marine-Earth Science and Technology (JAMSTEC), Yokosuka, Japan, [2]Geological Survey of Japan, National Institute of Advanced Industrial Science and Technology (AIST), Tsukuba, Japan, [3]Earthquake Research Institute, The University of Tokyo, Tokyo, Japan

Sudden changes of eruption styles and magma compositions at arc volcanoes are enigmatic processes. Nishinoshima volcano, western Pacific, has had historical eruptions in 1973–1974 and from 2013 on and off to the present day. These eruptions were characterized by effusive Strombolian eruptions of andesite magmas until mid-June 2020, when they suddenly transitioned to violent explosive Strombolian eruptions that produced tephra fallout over a wide area. To understand this transition, we conducted marine surveys and sampling of the extensive submarine deposits of the tephra fallout. Our new data demonstrate that the full compositional range of the 2020 eruptions spans from basalt to dacite. We present evidence for magma mixing of newly injected basalt with andesite magmas. Nishinoshima consists of an andesitic main edifice surrounded by basaltic knolls: previous studies have shown that Nishinoshima andesite compositions can be generated by olivine fractionation of primary andesitic magmas that result from partial melting of hydrous mantle at relatively low pressures under the thin crust of the Ogasawara arc; knoll basalt compositions can be generated by partial melting of mantle at greater depths and were interpreted as older events of the volcano. We show that basalt magmas could have been generated throughout the entire history of Nishinoshima. In addition, we show that andesites from Nishinoshima and nearby Nishinoshima-Minami Knoll, which are only ~8 km apart, have distinct subduction components. Together, these data improve our understanding of the diverse primary magmas responsible for the construction and continuing eruptive activity of an active island arc volcano.

KEYWORDS

basalt, andesite, mission immiscible, magma mixing, violent eruption, new continent

1 Introduction

Sudden changes of eruption styles and magma compositions at arc volcanoes are enigmatic processes that must be better understood in order to prepare for volcanic disasters. Recent eruptions of Nishinoshima volcano, a highly active island arc volcano in the Izu-Ogasawara arc in the western Pacific, have exhibited such a change in eruption style and magma composition. These recent eruption deposits therefore provide important geochemical data for investigating this phenomenon.

The Izu-Ogasawara arc extends for 1,330 km between the island of Honshu, Japan, and the northern part of the Mariana arc. It consists of 21 active island volcanoes and submarine volcanoes, from Izu-Oshima Island in the north to Nikko Seamount in the south (https://www.data.jma.go.jp/vois/data/tokyo/STOCK/souran_eng/menu.htm) (Figure 1). The arc results from the subduction of old ocean floor (135–180 Ma) of the western Pacific Plate beneath the Philippine Sea Plate along the Izu-Ogasawara Trench. In the Ogasawara segment of the arc (south of ~30°N), the crust is divided by the Ogasawara Trough into the Eocene–Oligocene Ogasawara Ridge, including Chichijima island, and the present active Ogasawara arc, which has thin underlying crust (16–21 km, Kodaira et al., 2007) and consists mostly of submarine volcanoes.

Nishinoshima, a small island located ~1,000 km south of Tokyo in this active Ogasawara arc, is the subaerial summit of a much larger submarine volcano. The existence of this island has been known since 1702 (Aoki and Ossaka, 1974), but its first recorded eruption was in 1973. Following a lull of four decades, it suddenly began erupting again in November 2013 and activity has continued on and off until the present day.

A previous study (Tamura et al., 2019) reported whole rock geochemistry of lavas and scoria dredged from the main submarine volcanic edifice in 2015 (eruption age unknown) and subaerial lava blocks from the 2015 eruption sampled by unmanned helicopter. Both the submarine and subaerial samples are andesitic in composition (58–62 wt% SiO_2), and similar to the andesitic composition of the 1973 eruption products and pre-1973 edifice (Osaka, 1973; Osaka, 1974; Osaka, 1975; Osaka et al., 1974; Aoki et al., 1983; Ishizuka et al., 2007; Umino and Nakano, 2007). The crust underlying Nishinoshima volcano is 21 km thick, without any thinning due to rifting, and thus Nishinoshima is one of the closest arc volcanoes to the mantle on the Earth (Kodaira et al., 2007). Tamura et al. (2016) showed a relationship between crustal thickness and magma type in the Izu-Ogasawara and Aleutian oceanic arcs, where volcanoes on thin crust erupt predominantly andesitic magmas whereas volcanoes on thick crust erupt predominantly basaltic magmas. To explain this relationship Tamura et al. (2016) reviewed geochemical and petrological data and hypothesized that where the crust is thin, partial melting of hydrous mantle occurs at low pressure below the thin crust, producing andesitic primary magmas. Where the crust is thick, melting pressures are higher and only basaltic magmas tend to be produced. Although this may seem counter-intuitive, the implications of this hypothesis are: 1) the rate of continental crust accumulation, which is andesitic in composition, would have been greatest soon after subduction initiated on Earth, when most crust was thin; and 2) most andesite magmas erupted on continental crust could be recycled from "primary" andesite originally produced in oceanic arcs (Tamura et al., 2016). The geochemical data from the Nishinoshima andesites collected in and prior to 2015 have been interpreted as evidence for this process occurring at Nishinoshima volcano, i.e., the andesite magmas derive from a shallow mantle source (Tamura et al., 2019).

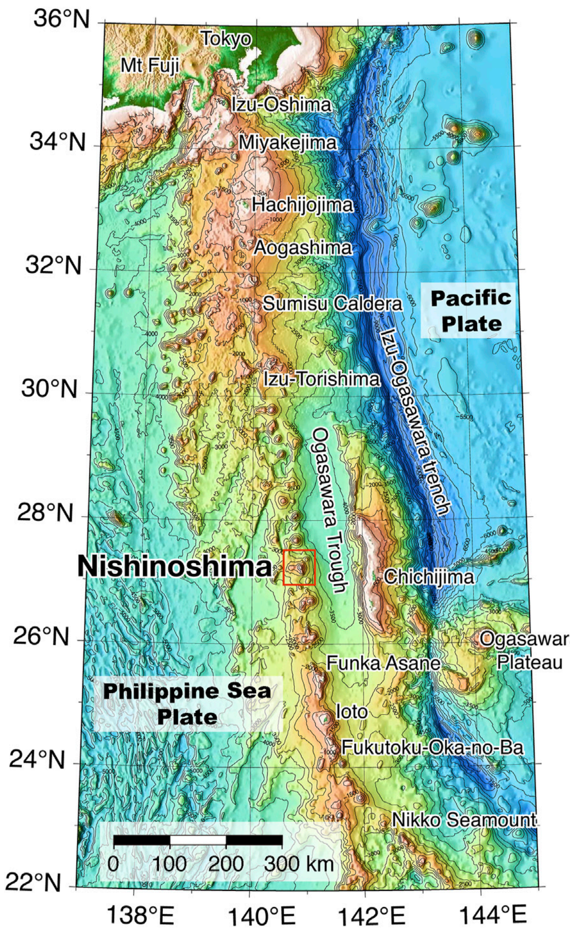

FIGURE 1
Bathymetric features of the Izu-Ogasawara arc system. Old ocean floor (135–180 Ma) of the western Pacific Plate is subducting beneath the active Izu-Ogasawara arc at the Izu-Ogasawara Trench. This island arc has 21 active island and submarine volcanoes from Izu-Oshima in the north to Nikko Seamount in the south (https://www.data.jma.go.jp/vois/data/tokyo/STOCK/souran_eng/menu.htm). The Ogasawara Trough divides the Ogasawara arc crust into the Eocene–Oligocene Ogasawara Ridge, including Chichijima, and the present Ogasawara arc, which has thin underlying crust (16–21 km) and consists mostly of submarine volcanoes. The map was created by using GMT v. 5.1.1 (http://gmt.soest.hawaii.edu/). Numbers on the contour lines are in meters. Nishinoshima means Western Island in Japanese, which could be a reference to the location of the island, approximately 130 km west of Chichijima.

Since the 2015 submarine and subaerial sampling Nishinoshima has continued to erupt, including a transition to more explosive activity. Maeno et al. (2021) reported the detailed sequence of Nishinoshima's eruptive activity from 2013 to 2020, which can be divided into four episodes (Figure 2A). The duration of the eruptive episodes was initially 2 years (Episode 1), and 120 days (Episode 2), but shortened to a week by Episode 3, with decreasing

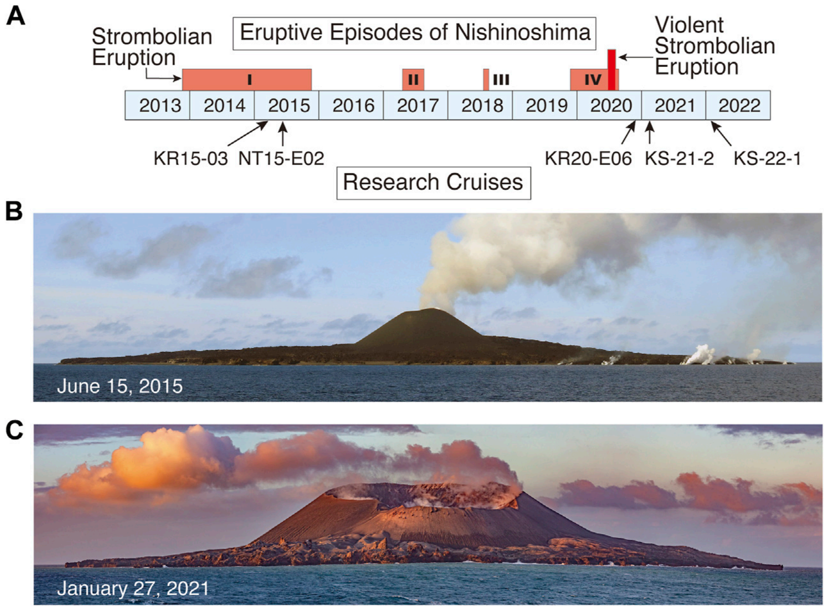

FIGURE 2
(A) Eruptive episodes of Nishinoshima and the timing of JAMSTEC research cruises. The duration of the eruptive episodes was initially 2 years (Episode 1), and 120 days (Episode 2), but shortened to a week by Episode 3, with decreasing eruptive volume with time. The Episode 4 lasted for 270 days. The eruption style changed in mid-June 2020 from mostly effusive Strombolian to violent Strombolian, after which eruption columns continuously reached a height of 2–6 km (maximum 8 km) and a large amount of tephra fall out occurred over more than several tens of kilometer from the island (Yanagisawa et al., 2020). We sampled the Nishinoshima area in February 2015, June 2015, December 2020, January 2021, and January 2022, during the JAMSTEC cruises KR15-03, NT15-E02, KR20-E06, KS-21-2, and KS-22-1, respectively. **(B)** Nishinoshima seen from the west on 15 June 2015, during NT15E-02. The height of the central cone is ~150 m. **(C)** Nishinoshima seen from the south on 27 January 2021, during KS-21-2. The height of the central cone is ~250 m (photographed by Chong Chen).

eruptive volume with time. Something, however, changed from 2019 to 2020 during Episode 4, which lasted for 270 days. The average effusion rates for the 2013–2015 eruption (Episode 1) and the 2017 eruption (Episode 2) were estimated to be 2.0 × 10^5 m^3/day and 1.5 × 10^5 m^3/day, respectively (Maeno et al., 2016; Maeno et al., 2021; Kaneko et al., 2019). The activity that began in December 2019 (Episode 4) however was intense, with a maximum magma discharge rate of 2.6 × 10^6 m^3/day (Maeno et al., 2021; Kaneko et al., 2022). Moreover, in June 2020 the eruption style switched from mostly effusive Strombolian to violent Strombolian, during which time eruption columns continuously reached a height of 2–6 km (maximum 8 km) and a large amount of tephra fall out occurred extending several tens of kilometers from the island (Yanagisawa et al., 2020). Long-term geochemical monitoring of 2013–2020 subaerial eruption products showed that this transition in eruption style was associated with a change from the initial andesite magma with ~60 wt% SiO_2 to a more mafic basaltic andesite magma with ~55 wt% SiO_2 in Episode 4 (Maeno et al., 2021). After Episode 4, small eruptions were observed by a weather satellite in October 2022 and by an aircraft of the Japan Coast Guard in January 2023.

Following the Episode 4 transition in eruption style and magma composition we returned to the Nishinoshima area to conduct further submarine survey and sampling (JAMSTEC cruises KR20-E06 in December 2020, KS-21-2 in January 2021, and KS-22-1 in January 2022; Figure 2A). Figures 2B, C show Nishinoshima island in profile on 15 June 2015 and 27 January 2021, as seen from the ship during the previous 2015 NT15E-02 cruise (Tamura et al., 2019) and 2021 KS-21-2 cruise, respectively. There were drastic changes before and after Episode 4; the height of the central cone increased from 150 to 250 m and the crater had been enlarged from 150 to 570 m in diameter (Maeno et al., 2021). The dimensions of the island were 2.0 km from east to west and 1.8 km from north to south in May 2019. The huge volumes of lava subsequently erupted during Episode 4 increased the landmass of the island by 33 percent from 2.89 km^2 in May 2019 to ~3.9 km^2 in August 2020, according to GSI (Geospatial Information Authority of Japan) analysis of satellite images. The island now measures 2.3 km from east to west and 2.4 km from north to south.

In this study we present whole-rock geochemical data for the submarine volcanic products (plausibly from the 2019-2020 eruptions) obtained by the KR20-E06, KS-21-2 and KS-22-1 cruises. These supplement the whole-rock geochemical data of the subaerial and submarine volcanic products sampled in 2015 that have already been reported in Tamura et al. (2019). We explore the possibility that the change in erupted magma composition in 2020 from andesite to basaltic andesite reflects a change in the composition of primary magmas resulting from partial melting of the mantle, from primary andesite produced at shallow depths beneath thin crust to primary basalt produced at considerable depth. Basalt magmas have recently been shown to have triggered the 2021 explosive pumice eruption of Fukutoku-Oka-no-Ba volcano, 300 km south of Nishinoshima in the same arc (Yoshida et al., 2022), providing another example where hydrous

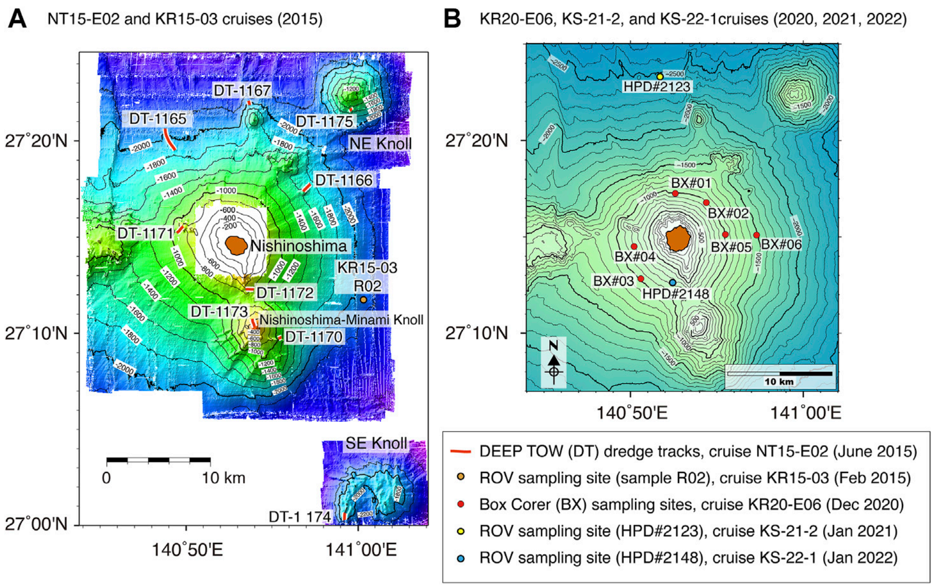

FIGURE 3
(A) The dredge tracks of the DEEP TOW system during cruise NT15-E02 in 2015. The old knolls around Nishinoshima (NE and SE Knolls) consist of basalt lavas, but the main body of the Nishinoshima volcano is andesitic in composition (Tamura et al., 2019) A loose sample collected by submersible during cruise KR15-03 in 2015 is also shown. **(B)** Red circles show sampling sites around Nishinoshima using box corer (prefix BX) during cruise KR20-E06 in 2020. Yellow circle is sampling sites ~15 km north of Nishinoshima using ROV Hyper Dolphin during cruise KS-21-2 in 2021 (denoted HPD#2123). Blue circle is sampling site ~3 km south of Nishinoshima using ROV Hyper Dolphin during cruise KS-22-1 in 2022 (denoted HPD#2148).

basaltic magmas in oceanic arcs produce explosive eruptions. In this context, our geochemical data yield new insights into the magma system of Nishinoshima volcano and the generation and interaction of magmas involved in explosive eruptions at island arc volcanoes.

2 Materials and methods

2.1 Research cruises

A brief summary of the 2015 sampling is given here; full details are given in Tamura et al. (2019). Cruise KR15-03 of R/V Kairei in February 2015 collected loose boulders ESE of Nishinoshima in water depths of 2,100 m below sea level (b.s.l.) using the remotely operated submersible KAIKO Mk-IV. Cruise NT15E-02 of R/V Natsushima in June 2015 conducted dredges using the deep ocean floor towed survey system (DEEP TOW) on the submarine flank of Nishinoshima, the summit and flank of Nishinoshima-Minami Knoll (8 km south of the island), and the steep cliffs of the adjacent NE Knoll and SE Knoll, located 18 km and 28 km from the island, respectively (Figure 3A). These dredges spanned water depths between 203 m b.s.l. and 2,060 m b.s.l. and collected lavas and scoria (Tamura et al., 2019). Finally, subaerial lava blocks from the 2015 eruption were collected using an unmanned helicopter during the cruise of the R/V Daisan Kaiyomaru in June-July 2015.

Cruise KR20-E06 of R/V Kairei in December 2020 sampled the surface sediments (very recent volcaniclastics) of the submarine flanks of Nishinoshima, from 5 to 7 km from the volcanic center and water depths between 500 m b.s.l. and 1,500 m b.s.l., using a Box Corer (Figure 3B). The Box Corer is 120 cm (width) * 130 cm (length) * 150 cm (height) and weighs 260 kg. When it reaches the seafloor, its box covers an area of 0.1 m^2 and strips the upper 10–20 cm of seafloor sediments.

Cruise KS-21-2 of R/V Shinseimaru in January 2021 sampled the surface sediments (very recent volcaniclastics) of the submarine flank of Nishinoshima at 15 km to the north of the volcanic center at a water depth of 2,500 m b.s.l. using the remotely operated submersible Hyper Dolphin (HPD#2123 in Figure 3B). The Hyper Dolphin made a video survey of the seafloor and sampled seafloor sediments using a 40 cm-long push core held by the submersible's manipulator arm.

Cruise KS-22-1 of R/V Shinseimaru in January 2022 collected additional lava fragments from the southern slope of Nishinoshima at 4 km from the volcanic center and a water depth of 790 m b.s.l. using the Hyper Dolphin manipulator arm (HPD#2148 in Figure 3B).

Samples recovered by these 2020–2022 Box Corer and Hyper Dolphin sampling surveys are deemed to be the products of the most recent Episode 4 eruptions in 2020, due to their proximity to the volcanic center and similarity to subaerial observations. The submarine outcrops observed to the north at 2,500 m b.s.l. (HPD#2123) exhibit alternate layers of white pumice and black scoria tuffs, reflecting the known bimodal nature of the Episode 4 eruptions (Figures 4A, B). Although land sampling surveys were not possible during the period of the 2020 and 2021 cruises, Maeno et al. (2021) used an aerial drone in December 2020 to show that nearly the entire lava flow field had been covered by pyroclastic deposits except for a few locations on the southwest and northwest coasts. In the north, the tephra deposit was more than 5 m thick, reflecting the northward direction of the major tephra dispersal axis

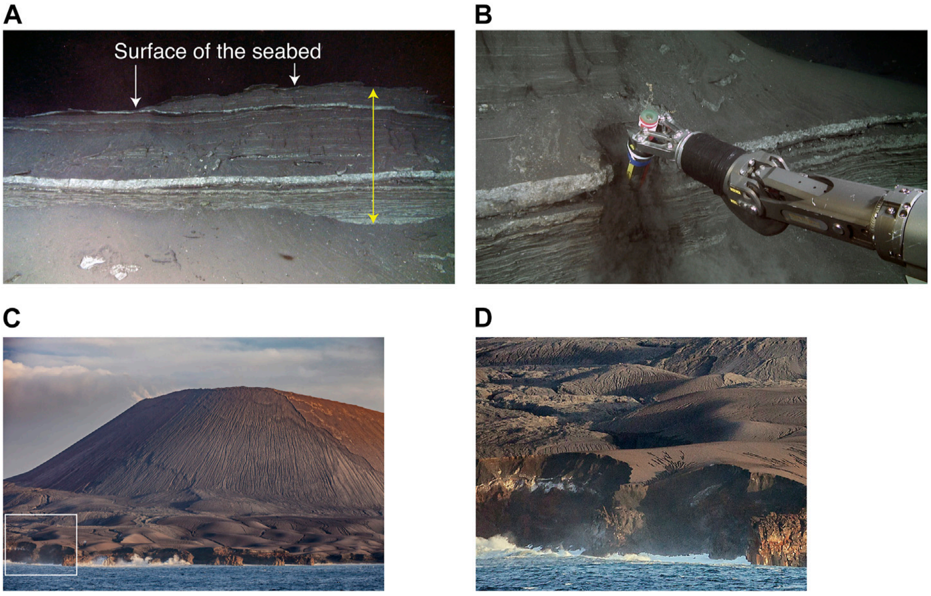

FIGURE 4
(A) Alternate layers of black and white tephra observed ~15 km north of Nishinoshima at a depth of 2,473 m b.s.l. (27°23.2934′N and 140°51.6102′E) during HPD#2123 dive of ROV Hyper-Dolphin on 23 January 2021. The yellow double-ended arrow shows a length of ~1 m. **(B)** Pushing a plastic cylinder (push-core) to sample the outcrop using Hyper-Dolphin. The layers are, however, soft, unconsolidated, and fragile and are difficult to keep in the original shape of the sediment. **(C)** Nishinoshima seen from the northwest on 27 January 2020, by Chong Chen. The white rectangle in the lower left of the photo is enlarged in **(D)**. The central cone is ~250 m in height. **(D)** An enlarged part of the previous photo, which shows the coast of Nishinoshima eroded by sea, consisting of lava flows and overlying tephra layers. Alternate bands of white and black color exist between the thick black ash layers and underlying lava flows: these tephra layers may correlate with the submarine layers 15 km away from the island shown in **(A)**.

during the explosive phase (Maeno et al., 2021). Figure 4C shows Nishinoshima taken from the northwest on 27 January 2020. The central cone is ~250 m in height. The white rectangle in the lower left of the photo is enlarged in Figure 4D. This part of the sea cliff of Nishinoshima has been eroded by the sea and consists of lava flows and overlying tephra layers. Alternate bands of white and black color exist between the overlying thick black ash layers and the underlying lava flows: we suggest these distinctive tephra layers correlate with the HPD#2123 submarine layers 15 km further to the north that are shown in Figures 4A, B.

Figures 5A, B show seafloor sediments (the uppermost tephra) from the December 2020 Box Corer samples BX#01 and BX#02, respectively, whose locations are shown in Figure 3B. Here the seafloor was mostly covered by black tephra (scoria), but some light-colored material (pumice) was observed along with the scoria. Figures 5C, D show pumice from BX#01 and scoria from BX#06, respectively. Figures 5E, F show pumice and scoria recovered from the white and black layers, respectively, sampled in January 2021 during dive HPD#2123 and seen in Figure 4B. Figures 5G, H show a sample collected in January 2022 during dive HPD#2148, and an Si X-ray map of a thin section of this sample is shown in Figure 5I.

2.2 Analytical methods

Samples with "R" in the sample number except for BX03-R05 were pulverized using a polycarbonate tube and alumina rod. Other samples were pulverized in an agate mortar. Major elements were determined on fused glass discs by XRF (ZSX Primus II, Rigaku) at Japan Agency for Marine-Earth Science and Technology (JAMSTEC) following the method of Tani et al. (2005). A mixture of ~0.4 g powdered sample and 4 g of anhydrous lithium tetraborate ($Li_2B_4O_7$) was used; no matrix correction was applied because of the high dilution. All discussion in this paper refers to analyses that have been normalized to 100% on a volatile-free basis with total iron calculated as FeO.

Concentrations of other trace elements, including the rare earth elements (REE), V, Cr, Rb, Sr, Y, Zr, Nb, Cs, Ba, Hf, Ta, Pb, Th, and U were determined by ICP-MS using a Agilent 7900 instrument at the Geological Survey of Japan/AIST. About 100 mg of sample powder was dissolved in a HF-HNO_3 mixture (5:1). After evaporation to dryness, the residues were redissolved with 2% HNO_3 prior to analysis. Reproducibility is better than ±4% [2 standard deviations (SD)] for the REE, Rb and Nb, and better than ±6% (2 SD) for other elements.

For a sample from KS-22-1, trace element concentrations were determined by ICP-MS (iCAP Qc, ThermoFisher Scientific, Bremen, Germany) at the JAMSTEC. Sample preparation followed the procedures of Chang et al. (2003). In brief, an aliquot of 50–100 mg rock powder was digested with a mixture of HF-$HClO_4$, followed by $HClO_4$ and HNO_3. Finally, the residues were dissolved in 2% HNO_3 with trace amount of HF to maintain the stability of elements in solution. ICP-MS analysis signals were normalized using In and Bi as internal standards. Reproducibility of data for JB-2 in this study at JAMSTEC is better than 2% RSD.

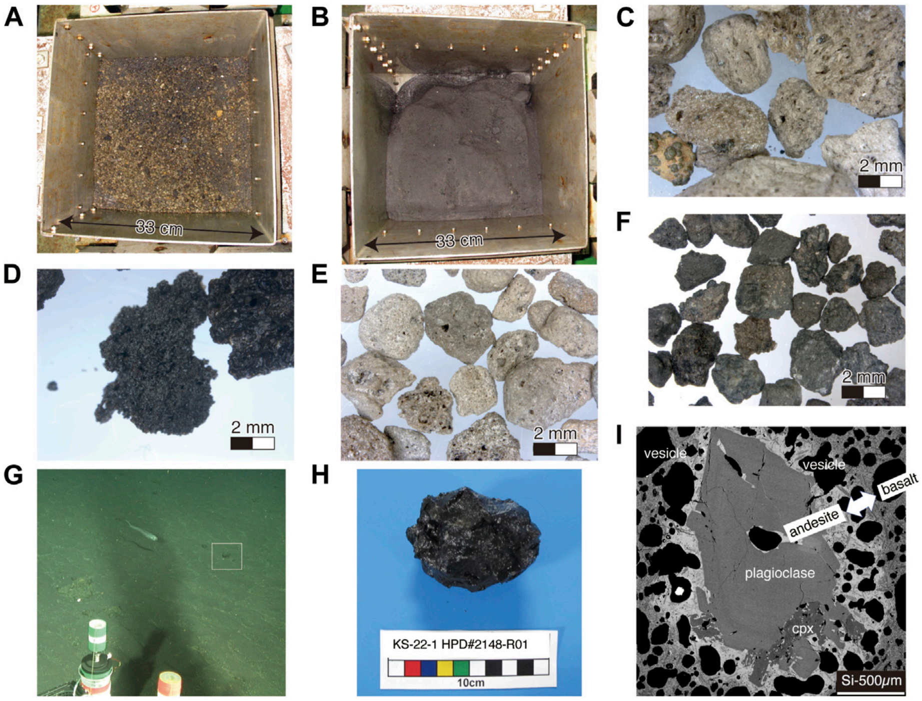

FIGURE 5
(A,B) Seafloor sediments (the latest tephra in December 2020) recovered by the Box Corer whose sites are shown in Figure 3B. The Box Corer covers an area of 0.1 m^2 (33 cm * 33 cm). The seafloor was mostly covered by black tephra (scorias), but some light-colored materials (pumices) were observed along with the scorias. **(A)** BX#01 recovered from 945 m b.s.l. **(B)** BX#02 from 952 m b.s.l. **(C)** Pumices from BX#01. **(D)** Scorias from BX#06 recovered from 1,500 m b.s.l. **(E)** Pumices recovered from a white layer in Figure 4B during HPD#2123. **(F)** Scorias recovered from a black layer just below the white layer in Figure 4B during HPD#2123 at a depth of 2,500 m b.s.l., 15 km in the north of Nishinoshima. **(G)** Seafloor at a depth of 760 m observed during HPD#2148 (Figure 3B) by using ROV Hyper Dolphin in the cruise of KS22-1 cruise in 2022. White rectangle frames recovered sample shown in **(H)**. **(H)** Larger basaltic andesite sample (HPD#2148-R01) collected from the sea floor at the southern slope of Nishinoshima, 3.3 km south of the island. **(I)** Si X-ray map taken from a thin section of sample HPD#2148-R01, which has a whole-rock composition of basaltic andesite. The Si-rich light-colored groundmass is andesitic magma containing Ca-poor plagioclase (An_{44-50}) and clinopyroxene (cpx), which exhibits a mingling texture with the surrounding Si-poor dark-colored groundmass of basaltic magma.

Isotopic compositions of Sr, Nd, and Pb were determined on 200 mg of hand-picked 0.5–1 mm rock chips. The chips were leached in 6 M HCl at 140°C for 1 h prior to dissolution in HF–HNO_3. Sr and Nd isotope ratios were measured on a seven-collector VG Sector 54 mass spectrometer at the Geological Survey of Japan/AIST. Sr was isolated using Sr resin (Eichrom Industries, Illinois). For Nd isotopic analysis, the REE were initially separated by cation exchange before isolating Nd on Ln resin (Eichrom Industries) columns. Sr and Nd isotopic compositions were determined as the average of 150 ratios by measuring ion beam intensities in multidynamic collection mode. Isotope ratios were normalized to $^{86}Sr/^{88}Sr = 0.1194$ and $^{146}Nd/^{144}Nd = 0.7219$. Measured values for NBS SRM-987 and JNdi-1 [$^{143}Nd/^{144}Nd = 0.512115$ (Tanaka et al., 2000)] were $^{87}Sr/^{86}Sr = 0.710276 \pm 0.000006$ (2 SD, $n = 4$) and $^{143}Nd/^{144}Nd = 0.512104 \pm 0.000012$ (2 SD, $n = 4$) during the measurement period. Pb was isolated using AG1-X8 200–400 mesh anion exchange resin. Procedural Pb blanks were <30 pg, considered negligible relative to the amount of sample analyzed. Pb isotopic measurements were made in multidynamic collection mode using the double spike technique (Ishizuka et al., 2003; Taylor et al., 2015) (Southampton-Brest-Lead 207–204 spike SBL74) at GSJ/AIST. Natural (unspiked) measurements were made on 60%–70% of collected Pb, giving ^{208}Pb beam intensities of $(2.5–3.0) \times 10^{-11}$ A. Fractionation-corrected Pb isotopic compositions and internal errors were obtained by a closed form linear double-spike deconvolution (Johnson and Beard, 1999). The reproducibility of Pb isotopic measurement (external error of 2 SD) by double spike is <200 ppm for all $^{20x}Pb/^{204}Pb$ ratios. Measured values for NBS SRM-981 during the measurement period were $^{206}Pb/^{204}Pb = 16.9401 \pm 0.0011$, $^{207}Pb/^{204}Pb = 15.5003 \pm 0.0025$, and $^{208}Pb/^{204}Pb = 36.7236 \pm 0.0041$.

Electron microprobe analyses were carried out on a JEOL JXA-8500F instrument equipped with five wavelength-dispersive spectrometers (WDS) at JAMSTEC using an accelerating voltage of 15 kV, 10 nA beam current, and 3–5 μm spot diameter. Peak and background counting times were 10 and 5 s, respectively. Calibrations were performed using mineral standards.

Supplementary Table S1 shows major element analyses by XRF, trace element analyses by ICP-MS, and Sr-Nd-Pb isotopic compositions of selected samples.

3 Results

3.1 Major elements

Variation diagrams of wt% SiO_2 vs. major elements and Mg-value of lavas and pyroclastic materials from Nishinoshima and

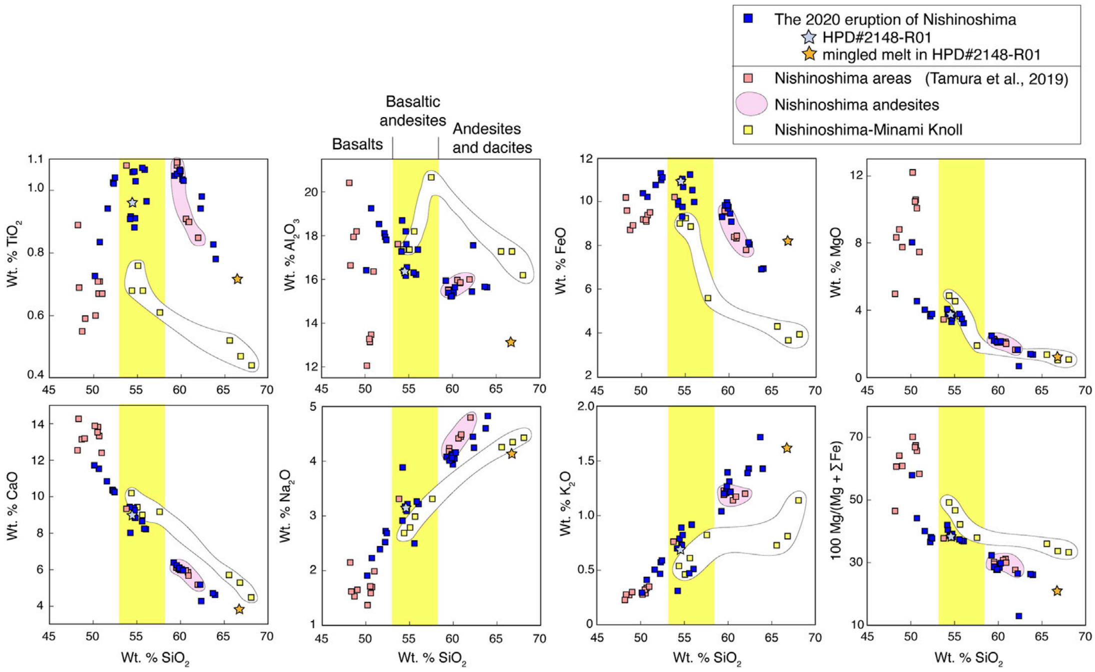

FIGURE 6
Variation diagrams of wt% SiO$_2$ vs. major elements and Mg-value of lavas and pyroclastic materials from Nishinoshima and surrounding areas. Blue squares indicate new data for submarine deposits of Episode 4 eruptions in 2020 (cruises KR20-E06, KS-21-1, and KS-22-1); stars indicate sample R01 collected during dive HPD#2148. Orange squares indicate samples collected from the Nishinoshima area in 2015 (Tamura et al., 2019), which include older basalts from the NE and SE Knolls; pink shading indicates data range of 1973 eruption products and pre-1973 edifice (Tamura et al., 2019 and references therein). Yellow squares indicate samples collected from Nishinoshima-Minami Knoll in 2015 (Tamura et al., 2019). Compositional boundaries between basalts, basaltic andesites, and andesites and dacites are marked.

surrounding areas (both new and previously published) are shown in Figure 6. Collectively the data range from 48 to 68 wt% SiO$_2$, 0.7 to 12.2 wt% MgO, and 0.2 to 1.72 wt% K$_2$O, defining a low-to medium-K suite as defined by Gill (1981). Mg-values range from 13 to 70. The scoria, pumice, and lava fragments from the 2020 eruption (Box Corer and Hyper Dolphin samples) range from 50 to 64 wt% SiO$_2$, 0.7 to 8 wt% MgO, 0.2 to 1.72 wt% K$_2$O, and 13 to 58 Mg-values. These values overlap previously reported data for andesite lavas from the Nishinoshima main edifice (59–62 wt% SiO$_2$) and basalts from the surrounding knolls (48.3–51 wt% SiO$_2$) (Tamura et al., 2019). Tephras from the 2020 eruption collected on the island were basaltic andesite (54–56 wt% SiO$_2$; Maeno et al., 2021); thus, basaltic andesites were deemed to be most voluminous and representative of the 2020 eruption (Maeno et al., 2021). However, our submarine samples, which we infer to be from the same 2020 eruption, have a wider compositional variation ranging from basalt (50 wt% SiO$_2$) to dacite (64 wt% SiO$_2$). It is possible that a similarly wide range was not recovered from the island itself due to the limited opportunity for sampling.

Lavas from Nishinoshima-Minami Knoll (collected in 2015; Tamura et al., 2019) are distinctly lower in TiO$_2$ (0.4–0.8 wt%), FeO (3.6–9.2 wt%), Na$_2$O (2.7–4.4 wt%) and K$_2$O (0.5–1.1 wt%) and higher in CaO (4–10 wt%) and Mg-values (33–49) than the main Nishinoshima edifice (0.8–1.1 wt% TiO$_2$, 7–11 wt% FeO, 3–5 wt% Na$_2$O, 0.6–1.5 wt% K$_2$O, 4–9 wt% CaO, 30–40 Mg-values) at the same SiO$_2$ contents in the range of 54–68 wt % SiO$_2$.

3.2 Trace element ratios

Variation diagrams of wt% SiO$_2$ vs. selected trace element ratios are shown in Figure 7. These element ratios are used as proxies for mantle and subduction components based on data and interpretations made by Pearce et al. (2005) for the Mariana arc. Accordingly, Ba/Nb is a proxy for total subduction addition, with high Ba/Nb indicating high total subduction addition (since Ba is released over a wide range of subduction temperatures). Similarly, Ba/Th is a proxy for shallow subduction addition (because Ba is mobilized in lower temperature fluids but Th is not), and Th/Nb is a proxy for deep subduction addition (because high temperature melts are required to mobilize Th). Nb/Yb is a proxy for degree of melting in an inverse way, with low Nb/Yb indicating high degrees of melting (because Nb is more incompatible than Yb in the source mantle and incompatible elements are more concentrated in melts resulting from lower degrees of melting) (Pearce et al., 2005). Both La/Sm and Zr/Y could be proxies for partial melt from subducted sediment, with higher La/Sm and Zr/Y indicating higher partial melt content from subducted sediment. Additionally, lower Zr/Y can also indicate higher degrees of mantle melting.

The 2020 basalts have a narrower range of Ba/Nb (100–130) and Ba/Th (330–420) than the previously reported basalts, which range from 40 to 150 and from 150 to 600, respectively. Basalts from the NE Knoll have higher Ba/Nb (~150) and Ba/Th (~600) than those from the SE Knoll (Ba/Nb, 40–57; Ba/Th, 260–350), and the 2020 basalts are plotted intermediate between them.

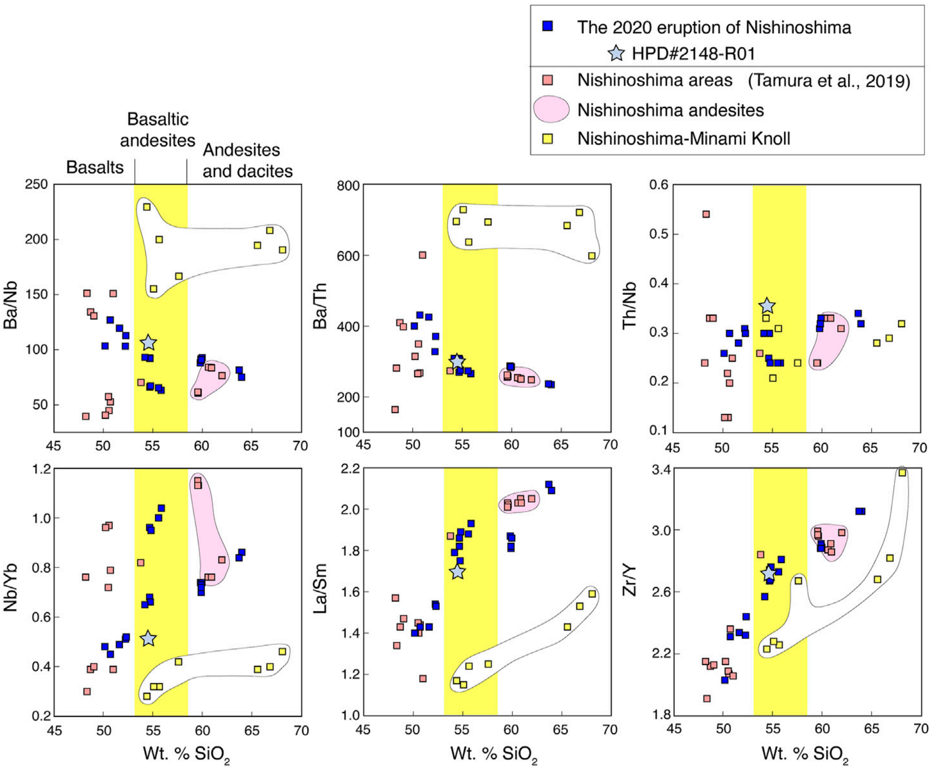

FIGURE 7
Variation diagrams of wt% SiO_2 vs. selected trace element ratios. Blue squares indicate new data for submarine deposits of Episode 4 eruptions in 2020 (cruises KR20-E06, KS-21-1, and KS-22-1); star indicates sample R01 collected during dive HPD#2148. Orange squares indicate samples collected from the Nishinoshima area in 2015 (Tamura et al., 2019), which include older basalts from the NE and SE Knolls; pink shading indicates data range of 1973 eruption products and pre-1973 edifice (Tamura et al., 2019 and references therein). Yellow squares indicate samples collected from Nishinoshima-Minami Knoll in 2015 (Tamura et al., 2019). Compositional boundaries between basalts, basaltic andesites, and andesites and dacites are marked.

Basaltic andesites, andesites, and dacites from the 2020 eruption have Ba/Nb (50–100) and Ba/Th (200–300), which are lower than the 2020 basalts, but similar to Nishinoshima andesites of Tamura et al. (2019). Notably, basaltic andesites and dacites from Nishinoshima-Minami Knoll have higher Ba/Nb (150–230) and Ba/Th (600–730) than those from Nishinoshima and surrounding areas.

The range of Th/Nb (0.24–0.33) of the 2020 eruption is almost similar to the previously reported data around Nishinoshima by Tamura et al. (2019) except for the lowest values of SE Knoll basalts (0.13–0.22) and the highest value (0.54) of the Northern Knoll basalt (DT-1167).

In the 2020 eruption, basaltic andesites have the highest Nb/Yb ranging from 0.51 to 1.04. Andesites and dacites are between 0.70 and 0.86. Basalts range from 0.45 to 0.52. All these values are, however, in the range for the Nishinoshima area reported in Tamura et al. (2019), for which basalt has the lowest value (0.3) and andesite has the highest (1.15). These wide variations in Nb/Yb values make a sharp contrast to Nishinoshima-Minami Knoll, which has generally low Nb/Yb values ranging from 0.28 to 0.46.

In summary, these trace element ratios are similar between the scorias, lava fragments, and pumices from the 2020 eruption and the previously reported andesite lavas from the main Nishinoshima edifice and basalts from the surrounding knolls. However, the lavas from Nishinoshima-Minami Knoll, which is only 8 km south of Nishinoshima island, are distinct from those of the Nishinoshima main body and surrounding knolls.

3.3 Rare earth element (REE) patterns

Figure 8 shows C1 chondrite (McDonough and Sun, 1995)-normalized REE patterns for lavas from the Nishinoshima area. Patterns of basalts from the 2020 eruption (Figure 8A) are similar to patterns of old basalts from the NE Knoll and SE Knoll of Nishinoshima (Figure 3A; Tamura et al., 2019). Basaltic andesites, andesites, and dacites from Nishinoshima (Figure 8B) also exhibit similar patterns between the new samples from the 2020 eruption and the old samples reported in Tamura et al. (2019). Interestingly, a 2015 sample of basaltic andesite from the eastern submarine flank of Nishinoshima (sample KR15-03-R02, Figure 3A), which was reported in Tamura et al. (2019) but not discussed in detail because it was an accidentally sampled rolling stone, has almost the same pattern as the basaltic andesites from the 2020 eruption. Basaltic andesites and dacites from Nishinoshima-Minami Knoll, however, have distinct patterns (Figure 8C). Comparisons between Nishinoshima basalts, Nishinoshima-Minami Knoll, and Nishinoshima andesites and dacites are summarized in Figure 8D.

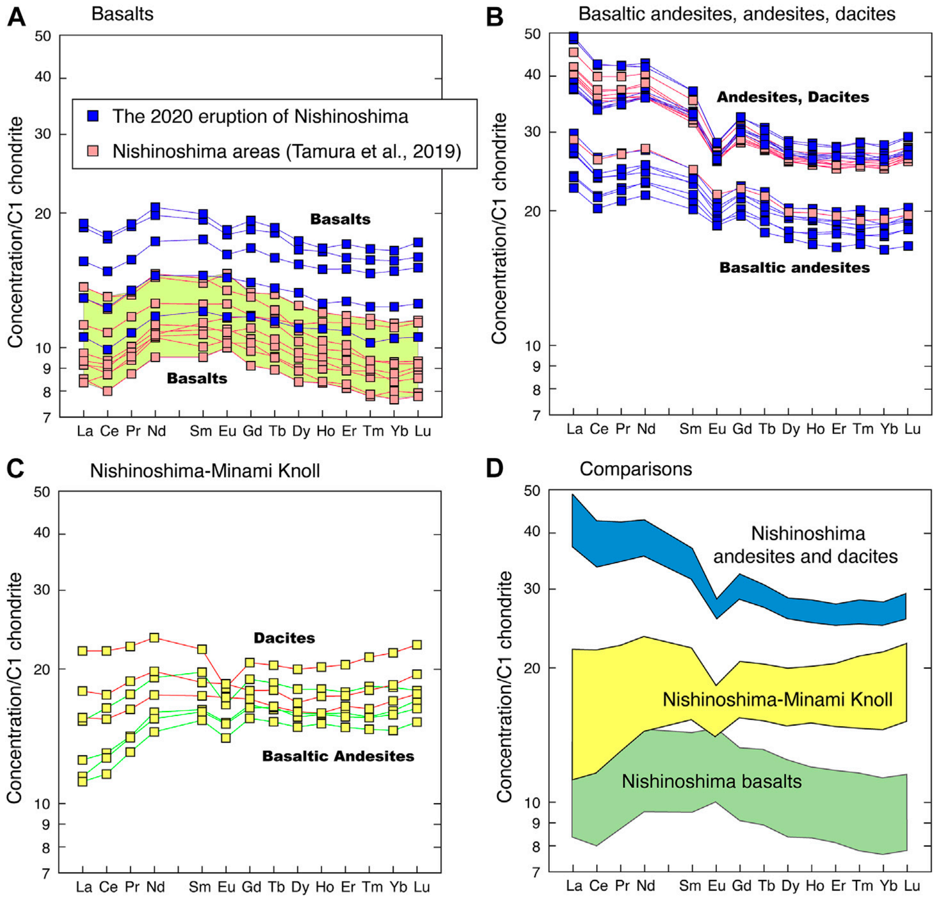

FIGURE 8
C1 chondrite (McDonough and Sun, 1995)-normalized REE patterns for lavas from Nishinoshima area. Blue squares indicate new data for submarine deposits of Episode 4 eruptions in 2020 (cruises KR20-E06, KS-21-1, and KS-22-1). Orange squares indicate samples collected from the Nishinoshima area in 2015 (Tamura et al., 2019), which include older basalts from the NE and SE Knolls. Yellow squares indicate samples collected from Nishinoshima-Minami Knoll in 2015 (Tamura et al., 2019). **(A)** Basalts. **(B)** Basaltic andesites, andesites, and dacites from Nishinoshima. **(C)** Basaltic andesites and dacites from Nishinoshima-Minami Knoll. **(D)** Comparisons between Nishinoshima basalts, Nishinoshima-Minami Knoll, and Nishinoshima andesites and dacites.

3.4 Normal (N)-MORB-normalized trace element patterns

N-MORB (Sun and McDonough, 1989)-normalized trace element patterns of lavas and pyroclastic rocks from the Nishinoshima area are shown in Figure 9. Panels (A), (B), and (C) show basalts, basaltic andesites, and andesites and dacites from the 2020 eruption, respectively, which are compared with the previous data for the Nishinoshima area of Tamura et al. (2019). Panel (D) shows basaltic andesites and dacites from Nishinoshima-Minami Knoll from Tamura et al. (2019).

Basalts of the 2020 eruption (Figure 9A) show the typical signature of subduction zones, being enriched in elements mobile in aqueous fluids and sediment melts (e.g., Rb, Ba, Th, U, K, Pb, and Sr). These basalts are depleted in Nb and Ta, and Zr, Hf, and Ti, which is also typical of subduction zone basalts. These basalts are more differentiated, and thus, the total values are higher, but they are similar and parallel to the previously reported basalts of Tamura et al. (2019).

As suggested by Tamura et al. (2019), the other lava compositions from the Nishinoshima area, including the new 2020 eruption samples, also show the typical signature of subduction zones, enriched in elements mobile in aqueous fluids and sediment melts (e.g., Rb, Ba, Th, U, K, and Pb), but the positive Sr anomalies of the Nishinoshima basalts, basaltic andesites, and Nishinoshima-Minami rocks are absent in the Nishinoshima andesites and dacites.

3.5 SiO_2 vs. La/Sm and Ba/Th vs. La/Sm

$(La/Sm)_N$ is La/Sm normalized to primitive mantle values, which were suggested by Sun and McDonough (1989). $(La/Sm)_N$ can be used as a proxy for partial melt from subducting sediments (Elliott, 2003). Figure 10 shows variation of $(La/Sm)_N$ vs. SiO_2 and Ba/Th for lavas from the Nishinoshima area. Nishinoshima andesites have $(La/Sm)_N$ values ranging from 1.2 to 1.4, which indicate the highest sediment component in this area. Nishinoshima basaltic andesites have values ranging from 1.13 to 1.25, which are plotted between the

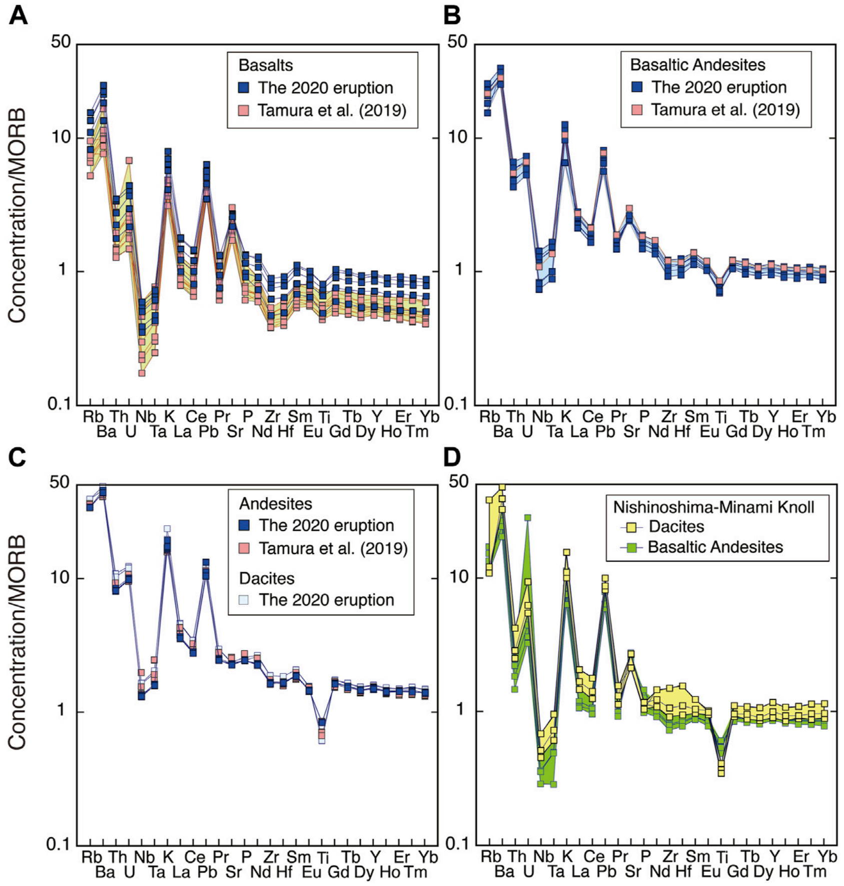

FIGURE 9
Normal (N)-MORB (Sun and McDonough, 1989)-normalized incompatible element patterns of lavas from Nishinoshima area. Blue and white squares indicate new data for submarine deposits of Episode 4 eruptions in 2020 (cruises KR20-E06, KS-21-1, and KS-22-1). Orange squares indicate samples collected from the Nishinoshima area in 2015 (Tamura et al., 2019), which include older basalts from the NE and SE Knolls. Yellow and green squares indicate samples collected from Nishinoshima-Minami Knoll in 2015 (Tamura et al., 2019). **(A)** Basalts. **(B)** Basaltic andesites. **(C)** Andesites and Dacites from Nishinoshima. **(D)** Basaltic andesites and dacites from Nishinoshima-Minami Knoll.

Nishinoshima andesites and basalts (0.76–1.01). Lavas from Nishinoshima-Minami Knoll and Nishinoshima basalts have the lowest $(La/Sm)_N$, ranging from 0.74 to 1.03, and 0.76 to 1.01, respectively, and thus the lowest sediment component in this area.

Ba/Th is used as a proxy for fluid from subducting oceanic crust (Elliott, 2003). Nishinoshima-Minami Knoll lavas have the highest Ba/Th values ranging from 600 to 730, which contrast with Nishinoshima andesites, whose Ba/Th values range from 250 to 280.

3.6 Sr, Nd, and Pb isotope ratios

The new Sr-Nd-Pb isotope ratios of the rocks from the 2020 eruption are plotted along with the data from Tamura et al. (2019) in Figures 11, 12. Basalts from the 2020 eruption have $^{87}Sr/^{86}Sr$ values ranging from 0.70330 to 0.70334, and $^{143}Nd/^{144}Nd$ values ranging from 0.513072 to 0.513087, which are plotted within the Sr-Nd isotopic range (0.70328–0.70360 and 0.513048–0.513131, respectively) of the other basalts reported in the Nishinoshima area (Figure 11). Basalts from the SE knoll (DT-1174) have the highest $^{87}Sr/^{86}Sr$ (0.70360) and the lowest $^{143}Nd/^{144}Nd$ (0.513048) in the Nishinoshima area. $^{87}Sr/^{86}Sr$ and $^{143}Nd/^{144}Nd$ values of Nishinoshima andesites range from 0.70328 to 0.70335 and from 0.51307 to 0.51308, respectively, and those of basaltic andesites are 0.70323–0.70333 and 0.513075–0.513098, respectively. Basaltic andesites have slightly higher $^{143}Nd/^{144}Nd$ than andesites. Nishinoshima-Minami Knoll has $^{87}Sr/^{86}Sr$ and $^{143}Nd/^{144}Nd$ values ranging from 0.70343 to 0.70351 and 0.51311 to 0.513135, respectively, and these are both higher than Nishinoshima andesites and basaltic andesites.

Nishinoshima andesites and basaltic andesites have higher $(La/Sm)_N$ and lower $^{143}Nd/^{144}Nd$ values than Nishinoshima-Minami Knoll (Figure 11), and these values show negative correlations. Basalts have wider $^{143}Nd/^{144}Nd$ values ranging from 0.51305 to 0.51313, but $(La/Sm)_N$ values have a limited range (0.76–1.02).

Figure 12 shows Pb isotope variations. Nishinoshima andesites show a limited range of $^{206}Pb/^{204}Pb$ values, ranging from 18.67 to 18.75, which are positively correlated to $^{87}Sr/^{86}Sr$ from 0.70329 to 0.70335 (Figure 12A), $^{207}Pb/^{204}Pb$ from 15.540 to 15.547 (Figure 12C), and $^{208}Pb/^{204}Pb$ from 38.41 to 38.48 (Figure 12D). Basaltic andesites have slightly wider ranges than andesites in $^{206}Pb/^{204}Pb$, $^{207}Pb/^{204}Pb$, and $^{208}Pb/^{204}Pb$, which are 18.66–18.76,

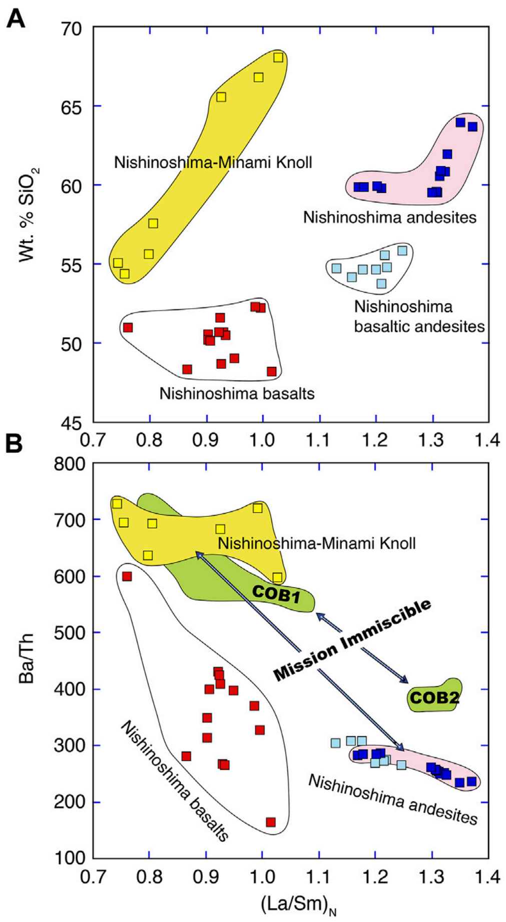

FIGURE 10
Variation of La/Sm normalized to primitive mantle (Sun and McDonough, 1989) vs. SiO_2 **(A)** and Ba/Th **(B)** for lavas from the Nishinoshima area. Samples are grouped by composition and geographical location, regardless of eruption or sampling date. Green COB1 and COB2 fields relate to data from Pagan Volcano in the Mariana arc (Tamura et al., 2014; see main text for details).

15.538–15.548, and 38.394–38.49, respectively. Basalts cover the widest ranges of ^{206}Pb/^{204}Pb, ^{207}Pb/^{204}Pb, and ^{208}Pb/^{204}Pb, ranging from 18.52 to 18.83, from 15.538 to 15.549, and from 38.29 to 38.59, respectively. Nishinoshima-Minami Knoll has the highest ^{206}Pb/^{204}Pb, ^{143}Nd/^{144}Nd, and ^{208}Pb/^{204}Pb values ranging from 18.80 to 18.86, 0.51311 to 0.513135, 38.48 to 38.56, respectively, which positively correlate each other (Figures 12B, D). Nishinoshima andesites and Nishinoshima-Minami Knoll have similar ^{207}Pb/^{204}Pb, but Nishinoshima andesites have lower ^{87}Sr/^{86}Sr, ^{143}Nd/^{144}Nd, and ^{206}Pb/^{204}Pb than those of Nishinoshima-Minami Knoll.

3.7 Petrography of basaltic andesite

HPD#2148-R01 is a key sample of basaltic andesite that was collected from the sea floor at the southern slope of Nishinoshima, 3.3 km south of the island (Figures 3B, 5G), using ROV Hyper Dolphin (HPD#2148) in the cruise of KS-22-1 in 2022. This sample (Figure 5H) represents basaltic andesites erupted in the 2019-2020 eruption, which have similar major element contents (Figure 6) and trace element ratios (Figure 7) to other basaltic andesites from the Nishinoshima area.

This sample is particularly important because it exhibits mingling between basaltic and andesitic magmas (Figure 5I). The major parts of the rock have plagioclase with Ca-rich ($An_{>90}$) cores, clinopyroxene, and olivine phenocrysts with Mg-rich ($Fo_{\sim 83}$) cores within a microlite-rich groundmass. Limited domains have Ca-poor plagioclase ($An_{44\text{-}50}$) accompanying a microlite-poor domain. The volcanic glass in the outer parts in Figure 5I is andesitic and the inner parts are dacitic in composition. These differences in phenocrysts and groundmass compositions suggest the mingling between basaltic and andesitic magmas during the 2020 eruptions.

4 Discussion

4.1 Andesites from Nishinoshima volcano

The andesites that erupted in Episode 4 from 2019 to 2020 overlap with the range of the previous Nishinoshima andesites in terms of major elements (Figure 6), trace element ratios (Figure 7), REE patterns (Figure 8), incompatible trace element patterns (Figure 9), and Sr-Nd-Pb isotopic ratios (Figures 11, 12). Thus, almost the same andesite magmas as historical andesite lavas erupted from Nishinoshima volcano in 2019–2020.

Phenocryst-poor Nishinoshima andesites contain olivine phenocrysts with Fo mol% [100 Mg/(Mg + Fe)] ranging from Fo_{60} to Fo_{86}. Variation in NiO wt% versus Fo mol% for olivine phenocrysts agrees with calculated olivine fractionation trends, which were produced by adding equilibrium olivine compositions into the bulk rock composition iteratively in 1 wt% increments and allowing the bulk rock composition to evolve (Tamura et al., 2019). Additions of 18%–24% equilibrium olivine to Nishinoshima andesites result in primary andesites with ~57 wt% SiO_2 and 9–11 wt% MgO (Tamura et al., 2019). These liquids are in equilibrium with mantle olivines [$Fo_{89\text{-}91}$ with 0.4 wt% NiO; see Tamura et al. (2014) for references of mantle olivines]. The estimated primary andesites have higher TiO_2 (0.67–0.75 wt%) and lower CaO (4.2–4.9 wt%) than recently erupted high-Ca boninites from the active Tonga Arc (Cooper et al., 2010), but have an affinity with type-2 low-Ca boninites such as those from the Setouchi area in southwestern Japan (Crawford et al., 1989).

Because of the thin crust (Kodaira et al., 2007), the mantle beneath Nishinoshima could be shallow enough (<1.0 GPa) for plagioclase peridotites to be stable in the mantle source of the Nishinoshima andesites (e.g., Kushiro and Yoder, 1966; Green and Ringwood, 1970; Presnall et al., 2002). Approximately, 10% partial melting of source mantle without Eu anomalies can produce the Eu anomalies of Nishinoshima andesites [$(Eu/Sm)_N < 0.83$ and $(Eu/Gd)_N < 0.92$], when their residues are plagioclase peridotites having 3%–14% plagioclase (Tamura et al., 2019).

4.2 Basalts from Nishinoshima volcano in Episode 4

The activity that started from December 2019 (Episode 4) was intense, with a transition in eruption style from mostly effusive

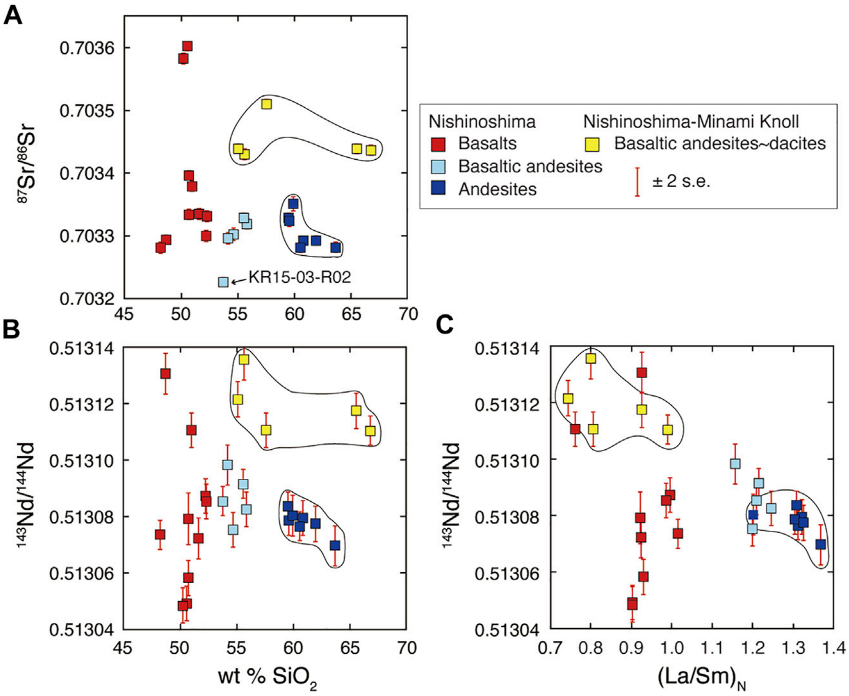

FIGURE 11
(A) $^{87}Sr/^{86}Sr$ vs. SiO_2, **(B)** $^{143}Nd/^{144}Nd$ vs. SiO_2, and **(C)** $^{143}Nd/^{144}Nd$ vs. $(La/Sm)_N$ for lavas from the Nishinoshima area. Samples are grouped by composition and geographical location, regardless of eruption or sampling date.

Strombolian to violent Strombolian in mid-June 2020 that caused a large amount of tephra to fall out over more than several tens of kilometer from the island (Yanagisawa et al., 2020). Although the subaerial samples of this tephra were basaltic andesite in composition (Maeno et al., 2021), our new data for submarine deposits of this tephra (Figures 3B, 4, 5) show that the pyroclastic rocks from Episode 4 range from basalt to dacite (Figures 6, 7). Thus, basalt was a part of the most recently erupted materials. Magma compositions therefore changed from andesite to basaltic andesite and basalt in the middle of June 2020. The small amount of dacite is not discussed in this paper, but could result from partial melting of the existing andesite edifice (Tamura et al., 2009).

Tamura et al. (2019) concluded that small knolls near Nishinoshima including the NE and SE Knolls (Figure 3) consist of old basalts whereas the main body of Nishinoshima consists of new andesites, which were derived from primary basalt and primary andesite magmas from deep and shallow mantle sources, respectively. Old basalt magmas were found spread over a wide Nishinoshima area, but new andesite magmas were concentrated in a smaller area that comprised the main body of Nishinoshima (Tamura et al., 2019). This previous understanding of the sequential and spatially demarcated evolution of Nishinoshima volcano from basalt to andesite magmas has been transformed by the 2020 Episode 4 eruption.

Now, the newest magmas erupted from the Nishinoshima volcanic center are basaltic in composition. Moreover, the new basalt from the eruptive center is distinctly less primitive than the old basalts erupted from the surrounding knolls. Figures 6–9 show major element, trace element ratios, REE patterns, and incompatible element patterns, respectively. Some basalts from the knolls are magnesian, having >10 wt% MgO and higher Mg-numbers than the basalts from the 2020 eruption (Figure 6), but there are no systematic differences in trace element ratios (Figure 7). REE patterns and incompatible trace element patterns also suggest that the 2020 basalts are more differentiated than the old submarine basalts, but their patterns are mostly parallel to the old basalts (Figures 8, 9). Pb-Sr-Nd isotope ratios of the new basalts overlap the old basalts (Figures 11, 12). These lines of evidence suggest that the new and old basalt magmas were derived from either the same, or similar, magma source beneath Nishinoshima. Importantly, however, the basaltic products are heterogeneous in some trace element ratios (i.e., Ba/Nb) and isotopic ratios (i.e., $^{143}Nd/^{144}Nd$) and it is difficult to explain the origin of this heterogeneity.

The basalts have both weakly positive and negative Eu-anomalies, possibly because the source mantle itself can have Eu anomalies. Prinzhofer and Allègre (1985) report systematic negative Eu anomalies in peridotites of the New Caledonia ophiolite (Southwest Pacific). Ulrich et al. (2010) further showed that the ophiolite samples had both negative and positive Eu anomalies (Eu/Eu* = 0.33–6.78).

The key difference between prior eruptions of basalt lavas at Nishinoshima and the 2020 eruption is that the 2020 eruption began as andesite and transitioned to basalt at a vent that normally erupts andesite.

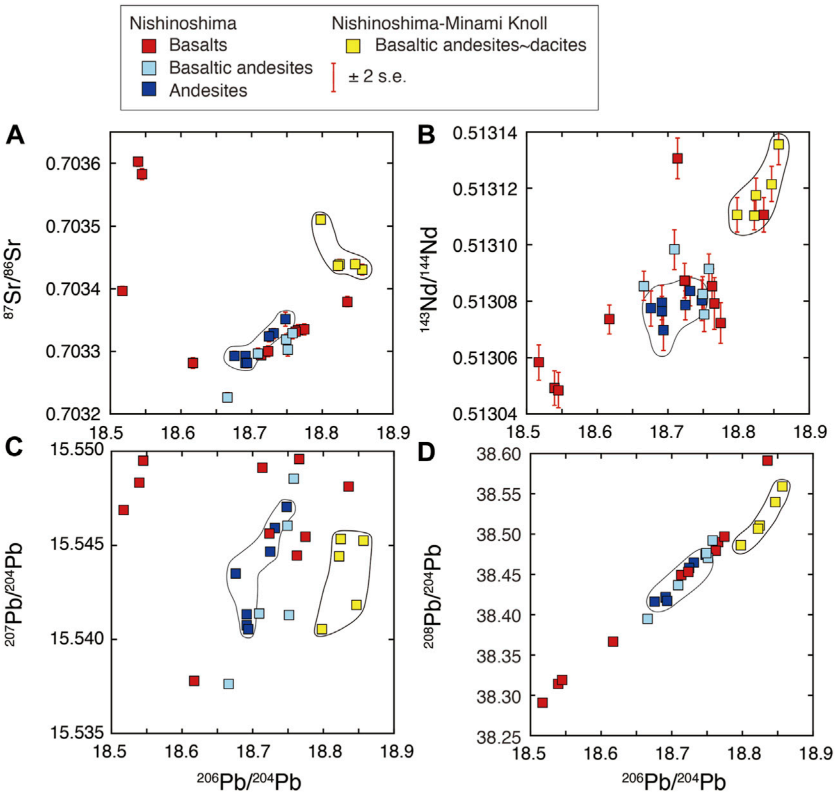

FIGURE 12
(A) $^{87}Sr/^{86}Sr$ vs. $^{206}Pb/^{204}Pb$, **(B)** $^{143}Nd/^{144}Nd$ vs. $^{206}Pb/^{204}Pb$, **(C)** $^{207}Pb/^{204}Pb$ vs. $^{206}Pb/^{204}Pb$, and **(D)** $^{208}Pb/^{204}Pb$ vs. $^{206}Pb/^{204}Pb$ for lavas from the Nishinoshima area. Samples are grouped by composition and geographical location, regardless of eruption or sampling date.

4.3 Basaltic andesites from Nishinoshima volcano in Episode 4

A large amount of the tephra erupted in Episode 4, representing the most voluminous magmas in 2020, were basaltic andesite in composition ranging from 53 to 58 wt% SiO_2 (Maeno et al., 2021). Major element compositions of basaltic andesites from Nishinoshima are intermediate between basalts and andesites (Figure 6). Trace element ratios are similar to those of Nishinoshima andesites (Figure 7).

REE patterns of Nishinoshima basaltic andesites and andesites are mostly parallel, except for negative Eu-anomalies that are strong in andesites but weak in basaltic andesites (Figure 8B). The strong negative Eu-anomalies of the andesites were interpreted to have resulted from their shallow mantle source and plagioclase-bearing residue (plagioclase lherzolite) (Tamura et al., 2019). The basaltic andesites have REE patterns intermediate between basalts and andesites.

Incompatible trace element patterns of Nishinoshima basaltic andesites are also intermediate between basalts and andesites (Figure 9), and positive Sr-anomalies are strong in basalts, weak in basaltic andesites and absent in andesites (Figure 9). However, both basaltic andesites and dacites from Nishinoshima-Minami Knoll have strong positive Sr-anomalies (Figure 9D).

The large amount of basaltic andesite explosively erupted in Episode 4 was the first basaltic andesite that was erupted from the Nishinoshima vent since historical eruptive activity began in 1973. That was unexpected and unusual because Episodes 1, 2, and 3 as well as the previous 1973 episode consisted of andesite eruptions (Maeno et al., 2021). However, this new eruption of basaltic andesite solved a small riddle, which could not be understood in Tamura et al. (2019).

As shown in Figures 6–9, we already reported a basaltic andesite from Nishinoshima in Tamura et al. (2019). This loose boulder stone (KR15-03-R02) was collected at a depth of 2,100 m ESE of Nishinoshima during cruise KR15-03 in 2015 (Figure 3A). This boulder and Episode 4 basaltic andesites are similar in major elements (Figure 6), trace element ratios (Figure 7), REE patterns (Figure 8B), and incompatible trace element patterns (Figure 9B). This boulder, however, has the lowest $^{87}Sr/^{86}Sr$ (0.703227) in the Nishinoshima area (Figure 11A), which is the only difference from the Episode 4 basaltic andesites. Evidently, basaltic andesites of similar composition to those of Episode 4 had previously been erupted from the volcanic center of Nishinoshima during prehistoric (pre-1973) eruptions.

As outlined above, andesites erupted from Nishinoshima are interpreted to have been produced by olivine fractionation of primary andesitic magmas generated at shallow depth whereas older basalts were derived from primary basaltic magmas generated at greater depth (Tamura et al., 2016; Tamura et al., 2019). In this scenario, the chemically intermediate basaltic andesite could be produced by mixing between mantle-derived andesite and mantle-derived basalt magmas in a magma chamber. It should be noted that the possible end-member basaltic magmas needed to produce the observed basaltic andesite compositions through mixing should have higher Ba/Nb ratios (Figure 7), higher Ba/Th ratios (Figure 10), and higher $^{143}Nd/^{144}Nd$ ratios than some basalt samples presented here, but our data show that geochemically heterogeneous basaltic magmas do exist at Nishinoshima.

Evidence for the proposed mixing between andesite and basalt magmas is seen in sample HPD#2148-R01 (Figure 5I), and a magma mixing scenario is consistent with the eruption sequence of Episode 4 (Maeno et al., 2021). Moreover, the existence of prehistoric basaltic andesite in the main body of Nishinoshima suggests that intrusions of basalt magmas might have happened before and may not be an unusual event for this volcano.

4.4 Nishinoshima-Minami Knoll and "mission immiscible"

Nishinoshima-Minami Knoll is 8 km south of Nishinoshima island and is built on the southern submarine flank of Nishinoshima. Despite this proximity, the lavas from Nishinoshima-Minami Knoll are distinct from those of the Nishinoshima main body and surrounding knolls. Compared with Nishinoshima andesites, Nishinoshima-Minami Knoll is low in TiO_2, FeO, Na_2O, and K_2O, and relatively high in Al_2O_3, CaO, and Mg value (Figure 6). High Ba/Nb and Ba/Th values suggest that the lavas from Nishinoshima-Minami Knoll are enriched in shallow subduction addition (e.g., Elliott, 2003; Pearce et al., 2005), while their low Nb/Yb values suggest a higher degree of mantle melting than Nishinoshima lavas (Figure 7). Moreover, light rare earth element (LREE; La, Ce, Pr, and Nd) concentrations are low in lavas from Nishinoshima-Minami Knoll compared to middle and heavy rare earth elements (MREEs and HREEs), suggesting that subducting sediment does not play an important role in the subduction components of these lavas (Figure 8). Instead, their high $^{87}Sr/^{86}Sr$, $^{143}Nd/^{144}Nd$, $^{206}Pb/^{204}Pb$, and $^{208}Pb/^{204}Pb$ (Figures 11, 12), coupled with high Ba/Th and low La/Sm (Figure 10), indicate sources enriched in hydrous fluids derived from the subducting Pacific Plate (e.g., Elliott, 2003; Pearce et al., 2005).

By contrast, the Nishinoshima andesites have LREE-enriched patterns with negative Eu anomalies that are different from the flat to LREE-depleted patterns of Nishinoshima-Minami Knoll (Figures 8B, C). The MORB-normalized incompatible element patterns (Figure 9) show that the lavas from the Nishinoshima area have the typical signature of subduction zones, enriched in elements mobile in aqueous fluids and sediment melts (e.g., Ba, U, K, and Pb). Interestingly, however, the positive Sr anomalies observed in the Nishinoshima-Minami rocks are absent in the Nishinoshima andesites (Figure 9C). The Nishinoshima andesites have lower $^{87}Sr/^{86}Sr$, $^{143}Nd/^{144}Nd$, $^{206}Pb/^{204}Pb$, and $^{208}Pb/^{204}Pb$ ratios than the Nishinoshima-Minami Knoll lavas (Figures 11, 12), and their combination of low $^{143}Nd/^{144}Nd$ with high La/Sm and low Ba/Th (Figure 10) suggests that their sources are instead enriched in the sediment melt component.

To interpret these differences between the Nishinoshima and Nishinoshima-Minami Knoll lavas, which occur within 8 km of each other, it is useful to make a comparison with a previous study of primitive arc basalt lavas from Pagan Volcano in the Mariana arc (Tamura et al., 2014). At Pagan, two geochemical groups of fresh basalt lavas can be distinguished at similar 10–11 wt% MgO; these erupted recently, at about the same time, and are only 500 m apart. Tamura et al. call these groups COB1 and COB2 (Figure 10B) because the two varieties have similar phenocryst assemblages (clinopyroxene and olivine) but can be distinguished on the basis of their "subduction component"; that is, what has been added from the subducted Pacific plate to their mantle source.

Ba/Nb and Ba/Th variations suggest that COB1 lavas have total and shallow subduction additions (Pearce et al., 2005) that are larger than those for COB2 lavas; meanwhile, Th/Nb and La/Sm indicate that sediment melts are more important for COB2 than for COB1. The negative correlation between Ba/Nb and Nb/Yb suggests that both total subduction addition and degree of melting of the COB1 source are higher than for the COB2 source. The higher total subduction addition might itself have resulted in a higher degree of melting of the COB1 mantle source; importantly, the subduction addition that caused higher degrees of melting of the COB1 source was mostly hydrous fluid, not sediment melt.

The alternative explanation—that COB1 and COB2 compositions reflect mixing between two endmembers, of a single subduction component and a single mantle component—is shown to be unlikely on the basis of their Pb isotope ratios, which do not define a linear trend in Pb isotope space. Instead, Tamura et al. (2014) suggest that Pb from subducted sediment is important for COB2 lavas, but Pb in aqueous fluid is more important for COB1 lavas. Together these lines of evidence suggest that aqueous fluid and sediment melt coexist when they are released from the subducting slab (Mibe et al., 2011; Kawamoto et al., 2012). These slab components can then be added separately to the source mantle, independently generating COB1 and COB2 magmas. The "mission" of a subducted slab is to add subduction components to the overlying mantle wedge to produce arc magmas. Thus, this coexistence of fluid and melt was referred to as "Mission Immiscible" (Tamura et al., 2014).

This model of separate addition of immiscible fluid and sediment melt components to the source mantle, resulting in independent generation of magmas with different compositions, can be applied to the case of Nishinoshima. Accordingly, lavas from Nishinoshima-Minami Knoll (with higher Ba/Th) derive from source mantle enriched in fluid from altered oceanic crust, whereas Nishinoshima andesites (with higher La/Sm) derive from source mantle enriched in partial melt from subducted sediment (Figure 10B).

Green et al. (2004) suggest that depleted mantle sources may be fertilized by slab-derived carbonatite fluid, which enriches CaO relative to Al_2O_3 in the primary magma derived from the mantle source. Evidence for carbonatite metasomatism in spinel peridotite xenoliths is reported from western Victoria, Australia (Yaxley et al., 1998). The model of Green et al. (2004) could explain the enigmatic enrichment of CaO in COB1 and Nishinoshima-Minami Knoll lavas compared to COB2 and Nishinoshima lavas (Figure 6), respectively, and thus the mantle source of COB1 and Nishinoshima-Minami Knoll might have been fertilized by slab-derived hydrous carbonatite fluid.

Moreover, carbonatite fluid and silicate melt are immiscible, and the miscibility gap expands with increasing pressure and decreasing temperature (e.g., Mattey et al., 1990; Brooker and Kjarsgaard,

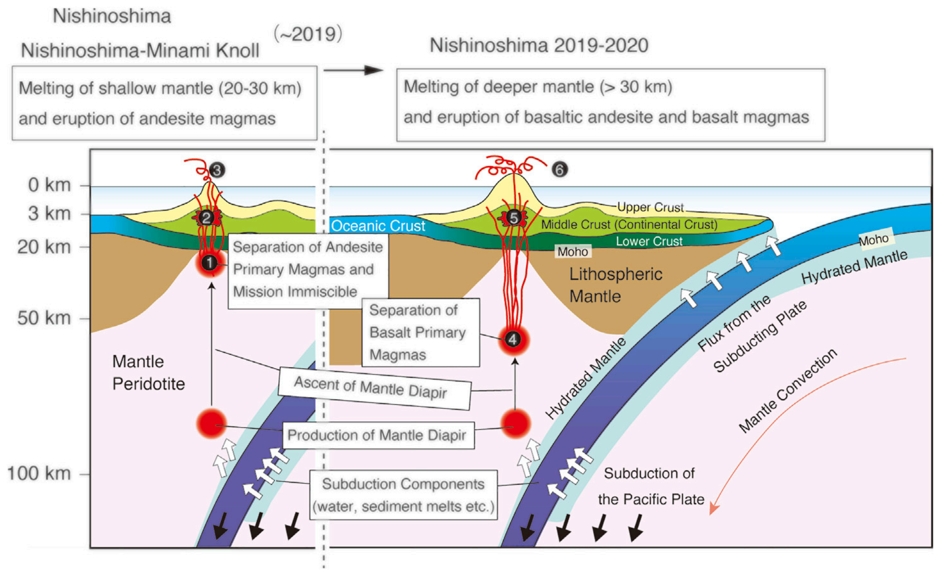

FIGURE 13
Schematic diagram showing the genesis of andesite magmas before 2019 and the genesis of basalt magmas and subsequent mixing with andesite magmas between 2019 and 2020. 1, mantle melting beneath thin crust (low pressure) and production of primary andesite. The "Mission Immiscible" process (Tamura et al., 2014) produced two different primary andesites in the Nishinoshima area (Nishinoshima main body and Nishinoshima-Minami Knoll); 2, efficient olivine fractionation from primary andesite magma in the crust (Tamura et al., 2019); 3, eruption of Nishinoshima andesites; 4, mantle melting at higher pressure and production of primary basalt, which is followed by assimilation of pyroxenes and fractional crystallization of olivines during ascent to the crust (AFC in the mantle, Tamura et al., 2019); 5, ascending basalt magma pushes the existing andesite magma out of the reservoir and then mixes with the andesite magma; 6, extrusion of andesite lava flows in 2019, followed by explosive eruptions of basalt and basaltic andesite in 2020.

2011). The hydrous fluid and sediment melt components are suggested to be immiscible, thus the former could be hydrous carbonatite fluid (Tamura et al., 2014). This immiscibility can make it possible for magmas derived from partial melting of source mantle affected by each component to coexist in the same volcano. Thus, magmas enriched in a sediment component (COB2/Nishinoshima andesites, with high La/Sm and low Ba/Th; Figure 10) and magmas enriched in a hydrous fluid (carbonatite) component (COB1/Nishinoshima-Minami Knoll, with low La/Sm and high Ba/Th), can be erupted within close proximity to each other—within 500 m at Pagan Volcano and at a distance of 8 km in the case of Nishinoshima and Nishinoshima-Minami Knoll.

In summary, primary magmas of Nishinoshima andesites and Nishinoshima-Minami Knoll lavas are derived from the partial melting of plagioclase peridotites at relatively low pressures under the thin crust (Tamura et al., 2019), to which the process of "Mission Immiscible" adds a subduction component of either sediment melt (yielding Nishinoshima andesites) or hydrous carbonatite fluid (yielding Nishinoshima-Minami Knoll basaltic andesites and dacites).

4.5 Evolution of magmas in Nishinoshima

Prior to the construction of Nishinoshima submarine volcano (~1 Ma), basalts erupted from the knolls that surround Nishinoshima (Tamura et al., 2019). Here we present a schematic diagram (Figure 13) to summarize the genesis of andesite magmas before 2019 and the genesis of basalt magmas and subsequent mixing with andesite magmas between 2019 and 2020.

The thin crust underlying Nishinoshima volcano is only 21 km thick (Kodaira et al., 2007). Andesite magmas with Eu anomalies (Figure 8B) can be produced by ~10% partial melting of source mantle without Eu anomalies when their residues are plagioclase peridotites having 3%–14% plagioclase (Tamura et al., 2019) (Figure 13, no. 1).

The "Mission Immiscible" process (Tamura et al., 2014) produced two different primary andesites in the Nishinoshima area (Nishinoshima main body and Nishinoshima-Minami Knoll), through enrichment in immiscible subduction components consisting of silicate melt (sediment melt) and hydrous carbonate fluid (carbonatite), respectively (Figure 13, no. 1). Immiscible subduction components result in mantle melting separately: Nishinoshima summit and Nishinoshima-Minami Knoll are only 8 km apart.

Efficient olivine fractionation from primary andesite magma in the crust produced Nishinoshima andesites (Tamura et al., 2019) (Figure 13, no. 2), which erupt from the summit of the volcano (Nishinoshima island) (Figure 13, no. 3).

Mantle melting at higher pressure produces primary basalt magmas, which is followed by assimilation of pyroxenes and fractional crystallization of olivines during ascent to the crust (AFC in the mantle, Tamura et al., 2019) (Figure 13, no. 4). Because old and new basalts are chemically similar, and because basaltic andesite, which is deemed to have resulted from mixing of basalt and andesite magmas, erupted prehistorically, it is possible that basalt magmas have been generated throughout the entire history of Nishinoshima, but their eruption center moved to Nishinoshima island in 2020.

Ascending basalt magma pushed the existing andesite magma out of the reservoir, resulting in continuous extrusion of andesite lava flows in 2019. As the ascending basalt magma interacted with the andesite magma some basaltic andesite was produced by magma mixing within the reservoir and/or conduit (Figure 13, no. 5). Explosive eruptions of basaltic andesite and basalt subsequently occurred in 2020 (Figure 13, no. 6). The explosivity is possibly related to the hydrous fluid and/or melt components from the subduction zone.

5 Conclusion

Analysis of submarine deposits has revealed that the 2020 eruption of Nishinoshima consisted of basalt, basaltic andesite, andesite, and dacite magmas. The andesites are similar to those which have erupted from the island since 1973. Nishinoshima andesite primary magmas originate directly from the mantle as a result of shallow and hydrous melting of plagioclase peridotite (Tamura et al., 2019).

The 2020 basalts are comparable to the older previously erupted basalts in the surrounding knolls reported in Tamura et al. (2019). Thus, basalt magmas could have been generated throughout the entire history of Nishinoshima, but their eruption center moved to the island summit in 2020.

In Episode 4, continuous extrusion of andesite lava flows in 2019 was followed by explosive eruptions of basalt and basaltic andesite in 2020. Apparently, ascending basalt magma pushed the existing andesite magma out of the reservoir in Episode 4 and then mixed with the andesite magma to produce basaltic andesite.

Basaltic andesites, which are similar to those of Episode 4, had previously been erupted from the volcanic center of Nishinoshima during prehistoric (pre-1973) eruptions.

Nishinoshima and Nishinoshima-Minami Knoll have distinct subduction components: the former is sediment melt and the latter is hydrous carbonatite fluid. The "Mission Immiscible" process of Tamura et al. (2014) could explain the production of different primary andesite magmas in the shallow mantle beneath Nishinoshima at a lateral distance of only ~8 km.

Generally, silicic volcanism tends to be more explosive than mafic (basaltic) eruptions. However, in oceanic arcs, basaltic volcanism can be more explosive than andesite volcanism.

Data availability statement

The original contributions presented in the study are included in the article/Supplementary Material, further inquiries can be directed to the corresponding author.

Author contributions

YT prepared the manuscript with feedback and contribution from all the coauthors. OI and QC, TS, and KY performed ICP-MS and isotopes, XRF, and EPMA analyses, respectively. All authors listed have made a substantial, direct, and intellectual contribution to the work and approved it for publication.

Funding

This work was supported by JSPS KAKENHI Grant Numbers JP17H02987 and JP21H01195.

Acknowledgments

Sampling of volcanic products from Nishinoshima were carried out in cooperation with shipboard scientists and technical personnel on multiple research vessels (Kairei, Natsushima, and Shinseimaru). Calvin Miller, Sean O'Donnell, and Takeshi Kuritani are thanked for their helpful comments, which improved the paper very much. Kristen Fauria and Valerio Acocella are thanked for the editorial handling.

Conflict of interest

The authors declare that the research was conducted in the absence of any commercial or financial relationships that could be construed as a potential conflict of interest.

Publisher's note

Supplementary material

The Supplementary Material for this article can be found online at: https://www.frontiersin.org/articles/10.3389/feart.2023.1137416/full#supplementary-material

References

Aoki, H., and Ossaka, J. (1974). *A mystery of submarine volcanoes – the exploration records of Nishinoshima (kaiteikazan No nazo)*. Tokyo: Tokai Univ. Press, 250.

Aoki, H., Utsunomiya, Y., Okitsu, H., Kawakami, M., Nakajima, I., and Ichikawa, M. (1983). Petrochemistry of the Nishinoshima islands. *La Mer.* 22, 248–256.

Brooker, R. A., and Kjarsgaard, B. A. (2011). Silicate-carbonate liquid immiscibility and phase relations in the system SiO_2-Na_2O-Al_2O_3-CaO-CO_2 at 0.1-2.5 GPa with applications to carbonatite Genesis. *J. Petrology* 52, 1281–1305. doi:10.1093/petrology/egq081

Chang, Q., Shibata, T., Shinotsuka, K., Yoshikawa, M., and Tatsumi, Y. (2003). Precise determination of trace elements in geological standard rocks using inductively coupled plasma mass spectrometry (ICP-MS). *Front. Res. Earth Evol.* 1, 357–362.

Cooper, L. B., Plank, T., Arculus, R. J., Hauri, E. H., Hall, P. S., and Parman, S. W. (2010). High-Ca boninites from the active Tonga Arc. *J. Geophys. Res.* 115, B10206. doi:10.1029/2009JB006367

Crawford, A. J., Falloon, T. J., and Green, D. H. (1989). “Classification, petrogenesis and tectonic setting of boninites,” in *Boninites and related rocks*. Editor A. J. Crawford (London: Unwin Hyman), 1–49.

Elliott, T. (2003). “Tracers of the slab,” in *Inside the subduction factory*. Editor J. Eiler (Geophysical Monograph, American Geophysical Union), 138, 23–45.

Gill, J. B. (1981). *Orogenic andesites and plate tectonics*. Berline: Springer, 390.

Green, D. H., and Ringwood, A. E. (1970). Mineralogy of peridotitic compositions under upper mantle conditions. *Phys. Earth Planet. Interiors* 3, 359–371. doi:10.1016/0031-9201(70)90076-2

Green, D. H., Schmidt, M. W., and Hibberson, W. O. (2004). Island-arc ankaramites: Primitive melts from fluxed refractory lherzolitic mantle. *J. Petrology* 45, 391–403. doi:10.1093/petrology/egg101

Ishizuka, O., Taylor, R. N., Milton, J. A., and Nesbitt, R. W. (2003). Fluid–mantle interaction in an intra-oceanic arc: Constraints from high-precision Pb isotopes. *Earth Planet. Sci. Lett.* 211, 221–236. doi:10.1016/S0012-821X(03)00201-2

Ishizuka, O., Taylor, R. N., Yuasa, M., Milton, J. A., Nesbitt, R. W., Uto, K., et al. (2007). Processes controlling along-arc isotopic variation of the southern Izu-Bonin arc. *Geochem. Geophys. Geosystems* 8, Q06008. doi:10.1029/2006GC001475

Johnson, C. M., and Beard, B. L. (1999). Correction of instrumentally produced mass fractionation during isotopic analysis of Fe by thermal ionization mass spectrometry. *Int. J. Mass Spectrom.* 193, 87–99. doi:10.1016/s1387-3806(99)00158-x

Kaneko, T., Maeno, F., Ishihara, M., Yasuda, A., Ohminato, T., Nogami, K., et al. (2022). Episode 4 (2019-2020) Nishinoshima activity: Abrupt transitions in the eruptive style observed by image datasets from multiple satellites. *Earth Planet Space* 74, 34. doi:10.1186/s40623-022-01578-6

Kaneko, T., Maeno, F., Yasuda, A., Takeo, M., and Takasaki, K. (2019). The 2017 Nishinoshima eruption: Combined analysis using himawari-8 and multiple high-resolution satellite images. *Earth Planet Space* 71, 140. doi:10.1186/s40623-019-1121-8

Kawamoto, T., Kanzaki, M., Mibe, K., Matsukage, K. N., and Ono, S. (2012). Separation of supercritical slab-fluids to form aqueous fluid and melt components in subduction zone magmatism. *PNAS* 109, 18695–18700. doi:10.1073/pnas.1207687109

Kodaira, S., Sato, T., Takahashi, N., Miura, S., Tamura, Y., Tatsumi, Y., et al. (2007). New seismological constraints on growth of continental crust in the Izu-Bonin intra-oceanic arc. *Geology* 35, 1031–1034. doi:10.1130/g23901a.1

Kushiro, I., and Yoder, H. S., Jr. (1966). Anorthite-forsterite and anorthite-enstatite reactions and their bearing on the basalt-eclogite transformation. *J. Petrology* 7, 337–362. doi:10.1093/petrology/7.3.337

Maeno, F., Nakada, S., and Kaneko, T. (2016). Morphological evolution of a new volcanic islet sustained by compound lava flows. *Geology* 44 (4), 259–262. doi:10.1130/G37461.1

Maeno, F., Yasuda, A., Hokanishi, N., Kaneko, T., Tamura, Y., Yoshimoto, M., et al. (2021). Intermittent growth of a newly-born volcanic island and its feeding system revealed by geological and geochemical monitoring 2013–2020, Nishinoshima, Ogasawara, Japan. *Front. Earth Sci.* 9, 773819. doi:10.3389/feart.2021.773819

Mattey, D. P., Taylor, W. R., Green, D. H., and Pillinger, C. T. (1990). Carbon isotopic fractionation between CO_2 vapour, silicate and carbonate melts: An experimental study to 30 kbar. *Contributions Mineralogy Petrology* 104, 492–505. doi:10.1007/bf01575626

McDonough, W. F., and Sun, S.-S. (1995). The composition of the Earth. *Chem. Geol.* 120, 223–253. doi:10.1016/0009-2541(94)00140-4

Mibe, K., Kawamoto, T., Matsukage, K. N., Fei, Y., and Ono, S. (2011). Slab melting versus slab dehydration in subduction-zone magmatism. *PNAS* 108, 8177–8182. doi:10.1073/pnas.1010968108

Osaka, J. (1973). On the submarine eruption of Nishinoshima. *Bull. Volcanol. Soc. Jpn.* 18, 97–98.

Osaka, J. (1974). On the activity and development of Nishinoshima volcano, bonin islands. *J. Geogr. (Chigaku Zasshi)* 83, 61–69.

Osaka, J., Ohira, Y., and Minato, I. (1974). On the submarine eruption of Nishinoshima (3). *Bull. Volcanol. Soc. Jpn.* 19, 37–38.

Osaka, J. (1975). On the activity and observation of volcano Nishinoshima (2). *Chishitsu News* 246, 1–9.

Pearce, J. A., Stern, R. J., Bloomer, S. H., and Fryer, P. (2005). Geochemical mapping of the Mariana arc-basin system: Implications for the nature and distribution of subduction components. *Geochem. Geophys. Geosystems* 6. doi:10.1029/2004GC000895

Presnall, D. C., Gudfinnsson, G. H., and Walter, M. J. (2002). Generation of mid-ocean ridge basalts at pressures from 1 to 7 GPa. *Geochimica Cosmochimica Acta* 66, 2073–2090. doi:10.1016/s0016-7037(02)00890-6

Prinzhofer, A., and Allègre, C. J. (1985). Residual peridotites and the mechanisms of partial melting. *Earth Planet. Sci. Lett.* 74, 251–265. doi:10.1016/0012-821x(85)90025-1

Sun, S.-S., and McDonough, W. F. (1989). Chemical and isotopic systematics of oceanic basalts: Implications for mantle composition and processes. *Geol. Soc. Lond. Spec. Publ.* 42, 313–345. doi:10.1144/gsl.sp.1989.042.01.19

Tamura, Y., Gill, J. B., Tollstrup, D., Kawabata, H., Shukuno, H., Chang, Q., et al. (2009). Silicic magmas in the Izu-Bonin oceanic arc and implications for crustal evolution. *J. Petrology* 50, 685–723. doi:10.1093/petrology/egp017

Tamura, Y., Ishizuka, O., Sato, T., and Nichols, A. R. L. (2019). Nishinoshima volcano in the Ogasawara arc: New continent from the ocean? *Isl. Arc* 28, e12285. doi:10.1111/iar.12285

Tamura, Y., Ishizuka, O., Stern, R. J., Nichols, A. R. L., Kawabata, H., Hirahara, Y., et al. (2014). Mission immiscible: Distinct subduction components generate two primary magmas at Pagan Volcano, Mariana arc. *J. Petrology* 55, 63–101. doi:10.1093/petrology/egt061

Tamura, Y., Sato, T., Fujiwara, T., Kodaira, S., and Nichols, A. (2016). Advent of continents: A new hypothesis. *Sci. Rep.* 6, 33517. doi:10.1038/srep33517

Tanaka, T., Togashi, S., Kamioka, H., Amakawa, H., Kagami, H., Hamamoto, T., et al. (2000). JNdi-1: A neodymium isotopic reference in consistency with LaJolla neodymium. *Chem. Geol.* 168, 279–281. doi:10.1016/S0009-2541(00)00198-4

Tani, K., Kawabata, H., Chang, Q., Sato, K., and Tatsumi, Y. (2005). Quantitative analyses of silicate rock major and trace elements by X-ray fluorescence spectrometer: Evaluation of analytical precision and sample preparation. *Front. Res. Earth Evol.* 2, 1–8.

Taylor, R. N., Ishizuka, O., Michalik, A., Milton, J. A., and Croudace, I. W. (2015). Evaluat-ing the precision of Pb isotope measurement by mass spectrometry. *J. Anal. At. Spectrom.* 30, 198–213. doi:10.1039/c4ja00279b

Turner, S., Bourdon, B., and Gill, J. (2003). “Insights into magma Genesis at convergent margins from U-series isotopes,” in *Uranium-series geochemistry*. Editors B. Bourdon, G. M. Henderson, C. C. Lundstrom, and S. P. Turner (Mineralogical Society of America and Geochemical Society, Reviews in Mineralogy and Geochemistry), 52, 255–315.

Ulrich, M., Picard, C., Guillot, S., Chauvel, C., Cluzel, D., and Meffre, S. (2010). Multiple melting stages and refertilization as indicators for ridge to subduction formation: The New Caledonia ophiolite. *Lithos* 115, 223–236. doi:10.1016/j.lithos.2009.12.011

Umino, S., and Nakano, S. (2007). *Geology of the Chichijima retto district, quadrangle series, 1:50,000*. Tsukuba: Geological Survey of Japan, AIST.

Yanagisawa, H., Iino, H., Ando, S., Takagi, A., and Oikawa, T. (2020). Violent strombolian eruption from June to August 2020 of Nishinoshima island, Ogasawara islands, Japan. *Bull. Vol. Soc. Jpn.* 65, 119–124.

Yaxley, G. M., Green, D. H., and Kamenetsky, V. (1998). Carbonatite metasomatism in the southeastern Australian Lithosphere. *J. Petrology* 39, 1917–1930. doi:10.1093/petroj/39.11-12.1917

Yoshida, K., Tamura, Y., Sato, T., Hanyu, T., Usui, Y., Chang, Q., et al. (2022). Variety of the drift pumice clasts from the 2021 Fukutoku-Oka-no-Ba eruption, Japan. *Isl. Arc* 31, e12441. doi:10.1111/iar.12441

frontiers | Frontiers in Earth Science

TYPE Original Research
PUBLISHED 24 August 2023
DOI 10.3389/feart.2023.1153288

OPEN ACCESS

EDITED BY
Tobias Dürig,
University of Iceland, Iceland

REVIEWED BY
Pierfrancesco Dellino,
University of Bari Aldo Moro, Italy
Arran Peter Murch,
National Museum of Nature and Science, Japan
Pierre-Simon Ross,
Université du Québec, Canada

*CORRESPONDENCE
J. Schmith,
johanneschmith@gmail.com

RECEIVED 29 January 2023
ACCEPTED 02 August 2023
PUBLISHED 24 August 2023

CITATION
Schmith J and Swanson DA (2023), Complex styles of phreatomagmatic explosions at Kīlauea Volcano, Hawaii, controlled by magma structure.
Front. Earth Sci. 11:1153288.
doi: 10.3389/feart.2023.1153288

Complex styles of phreatomagmatic explosions at Kīlauea Volcano, Hawaii, controlled by magma structure

J. Schmith[1]* and D. A. Swanson[2]

[1]Visiting Scientist, U.S. Geological Survey, Hawaiian Volcano Observatory, Hilo, HI, United States, [2]U.S. Geological Survey, Hawaiian Volcano Observatory, Hilo, HI, United States

Explosive eruptions at basaltic volcanoes remain poorly understood. Kīlauea Volcano is a type locality for basaltic eruptions and is well-known for effusive activity. However, more than 7 m of phreatomagmatic Keanakākoʻi Tephra unit D deposits from explosive eruptions crown the southern rim of the summit caldera and provide a stark reminder of Kīlauea's explosive past and future potential. We used detailed field observations as well as granulometric and morphological analysis of 100 samples from two proximal sections to assess the eruption style and fragmentation mechanism. The deposits can be divided into four subunits, six different lithofacies, and contain three juvenile tephra components. Each juvenile component shows distinct shape variability resulting from molten fuel-coolant interaction (MFCI) explosions of magma of variable vesicularity. Fragmentation of dense glass generates olive-green ash, fragmentation of low to moderately vesicular magma generates a dark gray ash-lapilli component, and fragmentation of highly vesicular magma generates light-yellow pumice. Our work shows that magma structure impacts MFCI explosion efficiency. Small-scale planar bedding throughout most of the deposit points to a general eruption style of small, frequent explosions generating low plumes. Thicker beds of accretionary lapilli of fine-extremely fine ash are related to very efficient magma-water mixing. Pyroclastic density current (PDC) deposits in the upper part of the stratigraphy contain at least three flows but show no significant dune or cross-bedding structures. We suggest that this is a function of the vent being situated in a caldera that was then ~600 m deep, where the caldera wall acted as a barrier and changed the flow dynamics to very dilute overspills and co-PDC plume falls over the wall. Deconvolution modeling of the polymodal grain size distributions is used to assess grain size changes of each juvenile component for this deposit, which greatly improves interpretation of lithofacies generation and eruption dynamics. Size-correlated shape parameters show that shape data across a wide size range are needed to accurately track grain shapes. This study demonstrates how careful examination of grain size and shape of juvenile tephra clasts can help volcanologists understand how effusive basaltic volcanoes can become violently explosive.

KEYWORDS

phreatomagmatic, explosive, stratigraphy, grain size, grain shape, Kīlauea, Keanakākoʻi, basaltic

1 Introduction

Hazards from volcanic eruptions are largely dependent on eruption style (Brown et al., 2017) and the distinction between effusive and explosive eruptions is particularly important (Cassidy et al., 2018). Lava flows typically provide a local hazard (Blong, 1984), whereas explosive eruptions can impact large areas and cause severe disruption and death (Cassidy et al., 2018). Thus, one of the most important questions is to understand how, why, and when volcanic eruptions become explosive rather than effusive.

Kīlauea Volcano in Hawai`i is the type locality for low-hazard Hawaiian fountains (Houghton and Gonnermann, 2008) and is famous for its effusive lava flows, but several meters of tephra deposits at the summit points to a more violent past of explosive activity (Swanson et al., 2014). It is therefore an ideal place to study processes that turn effusive volcanoes explosive. One such process is interaction of erupting magma with external water. In this paper we develop evidence that such phreatomagmatic interaction was crucial for driving some of Kīlauea's past explosions.

Kīlauea is an ocean island basalt shield volcano rising 1,247 m above sea level in the middle of the Pacific Ocean. Eruptive activity is concentrated in the 3–5 km wide summit collapse caldera and the East and Southwest Rift Zones (Figure 1). Geochemical studies show predominance of tholeiitic basalts (Garcia et al., 2018) and point to a two-tiered summit reservoir system together with geophysical evidence (Poland et al., 2014).Recent studies have recognized a cyclic eruptive behavior at Kīlauea with alternating explosive and effusive eruptive periods lasting several centuries (Swanson et al., 2014). The explosive periods are characterized by lower erupted volumes than those of the effusive periods, and the source area of the largest explosive eruptions is constrained to the summit caldera area. The explosive periods are preceded by large-volume effusive activity and large-scale summit caldera collapse event(s) (Powers, 1948; Swanson et al., 2014; Lynn and Swanson, 2022), but the mechanism responsible for the shift in the dominating eruptive style is still unknown.

When part of the caldera collapsed in 2018 (Neal et al., 2019), there was speculation about the nature of the next eruption at Kīlauea summit (Nadeau et al., 2020). In July 2019 a water lake formed in Halema'uma'u Crater within the caldera and became the first documented presence of a lake at Kīlauea summit. Immediately, the lake's presence raised concerns about explosive magma-water interaction if magma were to erupt though the lake (Nadeau et al., 2020), and it became timely to better understand the past phreatomagmatic activity at the summit.

The Keanakāko'i Tephra (Keanakāko'i) is the youngest and best exposed tephra package of Kīlauea (e.g., Powers, 1948; McPhie et al., 1990; Swanson and Houghton, 2018). It consists of up to 11 m of

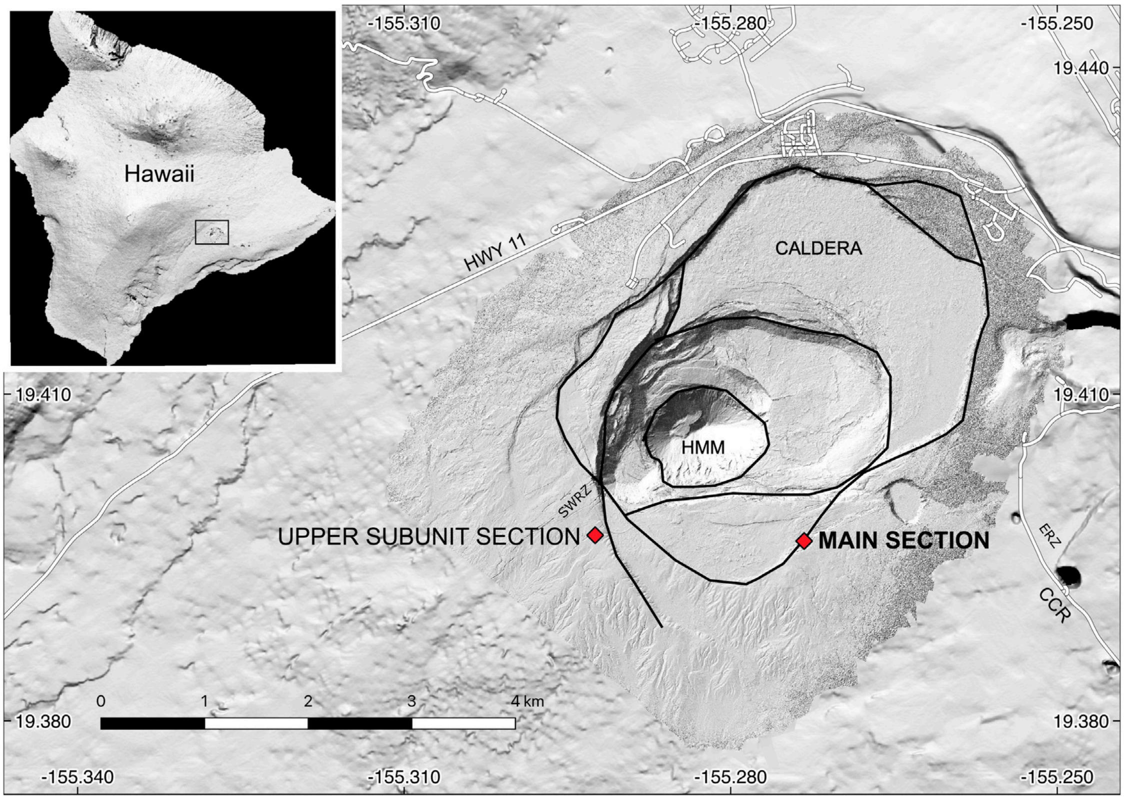

FIGURE 1
Map of Kīlauea summit with insert of map of the Island of Hawai'i with rectangle showing main map area. The summit caldera of Kīlauea (CALDERA) and Halema'uma'u Crater (HMM) are outlined with solid black lines. The Southwest Rift Zone (SWRZ) and East Rift Zone (ERZ) are indicated by labels. Red diamonds mark the field sections in the south caldera area that were used in this study. At the main section 723 cm of unit D was described and sampled (samples 1–93). At the upper subunit section 19 cm of the uppermost part of unit D was described and sampled (samples 94–100). CCR: Chain of craters road.

tephra (units A-L, Swanson and Houghton, 2018) with deposits from diverse eruption styles such as high Hawaiian lava fountains (units B, K1, and K2, May et al., 2015; Biass et al., 2019; Swanson and Houghton, 2018), subPlinian plumes (unit E, Swanson and Houghton, 2018), and phreatic plumes and pyroclastic density currents (PDCs) (units I, J1 and J2, Swanson et al., 2015).

Unit D of the Keanakākoʻi has long been interpreted as a phreatomagmatic deposit based on field appearance (Decker and Christiansen, 1984; McPhie et al., 1990; Swanson and Houghton, 2018) with some evidence of elevated glass volatile content associated with premature water-induced magma quenching (Mastin, 1997; Mastin et al., 2004). The deposits consist primarily of planar beds of juvenile clasts, which compose around 95% of the 1–2 mm size fraction according to componentry analysis (Swanson and Houghton, 2018). Most beds contain a small amount of wall-rock material, and some beds contain pumice lapilli up to 3–5 cm in diameter. The predominantly juvenile nature of the unit D deposits makes them ideal for granulometric and morphological study to evaluate the hypothesis that phreatomagmatism was responsible for the explosions.

The stratigraphy of Keanakākoʻi deposits has been redefined several times (Powers, 1948; Decker and Christiansen, 1984; McPhie et al., 1990). Here, we follow the stratigraphic nomenclature of Swanson and Houghton (2018): units A to L in order of decreasing age and deposit characteristics published therein. This latest revision of the Keanakākoʻi stratigraphy was informed by extensive field observations and ^{14}C ages obtained throughout the entire summit region (Swanson et al., 2012). Unit D can be correlated with subunits 2A (IIA) and 2B (IIB) from Decker and Christiansen. (1984) adapted by, e.g., Mastin. (1997) and Mastin et al. (2004) but is difficult to correlate directly with other stratigraphies.

Most of the Keanakākoʻi in the southern part of the summit area is made of unit D. The thickest exposure, about 7 m, is in the southern caldera wall. Exposures on the northern side of the caldera are less than 2 m thick, probably reflecting both a southern source area and deposition by the prevailing northeast trade wind (McPhie et al., 1990). An isopach map of unit D shows that the deposit abruptly thins in eastern and western directions from the summit caldera (Swanson and Houghton, 2018). The prevalence of trade wind deposition suggests that the plume(s) did not reach the jet stream at ca. 5 km above sea level. A smaller northern lobe probably indicates influence by the southerly winds, which blow at the summit 10%–15% of the time. The deposit also thins abruptly even in the downwind southwest direction consistent with low plume heights as well as poor preservation conditions.

Unit D was erupted after the caldera collapse ca. 1500 CE and ended before the mid 17th century as indicated by ^{14}C ages and stratigraphic relations to units B and E (Swanson et al., 2012). Unit D overlies small pockets of unit B reticulite on the southwest side of the caldera and thick unit C (a local block fall deposit) on the northeast side. Swanson and Houghton. (2018) suggested that unit D is capped by 1 cm of lithic-rich ash with accretionary lapilli in the southern caldera. However, our field data show that erosion cutting into strata took place between deposition of units D and E and that this 1 cm deposit was not part of unit D. Furthermore, the field data show that unit D had two different source areas in the caldera, such that the vent moved geographically in the later stage of the activity.

Here we present a detailed study of unit D deposits and focus on characterizing proximal deposits using systematic sampling of selected sections. We use new field observations of deposit components, lithofacies, and stratigraphy as well as granulometric and 2D shape parameter modeling to assess eruption style and fragmentation mechanism of this phreatomagmatic activity. This enables us to determine the style of the explosions that created the tephra and to evaluate the role of external water in the explosive processes at Kīlauea.

2 Methods

2.1 Deposit classification, stratigraphic subdivision, and sample collection

Lithofacies within unit D have been defined according to the classification scheme and grain size definitions following White and Houghton. (2006). Stratigraphic subdivisions in the form of subunits are based on lithofacies associations as well as regional unconformities.

The aim of the sampling was to get a high-resolution stratigraphic profile of the unit D deposits that would allow interpretation of temporal and process-related changes in eruptive activity. Two sections were sampled in detail (Figure 1) to characterize the deposit. Most of unit D was sampled in the southern part of the caldera wall at our main section (Figure 1), but the uppermost part was sampled at the upper subunit section (Figure 1) in a gully just southwest of the caldera. We sampled the thickest accessible exposure of each subunit, assuming this represents the proximal section with the highest temporal stratigraphic resolution. Induration of ash-dominated layers is common in the lower part of the section, and samples were scraped off as gently as possible with a toothless butterknife. All other samples were taken from loose deposits and were scooped out with spatulas and toothless knives. We collected a total of 100 samples for this study.

2.2 Grain size and quantitative 2D shape analysis

We used dynamic image analyzers CAMSIZER P4 and CAMSIZER X2 (hereafter P4 and X2) to obtain sample grain size distributions (GSDs) as well as quantitative shape parameters for all 100 samples. Both CAMSIZER instruments have a two-camera setup of a basal wide-angle camera and a high-resolution zoom camera to cover as wide a grain size range as possible with a frame rate of 300 frames per second. Both instruments disperse the sample from a vibrating feeder to ensure random orientation of the grains. The P4 instrument covers the size range 30,000–20 microns for reliable grain size data and analyses grains as they fall from the feeder in front of the cameras. However, a large size range within a single sample can be problematic, as larger grains create turbulent fall conditions for the finer particles, and the fine ash can aggregate into larger clumps that will skew the GSD. Therefore, we sieved the samples at 1 mm and split them between the two instruments. The X2 covers the size range 4,000–0.8 microns for grain size data and offers higher resolution for the ash size range than the P4. We chose an X2 instrument setup with an X-jet module using pressurized air to ensure laminar grain transport with good grain dispersal and to avoid fine ash aggregation.

Samples were dried at 65°C for at least 24 h, and indurated samples were mechanically disaggregated by hand. Loose lapilli-bearing samples were sieved at 1 mm, the splits were weighed, and grains larger than 1 mm were measured on the P4 whereas ash of less than 1 mm was measured on the X2. Samples of pure ash were analyzed only on the X2. Grain size distributions obtained from the P4 and X2 were merged using the split-weight proportions. In this study we use the minimum maximum chord Xc_{min} as the size parameter for all samples, because this parameter is compatible with traditional sieve sizes (CAMSIZER manual, 2020, version 0002). GSD statistics were obtained using GRADISTAT software (Blott and Pye, 2001).

For our quantitative 2D particle shape analysis we used means of shape data for half phi grain sizes for each sample (X2 ˂1 mm and P4 ˃1 mm) and whole sample means of X2 and P4 shape data weighted by sample weight fractions measured on each instrument. The resolution of the P4 was 67.3 microns per pixel for the basal camera and 11.8 microns per pixel for the zoom camera. The resolution was 9.9 microns per pixel for the basal camera and 0.84 microns per pixel for the zoom camera on the X2. This translates to a resolution of 173.4–624,255.3 pixels/particle for the P4 basal camera and 5,638–20,306,186.4 pixels/particle for the zoom camera for the 1 mm–3 cm grain size range. Particle resolutions of the X2 were 31.30–32,053.8 pixels/particle for the basal camera and 4,348–4,424,778,4 pixels/particle for the zoom camera for the modeled grains of 62.5 microns–1 mm. Zoom camera data are favored by the CAMSIZER software algorithm for fine fractions, and all shape parameters are well within the CAMSIZER resolution requirements. The number of particles analyzed per sample is in the range of several thousands, thus exceeding minimum recommendations from Schmith et al. (2017) of at least 1,500 analyzed grains per bulk sample.

We use the CAMSIZER parameters of sphericity, aspect ratio, compactness, and Krumbein roundness. Sphericity is defined as $SPHT = \frac{4\pi A}{P^2}$, where A is the area measured on the particle projection and P is the measured perimeter for the particle. Aspect ratio is defined as $AR = \frac{X_{c\,min}}{X_{Fe\,max}}$ and compactness as $COMP = \frac{\sqrt{\frac{4A}{\pi}}}{X_{Fe\,max}}$, where $X_{Fe\,max}$ is the maximum caliper dimension of the grain. Krumbein roundness is calculated as: "the average curvature radius of all relevant corners divided by the largest inscribed circle radius. The lower limit for detection is 20 pixels" (CAMSIZER manual, 2020, version 0002).

All parameters are dimensionless, ranging between 1 and 0, and were chosen so that grain size would not directly influence the shape modeling. Sphericity compares the area of the grain to the perimeter in a mathematical relation, so a perfect sphere (i.e., 2D circle) will have the value of 1, and it is a widely used measure of the overall regularity of the grain (e.g., Dürig et al., 2021; Edwards et al., 2021). Irregularities in grain morphology from either grain elongation (form), complex grain shapes (morphological roughness), surface perturbations (textural roughness) or a combination of all will result in relatively longer perimeters compared to the area increase and yield lower sphericity values. However, perimeter is also sensitive to resolution with higher resolutions resulting in longer perimeters (Schmith et al., 2017), but the CAMSIZERS use an image processing algorithm to minimize this effect. Aspect ratio compares width and length of the grain showing grain elongation (form) with values of 1 representing equant grains. Compactness compares the similar area circle diameter of the grain to the maximum caliper dimension (Fe_{max}), so a perfect sphere (i.e., 2D circle) will have the value of 1 and it is a measure of form/morphological roughness. Krumbein roundness is a mathematical adaption of the Krumbein roundness classification scheme (Krumbein, 1941) and is a measure for surface roughness of the grain.

3 Results

3.1 Deposit description

3.1.1 Unit D tephra components

Unit D contains three different juvenile components: olive-green ash, dark gray ash and lapilli, and light yellow pumice lapilli. Photos of typical component assemblages are shown in Figure 2. Deposits also contain a minor lithic component making up a few percent of the deposit (Mastin et al., 2004; Swanson and Houghton, 2018), which is often difficult to distinguish from the dark gray ash and lapilli (see grain in Figure 2). Deposits are generally loose, though high concentrations of fine-extremely fine ash form consolidated beds that stand out in eroded field sections.

The olive-green ash is a juvenile ash made of angular, dense, equant, blocky to platy sideromelane shards (see photo in Figure 2). It occurs throughout unit D. Grain size ranges from medium ash to extremely fine ash.

The dark gray ash and lapilli component consists of juvenile medium ash to medium lapilli of angular–subangular, dense to scoriaceous grains with vesicularities of ca. 0%–50% (visual estimate), mostly 10%–30% (see photo in Figure 2). Grains are commonly micro-vesicular, and larger vesicles are typically less than 100 microns in diameter. Most vesicles are spherical, though some are slightly ellipsoidal, and most are filled with fine olive-green ash (see photo in Figure 2). Grain shapes are blocky, typically with straight faces and edges. Phenocrysts of olivine or free olivine crystals are generally associated with the dark gray ash, which is commonly partly coated by olive-green ash.

Pumice clasts are light yellow, but some have orange palagonite patches. Clasts range between coarse ash and large lapilli in size. Vesicles are spherical to ellipsoidal and typically less than 100 microns in diameter. Medium–coarse fragments of pumice lapilli are typically angular-subangular. Some have millimeter-thick glassy rinds, interpreted as products of fast quenching, on one side of the grain. Many clasts are broken *in situ* in the deposit. Coarse pumice ash and fine lapilli are typically subangular to well-rounded with no quench rinds and can be extracted whole from the deposit (see photo Figure 2).

3.1.2 Unit D lithofacies

Unit D contains six different lithofacies (Figures 2A–F): fine homogeneous ash, coarse homogeneous ash, laminated ash, poorly sorted ash, ash-lapilli, and ash-lapilli couplets.

Fine homogeneous ash (F hom, Figure 2A) appears as millimeter-to centimeter-thick planar beds of well-sorted, olive-green, medium–extremely fine ash. A hard secondary silicic

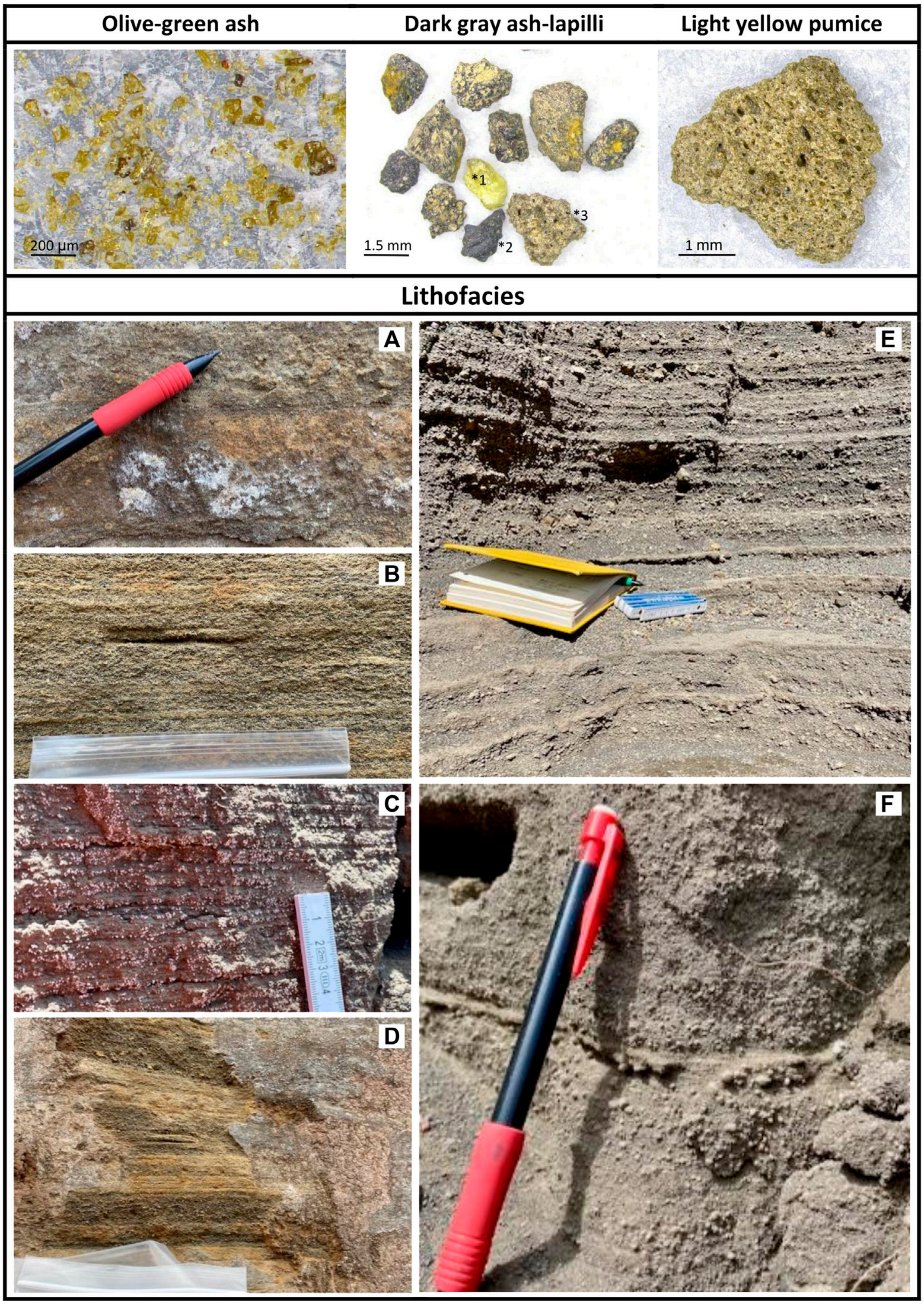

FIGURE 2
Top row: microscope photos in transmitted light of typical grains/grain assemblages representing the three juvenile components in the unit D deposits. See text for detailed descriptions. Free olivine (*1), lithic grain (*2), and pumice grain (*3) are included in the dark gray ash assemblage to represent the complete componentry of this size range. Notice how the olive-green ash fills vesicles on dark gray ash. Below: Representative photos of unit D lithofacies: **(A)** fine homogeneous ash—here shown with preserved accretionary lapilli features, **(B)** coarse homogeneous ash with noticeable content of olive-green ash and 15 cm wide sample bag, **(C)** laminated ash, **(D)** ash-lapilli beds with light yellow pumice lapilli showing after cleaning secondary outcrop coating with 15 cm wide sample bag, **(E)** couplets of ash-lapilli and ash beds with distributed clasts of pumice lapilli, **(F)** poorly sorted ash shown here with the most well-defined bedding exposed in the section. Notice clast-supported accretionary lapilli and grain size contrast of distributed clasts above and below fine ash trace.

surface shell on parts of the outcrop face makes it difficult to assess the presence of accretionary lapilli in a consistent manner. However, layers of framework-supported, moderately sorted, structured accretionary lapilli, typically with a dark gray coarse ash core, characterize some of the fine homogeneous ash layers.

Coarse homogeneous ash (C hom, Figure 2B) forms millimeter- to centimeter-thick planar beds of moderately sorted dark gray coarse ash. Close inspections shows that most coarse ash beds contain unstructured fine olive-green ash, which gives the beds a flecked appearance.

Laminated ash (PL, Figure 2C) is a collection of planar-bedded, millimeter-thick laminae of dark gray coarse ash and olive-green fine ash forming packages centimeters to decimeters thick. In a few places low-angle cross-bedding or very low amplitude (mm scale) pinch and swells are observed. The length scale of the pinching and swelling structures is difficult to assess but is probably on a decimeter scale. These structures are defined only by a few of the millimeter-thin laminae and are easily overlooked.

Poorly sorted ash (PS, Figure 2F) consists of decimeters to meters of fine to very fine olive-green ash with distributed, isolated coarse ash clasts of dark gray ash and rounded pumice grains covered in fine ash. A diffuse bedding is defined by slight color changes in the deposit as well as by millimeter-thin extremely fine ash traces of a light gray color, but it is difficult to discern actual bedding. Low-angle cross-bedding and low degree pinching- and swelling patterns are observed but uncommon, and it was not possible to measure the length or amplitude. No dune structures have been identified in this lithofacies.

Ash-lapilli (AL, Figure 2D) appears as centimeter thick planar beds of poorly sorted, dark gray coarse ash to medium lapilli containing a few percent free olivine crystals and lithic clasts as well as 10%–15% pumice lapilli.

Couplet deposits (CL, Figure 2E) are defined by planar-bedded couplets of very poorly sorted dark gray coarse ash to medium lapilli beds and moderately to well sorted fine olive-green ash beds. The dark gray ash-lapilli beds are typically 1–12 cm thick, whereas the olive-green ash beds are 0.2–2 cm. However, seemingly thick dark gray ash-lapilli beds commonly contain one or more millimeter-thin layers or traces of the olive-green ash. A few ash-lapilli beds show inverse size grading, but most are not graded. The dark gray beds contain a few percent free olivine crystals and lithic clasts, and both bed-types contain pumice clasts. Olivine crystals are typically 0.5–1 mm long and euhedral, though some crystals are broken. Lithic fragments are mainly of ash size and consist of dull, gray, angular basalt, some of which is oxidized. Pumice occurs in the coarse ash to large lapilli size range and dominates in the larger size ranges with average maximum length of ca. 0.5–1 cm. The medium-large pumice lapilli fragments are distributed as isolated clasts in the ash-lapilli beds but are commonly distributed along the olive-green ash traces within or at the interface between an ash-lapilli and an olive-green ash bed. The pumice clasts form 5%–70% of individual couplet beds based on visual field assessment.

3.2 Interpretation of the unit D deposit observations

Our study confirms that the unit D deposits are phreatomagmatic, in line with previous work (Decker and Christiansen, 1984; McPhie et al., 1990; Mastin, 1997; Mastin et al., 2004; Swanson and Houghton, 2018). More specifically, the dense, juvenile, blocky, and platy sideromelane olive-green shards that make up the fine–extremely fine ash fractions throughout the deposit (Figure 2) are prime examples of grains typical of phreatomagmatic interaction (e.g., Heiken, 1974; Wohletz, 1983a; Büttner et al., 2002; Murtagh and White, 2013; White and Valentine, 2016; Schmith et al., 2017; Verolino et al., 2022). The same can be said for the blocky and equant juvenile dark gray ash–lapilli grains with spherical/elliptical isolated microvesicles and variable but low vesicularities (e.g., Walker and Croasdale, 1972; Mastin et al., 2004; Verolino et al., 2022), and previous studies have already demonstrated the association of the less characteristic pumice component with phreatomagmatic eruption(s) (Mastin, 1997; Mastin et al., 2004).

Phreatomagmatic activity generating wet eruption plumes is also supported by observations of coating of the observed dark gray ash with olive-green ash (e.g., Nemeth and Kosik, 2020) and the prevalent poor sorting of the deposit, including the large intra-bed grain size range, and fine to extremely fine ash presence across the entire deposit (Walker and Croasdale, 1972; Sheridan and Wohletz, 1983; Wohletz, 1986; Nemeth and Kosik, 2020). Clast-supported accretionary lapilli beds with structured aggregates that have well-defined finer ash rinds point to a wet plume environment with high fine ash content and liquid water droplets nucleating on coarse ash grains (Van Eaton et al., 2012), which is typically observed in association with phreatomagmatic activity (Brown et al., 2012; Durant and Brown, 2016).

Based on the planar bedding, we interpret the lithofacies of fine homogeneous ash, coarse homogeneous ash, laminated ash, ash-lapilli beds, and all couplets as fall deposits. The regional distribution pattern indicates that they were deposited by small plumes or jets. The laminated deposits show a nice separation between coarser and finer ash, which suggests short-lived bursts with enough time for material to settle gravitationally between explosions, but not enough time for the winds on the southern side of the caldera to rework these deposits. This suggests fast accumulation rates of this lithofacies.

The homogeneous lithofacies suggests continuous settling of material related to sustained tephra generation at the vent. The relatively fine grain sizes could either result from a low plume height or indicate intense fragmentation. The coarser grain size of the ash-lapilli beds suggests higher plumes or less intense fragmentation at the vent.

The couplets are the most complex fall deposits. Their well-defined layering indicates either swift waxing and waning of the plume or discrete explosive episodes. The thin fine ash layers within the thicker ash-lapilli beds suggest that these lithofacies result from discrete explosive episodes of variable size and duration. The distribution of the pumice along traces of olive-green ash indicates some density-driven fractionation from the tephra plume; however, the generally poorly sorted nature and distribution of pumice throughout the beds also point to a proximal source and a densely tephra-laden plume.

The poorly sorted ash lithofacies with cross-bedding, pinching-swelling patterns, and matrix-supported distributed coarse ash grains covered in fine ash suggest dilute PDC deposits with poorly structured matrix-supported accretionary lapilli. The poorly defined bedding makes it difficult to subdivide the

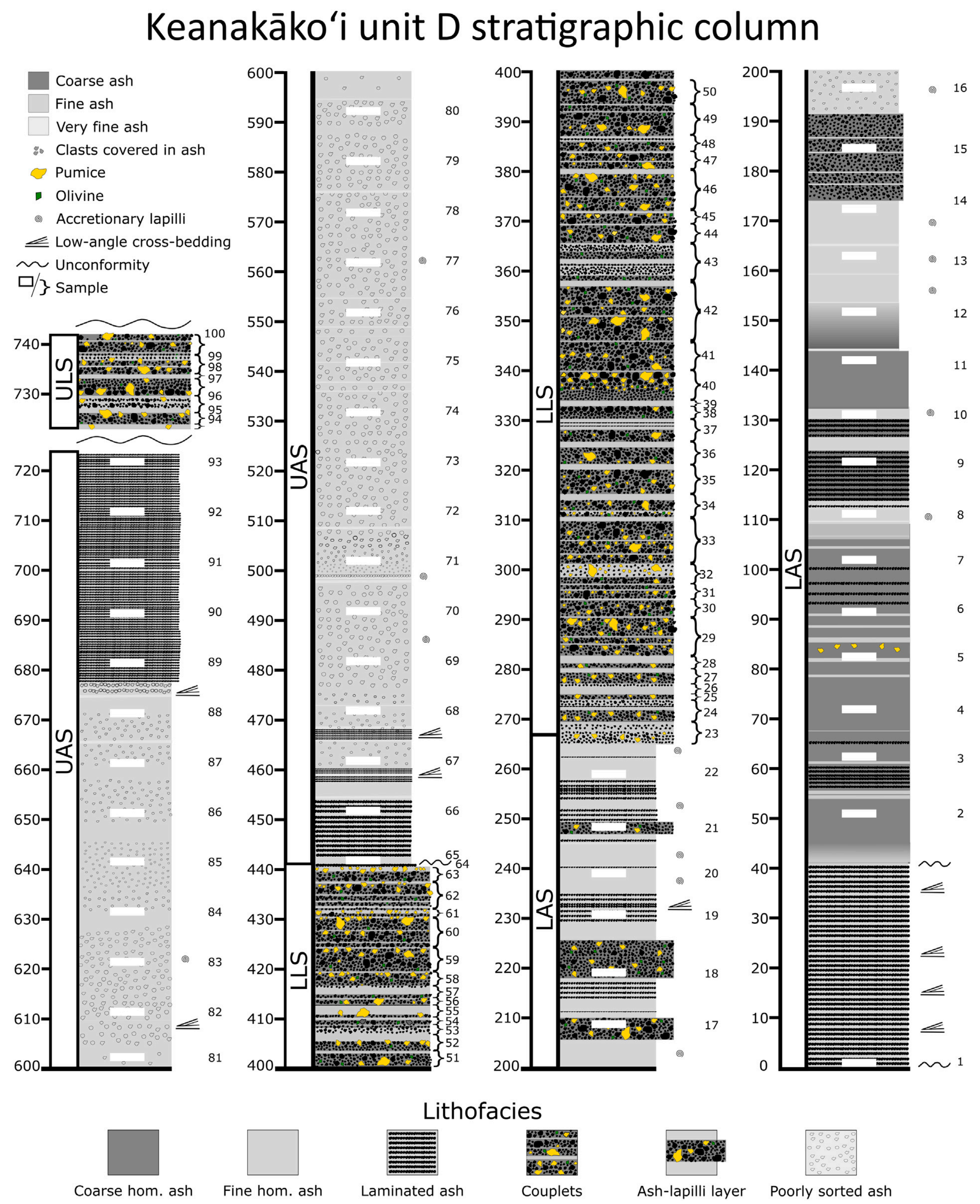

FIGURE 3
Composite stratigraphic column of unit D in Kīlauea south caldera with scale in centimeters. Gray-scale colors of column indicate matrix grain size as outlined in legend, whereas individual clasts from coarse ash to medium lapilli are drawn as individual grains to depict main features of the deposit. Relative amount of pumice and olivine are scaled to field observation on individual layers, though the olivines are oversized here for visibility purposes. Horizontal width of column indicates approximate grain size of lithofacies. LAS: lower ash-dominated subunit, LLS: lower lapilli-bearing subunit, UAS: upper ash-dominated subunit, ULS: upper lapilli-bearing subunit. The LAS, LLS, and UAS were all measured at the main section (Figure 1), whereas the ULS was measured and sampled at the upper subunit location (Figure 1). Samples are marked with white rectangles for the ash-dominated subunits (LAS and UAS) and by curly brackets for the lapilli-bearing subunits (LLS and ULS) with all sample numbers noted to the right of each column. Please zoom in on electronic version to see details if needed and refer to Figure 2 and text for description of lithofacies. See text for detailed descriptions of stratigraphy.

lithofacies into individual flows or flow and fall units. Interestingly, the deposit does not show prominent dunes, and the pinching-swelling structures are small enough in amplitude to be easily overlooked. This is atypical for near-vent surge deposits and will be explored further in the discussion.

3.3 Stratigraphy

A stratigraphic column of unit D is presented in Figure 3. We divide unit D into four subunits based on the stratigraphic distribution of the lithofacies as well as the observation of several unconformities. The base of unit D rests on the pāhoehoe lava flows (age ca. 1350 CE, Neal and Lockwood, 2003; Swanson et al., 2012) and local erosional remnants of unit B across the southern caldera. The basal unit D subunit is dominated by ash lithofacies of coarse and fine homogeneous ash and planar bedded laminated ash, but also contains three ash-lapilli beds and is as thick as 265 cm in the caldera wall. We call it the lower ash-dominated subunit (LAS, Figure 3). It is conformably overlain by up to 176 cm of continuous couplets of dark gray ash and lapilli and olive-green ash, which we call the lower lapilli-bearing subunit (LLS, Figure 3). The top of the LLS represents a disconformity with an undulating top on small and large lateral scales cutting into the planar bedded strata in exposures across the south caldera area with the uppermost deposit stripped of fine ash, suggesting widespread regional erosion. The level of erosion varies randomly based on location, and in places several decimeters of the stratigraphy identified at the main section is missing. Therefore, the 176 cm of LLS exposed at the main section is likely less than the maximum original thickness of the subunit. An ash-dominated lithofacies overlies this erosional unconformity, with up to 282 cm of poorly sorted ash and planar bedded laminated ash lacking obvious signs of erosion at the top of the subunit at the main section. This is the upper ash-dominated subunit (UAS, Figure 3). All three subunits are thickest in the south caldera wall in the main section (Figure 1) and thin away from this area. The uppermost subunit of D, the upper lapilli-bearing subunit (ULS, Figure 3) consisting of another set of continuous couplets, deviates from this distribution pattern. Its thickest exposure is about 2 km farther west in a gully just west of the caldera wall (see upper subunit section, Figure 1). The deposit is as thick as 19 cm and conformably overlies the UAS in several places. This subunit is conformably overlain by a 1-cm-thick ash layer, which was interpreted by Swanson and Houghton (2018) as capping unit D with units E and F above. However, the lithology and color of the 1-cm ash layer is different from the ash-dominated subunits of unit D, and it was erupted after another erosion event that removed the ULS completely in some places. Therefore, we do not consider it part of unit D.

3.4 Sample classification

The stratigraphic position of the 100 samples from the composite section is shown in Figure 3. The ash-dominated subunits were sampled every 10 cm from top to bottom, and each sample is 2–3 cm thick. The lapilli-bearing subunits were sampled as couplets from top to bottom based on thicker olive-green ash layers. It was not possible to separate the olive-green ash layers from the loose ash-lapilli layers and often both layers contained traces of the other, so we decided the couplet sampling was the best approach in practice. Samples typically consist of an olive-green ash bed above an ash and lapilli bed, although the ash and lapilli beds often contain one or more millimeter traces of olive-green ash. The couplet samples range significantly in total thickness as well as relative thickness of olive-green ash beds and ash and lapilli beds. Samples 1–22 represent the LAS, samples 23–63 the LLS, samples 64–93 the UAS, and samples 94–100 the ULS couplets.

We classified the 100 samples according to their lithofacies. The classification is summarized in table 1. We noted 11 samples taken from planar bedded laminated deposits (PL) and 23 samples from the poorly sorted, diffusely bedded ash deposits (PS). There are 15 samples of homogeneous ash including nine samples of coarse homogeneous ash (C hom) and 6 of fine homogeneous ash (F hom). Samples from the ash-lapilli and olive-green ash couplets comprise two categories, couplet samples (CL) dominated by dark gray ash and lapilli and fine couplet samples (Fine CL) largely dominated by the olive-green ash beds. We also distinguish between couplets from the LLS and ULS, as they were extracted from different sections. In the LLS, there are 29 couplet samples (CL) and 12 fine-dominated couplet samples (Fine CL). The seven ULS couplet samples consist of five lapilli-bearing couplets (CL ULS) and two fine ash beds (CL fine ULS). Finally, three individual ash-lapilli beds come from the LAS (AL). All lithofacies are well represented by several samples.

3.5 Grain size characterization of lithofacies

3.5.1 Median and sorting of lithofacies

Traditionally, grain size data are often presented in terms of the global GSD statistics of central tendency and width (sorting) of the distribution (Inman, 1952; Blott and Pye, 2001). We used the classic diagram of median grain size *versus* Inman sorting to assess the distributions of the lithofacies (Figure 4). All lithofacies fall in distinct fields of median grain size- and Inman sorting ranges except for the fine-dominated couplet layers (Fine CL) and the planar bedded deposits (PL), which suggests that the lithofacies are related to the genesis of the deposits.

The fine and coarse homogeneous ash (F hom and C hom, Figure 4) deposits define fields separated in median grain size range, with the F hom samples ranging from 2.74 to 3.98 φ (fine–very fine ash) and the C hom samples spanning 1.28–2.51 φ (medium–fine ash). These measurements quantitatively confirm the field-based observations of size differences, and also support the field observation of a significant amount of finer olive-green ash in the coarse ash lithofacies. The lithofacies show similar poor sorting ranges at the low-value end of the unit D sorting spectrum. The coarse ash samples are shifted to slightly better sorting (lower values) of 1.13–1.64 φ compared to 1.31–1.82 φ for the fine ash, which might be linked to the observation of a population of coarse to very coarse ash cores and/or extremely fine ash rinds of the accretionary lapilli of the fine homogeneous ash deposits. Generally, these sorting values show that the homogeneous ash deposits are not as well-sorted as they appear in outcrop.

TABLE 1 Table shows sample lithofacies, grain size distribution type, and deconvolution model output quality for every unit D sample. Samples are marked by their consecutive stratigraphic numbers (in bold in table) as shown in Figure 3. Distribution type categories are shown in Figure 5 and model output evaluation is described in Section 3.5.3 Deconvolution modeling. See text for more details.

Sample ID	Sample lithofacies	Distribution type	Quality of modeling	Sample ID	Sample lithofacies	Distribution type	Quality of modeling
100	CL ULS	Bimodal fine mode	Good	**50**	CL	Trimodal	Good
99	CL ULS	Trimodal	Good	**49**	CL	Trimodal	Good
98	Fine CL ULS	Quadrimodal	Moderate	**48**	CL	Trimodal	Poor
97	CL ULS	Trimodal	Good	**47**	CL	Trimodal	Good
96	CL ULS	Bimodal fine mode	Good	**46**	CL	Quadrimodal	Moderate
95	CL ULS	Trimodal	Moderate	**45**	CL	Trimodal	Moderate
94	Fine CL ULS	Trimodal	Good	**44**	CL	Trimodal	Good
93	PL	Bimodal	Good	**43**	Fine CL	Trimodal	Moderate
92	PL	Bimodal coarse shoulder	Good	**42**	CL	Trimodal	Good
91	PL	Bimodal coarse shoulder	Good	**41**	CL	Trimodal	Moderate
90	PL	Bimodal coarse shoulder	Good	**40**	CL	Quadrimodal	Moderate
89	PL	Bimodal	Good	**39**	Fine CL	Quadrimodal	Poor
88	PS	Bimodal coarse shoulder	Good	**38**	CL	Bimodal fine mode	Good
87	PS	Bimodal coarse shoulder	Good	**37**	Fine CL	Trimodal	Good
86	PS	Unimodal symmetrical	Good	**36**	CL	Quadrimodal	Moderate
85	PS	Bimodal coarse shoulder	Good	**35**	CL	Trimodal	Good
84	PS	Bimodal coarse shoulder	Moderate	**34**	CL	Trimodal	Good
83	PS	Bimodal	Moderate	**33**	CL	Trimodal	Moderate
82	PS	Bimodal coarse shoulder	Good	**32**	CL	Bimodal fine mode	Good
81	PS	Bimodal coarse shoulder	Good	**31**	CL	Trimodal	Poor
80	PS	Bimodal coarse shoulder	Good	**30**	CL	Trimodal	Moderate
79	PS	Bimodal coarse shoulder	Good	**29**	CL	Trimodal	Moderate
78	PS	Unimodal symmetrical	Good	**28**	Fine CL	Bimodal fine mode	Good
77	PS	Bimodal coarse shoulder	Good	**27**	CL	Trimodal	Moderate
76	PS	Bimodal coarse shoulder	Good	**26**	Fine CL	Bimodal fine mode	Good
75	PS	Unimodal symmetrical	Good	**25**	CL	Trimodal	Moderate
74	PS	Bimodal coarse shoulder	Good	**24**	Fine CL	Trimodal	Moderate

(Continued on following page)

TABLE 1 (*Continued*) Table shows sample lithofacies, grain size distribution type, and deconvolution model output quality for every unit D sample. Samples are marked by their consecutive stratigraphic numbers (in bold in table) as shown in Figure 3. Distribution type categories are shown in Figure 5 and model output evaluation is described in Section 3.5.3 Deconvolution modeling. See text for more details.

Sample ID	Sample lithofacies	Distribution type	Quality of modeling	Sample ID	Sample lithofacies	Distribution type	Quality of modeling
73	PS	Bimodal coarse shoulder	Good	**23**	Fine CL	Bimodal fine shoulder	Good
72	PS	Bimodal coarse shoulder	Good	**22**	F Hom	Bimodal	Good
71	PS	Bimodal coarse shoulder	Good	**21**	AL	Trimodal	Good
70	PS	Bimodal coarse shoulder	Good	**20**	F Hom	Bimodal coarse shoulder	Good
69	PS	Bimodal coarse shoulder	Good	**19**	PL	Bimodal fine shoulder	Good
68	PS	Unimodal symmetrical	Good	**18**	AL	Trimodal	Good
67	PS	Unimodal symmetrical	Good	**17**	AL	Unimodal fine skewed	Good
66	PL	Bimodal coarse shoulder	Good	**16**	PS	Unimodal symmetrical	Good
65	PL	Bimodal fine shoulder	Good	**15**	C Hom	Bimodal coarse shoulder	Good
64	PL	Bimodal	Good	**14**	F Hom	Unimodal symmetrical	Good
63	CL	Quadrimodal	Moderate	**13**	F Hom	Unimodal symmetrical	Good
62	CL	Quadrimodal	Moderate	**12**	C Hom	Unimodal fine skewed	Good
61	Fine CL	Trimodal	Good	**11**	C Hom	Unimodal fine skewed	Good
60	CL	Trimodal	Good	**10**	F Hom	Bimodal fine shoulder	Good
59	CL	Trimodal	Moderate	**9**	PL	Unimodal fine skewed	Good
58	CL	Trimodal	Good	**8**	F Hom	Unimodal fine skewed	Good
57	Fine CL	Trimodal	Good	**7**	C Hom	Unimodal fine skewed	Good
56	CL	Trimodal	Good	**6**	C Hom	Unimodal fine skewed	Good
55	Fine CL	Trimodal	Moderate	**5**	C Hom	Bimodal coarse shoulder	Good
54	CL	Trimodal	Moderate	**4**	C Hom	Unimodal fine skewed	Good
53	Fine CL	Bimodal fine mode	Good	**3**	C Hom	Unimodal fine skewed	Good
52	Fine CL	Trimodal	Good	**2**	C Hom	Bimodal fine shoulder	Good
51	CL	Trimodal	Moderate	**1**	PL	Unimodal fine skewed	Good

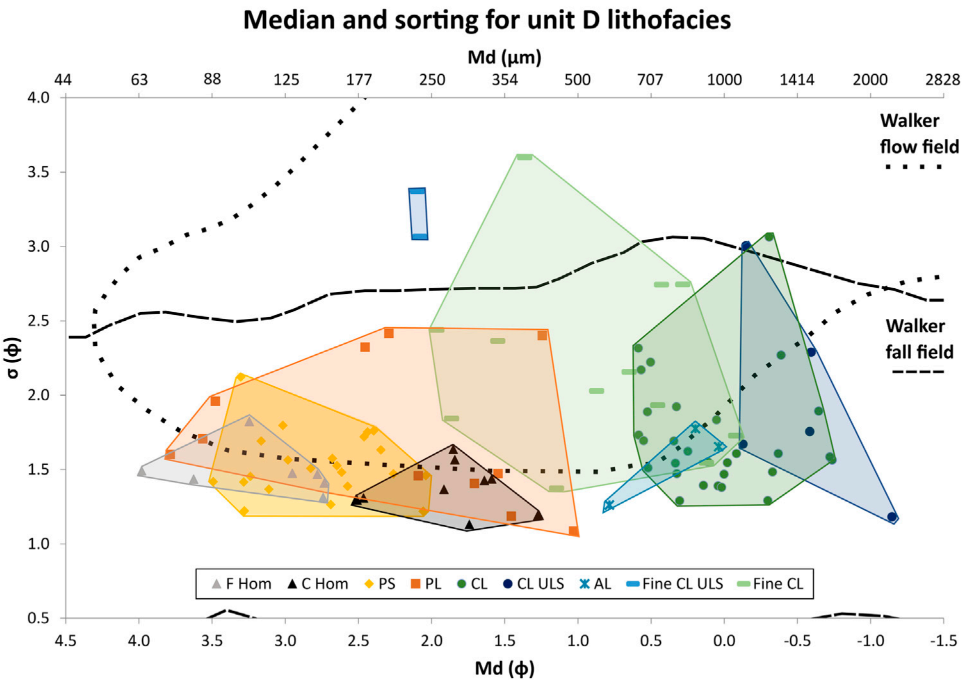

FIGURE 4
Grain size distribution median and sorting values in phi units for all 100 unit D samples. Samples are grouped according to lithofacies: fine homogeneous ash (F hom), coarse homogeneous ash (C hom), poorly sorted ash (PS), laminated ash (PL), couplets from main section (CL), couplets from upper subunit section (CL ULS), ash-lapilli layer (AL), fine-dominated couplet sample from main section (Fine CL), fine-dominated couplet sample from upper subunit section (Fine CL ULS). The median generally reflects the field observations, whereas the sorting is more similar across all lithofacies than estimated in the field. Fall and flow fields from Walker (1971) are outlined on plot, but as explained in the text they are not suitable for deposit interpretation. See text for further details.

The poorly sorted lithofacies (PS, Figure 4) samples overlap with both homogeneous ash fields and span only a slightly wider sorting range despite their poorly sorted appearance. Their medians are 2.06–3.49 φ (fine to very fine ash) and sorting is 1.22–2.12 φ (poorly sorted). The poorest sorting value beyond the homogeneous ash fields is for a single sample from a layer with low-angle cross-bedding.

The ash-lapilli beds (AL, Figure 4) of the LAS have Md_{φ}-values of −0.99–0.79 φ (coarse to very coarse ash) and sorting of 1.26–1.65 φ (poorly sorted), values reflecting the field observations of coarser beds in this lithofacies. The sorting values are in the same range as those of the ash-dominated deposits of the homogeneous and poorly sorted ash; thus sorting is not correlated with the overall grain size of the deposit.

The couplets (CL, CL ULS, Figure 4) from both subunits show overlapping fields with a relatively narrow median grain size but a wide range of sorting with values of Md_{φ}(CL) −0.74–0.59 φ (coarse to very coarse ash) and σ_{φ}(CL) 1.29–3.06 φ (poorly to very poorly sorted) and of Md_{φ}(CL ULS) −1.15–(-0.13) φ (very coarse ash to fine lapilli) and σ_{φ} (CL ULS) 1.18–3.01 φ (poorly to very poorly sorted), respectively. The wide sorting range is most likely related to the sampling of couplets of coarse- and fine-grained beds, but the narrow median-size range reveals that the overall distribution and ratio of different grain sizes remains relatively stable for these deposits. Most samples have sorting similar to that of the homogeneous and poorly sorted ash-deposits, an indication that overall grain size of the deposit is not correlated with sorting.

The fine-dominated couplet samples (Fine CL, fine CL ULS, Figure 4) have intermediate Md_{φ}-values of −0.08–1.96 φ (very coarse ash-medium ash), which fall between the couplet and the homogeneous and poorly sorted ash medians. The two fine-dominated samples from the ULS have finer medians of 2.08–2.1 φ (fine ash), consistent with field observations that these samples are dominated by a single olive-green ash bed. The fine-dominated couplets have the widest sorting range and show the poorest sorting of all sample types, with sorting values ranging from 1.37 to 3.6 φ (poorly to very poorly sorted). The ULS samples fall within the upper part of this sorting range, with values of 3.07–3.27 φ (very poorly sorted).

Finally, *the laminated deposits* (PL, Figure 4) have the widest range of Md_{φ}-values of all the lithofacies spanning 1.03 to 3.79 φ (medium to very fine ash) with sorting values of 1.09–2.42 φ (poorly sorted). The range of median and sorting values most likely reflects thickness variations in the coarse and fine laminae where each sample was taken and suggests considerable small-scale variability despite the rhythmic appearance in the field.

Walker (1971) used a median-sorting diagram to classify tephra deposits as fall or flow in origin. However, the Walker classification fields were based on sieved samples with a different resolution of the fine distribution than our modern dataset, which may influence values significantly. Furthermore, flows such as dilute PDCs are poorly classified by these fields, and we only show them here for reference.

3.5.2 Distribution analysis

To obtain detailed grain size information about the lithofacies, we analyzed the grain size frequency distributions for all 100 samples according to their visual modality and shape. We created separate

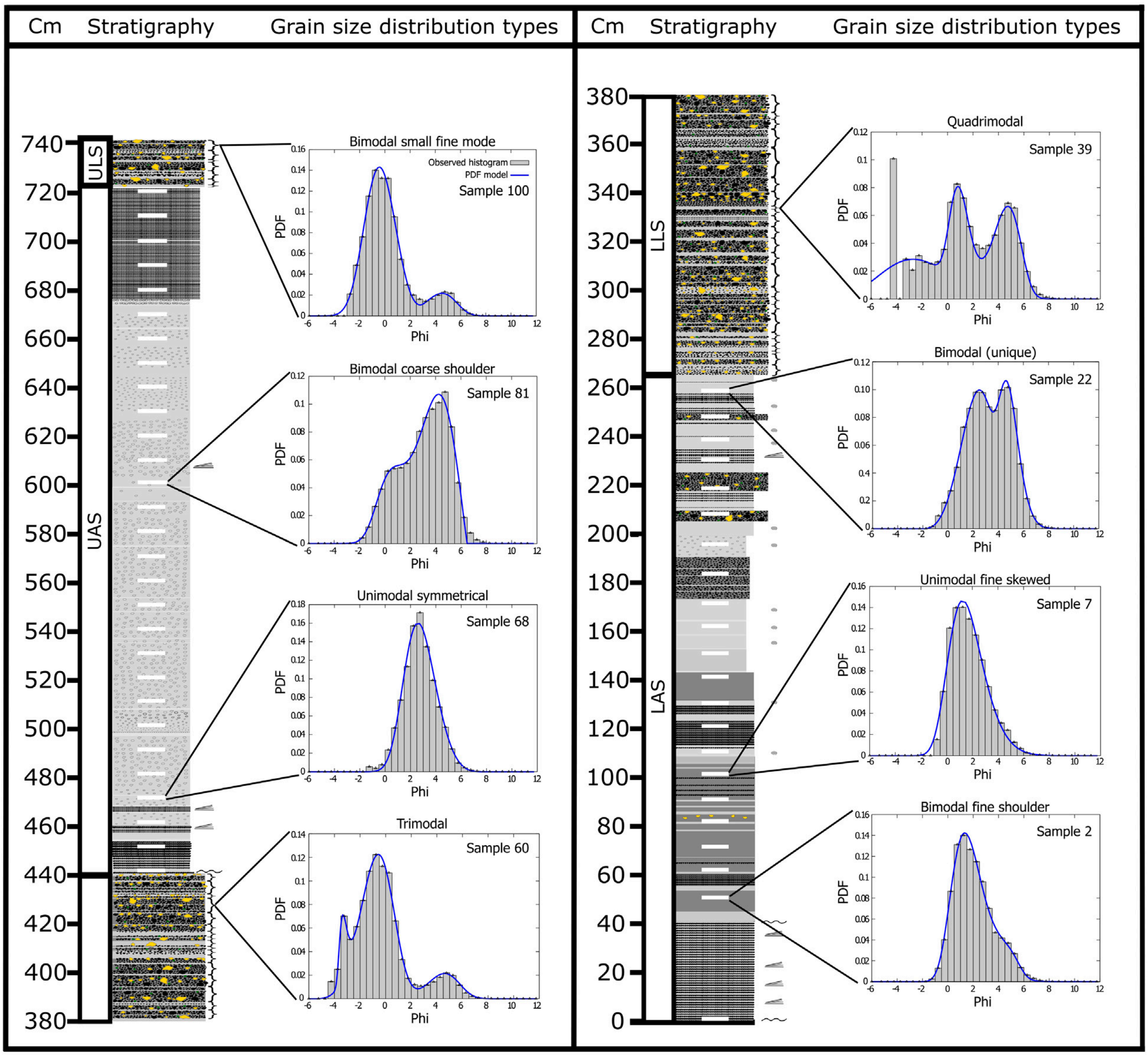

FIGURE 5
The eight grain size distribution types. Grain size distribution histograms are plotted as ½ phi retained (label is lower end of size interval) size bins. Frequency is in fraction values. Blue lines on grain size plots show the modeled deconvolution curve for the selected samples. The distributions shown in this figure are representative examples, but sample distributions vary within each category. Individual GSDs and distribution models for all samples can be found in supplementary data collection S1 and classifications of sample GSDs are outlined in table 1.

categories for common distribution shapes that are easily identified. Distribution plots for all samples are provided in supplementary data collection S1. We found distributions are uni-, bi-, tri-, or quadrimodal. The unimodal and bimodal samples show two to four distinct distribution shapes, whereas the trimodal and quadrimodal distributions are variable in shape. We group the frequency distribution shapes into eight categories (Figure 5): Unimodal symmetrical, unimodal fine skewed, bimodal fine shoulder, bimodal coarse shoulder, bimodal with a fine mode, bimodal (unique), trimodal, and quadrimodal distributions.

Only 18 samples show unimodal distributions of which 10 are symmetrical and 8 fine skewed. The other 82 distributions are multimodal, with 40 classified as bimodal, 35 as trimodal and 7 as quadrimodal. The bimodal samples are subdivided into 23 samples with coarse shoulder, 5 with fine shoulder, 12 had a separate second mode of which 7 samples have a smaller secondary fine mode and 5 are unique bimodal distributions (table 1).

Figure 6 shows the distribution types for each lithofacies. Even though seven of the nine sample lithofacies classes show a dominant distribution type, no lithofacies is uniquely defined by its GSD, and the GSD does not add significant detail about eruptive processes to the field observations in and of itself.

3.5.3 Deconvolution modeling

With more than 80 percent of our GSDs being polymodal, conventional statistical parameters beyond central measures (e.g.,

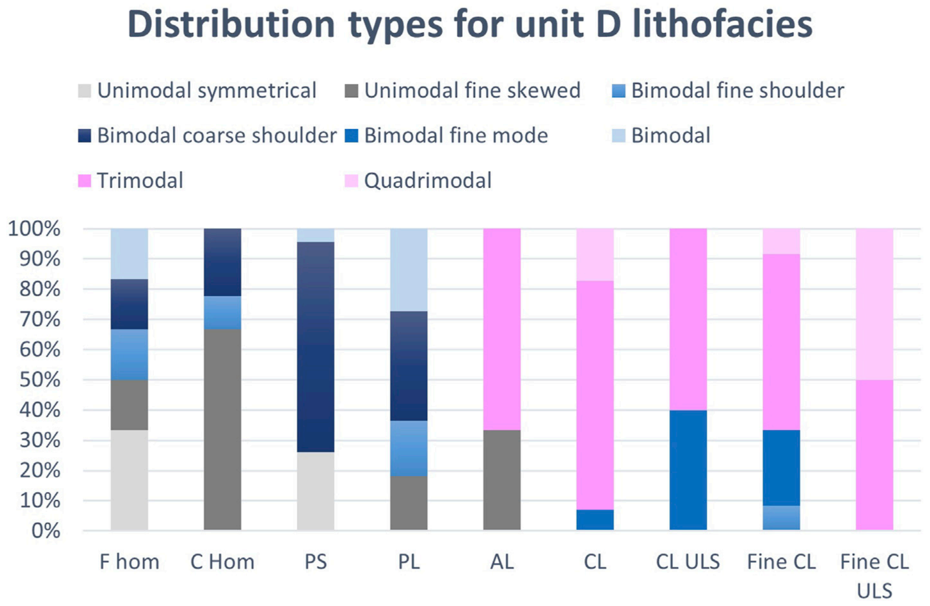

FIGURE 6
Grain size distribution types of samples from each lithofacies shown as percentage columns. Lithofacies key is similar to Figure 4 and distribution type categories are shown in Figure 5. C hom, PS, AL, CL, CL ULS, and CL fine lithofacies show dominant distribution types of unimodal fine skewed (C hom), bimodal coarse shoulder (PS), and trimodal (AL, CL, CL ULS, CL fine) distributions. F hom, PL, and Fine CL ULS lithofacies have no dominant distribution type.

mean and median) are mostly unreliable for our samples. Therefore, we used the DECOLOG software (Borselli and Sarocchi, 2022) for deconvolution modeling to obtain statistical information on each size sub-population. This method has provided useful information for interpreting multimodal grain size data from phreatomagmatic eruptions (Schmith et al., 2018). For fitting data and distribution graphs for all 100 samples, see supplementary data collection S1. The deconvolution modeling results are not unique solutions. Best fits are selected from a qualitative comparison between the distribution shape and the output modes. We estimate the quality of the deconvolution distribution as either good, moderate, or poor by visually comparing the original and model distributions. Distribution fit coefficients are consistently high for a wide range of model outputs. A good fit captures the visual modes well and shows a good visual overlap between frequency and cumulative distribution curves. A moderate fit captures the modes but may under- or overestimate their size/shape leading to a discrepancy between the cumulative curves–typically at either the fine or coarse extremes. Discrepancies between the number of visual modes and modeled modes automatically categorize the output as moderate or poor (see Table 1). Poorly modeled distributions either miss or misplace modes entirely. It was not possible to obtain a good fit for the quadrimodal samples, so they are all modeled with three modes only. Seventy-five samples have good modeling results, 22 have moderate fits, and three samples have poor fits (see Table 1).

3.5.4 Modes and sorting of lithofacies sub-populations

We compare mode and sorting of modeled subpopulation within each lithofacies to assess if the lithofacies show specific and/or stable size modes, which could be related to the eruptive activity. Figure 7 shows how mode- and sorting values are distributed for the modeled sub-populations of each lithofacies. Modes are numbered according to their influence on the distribution, so the mode that constitutes the largest fraction of the distribution is the first mode.

The fine homogeneous lithofacies (F hom, Figures 6, 7) has good model outputs and shows either symmetrical unimodal or one of the bimodal distribution types, though none of them has a separate secondary fine mode (Figure 6). Their dominant mode grain sizes are uniform and fall between 2.52 and 2.72 φ (fine ash) with a single outlier (sample 20) at 4.61 φ (Figure 7). However, the first mode of sample 20 falls within the narrow secondary mode interval 4.42–4.61 φ (extremely fine ash) and has a second mode within the primary mode interval (Figure 7). The narrow size ranges and an extremely fine ash second mode in some samples suggest that the overall poor sorting of this lithofacies is related to the extremely fine ash rinds observed on the accretionary lapilli. The finer modes are generally better sorted, with moderately–moderately well sorted values, whereas the coarser modes are still classified as poorly sorted–possibly in part due to the presence of the coarse ash accretionary lapilli cores.

The coarse homogeneous ash lithofacies (C hom, Figures 6, 7) samples all model well and show primarily poorly sorted, fine-skewed unimodal distributions with modes of 1.01–2.58 φ (coarse to fine ash) (Figure 6). Thus, the poor sorting noted in the statistical analysis is confirmed by the modeling. It is most likely caused by the substantial content of the finer olive-green ash as noted in the field observations, though sample 2 is the only sample with an actual modeled secondary mode of extremely fine ash (4.72 φ), in accordance with the observation of more olive-green ash in this deposit (Figure 7). Samples 5 and 15 have a secondary coarse mode

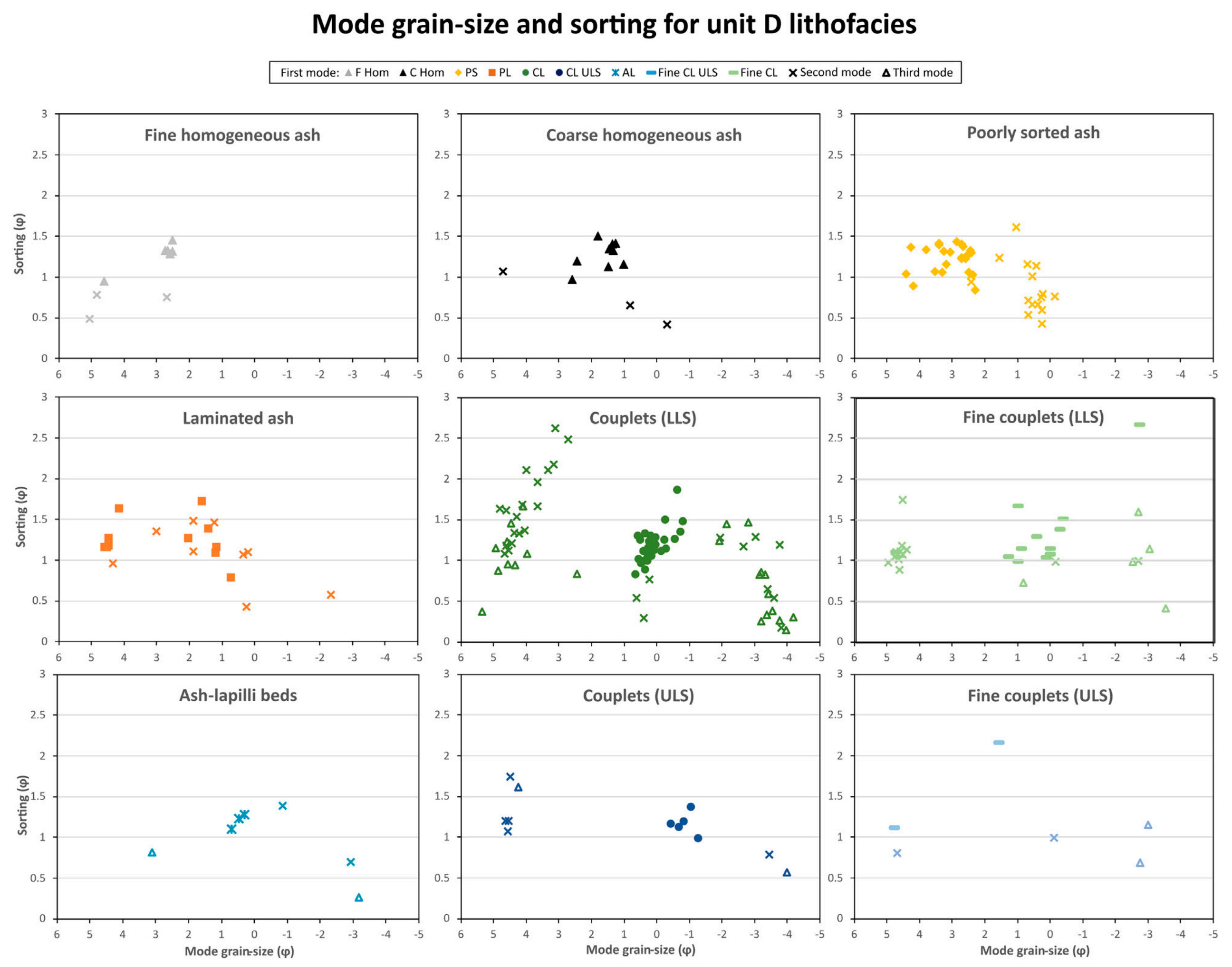

FIGURE 7
Modeled mode and sorting plots of grain size distribution subpopulations for each lithofacies. Both mode and sorting are shown in phi units. Data for this figure come from the deconvolution model output and modes are numbered according to their fraction of the distribution such that mode 1 is the largest mode of the distribution. The plots show that the lithofacies have well-defined mode size intervals, though the fraction of the distribution that is defined by this size mode may vary significantly.

corresponding to the observed clast populations of very coarse ash-size pumice and dark gray coarse ash, respectively (Figure 7).

The poorly sorted lithofacies (PS, Figures 6, 7) shows good model outputs except for samples 83 and 84, and distributions are primarily bimodal with a coarse shoulder (Figure 5). The dominant mode shows a considerable size range of 2.37–4.26 *φ* (fine to extremely fine ash) with a narrow secondary mode of −0.15–1.03 *φ* (very coarse to coarse ash) reflecting the field observation of a fine ash matrix and coarse distributed clasts (Figure 7). The rest of the poorly sorted deposits have symmetrical unimodal GSD with modes of 2.44–3.41 *φ* (fine to very fine ash), suggesting that the coarse ash clasts play a minor role in these samples. The modeling of sample 83 fails to capture a minor secondary mode in the lapilli size range, whereas the secondary mode of sample 84 poorly captures the actual size distribution and results in the only outlier between the primary and secondary mode size ranges (Figure 7).

The laminar ash lithofacies (PL, Figures 6, 7) models well and shows uni- or bimodal distributions with no clear primary distribution type (Figure 6). Their primary modes fall in two overall groups between 0.72 and 2.02 *φ* (coarse to medium ash) and 4.15 and 4.58 *φ* (extremely fine ash), respectively (Figure 7), reflecting the laminated nature of the deposit. The secondary modes are all in about the same size ranges except for samples 19 and 64. Sample 19 has the coarsest primary mode and a secondary mode between the two size fields, suggesting that grain sizes are in general shifted to higher values for this deposit. Sample 64 has a medium lapilli secondary mode, which most likely reflects a small population of pumice.

The *LLS couplet lithofacies samples (CL, Figures 6, 7)* are more difficult to model accurately, with 12 good model outputs *versus* 15 moderate and 2 poor. Almost all distributions are trimodal or quadrimodal with a few bimodal samples with a secondary fine mode (Figure 6), and models show a dominant size mode of −0.80–0.65 *φ* (coarse to very coarse ash) with most secondary modes of 2.72–4.93 *φ* (fine to extremely fine ash) and a third mode of −4.19–(−1.92) *φ* (fine to coarse lapilli) (Figure 7). This correlates with the observed lithofacies components of the dominant coarse-very coarse matrix ash with very fine olive-green ash beds and the fraction of pumice lapilli. Most of the moderate model outputs fail to capture a minor coarse mode that makes up the third or fourth mode or misplaces/misshapes the extreme modes slightly. This results in mode grain sizes migrating toward the dominant mode grain size and sorting values increasing for these samples (Figure 7).

The ULS couplets and all the fine-dominated couplets (CL ULS, fine CL, fine CL ULS, Figures 6, 7) show better model fits, with five moderate fits and 14 good, and distributions show similar systematics and size ranges to the LLS couplets. The ULS couplet dominant size mode is coarser and ranges between −0.44 and −1.28 φ (very coarse ash to fine lapilli) (Figure 7).

The three samples from *the ash-lapilli beds* (AL, Figures 6, 7) are well modeled. Two samples have trimodal distribution, whereas one has a fine skewed bimodal distribution (Figure 6). Primary modes range between −1.27 and 0.48 φ and coarse modes fall at −3.12–(−2.94) φ, which overlaps with the couplet modes, but only sample 21 shows a very fine ash mode at 3.10 φ (Figure 7). This fits the general similarity with the ash-lapilli beds of the LLS and ULS couplet lithofacies and supports the interpretation that the fine ash modes in these deposits are indeed correlated with the observed olive-green ash beds and traces.

3.6 Interpretation of grain size modeling

In general, the grain size modeling and field data for the lithofacies correlate very well, and the deconvolution modeling resolves the grain sizes and size variations of the lithofacies better than is possible with field estimates or general GSD statistics. The deconvolution subpopulations show relatively stable size modes for the lithofacies in spite of the variable distribution types, and variability can be linked to field observations. This indicates that processes controlling the size of the grains were stable for each lithofacies, but processes controlling the amount of each size fraction varied throughout the eruptive activity. From the size- and field data alone it is not possible to distinguish how fragmentation, transport, and depositional processes are responsible for the lithofacies grain size characteristics and internal variability. Therefore, we also looked at the grain shapes of the juvenile components to obtain more information.

3.7 Shape characteristics of unit D pyroclasts

We use the mean CAMSIZER 2D shape parameter data of sphericity, aspect ratio, Krumbein roundness, and compactness for each sample to assess the particle morphology of the juvenile unit D tephra. Aspect ratio shows the elongation of the grain and Krumbein roundness tracks features in the perimeter of the grain such as pointy corners or vesicle indentations. Compactness tracks changes in the area-based irregularity of the grain, such as elongation or shape distortion. Sphericity is affected both by area and perimeter changes of the grain and is one of the most widely used parameters in tephra shape parameter studies (e.g., Schmith et al., 2017; Dürig et al., 2021). Smooth, compact, equant grains will show high shape parameter values, and the value of the parameters will decrease with increasing irregularity of the grain shape.

To provide context to the scale of shape variability of unit D samples, we also measured a sample of lithic ash from the 1924 eruption of Kīlauea as well as a sample from the pumice deposit K1 and reticulite from deposit B1 of Keanakāko'i Tephra from a similar size range and compared them to the most extreme samples of unit D for each parameter. Results are shown in Figure 8. The most equant and blocky sample of unit D plots closely with the lithic phreatic deposit of the 1924 eruption, whereas the sample with the most irregular shapes shows lower shape values in all plots and falls between the 1924 sample and the K1 pumice sample. The reticulite B1 sample shows even lower shape values in all plots. This indicates that the unit D samples are clearly distinguishable from dry magmatic fountain deposits even though they display significant variation in shape parameter values.

3.7.1 Grain shape as a function of grain size

We look at the mean grain shape variation with grain size to see if the unit D shape variation is related to a specific grain size range. Shape variation with size might also add information about the fragmentation mechanism of the lithofacies grain size subpopulations, because the grains are predominantly juvenile. If rounding is seen for a range of grain sizes, it could also point to grain transportation processes associated with grain abrasion.

To check if sphericity values are influenced significantly by resolution, we plotted sphericity and aspect ratio (typically not sensitive to resolution) data from 1,000 random grains for the 0.5–2 mm size range (coarse–very coarse ash) from both the P4 basic, P4 zoom, and X2 basic cameras (supplementary materials S2). Grain resolution at 1 mm is approximately 173, 5,638, and 32,054 pixels/particle for the P4 basic, P4 zoom, and X2 basic camera, respectively. The plots show no significant difference in shape parameter values between cameras and show that resolution does not control our sphericity data.

Figure 9 shows the plots of mean shape parameter values for half phi size bins for each sample in the very fine ash to medium lapilli size ranges. Not all samples contained all grain size bins, so the number of samples plotted for each grain size varies. The grain-size ranges show three different distribution patterns for fine to very fine ash, medium ash to fine lapilli, and medium lapilli.

The very fine to fine ash ranges show distinct narrow sphericity values between 0.73–0.77 and 0.76–0.79, respectively, with a notable vertical spread in Krumbein roundness values of 0.15–0.35 and 0.10–0.30 for the bulk of the samples (Figure 9A) with fine ash shifted toward slightly lower Krumbein roundness values. Compactness values are between 0.83 and 0.86 for the very fine ash and 0.83–0.85 for the fine ash (Figure 9B) and aspect ratio values overlap between 0.67 and 0.72 (Figure 9C), though the fine ash is shifted to slightly higher values. Both size ranges show distinct distributions with vertical trends between sphericity and Krumbein roundness (Figure 9A), a slightly positive correlation between sphericity and compactness values (Figure 9B), and clear positive correlation with narrow distributions between aspect ratio and compactness (Figure 9D). There is no clear correlation between aspect ratio and Krumbein roundness or aspect ratio and sphericity (Figures 9C, E).

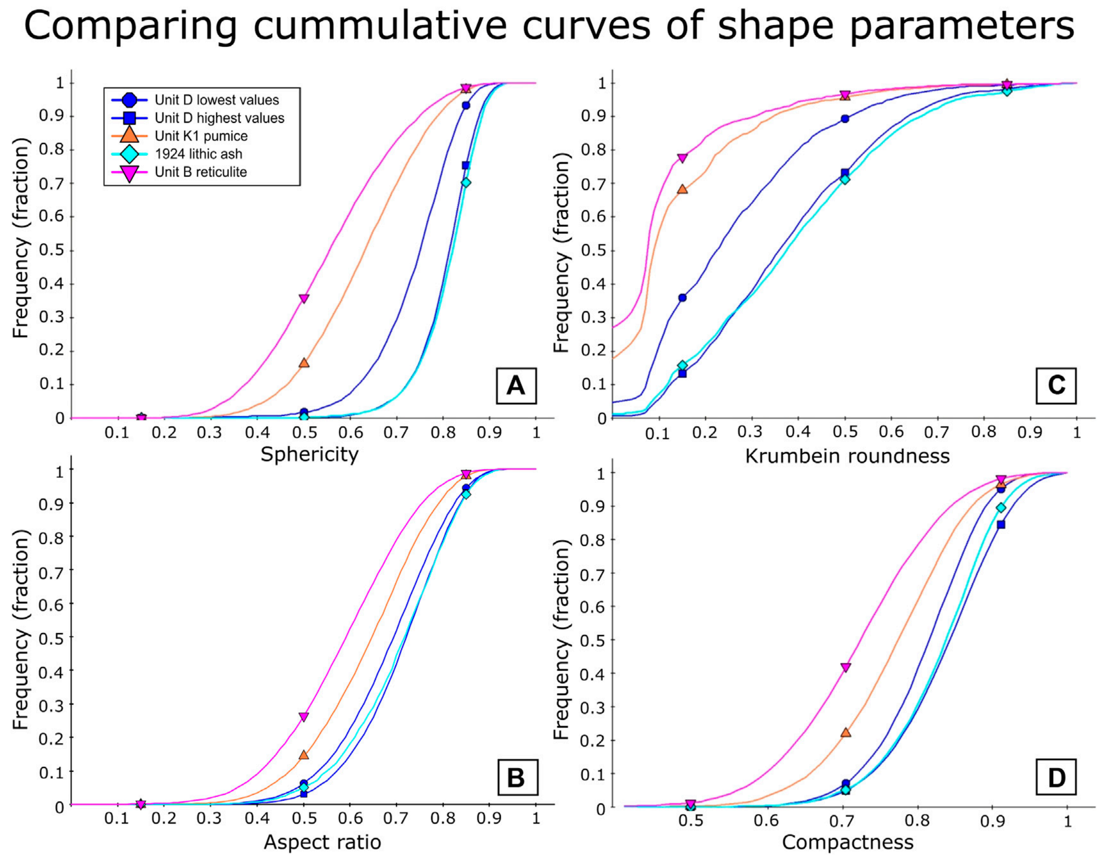

FIGURE 8
Cumulative shape parameter curves for the 0-5 phi size range for CAMSIZER shape parameters **(A)** sphericity, **(B)** aspect ration **(C)** Krumbein roundness, and **(D)** compactness. Unit D is shown as blue lines of the two most extreme samples for each parameter. Samples of the lithic 1924 deposit (light blue), the pumiceous K1 Keanakāko'i deposit (orange) and the Keanakāko'i unit B reticulite (pink) are shown for comparison. All shape parameters are dimensionless (see methods or CAMSIZER manual for definitions) and show increasingly equant and smooth shapes with increasing values. The samples span **(A)** sphericity values between 0.2 and 0.8, **(B)** aspect ratio values between 0.2 and 0.8, **(C)** Krumbein roundness values between 0.07 and 0.9, and **(D)** compactness values between 0.5 and 0.95. This suggests that the natural variation in parameter values is highest for Krumbein roundness, then sphericity and aspect ratio, and lowest for compactness. All plots show that Keanakāko'i unit B has the most irregular grains followed by unit K1, whereas 1924 has the most equant and smooth grains. Unit D samples shows a wide range of shapes that overlap with 1924 for the sample with the most regular grains and falls between 1924 and unit K1 for the sample with the most irregular grains. Although each shape parameter shows a unique numerical value range for the entire set of samples, unit D samples spans similar fractions of this entire range for all parameters. Thus, the numerical changes in unit D shape parameter values are in line with the overall changes between deposit types. See text for more details.

In Figure 9A, medium ash to fine lapilli size ranges all show a positive correlation between sphericity and Krumbein roundness values. Medium and coarse ash ranges fall along this trend with sphericity values of 0.75–0.81 and 0.71–0.81 and Krumbein roundness values of 0.26–0.39 and 0.25–0.39, respectively. The trend shifts to relatively higher sphericity values for the high Krumbein roundness end of the range. Very coarse ash follows the same general trend but is more concentrated at higher values of sphericity at 0.79–0.82 and Krumbein roundness at 0.30–0.39. The fine lapilli size forms the high value extreme of this trend with sphericity values of 0.77–0.84 and Krumbein roundness values of 0.34–0.82. In Figure 9B medium ash to fine lapilli show two distinct trends. Medium and coarse ash show lower overall compactness values than the fine ash ranges and a lateral spread of points with narrow compactness intervals of 0.81–0.84 and 0.81–0.84, respectively. Very coarse ash and fine lapilli sizes show a similar sphericity-compactness correlation as the fine ash sizes in similar compactness values of 0.83–0.85 and 0.81–0.86, respectively. Figure 9C shows no correlation between Krumbein roundness and aspect ratio for medium ash to fine lapilli with lateral point distributions of aspect ratio ranges for the bulk of samples from 0.69 to 0.72 for medium ash, 0.70–0.73 for coarse and very coarse ash, and 0.71–0.73 for fine lapilli. There is a slight positive correlation between compactness and aspect ratio for medium to very coarse ash, but no clear correlation for fine lapilli (Figure 9D). Figure 9E shows no distinct correlation between sphericity and aspect ratio for the medium ash to fine lapilli.

The medium lapilli size range shows the largest shape diversity of all size ranges in all plots in Figure 9 with no clear parameter correlations. At least half of the values are lower for all parameters compared to the other size ranges. In Figure 9A, most sphericity values are 0.66–0.78, with Krumbein roundness values between 0.11 and 0.37. In Figure 9B compactness values are between 0.69 and 0.86. Aspect ratio values are 0.57–0.78, but plots in Figures 9C–E have been zoomed in to better see distributions of other size ranges.

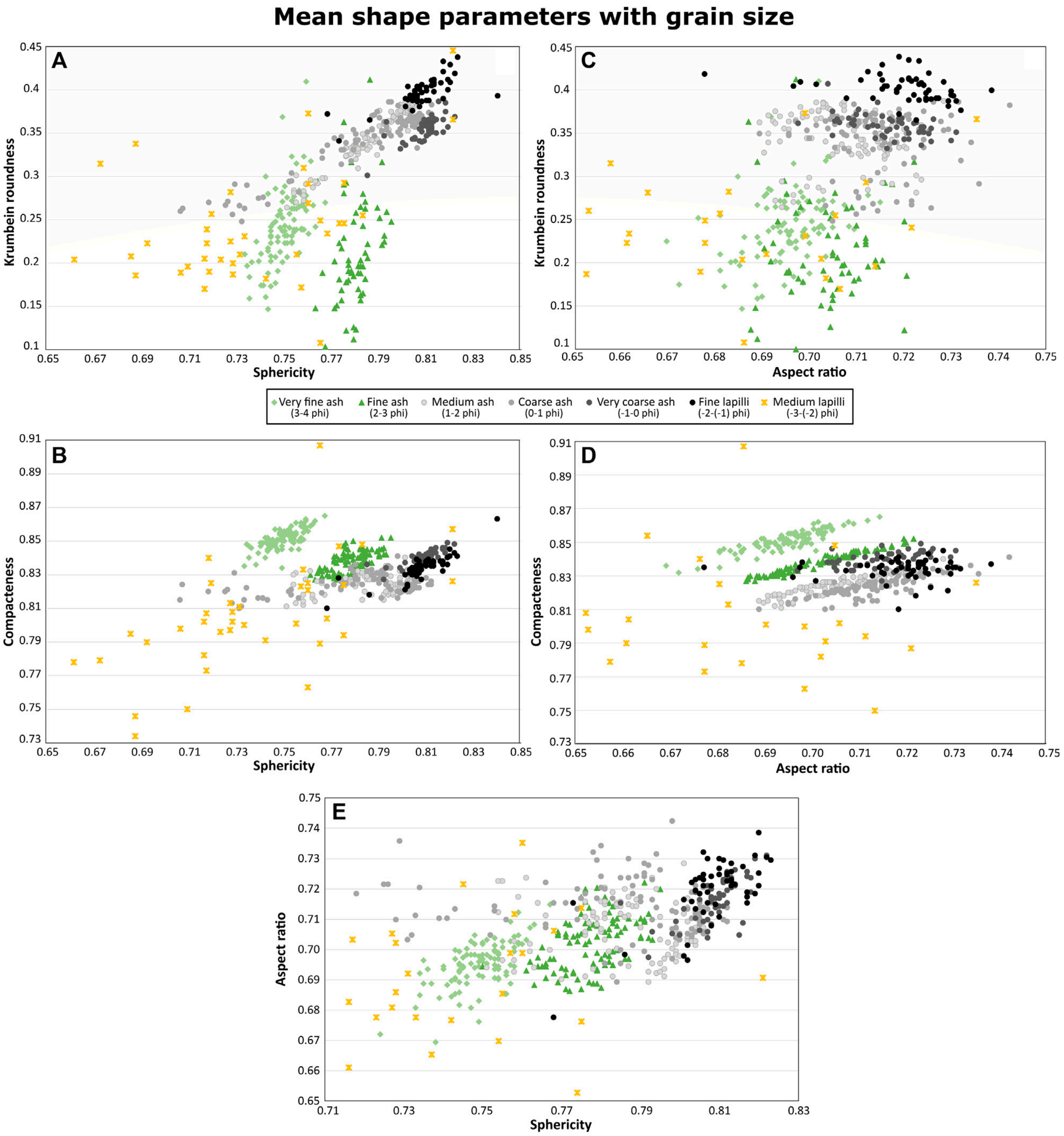

FIGURE 9
Plots of mean shape parameter of each sample for retained ½ phi size bins at very fine ash (4 φ), fine ash (3 φ) medium ash (2 φ), coarse ash (1 φ), very coarse ash (0 φ), fine lapilli (−1 φ), and medium lapilli (−2 φ). Plots contain **(A)** sphericity and Krumbein roundness, **(B)** sphericity and compactness, **(C)** aspect ratio and Krumbein roundness, **(D)** aspect ratio and compactness, and **(E)** sphericity and aspect ratio. Individual shape parameters are shown at the same scale across all plots except for sphericity in plot E, which is zoomed in to better show details of distributions. All shape parameters are dimensionless and grains are more regular, equant, and smooth with increasing values. Colors of sizes reflect interpreted unit D juvenile components with green colors representing olive-green ash, gray-scale colors representing the dark gray ash-lapilli, and the yellow color representing the pumice lapilli. Please note that not all samples contain all grain sizes and thus the number of samples (plotted points) may vary with grain size. Please refer to text for details.

3.7.2 Interpretation of shape changes with grain size

The distribution of fine to very fine ash in Figure 9A shows shape diversity mainly due to differences in perimeter pointiness. These differences do not cause relative elongation of the perimeter with respect to grain area/perimeter ratio, indicating morphological roughness diversity. This is supported by the lack of correlation between Krumbein roundness or sphericity with aspect ratio (Figures 9C, E) showing that grain elongation is not a defining factor. The positive correlation between compactness and sphericity

(Figure 9B) also indicates that shape diversity is related to morphological roughness changes rather than surface indentations from vesicles, for example, and the correlation between compactness and aspect ratio supports that (Figure 9D). The higher sphericity values of the fine ash relative to the very fine ash suggest that shape complexity of the grains increases with decreasing grain size. The narrow ranges in sphericity values associated with these sizes indicates that sphericity values are mainly controlled by the size-related decrease in projected area relative to perimeter between the two grain sizes.

The correlation trend between sphericity and Krumbein roundness for the medium ash to fine lapilli size ranges suggests that shape changes are related to differences in surface roughness that cause increase of the grain perimeter relative to area, such as vesicle indentations. The lateral trend in plot 9b for medium to coarse ash suggest that longer grain perimeters are not associated with grain elongation for this size range, which is in line with Figure 9C showing that surface roughness does not change significantly with aspect ratio. Interestingly, Figure 9D shows a correlation between compactness and aspect ratio suggesting that vesicles are big enough to cause some morphological roughness changes. This suggest that shapes in the medium to coarse ash range is controlled mainly by vesicle indentations and are thus a function of vesicularity. However, for grains in the very coarse ash to fine lapilli range, differences in grain shapes seem related to both grain elongation and surface perturbations, as suggested by the positive parameter correlations in Figures 9A, B, E. Neither surface roughness nor compactness change significantly with elongation (Figures 9C, D) suggesting that vesicles are now too small to impact overall grain shape. The shift to higher shape values with larger grain sizes indicates that grain shapes become more equant, smooth and less complex with increasing size.

There are no obvious distribution trends for the medium lapilli, but the low values for all shape parameters indicate that the grains have the roughest surfaces and morphological roughness of all the grain sizes. This is typical for highly vesicular grains.

Shape data plotted in terms of whole sample means of lithofacies show that lithofacies are well-defined in terms of shape data. Sample shape parameter means are correlated with the shape of the dominant grain size mode, and figures can be found in supplementary data S3. Rounding of grains across a range of grain sizes or for the interpreted PDC-related poorly sorted lithofacies are not observed. This shows that secondary abrasion is not a significant process modifying grain shapes.

The size ranges of the three distinctive shape distribution patterns correlate with the dominant grain size ranges of the three unit D components. Olive-green ash dominates the fine-extremely fine size range, the dark gray ash and lapilli dominate the coarse ash-fine lapilli sizes, and pumice dominates the medium lapilli size range. Thus, the shape distributions of Figure 9 allow us to assess fragmentation processes associated with each component.

3.8 Interpretation of fragmentation mechanism based on component shape parameters

Experimental work on phreatomagmatic fragmentation shows that molten fuel-coolant interaction (MFCI) is the preferred model for explosive magma-water interaction (e.g., Zimanowski et al., 1997; Büttner et al., 1999; Büttner et al., 2002; Dürig et al., 2012a; Zimanowski et al., 2015; Sonder et al., 2018; Dürig et al., 2020).Though alternative models such as turbulent shredding have been suggested for Kīlauea (Mastin, 2007), we find it unlikely to be a dominating process considering the high amount of fine ash in the unit D deposits. According to the MFCI model, explosive interaction needs an initial crude mixing of the magma and water on the scale of 1–10 cm length dimension of water domains (Zimanowski et al., 2015), where a vapor film forms a stable boundary layer between the magma and the water. The film can become unstable from an external pressure pulse (e.g., an earthquake) or local over-expansion and collapse across the mixing volume, leading to thermal coupling and high instantaneous heat transfer between water and magma (Wohletz et al., 2013). The high heat transfer leads to superheated and rapidly expanding water, which cannot be accommodated by the cooling magma that forms brittle stress cracks. The water intrudes into the cracks, causing further superheating, expansion, pressurization, and crack propagation in a positive feedback loop that finally produces a thermal detonation. The explosive energy is released as a thermohydraulic shock wave. The efficiency of this process is partly determined by the efficiency of the initial magma-water mixing as well as the elastic properties of the magma during the brittle stress wave propagation (Dürig et al., 2012b; Dürig and Zimanowski, 2012; Zimanowski et al., 2015). The maximum size of premix is limited by the speed of sound within the premix (Zimanowski et al., 2015).

The olive-green sideromelane ash morphology shows no influence from small surface perturbation such as vesicles or microlites, but grains are more pointed and equant than those of the dark gray ash, likely yielding a higher surface area. Thus, the fragmentation process generating the olive-green ash is related to the breakage of dense glass, where shape complexity increases with decreasing size, suggesting higher energy fragmentation was available to generate finer grains.

The dark gray ash-lapilli shape parameters generally reflect those of typical blocky and equant shapes of phreatomagmatic deposits and have less pointed grains than the other components. The most extreme shapes, overlapping or even surpassing the olive-green ash shapes in irregularity, are related to the large and medium ash fractions. Mele and Dioguardi. (2018) showed that, for vesicular grains, sphericity changes parabolically with grain size and is the lowest at a grain size slightly coarser than the coarsest vesicle diameter, which means that each vesicle indentation defines a significant percentage of the overall grain shape. Conversely, the coarser grain size ranges have higher sphericity values as grains become increasingly blocky and equant, with grain shapes less impacted by the vesicle indentations. Findings using 3D tomography to correlate grain shape with vesicularity, vesicle size, and solid structure thickness show a correlation between increasing particle irregularity and increasing vesicularity and decreasing solid structure thickness (Mele et al., 2018). Mastin et al. (2004) showed that the volume-fraction of bubbles was higher for medium and coarse unit D ash than for very coarse ash, though bubble number densities were lower, consistent with medium and coarse ash being more impacted by larger vesicle indentations than, very coarse ash. Our samples were generated by multiple explosive events, and part of the shape variation within each grain size bin is likely due to differences in melt vesicularity. Thus, the shape variation for the dark gray ash and lapilli is a function of grain size and vesicularity.

The pumice component has the most irregular grains as defined by the lowest shape parameter values, not surprising given that vesicular grains have more complex and irregular morphologies than blocky or dense grains (e.g., Heiken, 1974; Wohletz, 1983b; Schmith et al., 2017; Dürig et al., 2018; Comida et al., 2021; Ross et al., 2022). Interestingly, these grains are also the coarsest but do not follow the trend of increasingly blocky and equant shape with increased grain size shown by the dark gray component. This is consistent with measured high gas volume-fraction for this size range (Mastin et al., 2004) and indicates that the highly vesicular magma that fragmented to produce the pumice did not fragment the same way that the moderately vesicular magma did.

Previous studies show that the lapilli-bearing subunits are more vesicular than the ash-dominated subunits for a given grain size (Mastin, 1997; Mastin et al., 2004). Furthermore, the pumice component is almost exclusively associated with the lapilli-bearing subunits. Mastin. (1997) also found an intra-subunit increase in vesicularity with grain size. The increasing size of the grains with increasing vesicularity suggest less efficient fragmentation with increasing vesicularity. This in turn suggests that magmatic degassing decreased the intensity of the fragmentation, pointing to a dampening of the efficiency of the molten fuel-coolant interaction. Indeed, the presence of vesicles could influence the elastic response of the magma by allowing less energy build-up prior to the brittle failure of the magmatic foam. Furthermore, it is possible that elastic dampening of the pressure wave propagation also played a role, as foams are more compressible than a dense magma. The initial magma-water mixing could also be influenced by melt structure. Higher vesicularity is known to lower the magma viscosity (Giordano et al., 2008), which might facilitate initial magma-water mixing on smaller scale.

4 Discussion

4.1 Fragmentation mechanism and eruptive environment

The breakage faces, blocky morphologies, and generally high average shape parameter values of grain assemblages of the unit D deposits indicate that they were generated by brittle fragmentation (Zimanowski, 1998; Büttner et al., 2002; Dürig et al., 2020; Thivet et al., 2022). Numerical modeling shows that, for typical conditions, Kīlauea magmas reach neither a brittle fragmentation nor an inertial or fluid-dynamic fragmentation criterion while in the conduit (La Spina et al., 2021). The modeling also shows a strong coupling between gas and melt phase for Kīlauea ascending magmas, with a maximum gas-slip velocity (i.e., gas movement relative to melt phase) of 3 m/s. This indicates that a somewhat vesicular magma was coherently ascending when the magma-water interaction occurred. This scenario is supported by the predominantly spherical micro-vesicles with little coalescence or elongation and by elevated SO_2 content in pumice lapilli from the LLS and ULS interpreted as premature quenching prior to full magmatic outgassing (Mastin et al., 2004).

The modeling of La Spina et al. (2021) showed that magmatic temperature is one of the most important controls on eruptive style for basaltic magmas, as it is positively correlated with ascent rate and magma exit velocity at the vent. The highest ascent rates are associated with Hawaiian lava fountains (>50 m high), whereas effusive and explosive eruptions producing Plinian and sub-Plinian eruptions both have lower ascent rates. Studies of unit D major element geochemistry and olivine compositions show high MgO glass content (~7.5–11 wt percent), which corresponds to glass quench temperatures around 1,175°C (8 wt percent MgO) and up to 1,235°C (11 wt percent MgO), suggesting high temperature magmas for this period (Helz et al., 2014; Garcia et al., 2018; Lynn and Swanson, 2022). These temperatures are even higher than those used in the numerical modeling by La Spina et al. (2021) (1,160°C–1,060°C) and indicate that ascent rates and magma exit velocity at the vent could be higher throughout the unit D eruptions than for modern eruptions observed at Kīlauea. We hypothesize that the combination of high ascent rate and melt exit velocity, and the vesicular structure of the magma are the main controls for the efficiency of magma-water mixing and subsequent fragmentation.

Two layers within unit D have been studied in terms of olivine populations and melt inclusions to constrain outgassing and ascent history of the magma (Lynn et al., 2017; Garcia et al., 2018; Lerner et al., 2021). Samples were collected close to our main section, and we used stratigraphic height and the presence of pumice to correlate them roughly with our stratigraphy (Garcia et al., 2018; Lerner personal com.). Olivine from the middle of the LLS has high forsterite cores (Fo90–88), suggesting a deep origin from primitive mantle melts and melt inclusions show entrapment depths of 1–8 km except for two CO_2-rich inclusions from about 15 km depth (Lynn et al., 2017; Lerner et al., 2021). Most olivine from the upper portion of the LAS also has a high forsterite content, but a smaller olivine population has cores that crystallized in hybrid magma resulting from mixing of primitive melts with stored and fractionated melts at shallow depth (Lynn et al., 2017). Melt inclusion entrapment depths are about 1–7 km (Lerner et al., 2021). All olivine crystals, regardless of core Fo number, have diffusion rims indicating storage during ascent from the mantle, but the rims record poor mixing of the melts. This is in line with variable glass MgO within each layer (Garcia et al., 2018). Derived storage times before eruption are typically below 3 months, with 1–3 weeks for the lowest storage times (Lynn et al., 2017).

These interpretations constrain the rapid magma ascent to occur from a shallow magma reservoir and show overall similar gas content of the unit D magmas regardless of subunit and lithofacies. However, the LLS magmas may have vesiculated more before the magma-water interaction happened. This is consistent with measured H_2O concentrations (Mastin et al., 2004). We suggest that the poor mixing and variable storage times might lead to magma pockets of slightly heterogeneous volatile-content and temperature, which might explain the variability in pre-fragmentation vesicularity of the unit D magma.

Equilibrium H_2O saturation quench pressures indicate a fragmentation depth range of 10–100 m (lithostatic pressure) or 250 m (hydrostatic pressure) (Mastin et al., 2004). The sparsity of lithic wall-rock fragments in the deposit suggests that fragmentation did not happen far below ground, which would favor a hydrostatic model involving a standing water body at the surface. Depth to the water table at Kīlauea summit has been directly measured since 1973 at approximately 610 m above sea level ± 10 m (Keller et al., 1979; Hsieh and Ingebritsen, 2019). Resistivity studies have found a low-resistivity surface at the same level as well as at 800 m elevation below the central part of the caldera (Kauahikaua, 1993). Swanson et al. (2012) suggested that a 600 m deep (400 m above sea level) caldera formed shortly before or around ca. 1500 CE, where a standing water body in the caldera would be possible. The recent partial caldera collapse in 2018 reached a depth in Halema'uma'u Crater of about 500 m above sea level (Anderson et al., 2019; Neal et al., 2019) and after about 1 year a water lake appeared at the bottom of the crater (Nadeau et al., 2020). This water lake reached a depth of 50 m in about 17 months, with lake level increases of 5–15 cm/day and was interpreted as groundwater seepage from the recovering water table after collapse (Patrick et al., 2021). The recent observations support the idea of similar events on a larger scale following the large 1500 CE caldera collapse. Hawaiian oral traditions give no clear indication of a lake in the caldera, but they do hint at the presence of water as the caldera collapse ended.

We have not observed any fluidal grains such as Pele's tears or hair, which are commonly found in both proximal and distal deposits from explosive basaltic eruptions regardless of primary fragmentation mechanism (e.g., Büttner et al., 2002; Houghton et al., 2015). Thus, we infer that there was no dry magmatic fountaining activity concurrent with this eruptive activity. Furthermore, the absence of fluidal grains suggests either very efficient magma-water mixing that did not allow for ductile deformation, or that eruption dynamics preferentially segregated these grains during transport. We find transport segregation unlikely as we do not detect such effect on other components of the deposits. Thus, we think the absence of fluidal grains is a primary feature of the unit D fragmentation that suggests efficient MFCI fragmentation.

4.2 Evaluation of previous phreatomagmatic models for Kīlauea

The idea of explosive activity at Kīlauea involving external water originated from observations and interpretation of the 1924 explosive eruption from the summit crater of Halemaʻumaʻu. Most models envision water accessing the Halema'uma'u Crater and coming into contact with hot wall rock after a long standing lava lake drained and the walls of the crater started collapsing (e.g., Jaggar and Finch, 1924; Stearns, 1925; Finch, 1947; Houghton et al., 2015; Nemeth and Kosik, 2020), though this hypothesis has been questioned by recent modeling efforts (Hsieh and Ingebritson, 2019). Most interpretations of the Keanakākoʻi deposits were heavily influenced by the models of the 1924 eruption (Wentworth, 1938; Powers, 1948; Decker and Christiansen, 1984; McPhie et al., 1990; Swanson et al., 2012). Later work on unit D suggested the deposits originated from eruptions through a standing water lake based on pumice textures, vesiculation data, and glass volatile content to show premature quenching of the deposits compared to dry magmatic deposits of Keanakākoʻi units B and K1 and 1959 Kīlauea Iki (Mastin, 1997; Mastin et al., 2004). Our work clearly demonstrates that the 1924 eruption is not a good model for the unit D explosive activity or for the mechanism of phreatomagmatic eruptions at Kīlauea in general.

4.3 Summary of eruptive activity that generated the unit D deposits

Figure 10 shows a plot of the median grain size, modeled deconvolution modes, sphericity, Krumbein roundness, and compactness means as a function of stratigraphic height. We use this stratigraphic presentation of the data to outline the evolution of activity over time.

The eruption(s) initiate as hot basaltic magma rises to the surface from a magma chamber a few kilometers under the summit of Kīlauea. Degassing during ascent means that a moderately vesicular magma reaches the base of the water lake as indicated by the low value range of shape parameters of the early ash. The initial magma-water interaction results in frequent, small volume explosions generating low jets or plumes depositing laminated ash of mostly medium ash size. This activity might be similar to the intermittent jetting activity observed at Surtsey (Thorarinsson et al., 1964).

As about 2 m of deposit settles at our main section site, explosion frequency waxes and wanes and generates alternating homogeneous and laminated deposits (Figures 3, 10). The shape parameters all increase, showing increasing amounts of blocky and equant grains in the deposits, whereas grain size generally decreases as fragmentation becomes more efficient. The amount of fine ash increases, though the dominant medium ash size does not change until about 140 cm up in the deposit (Figure 10, median and modes). Just above 110 cm the first significant accretionary lapilli bed appears along with a drop in median and mode grain size to fine ash and a change in shard morphology indicated by the sharp increase in compactness (Figure 10). The accretionary lapilli bed also signifies a wetter plume phase. We suggest this represents more continuous magma-water mixing at the vent, which results in highly efficient fragmentation and larger entrainment of water in the plume. This might be similar to the continuous uprush described for Surtsey (Thorarinsson et al., 1964).

At the stratigraphic height of 205 cm, the first lapilli-bearing bed carrying pumice signifies that more vesicular magma has reached the surface. The ash-lapilli beds are interlayered with the finest and thickest homogeneous accretionary lapilli ash beds of the whole deposit (Figure 10, median and modes), showing very high fragmentation efficiency and wet plumes indicating high water availability. The grain size changes are clearly reflected in the variation of compactness values. Sphericity and Krumbein roundness generally increase at the top of the LAS showing the change from shard-dominated morphologies to the blocky, coarse dark gray ash and lapilli with higher parameter values.

The LAS contains two transitional phases (110–140 cm and 205–265 cm) that precede significant changes to the eruption style. The first change seems to be associated with the mode of magma-water interaction, whereas the second is associated with changes to a more vesicular magma.

At the stratigraphic height of 265 cm, the deposit changes to continuous couplets of ash-lapilli beds and layers of fine ash. The grain size modes are remarkably consistent throughout this eruptive phase, which is dominated by the blocky, coarse dark gray ash-lapilli, though relative amounts of each component may vary as indicated by variable layer thickness. Shape parameters change locally with these relative amounts of components in each

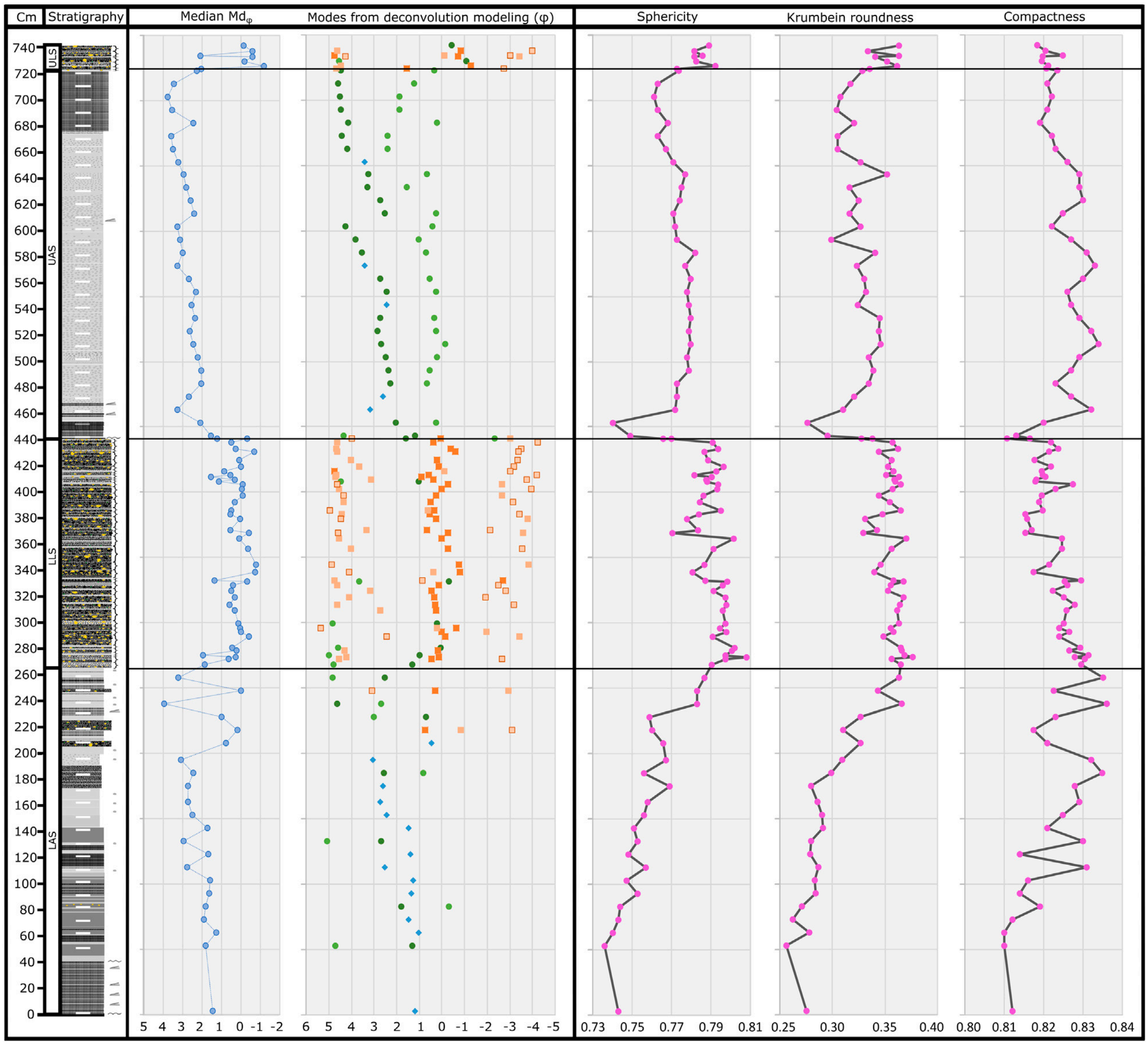

FIGURE 10
Median grain size (in phi), mode grainsizes (in phi), and the sample mean of the three dimensionless shape parameters of sphericity, Krumbein roundness, and compactness shown as a function of sample stratigraphic height and correlated with the stratigraphic column. Horizontal solid black lines show subunit borders as outlined in Figure 3. Refer to text for discussion of data.

sample but are also remarkably high and stable throughout the subunit, indicating a continuous and steady-state fragmentation of the more vesicular magma. The thickness differences likely reflect the volume of the magma-water premix at the vent for each explosion.

How this eruptive phase ends is unknown, as the top of the deposits is missing. Activity paused for long enough that both wind and local water erosion modified the top of the deposit. However, observed modern deposits have been substantially eroded within a few days at the summit of Kīlauea by heavy rainstorms. On the other hand, unit D was deposited between units B and C (~1500 CE) and unit E (~1650 CE) (Swanson et al., 2012), so decade-long pauses in activity are possible. Interestingly, when activity resumes it closely resembles the beginning of the eruption(s) in terms of lithofacies, grain size and shape parameters. We hypothesize that this indicates a fresh batch of magma rising from the shallow magma chamber, which supports the idea of a longer pause.

Poorly sorted lithofacies starting at the stratigraphic height of 460 cm marks a change in eruptive style to PDC deposition. The next 2.25 m of deposit show generally fining median grain size with repeated patterns of gradually decreasing Md$_\varphi$ grain sizes in ~0.2 φ increments with stratigraphic height from 490 to 525 cm, 550–605 cm and 610–670 cm, suggesting three packages of normally graded deposits. The packages are subtly visible from a distance and are defined by surface erosion patterns. We interpret this as three PDC events, where the surges become better developed with time as indicated by the package thickness and systematic grain size decrease. Shape parameters indicate steady state intense fragmentation of a poorly vesiculated magma. However, as previously stated, these are atypical proximal PDC deposits showing only subtle signs of flow deposition. With the vent being situated in a 600 m deep caldera, we suggest that the surges initially hit the caldera wall. Therefore, we interpret the PDC deposits as overspills and/or co-PDC plume deposits resulting from the caldera wall acting as a barrier.

After the PDC deposition, the eruption returns to the intermittent explosive style at the stratigraphic height of 675 cm. However, this time the deposits are dominated by a much finer grain size compared to the early stages of the eruption, suggesting more intense fragmentation.

After another break marked by erosion or nondeposition, the eruptive activity resumes farther north in the caldera and produces the ULS that defines the top of unit D west of the caldera. The ULS thins eastward and was not deposited at our main section location. As the PDC deposit remains regionally confined around the area of the main section, it remains to be seen if any overlap of these eruptive phases can be traced in the field. For now, there is no clear evidence of other activity at the northern vent than the couplets produced by more vesiculated magma interacting with water. The slight increase in median grain size suggests a slightly more vesiculated and hence unstable magma, which is supported by previous work on clast vesicularity (Mastin et al., 2004).

Thus, the unit D deposit is a result of complex phreatomagmatic processes resulting from variability in magma vesicularity, magma ascent rate, water mixing conditions, and water availability. Further field mapping and sampling could lead to a better understanding of the regional extent and thus hazard potential of PDCs and tephra fall. It would also be useful to obtain eruption source parameters for those parts of the deposit that can be mapped regionally; such parameters could be used for eruption scenario forecasts if water again returns to the surface at the summit of Kīlauea.

The repeated interaction of external water and rising magma found in this study can be expected in other basaltic calderas, and our work shows it clearly for a volcano typically characterized by volcanologists as effusive. Explosive deposits are relatively ephemeral, however, and over centuries or millennia can be eroded away, perhaps giving the false impression that the host volcano is docile. We are fortunate at Kīlauea that the Keanakāko‘i Tephra, and specifically Unit D, are well preserved so that a detailed deposit analysis such as we have done can lead to improved understanding of the potentially explosive nature of shield volcanoes.

5 Conclusion

Our study demonstrates that unit D of the Keanakāko‘i Tephra represents a complex phreatomagmatic deposit, which can be divided into four subunits, six different lithofacies, and three juvenile tephra components. The juvenile deposit components consist of:

- A fine-extremely fine olive-green ash of dense sideromelane grains,
- A medium ash to fine dark gray lapilli of moderately vesicular grains,
- A medium lapilli light yellow pumice of moderate vesicularity.

The stratigraphy contains:

- a lower ash-dominated subunit (LAS) of fall deposits with laminated, coarse, and fine ash lithofacies as well as coarser ash-lapilli lithofacies,
- a lower lapilli-bearing subunit (LLS) of fall deposits in the coupled ash-lapilli lithofacies,
- a break in activity suggested by a period of erosion or non-deposition,
- an upper ash-dominated subunit (UAS) of fall deposits of laminated, and fine ash, but primarily poorly sorted ash lithofacies reflecting dilute PDC deposits,
- another period of erosion or non-deposition, suggesting a longer halt of activity or a shift in vent location,
- an upper lapilli-bearing subunit (ULS) of coupled ash-lapilli lithofacies, which has a different vent area than the other three units.

The small-scale planar bedding throughout most of the deposit points to a general eruption style of small, frequent explosions generating low plumes. Variations in the time between explosions can explain the difference between laminated and coarse ash lithofacies, which are otherwise very similar in terms of grain size and shape metrics. Thicker beds of fine ash with accretionary lapilli are related to very efficient magma-water mixing as indicated by grain size and shape data, not by changes in plume dynamics. The coupled lithofacies show complex fragmentation dynamics, where a more vesicular magma interacts with the external water. We suggest that this change in vesicularity might be related to pockets of increased magma outgassing.

The poorly sorted lithofacies of PDC deposits contain at least three flows that are unconventional as they lack significant dune or cross-bedding structures. We suggest that this is a function of the vent location in a ~600-m deep caldera, where the caldera wall acted as a barrier and changed the flow dynamics to very dilute overspills and co-PDC plume falls over the top of the wall.

Grain-size modeling shows that most lithofacies are well-defined in terms of median and sorting metrics but have polymodal distributions and that global distribution statistics are inappropriate for quantitative modeling. Instead, deconvolution modeling can be used to assess the different subpopulations, and we found that it worked well for most of the distributions except for two very complex ones. We were able to track grain size changes of each juvenile component for this deposit, which greatly improved interpretation of lithofacies generation and eruption dynamics.

The 2D shape modeling of different grain size bins shows distinct shape values for the three grain size ranges of fine-very fine ash, medium ash-fine lapilli, and medium lapilli, which correspond to the olive-green ash, dark gray ash-lapilli, and pumice lapilli, respectively. The distinct shape profiles in turn reflect different fragmentation mechanisms for the three tephra components, though all were in the brittle fragmentation regime.

The pattern of size-correlated shape parameters shows that it is important to obtain shape data across a wide size range to accurately track grain shapes across the whole deposit. Our dataset was obtained from dynamic image analyzers CAMSIZER P4 and X2 with sample runs of ~2–5 min per sample per instrument. This method allowed for fast generation of a large internally consistent dataset, which has proven valuable to define and interpret complex phreatomagmatic processes.

Future work includes extensive mapping of the subunits of the unit D deposit in the summit and flank region of Kīlauea as well as generating eruption source parameters for hazard modeling.

A better understanding of explosions at basaltic volcanoes is vital for hazard analysis and risk mitigation. We have demonstrated how repeated interactions of external water and magma can lead to explosions, ranging from mild to strong and including pyroclastic density currents at a typical shield volcano. Our findings for Unit D of Kīlauea's Keanakāko'i Tephra may apply to other shield volcanoes, and at calderas where explosive deposits are poorly preserved, similar detailed textural analysis of tephra clasts may afford clues as to past water-magma interactions. We hope that our study helps researchers elsewhere as they deal with such important topics.

Data availability statement

The datasets presented in this study can be found in online repositories. The names of the repository/repositories and accession number(s) can be found below: ScienceBase: doi: 10.5066/P97WS3WS.

Author contributions

DS concieved the idea for the study, which was later developed further by JS. JS collected field observations and samples and DS provided critical guidance and feedback. JS carried out lab-analysis, data processing and modeling, and wrote the manuscript draft. DS provided critical revisions, intellectual discussions, and feedback. All authors contributed to the article and approved the submitted version.

Funding

This research was supported by the Carlsberg Foundation Internationalisation Postdoc Fellowship for JS. This work was also supported by the Additional Supplemental Appropriations for Disaster Relief Act of 2019 (P.L. 116-20) following the eruption of Kilauea Volcano in 2018 financing analytical instrumentation used in this study.

Acknowledgments

We are thankful for the social responsibility shown by the Carlsberg Foundation during the global pandemic by awarding JS additional funding allowing her to make up lost field- and laboratory time from the extensive COVID-19 shutdowns. We gratefully acknowledge Microtrac experts Gert Beckmann and Kai Düffels for assistance with finetuning the CAMSIZER instrument setup, and for their knowledgeable advice on data collection. We greatly appreciate scientific discussions with Kendra Lynn, Allan Lerner, Drew Downs, and Julie Chang as we progressed through fieldwork and data interpretations. We are grateful to Kristi Wallace for her helpful review of the manuscript during the internal USGS review process, and thank Pierfrancesco Dellino, reviewer, Pierre-Simon Ross, and editor Tobias Dürig for constructive journal reviews.

Any use of trade, firm, or product names is for descriptive purposes only and does not imply endorsement by the U.S. Government. Sample information, grain size, and 2D grain shape data from this work is available through a USGS data release and can be found here: doi:10.5066/P97WS3WS.

Conflict of interest

The authors declare that the research was conducted in the absence of any commercial or financial relationships that could be construed as a potential conflict of interest.

Publisher's note

Supplementary material

The Supplementary Material for this article can be found online at: https://www.frontiersin.org/articles/10.3389/feart.2023.1153288/full#supplementary-material

References

Anderson, K. R., Johanson, I. A., Patrick, M. R., Gu, M., Segall, P., Poland, M. P., et al. (2019). Magma reservoir failure and the onset of caldera collapse at Kīlauea Volcano in 2018. *Science* 366 (6470), eaaz1822. doi:10.1126/science.aaz1822

Biass, S., Swanson, D. A., and Houghton, B. F. (2019). "New perspective on the nineteenth-century golden pumice deposit of Kīlauea Volcano," in *Field Volcanology: A tribute to the distinguished career of don Swanson*. Editors M. P. Poland, M. O. Garcia, V. E. Camp, and A. Grunder (USA: Geological Society of America), 227–246.

Blong, R. J. (1984). *Volcanic hazards: A source book on the effects of eruptions*. Orlando Florida, US: Academic Press Inc.

Blott, S. J., and Pye, K. (2001). Gradistat: A grain size distribution and statistics package for the analysis of unconsolidated sediments. *Earth Surf. Process. Landforms* 26, 1237–1248. doi:10.1002/esp.261

Borselli, L., and Sarocchi, D. (2022). DECOLOG 6.0.1 (computer software). Avaliable at: https://www.lorenzo-borselli.eu/decolog/.

Brown, R. J., Bonadonna, C., and Durant, A. J. (2012). A review of volcanic ash aggregation. *Phys. Chem. Earth* 45 (46), 65–78. doi:10.1016/j.pce.2011.11.001

Brown, S. K., Jenkins, S. F., Sparks, R. S. J., Odbert, H., and Auker, M. R. (2017). Volcanic fatalities database: Analysis of volcanic threat with distance and victim classification. *J. Appl. Volcanol.* 6, 15. doi:10.1186/s13617-017-0067-4

Buttner, R., Dellino, P., La Volpe, L., Lorenz, V., and Zimanowski, B. (2002). Thermohydraulic ex-plosions in phreatomagmatic eruptions as evidenced by the comparison between pyroclasts and products from molten fuel coolant interaction experiments: Thermohydraulic explosions. *J. Geophys. Res. Solid Earth* 107, ECV 5-1–ECV 5-14. doi:10.1029/2001jb000511

Buttner, R., Dellino, P., and Zimanowski, B. (1999). Identifying magma-water interaction from the surface features of ash particles. *Nature* 401, 688–690. doi:10.1038/44364

CAMSIZER manual (2020). *Manual evaluation software CAMSIZER P4, version 0002*. Haan, Germany: Microtrac Retch GMbH.

Cassidy, M., Manga, M., Cashman, K., and Bachmann, O. (2018). Controls on explosive-effusive volcanic eruption styles. *Nat. Commun.* 9, 2839. doi:10.1038/s41467-018-05293-3

Comida, P. P., Ross, P. S., Durig, T., White, J. D. L., and Lefebvre, N. (2021). Standardized analysis of juvenile pyroclasts in comparative studies of primary magma fragmentation; 2. Choice of size fractions and method optimization. *Bull. Volc* 84, 5. doi:10.1007/s00445-021-01517-5

Decker, R. W., and Christiansen, R. L. (1984). *Explosive eruptions of Kilauea Volcano, Hawaii: Explosive volcanism: Inception, evolution, and hazards*. Washington, D.C.: National Research Council, National Academy Press, 122–132.

Durig, T., Bowman, M., White, J., Murch, A., Mele, D., Verolino, A., et al. (2018). PARTIcle shape ANalyzer PARTISAN – An open source tool for multi-standard two-dimensional particle morphometry analysis. *Ann. Geophys* 61. doi:10.4401/ag-7865

Durig, T., Mele, D., Dellino, P., and Zimanowski, B. (2012a). Comparative analyses of glass fragments from brittle fracture experiments and volcanic ash particles. *Bull. Volcanol.* 74, 691–704. doi:10.1007/s00445-011-0562-0

Durig, T., Ross, P. S., Dellino, P., White, J. D. L., Mele, D., and Comida, P. P. (2021). A review of statistical tools for morphometric analysis of juvenile pyroclasts. *Bull. Volc* 83, 79. doi:10.1007/s00445-021-01500-0

Durig, T., White, J. D. L., Murch, A. P., Zimanowski, B., Buttner, R., Mele, D., et al. (2020). Deep-sea eruptions boosted by induced fuel–coolant explosions. *Nat. Geosci.* 13, 498–503. doi:10.1038/s41561-020-0603-4

Durant, A. J., and Brown, R. J. (2016). "Ash aggregation in volcanic clouds," in *Volcanic ash* (Elsevier), 53–65. doi:10.1016/B978-008-100405-0.00006-9

Durig, T., Sonder, I., Zimanowski, B., Beyrichen, H., and Büttner, R. (2012b). Generation of volcanic ash by basaltic volcanism. *J. Geophys. Res.* 117, B01204. doi:10.1029/2011JB008628

Dürig, T., and Zimanowski, B. (2012). "Breaking news" on the formation of volcanic ash: Fracture dynamics in silicate glass. *Earth Planet. Sci. Lett.* 335-336, 1–8. doi:10.1016/j.epsl.2012.05.001

Edwards, M. J., Eychenne, J., and Pioli, L. (2021). Formation and dispersal of ash at open conduit basaltic volcanoes: Lessons from etna. *Front. Earth Sci.* 9, 709657. doi:10.3389/feart.2021.709657

Finch, R. H. (1947). Kīlauea in 1790 and 1823. *Volcano Lett.* 496, 1–2.

Garcia, M. O., Mucek, A. E., Lynn, K. J., Swanson, D. A., and Norman, M. D. (2018). "Geochemical evolution of Keanakako'i tephra, Kīlauea volcano, Hawai'i," in *Field Volcanology: A tribute to the distinguished career of don Swanson, 538*. Editors M. P. Poland, M. O. Garica, V. E. Camp, and A. Grunder (Boulder, Colorado, US: The Geological Society of America), 203–225.

Giordano, D., Russell, J. K., and Dingwell, D. B. (2008). Viscosity of magmatic liquids: A model. *Earth Planet Sci. Lett.* 271, 123–134. doi:10.1016/j.epsl.2008.03.038

Heiken, G. (1974). An atlas of volcanic ash. *Smithson. Contributions Earth Sci.* 12, 101.

Helz, R. T., Clague, D. A., Mastin, L. G., and Rose, T. R. (2014). *Electron micro-probe analyses of glasses from Kilauea tephra units, Kilauea Volcano*. Hawaii: U.S. Geological Survey Open-File Report 2014-1090, 24. doi:10.3133/ofr20141090

Houghton, B. F., and Gonnermann, H. M. (2008). Basaltic explosive volcanism: Constraints from deposits and models. *Chem. Erde* 68, 117–140. doi:10.1016/j.chemer.2008.04.002

Houghton, B., White, J. D. L., and Van Eaton, A. R. (2015). "Phreatomagmatic and related eruption styles," in *Encyclopedia of volcanoes*. Editor H. Sigurdsson (London: Academic Press), 537–552. doi:10.1016/B978-0-12-385938-9.00030-4

Hsieh, P. A., and Ingebritsen, S. E. (2019). Groundwater inflow toward a preheated volcanic conduit: Application to the 2018 eruption at Kīlauea Volcano, Hawai'i. *J. Geophys. Res. Solid Earth* 124 (2), 1498–1506. doi:10.1029/2018JB017133

Inman, D. L. (1952). Measures for describing the size distribution of sediments. *J. Sediment. Res.* 22 (3), 125–145. doi:10.1306/D42694DB-2B26-11D7-8648000102C1865D

Jaggar, T. A., and Finch, R. H. (1924). The explosive eruption of Kilauea in Hawaii, 1924, *Am. J. Sci.* 5 (47), 353–374. doi:10.2475/ajs.s5-8.47.353

Kauahikaua, J. (1993). Geophysical characteristics of the hydrothermal systems of Kilauea Volcano, Hawai'i. *Geothermics* 22, 271–299. doi:10.1016/0375-6505(93)90004-7

Keller, G. V., Grose, L. T., Murray, J. C., and Skokan, C. K. (1979). Results of an experimental drill hole at the summit of Kilauea Volcano, Hawai'i. *J. Volcanol. Geotherm. Res.* 5, 345–385. doi:10.1016/0377-0273(79)90024-6

Krumbein, W. C. (1941). Measurement and geological significance of shape and roundness of sedimentary particles. *J. Sediment. Pet.* 11, 64–72.

La Spina, G., Arzilli, F., Llewellin, E. W., Burton, M. R., Clarke, A. B., de' Michieli Vitturi, M., et al. (2021). Explosivity of basaltic lava fountains is controlled by magma rheology, ascent rate and outgassing. *Earth Planet. Sci. Lett.* 553, 116658. doi:10.1016/j.epsl.2020.116658

Lerner, A. H., Sublett, D. M., Cauley, C., Wallace, P. J., and Bodnar, R. J. (2021). *Magma storage depths and excess CO_2 fluids from the explosive Keanakāko'i tephra (Kīlauea Volcano, Hawai'i) based on measurements of melt and fluid inclusions*. Hawai: Abstract AGU Fall Meeting.

Lynn, K., Garcia, M. O., Shea, T., Costa, F., and Swanson, D. A. (2017). Time-scales of mixing and storage for Keanakako'i Tephra magmas (1500– 1820 C.E), Kilauea Volcano, Hawai'i. *Contributions Mineralogy Petrology* 172, 76. doi:10.1007/s00410-017-1395-4

Lynn, K., and Swanson, D. A. (2022). Olivine and glass chemistry record cycles of plumbing system recovery after summit collapse events at Kīlauea Volcano, Hawai'i. *J. Volcanol. Geotherm. Res.* 426, 107540. doi:10.1016/j.jvolgeores.2022.107540

Mastin, L. G., Christiansen, R. L., Thornber, C., Lowenstern, J., and Beeson, M. (2004). What makes hydromagmatic eruptions violent? Some insights from the Keanakako'i ash. *Kilauea Volcano, Hawai'i J. Volcanol. Geotherm. Res.* 137, 15–31. doi:10.1016/j.jvolgeores.2004.05.015

Mastin, L. G. (1997). Evidence for water influx from a caldera lake during the explosive hydromagmatic eruption of 1790 Kīlauea Volcano, Hawaii. *J. Geophys. Res.* 102, 20093–20109.

Mastin, L. G. (2007). Generation of fine hydromagmatic ash by growth and disintegration of glassy rinds. *J. Geophys. Res.* 112, B02203. doi:10.1029/2005JB003883

May, M., Carey, R. J., Swanson, D. A., and Houghton, B. F. (2015). "Reticulite-producing fountains from ring fractures in Kilauea Caldera ca. 1500 CE," in *Hawaiian volcanoes: From source to surface*. Editors R. Carey, V. Cayol, M. Poland, and D. Weis (Washington, DC: AGU, American Geophysical Union, Hoboken, New Jersey: John Wiley & Sons), 351–367. doi:10.1002/9781118872079.ch16

McPhie, J., Walker, G. P. L., and Christiansen, R. L. (1990). Phreatomagmatic and phreatic fall and surge deposits from explosions at Kilauea Volcano, Hawaii, 1790 A.D.: Keanakakoi ash member. *Bull. Volcanol.* 52, 334–354. doi:10.1007/BF00302047

Mele, D., Dioguardi, F., and Dellino, P. (2018). A study on the influence of internal structures on the shape of pyroclastic particles by X-ray microtomography investigations. *Ann. Geophys.* 61, AC27. doi:10.4401/ag-7868

Mele, D., and Dioguardi, F. (2018). The grain size dependency of vesicular particle shapes strongly affects the drag of particles. First results from microtomography investigations of Campi Flegrei fallout deposits. *J. Volcanol. Geotherm. Res.* 353, 18–24. doi:10.1016/j.jvolgeores.2018.01.023

Murtagh, R. M., and White, J. D. L. (2013). Pyroclast characteristics of a subaqueous to emergent Surtseyan eruption, Black Point volcano, California. *J. Volcanol. Geotherm. Res.* 267, 75–91. doi:10.1016/j.jvolgeores.2013.08.015

Nadeau, P. A., Diefenbach, A. K., Hurwitz, S., and Swanson, D. A. (2020). From lava to water: A new era at Kīlauea. *Eos* 101, 557. doi:10.1029/2020EO149557

Neal, C. A., Brantley, S. R., Antolik, L., Babb, J. L., Burgess, M., Calles, K., et al. (2019). The 2018 rift eruption and summit collapse of Kīlauea Volcano. *Science* 363 (6425), 367–374. doi:10.1126/science.aav7046

Neal, C. A., and Lockwood, J. P. (2003). *Geologic map of the summit region of Kilauea Volcano*, Hawaii: U.S. Geological survey geologic investigations series map I-2759.

Nemeth, K., and Kosik, S. (2020). Review of explosive hydrovolcanism. *Rev. Explos. hydrovolcanism Geosciences* 10, 44. doi:10.3390/geosciences10020044

Patrick, M. R., Swanson, D. A., Zoeller, M. H., Mulliken, K. M., Parcheta, C. E., Lynn, K. J., et al. (2021). *Water-level data for the crater lake at the summit of Kīlauea Volcano, Island of Hawai'i, 2019–2020*. Hawai: U.S. Geological Survey data release. doi:10.5066/P9262JDH

Poland, M. P., Miklius, A., and Montgomery-Brown, E. K., 2014, Magma supply, storage, and transport at shield-stage Hawaiian volcanoes, 178–235. In: M. P. Poland, T. J. Takahashi, and C. M. Landowski (Editors), *Characteristics of Hawaiian volcanoes*, U.S. Geological Survey 1801, 429. doi:10.3133/pp1801

Powers, H. A. (1948). A chronology of the explosive eruptions of Kilauea. *Pac. Sci.* 2, 278–292.

Ross, P. S., Dürig, T., Comida, P. P., Lefebvre, N., White, J. D., Andronico, D., et al. (2022). Standardized analysis of juvenile pyroclasts in comparative studies of primary magma fragmentation; 1. Overview and workflow. *Bull. Volcanol.* 84, 13–29. doi:10.1007/s00445-021-01516-6

Schmith, J., Hoskuldsson, Á., and Holm, P. M. (2017). Grain shape of basaltic ash populations: Implications for fragmentation. *Bull. Volc* 79, 14. doi:10.1007/s00445-016-1093-5

Schmith, J., Hoskuldsson, Á., Holm, P. M., and Larsen, G. (2018). Large explosive basaltic eruptions at Katla volcano, Iceland: Fragmentation, grain size and eruption dynamics. *J. Volcanol. Geotherm. Res.* 354, 140–152. doi:10.1016/j.jvolgeores.2018.01.024

Sheridan, M. F., and Wohletz, K. H. (1983). Hydrovolcanism: Basic considerations and review. *J. Volcanol. Geotherm. Res.* 17 (1-4), 1–29. doi:10.1016/0377-0273(83)90060-4

Sonder, I., Harp, A., Graettinger, A. H., Moitra, P., Valentine, G. A., Büttner, R., et al. (2018). Meter-scale experiments on magma-water interaction. *J. Geophys. Res. Solid Earth* 123 (10), 615. doi:10.1029/2018JB015682

Stearns, H. T. (1925). The explosive phase of Kilauea Volcano, Hawaii, in 1924. *Bull. Volcanol.* 2 (2), 193–208. doi:10.1007/BF02719505

Swanson, D. A., and Houghton, B. F. (2018). "Products, processes, and implications of Keanakāko'i volcanism, Kīlauea Volcano, Hawai'i," in *Field Volcanology: A tribute to the distinguished career of don Swanson*. Editors M. P. Poland, M. O. Garcia, V. E. Camp, and A. Grunder (Boulder, Colorado, US: The Geological Society of America), 159–190. doi:10.1130/2018.2538(07

Swanson, D. A., Rose, T. R., Fiske, R. S., and McGeehin, J. P. (2012). Keanakāko'i Tephra produced by 300years of explosive eruptions following collapse of Kīlauea's caldera in about 1500CE. *J. Volcanol. Geotherm. Res.* 215–216, 8–25. doi:10.1016/j.jvolgeores.2011.11.009

Swanson, D. A., Rose, T. R., Mucek, A. E., Garcia, M. O., Fiske, R. S., and Mastin, L. G. (2014). Cycles of explosive and effusive eruptions at Kīlauea Volcano, Hawai'i. *Hawai'i Geol.* 42, 631–634. doi:10.1130/g35701.1

Swanson, D. A., Weaver, S. J., and Houghton, B. F. (2015). Reconstructing the deadly eruptive events of 1790 CE at K lauea Volcano, Hawai'i. *Geol. Soc. Am. Bull.* 127, 503–515. doi:10.1130/B31116.1

Thivet, S., Carlier, J., Gurioli, L., Di Muro, A., Besson, P., Smietana, M., et al. (2022). Magmatic and phreatomagmatic contributions on the ash-dominated basaltic eruptions: Insights from the april and november–december 2005 paroxysmal events at karthala volcano, Comoros. *J. Volcanol. Geotherm. Res.* 424, 107500. doi:10.1016/j.jvolgeores.2022.107500

Thorarinsson, S., Einarsson, T., Sigvaldason, G., and Elisson, G. (1964). The submarine eruption off the vestmann islands 1963–64: A preliminary report. *Bull. Volcanol.* 27, 435–445. doi:10.1007/bf02597544

Van Eaton, A. R., Muirhead, J. D., Wilson, C. J. N., and Cimarelli, C. (2012). Growth of volcanic ash aggregates in the presence of liquid water and ice: An experimental approach. *Bull. Volcanol.* 74, 1963–1984. doi:10.1007/s00445-012-0634-9

Verolino, A., White, J. D. L., Baxter, R. J. M., Schipper, C. I., and Thordarson, T. (2022). Characteristics of sub-aerially emplaced pyroclasts in the Surtsey eruption deposits: Implications for diverse surtseyan eruptive styles. *Geosciences* 12, 79. doi:10.3390/geosciences12020079

Walker, G. P. L., and Croasdale, R. (1972). Characteristics of some basaltic pyroclastics. *Bull. Volcanol.* 35 (2), 303–317. doi:10.1007/bf02596957

Walker, G. P. L. (1971). Grain-size characteristics of pyroclastic deposits. *J. Geol.* 79, 696–714. doi:10.1086/627699

Wentworth, C. K. (1938). *Ash formations of the island of Hawaii*. Honolulu: Hawaiian Volcano Research Association, 183.

White, J. D. L., and Houghton, B. F. (2006). Primary volcaniclastic rocks. *Geology* 34, 677. doi:10.1130/g22346.1

White, J. D. L., and Valentine, G. A. (2016). Magmatic versus phreatomagmatic fragmentation: Absence of evidence is not evidence of absence. *Geosphere* 12, 1478–1488. doi:10.1130/ges01337.1

Wohletz, K. H. (1983a). Mechanisms of hydrovolcanic pyroclast formation: Grain-size, scanning electron microscopy, and experimental studies. *J. Volcanol. Geotherm. Res.* 17, 31–63. doi:10.1016/0377-0273(83)90061-6

Wohletz, K. H. (1983b). Chemical and textural features of pyroclasts from hydrovolcanic eruption sequences. report LA-UR-83–250. Los Alamos, New Mexico, US: Los Alamos National Laboratory.

Wohletz, K. H. (1986). Explosive magma-water interactions: Thermodynamics, explosion mechanisms, and field studies. *Bull. Volcanol.* 48, 245–264. doi:10.1007/bf01081754

Wohletz, K., Zimanowski, B., and Büttner, R. (2013). *Modeling volcanic processes*. New York: Cambridge University Press, 230–257.

Zimanowski, B. (1998). in *Phreatomagmatic explosions," in from magma to tephra, developments in Volcanology 4*. Editors A. Freundt and M. Rosi (Amsterdam: Elsevier), 25–54.

Zimanowski, B., Buttner, R., Lorenz, V., and Hafele, H. G. (1997). Fragmentation of basaltic melt in the course of explosive volcanism. *J. Geophys Res.* 102, 803–814. doi:10.1029/96jb02935

Zimanowski, B., Buttner, R., Delino, P., White, J. D. L., and Wohletz, K. (2015). "Magma-water interaction and phreatomagmatic fragmentation," in *Encyclopedia of volcanoes*. Editors H. Sigurdsson, B. Houghton, S. R. McNutt, H. Rymer, and J. Stix (London: Academic Press), 473–484.

Frontiers in
Earth Science

Investigates the processes operating within the major spheres of our planet

Advances our understanding across the earth sciences, providing a theoretical background for better use of our planet's resources and equipping us to face major environmental challenges.

Discover the latest Research Topics

See more →

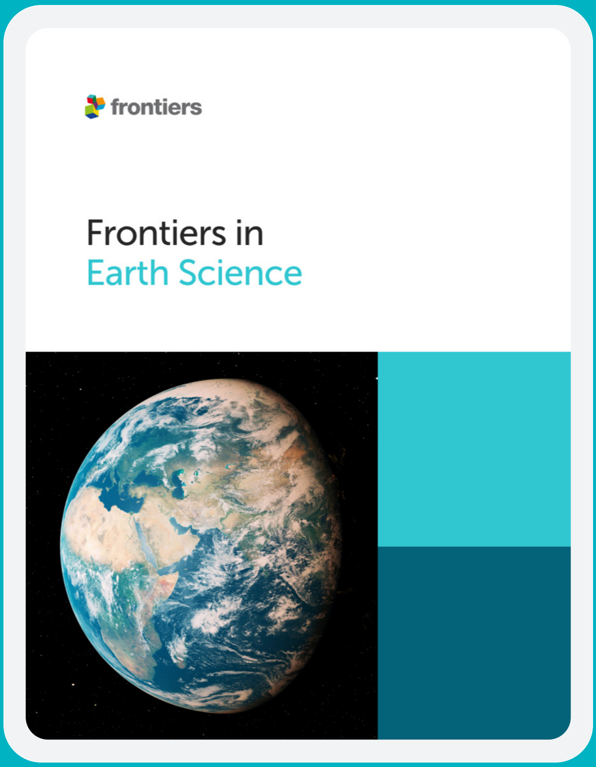

frontiers

Frontiers in
Earth Science

Frontiers

Avenue du Tribunal-Fédéral 34
1005 Lausanne, Switzerland
frontiersin.org

Contact us

+41 (0)21 510 17 00
frontiersin.org/about/contact